

(12)

AD A139726

PRELIMINARY METHOD FOR ESTIMATING
HINGE MOMENTS OF ALL-MOVABLE
CONTROLS

by

Jack N. Nielsen and Frederick K. Goodwin

DTIC
ELITE
S APR 2 1984 D
A

This document has been approved
for public release and sale; its
distribution is unlimited.

DTIC FILE COPY

NIELSEN ENGINEERING
AND RESEARCH, INC.

OFFICES: 510 CLYDE AVENUE / MOUNTAIN VIEW, CALIFORNIA 94043 / TELEPHONE (415) 968-9457

84 00 00 000

COPY NO. 122

PRELIMINARY METHOD FOR ESTIMATING
HINGE MOMENTS OF ALL-MOVABLE
CONTROLS

by

Jack N. Nielsen and Frederick K. Goodwin

NEAR TR 268

March 1982

DTIC
ELECTE
APR 2 1984
S A D

Prepared under Contract No. N00014-81-C-0267

for

OFFICE OF NAVAL RESEARCH
Arlington, Virginia 22217

by

NIELSEN ENGINEERING & RESEARCH, INC.
510 Clyde Avenue, Mountain View, CA 94043
Telephone (415) 968-9457

Unclassified

SECURITY CLASSIFICATION OF THIS PAGE (When Data Entered)

REPORT DOCUMENTATION PAGE		READ INSTRUCTIONS BEFORE COMPLETING FORM
1. REPORT NUMBER	2. GOVT ACCESSION NO.	3. RECIPIENT'S CATALOG NUMBER
	AD-A139 726	
4. TITLE (and Subtitle) PRELIMINARY METHOD FOR ESTIMATING HINGE MOMENTS OF ALL-MOVABLE CONTROLS		5. TYPE OF REPORT & PERIOD COVERED Final Report 03/01/81 to 11/30/81
		6. PERFORMING ORG. REPORT NUMBER NEAR TR 268
7. AUTHOR(s) Jack N. Nielsen and Frederick K. Goodwin		8. CONTRACT OR GRANT NUMBER(s) N00014-81-C-0267
9. PERFORMING ORGANIZATION NAME AND ADDRESS Nielsen Engineering & Research, Inc. 510 Clyde Avenue Mountain View, CA 94043		10. PROGRAM ELEMENT, PROJECT, TASK AREA & WORK UNIT NUMBERS
11. CONTROLLING OFFICE NAME AND ADDRESS Office of Naval Research Arlington, VA 22217		12. REPORT DATE March 1982
		13. NUMBER OF PAGES 334
14. MONITORING AGENCY NAME & ADDRESS (if different from Controlling Office)		15. SECURITY CLASS. (of this report) Unclassified
		15a. DECLASSIFICATION/DOWNGRADING SCHEDULE
16. DISTRIBUTION STATEMENT (of this Report) Approved for public release; distribution unlimited		
17. DISTRIBUTION STATEMENT (of the abstract entered in Block 20, if different from Report)		
18. SUPPLEMENTARY NOTES		
19. KEY WORDS (Continue on reverse side if necessary and identify by block number) Missile Airframes Aerodynamic Forces All-Movable Controls Supersonic Characteristics Hinge Moments Control Surfaces <i>Control Surfaces</i>		
20. ABSTRACT (Continue on reverse side if necessary and identify by block number) This report covers the first phase of a two-phase study of the hinge moments of all-movable controls. The objective of the first phase is to develop a hinge-moment prediction method for all-movable controls for angles of attack up to 20°, control deflections to 15°, the complete range of roll angles, and Mach numbers from subsonic to hypersonic if possible. Based on a review of the literature, it was decided to modify an existing computer program.		

Unclassified

SECURITY CLASSIFICATION OF THIS PAGE(When Data Entered)

Block 20 - Continued

MISSILE2, to improve its accuracy of hinge-moment prediction. A method based on strip theory and shock-expansion theory is used to improve the prediction of fin axial center-of-pressure position. A special method is included to account for canard and body vortices on fin axial center-of-pressure location. Special extrapolation procedures for the underlying data base were added. Comparison between hinge-moment data and prediction show good agreement at zero roll between Mach numbers of 1.3 and 3.7, but not at transonic speeds. When body or canard vortices are close to tail fins on the leeward side of the body, the predictions were usually not good. Canard fin hinge moments were generally well predicted. 7

Unclassified

SECURITY CLASSIFICATION OF THIS PAGE(When Data Entered)

PREFACE

This technical report covers the work performed under Contract N00014-81-C-0267 from March 1, 1981 to November 30, 1981. The program is sponsored by the Office of Naval Research, Arlington, Virginia. Dr. Robert E. Whitehead is the Scientific Officer.

Accession For
NHS GRA&I
DTIC TAB
Unannounced
Justification
By
Prescription
Availability Codes
Avail and/or
Dist. Special
A-1

SUMMARY

This report is the technical report on the first phase of a two-part investigation of the hinge moments of all-movable controls as utilized in cruciform missiles. In the first phase, an attempt has been made to develop as general as possible a hinge-moment prediction method from subsonic to hypersonic speeds for angles of attack to 20° and control deflections up to 15° . The complete range of roll angles has been included. In the second phase, a study is to be carried out to minimize hinge moments, and an experimental investigation is to be undertaken to see if the low hinge moments are realized.

Initially a literature survey was made to collect systematic data on hinge moments and to seek methods of hinge-moment prediction. The state of the art was reviewed with respect to a number of factors which can influence hinge moments including wing-alone nonlinearities, airfoil section effects, fin-fin and fin-body interferences, gaps, canard and body vortices, and trailing-edge shock-wave, boundary-layer interaction. One effect found to be of significance is that of airfoil thickness ratio and thickness distribution which can have a significant effect on the center of pressure of fin normal force. It was also found that vortices such as those of the body or canard fins passing in close proximity to the all-movable fin can significantly change its center-of-pressure position and normal force and hence its hinge moment. Sufficient systematic hinge-moment data were found to use for checking the results of any prediction method for the effects of angle of attack, roll angle, Mach number, fin planform, and fin airfoil section(s). An unpublished wing-alone data base provided systematic data on the effects of fin airfoil section(s), planform, angle of attack, and Mach number on normal force and axial center-of-pressure position.

To predict hinge-moment coefficient requires separate predictions of normal-force coefficient and axial center-of-pressure

location. An existing missile aerodynamic force and moment computer program (MISSILE 1 or MISSILE 2) generally predicts normal-force coefficients with sufficient accuracy, but not axial center-of-pressure locations. An equivalence was found between the axial center of pressure of the fin on body with that of the wing alone at the same value of the normal-force coefficient. Thus if experimental data on the axial center of pressure of the wing alone are available, they can be used in the hinge-moment prediction method provided its thickness distribution is the same as that of the fin. For those cases where such data are not available but where the leading-edge shock is attached viewed in planes normal to the fin planform but parallel to the body axis, a method was found for predicting axial center-of-pressure location. The method uses a combination of strip theory and shock-expansion theory in a separate computer program to obtain axial center-of-pressure location. This information is used as input to MISSILE 2. Also a method for determining the effects of vortices on the fin hinge moment was added to MISSILE 2. With these and several other modifications to improve accuracy, a version of MISSILE 2 to predict hinge-moment coefficient was developed. This program is applicable to fins with unswept trailing edges. However a means for treating fins with swept trailing edges is outlined.

For a fin of general planform it appears possible to obtain accurate hinge moments using a combination of the program DEMON II and the strip theory, shock-expansion program referred to above. However, no example is carried out.

The hinge-moment version of MISSILE 2 has been applied to a variety of cases to determine its range of applicability with reasonable accuracy. The following conclusions are borne out by comparison of experiment and theory.

1. The method has been successfully applied for the following range of Mach number, $1.3 < M_{\infty} < 3.7$.

2. While the method appears to be fairly good for leeward canard fins, it is not accurate for leeward tail fins near strong body vortices or canard vortices.

3. The use of the panel normal forces obtained from DEMON II can increase the accuracy of hinge-moment prediction for windward fins if used rather than the normal forces determined from MISSILE 2.

4. For zero roll angle the predicted tail fin hinge moments with no canard deflections are good and those with canard deflections are fair. At a roll angle of 45° , the predicted tail fin hinge moments are not good with or without canard deflection because the canard vortex effects on the tail fin are not well predicted for the vortices in close proximity.

5. The method is not accurate at transonic speeds principally because no method exists to account for wing section effects on axial center-of-pressure position.

TABLE OF CONTENTS

<u>Section</u>	<u>Page No.</u>
1. INTRODUCTION	9
2. GENERAL CONSIDERATIONS	11
2.1 General Observations	11
2.2 Parameters of Interest	11
2.3 Factors Influencing Hinge Moment	13
3. STATE OF THE ART	13
3.1 Introductory Remarks	13
3.2 Nonlinearities in the Wing-Alone Normal- Force Curve	14
3.3 Nonlinearities in the Wing-Alone Longitudinal Center-of-Pressure Position	15
3.4 Fin-Body Interference; No Body Vortices	20
3.4.1 Introductory remarks	20
3.4.2 Theory	21
3.4.3 Experiment	22
3.5 Fin-Body Interference Due to Body Vortices	23
3.5.1 Introductory remarks	24
3.5.2 Theory	25
3.5.3 Experiment	26
3.6 Fin-Fin Interference	26
3.6.1 Introductory remarks	26
3.6.2 Theory	28
3.7 Canard Vortices; Effects on Aft Surfaces	29
3.8 Adverse Fin-Body Interference	30
3.9 Boundary-Layer, Shock-Wave Interaction	32
3.10 Gap Effects	33
3.10.1 Introductory remarks	33
3.10.2 Theory	33
3.10.3 Experiment	34
3.11 Aeroelastic Effects, Fin Choking	35
4. PREDICTIVE METHOD FOR ESTIMATING HINGE MOMENTS	36
4.1 Introductory Remarks	36
4.2 Wing-Alone Center-of-Pressure Locations	38

<u>Section</u>	<u>Page No.</u>
4.2.1 Introductory remarks	38
4.2.2 Attached shock case	38
4.2.3 Detached shock case	45
4.3 Effect of Vortices on Fin Axial Center-of- Pressure Position	46
4.3.1 Panel method approach	46
4.3.2 Approximate engineering method	49
4.4 Other Changes in Program MISSILE	51
4.4.1 Introductory remarks	51
4.4.2 Wing-alone characteristics as input data	51
4.4.3 Interpolation and extrapolation for the fin-on-body data base	54
4.4.4 Changes in implementation of equivalent angle-of-attack concept	56
5. FINS OF GENERAL PLANFORM	57
6. COMPARISON OF EXPERIMENTS AND THEORY	60
6.1 Introductory Remarks	60
6.2 Data of Lamb and Trescot	61
6.2.1 Wing-alone characteristics	61
6.2.2 Comparison of experiment and theory	62
6.3 Comparisons for Army Generalized Missile	67
6.3.1 Preliminary remarks	67
6.3.2 Wing-alone normal-force coefficients and axial center-of-pressure positions	68
6.3.3 Comparisons for fin C ₄	70
6.3.4 Comparisons for fin C ₆	72
6.3.5 Comparisons for tail fin T ₂	74
6.3.6 Comparisons between data and theory for effects of roll angle on hinge moment	77
7. CONCLUDING REMARKS	78
8. RECOMMENDATIONS	83
REFERENCES	85

<u>Section</u>	<u>Page No.</u>
TABLES 1 THROUGH 3	89
FIGURES 1 THROUGH 89	101
APPENDIX A - CONTROL HINGE-MOMENT BIBLIOGRAPHY	A-1
APPENDIX B - EFFECT OF THICKNESS ON AIRFOIL CENTER-OF- PRESSURE POSITION IN ATTACHED SHOCK REGION	B-1
APPENDIX C - EQUIVALENT ANGLE OF ATTACK FORMULATION FOR LARGE ANGLES OF ATTACK	C-1
LIST OF SYMBOLS	

1. INTRODUCTION

The choice of fin size and planform shape to provide a missile with adequate control but small hinge moments has been a difficult problem at least since World War II. The problem has generally been studied by means of expensive and time-consuming wind-tunnel testing. The weights of the control actuators and their power supplies are substantial. While some attention has been given to analytical means for predicting hinge-moments for missiles, no attempt seems to have been made to develop general hinge-moment prediction technology and to apply it to the search for low hinge-moment all-movable controls (fins). It is the purpose of this report to describe a preliminary method for estimating hinge moments of all-movable controls. The Mach number range of interest is $0.5 < M_{\infty} < 4.0$.

Many missiles use all-movable controls for trim and maneuver because the greatest control effectiveness is usually obtained by utilizing all the potentially available fin area for control. Preliminary design methods for determining the characteristics of all-movable controls have been available only for the linear range of angle of attack and control deflection. As missiles have been pushed to higher angles of attack in search of greater maneuverability, the required control deflections have also increased. The nonlinearities resulting from higher angle-of-attack operation have made the prediction of the control characteristics even more difficult. Accordingly, the normal forces and hinge moments developed by such controls have usually been measured in wind tunnels during the design stage to assure that they will produce the desired trim and maneuverability within the hinge-moment capabilities of the control actuators.

Recent studies (ref. 1) of the forces acting on the fins of cruciform wing-body combinations at high angles of attack have had some success in predicting the high angle of attack nonlinearities. There is therefore now some prospect for developing a preliminary method for estimating hinge-moments of all-movable controls at high angles of attack. It is the purpose of the present report to present such a method. The method is preliminary because further work is planned under the contract, and the method is constructed so that it can utilize a better data base which is planned for the future.

This work is being conducted under Contract N00014-81-C-0267 from the Office of Naval Research which is supported by the Flight Dynamics Laboratory of the Air Force Wright Aeronautical Laboratories. The work is being carried out in two phases as follows.

Phase I - Development of an analytical capability for predicting hinge moment for aerodynamically-tailored fins, and validation and refinement of the analytical method following correlation of the results from the predictive method(s) with existing missile fin hinge-moment data.

Phase II - An unconstrained look at approaches for lowering fin hinge moment while retaining missile control effectiveness shall be made using the analytical capability developed during Phase I. Upon analysis of the results, not less than two and not more than six planforms reflecting the most promising approaches shall be selected and tested. The experimental data shall be analyzed for the purpose of refining the analytical capability further to improve the accuracy in predicting hinge moments of aerodynamically tailored, low hinge-moment fins.

In this report we start with a general discussion of the problem followed by a summary of the state of the art. Then the predictive method is described. A series of comparisons between experiment and theory are carried out and discussed.

In the concluding remarks, the successes and shortcomings of the method will be covered.

2. GENERAL CONSIDERATIONS

2.1 General Observations

The hinge moment depends on the normal force developed by a fin together with the center-of-pressure position of the normal force with respect to the hinge line. A number of methods exist for determining the fin normal force for various ranges of the relevant parameters. However, sufficiently accurate methods for determining longitudinal center-of-pressure position do not generally exist. This void is addressed herein.

In the estimation of hinge-moment coefficient and its comparison with data, care must be taken in assessing the accuracy of prediction. For a control with small hinge moments, the percent difference between the theory and data is not a good measure of accuracy since if the hinge-moment were zero, the error would be percentagewise infinite even for excellent agreement. A better measure is how much the differences between experiment and theory represents in terms of the hinge-moment lever arm expressed as percent of the root chord. Based on the present state of the art, if the error represents less than about 2 percent of the root chord, it is considered that good agreement is obtained.

2.2 Parameters of Interest

Some discussion of the ranges of the parameters to be considered will help fix ideas. First by an all-movable control we mean that the entire fin rotates about some lateral axis which projects from the missile body. The emphasis will be on the cruciform case rather than the planar case, although at $\phi = 0$ they are essentially the same. Also for small fin-fin interference

they do not differ substantially. Ratios of body diameter to wing span from 0 to well above 0.5 are covered.

With regard to fin parameters, we based the aspect ratio on two opposing fins joined together at their root chords. Aspect ratios from 1/2 to 2.0 are covered in the data base used in the method for the normal force of the fin mounted on the body. Extrapolation up to aspect ratio approaching 3 is possible. A future data base up to $AR = 4$ and $M_\infty = 4.5$ is planned. Taper ratios of 0 to 1 are included. For the most part we will be dealing with fins with unswept trailing edges in the data base. However, a means of specifying an equivalent fin with an unswept trailing edge will be given for fins with swept trailing edges. The method will be structured sufficiently broadly that fins of polygonal planform with many straight edges can be handled. For all-movable controls the aspect ratio range of importance is generally greater than unity.

Besides the geometric parameters of the basic configuration, we are interested in the following ranges of the parameters:

$$\begin{aligned} 0^\circ &\leq \alpha \leq 20^\circ; \text{ angle of attack} \\ -15^\circ &\leq \delta \leq 15^\circ; \text{ control deflection angle} \\ 0.5 &\leq M_\infty \leq 4.5; \text{ Mach number} \\ 0^\circ &\leq \phi \leq 180^\circ; \text{ roll angle} \end{aligned}$$

Most of our effort will be devoted to all-movable controls not operating in the wake of another set of cruciform surfaces. The computer program will be applicable to the case of all-movable controls operating in the wake of forward fins, but the nonlinearities encountered are more numerous than for forward controls because of the wake of the forward controls and that generated by the afterbody behind the forward surfaces. We will make some comparisons between experiment and theory for this case to determine our ability to handle it.

2.3 Factors Influencing Hinge Moment

A number of factors have an influence on the hinge-moment coefficients of all-movable controls. A list is given below as a guide to the discussion of the state of the art in the following section.

1. Nonlinearities in the wing-alone normal-force curve (versus α)
2. Nonlinearities in the wing-alone longitudinal center-of-pressure curve (versus α)
3. Fin-body interference (no body vortices)
4. Fin-body interference due to body vortices
5. Fin-fin interference
6. Canard vortices (effects on aft surfaces)
7. Adverse fin-body interference
8. Fin trailing-edge shock-wave/boundary-layer interaction
9. Gap effects
10. Aeroelastic effects
11. Fin choking

3. STATE OF THE ART

3.1 Introductory Remarks

A literature survey has been made through Defense Technical Information Center (DTIC) and NASA Scientific and Technical Information Facility to find references regarding all-movable controls. The references found have been classified under the following headings.

- A. Gap Effects
- B. Work at Ames Research Center
- C. Work at Langley Research Center
- D. General

The bibliography is presented in Appendix A. The overall methods for determining the characteristics of all-movable controls are generally fluid dynamic computer programs which determine the entire flow field with the exception of reference 2 which presents an engineering method. The present method is a considerable extension of that method.

3.2 Nonlinearities in the Wing-Alone Normal-Force Curve

One of the inputs to the calculation method is the wing-alone normal-force curve. There are numerous theories for determining wing normal-force coefficient, but they are not adequate to determine the wing normal force to high angles of attack with confidence for general planforms. It is not our intent to try to remedy this general defect of theory, but instead we will rely on data base methods.

Previously, the only wing-alone data base for the normal-force coefficients from low to high Mach numbers and to high angle of attack of wings which systematically vary in aspect ratio and taper ratio was obtained on a reflection plane and contained unknown effects of the plate boundary layer. Wing-alone normal-force curves have been "constructed" from existing data for aspect ratios of 0.5, 1.0, 2.0; taper ratios of 0, 0.5, and 1.0; and Mach numbers of 0.8, 1.2, 2.0, and 3.0 for use in reference 1.

Recently Stallings and Lamb, reference 3, published a wing-alone data base for Mach numbers from 1.6 to 4.50 based on pressure distribution models. The set of wings tested by Stallings and Lamb have the geometric characteristics shown in Figure 1. It is noted that the aspect ratio goes up to 4.

These airfoil sections are not of uniform thickness ratio but are of constant thickness because of the necessity of housing the pressure tubing. The values of normal-force coefficient agree closely enough with those of reference 1 for the range tested so that no changes are required on reference 1.

Recently the Stallings-Lamb wings were tested in the Ames 6- by 6-Foot Supersonic Wind Tunnel at $M_\infty = 0.6, 0.8, 0.9,$ and 1.2 to complete the Mach number range. The data have been reduced and some of them are utilized in the present report. This work was accomplished under Contract DAAG29-79-C-0020 for the Army Research Office, Durham, N.C. with support from ARO, NAVAIR, and MICOM. The models for the supersonic testing were designed and constructed by the Langley Research Center and lent to Nielsen Engineering & Research, Inc. (NEAR) for testing in the Ames Research Center 6- by 6-Foot Wind Tunnel. Dr. Robert E. Singleton, Director, Engineering Sciences Division, AROD, has given us permission to use some of these unpublished data in this report.

A wing-alone data base due to Baker (ref. 4) was obtained on a reflection plane using semispan models. The aspect-ratio range was $1/2$ to 2 and the Mach number range up to $M_\infty = 3$. At high angles of attack and Mach numbers, the data are known to exhibit loss of normal force of unknown extent due to boundary-layer effects of the reflection plane. This data base will be termed the Fidler-Baker data base hereafter since the wings tested by Baker are similar to wings tested earlier by Fidler.

3.3 Nonlinearities in the Wing-Alone Longitudinal Center-of-Pressure Position

The longitudinal center-of-pressure position determines the lever arm for the hinge moment. Any variation of this position with angle of attack for the wing alone would be

expected to also be present to some degree for the fin in the presence of the body.

The theoretical determination of the wing-alone center-of-pressure location is in the same state of development as the prediction of the wing-alone normal force. We must rely on data to a large extent. With this in mind we examine the question of the available systematic data on the matter. However, first consider what symmetrical thickness can do to the center-of-pressure location of a two-dimensional supersonic airfoil.

It is known that a symmetric thickness distribution causes the airfoil center-of-pressure location at supersonic speed to move forward from the zero thickness position by an amount that increases with thickness ratio and Mach number. In fact, it is possible to use Busemann second-order theory or shock-expansion theory to show this.

Using both of these theories, calculations have been made for the effect of thickness on center-of-pressure positions for the three airfoils of Figure 2. These airfoils have the same thickness ratio but vary in the length of the region of maximum thickness. Without any thickness, the center-of-pressure position denoted by \bar{x}/c is at the midcord of the airfoil, and with thickness is moved forward an amount $(\Delta\bar{x}/c)_t$. The values of this latter quantity are given in Figure 3 for the three airfoils as calculated by the two theories for $M_\infty = 4.5$. It is noted that large forward shifts occur which must be accounted for if \bar{x}/c is to be predicted to within say 0.02. Note that the Busemann theory and shock-expansion theory agree at $\alpha = 0^\circ$, but shock-expansion theory exhibits an angle-of-attack effect. Also the double-wedge airfoil shows the least effect of thickness. Figure 4 shows the effects of Mach number for one of the airfoils, and demonstrates how $(\Delta\bar{x}/c)_t$ increases with M_∞ . These effects occur when the leading-edge shock wave is attached.

The foregoing results show why center-of-pressure data from a set of wings of systematic planforms do not yield systematic center-of-pressure locations unless the airfoil sections are uniform or vary systematically wing to wing. They also show that a systematic hinge-moment data base requires systematic airfoil sections.

There exist two sets of wings varying systematically in aspect ratio and taper ratio for which longitudinal center-of-pressure data have been obtained to large angles of attack; the set shown in Figure 1 and the Fidler-Baker set shown in Figure 5. It is noted that the two sets of wings have dissimilar airfoil sections, and the airfoil section changes from wing to wing within each set. A comparison of thickness ratios is made in the following tabulation between the two sets of wings for wings of the same aspect ratio and taper ratio.

Stallings-Lamb		Fidler-Baker		\overline{AR}	λ
Wing (fig. 1)	$(t/c_r)_{\text{root}}$	Wing (fig. 5)	$(t/c_r)_{\text{root}}$		
P ₂	.044	T31	.025	0.5	0.5
P ₄	.042	T14	.025	1.0	0
P ₅	.062	T15	.037	1.0	0.5
P ₆	.083	T11	.037	1.0	1.0
P ₈	.088	T23	.049	2.0	0.5

The Fidler-Baker wings were tested on a boundary-layer reflection plate, and induced plate boundary-layer separation at large values of α which invalidated the data. The Stallings-Lamb wings were tested as pressure-distribution wings, a fact accounting for their greater thickness ratios. Comparisons between \bar{x}/c_r for the two sets of wings will now be made for $M_\infty = 0.8, 1.2, 2.0, \text{ and } 3.0$.

In Figures 6-13 comparisons will be made between the normal-force coefficients and axial center-of-pressure locations

for the five wing planform common to the Fidler-Baker and Stallings-Lamb data bases for Mach numbers of 0.8, 1.2, 2.0, and 3.0. Before the presentation of these comparisons some points with regard to the data are noteworthy. First the data for the wings of the Fidler-Baker data base were corrected for the tares in normal-force and hinge-moment coefficients at $\alpha = 0$ before determining axial center-of-pressure position, \bar{x}/c_r . The Fidler-Baker wings were not tested at $M_\infty = 1.2$ but were tested at $M_\infty = 1.15$ and 1.3. The results presented for $M_\infty = 1.2$ represent a linear interpolation between the data for these two Mach numbers. No data for the T14 wing exist for $M_\infty = 0.8$ or 1.2, but the P4 data are included for completeness.

Consider now the comparison of the wing normal-force curves at $M_\infty = 0.8$ given in Figure 6. The first apparent result is that the two sets of wings have quite different normal-force curves at $M_\infty = 0.8$ as a result of different wing sections. There is a difference in their stall characteristics, the thinner wings of the Fidler-Baker data base generally stalling at higher angles of attack for aspect ratios of 1 or more.

Consider now the values of \bar{x}/c_r for the same wings in Figure 7. The wings of the Fidler-Baker data base show large rearward travel of the center-of-pressure as angle of attack increases in all cases. The wings P6 and P8 do not exhibit such large rearward shifts. The two sets of wings show generally much different \bar{x}/c_r characteristics.

Figures 6 and 7 show the large effects of wing section on C_N and \bar{x}/c_r which have implications with regards to predicting hinge moment. Since a general data base including planform and wing-section effects is not available, we must confine our predictive capability to wings with existing data or must rely on theory. However, a theory which accounts for wing-section effects on \bar{x}/c_r does not exist for the angle of attack in which we are interested. Possibly transonic full

potential theory would work at the lower angles, but its application is expensive and limited. A general prediction method for hinge moment around $M_\infty = 0.8$ thus requires more basic work.

We will now consider the state of affairs for $M_\infty = 1.2$. Figure 8 presents the comparisons for the normal-force coefficients. Generally the effects of wing section on normal-force coefficients are small up to wing stall. The thinner wings of the Fidler-Baker data base exhibit no significant stall while P_5 , P_6 , and P_8 do.

The \bar{x}/c_r comparisons of the wings for $M_\infty = 1.2$ are given in Figure 9. The thinner wings generally have centers of pressures near the DATCOM values for small angles of attack, which move rapidly backward with increasing angle of attack. For the P_5 , P_6 , and P_8 wings which exhibited normal-force stall, the centers of pressure are in front of those for the corresponding Fidler-Baker wings above the stall. At low angles of attack the center-of-pressure positions are aft of those of the Fidler-Baker wings.

We have a problem at $M_\infty = 1.2$ with regard to predicting center-of-pressure positions at high angle of attack because of the lack of a suitable theory. For low angles, where the leading-edge shock may be attached, we will subsequently present a method.

Consider now the comparison of the normal-force curves for the two sets of wings at $M_\infty = 2.0$ as given in Figure 10. The curves are in very good agreement except at the highest angles of attack where wings T31 and T14 exhibit stall at angles less than 50° . The corresponding center-of-pressure locations are given in Figure 11. The points in the stalled region for T14 and T31 have been marked with flags since the stall may be induced by reflection plate boundary layer. It is noted that the Stallings-Lamb wings generally exhibit center-of-pressure locations in front of those for the Fidler-Baker wings, a result that would be

expected in the range of shock attachment because of their greater thickness. This difference would also be expected near $\alpha = 0^\circ$, but this is not the case for T31 and T14. This result may be due to inaccuracies in determining \bar{x}/c_r near $\alpha = 0^\circ$. For the $R = 1$, $\lambda = 1$ wings larger differences are shown at small α than at large α . This, again, may be an accuracy problem.

The normal-force curves and the axial center-of-pressure curves for the two sets of wings at $M_\infty = 3.0$ are shown in Figures 12 and 13, respectively. The Fidler-Baker wings T31, T14, T15, and T11 show earlier stall than the corresponding Stallings-Lamb wings. This phenomenon is reflected in the axial center-of-pressure positions shown in Figure 13 with flagged symbols in the neighborhood of $\alpha = 50^\circ$ and above. These flagged data points are suspect. The observations made concerning the differences in the results for the two sets of wings at $M_\infty = 2.0$ also hold generally at $M_\infty = 3.0$. The fairly regular differences shown give hope of predicting these differences.

3.4 Fin-Body Interference; No Body Vortices

3.4.1 Introductory remarks.- A fin in the presence of the body can act differently than it does when part of the wing alone because of the nonuniform flow field induced at the fin location by the body and because the round body does not present an infinite reflection plane. We now consider the effects of fin-body interference without the complicating effects of body vortices which are taken up in the next section.

We are interested in the effects of fin-body interference on the quantities $C_{N_{W(B)}}$ and $\bar{x}_{W(B)}$ since both of these quantities are used in calculating hinge moment. The fin-body interference depends on the following parameters in a complicated way.

α ; angle of attack
 M_∞ ; free-stream Mach number
 ϕ ; roll angle
 a/s_m ; radius/semispan ratio
 n ; number of fins (equally spaced)
 $\delta_1, \delta_2, \delta_3, \delta_4$; fin deflection angles
 \mathcal{R} ; fin aspect ratio
 λ ; fin taper ratio

We will confine our attention to $n = 4$.

Consider now what theories are available for determining $C_{NW(B)}$ and $(\bar{x}/c_r)_{W(B)}$.

3.4.2 Theory.— For subsonic speeds several theories are available for determining the fin load distribution. First there is the slender-body theory of Spreiter and Sacks (ref. 7) for $\delta = 0$, Adams and Dugan (ref. 8) for $\delta \neq 0$. There are also various lifting-line theories and lifting-surface theories. These methods, however, are generally worked out for zero wing thickness and apply to the linear range of angle of attack characteristics. A special vortex-lattice program has been developed by Dillenius (ref. 9) which applies to empennages of quite general geometric configuration. This program, applicable to $M_\infty = 0$, treats multiple fins which are not alike and which can be unequally spaced around the fuselage.

For supersonic speeds, there are a number of linear methods that can be used including quasi-cylindrical theory (ref. 10) and paneling methods. Of this latter type, the PANAIR program (ref. 11) is an example as well as DEMON II (ref. 12), which is a panel program especially adapted to cruciform missiles. For supersonic speeds, DEMON II can be used for fins of arbitrary planforms. Codes based on the Euler equations have been used for supersonic wing-body combinations for supersonic axial Mach numbers. The code of

Soloman, Wardlaw and Baltakis (ref. 13) and that of Klopfer and Nielsen (ref. 14) are examples.

Generally the panel codes applicable to wing-body combinations require significant amounts of computer time. They are applied to unusual planforms or for calculation of benchmark cases. For preliminary design we will rely as much as possible on a data base or on engineering methods for determining both $C_{N_{W(B)}}$ and $(\bar{x}/c_r)_{W(B)}$.

3.4.3 Experiment.- A data base for $C_{N_{W(B)}}$ and $(\bar{x}/c_r)_{W(B)}$ should cover a range of wing planforms, angles of attack, roll angles, Mach numbers, and deflection angles. Such a data base does not exist for variable δ . For $\delta = 0$ the Fidler-Baker data base exists from which only the $C_{N_{W(B)}}$ results have been incorporated into Program MISSILE (Refs. 1 and 2). The data base for $(\bar{x}/c_r)_{W(B)}$ is not systematic since the airfoil sections varied among wings of the set.

In reference 2 it was shown that $(\bar{x}/c_r)_{W(B)}$ was closely approximated by $(\bar{x}/c_r)_W$ for the wing alone. The correspondence of the center of pressure of the wing alone and the fin in the presence of the body is based on an equivalence assumption. One way of putting the assumption is that at the same value of normal-force coefficient based on planform, the longitudinal and lateral center-of-pressure positions of the wing alone and the fin are the same. In other words, the fin is assumed to exhibit the same nonlinearities as the wing at a given value of fin normal-force coefficient.

We will now compare the axial center-of-pressure positions of the wings alone, $(\bar{x}/c_r)_W$, as a function of fin normal-force coefficient (ref. 5) with those for the fins in the presence of the body, $(\bar{x}/c_r)_{W(B)}$, using data (ref. 15) for the wings of the Fidler-Baker data base. The first such wing results are shown in Figure 14 for Mach numbers of 0.8, 1.2, 2.0, and 3.0 for $M_R = 0.5$ and $\lambda = 0.5$. Some explanation of the results are necessary. The data for the fin in the presence of the

body, taken from reference 15, are given for various roll positions on the windward side of the body to minimize any effects of body vortex interference. They have not been corrected for zero shifts of normal force or hinge moment, and therefore contain some degree of uncertainty. The wing-alone data have been taken from reference 5, and they have been corrected for zero shifts.

For all Mach numbers it is noted that the data for \bar{x}/c_r for the fin at different values of ϕ tend to correlate in a small band. Also the wing-alone data generally goes through this band within about ± 0.02 . The nonlinear trend of the center of pressure with angle of attack measured for the wing alone is thus duplicated by the fin in the presence of the body. It is also apparent that the equivalence principle described above does a good job of correlating the data for different roll angles and angles of attack.

The results for four more wings are given in Figures 15 to 18 in accordance with the following table:

Configuration (ref. 15)	AR	λ	Figure
B1T14	1	0	15
B1T15	1	1/2	16
B1T11	1	1	17
B1T23	2	1/2	18

In Figure 15 for B1T14, wing-alone data are not available for T14 at $M_\infty = 0.8$ and 1.2 so that only the data for the fin in the presence of the body are shown for this combination*. A mean line has been drawn through the data for these two Mach

* While a wing of comparable planform was tested at these Mach numbers in the Stallings-Lamb data base, it has a different thickness distribution from that for T14.

numbers to simulate the missing wing-alone results. It is noted for this delta fin that the center-of-pressure variations with angle of attack and Mach number are not large, possibly making it a candidate for a low hinge moment all-movable control.

Figure 16 for BlT15 exhibits an interesting phenomenon at $M_\infty = 0.8$. For a range of C_N between 0.87 and 0.97, \bar{x}/c_r of the wing alone is triple valued for a given C_N . It is not clear from the data for the fin in the presence of the body whether this nonlinearity is present for the fin. We have compared the data for the wing alone with that of the fin at two different roll angles in Figure 19. Note that at the horizontal position, the fin duplicates the wing alone nonlinearity past stall. For $\phi = 30^\circ$ the fin-on-body duplicates the wing alone up to the stall. To predict fin center-of-pressure beyond the stall from wing alone data in the transonic range is thus not promising.

Figure 17 for BlT11 shows a slight stall for the $AR = 1$, $\lambda = 1$ fin at $M_\infty = 0.8$ but it appears not to be important. The large center-of-pressure travel for $AR = 1$, $\lambda = 1.0$ and that for $AR = 2$, $\lambda = 0.5$ shown in Figures 17 and 18 at $M_\infty = 0.8$ and 1.2 make it difficult to obtain small hinge-moment coefficients with them in the transonic range.

It appears that the wing-alone axial center-of-pressure position is thus a good approximation to that for the fin in the presence of the body for the five wings of the Fidler-Baker data base for the Mach number range $M_\infty = 0.8$ to 3.0. However, in cases of severe wing-alone stall, the approximation breaks down.

3.5 Fin-Body Interference Due to Body Vortices

3.5.1 Introductory remarks.- A body of revolution above an angle of attack depending principally on its length-to-diameter ratio will generate a pair of symmetric vortices on

its leeward side. At a still larger angle of attack the symmetric pair can become asymmetric particularly for subsonic flow. The present method of predicting hinge moments could be applied to the asymmetric vortex case if we knew the vortex positions and strengths. A rough rule of thumb is that asymmetric vortices do not develop if the crossflow Mach number is greater than about 0.5 (ref. 16). This fact taken together with the fact that asymmetric vortices form at angles of attack above about 20° - 30° for body of moderate length-to-diameter ratio leads to the plot shown as Figure 20. The present method has not been applied to the region marked "Subcritical, asymmetric."

In the region above the curve $M_C = M_{\infty} \sin \alpha = 0.5$, there are generally shock waves in the crossflow plane which appear to emanate from the body surface. These shock waves tend to eliminate the asymmetric vortices. The vortical regions are not so concentrated as for subcritical crossflow Mach numbers, but tend to be elongated elliptical regions.

Body vortices are generally characterized for engineering purposes by their strengths and their positions. Their strengths are given by a nondimensionalized value of the circulation about a contour including the vorticity. The vortex position is characterized by the location of the core of the vortex in the crossflow plane. This position can usually be deduced from flow surveys, vapor-screen photographs, and sometimes schlieren photographs. A description of the vortices in terms of strengths and positions is the first step in determining the effect of the body vortices on the fin. The second step is determining what effect these vortices have on fin forces and moments using aerodynamic theory.

3.5.2 Theory.- We consider first the available theories for determining the vortex strengths and positions. These theories fall into two classes, vortex tracking methods and

Euler equations methods. Vortex tracking methods consider the crossflow planes of a body of revolution and introduce point vortices at the body separation line, as calculated or as input empirically. The calculation proceeds downstream with the shed vortices following the calculated streamlines. The method of Mendenhall, et al. (refs. 17-19) is an example of this type of theory. A second method makes use of the Euler equations and known positions of the body primary vortex shedding lines. By the application of appropriate boundary conditions at the separation line, the entire flow field is calculated in a supersonic marching procedure. The method of Nielsen and Klopfer (ref. 20) is the only present example of this approach.

We next consider methods for calculating the effect of the vortices on the fin aerodynamics. These methods include reverse-flow methods (ref. 1), panel methods (ref. 12), and Euler methods (ref. 20). In the reverse-flow method, the upwash distribution induced at the fin by the external vortices and their images is first determined. Then a span-wise integral of this upwash distribution multiplied by a weighting factor is used to determine the fin normal force due to the vortices. Another weighting factor yields the lateral center of pressure. This method is used in Program MISSILE (ref. 1). However, the method as originally formulated is not suitable for determining hinge moments, and an engineering means has to be developed where none now exists.

Panel methods are applicable to determining hinge moments due to vortices. The use of Program DEMON II (ref. 12) in this connection will be demonstrated subsequently. The Euler equation method of determining the effect of body vortices on the fin loading was recently developed by NEAR and is a finite-difference method not presently suitable for preliminary design.

3.5.3 Experiment.- Consider first the experimental data with respect to strengths and positions of symmetric body

vortices above bodies of revolution at angles of attack. Vapor-screen photographs and conventional pitch-yaw probes were used in the 1950's to obtain vortex positions, and the vortex strengths were inferred principally from normal forces or normal-force distributions. These data have been correlated for use in preliminary design by several investigators. A correlation of these data by Mendenhall and Nielsen given in reference 17 has been used in Program MISSILE.

In recent years additional measurements in this area have been made by Oberkampf (ref. 21) using conventional probes. Schwind, et al. (refs. 22 and 23) and Yanta, et al. (ref. 24) have also made measurement using laser-doppler velocimetry.

With regard to measuring the effect of vortices on a wing pressure distribution, two studies have been made at low speed by Smith and Lazeroni (ref. 25) and McMillan, et al. (ref. 26). The latter authors found that reverse-flow theory provides loads of sufficient accuracy compatible with economy. To obtain better accuracy probably requires accounting for the effect of the fin on the vortex path in a fully mutual interference calculation.

3.6 Fin-Fin Interference

3.6.1 Introductory remarks.- Fin-fin interference occurs when the aerodynamic characteristics of a given fin are changed as the result of the presence of another fin of the set. There is also fin-fin interference if the aerodynamic characteristics of a given fin are influenced by control deflection of any other member of the set. It is clear that fin-fin interference can influence all-movable control effectiveness and hinge moment and must be accounted for in a hinge-moment prediction method. A severe case of fin-fin interference can result in serious control cross-coupling. In this case a pitch control command might result in yaw control and/or roll control as well. It

is clear that fin-fin interference is more severe for cruciform fins than for planar fins simply because of the closer proximity of the neighboring fins.

Fin-fin interference occurs when one fin falls within the zone of influence of another fin as at subsonic speed. At supersonic or hypersonic speed, it is possible that the fins are not within each others fields of influence so that no fin-fin interference occurs.

3.6.2 Theory.- Several methods exist for calculating fin-fin interference due to control deflection and the simplest of these is probably reverse-flow theory. Appendices A and B of reference 1 developed this theory using a combination of slender-body theory and reverse-flow theorems. The method determines the effect of control deflection on fin normal force and lateral center of pressure, but is not adaptable to determining the effect on longitudinal center-of-pressure position. Fin-fin interference for no control deflection has already been accounted for in the data base of Program MISSILE.

Panel methods such as Program DEMON (ref. 12), specially constructed for cruciform missiles, can be used to study fin-fin interference. Euler codes can be developed to handle general fin-fin interference in cruciform missiles for the case of supersonic marching.

Theoretical fin-fin interference factors for unit fin deflections have been calculated using Program MISSILE and are presented in Table 1 of reference 1. These factors are applicable to fins which are wholly within each others zones of influence. For a fin partially within the field of influence of other fins, the percentage of the fin planform within the field of influence is determined. This percentage is applied to the above mentioned fin-fin interference factors as a multiplication factor. The method gives the right

limit when a fin is not within the field of influence of a deflected fin.

3.7 Canard Vortices; Effects on Aft Surfaces

The influence of canard vortices on the hinge moments of all-movable tail controls is complicated. For angles of attack which are relatively small and for zero roll angle, the horizontal canard fins produce vortices which may be sufficiently close to the tail fins to influence their hinge moments. At high angles of attack ($\phi = 0^\circ$) the canard vortices can pass high enough above the tail fins to have a small effect on their hinge moments. However, at high angles of attack the afterbody between the canards and the empennage can shed its own vorticity which interacts with the tail fins and has a strong effect on their hinge moments. The interaction between the canard vortices and the afterbody will influence the strengths and positions of both the afterbody and canard vortices.

The foregoing effects encountered at zero roll angle are made more complicated at nonzero roll angle by vortices from all four canard panels which interact with each other and with the afterbody in an asymmetric way. To account for these vortex effects on tail hinge moments requires a knowledge of the vortex strengths and positions at the tail axial location and then an application of a method for determining the tail fin reactions. The strengths and positions of the canard vortices at the canard trailing edge can be obtained from some knowledge of the span loading distribution; then the canard vortices must be tracked over the afterbody, the origin of the afterbody vortices determined, and the strengths and positions of the afterbody vortices determined accounting for their interaction with the canard vortices.

MISSILE 2 (ref. 2) contains a vortex-tracking routine to take account of the above phenomena. In principle it can

be applied to the problem of determining the vortex strengths and positions at the tail location. The method subsequently to be described for determining the effects of vortices on fin hinge moments can then be used to determine the tail fin hinge moments. To be able to account accurately for all nonlinearities on tail fin hinge moments is probably more than can be expected for the present method, but some comparisons will be made to determine the state of the art.

3.8 Adverse Fin-Body Interference

At supersonic speeds at moderate angles of attack and at hypersonic speeds at low angles of attack significant nonlinear effects occur on the fin normal force due to the interference of the body. Account of these nonlinearities must be taken in determining hinge moments.

The fin in the presence of the body at $\delta = 0^\circ$ and $\phi = 0^\circ$ has a normal-force coefficient $C_{N_W(B)}$ based on its planform area, and the wing alone at the same angle of attack has a normal force coefficient C_{N_W} . The interference of the body on the fin is measured by a factor K_W given by

$$K_W = \frac{C_{N_W(B)}}{C_{N_W}}$$

This factor is normally greater than unity at low speeds and low angles of attack because of body upwash, denoting favorable interference. The experimental values of these factors for an aspect ratio 1 delta wing on a body are shown in Figure 21. The body vortex effects have been taken out of $C_{N_W(B)}$ by theoretical means. It is seen that the favorable interference at low Mach numbers and low angles of attack can become very unfavorable at high Mach numbers and high angles of attack.

The favorable interference manifest at low Mach numbers and angles of attack is known to be the result of body upwash which increases the fin normal force. However, at high Mach

numbers and angles of attack, the net interference is a result of changes in flow upwash angle, dynamic pressure, and Mach number at the positions to be occupied by the fin in the body flow field. The effect of compressibility and the bow wave on these quantities basically controls the value of K_W .

A fair estimate of the fin normal force can be made by strip theory if the flow field in the position to be occupied by the fin is known. Euler codes exist which will calculate this flow field quickly for supersonic marching. However, since Program MISSILE uses a data base for $C_{N_W(B)}$, the values of K_W are known experimentally from the data base. They are used in extending the data base to configurations with a/s_m ratios different from 0.5, that of the data base.

3.9 Boundary-Layer, Shock-Wave Interaction

At an unswept (or supersonic) sharp trailing edge of a supersonic wing on the upper surface, the flow is above free-stream speed, and must traverse an oblique shock to come back to free-stream static pressure behind the wing. Under certain circumstances the shock moves forward from the trailing edge and separates the boundary layer approaching the trailing edge. The results presented by Ferri, reference 27, for a biconvex airfoil with semiapex angle of $11^\circ 20'$ tested at $M_\infty = 2.13$ at $R_e = 710,000$ are interesting. They show effects of boundary-layer separation at $\alpha = 0^\circ$ over the last 15 percent of the chord and at $\alpha = 20^\circ$ over the last 50 percent of the chord.

If boundary-layer, shock-wave interaction occurs on the upper surface, the pressure coefficients on the top rear part of the wing are increased, so that the normal force per unit area is decreased. As a result the center-of-pressure location should move forward and change the hinge moment.

The pressure distributions taken by Stallings and Lamb on their wings sheds some light on the extent of separated flow

on the upper surface of the wings near the trailing edge. For this purpose the pressure distributions on the $AR = 2$ rectangular wing have been examined. This wing has 15° semi-wedge angles at the leading, side, and trailing edges. It was tested at a Reynolds number of slightly over 700,000 based on the wing chord. The orifices numbered 52, 57, and 63 in Figure 22 have the following distances from the trailing edge:

Orifice	x'/c_r
52	0.177
57	0.118
63	0.059

The measured pressure distributions on the upper and lower surfaces of the wing at $\alpha = 10^\circ$ are compared in Figure 23(a) with the predictions of shock-expansion theory. Note that on the upper surface the last three orifices show uniform pressure on the beveled trailing edge. The pressure is slightly higher than predicted by shock-expansion theory. Some separation from the shoulder to the trailing edge seems to be present. At any rate the difference between experiment and theory accounts for about 0.015 in \bar{x}/c_r . The data in Figure 23(b) for $\alpha = 20^\circ$ probably exhibit separation. No comparison is made with theory since the angle of attack is above that for shock detachment.

Data and theory are compared in Figures 23(c) and (d) for $M_\infty = 4.60$ for $\alpha = 20^\circ$. There is little or no evidence of trailing-edge separation. These data show that the pressure coefficient on the upper surface of a wing at high angle of attack and Mach number is so close to the free-stream value that boundary-layer, shock-wave interactions on the upper surface approaching the trailing edge could not have a significant effect on normal-force or center-of-pressure position.

We will generally ignore the effects of trailing-edge, shock-wave, boundary-layer interaction on center of pressure in the hinge-moment predictive method. This should prove to be a fair approximation for wedge-shaped trailing edges. However, on the basis of the results of Ferri the same assumption should not be made for wings with airfoil sections curved at the trailing edge such as biconvex sections.

3.10 Gap Effects

3.10.1 Introductory remarks.- A gap exists between an all-movable control and the body on which it is mounted. Two kinds of gaps occur in practice which are worth differentiating. For a fin at $\delta = 0$ there is generally a streamwise gap of nearly uniform width between the fin and the body. This is the kind of gap which is generally modeled in theory. In practice the fin is rotated about a hinge line so that a gap of non-uniform width occurs between the body and the fin for $\delta \neq 0$. For very large deflections, the fin can even project above the body. To treat this kind of nonuniform gap analytically is clearly very difficult but it is amenable to panel methods with some complexity. However, for small control deflections the gap is fairly well approximated by a uniform gap.

Principally as a result of theoretical studies the effect of gaps on the fin characteristics have at times thought to be large. On the basis of potential theory, the span loading at the gap falls to zero from the substantial value it has for no gap. However, it appears that for gap sizes used in practice, much of the adverse effect predicted theoretically is overcome by viscosity. That is not to say that for nonuniform gaps due to δ there are not substantial effects. Let us examine the theoretical basis for gap effects as well as the experimental results.

3.10.2 Theory.- There are two theoretical methods that have been pursued in the study of gap effects. The first

approach is that of Bleviss and Struble (refs. 28 and 29) who use linearized supersonic wing theory to study the effect of a gap between a wing panel and a vertical reflection plane. The second approach based on slender-body theory has been used by Mirels (ref. 30) and Dugan and Hikido (ref. 31) to study slender wings mounted on bodies of revolution with nonuniform gaps. Bleviss and Struble find that the presence of a gap, as small as 0.05 of the exposed semispan, can cause losses in lift as large as 40 percent of that for no gap (ref. 28, Fig. 4). Dugan and Hikido also find large losses of lift even for minute gaps. Those theoretical results are considerably modified by viscosity.

3.10.3 Experiment.- Several experimental investigations of gap effects are available (refs. 32 and 33). Careful systematic measurements were reported by Dugan (ref. 32) on the effects of a gap on the lift developed by an aspect ratio 2.31 delta wing mounted on a body of revolution with a body diameter to span ratio of 0.216 for zero gap. The tests were carried out at a Mach number of 1.4 and a Reynolds number of slightly less than 4×10^6 based on the wing root chord. Two cases were tested, the effect of α at $\delta = 0$ and the effect of δ at $\alpha = 0$. Some results are now quoted from Figure 5 of the report.

For a gap/wing semispan ratio of 0.025, the ratio of lift with a gap to that with no gap was 0.75 at $\alpha = 1^\circ$, 0.95 at $\alpha = 5^\circ$, and 0.97 at $\alpha = 10^\circ$. For $\alpha = 0$ but variable δ , the comparable results are 0.72 at $\delta = 1^\circ$, 0.94 at $\delta = 5^\circ$, 0.97 at $\alpha = 10^\circ$. At very small angles of attack or control deflection significant loss of lift occurred; by the time α reaches 5° and δ reaches 10° very little loss occurs.

An investigation (ref. 34) of an aspect ratio 4 all-movable delta wing on a body of revolution also contains some data on gap effects. The results quoted here are for

gap/wing semispan ratios of 0.0057 and 0.023, a Mach number of 1.46, and a Reynolds number of 5.7×10^6 based on a body length of 10.5 inches with a root chord of 2.25 inches. It was concluded that over the range of gap/semispan ratios tested there was little or no effect on lift, drag, or hinge moment at $M_\infty = 1.46$.

It thus appears that for gap/semispan ratios up to about 0.025 significant loss of fin lift occurs only at very small values of α or δ . At higher values of α or δ , the loss disappears so that there is generally no basic loss in maneuver capability. If larger gaps are used, larger losses occur (ref. 33). These results are not confirmed for high supersonic or hypersonic Mach numbers.

3.11 Aeroelastic Effects, Fin Choking

Several other factors can influence hinge moments, and they are mentioned here for the sake of completeness. The first factor to be considered is aeroelasticity. If fins are made as thin as possible to reduce weight and are still subject to large loads in order to produce high maneuverability, then significant deformation of fins under load is to be expected. A study to determine to what extent the normal forces and hinge moments of an all-movable control are changed as a result is needed. In particular, it appears that some reduction in hinge moments could be made possible by aeroelastic tailoring. The determination of aeroelastic effects on hinge moments will not be taken into account in the present prediction method.

The second factor which can influence hinge moments is "fin choking" which can occur under special circumstances. In this phenomenon the axial flow between the two lower fins of a cruciform wing-body combination in the x roll position suddenly chokes by means of a shock normal to the axial direction. A high pressure region exists between the fins and the lines of constant pressure are nearly lateral. An example

of the pressure field in this case is given in Figure 25 of reference 35 based on data provided by Mr. R. L. Stallings and Mr. W. J. Monta of Langley Research Center, NASA. The conditions under which this example of fin choking occurred are $\phi = 45^\circ$, $\alpha = 50^\circ$, and $M_\infty = 2.7$. The limits of operation to avoid choking have not been determined.

4. PREDICTIVE METHOD FOR ESTIMATING HINGE MOMENTS

4.1 Introductory Remarks

A method for estimating hinge moments for the range of angle of attack, 0° - 20° , and the range of control deflection $\pm 15^\circ$, is not generally available. A method applicable to the linear range is given in reference 36. Without going into the details of that method, it can be said that the present method is an extension of that method to increase its range of applicability. It is our desire that the present method include effects of roll angle and be applicable from subsonic* to high supersonic speeds. It will also turn out that the method we are adopting will include within its framework the possibility of determining the hinge moments for all-movable tail controls affected by wing-tail interference. It is also an objective to treat wing planforms of quite general shape so long as these can be represented by connected straight line segments.

Calculating hinge moment involves determining the fin normal-force coefficient and its longitudinal center-of-pressure position. We have available an engineering tool for predicting fin normal force coefficients (MISSILE 2, ref. 2) but it does not predict axial center-of-pressure location with sufficient accuracy for hinge-moment purposes. Accordingly, our approach is to use MISSILE 2 as the starting point

* It will turn out that the present method needs further work for application at transonic speeds.

of the prediction technique and to make the necessary changes to it to improve hinge-moment prediction.

There are a number of changes or additions required to MISSILE 2, and a list follows.

1. Provide accurate wing-alone center-of-pressure positions as a function of angle of attack as input.
2. Add the capability for determining the effect of free vortices on fin axial center-of-pressure position.
3. Add a better means for extrapolation outside the $AR = 2$ limit of the data base of MISSILE 2.
4. Add a better means of extrapolation above $M_\infty = 3$ in the data base.
5. Change the method of accounting for fin-fin interference.
6. Determine a method for handling fins with swept trailing edges within the framework of MISSILE 2.

Item 1 comes about because the most accurate available means for obtaining $(\bar{x}/c_r)_w$ is needed to predict hinge moments. The most accurate means available differs from case to case so the calculation is done external to the main program. Item 2 is needed because no engineering method for carrying out this task has hitherto existed. Items 3 and 4 are needed because much of the available data for evaluating the method lie above $AR = 2$ and $M_\infty = 3.0$. Also much of the region of interest lies above these values. Item 5 changing the method of accounting for fin-fin interference is incorporated into the program for technical reasons which will be more important in the future. Item 6 is included to increase the configurational range of applicability of the program.

In the following sections, we will describe these above items. We will not, however, give a full description of MISSILE 2 since this information is covered in references 1 and 2.

4.2 Wing-Alone Center-of-Pressure Locations

4.2.1 Introductory remarks.- The wing-alone longitudinal center-of-pressure location is not solely a function of angle of attack, Mach number, and planform, but depends also on the airfoil section or sections used by the wing. There are several options in determining the curve of $(\bar{x}/c_r)_w$ versus α for the wing alone, and this information is generated external to the computer program for convenience. The first and best option is to have experimental data for the wing alone (with the correct wing thickness distribution) and use this directly. In case such data are not available, we have several options open to us. If the leading-edge shock wave is attached at any angle of attack when considering planes normal to the wing planform and parallel to the body axis, then a combination of linear theory (DATCOM), shock-expansion theory and data is used to establish the curve. In case the shock wave is not attached at any angle of attack, only special cases can be handled. Let us consider the attached shock case first.

4.2.2 Attached shock case.- A brief description of the method is given before a detailed explanation of how it is carried out. First, the center of pressure for an infinitely thin wing is determined from DATCOM or elsewhere, and a correction for thickness is obtained using shock-expansion theory. This establishes the center-of-pressure location up to the shock detachment angle of attack, α_{det} . For $\alpha = 45^\circ$ it is assumed that wing section has little effect on \bar{x}/c_r , and an empirical correlation of this quantity is used to establish its value at $\alpha = 45^\circ$. Between α_{det} and $\alpha = 45^\circ$, the curve is

faired by hand using the data for the closest wing of the data base as a guide. We will be considering only wings with symmetric thickness distributions.

To determine if the leading-edge shock of the wing is attached, we need only consider the $\alpha = 0$ case. Let the nose semi-apex angle in the streamwise direction be θ_n , and let the semi-vertex angle of a wedge for shock detachment be θ_{det} . Then if

$$\theta_n > \theta_{det} \quad (1)$$

the shock is detached. If

$$\theta_n < \theta_{det} \quad (2)$$

then the shock is attached for the angle of attack range

$$0 \leq \alpha < \theta_{det} - \theta_n$$

We have chosen to apply shock-expansion theory to planes parallel to the body axis since the flow near the fin-body juncture is principally in this direction. For a swept-back wing of high aspect ratio, simple sweep theory dictates use of simple sweep theory in planes normal to the wing leading edge. However, such wings are not usually used for all-movable controls.

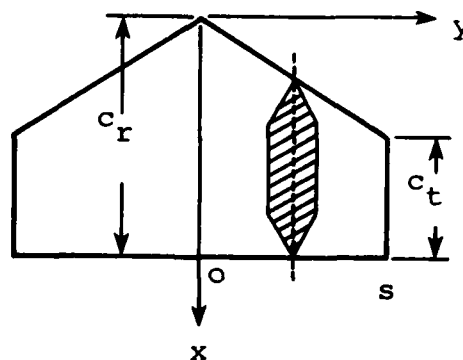
Consider now the determination of the wing longitudinal center-of-pressure position for the shock-attached case. The first step is the determination of the center-of-pressure position for the wing with no thickness using linear theory. For most planforms this quantity is conveniently obtained from DATCOM. For delta wings the center of pressure is always at the $2/3$ root chord. For rectangular wings with effective aspect ratios, βAR , of unity or greater

$$\frac{\bar{x}}{c_r} = \frac{1}{2} \frac{[1 - 2/(3 \beta R)]}{[1 - 1/(2 \beta R)]} \quad (3)$$

For wings, the leading and trailing edges of which are composed of straight line segments, a panel method such as DEMON II, reference 12, can be used. If time and cost permits, DEMON II can be used to determine the fin center-of-pressure in the presence of the body, which can be used rather than that of the wing alone for greater accuracy of prediction.

The second step in determining \bar{x}/c_r is to correct the lifting-surface theory value for wing thickness effects. This correction gives a forward movement of the center-of-pressure position which varies with angle of attack.

Consider now the change in center-of-pressure location due to wing thickness distribution. Let the wing have a straight* trailing edge, and consider the following sketch.



*The derivation is valid for a wing planform composed of any number of straight line segments.

A given streamwise section as shown will be considered to act at the given angle of attack, α , and the given Mach number M_∞ . By shock-expansion theory the section will have a longitudinal center-of-pressure location \bar{x}/c where \bar{x} is measured from the leading edge and c is the local chord. It will also have section lift coefficient $c_\ell(y)$. For no thickness, the local section center of pressure will be at $\bar{x}/c = 0.5$.

Accordingly, the contribution to the moment due to thickness is proportional to $cc_\ell(\bar{x} - c/2)$. The shift in \bar{x} for the entire wing is using strip theory

$$(\Delta\bar{x})_t = \frac{\int_0^s cc_\ell(\bar{x} - c/2)dy}{\int_0^s (cc_\ell)dy} \quad (4)$$

$$\left(\frac{\Delta\bar{x}}{c_r}\right)_t = \frac{\int_0^s \frac{c^2}{c_r} c_\ell\left(\frac{\bar{x}}{c} - \frac{1}{2}\right)dy}{\int_0^s (cc_\ell)dy} \quad (5)$$

To carry out the calculations based on Equation (5), a computer program has been constructed. First the section normal-force coefficient and section center-of-pressure positions are calculated at specified spanwise locations on the wing. The equations to carry out these calculations for the airfoil sections by shock-expansion are given in Appendix B. It is assumed that the airfoil sections are symmetrical and that the surface can be approximated by a connected series of straight line segments. The computer program then carries out the calculation indicated by Equation (5).

At this point we compare the measured center-of-pressure locations of Stallings-Lamb wings (ref. 3) with the predictions of the above method for the angle of attack and Mach number ranges of shock attachment. Comparisons are made for 10 wings from $M_\infty = 1.60$ to 4.60 as follows:

Figure	AR	λ
24	0.5	0
25	1.0	0
26	2.0	0
27	0.5	0.5
28	1.0	0.5
29	2.0	0.5
30	4.0	0.5
31	0.5	1.0
32	1.0	1.0
33	2.0	1.0

The degree of correlation between experiment and prediction is now systematically reviewed.

Considering first Figure 24, it is noted that three sets of information for each Mach number are given; the data, the linear theory, and the linear theory plus thickness correction. The angle of attack for shock detachment increases as the Mach number increases. The thickness correction increases as Mach number increases. Considering Figures 24-26 for all three delta wings, the prediction with thickness correction and the data are in satisfactory agreement. Forward shifts of the center-of-pressure position up to 6 percent of the root chord are exhibited.

Consider now the results for $\lambda = 0.5$ wings in Figures 27 through 30. For $AR = 0.5$ the agreement is not good at all. DATCOM predicts positions generally in front of the experimental center-of-pressure position, and the thickness correction further aggravates the agreement. It is clear that some

phenomenon not accounted for by the theory is involved for the $AR = 0.5$, $\lambda = 0.5$ wing which did not act for the $AR = 0.5$, $\lambda = 0$ wing. There is a strong component of nonlinear normal force proportional to α^2 due to leading-edge and side-edge separation which could act well back on the wing and cause the observed effect. This possibility was not pursued in an attempt to verify it or to improve the prediction method for several reasons. First, $AR = 0.5$ controls are not common. Secondly, for a wing of the same planform but of different thickness distribution, we can use the data of Figure 27 and correct it for thickness distribution. The data of Figure 28 for the $AR = 1.0$, $\lambda = 0.5$ wing exhibit the same disagreement between experiment and theory for $M_\infty = 1.6$ and 2.5, but at the higher Mach number the agreement is much better. The $AR = 2$, $\lambda = 0.5$, and $AR = 4$, $\lambda = 0.5$ wings shows good agreement everywhere in the attached shock regime.

Consider now the $\lambda = 1.0$ wings in Figures 31-33. The $AR = 0.5$ wing shows some disagreement at $M_\infty = 2.86$ but is good at the higher Mach numbers. The $AR = 1$ and 2 wings show good agreement.

In the discussion we have considered two approaches:

Method A: DATCOM plus thickness corrections

Method B: Use the data with corrections to account for any change in thickness distribution.

For wings of various taper ratio, the method is now summarized.

- | | | |
|----|-----------------|---|
| 1. | $\lambda = 0$ | Method A |
| 2. | $\lambda = 0.5$ | $\left\{ \begin{array}{ll} AR = 0.5: & \text{Method B} \\ AR = 1: & M_\infty < 3 \quad \text{Method B} \\ & M_\infty > 3 \quad \text{Method A} \\ AR = 2, 4: & \text{Method A} \end{array} \right.$ |
| 3. | $\lambda = 1.0$ | $\left\{ \begin{array}{ll} AR = 0.5: & M < 3.0 \quad \text{Method B} \\ & M > 3.0 \quad \text{Method A} \\ AR = 1, 2: & \text{Method A} \end{array} \right.$ |

Above the angles of shock detachment from the wing leading edge, the center-of-pressure position tends toward the centroid especially at very high angles of attack. If a value of \bar{x}/c_r for a wing at some large angle of attack such as 45° were known, then the values given by the above method for the range of shock attachment could be faired to the $\alpha = 45^\circ$ value to obtain an estimate over a broad angle-of-attack range. With this approach in mind, the center-of-pressure positions for $\alpha = 45^\circ$ have been plotted versus Mach number for $M_\infty \geq 1.6$ in Figure 34 for the wings of the Fidler-Baker data base (ref. 5) and the Stallings-Lamb data base (ref. 3). Curves have been faired through the data of the Stallings-Lamb data base for design purposes. The Stallings-Lamb wings were chosen because the Fidler-Baker wings were tested as semispan models on a reflection plane and may be affected by boundary-layer separation at high angles of attack. In any event, there is not much difference between the two sets of data in Figure 34. It is noted that the effect of M_∞ is small in the range of 1.6 to 4.6 shown in the figure. For the $\lambda = 1$ wings the center of pressure is somewhat forward of $\bar{x}/c_r = 0.5$, the centroid position. For the $\lambda = 0$ wings it is also forward of 0.667, the centroidal position.

Consider now results for \bar{x}/c_r at $\alpha = 45^\circ$ for $M_\infty \leq 1.6$ as shown in Figure 35. The results for $AR = 0.5$ shown in Figure 35(a) show definite effects of Mach number on \bar{x}/c_r below a Mach number of unity. An effect of wing section on \bar{x}/c_r at $\alpha = 45^\circ$ in the lower transonic range, $M_\infty = 0.6$ to 1.0, is evident for the $\lambda = 0.5$ wing. For $AR = 1$ the wings of Figure 35(b) show a significant effect of wing section for the $\lambda = 1$ wings only (around $M_\infty = 1.0$). The same is true for the $AR = 2$ wings data shown in Figure 35(c). Whether this effect is a true transonic effect or is due to problems of testing a semispan model on a reflection plate is not known.

For help in estimating the \bar{x}/c_r positions for a wing which has an angle-of-attack region of attached flow at the leading edge in the supersonic range, the data in Figures 34 and 35 is presented in tabular form in Table 1. This table includes the $AR = 4$ results not given in the figures but which are needed for wings with $AR > 2$. The data are sufficient to cover the range $0.5 \leq AR \leq 4.0$ and $0 \leq \lambda \leq 1.0$. For wings which do not fall on the precise values of AR and λ of the wings in the data base, interpolation is to be used. Generally, interpolation is best done linearly in taper ratio, inversely as aspect ratio, and inversely as $\sqrt{M_\infty^2 - 1}$. Normal-force curves for the Fidler-Baker data base are available in reference 5, and normal-force curves for the Stalling-Lamb wings are available for $M_\infty \geq 1.6$ in reference 3. Tabulated normal-force coefficients for the 10 Stalling-Lamb wings are given in Table 2 for $M_\infty \geq 1.6$.

4.2.3 Detached shock case.— The detached shock case covers all wings for which the shock is not attached to the leading edge for any angle of attack when considering two-dimensional flow in streamwise planes normal to the wing planform and parallel to the root chord. The leading edge semiapex angle for which the shock wave detaches at $\alpha = 0^\circ$ is given in Figure 36.

We have seen that wing thickness effect can have a large influence on the axial center-of-pressure position when the leading-edge shock is attached. When the leading-edge shock is not attached even at $\alpha = 0^\circ$ the data at $M_\infty = 1.6$ in Figures 26 and 29-33 still exhibit large effects of wing thickness (airfoil section) on axial center-of-pressure position. Let us now inquire how we might determine this quantity theoretically.

Linear theories based on the wave equation for determining the center-of-pressure position of a wing alone with or without thickness at supersonic speed are well known.

However, we know that the use of linear theory to obtain the velocity field combined with Bernoulli's equation to calculate the pressure does not accurately account for thickness effects on $(\bar{x}/c_r)_w$ for attached leading-edge shocks. There is thus no promise this procedure will do so for detached shocks. In fact, no proven method is now available for determining thickness effects on \bar{x}/c_r for detached shocks. A method based on the Euler equations has promise but is not currently available. Thus, we must rely for the present on experiment.

With respect to the experimental approach, there seems only a few alternatives available. First one might use a fin for which the wing alone corresponds closely to one of the wings of the Fidler-Baker or Stallings-Lamb data bases or may be found by interpolating within them. Again the fin may correspond to a wing alone for which data are otherwise available. As a final resort, one could measure the properties of the wing alone in a wind tunnel.

4.3 Effect of Vortices on Fin Axial Center-of-Pressure Position

4.3.1 Panel method approach.- Body or canard vortices can have a significant effect on the hinge moment of an all-movable control if they pass in close proximity to it. This can occur when a fin is rolled well up into the first or second quadrants at the moderate to large angles of attack for which body vortices exist. It can also occur when the vortices from canard fins pass near an empennage. It is not known how to determine the effect of such vortices on axial center-of-pressure position using reverse-flow methods as is possible for normal force and lateral center-of-pressure position. We are therefore interested in developing a simple means for determining the effect of vortices on axial center-of-pressure positions.

In order to gain the necessary insight to model the phenomenon in question, we will make calculations using a panel method (ref. 12) to study the vortex effects. For this purpose we have chosen the configuration shown in Figure 37 for which fin data are available in reference 37. In the figure comparison is made between data and the prediction of the panel method for fin normal-force coefficient, root bending-moment coefficient, and hinge-moment coefficient. The comparisons, for $M_\infty = 1.6$ for fin deflections of 0° and -15° , show excellent agreement for fin normal force and bending moment but not for hinge moment. The $\phi_f = 45^\circ$ results include significant body vortex effects, and the $\phi_f = 135^\circ$ results are free of such effects. Nevertheless the hinge-moment results for the $\phi_f = 135^\circ$ fins are not well predicted. This result is associated with the fact that panel methods do not properly account for the second-order effects of thickness on axial center-of-pressure locations as discussed previously. (This configuration will be discussed subsequently with such second-order effects accounted for.) We feel, however, that the increment in wing loading due to the body vortices is probably well predicted by the panel method.

In order to obtain accurate axial center-of-pressure positions one might inquire how many chordwise panels are required. A systematic set of calculations has been made varying the number of chordwise panels from 3 to 7, while keeping the number of spanwise rows equal to 5. The calculations were made for the example configuration of the previous figure for the leeward fin at $\phi_f = 45^\circ$. Calculations were made with and without body vortices. The vortex strengths and positions were estimated from correlation curves in reference 17. Figure 38 presents the results of the calculations for the center-of-pressure positions with and without body vortices plotted versus $1/n$, where n is the number of chordwise panels. It is noted that without vortices the value of \bar{x}/c_r

is close to that obtained from DATCOM for all values of l/n . The body vortices cause about a 3.5 percent forward shift in the fin center-of-pressure position for all values of l/n , a shift which can significantly influence hinge moment.

A series of calculations has been made for the same conditions as those of Figure 38, but the fin taper ratio has been varied from $\lambda = 0$ to 0.423 to 1.0 with a fixed exposed semi-span of 11.43 as shown in Figure 37. The results plotted in Figure 39 form the basis for the simplified method of determining vortex effects on fin axial center-of-pressure position. Figure 39(a) for $\lambda = 0$ shows the local center-of-pressure positions at five spanwise stations with and without body vortex effects. The lines joining these positions are nearly straight and can be thought of as lifting lines. Consider now the wing center of pressure without vortices and the center of pressure of the vortex normal force. The vortex normal-force center of pressure is inboard and lies close to the lifting line without vortex effects. Since the vortex induced normal force is downward, the fin center of pressure is moved aft by vortex effects.

Examine now figure 39(b) for a fin with $\lambda = 0.423$. The results are qualitatively similar to those for $\lambda = 0$, and a significant shift of the fin center of pressure in a rearward direction is due to the body vortices. Examine now Figure 39(c) for the rectangular fin with the same exposed semispan as the other fins. The lifting lines are now essentially unswept, and the lifting line for no body vortex effects is not straight. The center of pressure of the vortex normal force lies slightly behind this lifting line, unlike the situation for the other two cases. However, because the lifting lines are nearly unswept, the effect of the vortices on axial center-of-pressure location is only about 1 percent of the root chord.

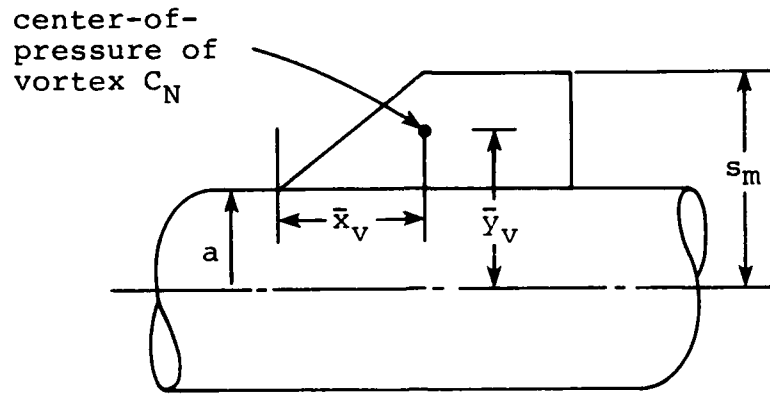
4.3.2 Approximate engineering method.— The foregoing results suggest assumptions that lead to a simple method for determining the effect of the vortices on fin center-of-pressure positions. It is first assumed that the lifting line is a straight line passing through the fin center-of-pressure position without vortex effects at a constant percent local chord. It is also assumed that the center of pressure of the vortex normal force lies on this lifting line. We can get an idea of the degree of approximation of this assumption from the following values for three cases of Figure 39 for the center-of-pressure locations in terms of percent local chord.

λ	$(x - x_{le})/c$ No Vortices	$(x_v - x_{le})/c$
0	0.452	0.423
0.423	0.459	0.427
1.00	0.439	0.491

c = local chord through center of pressure

We have values for the coordinates of \bar{x}, \bar{y} of the fin center-of-pressure position with no vortex effect from the computational method. We obtain \bar{y}_v due to the loading induced on the fin by the vortex (vortices) in the program using reverse flow methods. Knowing the value of $(x_v - x_{le})/c$ by the above assumption and knowing \bar{y}_v , we have fixed \bar{x}_v .

We now list the steps required to determine the center of pressure of the vortex induced normal force as a fraction of the root chord $(\bar{x}/c_r)_v$.



1. Determine the lateral center-of-pressure position of the vortex normal force, $(\bar{y}/a)_v$, from MISSILE 2 as now constituted.

2. Determine $(\bar{x}/c_r)_{W(B)}$ by the methods discussed in the previous section (section 4.2) for C_{NF} with no vortices.

3. Determine the lateral center of pressure of the fin (with or without deflection) and with no vortex effects $(\bar{y} - a)/(s_m - a)_{W(B)}$ by interpolating or extrapolating in the results of Program MISSILE.

4. Determine the local fractional chord τ of the fin center of pressure with no vortex effects from

$$\tau = \frac{\left(\frac{\bar{x}}{c_r}\right)_{W(B)} - (1 - \lambda) \left(\frac{y - a}{s_m - a}\right)_{W(B)}}{1 - (1 - \lambda) \left(\frac{y - a}{s_m - a}\right)_{W(B)}}$$

5. Determine the percent root chord corresponding to the axial position of the normal force induced on the fin by the vortices, $(\bar{x}/c_r)_v$.

$$\left(\frac{\bar{x}}{c_r}\right)_v = \tau + (1 - \tau)(1 - \lambda) \left(\frac{y - a}{s_m - a}\right)_v$$

We know the normal force induced on the fin by the vortices and we are now in a position to determine its contribution to the hinge-moment coefficient. It is

noted that in this approximate method the normal force and hinge moment induced by the body vortices go to zero together. No induced camber effects can be handled.

4.4 Other Changes in Program MISSILE

4.4.1 Introductory remarks.- We have made a number of changes in MISSILE 2 for more accurate calculation of hinge moments. The first major change is that we now require as input a table which gives the wing-alone axial center-of-pressure position as a function of fin normal-force coefficient as well as the normal-force coefficient as a function of angle of attack. Methods of interpolating or extrapolating in the wing-alone data base to obtain this information for a wing not in the data base are given below. Methods for extrapolating the fin normal force with no vortex effects as given in the data base to high aspect ratios and high Mach numbers have been improved. Also, the application of the equivalent angle of attack concept* has been modified to account for vortex effects prior to accounting for fin deflection effects. The two effects are commutative only for a linear normal-force curve. Finally, improvements have been made in the treatment of fin-fin interference due to control deflection using the equivalent angle of attack concept based on certain physical arguments.

4.4.2 Wing-alone characteristics as input data.-

1. Effect of Mach number on normal force. In case we do not have data for the wing alone at the conditions of interest, we may choose to interpolate (or extrapolate) in the Fidler-Baker or the Stallings-Lamb data bases. Such interpolations may be made with respect to AR , λ , or M_∞ . With regard to extrapolating above $M_\infty = 3.0$ in the Fidler-Baker data

* See Appendix C for a description of the equivalent angle-of-attack concept.

base, the Stallings-Lamb data base which goes up to $M_\infty = 4.6$ sheds light on this question. In Figure 40 the wing normal-force coefficient from Table 2 has been plotted versus M_∞ for constant angle of attack for wings with $AR = 0.5$, $\lambda = 1$, and $AR = 4.0$, $\lambda = 0.5$ as extreme cases. Straight line projections have been drawn through the $M_\infty = 2.16$ and 2.86 data points to illustrate the accuracy of straight-line extrapolation to higher Mach numbers. It is clear that significant errors can be made if such extrapolation is carried out very far above $M_\infty = 3.0$.

A better extrapolation means should take advantage of the known fact that the aerodynamic coefficients change slowly with Mach number and become asymptotic as $M_\infty \rightarrow \infty$. A parameter which has this property is $(M_\infty^2 - 1)^{-1/2}$. The data of Figure 40 have been plotted versus $(M_\infty^2 - 1)^{-1/2}$ in Figure 41. Extrapolating to higher Mach numbers based on the $M_\infty = 2.16$ and 2.86 data shows great improvement in accuracy over the linear extrapolation. As a consequence we have used this type of interpolation in the computer program for data above $M_\infty = 3$ for both the wing alone and the fin in the presence of the body. The linear interpolation is retained within the Mach number range of the fin-on-body data base, $0.8 \leq M_\infty \leq 3.0$.

If the Mach number, aspect ratio, and taper ratio do not correspond to values in the wing-alone data base, it is suggested that linear interpolation be performed in the data base. The three closest wings to the subject wing are selected, and their characteristics are interpolated to the correct Mach number before the aspect-ratio, taper-ratio interpolation. If the Mach number of interest is outside the realm of the data base, that Mach number extrapolation is done as described above before aspect-ratio, taper-ratio interpolation.

2. Effect of Mach number on axial center-of-pressure location. A study similar to that for extrapolation of normal force has been carried out for extrapolation of axial

center-of-pressure location. The results are shown in Figures 42 and 43. They show that axial center-of-pressure positions cannot be extrapolated in Mach numbers above 3 with confidence either linearly or as $1/\sqrt{M_\infty^2} - 1$. Generally, the methods of predicting \bar{x}/c_r previously described should be relied on. For $M_\infty > 3$ practically all wings will have a region of attached leading-edge shock waves.

3. Extrapolation of normal-force coefficient for $AR > 2.0$. There is a requirement to extrapolate the wing alone and fin-on-body normal-force coefficients to aspect ratios greater than 2. Since, for a given angle of attack, normal-force coefficient becomes asymptotic to the two-dimensional value as $AR \rightarrow \infty$, it is not accurate to extrapolate linearly in AR without limit. Instead, extrapolation in $1/AR$ has the correct asymptotic behavior. Consider that data are available for $AR = 1$ and $AR = 2$ and we desire the extrapolation to $AR > 2$. We can use the Stallings-Lamb data of Table 2 to test our extrapolation scheme for $\lambda = 0.5$ since data are available to $AR = 4$. Wing-alone normal-force coefficient is plotted versus $1/AR$ for constant α in Figure 44 for two Mach numbers for $\lambda = 0.5$ wings. It is seen that straight line extrapolation predicts the $AR = 4$ results quite well in all cases.

4. Extrapolation of axial center-of-pressure position for $AR > 2$. Plots were made similar to Figure 44 to test the feasibility of extrapolating axial center-of-pressure results to aspect ratios greater than $AR > 2$. The Stallings-Lamb wing data for $\lambda = 0.5$ and $M_\infty = 1.6$ and $M_\infty = 3.5$ are plotted versus $1/AR$ in Figures 45(a) and 45(b). The lines connecting the $AR = 1$ and $AR = 2$ data extended to $AR = 4$ sometimes provide a good prediction and sometimes do not. Accordingly, we do not recommend extrapolating axial center of pressure in aspect ratio.

5. Interpolation of wing-alone C_N and \bar{x}/c_r in wing taper ratio. The question of interpolating in a data base to obtain wing alone or fin-on-body C_N and \bar{x}/c_r for values of λ not in the data base arises in preparing input data for the program and in the program itself in obtaining fin-on-body normal force. Generally, values of λ run from 0 to 1.0, and the question of extrapolating to values greater than 1 does not arise. Data exist for the Stallings-Lamb wings to show the effect of λ on the measured aerodynamic quantities for $R = 0.5, 1.0, \text{ and } 2.0$. We show the effect of λ on wing C_N for $R = 2$ wings in Figure 46 for $M_\infty = 1.6$ and $M_\infty = 3.50$. The curves drawn through the data have very little curvature so that straight line interpolation between data points is sufficiently accurate for our purposes.

Considering now axial center-of-pressure position, this quantity is shown for the same parameters in Figures 47(a) and 47(b). Curves are faired through the data. Straight lines between the data points deviate from the faired curves by less than 0.01. Thus, linear interpolation in λ for \bar{x}/c_r should be adequate for hinge-moment purposes in most cases.

4.4.3 Interpolation and extrapolation for the fin-on-body data base.- The fin-on-body data base is needed solely for finding the normal force of the fin on the body including all interference effects except body vortices; it is not used to determine the axial center-of-pressure location of the fin on the body. Accordingly, we are interested only in interpolation or extrapolation with respect to fin normal-force coefficient. Much of section 4.4.2 applies to this question because under the equivalent angle-of-attack concept a parallelism has been set up between the nonlinear characteristics of the wing alone and the fin in the presence of the body.

Consider the aspect ratio, Mach number domain of the present data base shown in Figure 48. The aspect ratio-Mach number combinations for which data are available in the present data base are shown as circles, and the domain of the present data base is contained within the boundary enclosing these circles. The dotted boundary is that for a tri-service effort presently underway which can be used to extend the domain of application of the present effort at a later date (ref. 38).

With regard to interpolation within the present data base, we retain linear interpolation in M_∞ , \mathcal{AR} , and λ as in MISSILE 2. However, the new feature added to the hinge-moment program is the ability to extrapolate in \mathcal{AR} and M_∞ in the directions shown in the figure by a more accurate means. The extrapolation in aspect ratio is done inversely on \mathcal{AR} . The extrapolation with respect to M_∞ has been done proportional to $(M_\infty^2 - 1)^{-1/2}$.

Another change has been introduced into the hinge-moment program. In Program MISSILE an approximate wing-alone C_N data base has been built into the program. This together with the fin-on-body C_N data base gives values of K_W used in the equivalent angle-of-attack method. Since for the hinge-moment program the wing-alone normal-force curve is input data, it is necessary to reevaluate K_W . This is done internal to the program. Since wing-alone normal force is not influenced greatly by airfoil section, this change should not influence the calculated hinge moment very much (except at transonic stall) and is done for internal consistency.

The present model for the strengths and positions of the body vortices includes Mach number up to 3.0. For higher Mach numbers linear extrapolation is used based on the $M_\infty = 2$ and $M_\infty = 3$ results.

4.4.4 Changes in implementation of equivalent angle-of-attack concept.- We will now describe two changes in the implementation of the equivalent angle-of-attack concept which have been incorporated into the hinge-moment program and which are not in MISSILE 2. A detailed description of the equivalent angle of attack with instructions for its use are given in reference 38.

Briefly the equivalent angle of attack is the angle of attack of the wing alone for which it has twice the normal force of the fin in the presence of the body. The equivalent angle of attack of the fin depends on body upwash (angle of attack and roll angle), body vortex induced downwash on the fin, and wash induced on the fin by deflection of other fins. The equivalent angle of attack depends on the order of application of the vortex effects and fin deflection effects because the fin-fin interference factors entering the method depend on angle of attack. In Program MISSILE the body vortex effects were imposed after the fin deflection effects. In this hinge-moment program this procedure has been reversed. The fin-fin interference factors for use in the method can then be determined from wind-tunnel data without first removing body vortex effects from the data, a process of some uncertainty.

The second change made in anticipation of the tri-service data base is simplification of the fin-fin interference treatment. In Program MISSILE the effect of panel deflections on the equivalent angle of attack of a particular panel was obtained by a tangent addition theorem which did not permit the equivalent angle of attack to exceed 90° . However, it is clear that fin deflection increases the fin equivalent angle of attack linearly and that an equivalent angle of attack greater than 90° is possible. Thus, if $\hat{\alpha}_{eq_i}$ is the equivalent angle of attack of fin i with no fin deflection and α_{eq_i} is that with all fins deflected, then

$$\alpha_{eq_i} = \hat{\alpha}_{eq_i} + \sum_{j=1} \Lambda_{ij} \delta_j$$

where Λ_{ij} are fin-fin interference factors. For instance, Λ_{ij} is the amount the equivalent angle of attack of fin i is increased by unit deflection of fin j . The factor Λ_{ii} should be close to unity. Theoretical values of Λ_{ij} obtained from slender-body theory (ref. 1) are now used in the hinge-moment program with corrections for how much of fin i lies within the zone of influence of fin j . The zone of influence correction is also used in the present version of MISSILE 2.

5. FINS OF GENERAL PLANFORM

As a result of the present study, a method can be specified for application to fins of general planform. The method will be described for possible future development and verification.

By a fin of general planform we mean one for which the leading, trailing, and side edges can be approximated by straight line segments. The airfoil sections should be such that their contours can be approximated by straight line segments. Its leading edges should be sharp.

The method is meant to apply only to the range of leading-edge shock attachment in $\alpha - M_\infty$ space. The criterion for shock attachment shall be applicability of shock-expansion theory in planes normal to the fins and parallel to the body axis.

The first task in the method is to determine the normal-force coefficient and axial center of pressure for the wing alone using the panel theory of reference 12 with no thickness effects in the calculation. These quantities are determined up to an angle of attack of about 20° . Some nonlinearities are accounted for by the method. Then the shock-expansion

theory computer program to determine the shift in axial center-of-pressure position due to wing thickness is applied. This establishes the axial center-of-pressure position up to leading-edge shock detachment. An estimate of \bar{x}/c_r at $\alpha = 45^\circ$ is made next. This is done by determining the wing planform centroid, and then subtracting an estimated quantity from it using the results of Figures 34 and 35 as a guide. A hand fairing between the results of shock-expansion theory and that for $\alpha = 45^\circ$ is then made.

The second main task is to choose an equivalent wing in the fin-on-body data base to replace the general planform in determining the normal force on the fin in the presence of the body. (If the angle of attack range is below 20° , we can circumvent this step by using the panel program for the wing-body combination to calculate this quantity directly.) However, if we desire to use the engineering method, we must choose an equivalent wing for normal force in the following way.

1. The normal force of the equivalent clipped delta wing should equal that of the wing of general planform at the same angle of attack and Mach number.

$$S_e C_{N_e} = S_f C_{N_f}$$

S ~ reference area

e ~ equivalent wing

f ~ wing of general planform

2. The exposed semispans shall be equal.

The first requirement is based on the assumption that if the wing-alone normal forces have the same magnitude, then the normal forces acting on the corresponding fins on the body will be the same. The assumption is suggested by the following arguments. The normal force on a fin in the presence of the body is related to that on the fin as part of the wing alone

by a factor K_w which depends principally on the a/s_m ratio independent of planform. This condition is met by having the fin of general planform and the equivalent fin have the same exposed semispans. Also the effect of body vortices on the fin normal force depends on a reverse flow method which uses weighting factors depending only on a/s_m and which are independent of planform. In applying the first rule it may be enough to match normal-force curve slope times reference area. The whole purpose of the "equivalent wing" is to use the fin-on-body data base in the program to get an estimate of the normal force of the fin of general planform mounted on the body. Any considerations of planform on axial center-of-pressure position are extraneous since this is handled through the wing-alone data which are input.

The third main task in the procedure is to apply MISSILE 2 as modified to the problem using the equivalent wing to get fin normal-force coefficient. This quantity and the axial center-of-pressure position estimated for the fin of general planform then yield the hinge-moment coefficient. In case the fin-on-body normal forces are calculated by the panel program, the axial center-of-pressure position estimated for the fin of general planform should still be used in calculating the hinge moment rather than that from the panel program. In this step a refinement may be necessary. It may be necessary to determine the incremental distance between the axial center-of-pressure positions of the vortex normal force and normal force without vortices present by using the panel method. The normal force for no vortices would then be applied at the axial center-of-pressure position estimated for the fin of general planform and the vortex normal force would be applied at the incremental distance from this position determined on the basis of the panel method.

At the present time it is not clear how to treat the fin of general planform in the case where the shock is detached from the leading edge at zero angle of attack unless experimental wing-alone data on normal force and axial center-of-pressure positions are available.

6. COMPARISON OF EXPERIMENTS AND THEORY

6.1 Introductory Remarks

Comparisons will be made between prediction and experiment for a number of cases to investigate the accuracy and range of applicability of the method. The range of applicability will be defined in terms of wing aspect ratio, wing taper ratio, angle of attack, fin deflection, and Mach number. In addition, roll angle is a parameter. The configurations will be principally cruciform wing-body combinations although we also consider an exploratory application to a wing-body-tail combination.

Two sets of data are particularly useful for making the comparisons. The first set is that of Lamb and Trescot (ref. 39) and of Lamb, Sawyer, Wassum, and Babb (refs. 37, 40, and 41). These data are particularly interesting because the fin pressure distributions are available to diagnose any significant differences between experiment and theory. The configurations investigated are shown in Figure 49. The second set of data is that for the Army Generalized Missiles described in reference 42 and shown in Figures 50 and 51. While no pressure distribution data are available, there are fin force and moment data for wing-body and wing-body-tail combinations for several different fins at a number of roll angles and at subsonic and supersonic speeds. Other data exist in the public domain, but they are not so extensive nor so systematic as the foregoing sources. We start by considering the first set of data.

6.2 Data of Lamb and Trescot

6.2.1 Wing-alone characteristics.- Comparisons will be shown for fin B of Figure 49 at Mach numbers of 1.6, 2.35, and 3.7. The first task is to find the wing-alone values of C_N and \bar{x}/c_r for this fin at the various Mach numbers for input into the program. To obtain the normal-force characteristics, we have used interpolation in the Stallings-Lamb data base (ref. 3). The geometric parameters for fin T_B are:

$$AR = 2.812$$

$$\lambda = c_t/c_r = 0.423$$

$$a/s_m = 0.25$$

$$x_{HL}/c_r = 0.589$$

The normal-force curves of the Stallings-Lamb data base have been fitted by least squares with a truncated sine series of the following form.

$$C_N = A_1 \sin \alpha + A_2 \sin 3\alpha + A_3 \sin 5\alpha$$

The values of the coefficients A_1 , A_2 , and A_3 are given in Table 3. Good fits to the data were obtained in all cases. To obtain the values of A_1 , A_2 , A_3 for T_B , linear interpolation in aspect ratio between the $AR = 2$, $\lambda = 0.5$, and $AR = 4$ and $\lambda = 0.5$ wings was used. The taper ratio effect was obtained by linear interpolation between the $AR = 2$, $\lambda = 0$ wing and the $AR = 2$, $\lambda = 0.5$ wing. Linear interpolation between Mach numbers was used for the particular Mach numbers 1.60, 2.36, and 3.70. The normal-force curves so obtained are shown in Figure 52.

To obtain the wing-alone center-of-pressure positions for T_B , interpolation was also made in the Stallings-Lamb data base. As has been previously pointed out, the wing-alone axial center-of-pressure position is influenced by airfoil section.

Therefore, the dimensions of equivalent wing of the Stallings-Lamb data base for $AR = 2.812$ and $\lambda = 0.423$ were found by linear interpolation. The semiapex angle normal to the leading and trailing edges of the data base wing is 15° while for fin T_B , it is 13.1° . Since the wings are fairly close, it was decided not to correct the interpolation data for center-of pressure positions. Also, shock-expansion theory will not go through at $M_\infty = 1.60$ because the leading-edge shock is always detached. The resulting center-of-pressure curves are shown in Figure 53. The data from Figures 52 and 53 go into the computer program as input.

6.2.2 Comparison of experiment and theory.- Comparisons have been made between prediction and data for fin T_B for the following matrix of conditions:

$$M_\infty = 1.6, 2.36, \text{ and } 3.70$$

$$0^\circ < \alpha < 20^\circ$$

$$\delta = 0^\circ, -15^\circ$$

$$\phi_f = 45^\circ, 90^\circ, 135^\circ$$

Consider first the $M_\infty = 1.60$ results shown in Figure 54. The results for the horizontal fin position ($\phi_f = 90^\circ$) as shown in Figure 54(a) and 54(b) show good agreement for both fin normal-force and hinge-moment coefficients for $\delta = 0$ and -15° . The same quantities for the windward fin location ($\phi_f = 135^\circ$) are shown in Figures 54(c) and 54(d). The $\delta = 0^\circ$ results are in good agreement, but the $\delta = -15^\circ$ results are not good in the high angle-of-attack range. This effect appears to be the result of fin unporting in the wing-body juncture. We will subsequently discuss this phenomenon. Consider the comparison for the fin on the leeward side of $\phi_f = 45^\circ$ shown in Figures 54(e) and 54(f). For $\delta = 0$ the normal-force results are nonlinear and in fair accord with experiment suggesting that the vortex effects have been fairly well modeled for normal force. For $\delta = 0$ the hinge-moment nonlinearities are somewhat

stronger than predicted. For $\delta = -15^\circ$ both C_{NF} and C_{HM} are well predicted at low α but neither is well predicted at high α .

We now consider what the pressure distributions show concerning the behavior of fin T_B for $\phi = 135^\circ$ and $\delta = -15^\circ$ as shown in Figures 54(c) and 54(d). To obtain an idea of the upwash distribution at the fin location with no fin present, we have calculated it using the supersonic linear theory for the body alone. Body vortex effects are negligible for $\phi_f = 135^\circ$. The resultant local angles of attack with respect to the fin chord plane are shown in Figure 55 for $\delta = 0$ and $\delta = -15^\circ$. The pressure distributions from reference 37 are shown in Figure 56 for the upper and lower surfaces at 0.02 and 0.22 of the exposed semispan. Inspecting first the pressure on the leading edge wedge for $y/s = 0.02$, we note that the upper surface has pressures about equal to those of the lower surface despite a calculated upwash angle of 10° . This result corresponds to nearly zero local angle of attack rather than the predicted angle. Behind the $x/c = 0.2$ location, the data show a more normal behavior with regard to the magnitude of the pressure distributions on the upper and lower surfaces. However, they do not show uniform pressure on the flat surfaces. Inspecting the pressure distributions for the $y/s = 0.22$ station reveals the pressure distributions to be similar to what might be expected for the airfoil at a slight positive angle of attack. It thus appears some wing-body juncture phenomenon occurs which nearly disappears by $y/s = 0.22$. It is suspected this is a local gap effect associated with unporting and possibly separation of the boundary layer. However, pressure distributions at the next higher Mach number, $M_\infty = 2.36$, show that the nonlinear effect has substantially disappeared.

Curves directly analogous to those of Figure 54 for $M_\infty = 1.6$ are plotted in Figure 57 for $M_\infty = 2.36$ and in

Figure 58 for $M_\infty = 3.7$. The predictions for $M_\infty = 3.7$ involved extrapolating in M_∞ out of the present fin-on-body data base. We now look at the various cases as a function of Mach number to see how the nonlinearities exhibited at $M_\infty = 1.6$ change with Mach number.

Comparing parts (a) of Figures 54, 57, and 58, we see that the prediction of C_{NF} for all Mach numbers are fairly good except that the $\delta = -15^\circ$ case shows more download in the low α range than predicted. The difference between the $\delta = 0$ and $\delta = -15^\circ$ normal forces are associated with the fin interference factor for deflection, k_w , which is known to vary with α and δ , but no data base for this variation is yet available. It is planned to obtain such data in the tri-service study (ref. 38).

Consider now parts (b) of the figures. We see that hinge-moment coefficients are fairly well predicted, and that the hinge-moment curves are more nonlinear than the normal-force curves as a result of movements in \bar{x}/c_r with changes in C_{NF} .

Consider now the fin rolled to the windward side of the body with $\phi_f = 135^\circ$, and examine the normal-force curves of parts (c) of the figures. The fin normal-force coefficient at $M_\infty = 1.6$ and 2.36 is well predicted for $\delta = 0$ but is underpredicted for $M_\infty = 3.7$. This probably is the result of the large extrapolation. What is of interest is that the change of C_{NF} between $\delta = 0$ and $\delta = -15^\circ$ is underpredicted by the calculation. At the two higher Mach numbers 15° of deflection produces more normal force than 15° of angle of attack with $\delta = 0$. This again points to the desirability of building a k_w data base into the prediction method when it becomes available. Another method of improvement based on the panel method will be subsequently discussed.

Consider now parts (d) of the figures which show hinge-moment comparisons for $\phi_f = 135^\circ$. For $\delta = 0$ the prediction of hinge-moment coefficient is within expected accuracy. However, for $\delta = -15^\circ$ the predictions are satisfactory only at low angles of attack. A means of improving the accuracy of prediction for the higher angle of attack range for $\phi_f = 135^\circ$ will be described subsequently.

Consider now parts (e) of Figures 54, 57, and 58 which show the predicted and measured fin normal-force coefficients for $\phi_f = 45^\circ$. The $M_\infty = 1.6$ comparisons for $\delta = 0$ are good, but the predictions for $\delta = -15^\circ$ are not good at the higher angles of attack. The $M_\infty = 2.36$ and 3.7 predictions are not good at all. The reason for the discrepancy is not known.

The hinge-moment results for the leeward fin at $\phi_f = 45^\circ$ are shown in parts (f) of the three figures for $M_\infty = 1.6$, 2.36 , and 3.7 . The predictions are good only for $\delta = 0$ at low angles of attack, but otherwise are not satisfactory.

Some calculations have been made with the supersonic panel method of reference 12 at $M_\infty = 1.60$ to study further the problems of predicting fin-normal forces and hinge moments for the subject wing-body combination. In these calculations the fins were treated as lifting surfaces, with seven chordwise and five spanwise rows of panels on each fin. Calculations were made for $\phi_f = 45^\circ$ and 135° , for $\delta = 0^\circ$ and -15° , and for $\alpha = 0^\circ$, 15° , and 20° , a total of 12 cases. The results of these calculations are compared with the data of reference 39 in Figure 37. What is immediately clear is that for nearly all cases the fin normal-force coefficient and the fin bending-moment coefficient are predicted well by the panel theory which uses the same vortex strengths and positions as the engineering prediction method. However, hinge-moment coefficients are not satisfactorily predicted. The reason that the hinge-moment coefficients are not well predicted is that the panel theory

does not give accurate axial center-of-pressure positions. An important reason for this shortcoming is that it does not account for second-order effects of thickness on \bar{x}/c_r .

The panel method yields good normal-force coefficients at $\phi_f = 45^\circ$ and 135° even at angles of attack up to 20° where the engineering prediction method does not. It is natural, then, to try to calculate the hinge moments by a hybrid method using the panel-method normal-force coefficient and the experimental values of \bar{x}/c_r for the wing alone. This is certainly promising for the windward fins when no vortex effects of any significance occur. Consider now Figure 59 which is a reproduction of Figures 54(d), (e), and (f). Figure 59(a) shows that the hinge-moment coefficient at $\phi_f = 135^\circ$ and $\delta = -15^\circ$ is much better predicted by the hybrid method than by the engineering prediction method. Excellent agreement is still not achieved at large angles of attack probably because of the unporting effect discussed in connection with Figures 55 and 56.

In principal the hybrid method as used for the windward fins does not apply to the leeward fin ($\phi_f = 45^\circ$) because the fin normal-force increment due to body vortex effects acts at a different position than that of the normal force without vortices present. For $\delta = 0$ the engineering method does a good job of calculating normal force and the panel method does not at high α , see Figure 59(b). The fact that the panel method does a good job of calculating normal force at $\delta = -15^\circ$ is thus an anomaly. Hence, do not think the hybrid method is reliable for leeward fins near the vortex.

In summary, the engineering method appears to predict hinge moments for $\phi_f = 90^\circ$ well enough to give trends with α , δ , and M_∞ . For the windward fins at $\phi_f = 135^\circ$, a hybrid method based on the panel method and the engineering method yields improved accuracy. At high angles of attack with negative deflection ($\delta = -15^\circ$) and large angles of attack,

15°-20°, satisfactory predictions have not been made for leeward fins. It is to be remembered that the data base has been extrapolated both in aspect ratio and Mach number. Additional comparisons are made in the next section.

6.3 Comparisons for Army Generalized Missile

6.3.1 Preliminary remarks.- A considerable number of comparisons have been made for the Army Generalized Missile, the body of which is shown in Figure 50. We will consider results for two canard fins and one tail fin shown in Figure 51 from tests described in reference 42. Fin C_4 was mounted at the mid hinge-line position and C_6 at the aft hinge-line position for the canards as shown in Figure 50. Tail fin T_2 was mounted at the mid hinge-line tail position. Comparisons will be made for the tail fins with and without the canard fins present.

It is helpful to tabulate the various conditions for which comparisons have been made before getting into the details.

Model	M_∞	ϕ	δ_c
B_1C_4	1.5, 2.0	0	0, 15°
	1.5, 2.0	45°	0, 15°
B_1C_6	1.3, 1.75	0, 45°	0, 15°
	0.8	0	0, 15°
B_1T_2	1.75	0, 45°	0
$B_1C_6T_2$	1.75	0, 45°	0, 15°

Roll Angle Sweeps

Model	M_∞	α	δ_c
B_3C_6	1.3, 1.75	10°, 20°	0
B_3T_2	1.75	10°, 20°	0

It was not possible to deflect the tail fins so that δ_t is zero in all cases.

The geometric properties of the fins are:

	S_F (ins. ²)	R	λ	c_t (ins.)	c_r (ins.)	$s_m - a$ (ins.)
C_4	3.90	2.31	0.30	0.848	2.829	2.121
C_6	7.97	3.53	0.06	0.25	4.00	3.75
T_2	18.40	1.333	0.50	3.50	7.00	3.50

Both canard fins are outside the aspect-ratio boundaries of the fin-on-body data base although C_4 requires only a minor extrapolation.

6.3.2 Wing-alone normal-force coefficients and axial center-of-pressure positions.- The C_4 fin results are for M_∞ of 1.5 and 2.0, the C_6 fin results for 0.8, 1.3, and 1.75, and the T_2 results for 1.75. The data base for wing-alone normal-force coefficient in reference 1 was used to predict C_N for the fins in the following steps for fin C_4 .

Step 1: Linearly extrapolate in $1/R$ in the $\lambda = 1/2$ data to get C_N at $R = 2.31$, $\lambda = 1/2$ for each α .

$$C_{N_{2.31, 1/2}} = \left(\frac{\frac{1}{2.31} - \frac{1}{1}}{\frac{1}{2} - \frac{1}{1}} \right) (C_{N_{T23}} - C_{N_{T15}}) + C_{N_{T15}}$$

Step 2: Linearly interpolate in λ in the $R = 1$ data to get a ΔC_N due to going from $\lambda = 0.5$ to $\lambda = 0.3$.

$$\Delta C_N = \left(\frac{0.3 - 0.5}{0 - 0.5} \right) (C_{N_{T14}} - C_{N_{T15}})$$

Step 3: Add ΔC_N to $C_{N_{2.31, 1/2}}$ to get C_N at $R = 2.31$ and $\lambda = 0.3$.

Step 4: Plot $C_{N_{2.31,0.3}}$ versus $1/M_\infty$ for $M_\infty = 1.2, 2,$ and 3 for all α 's.

Step 5: Read desired values of C_N from plot for $M_\infty = 1.5$ and 2.0

Fin C_6 is in the wing-alone and fin-on-body data bases of reference 1 for $M_\infty = 0.8$ and 1.3 . However, we have used the above procedure to get the desired wing alone normal-force coefficients by extrapolating from $AR = 2$ to $AR = 3.53$. The extrapolated normal-force curve for $M_\infty = 1.3$ is compared in Figure 60 with the data given in Table 3 of reference 1 to give an idea of the errors arising in extrapolation from $AR = 2$ to $AR = 3.53$. The C_N curve for $M_\infty = 0.8$ was estimated from the data of reference 6, but because the nonlinearities at transonic speeds are wing-section dependent, the curves did not compare well.

Fortunately, fin T2 is within the wing-alone data base in reference 1, and its normal-force curve at $M_\infty = 1.75$ was obtained following the five steps of the procedure outlined above.

Now with respect to axial center-of-pressure positions for the wings alone, the following procedure was used in all cases.

Step 1: Determine the center-of-pressure position from DATCOM based on a lifting surface; $(\bar{x}/c_r)_{LT}$.

Step 2: Determine the change in center-of-pressure position due to thickness $\Delta(\bar{x}/c_r)_t$ for angles of attack up to that for shock detachment by using the program described in Appendix B.

Step 3: Add the quantities in steps 1 and 2 to get the wing alone axial center-of-pressure position.

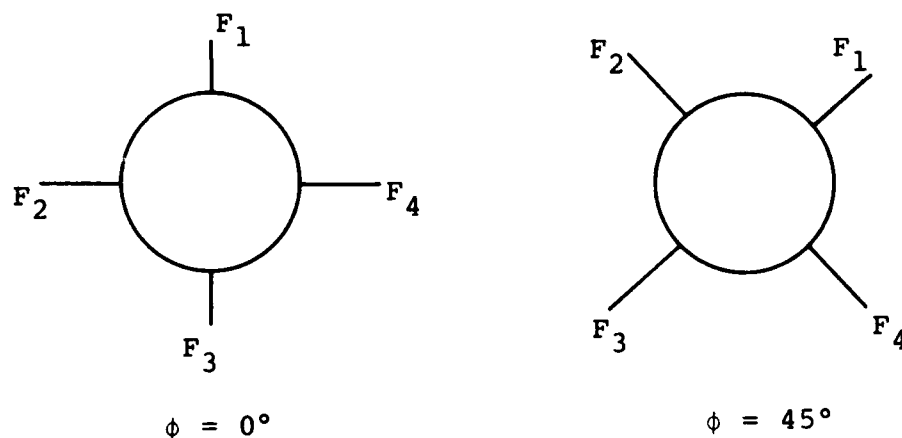
$$(\bar{x}/c_r)_W = (\bar{x}/c_r)_{LT} + \Delta(\bar{x}/c_r)_t$$

Step 4: Determine the axial center-of-pressure position at $\alpha = 45^\circ$ from the curves of Figures 34 or 35.

Step 5: Fair a curve between the results of steps 3 and 4.

The $(\bar{x}/c_r)_w$ curves for wing C_4 at $M_\infty = 1.5$ and 2.0 based on this method are shown in Figure 61; those for wing C_6 in Figure 62 for Mach numbers of 1.3 and 1.75; and that for wing T_2 at $M_\infty = 1.75$ in Figure 63. We now make comparisons between experiment and theory in the order listed in Section 6.3.1.

6.3.3 Comparisons for fin C_4 .— The comparisons between experiment and prediction for normal force and hinge moment for fin C_4 are contained in Figure 64. The comparisons were made for $M_\infty = 1.5$ and no roll with the horizontal canards undeflected and deflected $+15^\circ$. The notation for the canard fins F_1 , F_2 , F_3 , and F_4 follows the convention below looking upstream.



We note that the fin normal-force coefficients are well predicted by the method. The hinge-moment coefficients are small and the trends with angle of attack are fairly well predicted even though the data and predictions have opposite signs. Inquiring more closely into the agreement between data and prediction, we note that the normal-force coefficients at high angles of attack are well predicted for both $\delta = 0^\circ$

and $\delta = 15^\circ$ so that any disagreement for hinge-moment coefficient is due mainly to axial center-of-pressure position. For $\delta = 15^\circ$ and $\alpha = 12.5^\circ$ the difference between data and prediction represents an error in axial center-of-pressure position of about 3 percent of the root chord for fin F_4 and about 5 percent for fin F_2 . It is noted that the experimental difference of 2 percent between the two fins is not much less than the difference between experiment and theory for fin F_4 . The agreement might thus range from good to fair.

Results are shown in Figure 65 for $M_\infty = 2.0$ similar to those in Figure 64 for $M_\infty = 1.5$ with the same accuracy of comparison. There are no significant body vortex effects for the range of angles of attack tested.

Comparison for a roll angle of 45° and Mach number of 1.5 with no fin deflection is shown in Figures 66 and 67. It is noted that data are available on the fin C_4 quantities with and without tail fins present, and the duplicate data are shown in the figures. For the upper fins the normal-force data in Figure 66(a) do not show good agreement for left and right fins. For the lower fins all the data agree well in Figure 66(b) and are in good agreement with prediction. The hinge-moment results of Figure 67 are also satisfactory.

Figures 68 and 69 give normal-force coefficient and hinge-moment results, respectively, for $M_\infty = 1.5$ and $\phi_c = 45^\circ$ with all four fins positively deflected 15° . For the upper two fins, F_1 and F_2 , the experimental normal-force coefficients and the hinge-moment coefficients do not agree well but for the lower fins the data are very repeatable. The comparisons between experiment and theory are judged to be good.

In Figures 70 and 71 normal-force and hinge-moment coefficients are presented for $M_\infty = 2.0$, $\alpha_c = 45^\circ$ with all fins undeflected. All results are in good agreement and repeatable except for the F_1 and F_2 normal-force coefficients. Despite

the fact that F_1 and F_2 are different, they repeat tail on and tail off. However, the theory is well below the data for either or them. This tendency was also seen for fin T_B at $\phi_f = 45^\circ$ in Figure 57. The comparable quantities are:

	M_∞	ϕ_c	AR	λ	a/s_m
Fin T_B :	2.00	45°	2.812	0.423	0.25
Fin C_4 :	2.36	45°	2.31	0.30	0.54

We do not know the reason for this discrepancy but suspect that the values of normal-force coefficient in the data base for any of the three fins or two Mach numbers which yield the predicted normal-force coefficients are low. The data in the fin-on-body data base was taken with the fin trailing edge aligned with the base of the body. At angle of attack and $\phi_c = 45^\circ$ some possible base effect on fin normal force might occur. Both fins T_B and C_4 had at least some afterbody behind their trailing edges. The fins in the tri-service data base are being tested with some afterbody, and these data should resolve this question.

Data similar to those for Figures 70 and 71 are shown in Figures 72 and 73 except will all fins deflected 15° rather than 0° . Again the repeatability of the data and the agreement with prediction are good except for the normal-force coefficient on fins F_1 and F_2 . While CNC1 and CNC2 are repeatable tail-on and tail-off, they are not equal as required by lateral symmetry. If F_2 is correct, then the agreement with prediction is fair.

6.3.4 Comparisons for fin C_6 .— As mentioned previously, the experimental fin-on-body normal-force coefficients at $M_\infty = 0.8$ and $M_\infty = 1.3$ are included in the data base used in the predictive method. Nevertheless, comparisons are made between data and predictions for C_6 because hinge moments are not in the

data base and because $M_\infty = 1.75$ predictions will be made. The wing-alone normal-force curve has been estimated as described previously.

We first look at normal-force and hinge-moment coefficients in Figure 74 for $M_\infty = 1.3$, $\phi_C = 0^\circ$, and $\delta_1 = \delta_3 = 0$ and 15° . The equality of the normal-force coefficients left to right is good, but for the hinge-moment coefficients it could be better. However, the predictions for normal-force coefficients are very good at $\delta = 0^\circ$ and $\delta = 15^\circ$, and the hinge-moment predictions match the data well in the mean. It is to be noted that the significant error in estimating the wing-alone normal-force coefficient shown in Figure 60 apparently has little effect on the accuracy of the predicted fin-on-body normal force since K_W is calculated internal to the program from the fin-on-body data base.

Data for $M_\infty = 1.75$ at $\phi_C = 0$ with $\delta_2 = \delta_4 = 0$ and 15° are exhibited in Figure 75. The agreement between the data for left and right fins and the comparison of experiment and prediction are comparable to those for $M_\infty = 1.30$ in the previous figure.

Data for $M_\infty = 1.30$ at $\phi_C = 45^\circ$ with $\delta_1 = \delta_2 = \delta_3 = \delta_4 = 0^\circ$ and 15° are given in Figure 76. The data for the upper fins, F_1 and F_2 , show some difference left to right at $\delta = 0$ and $\delta = 15^\circ$ for both normal-force and hinge-moment coefficients. However, the agreement between experiment and theory is considered fairly good up to $\alpha = 20^\circ$. The lower fins, F_3 and F_4 , show good repeatability of the data left to right for both $\delta = 0$ and $\delta = 15^\circ$ for both coefficients. The comparison between experiment and theory are good for normal-force coefficient and for hinge moment for $\delta = 0$. For $\delta = 15^\circ$ the hinge-moment agreement is only fair. It is suspected that body vortex effects are not important in this case, and unporting may be a contributing factor through its effect on axial center-of-pressure position.

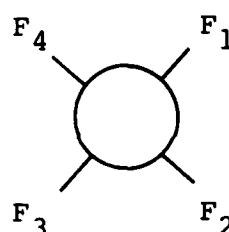
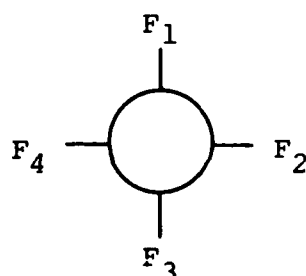
Data for $M_\infty = 1.75$ are given in Figure 77 paralleling that for $M_\infty = 1.3$ in Figure 76. The agreement of the normal-force and hinge-moment coefficients left to right for the upper fins F_1 and F_2 is not good for $\delta = 0$ nor $\delta = 15^\circ$. For $\delta = 0^\circ$ the normal-force prediction for F_1 and F_2 is low, but at $\delta = 15^\circ$ it is good up to $\alpha = 20^\circ$. The hinge-moment comparisons for $\delta = 0$ is fair up to 20° and for $\delta = 15^\circ$ is good in the mean. For the windward fins F_3 and F_4 the data are very close left to right and the comparisons between experiment and theory are good for all cases.

An attempt was made to predict the hinge moments of fin C_6 at $M_\infty = 0.8$, $\phi_c = 0$, with $\delta = 0$ and $\delta = 15^\circ$. However, the attempt was not successful. The wing-alone characteristics for C_6 had to be estimated from the Stallings-Lamb data base since one of the required wings alone was not present in the Fidler-Baker data base. However, the differences in wing sections between C_6 and the equivalent Stallings-Lamb wing were too large to yield accurate center-of-pressure predictions at $M_\infty = 0.8$.

6.3.5 Comparisons for tail fin T_2 . Tail fins T_2 exhibited phenomena different from canard fins C_4 and C_6 because they are mounted well back on the body where vortex effects are significant. Also they were tested with and without canard fins present so that the effects of wing-tail interference on hinge moments could be investigated. The following listing shows the various conditions for which comparisons between experiment and prediction are made. The model did not permit tail fin deflection. When the canard fins were deflected, all four fins were positively deflected 15° at $\phi_c = 45^\circ$, but only the horizontal canards were deflected at $\phi_c = 0^\circ$ for the cases presented.

<u>Figure</u>	<u>M_∞</u>	<u>ϕ_c</u>	<u>δ_T</u>	<u>Canard</u>	<u>δ_c</u>
78	1.75	0	0	None	
79	1.75	45°	0	None	
80	1.75	0	0	C ₆	0
81	1.75	0	0	C ₆	15°
82	1.75	45°	0	C ₆	0
83	1.75	45°	0	C ₆	15°

For the tail fins the numbering of the fin has been done clockwise rather than counterclockwise as for the canard fins. Thus, the fin numbering for the $\phi_c = 0^\circ$ and $\phi_c = 45^\circ$ cases is as follows.



The agreement of the data between fins F_2 and F_4 (body-tail configuration) in Figure 78 is very good, and the agreement between data and theory for normal-force coefficient is also very good. The hinge-moment coefficient prediction is only fair at angles of attack approaching 20° . At the highest angle of attack, the error in center-of-pressure position is .05.

For $\phi_c = 45^\circ$ and no canards present, Figure 79 also shows excellent agreement between the measured results for the two upper fins and for the two lower fins. The lower fins, 2 and 3, show very good agreement between experiment and theory for normal force, and the upper fins, 1 and 4, show good agreement when allowance is made for the large reduction

in normal force associated with the body vortices. The hinge-moment coefficients for the windward fins are underpredicted in about the same way as for the horizontal fins in Figure 78. This result is not a vortical effect. The leeward fins show a substantial reduction in hinge-moment coefficients below that for the windward fins for which the prediction is fair.

Figure 80 shows the normal-force coefficient and hinge-moment coefficients when canard fins are added to the body-tail combination which is treated in Figure 78. Some reduction in normal force occurs, but not as much as predicted at angles of attack of 20° or greater. The measured hinge moments increased only very slightly, but the prediction is now in better agreement with the data. Vortices from the canard fins have trailed back and passed over the tail fins, but are fairly far above them before the vortex strength is large. Therefore, vortex effects are small.

In Figure 81 the same results are shown as for Figure 80 except that the forward canards have now been deflected positively by 15° . Canard vortices thus pass below the horizontal tail fins near zero angle of attack. However, they intersect the tail fins at an angle of attack near 5° causing the bumps in predicted normal-force and hinge-moment coefficient curves. At $\alpha = 0$ the download on the tail fins is due entirely to the canard vortices and is fairly well predicted. However, the hinge-moment coefficient predicted at $\alpha = 0$ has the wrong sign. This result warrants refinement in the method of determining vortex effects on hinge moments. Overall the trends with angle of attack are fairly well predicted.

In Figure 82 data and theory are compared for tail-fin hinge moments with the model rotated to the $\phi = 45^\circ$ position. In this case there is a pair of canard vortices originating on the bottom fins which does not intersect the lower pair of tail fins but which intersects the upper pair at an angle of attack near $\alpha = 13^\circ$. The bumps in the predictions for

normal-force and hinge-moment coefficients are a manifestation of this fact together with the way in which the computer program treats vortices in close proximity to the fin. The agreement between experiment and theory for the upper fins is not good. The lower fins are not intersected by canard vortices, and the agreement between experiment and theory is good to fair.

In Figure 83, the same case is handled as for Figure 82 except that the canard fins are all positively deflected 15° . Strong vortices exist even at $\alpha = 0^\circ$. The agreement between experiment and theory in this case is unsatisfactory.

To summarize, the prediction method gives fair to good results for the body-tail combination at $\phi_c = 0$ and $\phi_c = 45^\circ$. For $\phi_c = 0$ and addition of the canards with or without deflection of the horizontal canards, the predictions of the method are fair to good. For $\phi_c = 45^\circ$ and addition of the canards with $\delta = 0$ the predictions are not good and deflection of all four canards makes prediction even worse.

6.3.6 Comparison between data and theory for effects of roll angle on hinge moment.- Sufficient data are available to see how the method predicts normal-force and hinge-moment coefficient for a roll angle range of 180° for fixed angles of attack for both canard fins and tail fins. Since all four fins are instrumented, such data can be generated by rolling the model only 45° . Comparisons have been made for the following cases:

Figure	Model	M_∞	α	δ	Coefficient
84	BN ₃ C ₆	1.3	10°, 20°	0	CN
85	BN ₃ C ₆	1.3	10°, 20°	0	CHM
86	BN ₃ C ₆	1.75	10°, 20°	0	CN
87	BN ₃ C ₆	1.75	10°, 20°	0	CHM
88	BN ₃ T ₂	1.75	10°, 20°	0	CN
89	BN ₃ T ₂	1.75	10°, 20°	0	CHM

From Figures 84 and 85 it is seen that the data and predictions are in good accord everywhere. In these plots $\phi_c = 0$ is the horizontal fin, $\phi_c = 90^\circ$ the windward fin, and $\phi_c = -90^\circ$ the leeward fin. The data on hinge moments of two different fins at the same condition give a measure of the minimum error of the data.

Figure 86 for $M_\infty = 1.75$ shows an underprediction of the leeward fin normal-force coefficient for both 10° and 20° . The prediction involves extrapolation both in Mach number (from 1.3) and aspect ratio. Figure 87 exhibits good comparison between data and theory for hinge-moment coefficient at $\alpha = 10^\circ$, but underprediction of the data for $\phi_c < -30^\circ$ for $\alpha = 20^\circ$. The discrepancies here are not vortex effects since they are small for the canard fins.

For tail fin T₂ the normal-force coefficients in Figure 88 are well predicted including the severe body vortex effects exhibited at $\alpha = 20^\circ$. Despite good normal-force prediction, the hinge moment is consistently underpredicted at both angles of attack in Figure 89.

7. CONCLUDING REMARKS

A comprehensive engineering hinge-moment predictive method for cruciform missiles with all-movable controls has been formulated in preliminary form, and a series of comparisons have been made between experiment and prediction to

determine the range of applicability of the method together with its shortcomings. In addition, the applicability of a supersonic panel method for cruciform missiles has been investigated with respect to calculation of hinge moments for all-movable controls. The engineering method in principle is applicable from transonic to high supersonic speed for wing-body or wing-body-tail combinations employing cruciform all-movable controls. The method applies to large angles of attack and control deflections, the sum of which can approach 50°. The panel method is applicable in the supersonic range but covers a much broader spectrum of configurations than the engineering method. It is, however, limited to about 20° of angle of attack plus control deflection.

For accurate hinge-moment prediction, it has been found that accurate knowledge is required of the fin axial center-of-pressure positions—within about 2 percent of the root chord. Large changes in axial center-of-pressure position occur with angle of attack and Mach number, but existing analytical methods are not able to predict them within the desired accuracy. A hybrid method of determining axial center-of-pressure position of wings alone has been developed for wings having attached leading-edge shock waves when viewed in planes normal to the wing planform and parallel to the root chord. This method provides essential center-of-pressure information which is used in both the engineering method and the panel method for estimating hinge moments. In the low supersonic region ($M_\infty \leq 1.2$) and the high subsonic region ($M_\infty \geq 0.8$), the fin center-of-pressure position is a function of wing airfoil section in a way which cannot be currently estimated. Accordingly, in these regimes existing data-base information for wing-alone center-of-pressure position must be used. This fact limits the configuration range that can be treated.

Comparisons have been made for a number of configurations over a range of operating parameters to determine the

limitations of the engineering predictive method. Consider first the comparisons for a cruciform body-tail combination with fins T_B having $AR = 2.812$ and $\lambda = 0.423$. Comparisons were made for the following ranges of parameters:

M_∞ : 1.6, 2.35, 3.7

α : $0^\circ \leq \alpha \leq 20^\circ$

δ : $0^\circ, -15^\circ$

ϕ_f : $45^\circ, 90^\circ, 135^\circ$

For the unrolled case ($\phi_f = 90^\circ$) the prediction and data compared well for the ranges of the first three parameters. With a pair of fins on the windward side ($\phi_f = 135^\circ$) it was found that some times the engineering method predicted the fin normal force inaccurately, but the combined use of the panel and engineering method improved accuracy of prediction. For the leeward fins ($\phi_f = 45^\circ$), the fin hinge-moment predictions were usually poor. In these cases strong body vortices appeared at the high angles of attack.

A second set of systematic comparisons was made for a body with canard fins (C_4) having an aspect ratio of 2.36 and taper ratio of 0.30. The comparisons were made for the following ranges of parameters:

M_∞ : 1.5, 2.0

α : $0^\circ \leq \alpha \leq 20^\circ$

δ : $0^\circ, +15^\circ$

ϕ_f : $45^\circ, 90^\circ, 135^\circ$

In some cases the left and right fins did not give equal measured results when they should have by symmetry. However, one set of results agreed fairly well with prediction in all cases but one. In this one case of approximately 40 comparisons, significant disagreement between prediction and data occurred. This is a case for $M_\infty = 2.0$ at 45° roll with $\delta = 0$

where the normal-force coefficient for the leeward fins is significantly underpredicted, Figure 70(a). A conjecture concerning the cause is given in the text. Generally, the good agreement for this case between prediction and experiment can be ascribed to the absence of any significant body vortex effects in contrast, for example, to the previous case.

The third set of comparisons was made for another body-canard fin combination with fins (C_6) of aspect ratio of 3.53 with $\lambda = .06$. The ranges of parameters are:

$$\begin{aligned}M_\infty: & 1.3, 1.75 \\ \alpha: & 0^\circ \leq \alpha \leq 20^\circ \\ \delta: & 0^\circ, 15^\circ \\ \phi_f: & 45^\circ, 90^\circ, 135^\circ\end{aligned}$$

Essentially the same results were found for the previous body-canard combination. An attempt to predict hinge moments at $M_\infty = 0.8$ was unsuccessful because of the lack of a reliable way of predicting fin or wing-alone axial center-of-pressure position at subsonic speeds.

The fourth set of comparisons was made for a body-tail combination employing tail fins T_2 to which canard fins C_4 were then added to see how well the effect of wing-tail interference on hinge moments could be predicted. The tail fins have an aspect ratio of 1.333 and a taper ratio of 0.50. The parameters are:

$$\begin{aligned}M_\infty: & 1.75 \\ \alpha: & 0^\circ \leq \alpha \leq 20^\circ \\ \delta_c: & 0^\circ, 15^\circ \text{ (canards only)} \\ \phi_f: & 45^\circ, 90^\circ, 135^\circ \text{ (tail fins inline)}\end{aligned}$$

First the comparisons between prediction and data for the body-tail combination is discussed as a basis for evaluating the subsequent effects of adding canard fins. For $\phi_f = 90^\circ$ and 135° the fin normal forces are predicted quite closely.

The leeward fin normal-force coefficient is also predicted well considering the fact that at $\alpha = 20^\circ$ it is less than 30 percent of that for the windward fins. The hinge-moment coefficients are underpredicted by about 25 percent as a rough average.

Adding the undeflected canard fins at $M_\infty = 1.75$ does not have a large effect on the tail fins, and the agreement between prediction and data for the hinge moment is improved. Deflecting the horizontal canards 15° positive cause nonlinearities in normal force and hinge moment due to intersection of the tail fin by the canard vortices, nonlinearities which do not appear in the data. However, the agreement between prediction and data are still fair. When the configuration is rolled 45° , the effects of the canards on the tail fin hinge moments are not well predicted, with or without canard deflection.

The last set of comparisons were made to see how the effects of roll angle on normal force and hinge moment were predicted for a roll angle range of 180° . The first comparisons for the body-canard (C_6) configuration for $M_\infty = 1.3$ exhibited good agreement between experiment and theory at both $\alpha = 10^\circ$ and 20° over the roll angle range. At $M_\infty = 1.75$ there was a tendency to underpredict the normal force on the leeward fins at both $\alpha = 10^\circ$ and 20° . This tendency was reflected in the hinge-moment coefficient at $\alpha = 20^\circ$ only. To see the effect of body vortices on the preceding comparisons, similar comparisons were made for the body-tail (T_2) configuration. The normal-force comparisons are quite good, but the hinge-moment coefficients are underpredicted.

These comparisons indicate the following conclusions:

1. The method is applicable to the range $1.3 < M_\infty < 3.7$.
2. It is not applicable with accuracy to leeward fins near strong body vortices.

3. A hybrid theory is applicable to windward fins.
4. It will handle wing-tail interference effects for inline canards and tails with no roll angle both with and without canard deflection.

8. RECOMMENDATIONS

As a result of the present work, several problem areas have arisen in which further work should result either in increasing the accuracy of hinge-moment estimation or in extending the range of applicability of the present method.

1. For Mach numbers less than the Mach number of shock detachment for zero degrees angle of attack for the wing-alone, data have exhibited significant effects of wing thickness on axial center-of-pressure location. No method is available for calculating such effects. If one were available, the range of the hinge-moment prediction method could be significantly increased.

2. When strong body or canard vortices pass in close proximity to tail fins, the present calculative model for hinge moments seems to be inaccurate. This could result from inadequacy of the vortex itself or in the method of determining its effect on the fin. Resolution of this problem may depend on a good experiment measuring both vortex properties and fin pressure distributions. While this has been done at subsonic speeds, a parallel program is needed at supersonic speeds. Then an improved analytical method should be developed.

3. For wings of taper ratio 0.5, the strip theory/shock-expansion method of determining the effects of thickness on axial center-of-pressure position was not accurate at low supersonic Mach number even though the leading-edge shock was attached. It nevertheless was accurate for taper ratios of 0 and 1.0. Further study of the problem is required to resolve this apparent anomaly.

4. When the tri-service data base has been measured, the present program based on MISSILE 2 should be expanded to encompass the greater ranges of aspect ratio and Mach number. Also these data will yield systematic values of fin effectiveness as a function of the various parameters as well as fin interference factors, Λ_{ij} . This information should be used to improve the accuracy and range of applicability of the present program.

5. Systematic data are needed on all-movable controls of general planform, particularly ones with swept trailing edges so that the method outlined in this report to calculate their hinge moments can be properly tested.

6. In several instances it has been observed that zero fin normal force and zero fin hinge moments did not occur at the same conditions. This fact implies that some phenomena exist which exhibit induced camber effects. A special study to understand and predict these effects seems worthwhile.

7. There is evidence to suggest that the length of the afterbody behind the trailing edge of an all-movable control can have a significant effect on its normal force and hinge moment in certain circumstances. An experimental investigation of this question is recommended.

REFERENCES

1. Nielsen, J. N., Hensch, M. J., and Smith, C. A.: A Preliminary Method for Calculating the Aerodynamic Characteristics of Cruciform Missiles to High Angles of Attack Including Effects of Roll Angle and Control Deflections. Report ONR-CR215-226-4F, Nov. 1977. (MISSILE 1)
2. Smith, C. A. and Nielsen, J. N.: Prediction of Aerodynamic Characteristics of Cruciform Missiles to High Angles of Attack Utilizing a Distributed Vortex Wake. NEAR TR 208, Jan. 1980. (MISSILE 2)
3. Stallings, R. L., Jr. and Lamb, M.: Wing-Alone Aerodynamic Characteristics for High Angles of Attack at Supersonic Speeds. NASA Technical Paper 1889, July 1981.
4. Baker, W. B., Jr.: Static Aerodynamic Characteristics of a Series of Generalized Slender Bodies With and Without Fins at Mach Numbers from 0.6 to 3.0 and Angles of Attack from 0 to 180 Degs., AEDC-TR-75-124, Vols I and II, May 1976.
5. No author listed: High Alpha Aerodynamics - Fin Alone (Data reported in AEDC-TR-75-124). Vols 1 and 2, Propulsion Wind Tunnel Facility, ARO Inc., July 1974.
6. Briggs, M. M., Reed, R. E., and Nielsen, J. N.: Wing Alone Aerodynamic Characteristics to High Angles of Attack at Subsonic and Transonic Speeds. Nielsen Engineering & Research, Inc. TR 269. (To be published)
7. Spreiter, J. R. and Sacks, A. H.: A Theoretical Study of the Aerodynamics of Slender Cruciform Wing Arrangements and Their Wakes. NACA TR 1296, 1957.
8. Adams, G. J. and Dugan, D. W.: Theoretical Damping in Roll and Rolling Moment Due to Differential Wing Incidence for Slender Cruciform Wings and Wing-Body Combinations. NACA TR 1088, 1952.
9. Dillenius, M. F. E., Perkins, S. C., Jr., and Mullen, J., Jr.: A General Method for Determining the Forces and Moments on Components of Finned Sections of Underwater Vehicles. Report NCSC-TM319-81, Dec. 1981.
10. Nielsen, J. N.: Quasi-Cylindrical Theory of Wing-Body Interferences at Supersonic Speeds and Comparisons with Experiment. NACA Report 1252, 1955.
11. Carmichael, R. L. and Erickson, L. L.: PANAIR - A Higher-Order Panel Method for Predicting Subsonic or Supersonic Linear Potential Flow About Arbitrary Configurations. AIAA Paper No. 81-1255, June 1981.

12. Dillenius, M. F. E. and Nielsen, J. N.: Computer Program for Calculating Pressure Distributions Including Vortex Effects on Supersonic Monoplane or Cruciform Wing-Body-Tail Combinations with Round or Elliptical Bodies. NASA CR 3122, April 1979.
13. Wardlaw, A. B., Jr., Solomon, J. M., and Baltakis, F. P.: Supersonic Inviscid Flow Field Computations of Missile Type Bodies. AIAA Paper No. 80-0271, presented at AIAA 18th Aerospace Sciences Meeting, Pasadena, CA, January 1980.
14. Klopfer, G. H. and Nielsen, J. N.: Basic Studies of Wing-Body Interference at High Angles of Attack and Supersonic Speeds. Report ONR-CR215-263-1, October 1979.
15. Derrick, J., Spring, D., and Winn, G.: Aerodynamic Characteristics of a Series of Bodies With and Without Tails at Mach Numbers from 0.8 to 3.0 and Angles of Attack from 0 to 45°. MICOM-TR-RD-7T-3, July 1976.
16. Chapman, G. T., Keener, E. R., and Malcolm, G. N.: Asymmetric Aerodynamic Forces on Aircraft Forebodies at High Angles of Attack - Some Design Guides. Paper published in AGARD Conference Proceedings No. 199 on Stall-Spin Problems of Military Aircraft, November 1975.
17. Mendenhall, M. R. and Nielsen, J. N.: Effect of Symmetrical Vortex Shedding on the Longitudinal Aerodynamic Characteristics of Wing-Body-Tail Combinations. NASA CR-2473, January 1975.
18. Mendenhall, M. R., Spangler, S. B., and Perkins, S. C., Jr.: Vortex Shedding from Circular and Noncircular Bodies at High Angles of Attack. AIAA Paper No. 79-0026, presented at the AIAA 17th Aerospace Sciences Meeting, January 15-17, 1979.
19. Mendenhall, M. R.: Predicted Vortex Shedding From Noncircular Bodies in Supersonic Flow. J. Spacecraft and Rockets, Vol. 18, No. 5, September-October, 1981, pp. 385-392.
20. Klopfer, G. H. and Nielsen, J. N.: Basic Studies of Body Vortices at High Angles of Attack and Supersonic Speeds. NEAR TR 226, October 1980.
21. Oberkampf, W. L.: Supersonic Flow Measurements in the Body Wakes of an Ogive Nose Cylinder. AFATL-TR-78-127, November 1978.
22. Schwind, R. G. and Mullen, J., Jr.: Laser Velocimeter Measurements of Slender-Body Wake Vortices. AIAA Paper No. 79-0302, presented at the AIAA 17th Aerospace Sciences Meeting, Jan. 15-17, 1979.

23. Schwind, R. G. and Kline, D. M.: Data Report on Laser Anemometer Measurements of Missile Body-Separation Vortices. NEAR TR 91, June 1975.
24. Yanta, W. J. and Wardlaw, A. B., Jr.: Flowfield about and Forces on Slender Bodies at High Angles of Attack. AIAA Journal, Vol. 19, No. 3, pp. 296-302, March 1981.
25. Smith, W. G. and Lazzeroni, F. H.: Experimental and Theoretical Study of a Rectangular Wing in a Vortical Wake at Low Speed. NASA TN D-339, October 1960.
26. McMillan, O. J., Nielsen, J. N., Schwind, R. G., and Dillenius, M. F. E.: Rolling Moments in a Trailing Vortex Flow Field. AIAA Paper No. 77-670, presented at AIAA 10th Fluid and Plasma Dynamics Conference, Albuquerque, New Mexico, June 27-29, 1977.
27. Ferri, A.: Elements of Aerodynamics of Supersonic Flow. The MacMillan Co., N.Y., pp. 149-154, 1949.
28. Bleviss, Z. O. and Struble, R. A.: Some Aerodynamic Effects of Streamwise Gaps in Low-Aspect-Ratio Lifting Surfaces at Supersonic Speeds. Preprint No. 396, January 1953. Presented at the 21st Annual Meeting, January 26-29, 1953, Institute of the Aeronautical Sciences.
29. Bleviss, Z. O. and Struble, R. A.: Some Effects of Streamwise Gaps on the Aerodynamic Characteristics of Low-Aspect-Ratio Lifting Surfaces at Supersonic Speeds. Douglas Report SM-14627, April 1953.
30. Mirels, H.: Gap Effect on Slender Wing-Body Interference. Jour. of Aero. Sciences, Vol. 20, No. 8, pp. 514-575, Reader's Forum.
31. Dugan, D. W. and Hikido, K.: Theoretical Investigation of the Effects Upon Lift of A Gap Between Wing and Body of a Slender Wing-Body Combination. NACA TN 3224, August 1954.
32. Dugan, D. W.: Experimental Investigation of Some Aerodynamic Effects of a Gap Between Wing and Body of a Moderately Slender Wing-Body Combination at a Mach Number of 1.4. NACA RM A55D08, May 1955.
33. Zarin, N. A.: Wing Tunnel Tests of Rectangular Finned Variable Gap Tangent Ogive-Cylinder Model at Mach Numbers 1.75 to 4.50. BRL Memorandum Report No. 1583, August 1964.
34. Drake, W. C.: Lift, Drag, and Hinge Moments at Supersonic Speeds of an All-Moveable Triangular Wing and Body Combination. NACA RM A53F22, September 1953.

35. Nielsen, J. N.: Nonlinearities in Missile Aerodynamics. AIAA Paper No. 78-0020, paper presented at 16th Aerospace Sciences Meeting, New Orleans, LA, January 15-17, 1978.
36. Nielsen, J. N., Kaattari, G. E., and Drake, W.: Comparison Between Prediction and Experiment for All-Movable Wing and Body Combinations at Supersonic Speeds - Lift, Pitching Moment, and Hinge Moment. NACA RM A52D29, 1952.
37. Lamb, M., Sawyer, W. C., Wassum, D. L., and Babb, C. D.: Pressure Distributions on Three Different Cruciform Aft-Tail Control Surfaces of a Wingless Missile at Mach 1.60, 2.36, and 3.70. Volume II - Clipped Delta Tail. NASA TM 80097, August 1979.
38. Hemsch, M. J. and Nielsen, J. N.: Triservice Program for Extending Missile Aerodynamic Data Base and Prediction Program Using Rational Modeling. NEAR TR 249, September 1981.
39. Lamb, M., Trescot, C. D., Jr.: A Study of Panel Loads and Centers of Pressure of Three Different Cruciform Aft-Tail Control Surfaces of a Wingless Missile from Mach 1.60 to 3.70. NASA TM 81787, May 1980.
40. Lamb, M., Sawyer, W. C., Wassum, D. L., and Babb, C. D.: Pressure Distributions on Three Different Cruciform Aft-Tail Control Surfaces of a Wingless Missile at Mach 1.60, 2.36, and 3.70. Volume I - Trapezoidal Tail. NASA TM 80097, August 1979.
41. Lamb, M., Sawyer, W. C., Wassum, D. L., and Babb, C. D.: Pressure Distributions on Three Different Cruciform Aft-Tail Control Surfaces of a Wingless Missile at Mach 1.60, 2.36, and 3.70. Volume III - Cranked Tail. NASA TM 80097, August 1979.
42. Hemsch, M. J. and Nielsen, J. N.: Test Report for Canard Missile Test in Ames 6- by 6-Foot Supersonic Wind Tunnel. NEAR TR 72, August 1974.
43. Pitts, W. C., Nielsen, J. N., and Kaattari, G. E.: Lift and Center of Pressure of Wing-Body-Tail Combinations at Subsonic, Transonic, and Supersonic Speeds. NACA Report 1307, 1957.
44. Nielsen, J. N.: Missile Aerodynamics. McGraw-Hill Book Co., 1960.
45. Spreiter, J. R. and Sacks, A. H.: A Theoretical Study of Aerodynamics of Slender Cruciform-Wing Arrangements and Their Wakes. NACA Report 1296, 1957.

TABLE 1. - AXIAL CENTER-OF-PRESSURE LOCATIONS OF WINGS OF
STALLINGS-LAMB AND FIDLER-BAKER DATA BASES
AT $\alpha = 45^\circ$, $(\bar{x}/c_r)_{45^\circ}$

(a) Stallings-Lamb Data Base

Wing	λ	AR	ARC Tests					LRC Tests				
			M = .6	M = .8	M = .9	M = 1.2	M = 1.6	M = 1.6	M = 2.16	M = 2.86	M = 3.50	M = 4.60
P1	0	1/2	.5739	.5933	.6036	.6162	.6359	.632	.641	.645	.644	.644
P2	1/2	1/2	.5135	.5339	.5410	.5565	-	.558	.570	.575	.575	.576
P3	1	1/2	.4218	.4223	.4276	.4334	-	.432	.440	.440	.438	.440
P4	0	1	.5882	.5910	.5997	.6185	-	.619	.635	.640	.640	.640
P5	1/2	1	.5322	.5342	.5406	.5576	-	.557	.559	.566	.563	.565
P6	1	1	.4030	.4035	.4083	.4191	-	.430	.427	.428	.427	.427
P7	0	2	.5962	.5982	.6048	.6218	-	.618	.620	.631	.630	.632
P8	1/2	2	.5241	.5317	.5409	.5607	.5570	.547	.545	.548	.547	.550
P9	1	2	.3818	.3858	.3993	.4253	.4218	.417	.415	.412	.412	.412
P10	1/2	4	.5139	.5256	.5318	.5544	-	.558	.540	.535	.532	.533

TABLE 1. - CONCLUDED

(b) Fidler-Baker Data Base

Wing	λ	R	M = .6	M = .8	M = .9	M = 1.0	M = 1.15	M = 1.3	M = 1.76	M = 2.0	M = 2.5	M = 3.01
T31	1/2	1/2	.5478	.5508	.5534	.5598	.5632	.5673	.5730	.5786	.5816	.5873
T14	0	1	-	-	-	-	-	-	.6501	.6466	.6539	.6580
T15	1/2	1	.5376	.5402	.5416	.5628	.5619	.5720	.5774	.5779	.5825	.5846
T11	1	1	.4039	.4004	.4061	.4314	.4410	.4443	.4419	.4433	.4500	.4514
T23	1/2	2	.5275	.5328	.5433	.5587	.5684	.5782	.5773	.5789	.5737	.5678
T36	0	1/2	.5810	.5882	.5926	.6040	.6313	.6408	.6504	.6399	-	.6434
T32	1	1/2	.4174	.4165	.4184	.4332	.4280	.4280	.4276	.4252	.4361	.4374
T22	0	2	.6144	.6175	.6172	.6318	.6288	.6358	.6460	.6516	.6556	.6534
T21	1	2	.3788	.4008	.4140	.4314	.4458	.4502	.4371	.4484	.4421	.4221

TABLE 2.- STALLINGS-LAMB DATA BASE, $M_\infty \geq 1.6$

(a) $R = 0.5$, $\lambda = 0.0$

1	2	3	4	5	6	7	8	9	10
	$M_\infty = 1.60$			$M_\infty = 2.16$			$M_\infty = 2.86$		
α	C_N	$\frac{\bar{x}}{c_r}$	$\frac{\bar{y}}{b/2}$	C_N	$\frac{\bar{x}}{c_r}$	$\frac{\bar{y}}{b/2}$	C_N	$\frac{\bar{x}}{c_r}$	$\frac{\bar{y}}{b/2}$
-5	-.080	-	-	-.075	-	-	-.075	-	-
0	0	-	-	0	-	-	0	-	-
5	.080	.677	.410	.075	.655	.390	.075	.660	.378
10	.220	.657	.362	.180	.650	.355	.160	.650	.345
15	.340	.653	.350	.295	.648	.342	.240	.643	.335
20	.485	.652	.342	.425	.645	.335	.350	.642	.327
25	.645	.647	.328	.560	.643	.324	.480	.643	.323
30	.800	.645	.323	.680	.642	.317	.605	.644	.320
35	1.000	.635	.315	.850	.643	.317	.740	.645	.318
40	1.080	.628	.306	.985	.642	.317	.880	.644	.319
45	1.225	.632	.310	1.120	.641	.313	1.030	.645	.320
50	1.340	.630	.309	1.250	.641	.312	1.165	.645	.317
55	-	-	-	1.360	.640	.312	1.295	.645	.317
60	-	-	-	1.460	.641	.312	1.405	.645	.317

	$M_\infty = 3.50$			$M_\infty = 4.60$					
-5	-.060	-	-	-.04	-	-			
0	0	-	-	0	-	-			
5	.060	.653	.315	.04	.643	.360			
10	.125	.642	.340	.09	.633	.335			
15	.215	.642	.330	.17	.640	.326			
20	.310	.642	.325	.26	.635	.323			
25	.430	.640	.321	.38	.641	.320			
30	.555	.642	.320	.51	.640	.321			
35	.690	.640	.320	.65	.642	.321			
40	.840	.642	.319	.79	.643	.320			
45	.995	.644	.319	.94	.644	.320			
50	1.140	.645	.319	1.09	.645	.318			
55	1.280	.646	.319	1.23	.648	.319			
60	1.395	.647	.319	1.34	.655	.320			

TABLE 2.- CONTINUED.

(b) $AR = 1.0$, $\lambda = 0.0$

1	2	3	4	5	6	7	8	9	10
	$M_\infty = 1.60$			$M_\infty = 2.16$			$M_\infty = 2.86$		
α	C_N	$\frac{\bar{x}}{c_r}$	$\frac{\bar{y}}{b/2}$	C_N	$\frac{\bar{x}}{c_r}$	$\frac{\bar{y}}{b/2}$	C_N	$\frac{\bar{x}}{c_r}$	$\frac{\bar{y}}{b/2}$
-5	-.12	-	-	-.11	-	-	-.090	-	-
0	0	-	-	0	-	-	0	-	-
5	.13	.667	.408	.11	.655	.393	.090	.647	.378
10	.29	.657	.385	.24	.645	.372	.185	.640	.358
15	.46	.645	.362	.37	.642	.350	.295	.637	.340
20	.62	.644	.345	.50	.641	.337	.410	.637	.335
25	.78	.643	.335	.63	.640	.330	.630	.637	.326
30	.94	.641	.330	.78	.640	.325	.670	.638	.325
35	1.09	.635	.320	.92	.640	.322	.820	.640	.324
40	1.20	.625	.315	1.07	.639	.317	.960	.640	.323
45	1.29	.619	.310	1.19	.635	.313	1.100	.640	.320
50	1.41	.621	.309	1.30	.634	.312	1.235	.640	.316
55	-	-	-	1.39	.630	.312	1.340	.637	.315
60	-	-	-	1.49	.635	.312	1.430	.635	.315

	$M_\infty = 3.50$			$M_\infty = 4.60$					
-5	-.085	-	-	-.06	-	-			
0	0	-	-	0	-	-			
5	.080	.635	.370	.06	.625	.368			
10	.150	.633	.353	.13	.619	.345			
15	.245	.630	.335	.22	.620	.333			
20	.350	.631	.331	.31	.624	.327			
25	.470	.633	.325	.43	.628	.325			
30	.610	.635	.323	.56	.632	.323			
35	.750	.637	.322	.70	.635	.322			
40	.900	.638	.321	.85	.638	.321			
45	1.050	.640	.321	1.00	.640	.321			
50	1.200	.641	.319	1.15	.641	.318			
55	1.330	.640	.314	1.28	.640	.317			
60	1.420	.635	.313	1.38	.639	.315			

TABLE 2.- CONTINUED

(c) $AR = 2.0$, $\lambda = 0.0$

1	2	3	4	5	6	7	8	9	10
	$M_\infty = 1.60$			$M_\infty = 2.16$			$M_\infty = 2.86$		
α	C_N	$\frac{\bar{x}}{c_r}$	$\frac{\bar{y}}{b/2}$	C_N	$\frac{\bar{x}}{c_r}$	$\frac{\bar{y}}{b/2}$	C_N	$\frac{\bar{x}}{c_r}$	$\frac{\bar{y}}{b/2}$
-5	-.160	-	-	-.140	-	-	-.115	-	-
0	0	-	-	0	-	-	0	-	0
5	.190	.652	.385	.140	.635	.370	.115	.620	.370
10	.395	.647	.380	.290	.627	.367	.225	.615	.358
15	.590	.637	.362	.445	.622	.350	.340	.617	.345
20	.775	.632	.345	.590	.626	.340	.470	.620	.340
25	.940	.630	.332	.740	.627	.332	.600	.623	.335
30	1.080	.623	.322	.890	.630	.325	.740	.626	.330
35	1.190	.618	.315	1.035	.630	.322	.880	.630	.327
40	1.280	.617	.310	1.165	.628	.317	1.030	.631	.324
45	1.370	.618	.310	1.260	.620	.313	1.170	.631	.320
50	1.500	.623	.312	1.350	.619	.312	1.280	.626	.316
55	-	-	-	1.455	.626	.312	1.360	.625	.315
60	-	-	-	1.540	.634	.312	1.455	.631	.317

	$M_\infty = 3.50$			$M_\infty = 4.60$					
-5	-.095	-	-	-.075	-	-			
0	0	-	-	0	-	-			
5	.090	.605	.374	.075	.600	.393			
10	.180	.606	.360	.155	.601	.370			
15	.285	.609	.348	.240	.603	.357			
20	.400	.612	.340	.345	.606	.343			
25	.520	.615	.335	.465	.610	.335			
30	.665	.620	.330	.600	.618	.330			
35	.810	.625	.326	.750	.623	.328			
40	.960	.627	.324	.900	.630	.325			
45	1.105	.630	.322	1.060	.632	.323			
50	1.255	.630	.319	1.200	.632	.318			
55	1.345	.625	.314	1.300	.627	.315			
60	1.430	.621	.313	1.385	.626	.315			

TABLE 2.- CONTINUED.

(d) $R = 0.5$, $\lambda = 0.5$

1	2	3	4	5	6	7	8	9	10
	$M_\infty = 1.60$			$M_\infty = 2.16$			$M_\infty = 2.86$		
α	C_N	$\frac{\bar{x}}{c_r}$	$\frac{\bar{y}}{b/2}$	C_N	$\frac{\bar{x}}{c_r}$	$\frac{\bar{y}}{b/2}$	C_N	$\frac{\bar{x}}{c_r}$	$\frac{\bar{y}}{b/2}$
-5	-.10	-	-	-.09	-	-	-.09	-	-
0	0	-	-	0	-	-	0	-	-
5	.12	.527	.482	.10	.534	.465	.08	.550	.445
10	.27	.535	.484	.24	.548	.473	.20	.557	.458
15	.45	.545	.468	.35	.559	.460	.31	.561	.445
20	.62	.551	.457	.52	.562	.442	.43	.565	.435
25	.79	.557	.440	.65	.565	.434	.55	.569	.432
30	.95	.560	.436	.79	.567	.430	.68	.572	.430
35	1.08	.560	.431	.93	.567	.427	.83	.574	.429
40	1.20	.559	.422	1.06	.567	.426	.97	.575	.427
45	1.30	.558	.418	1.18	.570	.425	1.10	.575	.425
50	1.42	.563	.418	1.30	.571	.423	1.23	.576	.425
55	-	-	-	1.39	.571	.423	1.34	.575	.424
60	-	-	-	1.48	.575	.423	1.44	.577	.424

	$M_\infty = 3.50$			$M_\infty = 4.60$					
α	C_N	$\frac{\bar{x}}{c_r}$	$\frac{\bar{y}}{b/2}$	C_N	$\frac{\bar{x}}{c_r}$	$\frac{\bar{y}}{b/2}$			
-5	-.08	-	-	-.05	-	-			
0	0	-	-	0	-	-			
5	.08	.548	.440	.05	.522	.437			
10	.16	.553	.445	.12	.535	.435			
15	.26	.558	.435	.21	.550	.430			
20	.37	.565	.432	.31	.558	.428			
25	.48	.568	.430	.43	.562	.426			
30	.62	.570	.429	.56	.568	.427			
35	.76	.572	.429	.70	.572	.427			
40	.90	.574	.429	.85	.575	.427			
45	1.05	.575	.427	1.00	.576	.427			
50	1.20	.576	.427	1.15	.577	.427			
55	1.33	.577	.426	1.27	.577	.426			
60	1.43	.579	.425	1.38	.577	.425			

TABLE 2.- CONTINUED.

(e) $M_\infty = 1.0$, $\lambda = 0.5$

1	2	3	4	5	6	7	8	9	10
	$M_\infty = 1.60$			$M_\infty = 2.16$			$M_\infty = 2.86$		
α	C_N	$\frac{\bar{x}}{c_r}$	$\frac{\bar{y}}{b/2}$	C_N	$\frac{\bar{x}}{c_r}$	$\frac{\bar{y}}{b/2}$	C_N	$\frac{\bar{x}}{c_r}$	$\frac{\bar{y}}{b/2}$
-5	-.15	-	-	-.13	-	-	-.12	-	-
0	0	-	-	0	-	-	0	-	-
5	.17	.548	.435	.13	.528	.417	.10	.523	.430
10	.36	.542	.453	.28	.540	.440	.22	.530	.437
15	.56	.546	.460	.44	.547	.445	.34	.538	.437
20	.75	.551	.458	.59	.553	.442	.48	.545	.433
25	.94	.556	.445	.75	.555	.437	.62	.551	.432
30	1.09	.560	.435	.90	.560	.432	.77	.559	.431
35	1.20	.560	.430	1.05	.560	.429	.92	.562	.429
40	1.29	.559	.422	1.17	.560	.426	1.07	.565	.427
45	1.38	.557	.420	1.27	.559	.425	1.19	.566	.425
50	1.46	.562	.419	1.37	.560	.423	1.30	.563	.425
55	-	-	-	1.45	.565	.423	1.40	.566	.424
60	-	-	-	1.53	.575	.423	1.48	.570	.424

	$M_\infty = 3.50$			$M_\infty = 4.60$					
-5	-.09	-	-	-.07	-	-			
0	0	-	-	0	-	-			
5	.09	.510	.440	.06	.472	.450			
10	.19	.519	.443	.13	.492	.445			
15	.29	.527	.436	.23	.508	.440			
20	.40	.535	.435	.34	.523	.435			
25	.53	.545	.430	.46	.535	.430			
30	.68	.555	.430	.60	.545	.427			
35	.84	.560	.430	.76	.555	.427			
40	.98	.563	.429	.92	.563	.427			
45	1.13	.563	.427	1.08	.565	.427			
50	1.28	.563	.427	1.21	.566	.426			
55	1.37	.564	.426	1.32	.566	.426			
60	1.45	.565	.425	1.42	.568	.425			

TABLE 2.- CONTINUED.

(f) $Re = 2.0$, $\lambda = 0.5$

1	2	3	4	5	6	7	8	9	10
	$M_\infty = 1.60$			$M_\infty = 2.16$			$M_\infty = 2.86$		
α	C_N	$\frac{\bar{x}}{c_r}$	$\frac{\bar{y}}{b/2}$	C_N	$\frac{\bar{x}}{c_r}$	$\frac{\bar{y}}{b/2}$	C_N	$\frac{\bar{x}}{c_r}$	$\frac{\bar{y}}{b/2}$
-5	-.17	-	-	-.15	-	-	-.12	-	-
0	0	-	-	0	-	-	0	-	-
5	.21	.510	.405	.17	.490	.442	.13	.485	.451
10	.43	.522	.425	.33	.505	.440	.26	.495	.455
15	.66	.533	.435	.49	.515	.436	.40	.505	.449
20	.87	.534	.437	.65	.528	.435	.53	.513	.440
25	1.05	.534	.436	.82	.538	.434	.68	.522	.435
30	1.18	.534	.430	1.00	.543	.430	.84	.535	.431
35	1.26	.535	.423	1.13	.543	.430	1.01	.545	.429
40	1.35	.540	.422	1.23	.543	.426	1.15	.548	.427
45	1.44	.547	.422	1.33	.545	.425	1.27	.548	.425
50	1.55	.563	.424	1.40	.552	.425	1.36	.550	.425
55	-	-	-	1.52	.567	.426	1.45	.557	.427
60	-	-	-	1.59	.575	.427	1.55	.570	.427

	$M_\infty = 3.50$			$M_\infty = 4.60$					
-5	-.12	-	-	-.08	-	-			
0	0	-	-	0	-	-			
5	.10	.476	.448	.08	.458	.445			
10	.22	.489	.455	.17	.470	.450			
15	.34	.495	.456	.29	.485	.455			
20	.46	.507	.458	.41	.496	.453			
25	.62	.517	.437	.54	.508	.445			
30	.75	.527	.433	.68	.520	.437			
35	.90	.540	.430	.83	.530	.432			
40	1.07	.547	.429	.99	.545	.427			
45	1.22	.547	.427	1.15	.550	.427			
50	1.34	.547	.427	1.27	.551	.426			
55	1.42	.555	.427	1.37	.555	.426			
60	1.51	.567	.429	1.45	.562	.430			

TABLE 2.- CONTINUED.

(g) $AR = 4.0$, $\lambda = 0.5$

1	2	3	4	5	6	7	8	9	10
	$M_\infty = 1.60$			$M_\infty = 2.16$			$M_\infty = 2.86$		
α	C_N	$\frac{\bar{x}}{c_r}$	$\frac{\bar{y}}{b/2}$	C_N	$\frac{\bar{x}}{c_r}$	$\frac{\bar{y}}{b/2}$	C_N	$\frac{\bar{x}}{c_r}$	$\frac{\bar{y}}{b/2}$
-5	-.22	-	-	-.19	-	-	-.12	-	-
0	0	-	-	0	-	-	0	-	-
5	.24	.465	.418	.18	.462	.452	.13	.452	.442
10	.47	.485	.425	.38	.475	.450	.29	.474	.449
15	.69	.505	.427	.55	.485	.443	.46	.482	.452
20	.92	.508	.428	.71	.498	.437	.61	.488	.449
25	1.09	.510	.429	.89	.514	.436	.74	.497	.430
30	1.22	.518	.430	1.05	.518	.430	.89	.512	.435
35	1.30	.525	.430	1.18	.522	.430	1.03	.522	.434
40	1.36	.535	.431	1.26	.530	.431	1.15	.528	.433
45	1.49	.558	.432	1.35	.540	.433	1.27	.535	.433
50	1.55	.563	.432	1.48	.560	.434	1.36	.547	.435
55	-	-	-	1.56	.570	.435	1.48	.566	.435
60	-	-	-	1.63	.575	.435	1.56	.573	.436

	$M_\infty = 3.50$			$M_\infty = 4.60$					
-5	-.12	-	-	-.09	-	-			
0	0	-	-	0	-	-			
5	.12	.448	.445	.09	.440	.450			
10	.24	.463	.449	.21	.448	.450			
15	.39	.475	.450	.33	.460	.450			
20	.55	.485	.456	.47	.476	.453			
25	.69	.490	.448	.63	.483	.455			
30	.81	.503	.440	.76	.495	.443			
35	.95	.517	.435	.89	.511	.440			
40	1.11	.527	.430	1.04	.524	.435			
45	1.23	.532	.428	1.18	.533	.430			
50	1.33	.540	.433	1.27	.540	.430			
55	1.44	.558	.435	1.38	.552	.433			
60	1.54	.570	.435	1.50	.568	.435			

Table 2.- Continued.

(h) $Re = 0.5$, $\lambda = 1.0$

1	2	3	4	5	6	7	8	9	10
	$M_\infty = 1.60$			$M_\infty = 2.16$			$M_\infty = 2.86$		
α	C_N	$\frac{\bar{x}}{c_r}$	$\frac{\bar{y}}{b/2}$	C_N	$\frac{\bar{x}}{c_r}$	$\frac{\bar{y}}{b/2}$	C_N	$\frac{\bar{x}}{c_r}$	$\frac{\bar{y}}{b/2}$
-5	-.100	-	-	-.110	-	-	-.090	-	-
0	0	-	-	0	-	-	0	-	-
5	.120	.330	.490	.110	.322	.460	.090	.357	.462
10	.265	.365	.498	.235	.350	.480	.200	.365	.474
15	.440	.385	.499	.370	.377	.485	.315	.373	.477
20	.605	.402	.497	.510	.400	.487	.430	.382	.480
25	.780	.415	.495	.650	.412	.485	.550	.402	.482
30	.970	.418	.488	.795	.420	.483	.680	.417	.483
35	1.120	.425	.487	.950	.425	.481	.820	.430	.484
40	1.250	.432	.486	1.085	.435	.487	.965	.435	.484
45	1.340	.432	.486	1.210	.440	.487	1.100	.440	.485
50	1.425	.435	.485	1.320	.445	.486	1.230	.447	.485
55	-	-	-	1.420	.449	.486	1.345	.450	.485
60	-	-	-	1.515	.455	.485	1.440	.456	.485

	$M_\infty = 3.50$			$M_\infty = 4.60$					
-5	-.070	-	-	-.060	-	-			
0	0	-	-	0	-	-			
5	.080	.350	.458	.050	.310	.442			
10	.170	.363	.470	.130	.342	.460			
15	.280	.370	.475	.220	.357	.465			
20	.390	.375	.477	.325	.370	.467			
25	.490	.390	.480	.440	.379	.476			
30	.620	.412	.483	.570	.403	.480			
35	.760	.425	.485	.700	.423	.483			
40	.910	.433	.485	.850	.433	.484			
45	1.060	.438	.485	1.000	.440	.484			
50	1.200	.445	.485	1.145	.446	.486			
55	1.330	.450	.485	1.270	.450	.486			
60	1.430	.453	.485	1.385	.453	.486			

Table 2.- Continued.

(i) $AR = 1.0$, $\lambda = 1.0$

1	2	3	4	5	6	7	8	9	10
	$M_\infty = 1.60$			$M_\infty = 2.16$			$M_\infty = 2.86$		
α	C_N	$\frac{\bar{x}}{c_r}$	$\frac{\bar{y}}{b/2}$	C_N	$\frac{\bar{x}}{c_r}$	$\frac{\bar{y}}{b/2}$	C_N	$\frac{\bar{x}}{c_r}$	$\frac{\bar{y}}{b/2}$
-5	-.15	-	-	-.16	-	-	-.12	-	-
0	0	-	-	0	-	-	0	-	-
5	.17	.330	.450	.14	.350	.445	.12	.360	.450
10	.35	.370	.465	.30	.350	.463	.24	.372	.462
15	.54	.390	.474	.44	.370	.472	.37	.373	.469
20	.73	.405	.480	.59	.390	.478	.52	.373	.475
25	.93	.407	.481	.74	.402	.482	.63	.387	.478
30	1.08	.410	.484	.90	.410	.480	.77	.410	.480
35	1.21	.412	.487	1.05	.415	.481	.92	.417	.482
40	1.33	.422	.486	1.18	.422	.487	1.07	.423	.484
45	1.42	.430	.486	1.28	.427	.487	1.19	.428	.485
50	1.48	.435	.485	1.37	.432	.487	1.30	.433	.485
55	-	-	-	1.46	.440	.487	1.39	.438	.485
60	-	-	-	1.55	.450	.487	1.48	.448	.485

	$M_\infty = 3.50$			$M_\infty = 4.60$					
-5	-.10	-	-	-.07	-	-			
0	0	-	-	0	-	-			
5	.09	.350	.453	.07	.315	.448			
10	.20	.362	.460	.17	.340	.460			
15	.32	.370	.465	.27	.353	.465			
20	.45	.371	.470	.38	.367	.467			
25	.58	.377	.477	.52	.370	.473			
30	.70	.398	.480	.64	.388	.478			
35	.84	.415	.482	.78	.408	.480			
40	.98	.422	.484	.93	.421	.484			
45	1.14	.427	.485	1.09	.427	.484			
50	1.27	.430	.485	1.21	.432	.486			
55	1.38	.435	.486	1.32	.436	.486			
60	1.47	.442	.486	1.42	.440	.486			

Table 2.- Concluded.

(j) $Re = 2.0$, $\lambda = 1.0$

1	2	3	4	5	6	7	8	9	10
	$M_\infty = 1.60$			$M_\infty = 2.16$			$M_\infty = 2.86$		
α	C_N	$\frac{\bar{x}}{c_r}$	$\frac{\bar{y}}{b/2}$	C_N	$\frac{\bar{x}}{c_r}$	$\frac{\bar{y}}{b/2}$	C_N	$\frac{\bar{x}}{c_r}$	$\frac{\bar{y}}{b/2}$
-5	-.200	-	-	-.185	-	-	-.130	-	-
0	0	-	-	0	-	-	0	-	-
5	.220	.335	.442	.160	.337	.445	.130	.337	.465
10	.420	.360	.460	.350	.342	.458	.270	.349	.470
15	.620	.382	.483	.515	.358	.467	.430	.352	.469
20	.830	.392	.474	.670	.375	.472	.580	.355	.470
25	1.020	.395	.481	.830	.390	.476	.710	.375	.475
30	1.165	.398	.484	.980	.400	.479	.845	.392	.476
35	1.260	.402	.487	1.130	.403	.481	.995	.405	.480
40	1.325	.408	.486	1.230	.407	.487	1.140	.408	.484
45	1.415	.417	.488	1.325	.415	.488	1.245	.412	.485
50	1.530	.440	.485	1.400	.425	.489	1.335	.420	.487
55	-	-	-	1.520	.447	.489	1.430	.438	.488
60	-	-	-	1.580	.454	.490	1.520	.450	.488

	$M_\infty = 3.50$			$M_\infty = 4.60$					
-5	-.105	-	-	-.080	-	-			
0	0	-	-	0	-	-			
5	.110	.308	.467	.080	.263	.463			
10	.220	.327	.470	.180	.300	.470			
15	.360	.342	.470	.290	.323	.470			
20	.510	.349	.467	.425	.340	.470			
25	.640	.360	.470	.580	.348	.468			
30	.770	.380	.474	.710	.370	.474			
35	.920	.399	.480	.850	.390	.478			
40	1.080	.408	.483	1.000	.404	.480			
45	1.215	.412	.485	1.150	.412	.484			
50	1.320	.417	.487	1.260	.416	.486			
55	1.415	.427	.488	1.360	.425	.487			
60	1.510	.445	.488	1.460	.440	.488			

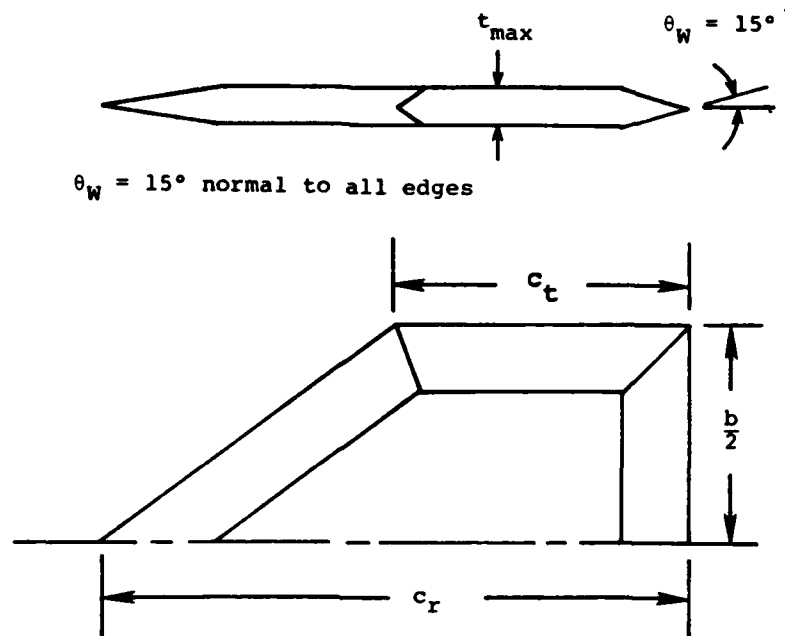
TABLE 3.- CURVE FITS TO THE WING-ALONE NORMAL-FORCE
CURVES OF THE STALLINGS-LAMB DATA

Least squares curve fits have been made using the following function:

$$C_N = A_1 \sin \alpha + A_2 \sin 3\alpha + A_3 \sin 5\alpha$$

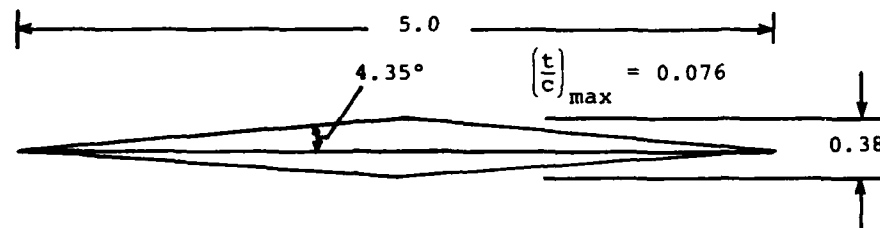
The coefficients for all wings are listed in the following table.

AR	LAMBDA	MACH NO.	A1	A2	A3
.500	0.000	1.600	1.63863	.291143E-01	-.104156
.500	0.000	2.160	1.61551	-.861637E-01	-.632322E-01
.500	0.000	2.860	1.57903	-.166955	-.432184E-01
.500	0.000	3.500	1.56544	-.206644	-.475144E-01
.500	0.000	4.600	1.47765	-.204498	-.681338E-01
1.000	0.000	1.600	1.50268	.240389	-.123309
1.000	0.000	2.160	1.66441	-.298765E-01	-.463506E-01
1.000	0.000	2.860	1.59687	-.963826E-01	-.570519E-01
1.000	0.000	3.500	1.59315	-.160454	-.565923E-01
1.000	0.000	4.600	1.54076	-.181507	-.589119E-01
2.000	0.000	1.600	1.92865	.799505E-01	.382202E-01
2.000	0.000	2.160	1.73963	.279736E-01	-.256099E-01
2.000	0.000	2.860	1.62166	-.382456E-01	-.545200E-01
2.000	0.000	3.500	1.59126	-.938359E-01	-.675902E-01
2.000	0.000	4.600	1.52894	-.117949	-.784421E-01
.500	.500	1.600	1.57452	.195151	-.102592
.500	.500	2.160	1.65113	-.179258E-01	-.485538E-01
.500	.500	2.860	1.61567	-.937858E-01	-.509234E-01
.500	.500	3.500	1.61623	-.169185	-.425366E-01
.500	.500	4.600	1.52538	-.172644	-.671093E-01
1.000	.500	1.600	1.61213	.295073	-.648054E-01
1.000	.500	2.160	1.70531	.623847E-01	-.459241E-01
1.000	.500	2.860	1.63332	-.142027E-01	-.689149E-01
1.000	.500	3.500	1.60389	-.793663E-01	-.776433E-01
1.000	.500	4.600	1.54452	-.120098	-.923145E-01
2.000	.500	1.600	1.96947	.144631	.535941E-01
2.000	.500	2.160	1.80255	.758850E-01	-.177179E-01
2.000	.500	2.860	1.70693	.207995E-01	-.635834E-01
2.000	.500	3.500	1.66844	-.356632E-01	-.743933E-01
2.000	.500	4.600	1.59519	-.777601E-01	-.857075E-01
4.000	.500	1.600	2.02696	.143905	.842598E-01
4.000	.500	2.160	1.90004	.680800E-01	.189451E-01
4.000	.500	2.860	1.78481	-.785871E-03	-.120058E-01
4.000	.500	3.500	1.73794	-.354389E-01	-.311429E-01
4.000	.500	4.600	1.65956	-.549661E-01	-.508460E-01
.500	1.000	1.600	1.38974	.349982	-.182388
.500	1.000	2.160	1.6A793	-.239781E-01	-.509075E-01
.500	1.000	2.860	1.62919	-.111045	-.369584E-01
.500	1.000	3.500	1.62445	-.166713	-.356818E-01
.500	1.000	4.600	1.54524	-.182116	-.528856E-01
1.000	1.000	1.600	1.56417	.343850	-.108281
1.000	1.000	2.160	1.73967	.423373E-01	-.345330E-01
1.000	1.000	2.860	1.66287	-.280788E-01	-.426710E-01
1.000	1.000	3.500	1.66505	-.105324	-.400927E-01
1.000	1.000	4.600	1.57580	-.113018	-.626461E-01
2.000	1.000	1.600	1.89382	.172125	.312991E-01
2.000	1.000	2.160	1.82154	.642086E-01	.124394E-02
2.000	1.000	2.860	1.71380	.136117E-01	-.306073E-01
2.000	1.000	3.500	1.68051	-.311690E-01	-.560945E-01
2.000	1.000	4.600	1.59810	-.567986E-01	-.761496E-01

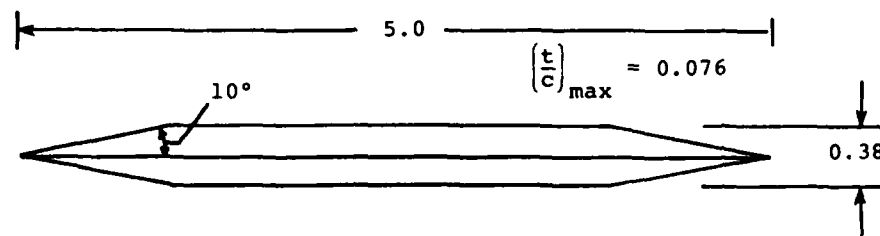


Wing	AR	b in.	c_t in.	c_r in.	λ	t_{\max} in.	$\frac{t_{\max}}{c_r}$
P ₁	0.5	4.243	0	16.971	0	0.500	0.029
P ₂	0.5	4.243	5.657	11.314	0.50	0.500	0.044
P ₃	0.5	4.243	8.486	8.486	1.00	0.500	0.059
P ₄	1.0	6.000	0	12.000	0	0.500	0.042
P ₅	1.0	6.000	4.000	8.000	0.50	0.500	0.062
P ₆	1.0	6.000	6.000	6.000	1.00	0.500	0.083
P ₇	2.0	8.486	0	8.486	0	0.500	0.059
P ₈	2.0	8.485	2.828	5.657	0.50	0.500	0.088
P ₉	2.0	8.485	4.243	4.243	1.00	0.500	0.118
P ₁₀	4.0	12.000	2.000	4.000	0.50	0.500	0.125

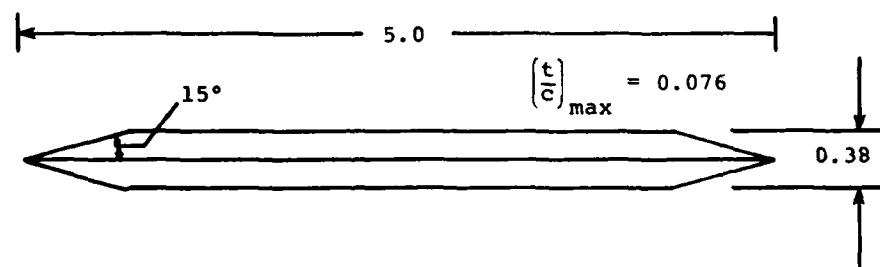
Figure 1.- Summary of characteristics of wings
of Stallings - Lamb data base.



(a) Airfoil 1



(b) Airfoil 2



(c) Airfoil 3

Figure 2.- Three airfoil sections with different wedge angles but the same thickness ratio.

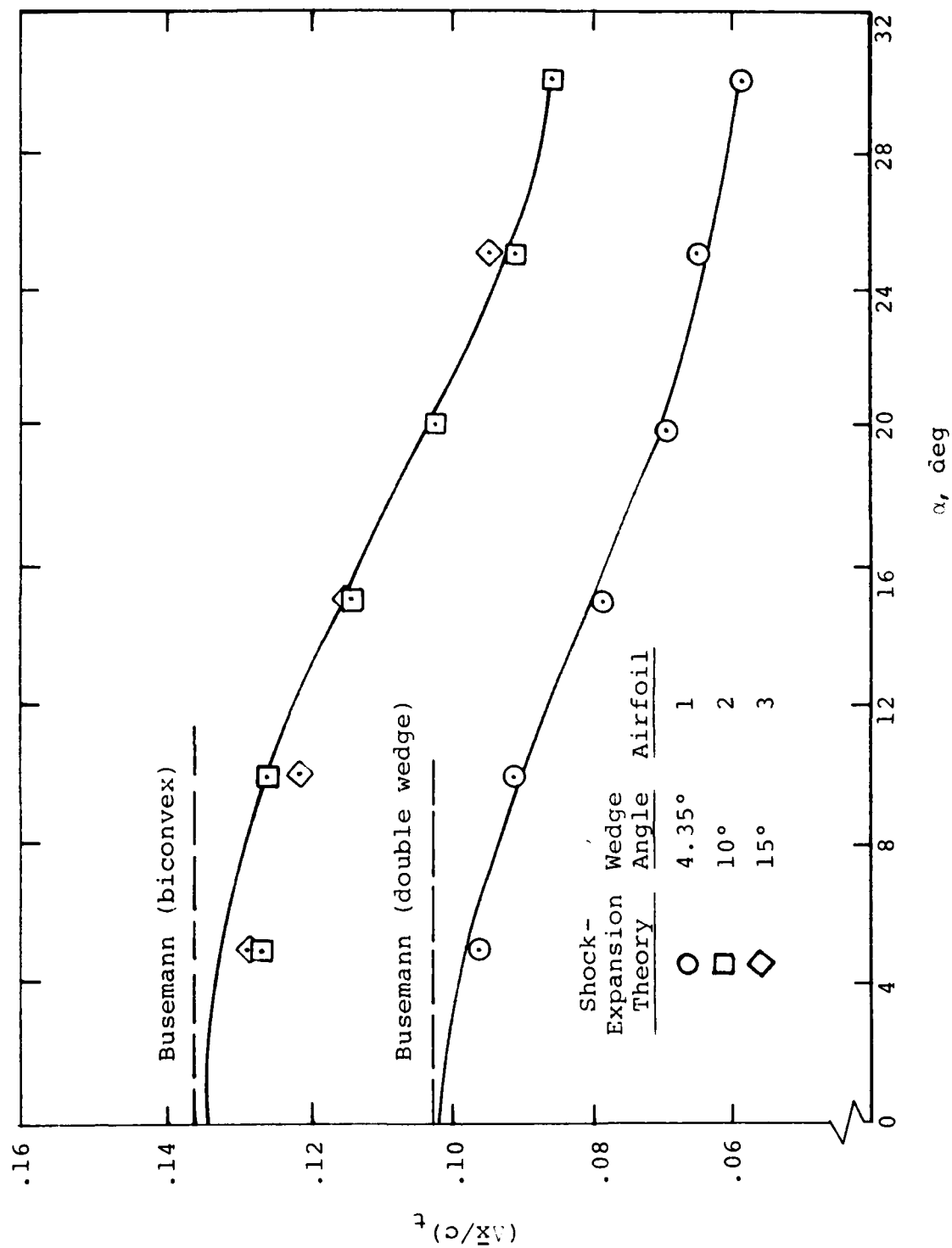


Figure 3. Effect of wedge angle on center-of-pressure position (positive forward from the 50 percent chord location) for three airfoils of the same thickness ratio; $M_\infty = 4.50$.

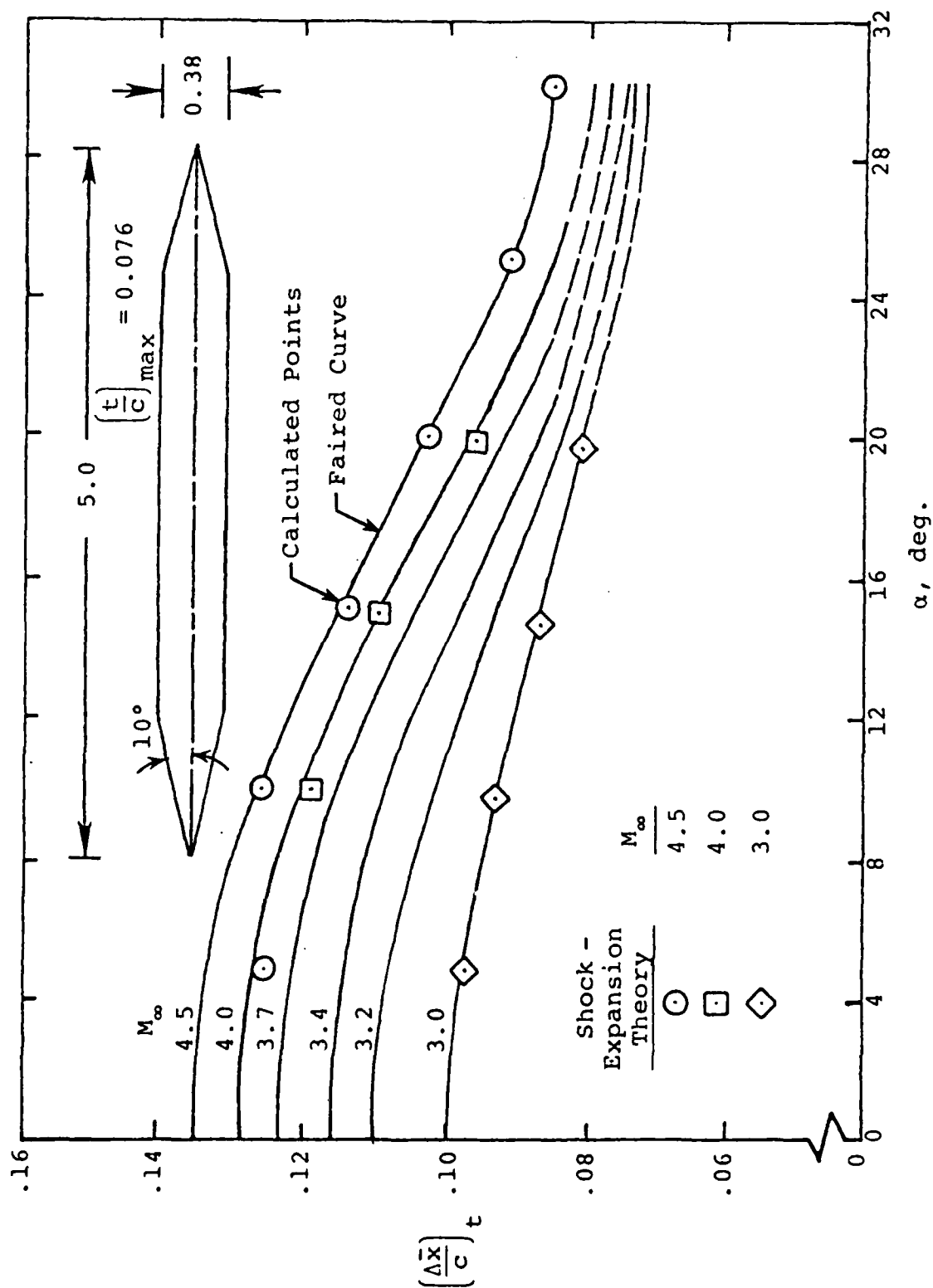


Figure 4. - Effect of Mach number on center-of-pressure position (positive forward from 50 percent chord location); airfoil 2.

Tall Fin Config	S _F in. ²	AR	b/2, in.	λ	Λ	Λ , in.	C _T ', in.	D, in.	C _R ', in.	HL/C _R	t _R ', in.	t _C ', in.	t _R C _R
16	7.916	2.0	2.821	1.0	90°	0.800	2.813	1.140	2.813	0.45	0.140	0.140	0.050
13	7.916	2.0	2.821	0.5	56°19'	1.158	1.873	1.140	3.749	0.55	0.187	0.187	0.050
12	7.942	2.0	2.821	0	26°34'	1.172	0	1.140	5.625	0.62	0.187	0.187	0.033
21	3.5119	2.0	1.874	1.0	90°	0.696	1.874	0.696	1.874	0.45	0.125	0.125	0.067
23	3.6066	2.0	1.875	0.5	55°38'	0.713	1.282	0.694	2.565	0.55	0.125	0.125	0.049
22	3.5156	2.0	1.875	0	26°34'	0.728	0	0.694	3.750	0.62	0.125	0.125	0.033
11	7.028	1.0	1.875	1.0	90°	0.800	3.749	0.800	3.749	0.45	0.140	0.140	0.037
15	7.024	1.0	1.875	0.5	36°54'	1.165	2.497	1.140	4.996	0.55	0.187	0.187	0.037
14	7.028	1.0	1.875	0	14°3	1.195	0	1.140	7.499	0.62	0.187	0.187	0.025
12	14.016	0.5	1.875	1.0	90°	1.587	7.499	1.587	7.499	0.45	0.250	0.250	0.033
31	14.030	0.5	1.875	0.5	20°36'	1.626	4.990	1.587	9.980	0.55	0.250	0.125	0.025
36	14.056	0.5	1.875	0	7°8'	1.682	0	1.587	14.998	0.62	0.250	0.250	0.017

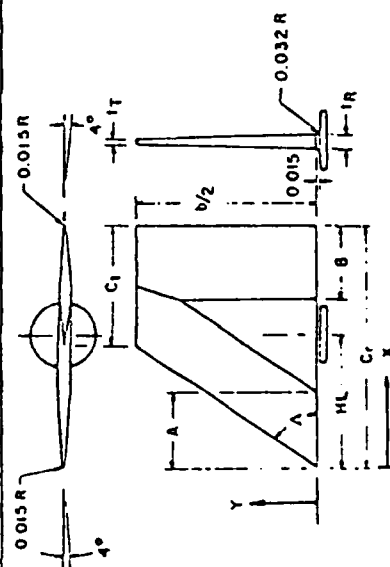
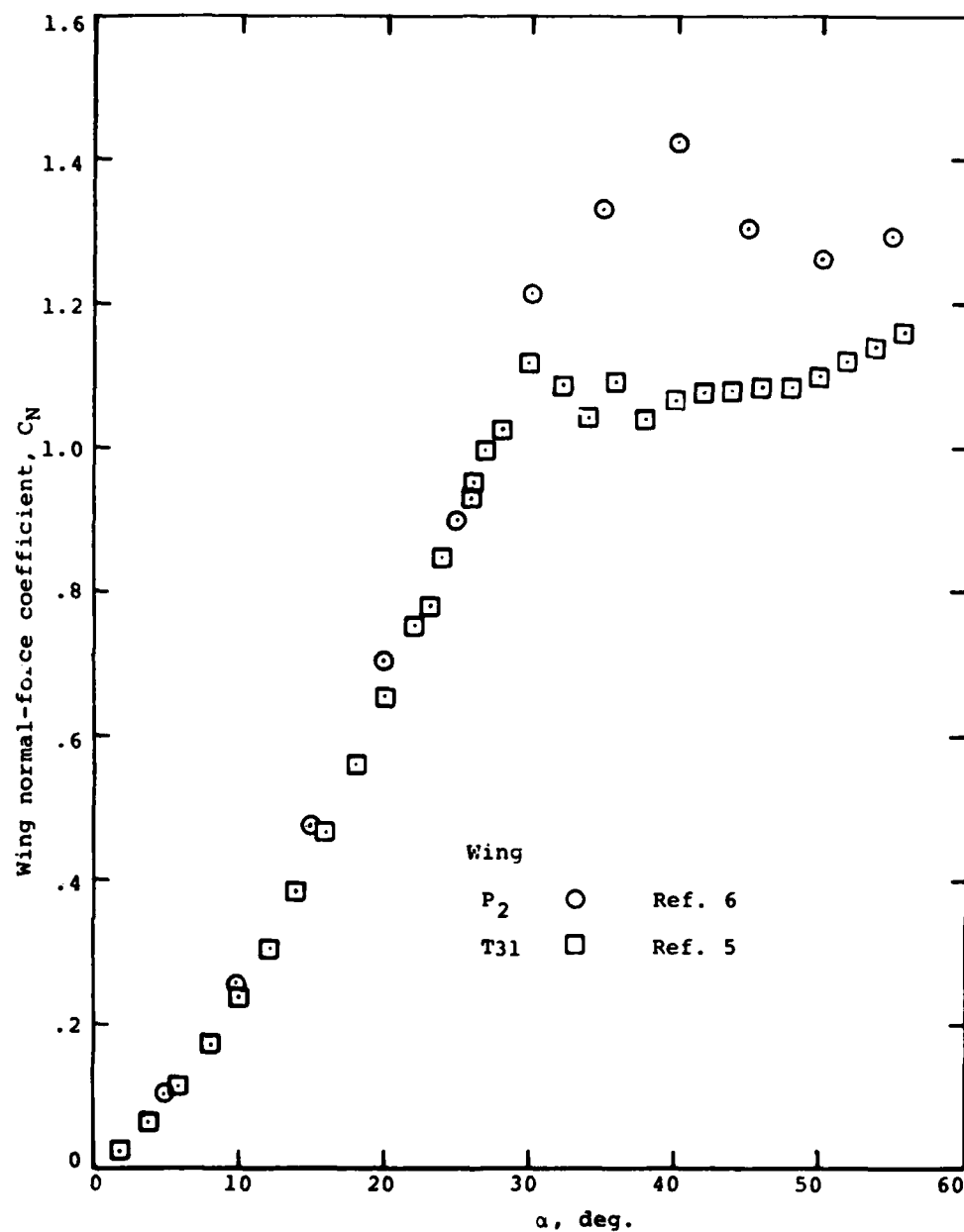
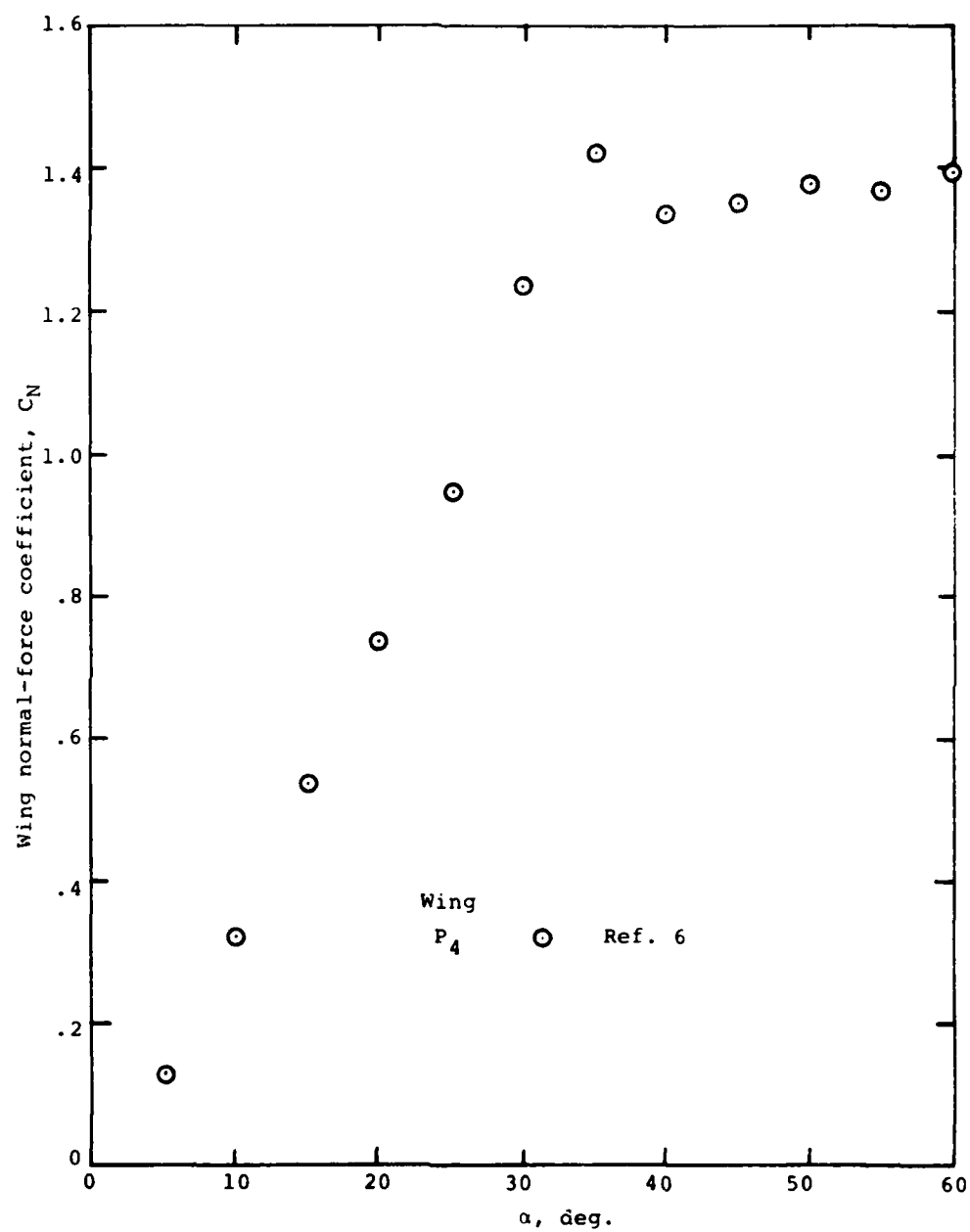


Figure 5.- Summary of characteristics of wings of Fidler-Baker data base.



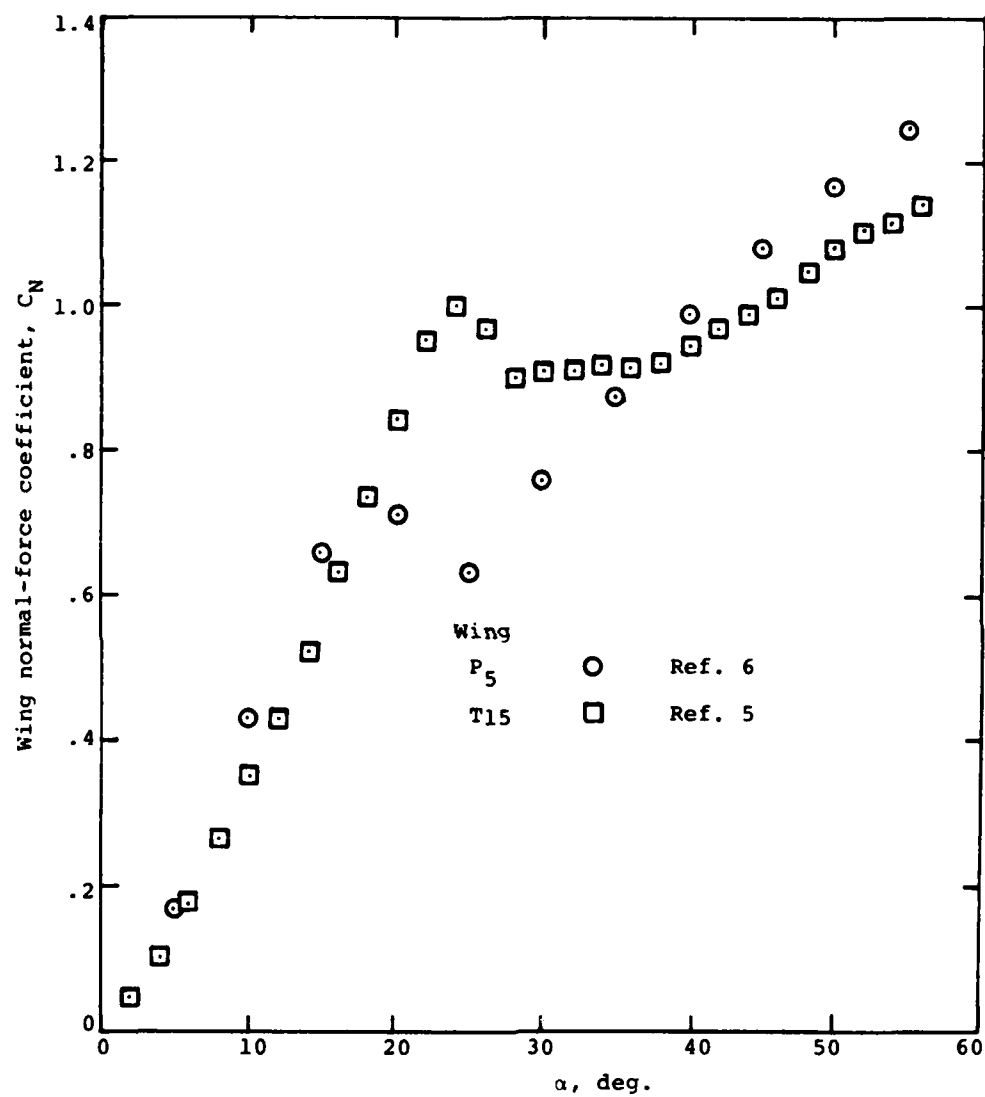
(a) $AR = 0.5$, $\lambda = 0.5$

Figure 6.- Comparison of wing normal-force curves
at $M_\infty = 0.8$.



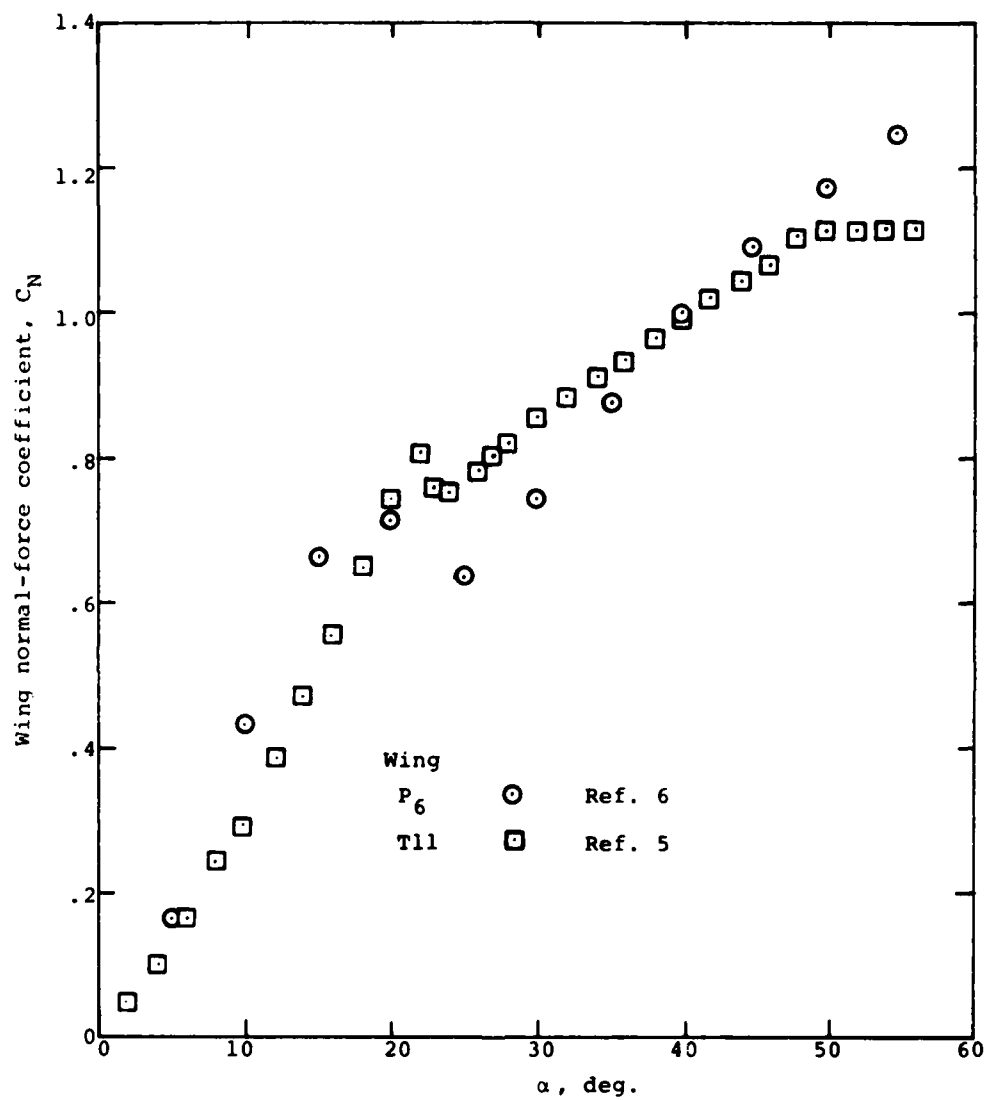
(b) $M = 1.0$, $\lambda = 0$

Figure 6.- Continued.



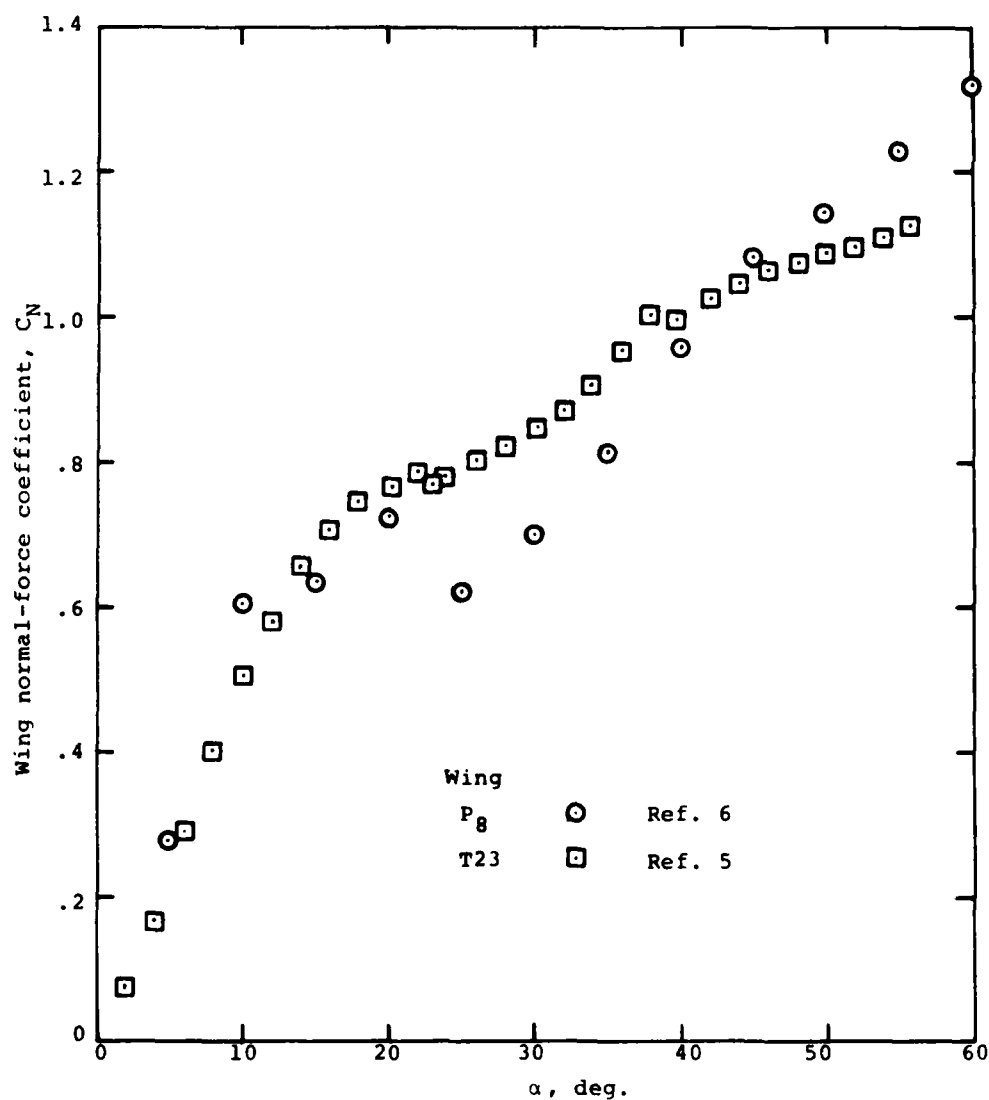
(c) $Re = 1.0$, $\lambda = 0.5$

Figure 6.- Continued.



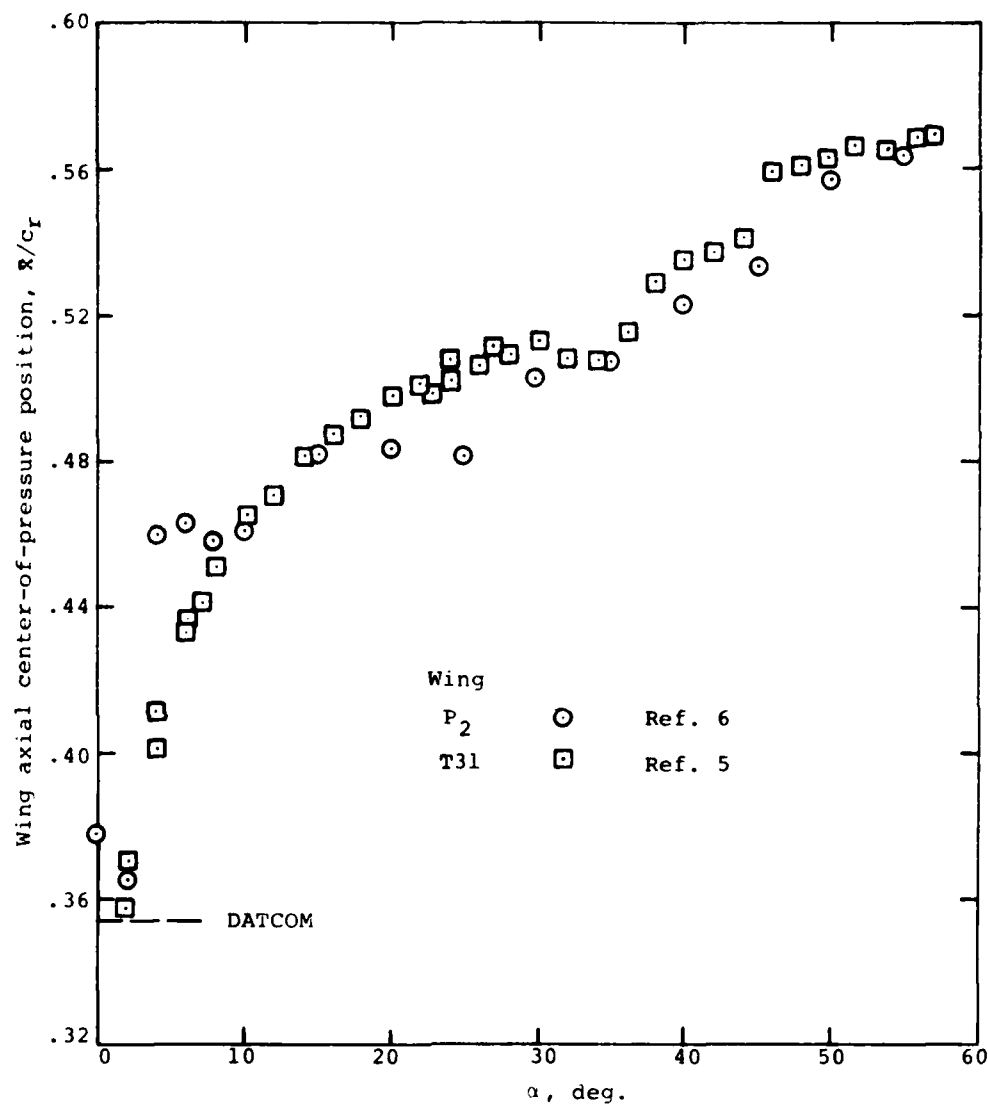
(d) $Re = 1.0$, $\lambda = 1.0$

Figure 6.- Continued.



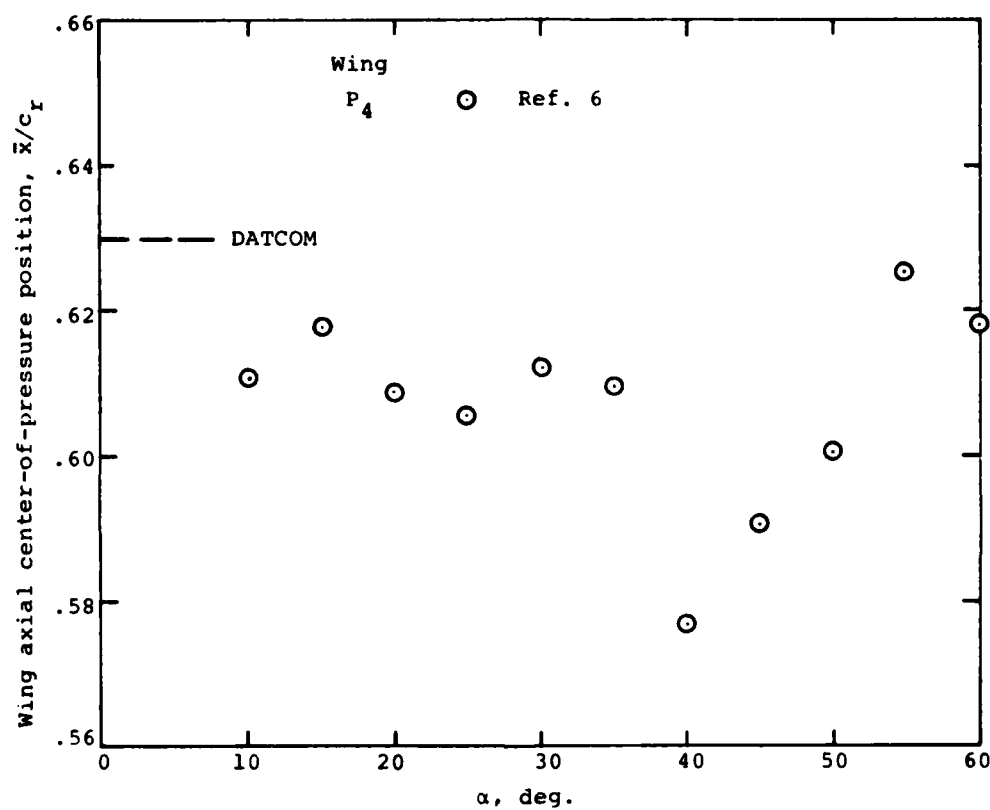
(e) $M = 2$, $\lambda = 0.5$

Figure 6.- Concluded.



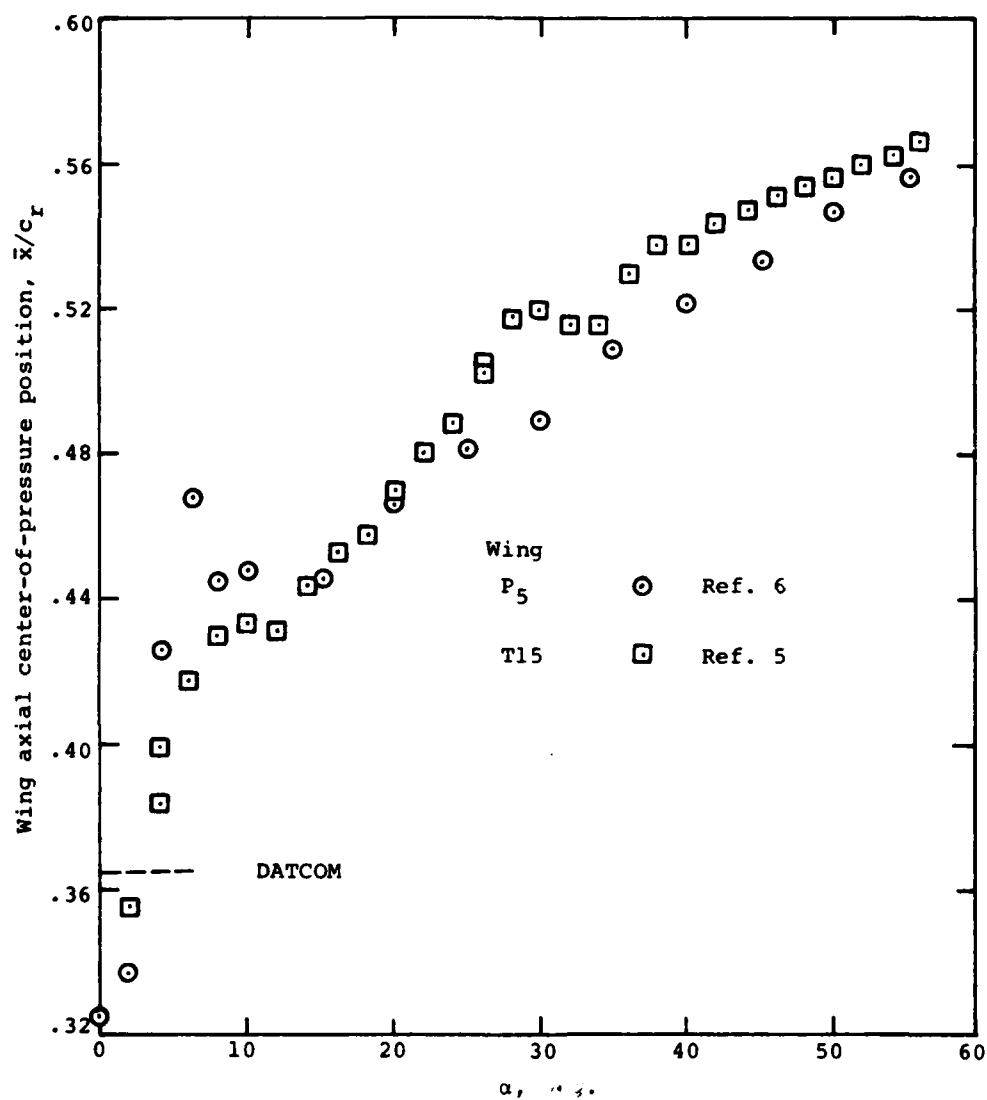
(a) $AR = 0.5$, $\lambda = 0.5$

Figure 7.- Comparison of wing axial center-of-pressure positions at $M_\infty = 0.8$.



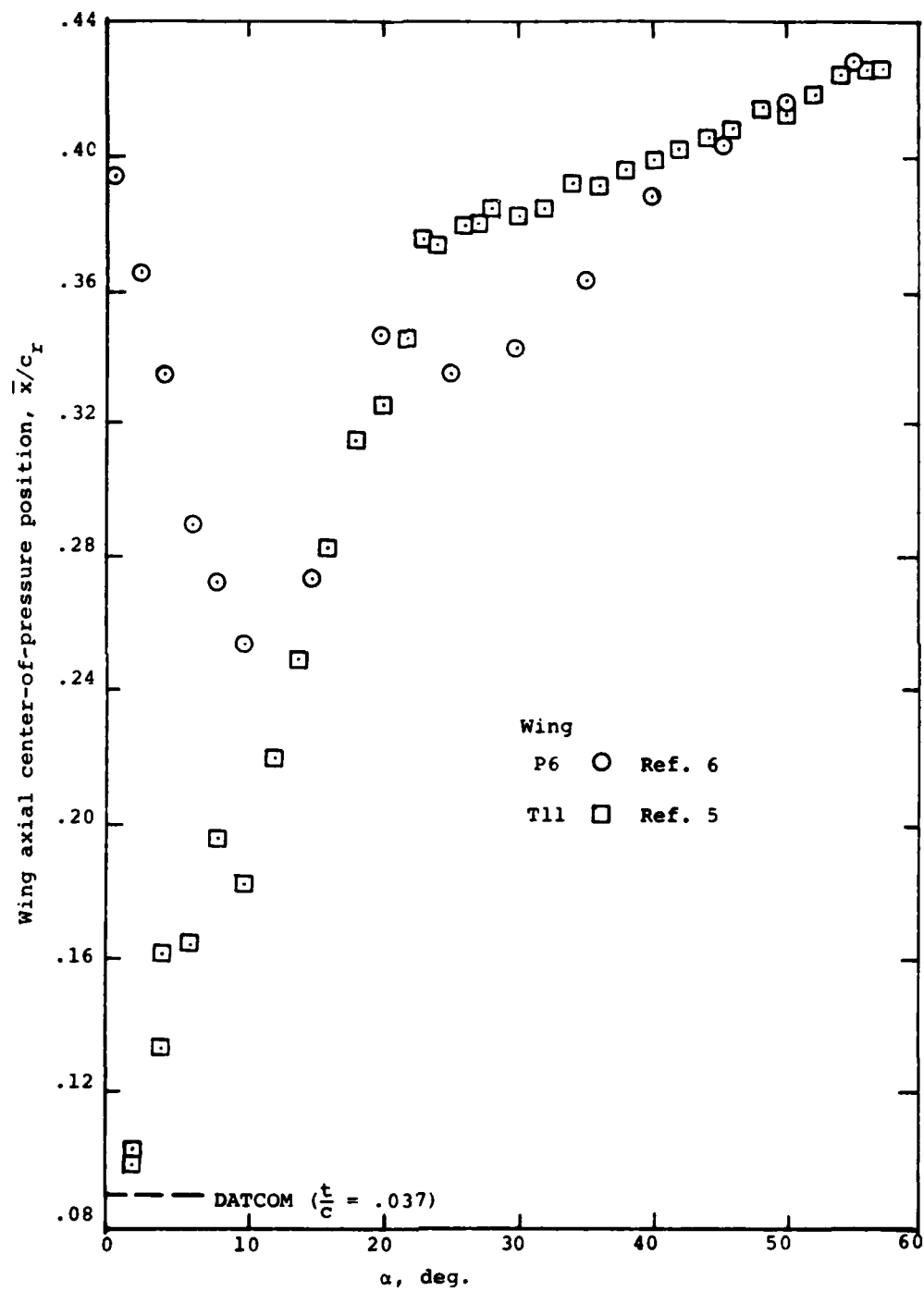
(b) $M = 1.0$, $\lambda = 0$

Figure 7.- Continued.



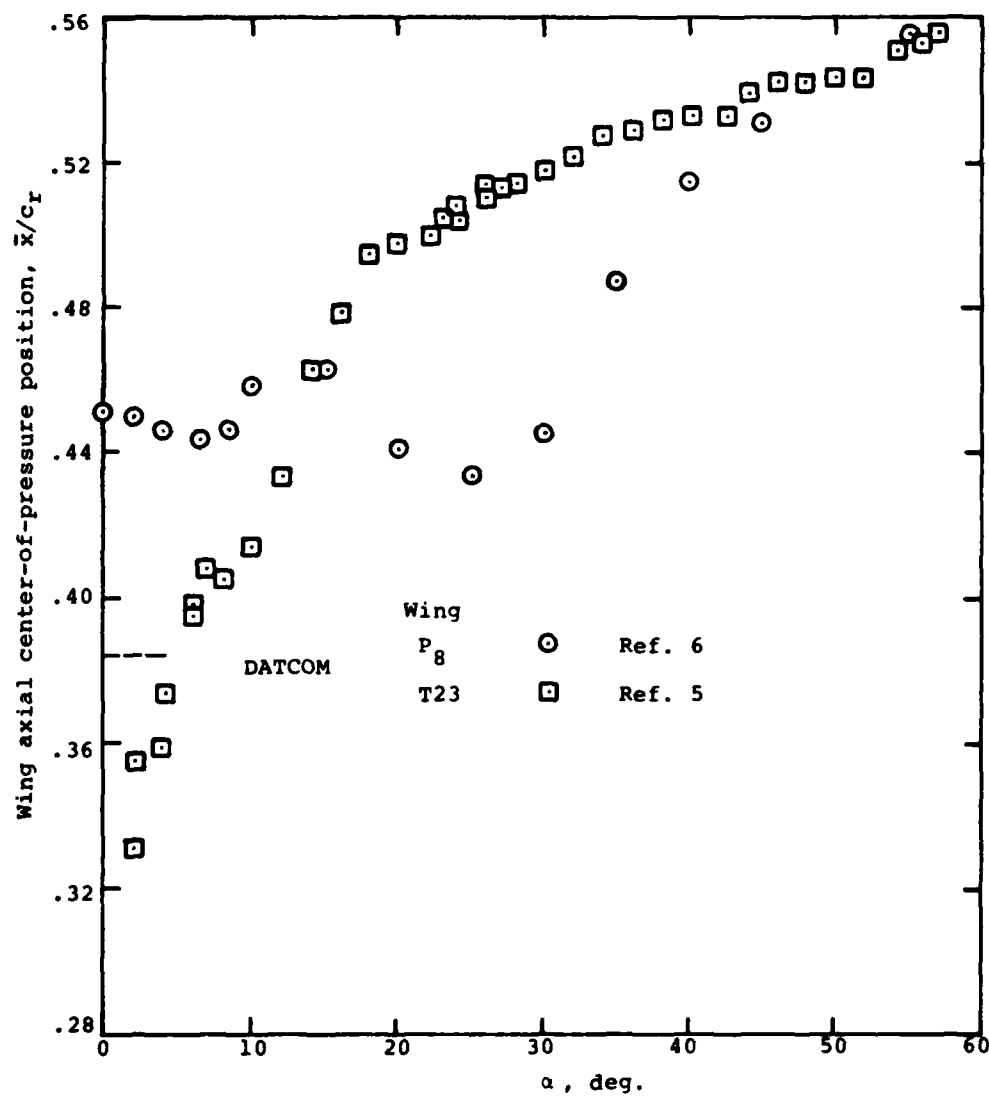
(c) $M = 1.0, \lambda = 0.5$

Figure 7.- Continued.



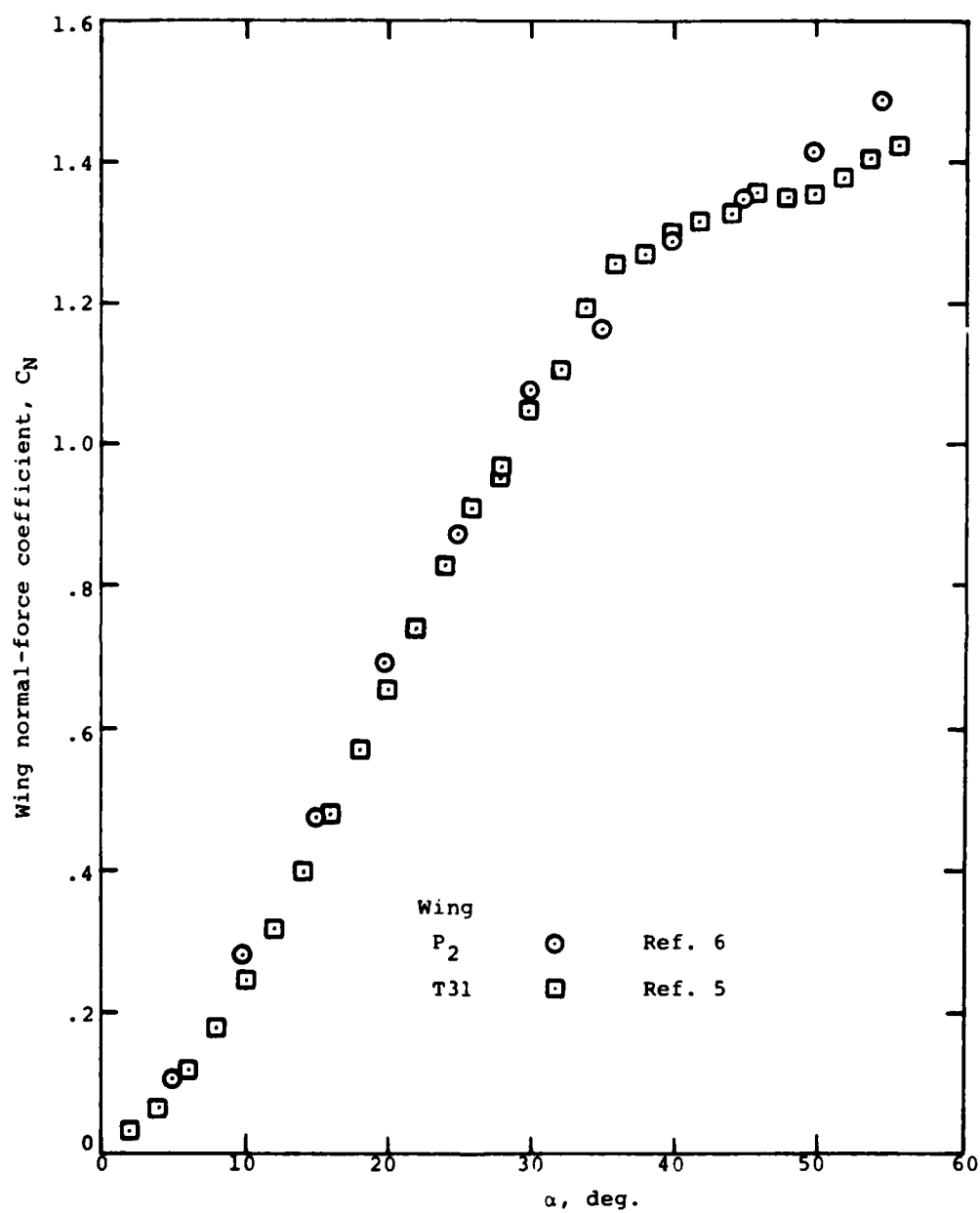
(d) $M = 1.0$, $\lambda = 1.0$

Figure 7.- Continued.



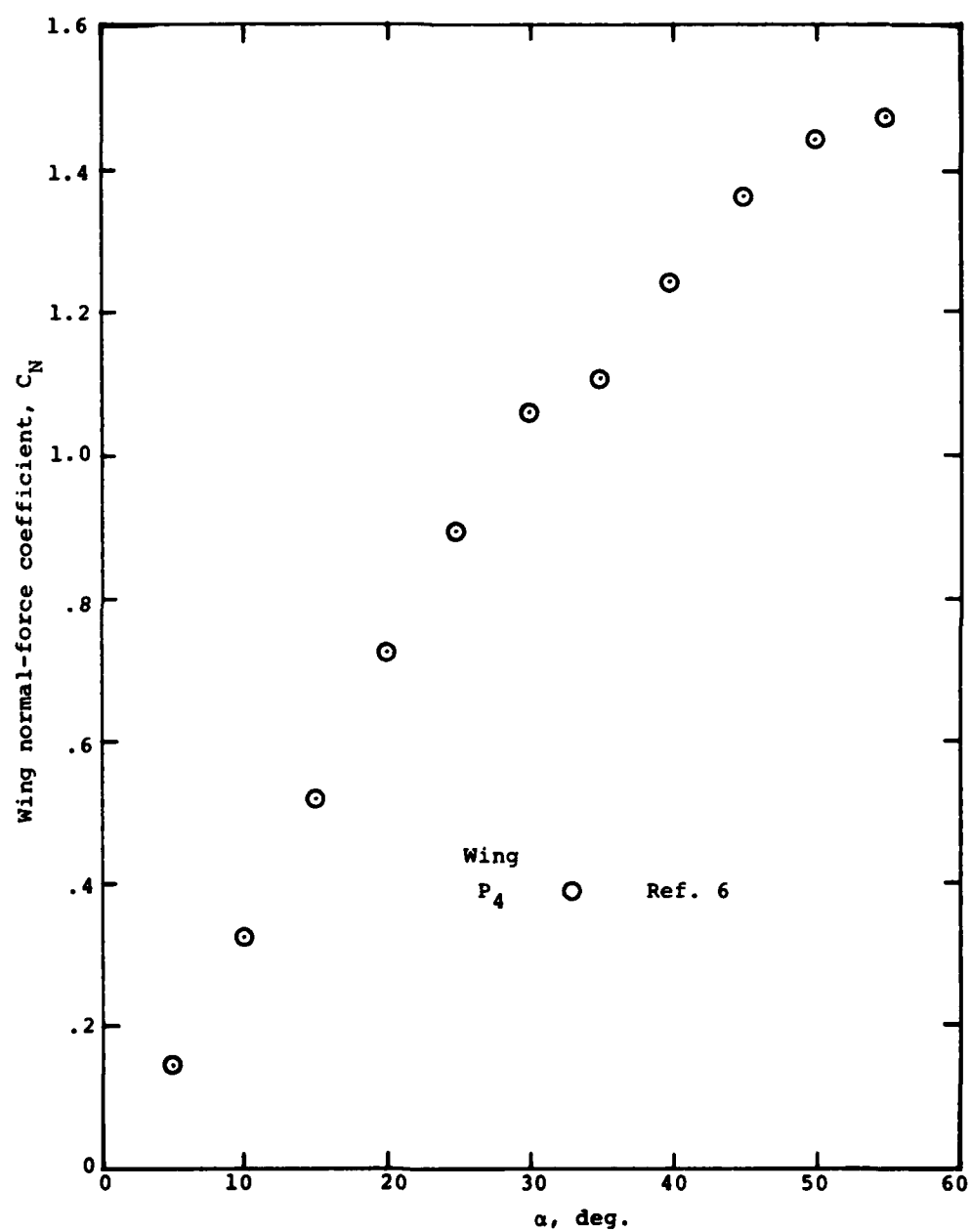
(e) $AR = 2$, $\lambda = 0.5$

Figure 7.- Concluded.



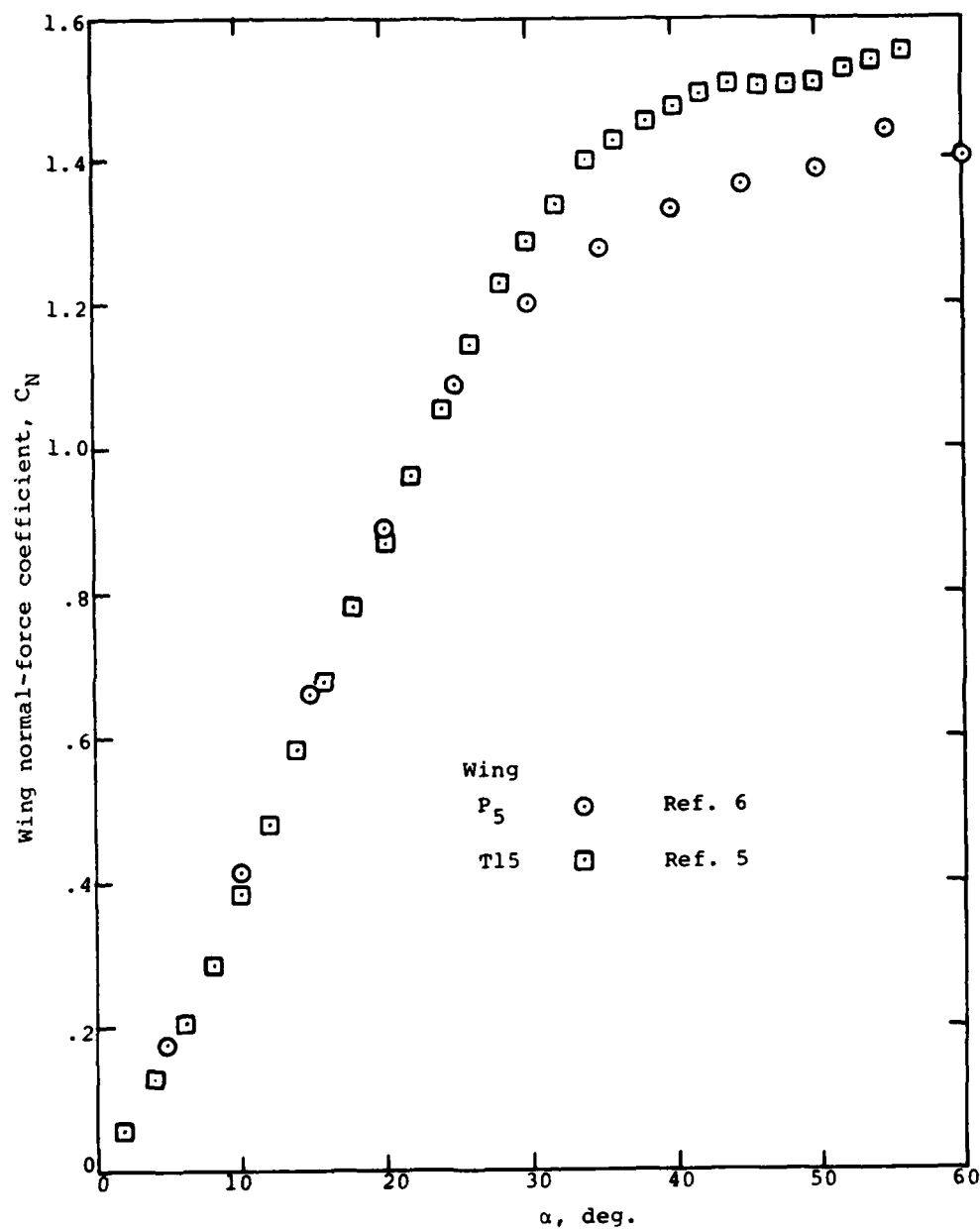
(a) $AR \approx 0.5$, $\lambda = 0.5$

Figure 8.- Comparison of wing normal-force curves at $M_\infty = 1.2$.



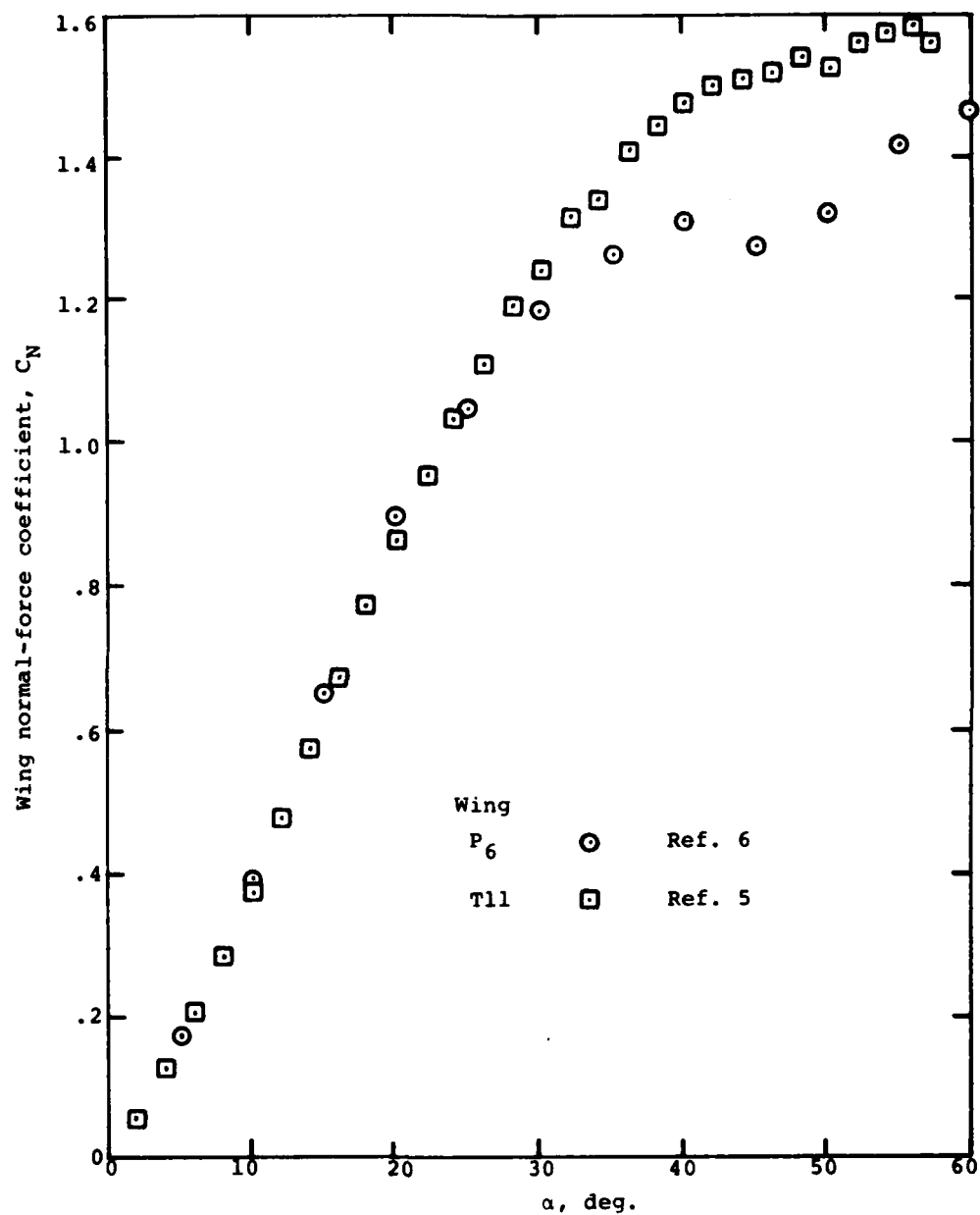
(b) $M = 1$, $\lambda = 0$

Figure 8.- Continued.



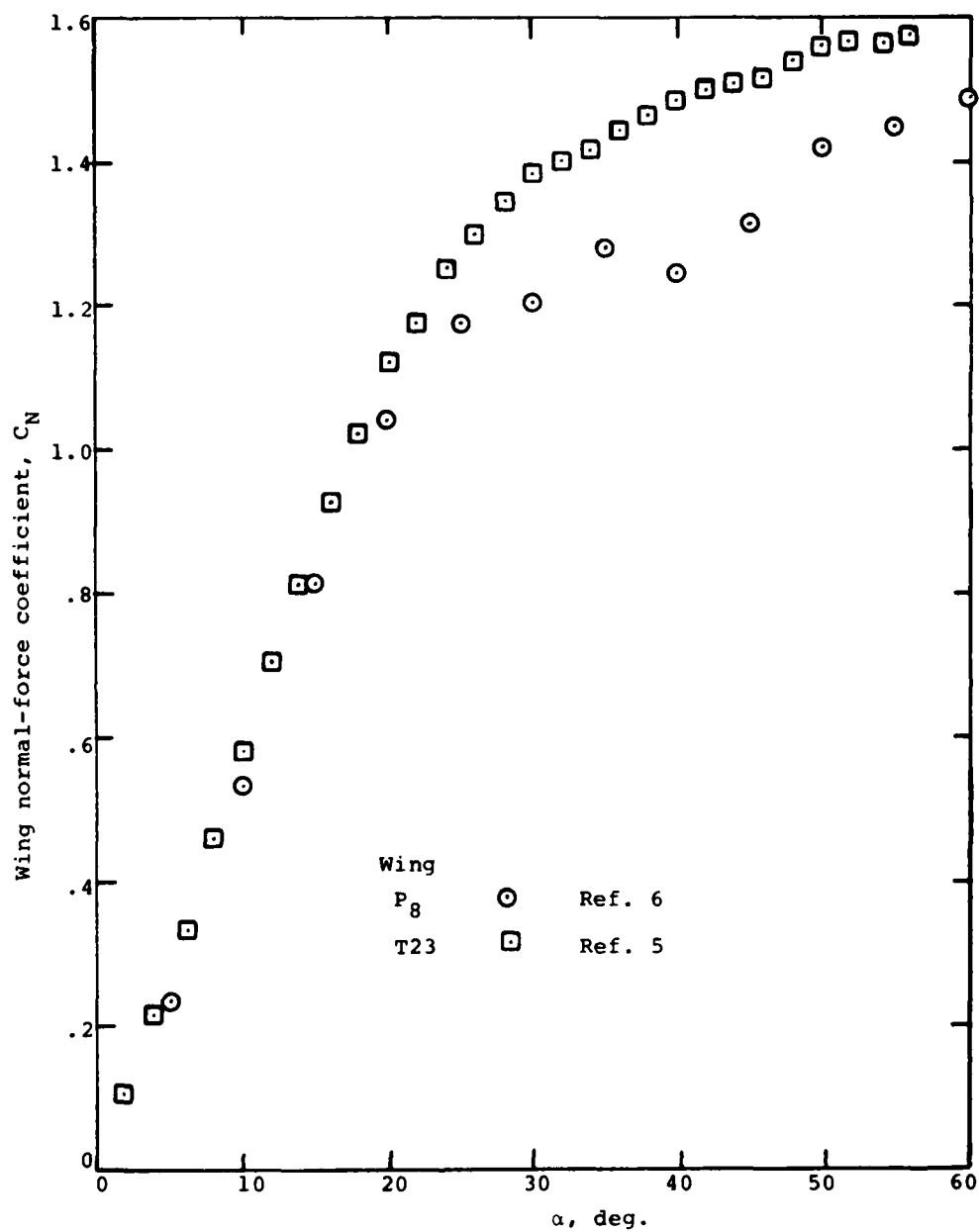
(c) $AR = 1$, $\lambda = 0.5$

Figure 8.- Continued.



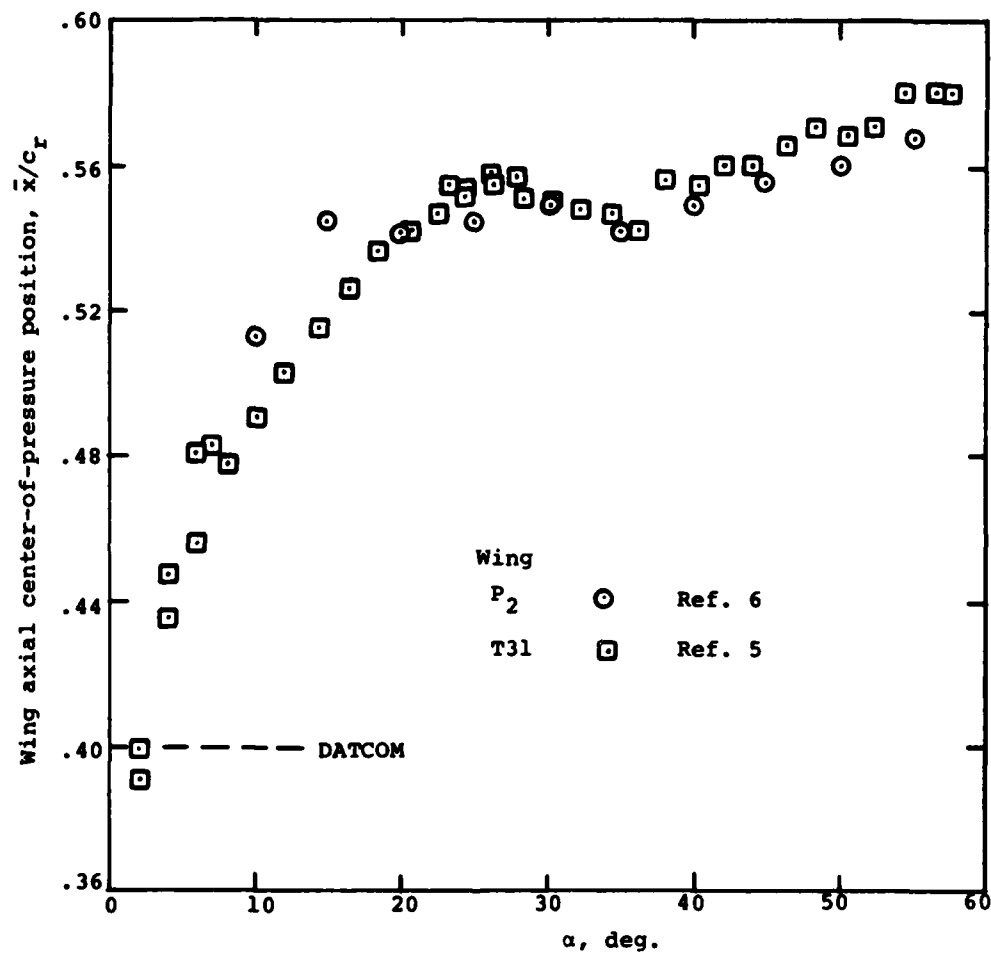
(d) $Re = 1$, $\lambda = 1$

Figure 8.- Continued.



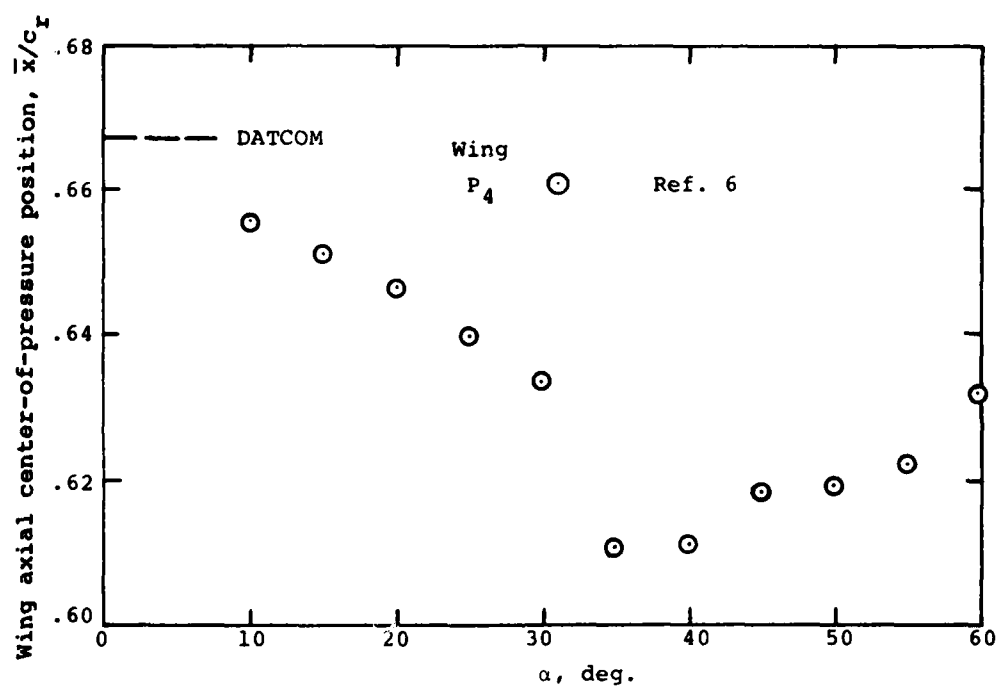
(e) $Re = 2, \lambda = 0.5$

Figure 8.- Concluded.



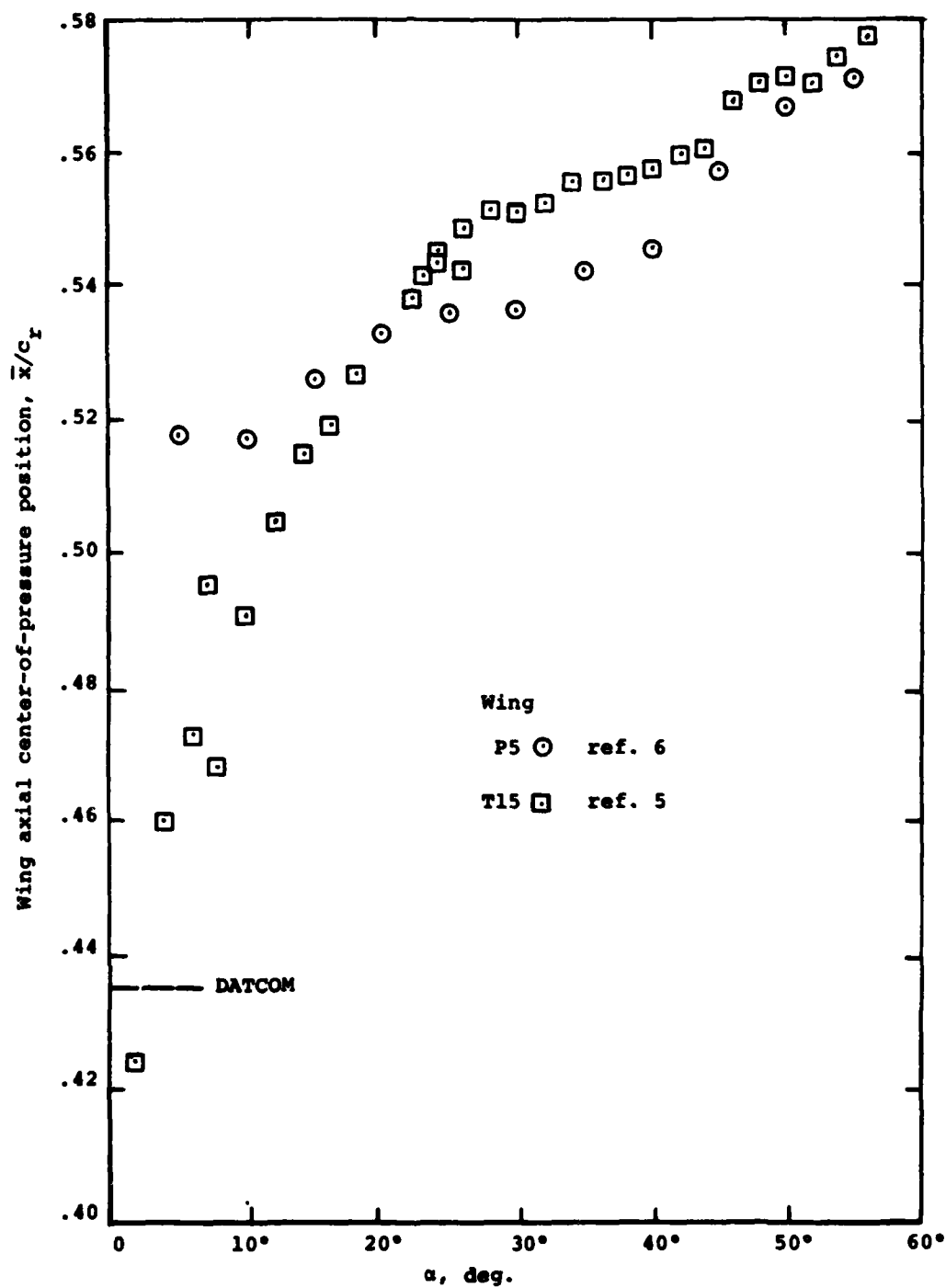
(a) $AR = 0.5, \lambda = 0.5$

Figure 9.- Comparison of wing axial center-of-pressure positions at $M_\infty = 1.2$.



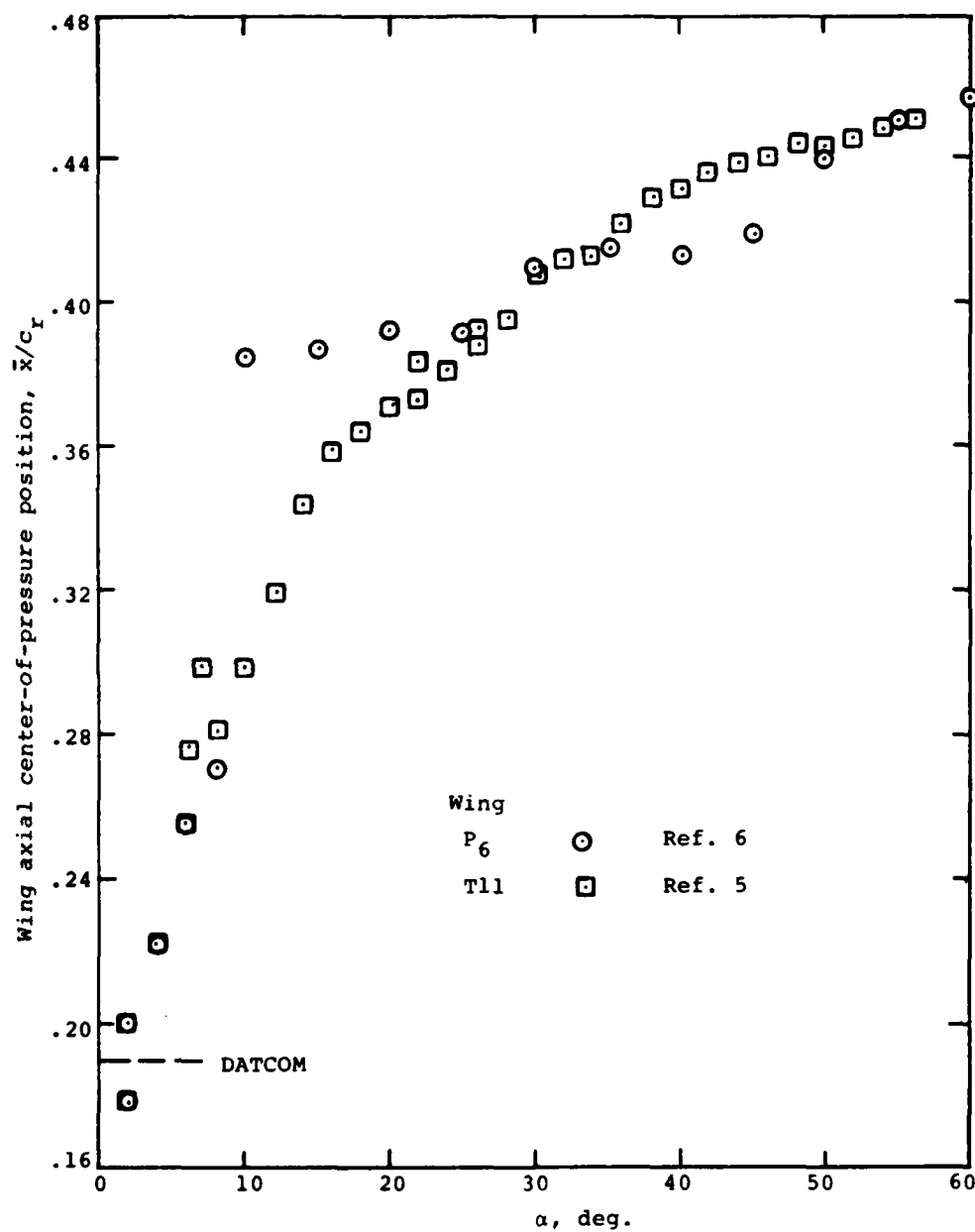
(b) $AR = 1$, $\lambda = 0$

Figure 9.- Continued.



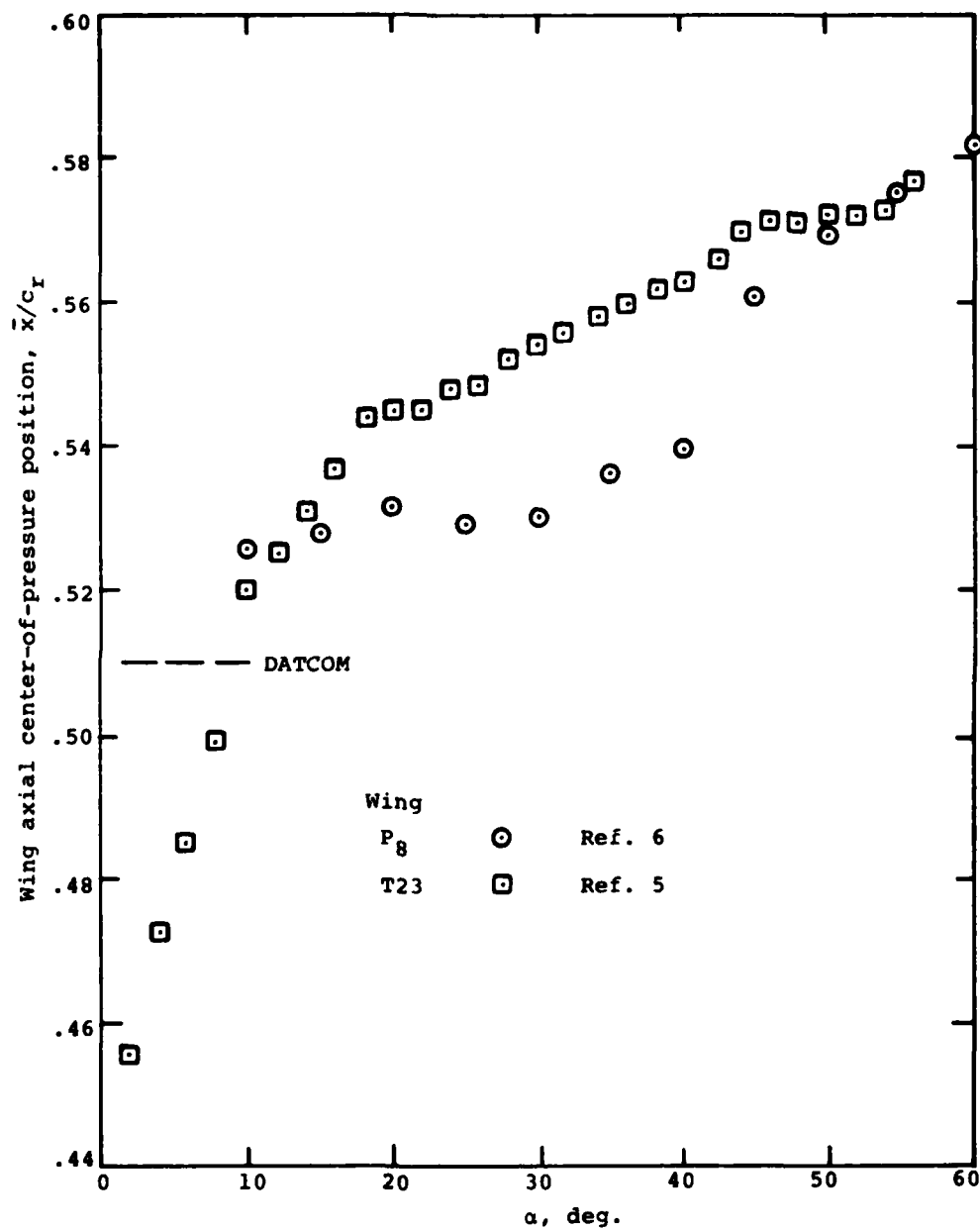
(c) $M = 1.0$, $\lambda = 0.5$

Figure 9.- Continued.



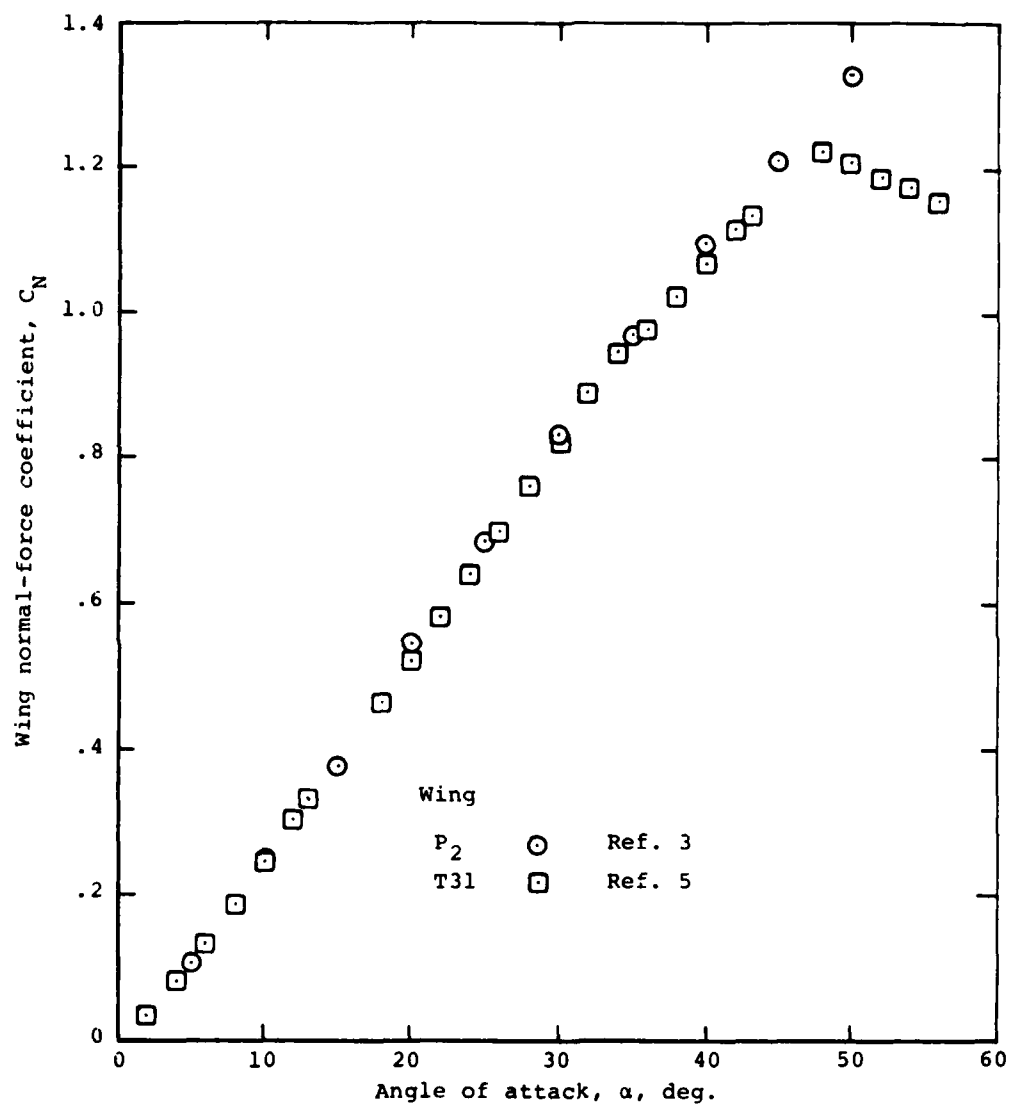
(d) $M = 1$, $\lambda = 1.0$

Figure 9.- Continued.



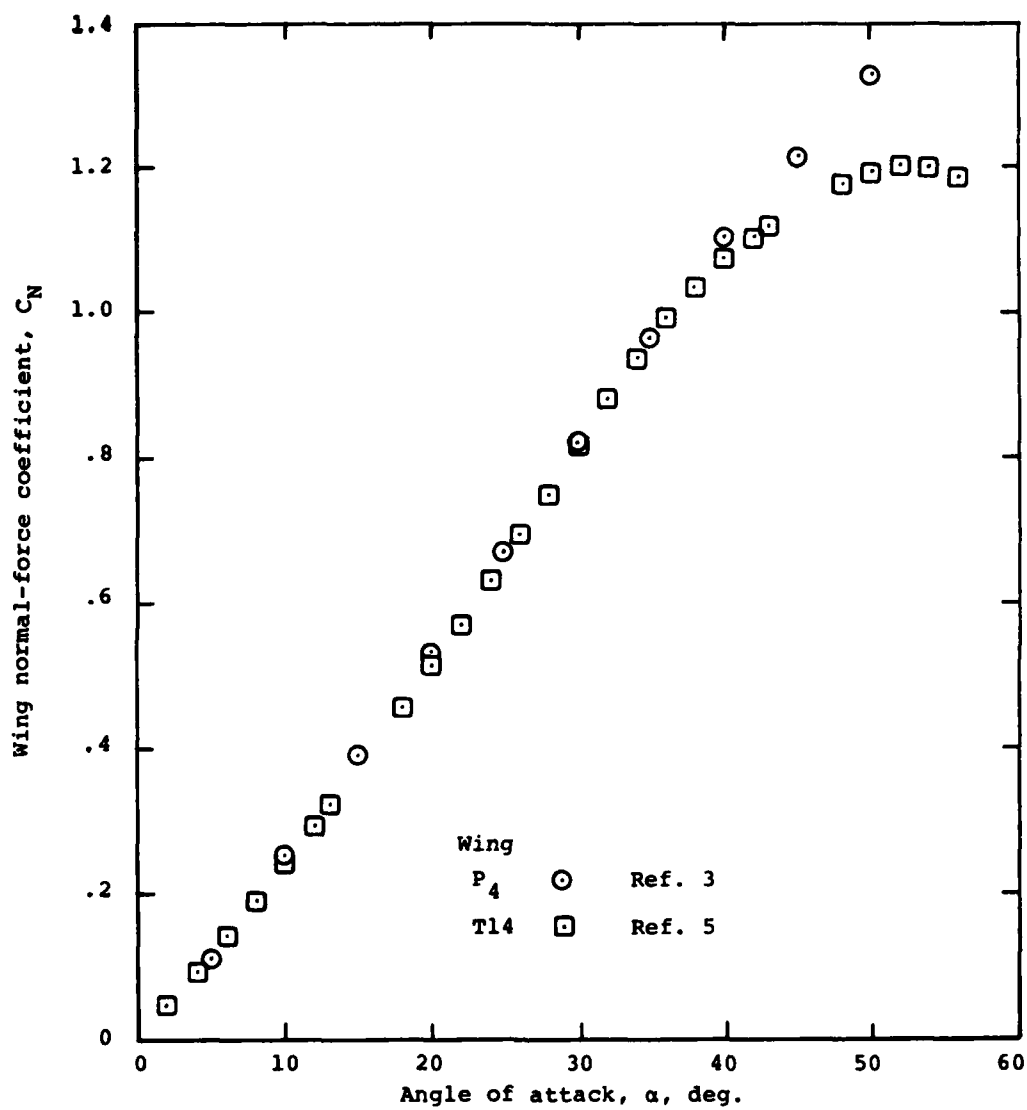
(e) $M = 2.0$, $\lambda = 0.5$

Figure 9.- Concluded.



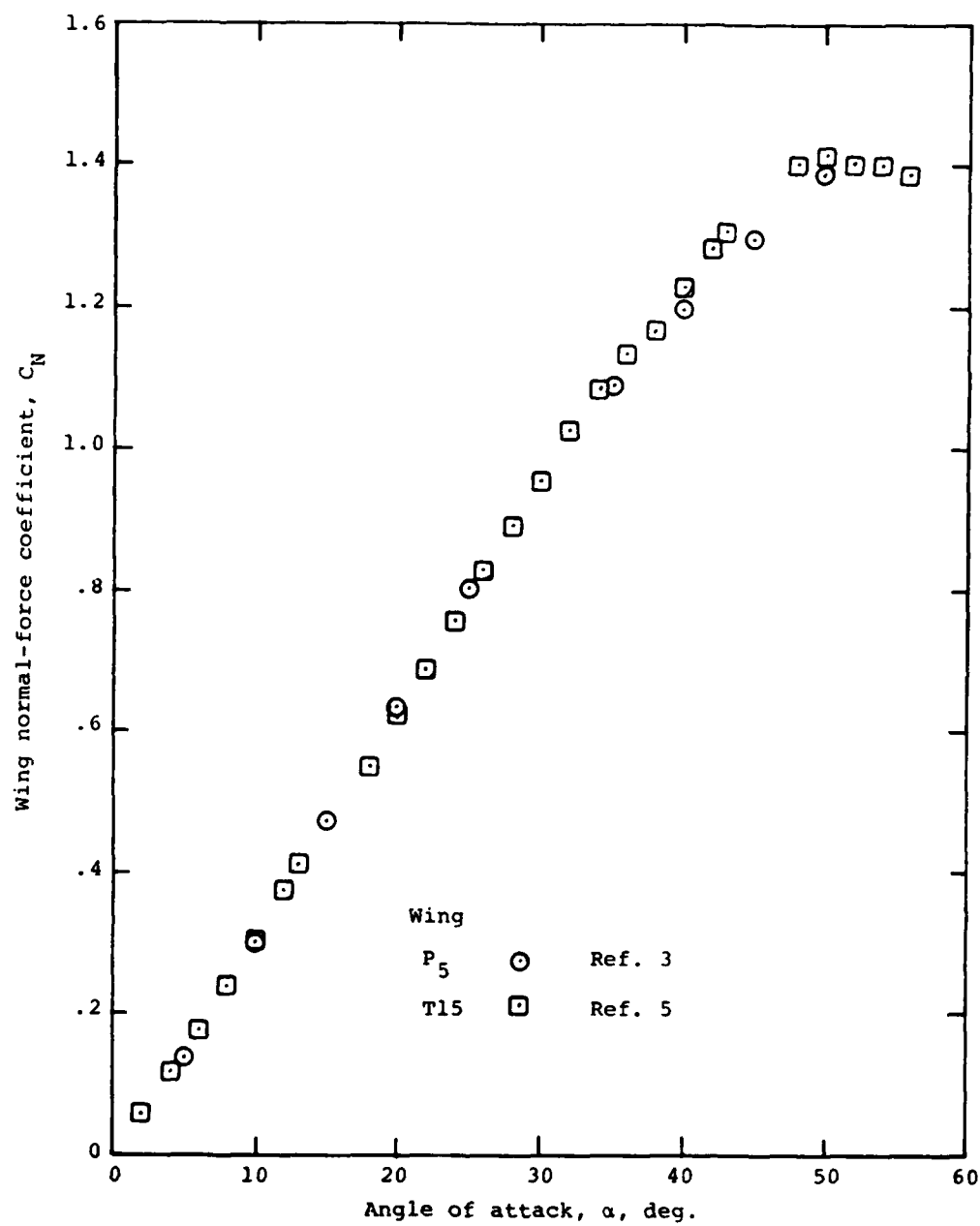
(a) $R = 0.5$, $\lambda = 0.5$

Figure 10.- Comparison of wing normal-force curves at $M_\infty = 2.0$



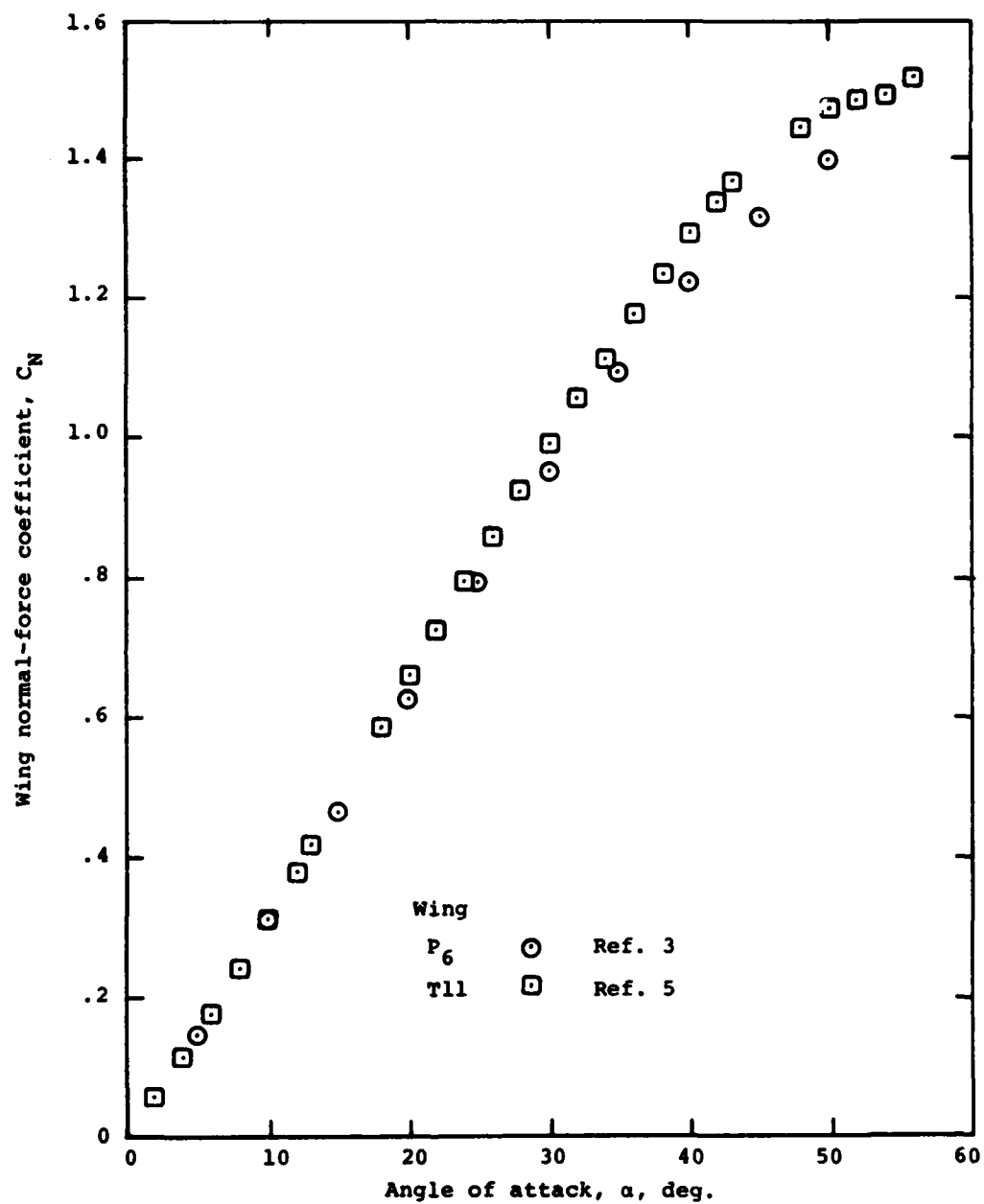
(b) $Re = 1.0, \lambda = 0$

Figure 10.- Continued



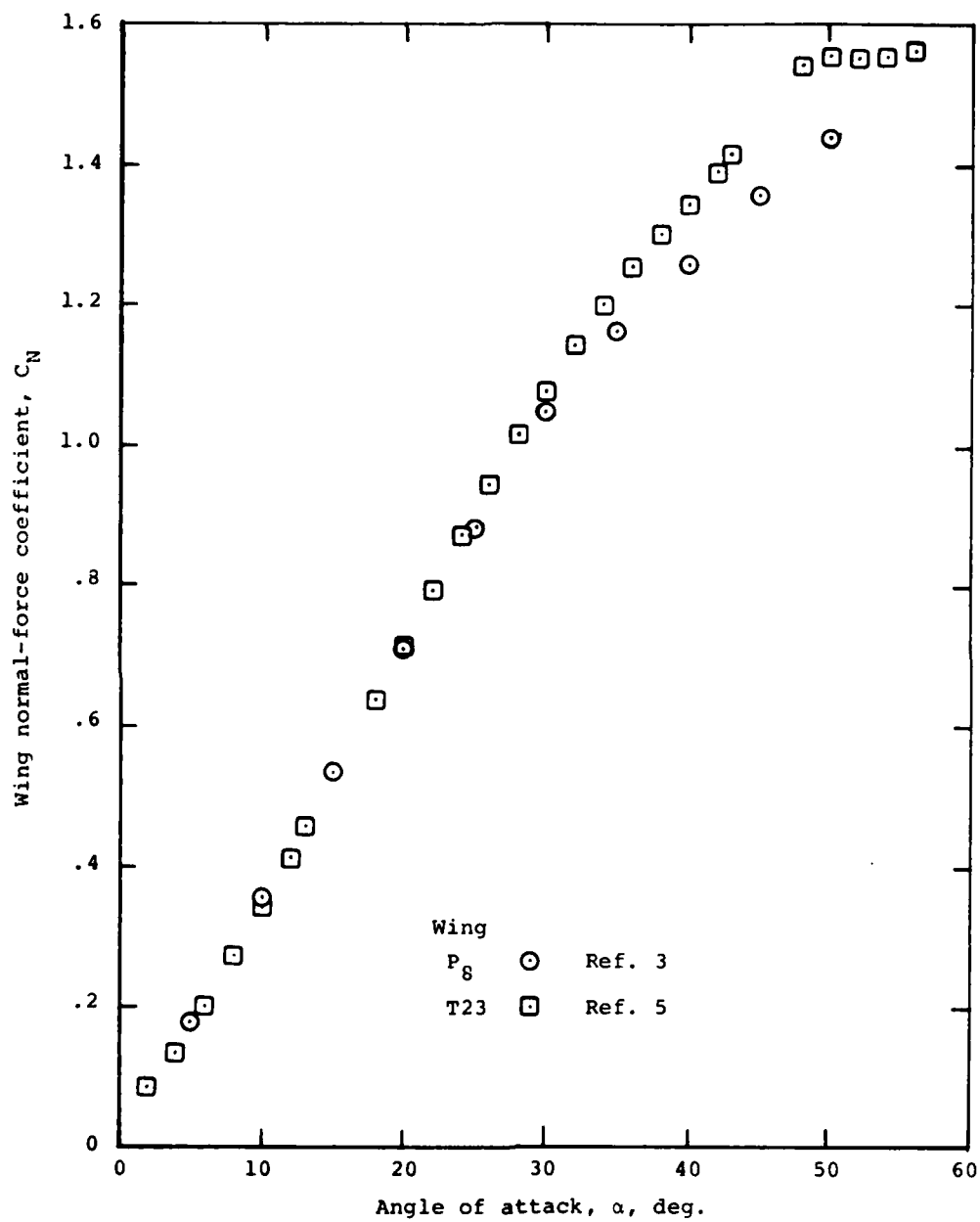
(c) $Re = 1.0$, $\lambda = 0.5$

Figure 10.- Continued



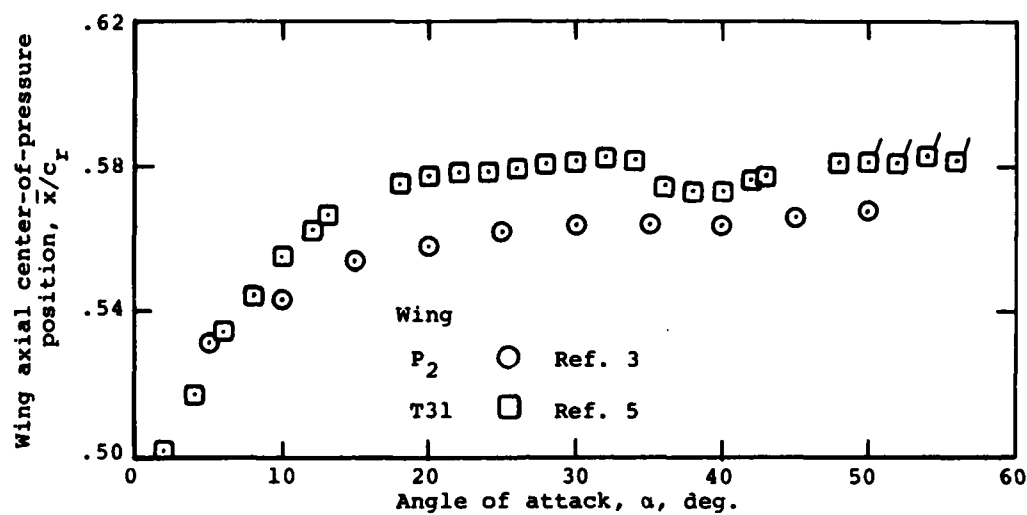
(d) $AR = 1.0$, $\lambda = 1.0$

Figure 10.- Continued

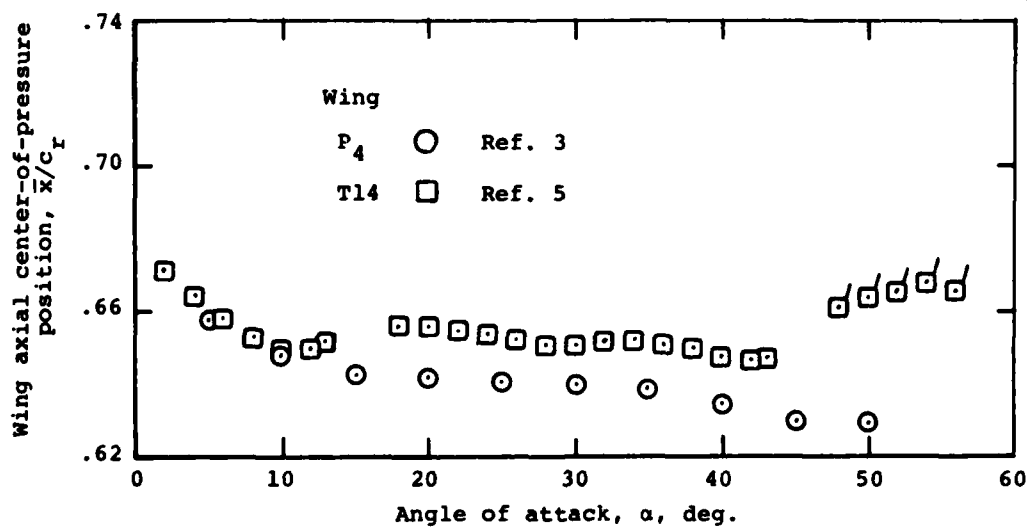


(e) $M = 2.0$, $\lambda = 0.5$

Figure 10.- Concluded

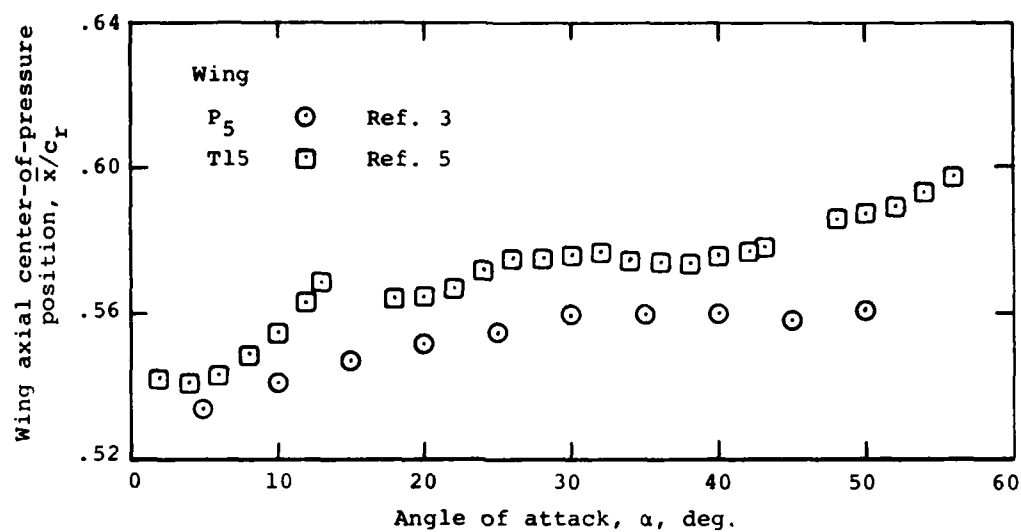


(a) $AR = 0.5$, $\lambda = 0.5$

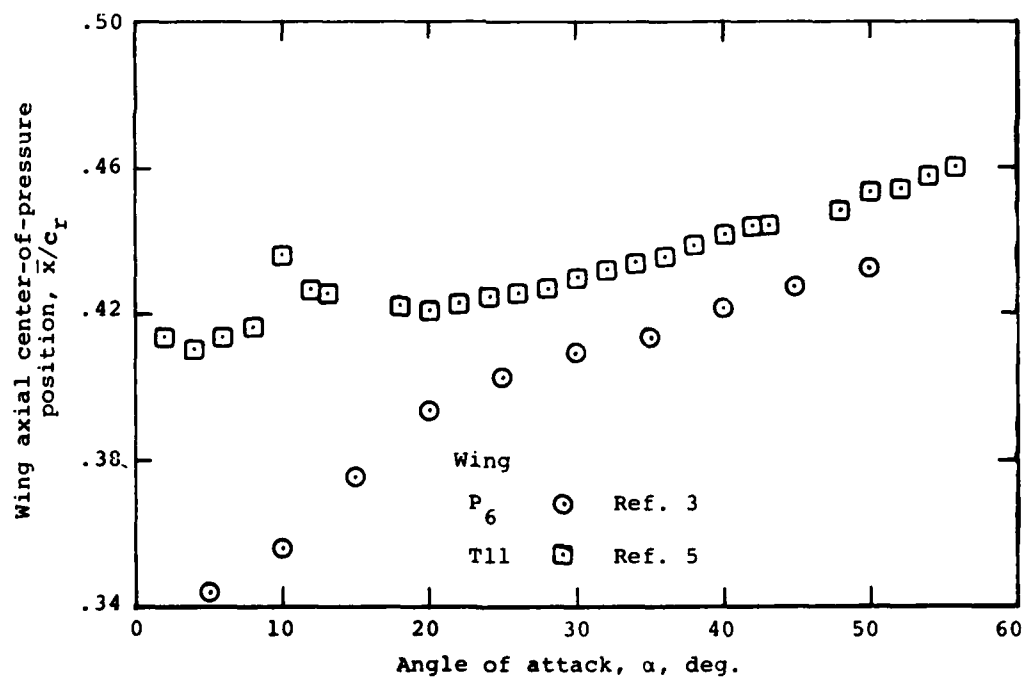


(b) $AR = 1.0$, $\lambda = 0$

Figure 11.- Comparison of wing axial center-of-pressure positions at $M_\infty = 2.0$

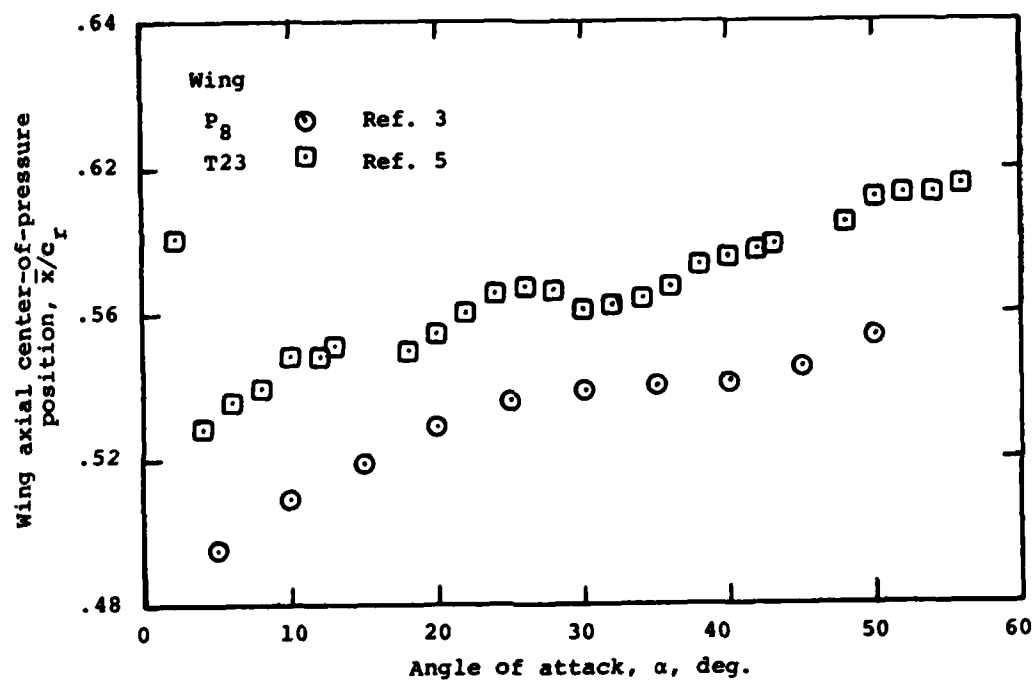


(c) $AR = 1.0$, $\lambda = 0.5$



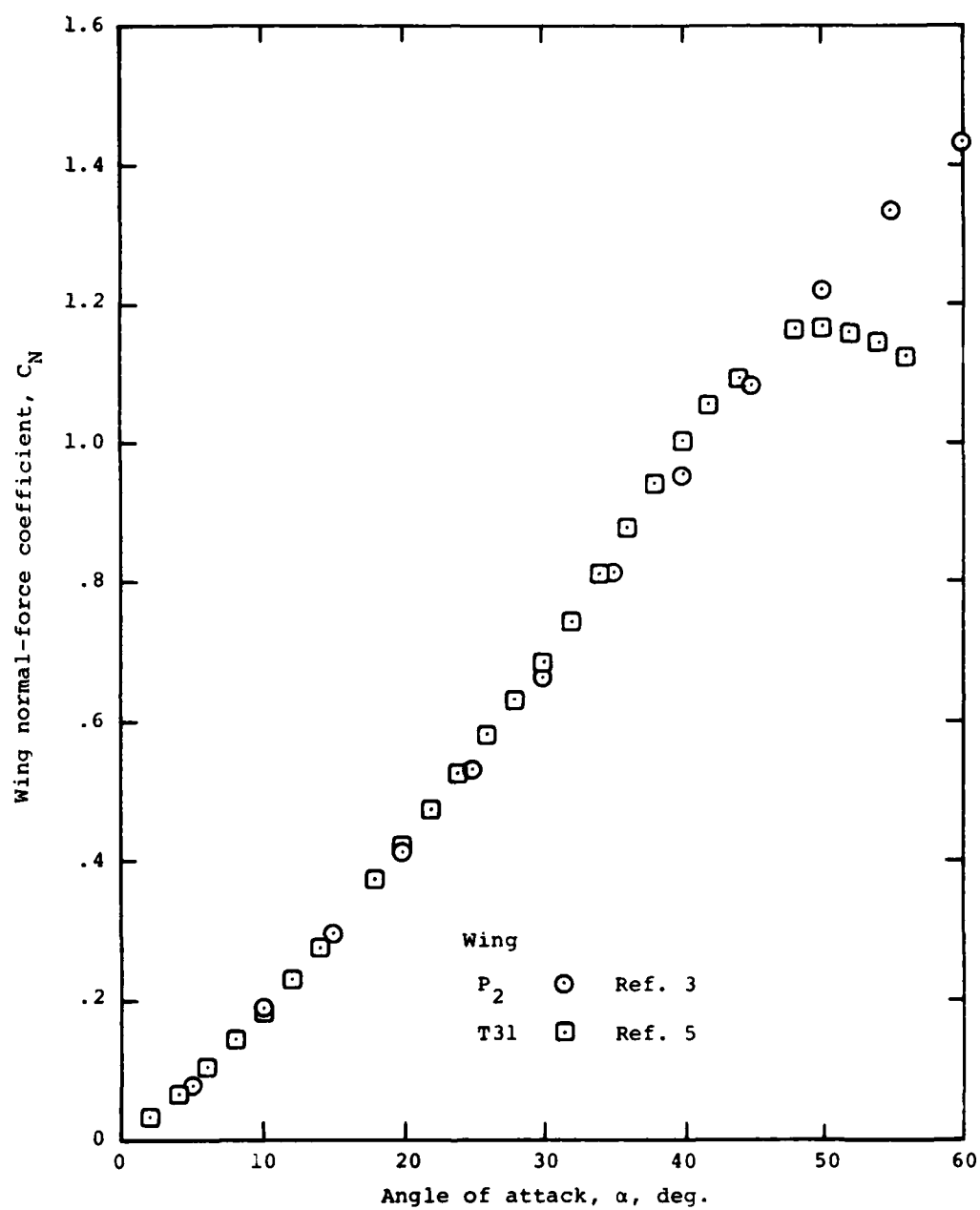
(d) $AR = 1.0$, $\lambda = 1.0$

Figure 11.- Continued



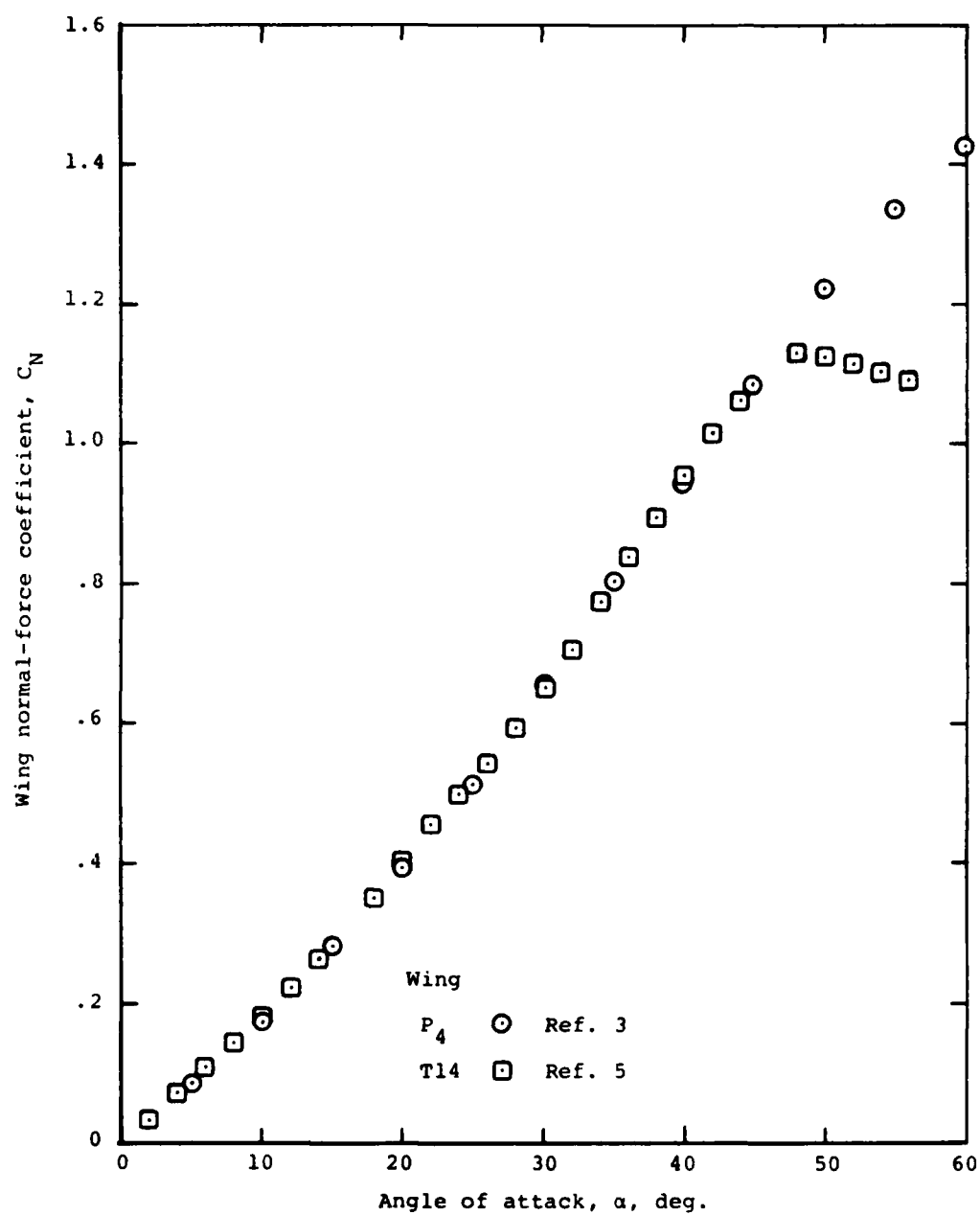
(e) $Re = 2.0, \lambda = 0.5$

Figure 11.- Concluded



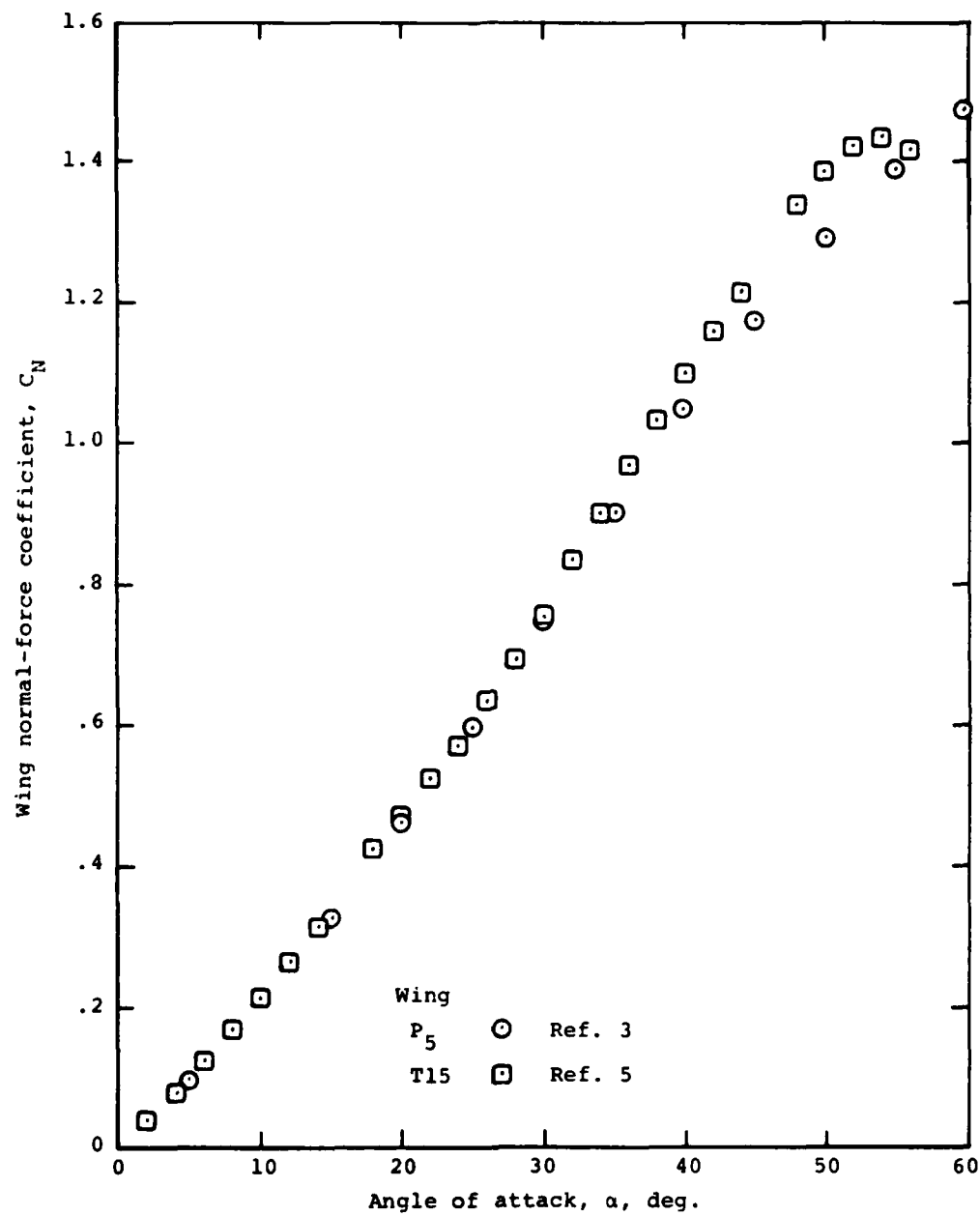
(a) $R = 0.5$, $\lambda = 0.5$

Figure 12.- Comparison of wing normal-force curves at $M_\infty = 3.0$



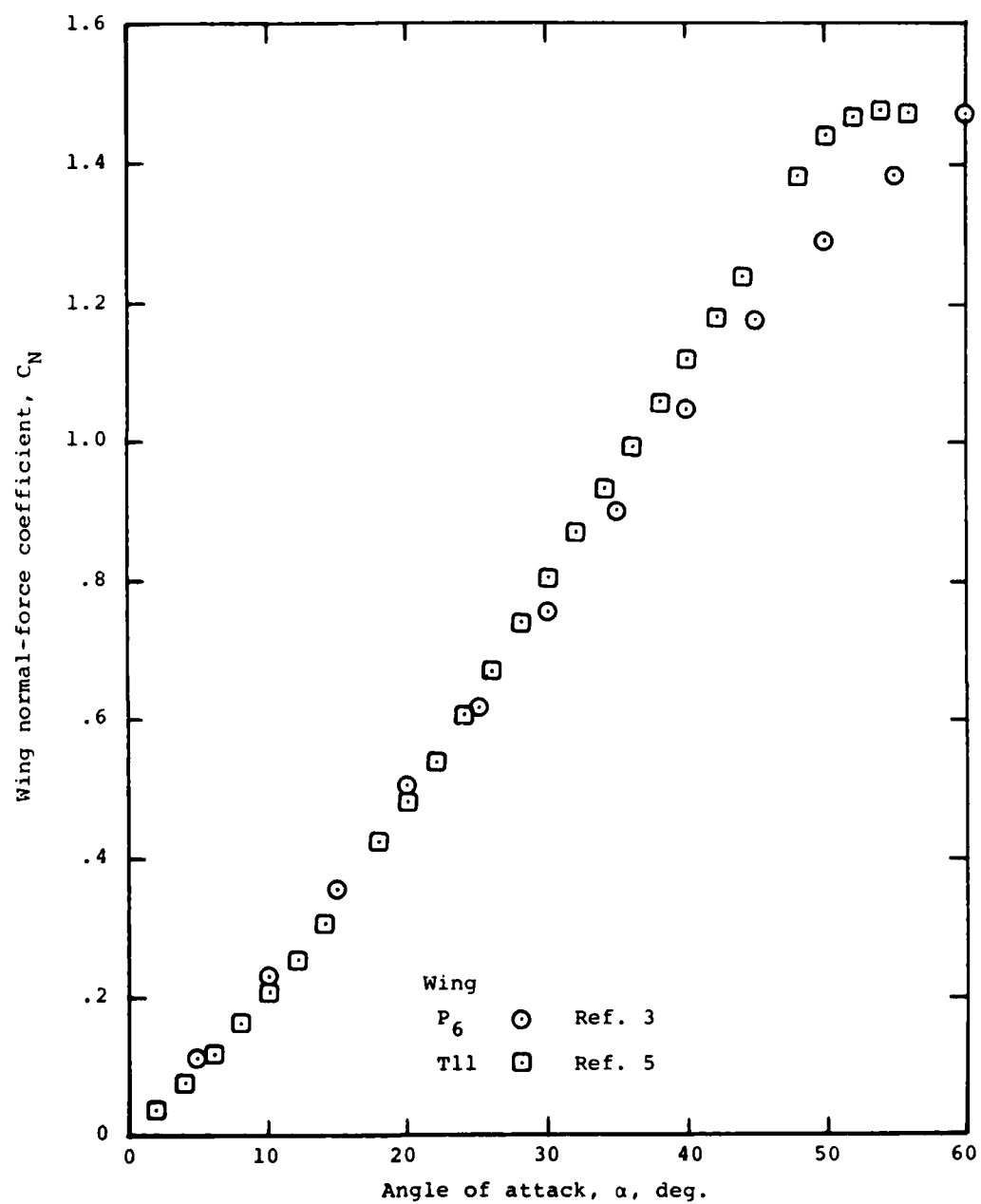
(b) $Re = 1.0$, $\lambda = 0$

Figure 12.- Continued



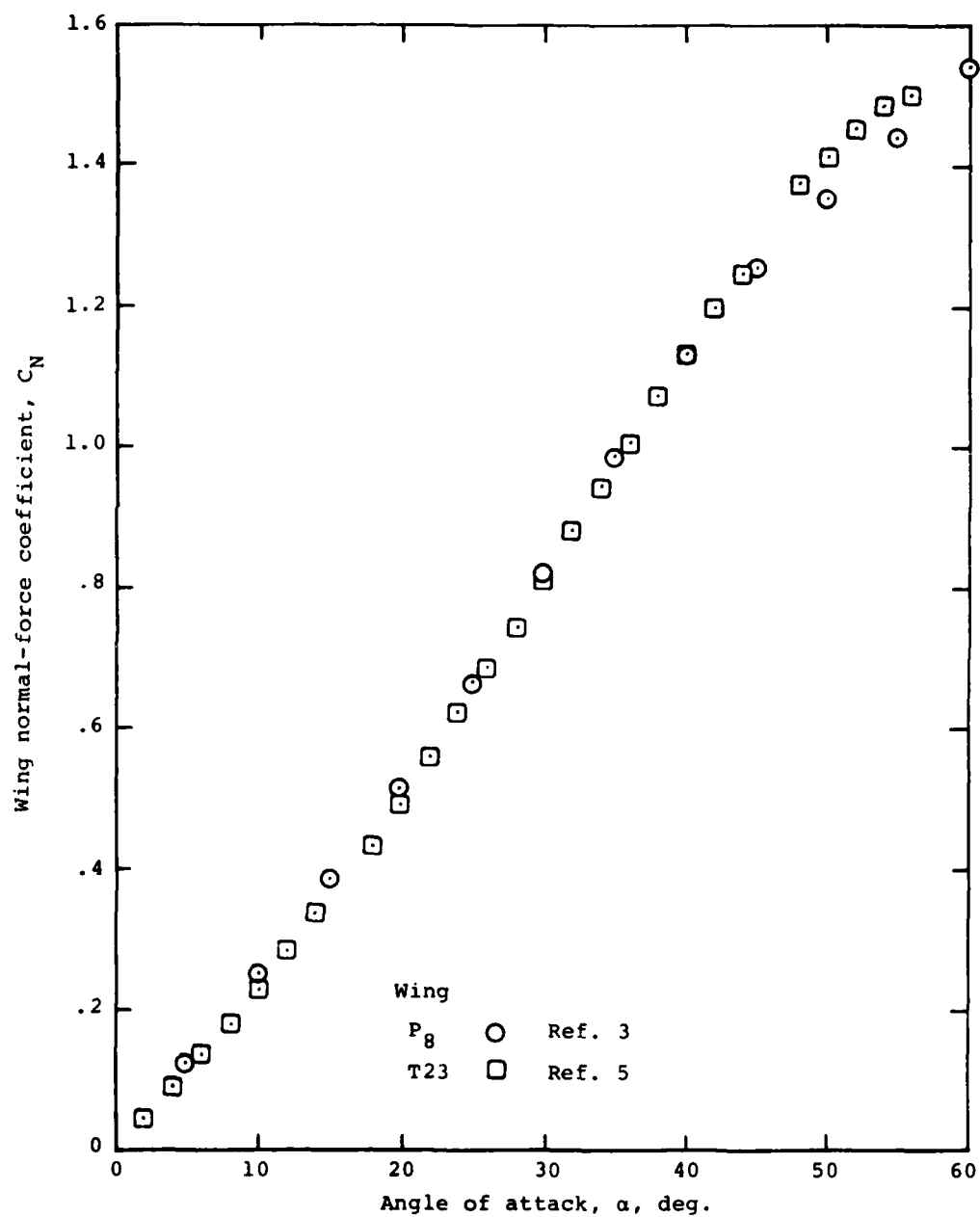
(c) $M = 1.0$, $\lambda = 0.5$

Figure 12.- Continued



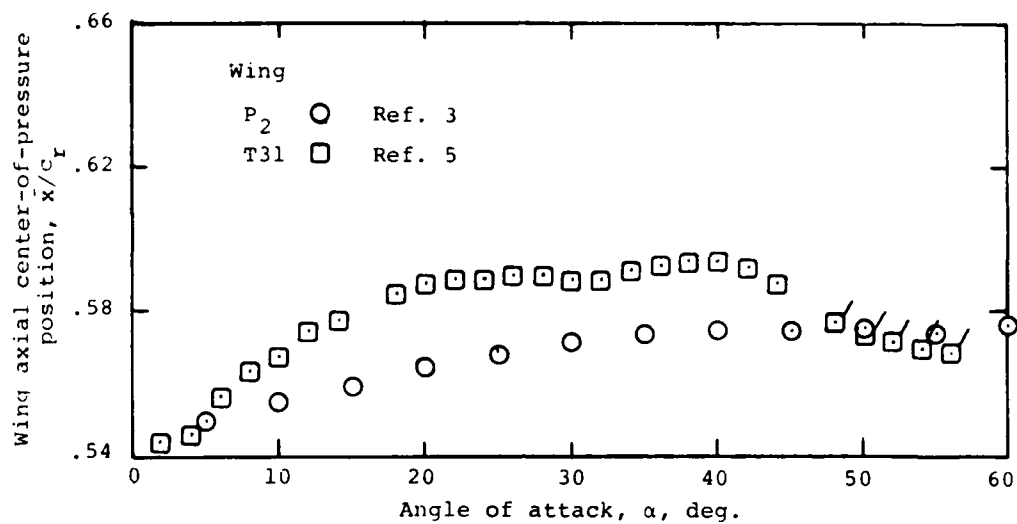
(d) $Re = 1.0$, $\lambda = 1.0$

Figure 12.- Continued

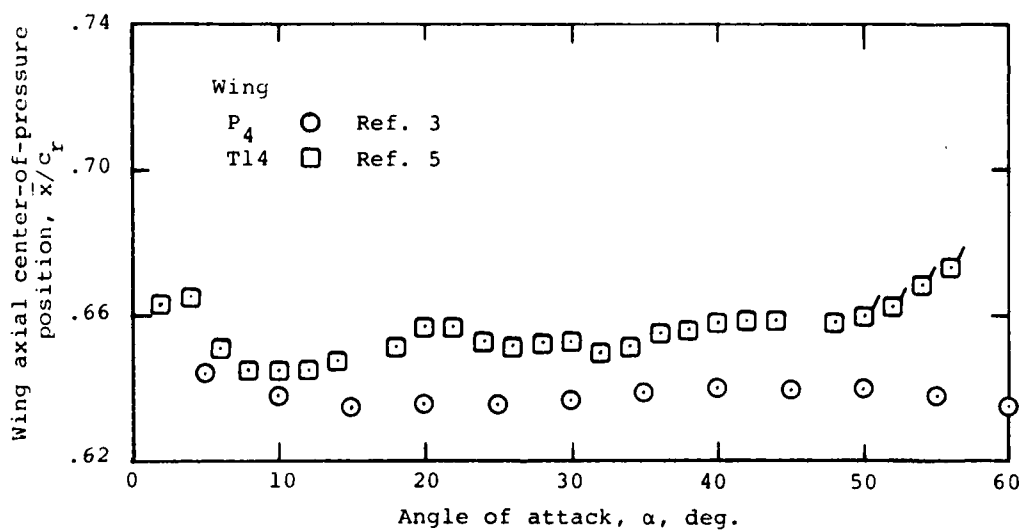


(e) $M = 2.0$, $\lambda = 0.5$

Figure 12.- Concluded

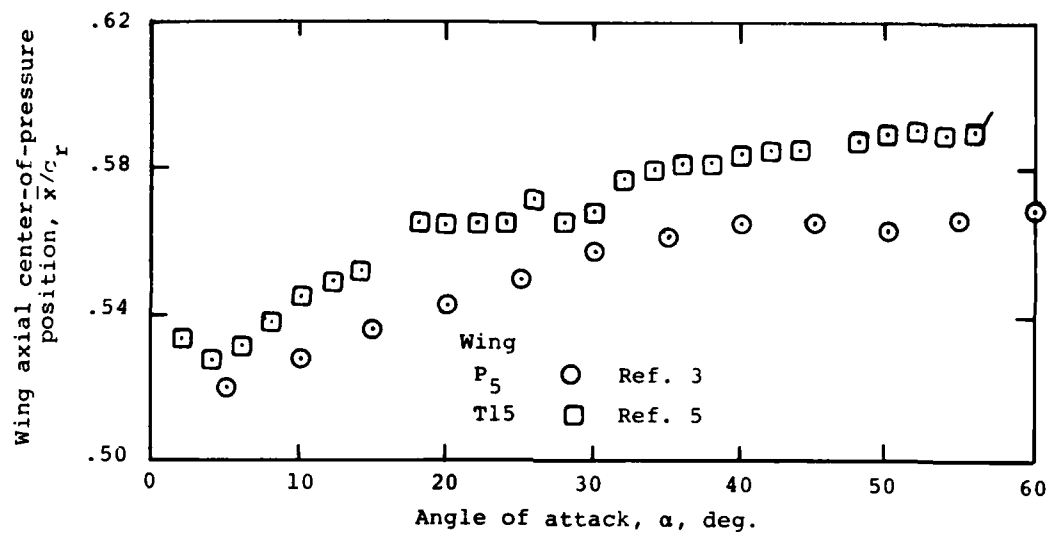


(a) $R = 0.5$, $\lambda = 0.5$

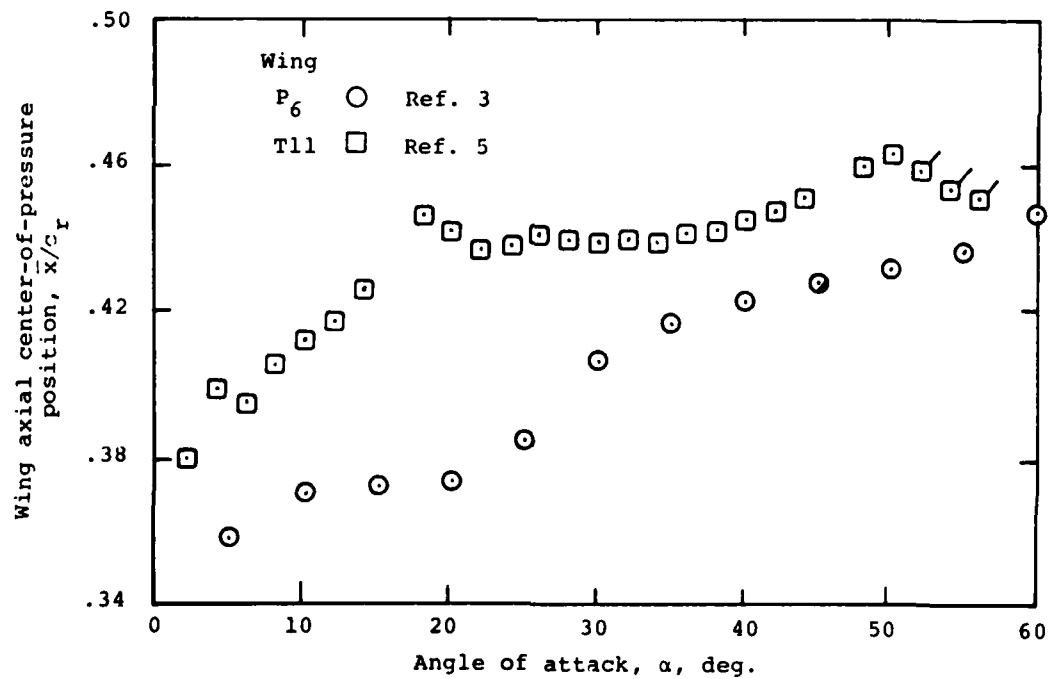


(b) $R = 1.0$, $\lambda = 0$

Figure 13.- Comparison of wing axial center-of-pressure positions at $M_\infty = 3.0$

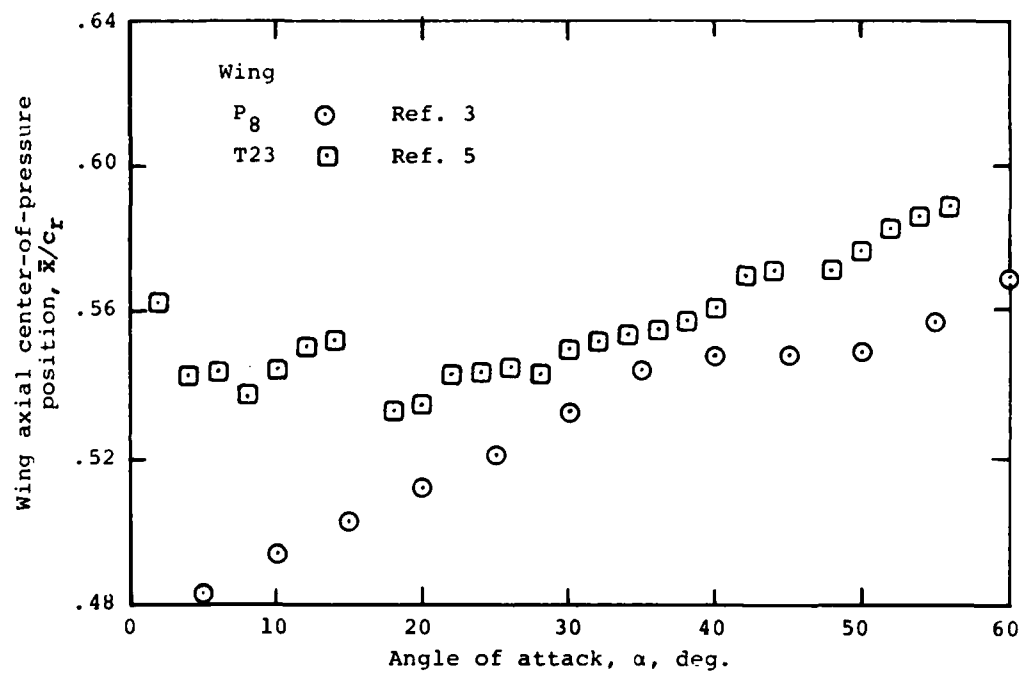


(c) $Re = 1.0$, $\lambda = 0.5$



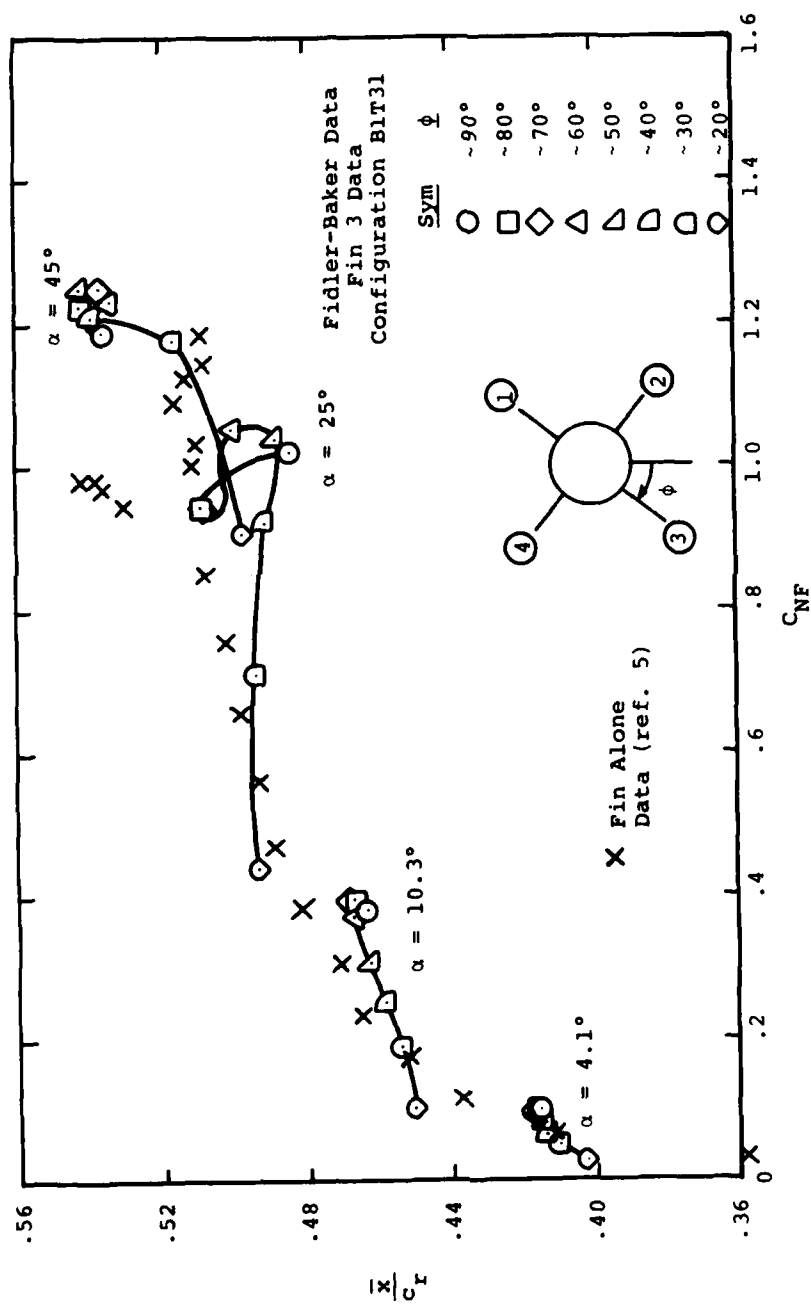
(d) $Re = 1.0$, $\lambda = 1.0$

Figure 13.- Continued

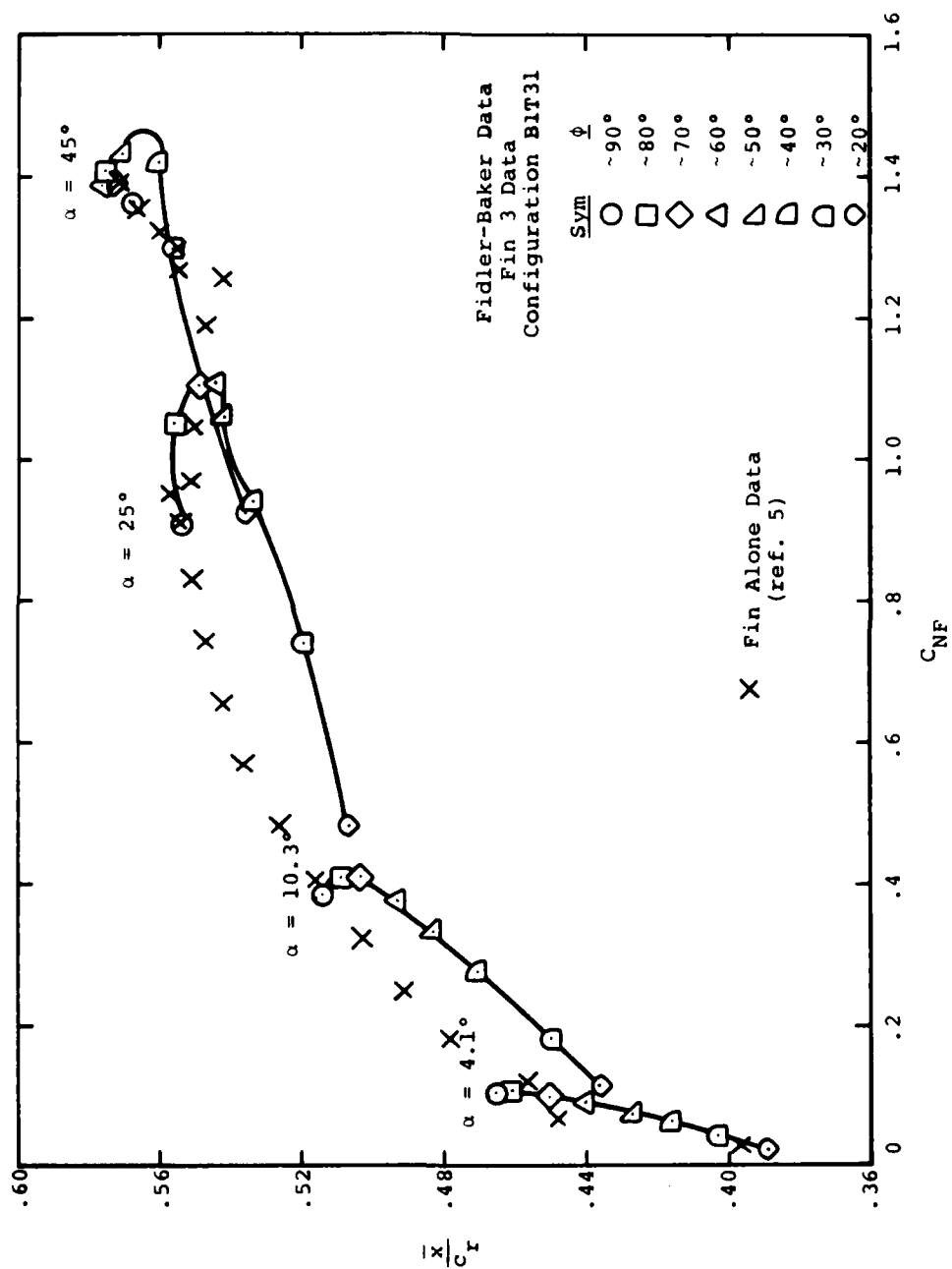


(e) $Re = 2.0, \lambda = 0.5$

Figure 13.- Concluded

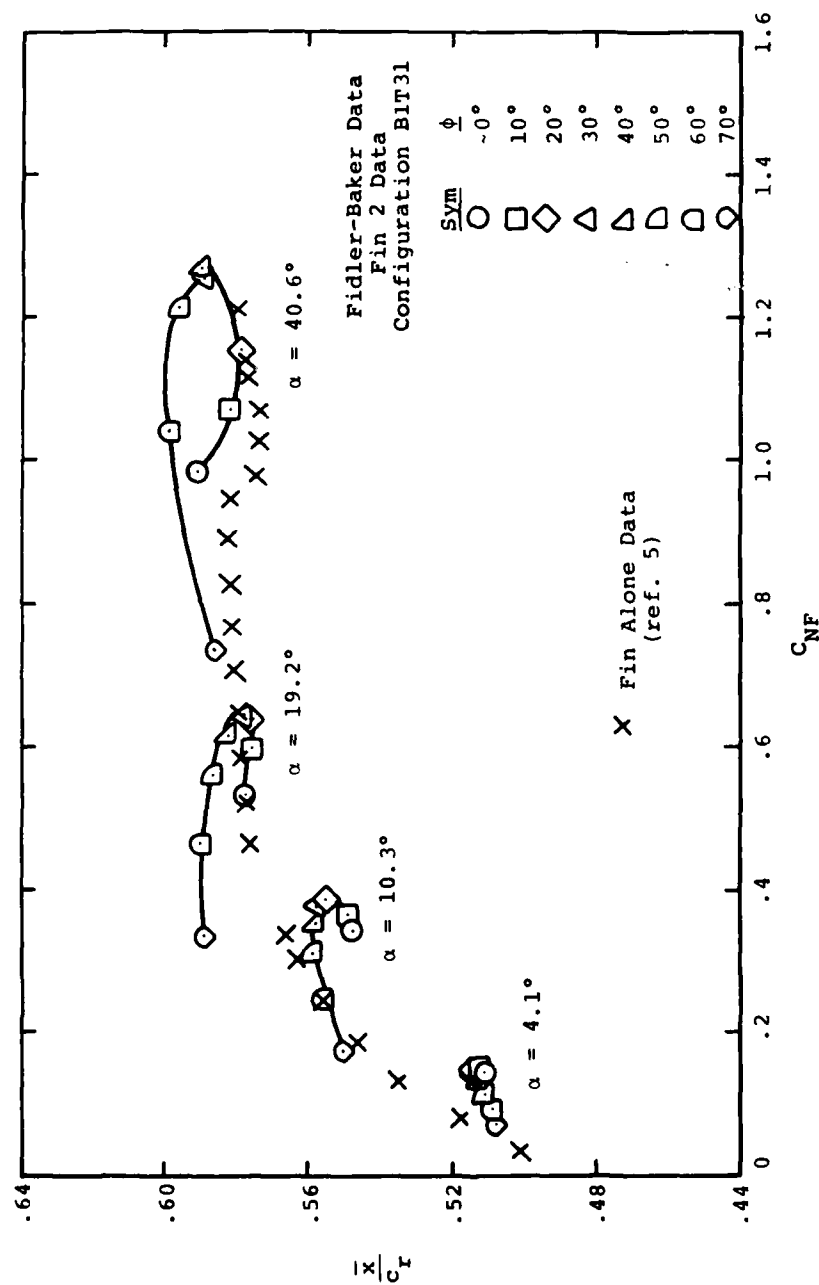


(a) $M_\infty = 0.8$
 Figure 14.- Comparison of axial center-of-pressure positions for wing-alone and fin-on-body at $\delta = 0^\circ$; $R = 0.5$, $\lambda = 0.5$.



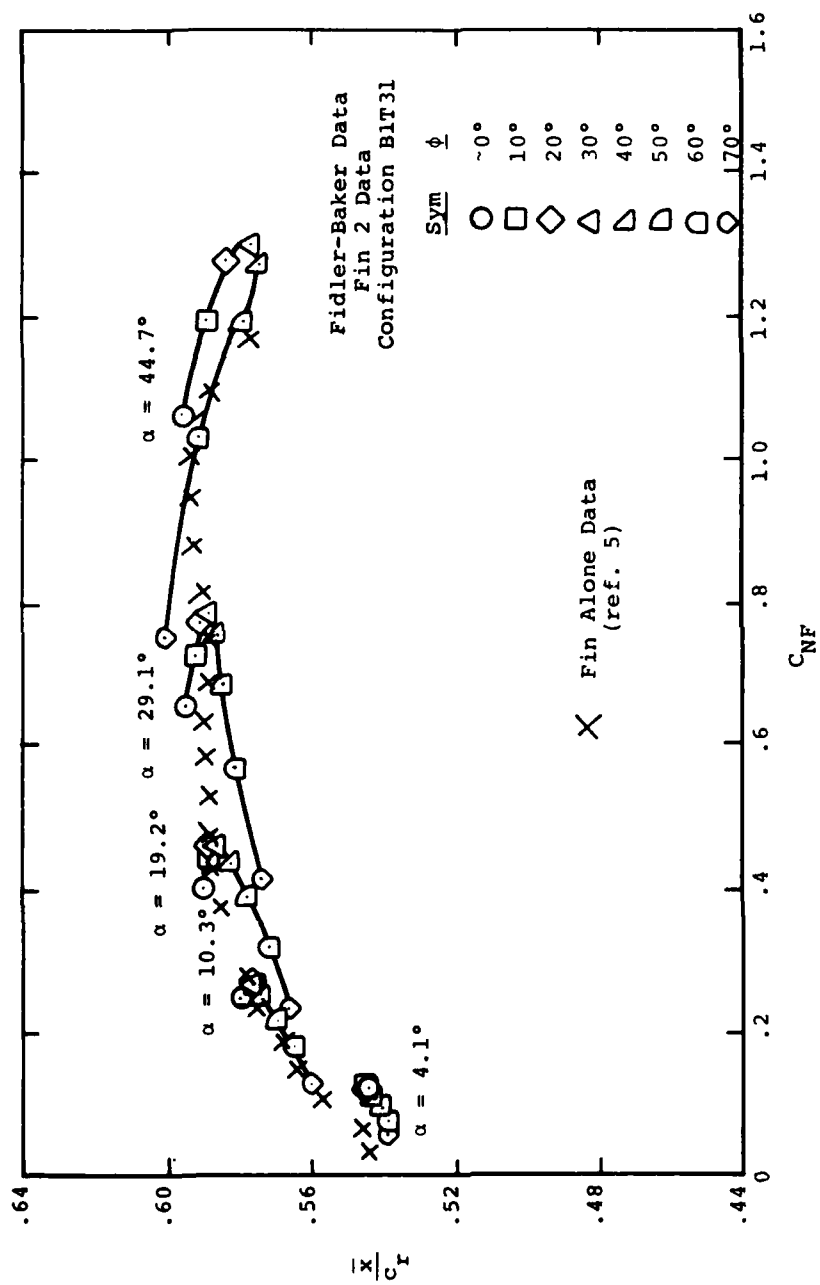
(b) $M_\infty = 1.2$

Figure 14.- Continued.

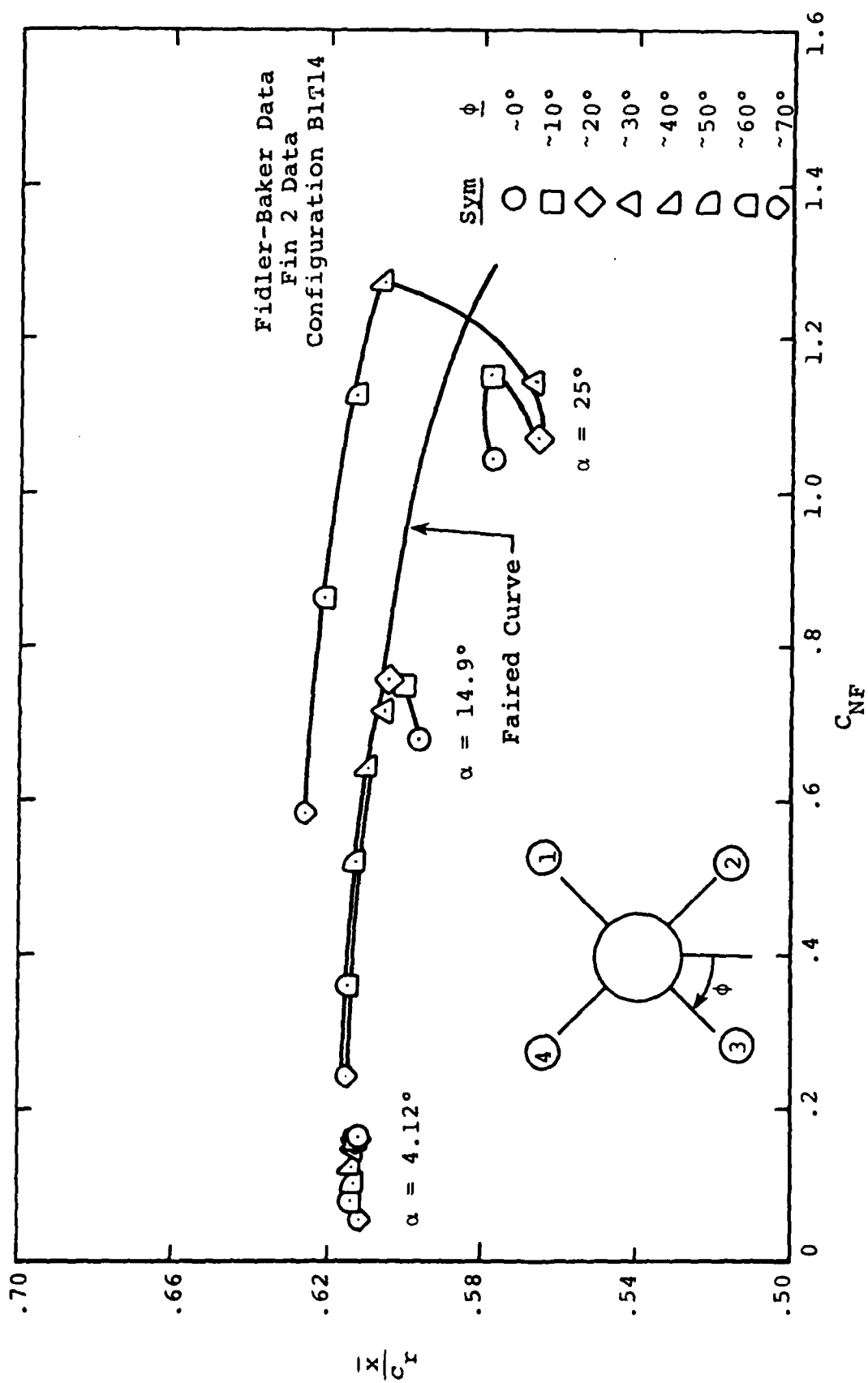


(c) $M_\infty = 2.0$

Figure 14.- Continued.

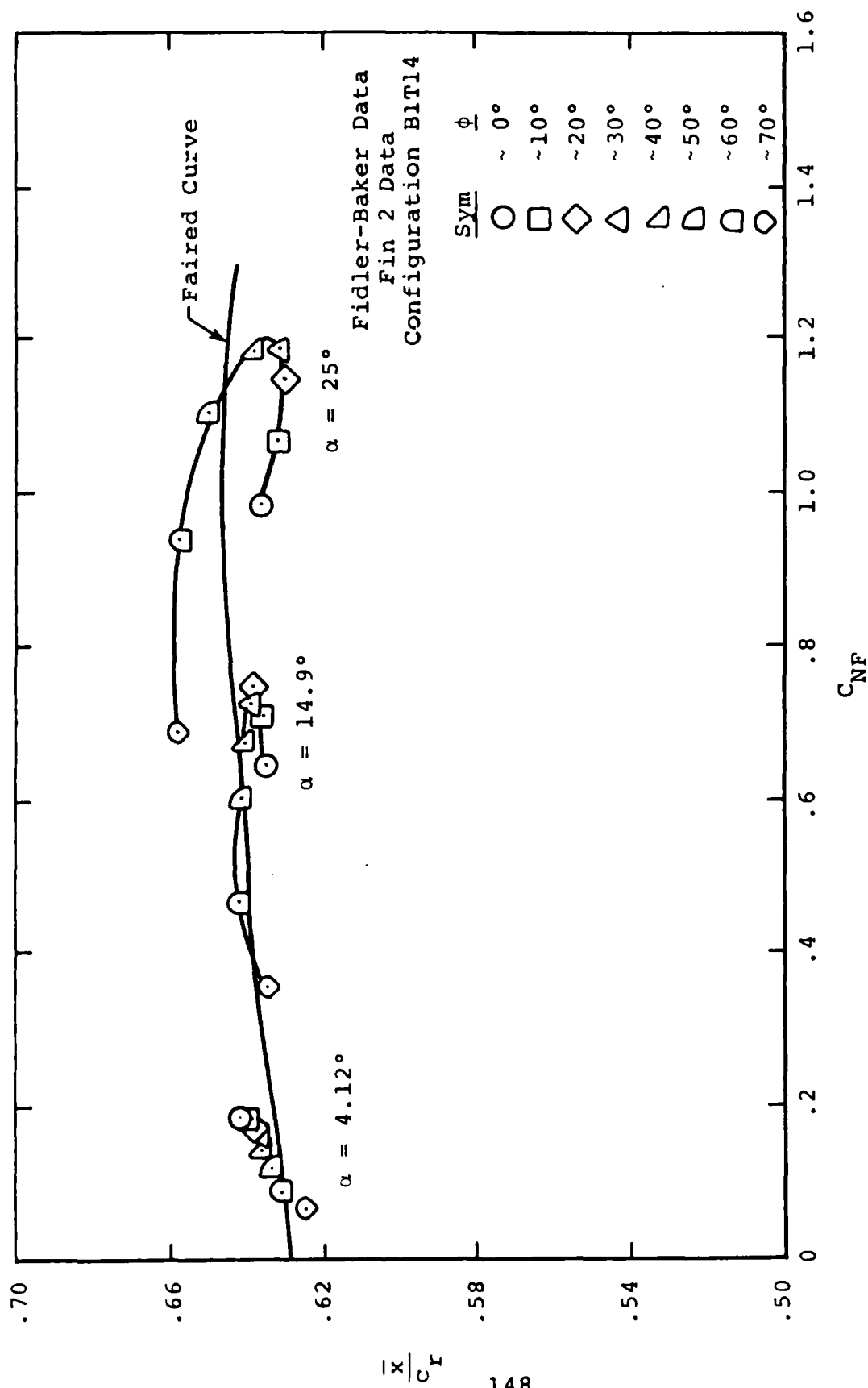


(d) $M_\infty = 3.0$
Figure 14.- Concluded.



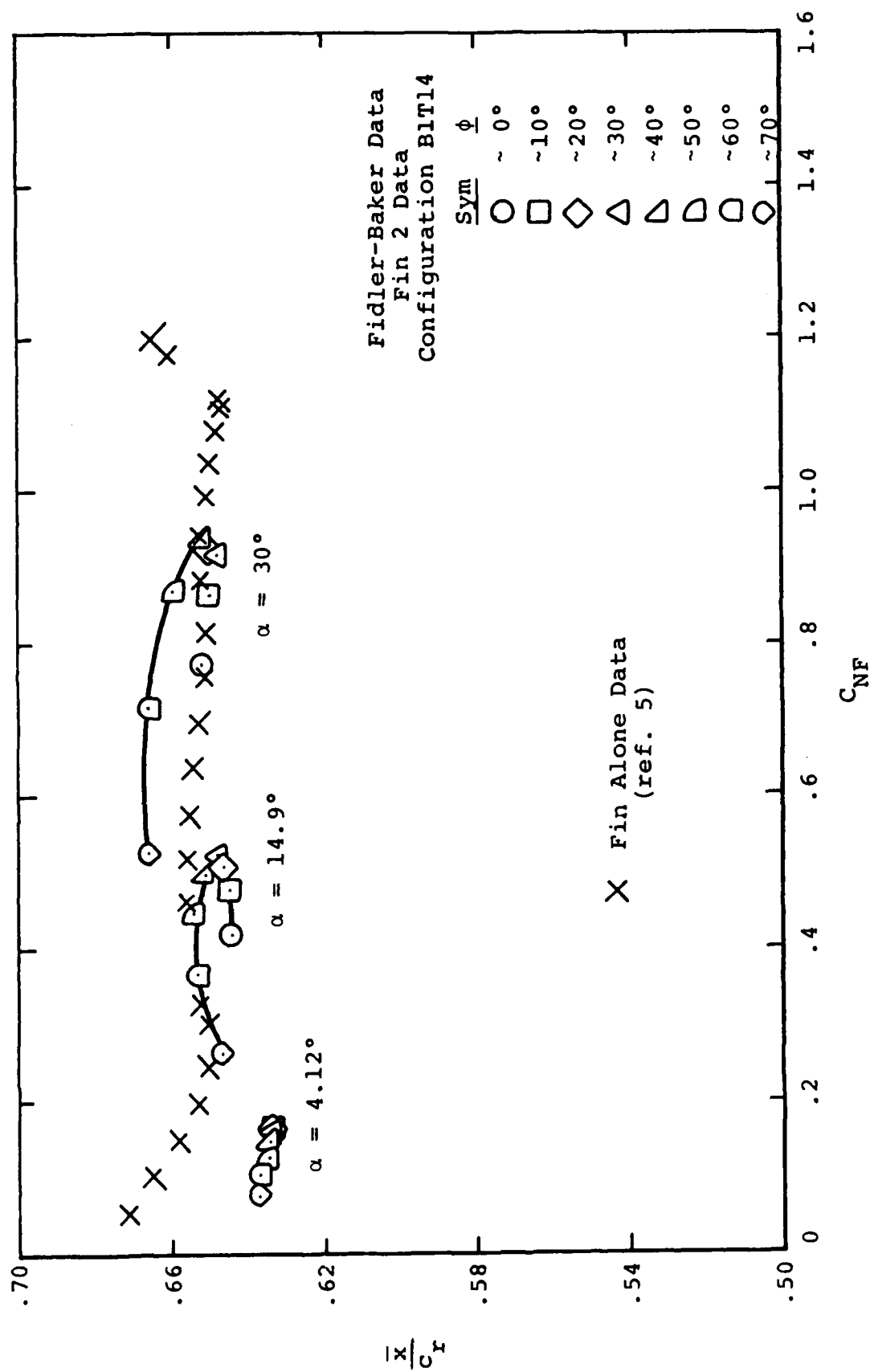
(a) $M_\infty = 0.8$

Figure 15.- Comparison of axial center-of-pressure positions for wing-alone and fin-on-body at $\delta = 0^\circ$; $AR = 1.0$, $\lambda = 0$.



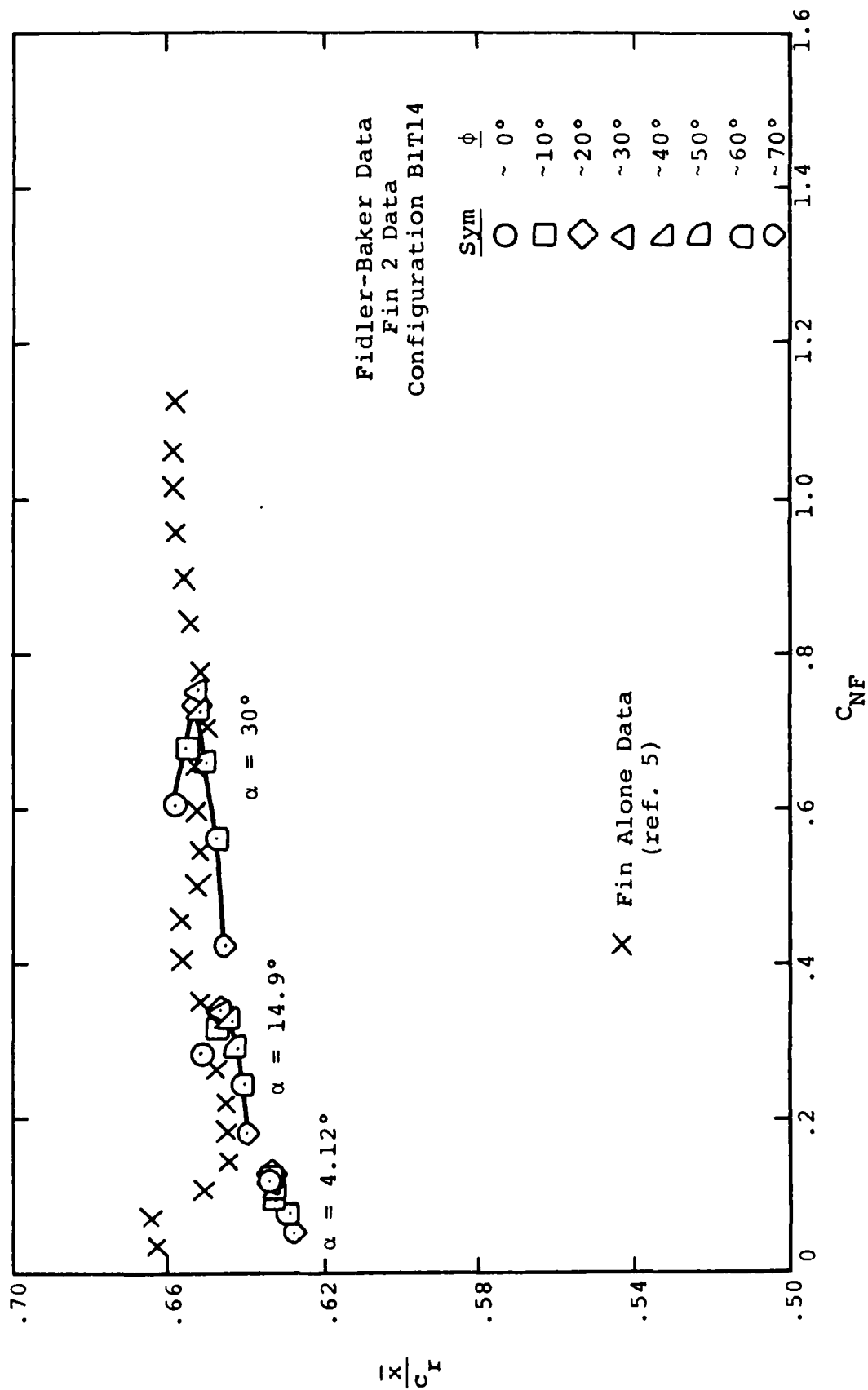
(b) $M_\infty = 1.2$

Figure 15.- Continued



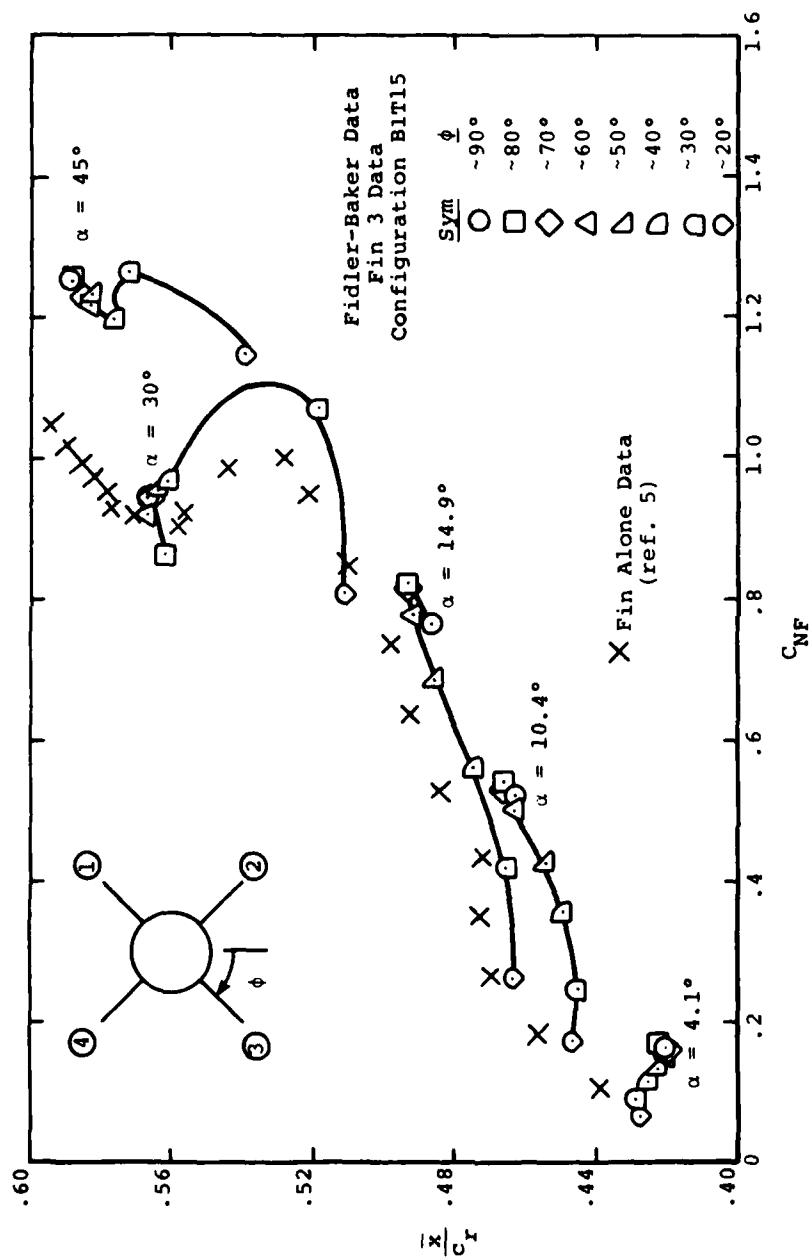
(c) $M_\infty = 2.0$

Figure 15.- Continued.



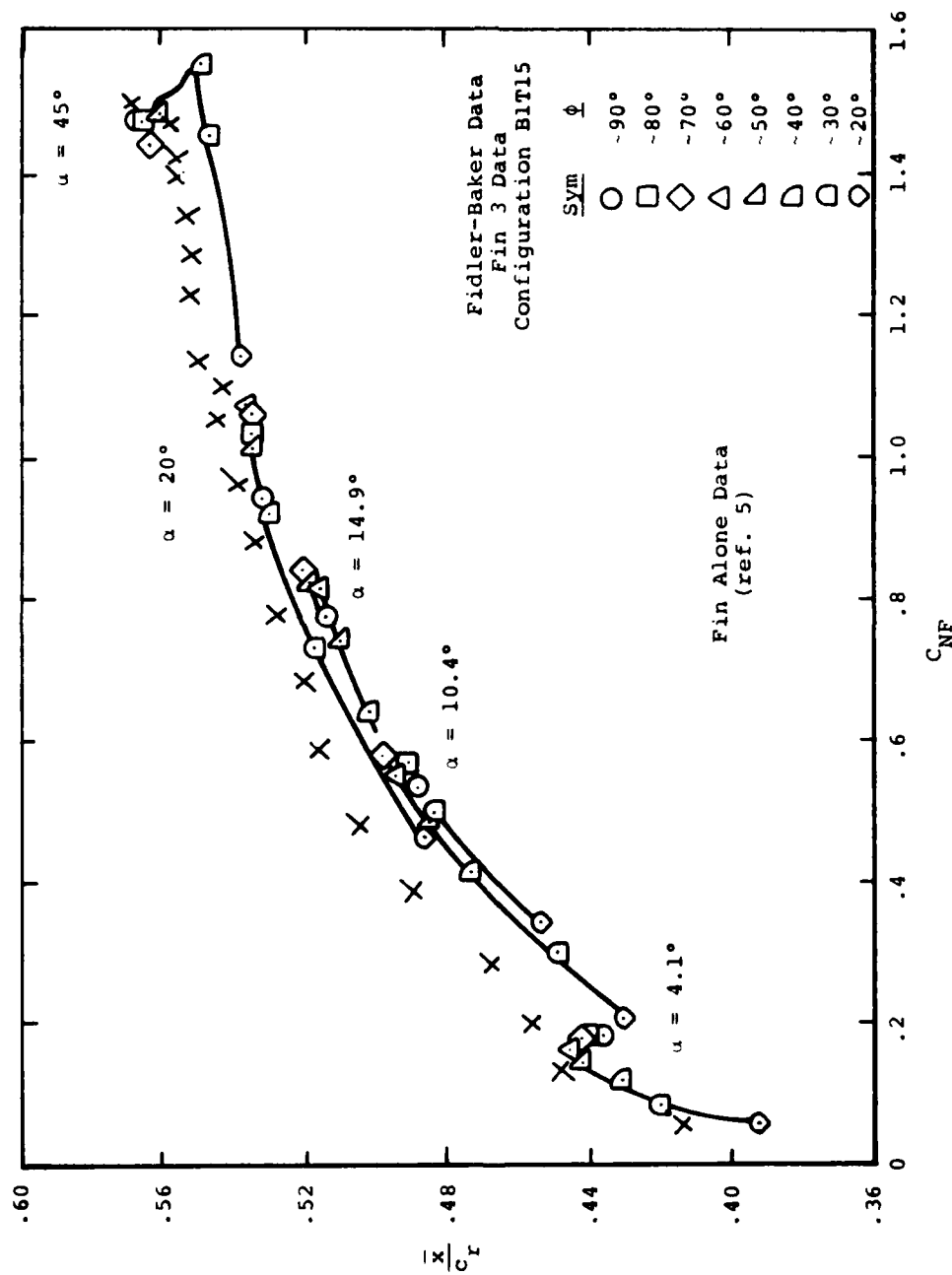
(d) $M_\infty = 3.0$

Figure 15.- Concluded.



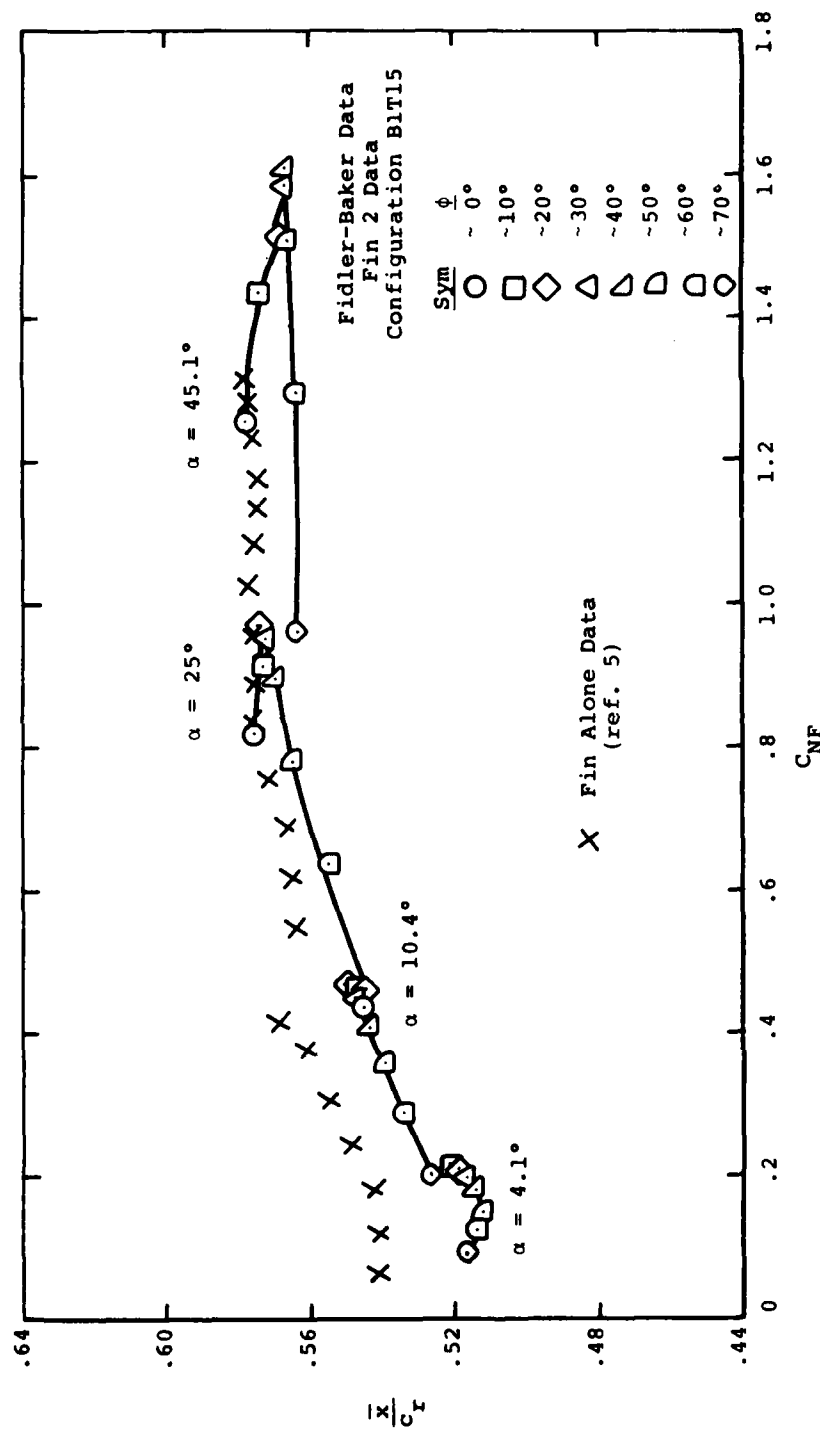
(a) $M_\infty = 0.8$

Figure 16.- Comparison of axial center-of-pressure positions for wing-alone and fin-on-body at $\delta = 0^\circ$; $Re = 1.0$, $\lambda = 0.5$.



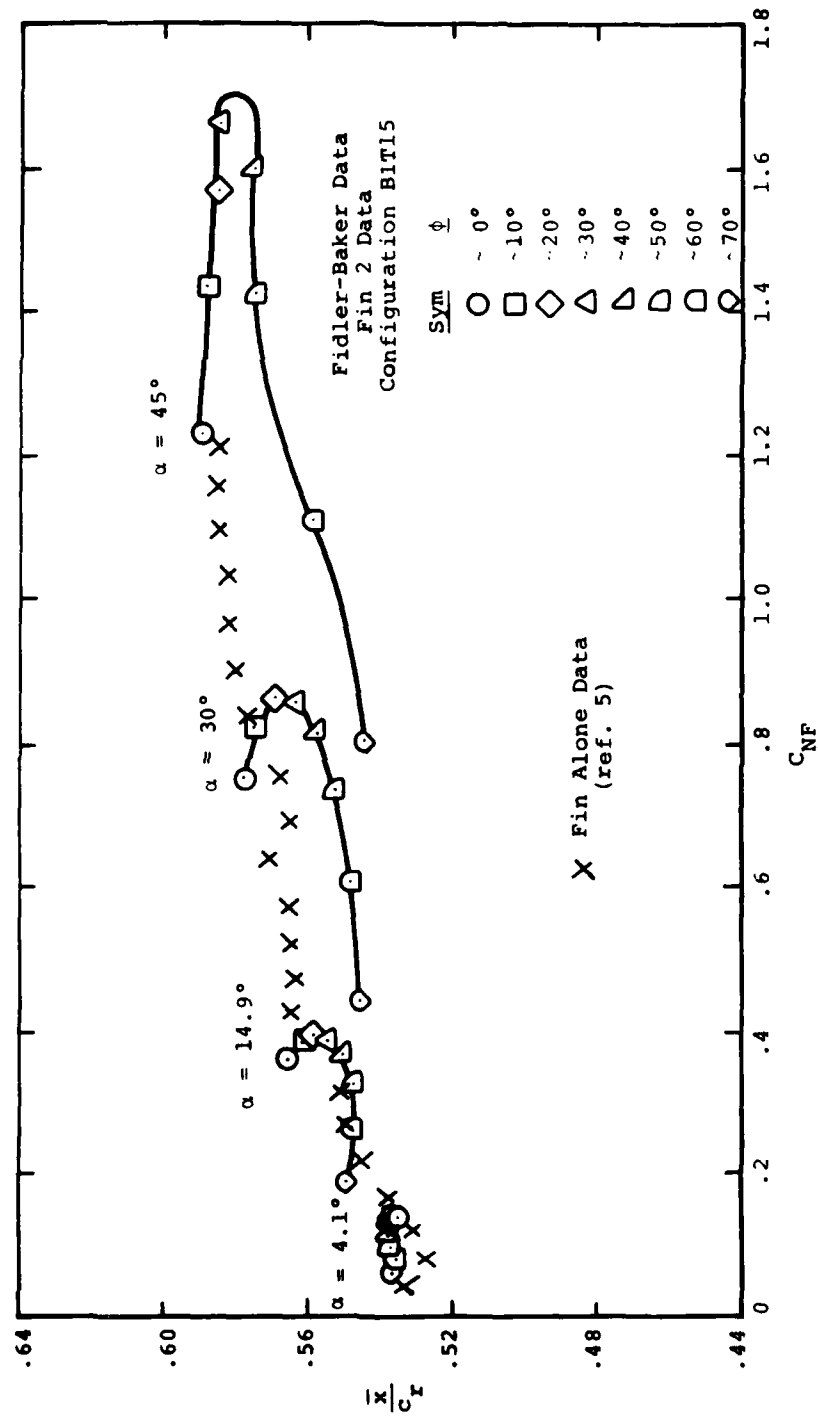
(b) $M_\infty = 1.2$

Figure 16.- Continued.



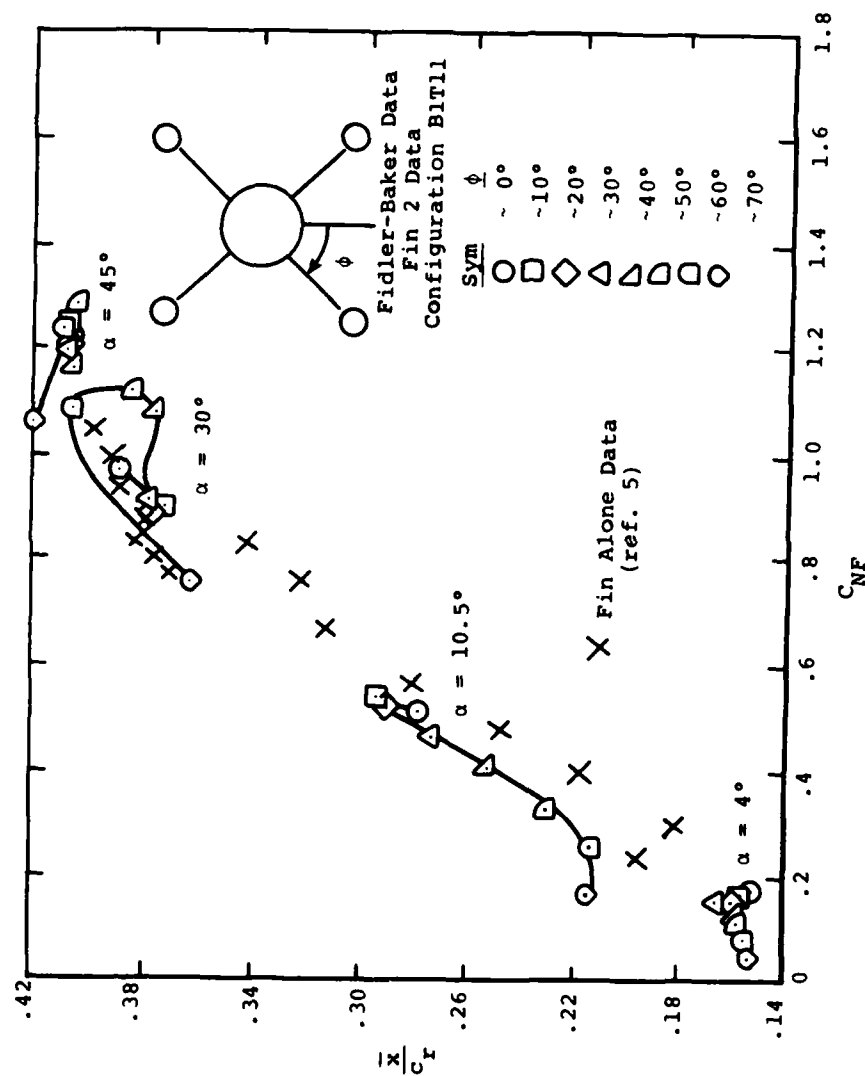
(c) $M_\infty = 2.0$

Figure 16.- Continued.



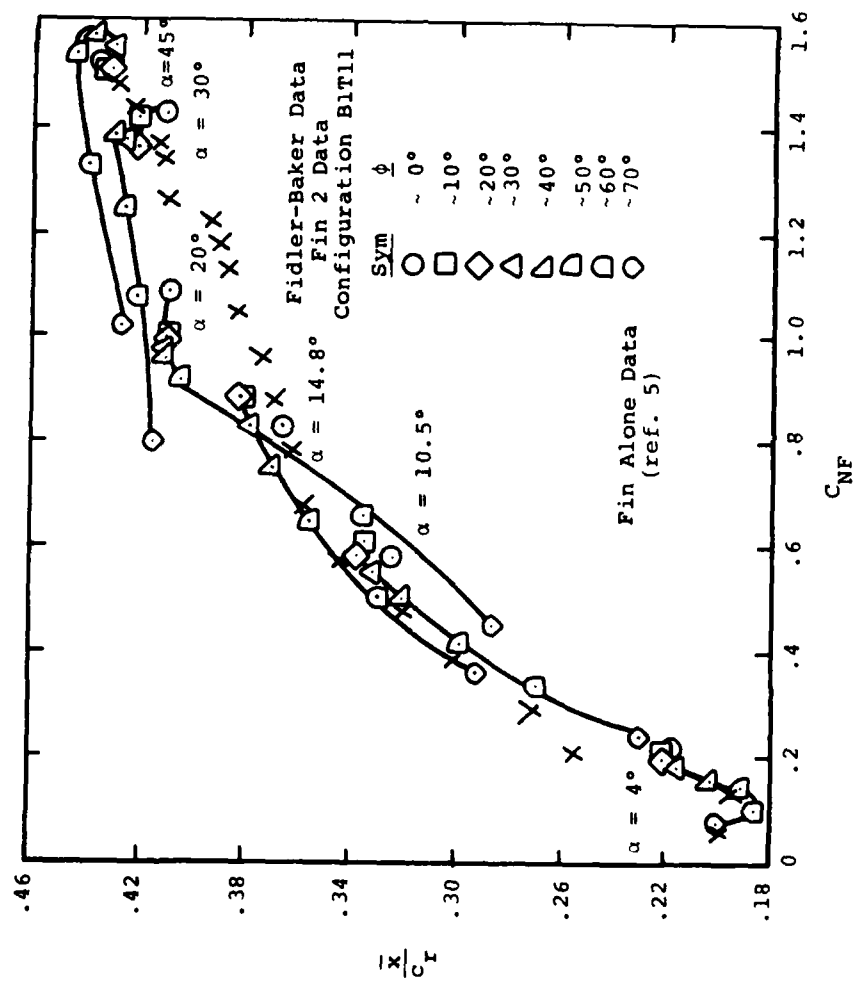
(d) $M_\infty = 3.0$

Figure 16.- Concluded.



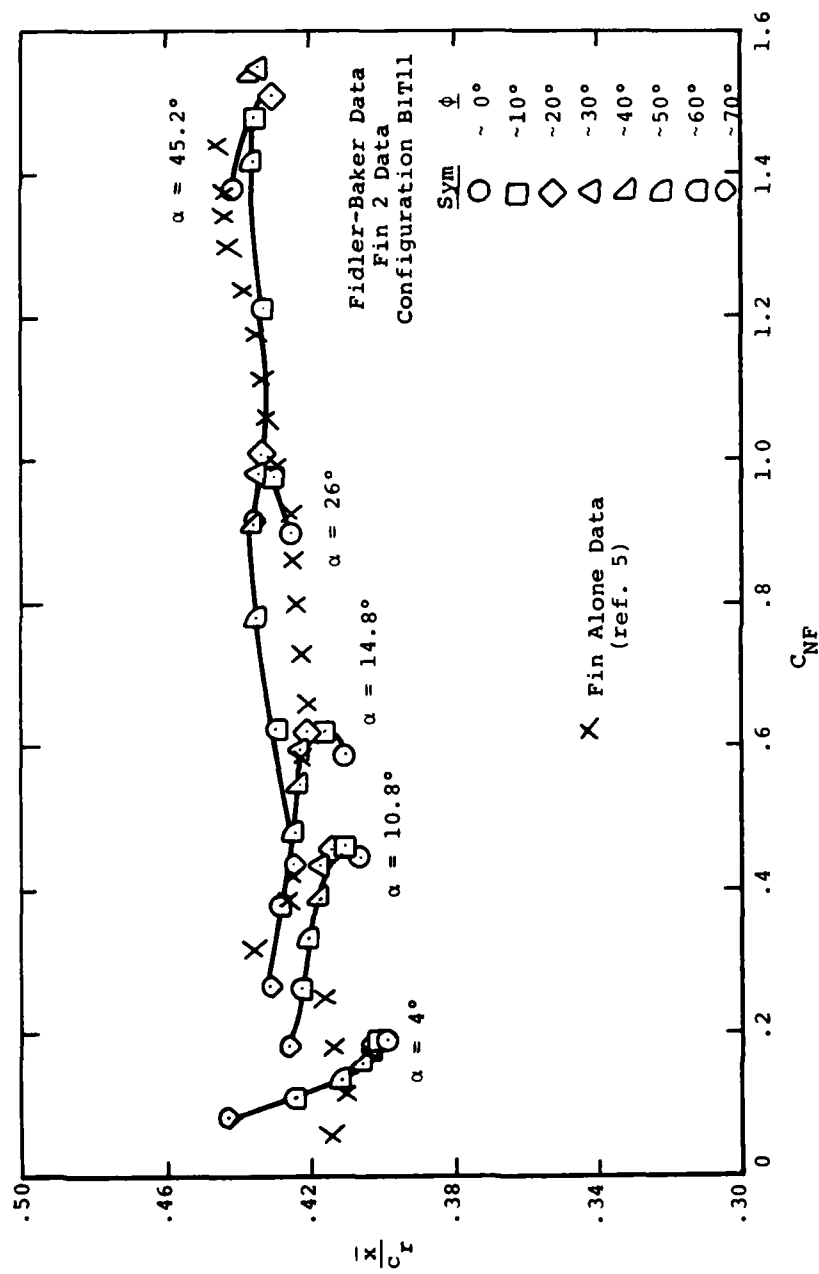
(a) $M_\infty = 0.8$

Figure 17.- Comparison of axial center-of-pressure positions for wing-alone and fin-on-body at $\delta = 0^\circ$; $AR = 1.0$, $\lambda = 1.0$.



(b) $M_\infty = 1.2$

Figure 17.- Continued.



(c) $M_\infty = 2.0$

Figure 17.- Continued.

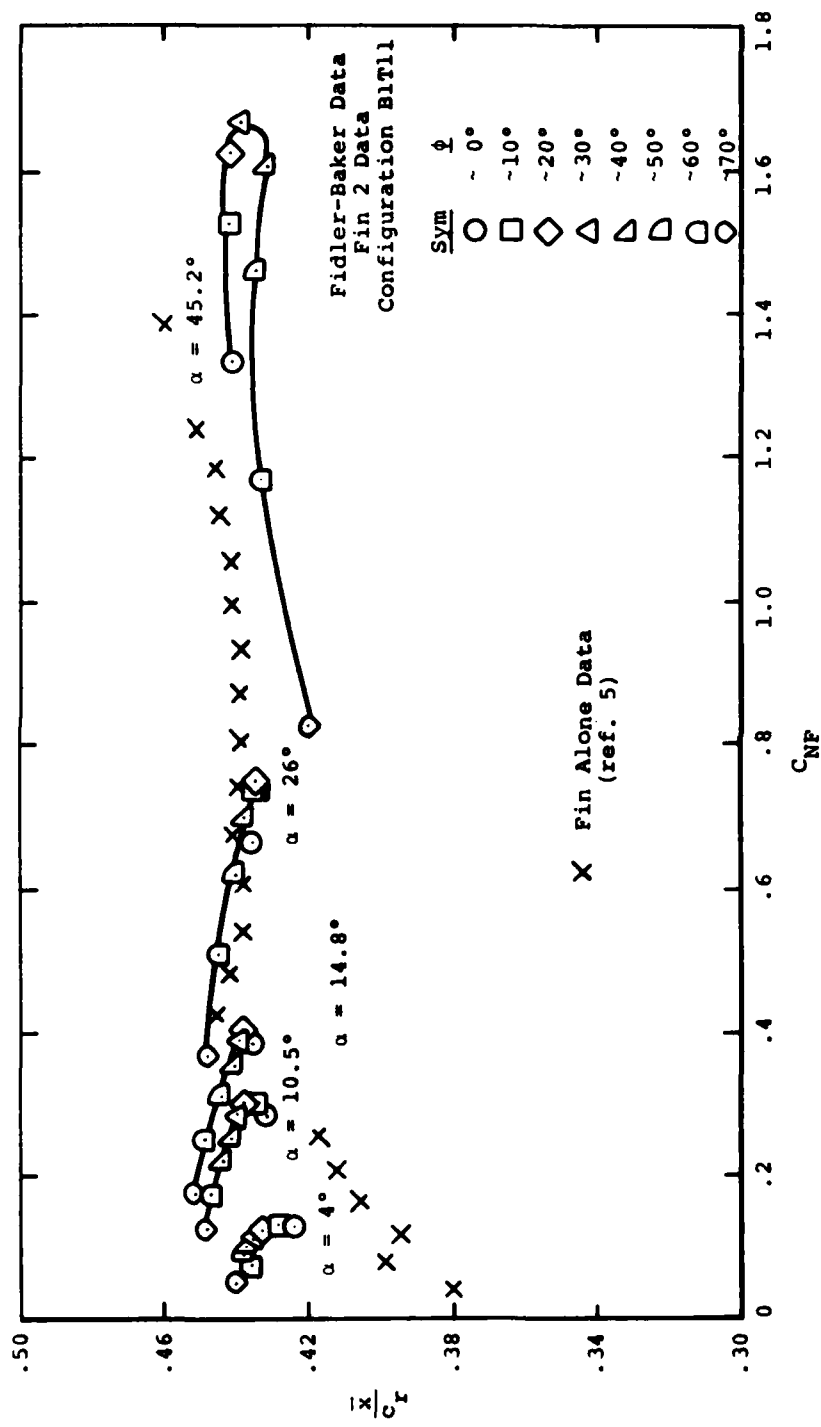
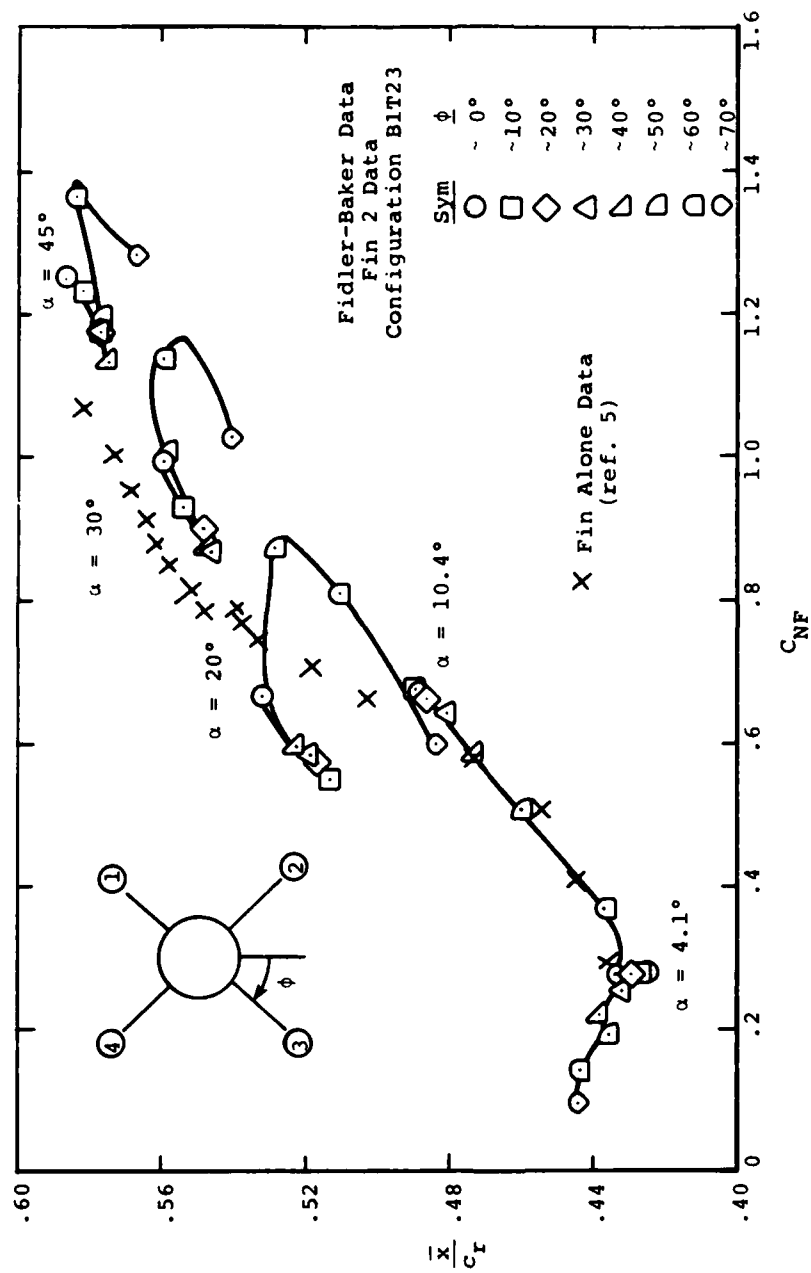
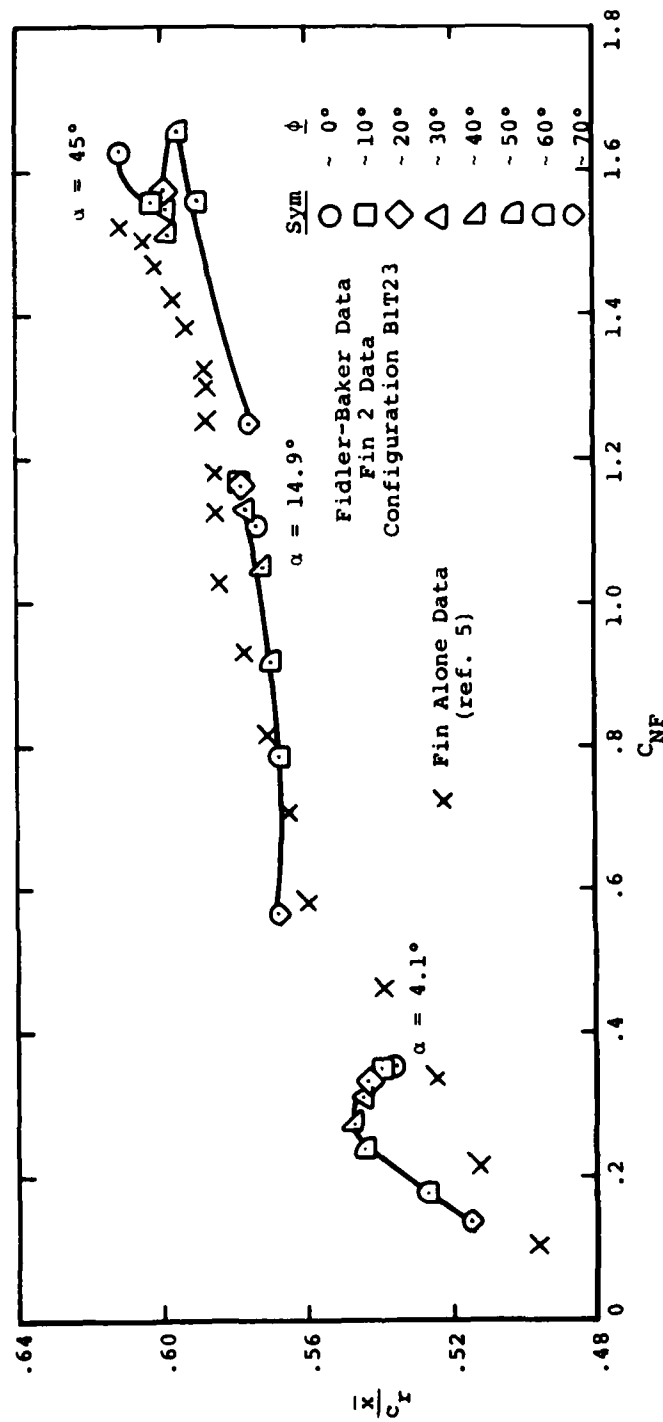


Figure 17.- Concluded.

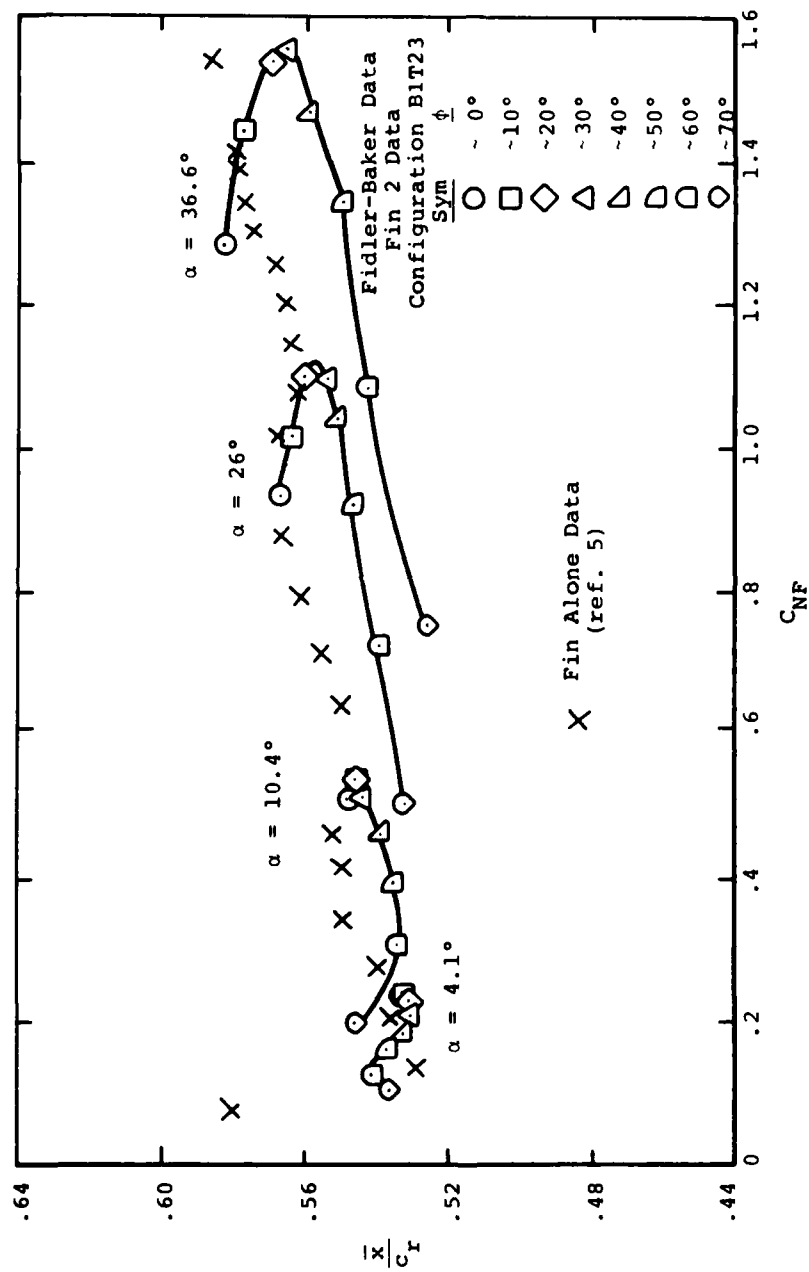


(a) $M = 0.8$
 Figure 18.- Comparison of axial center-of-pressure positions for wing-alone and fin-on-body at $\delta = 0^\circ$; $AR = 2.0$, $\lambda = 0.5$.



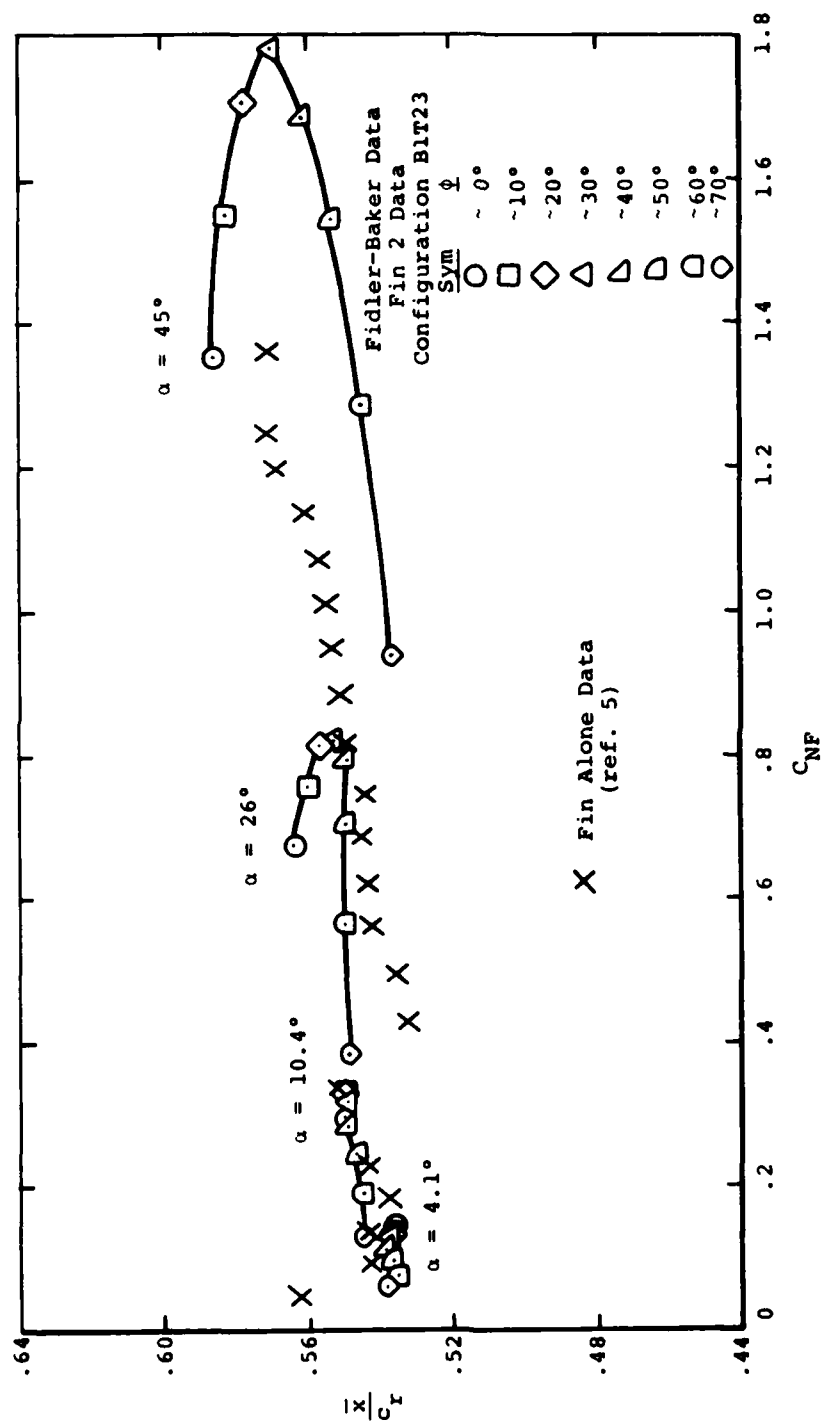
(b) $M_\infty = 1.2$

Figure 18.- Continued.



(c) $M_\infty = 2.0$

Figure 18.- Continued.



(d) $M_\infty = 3.0$

Figure 18.- Concluded.

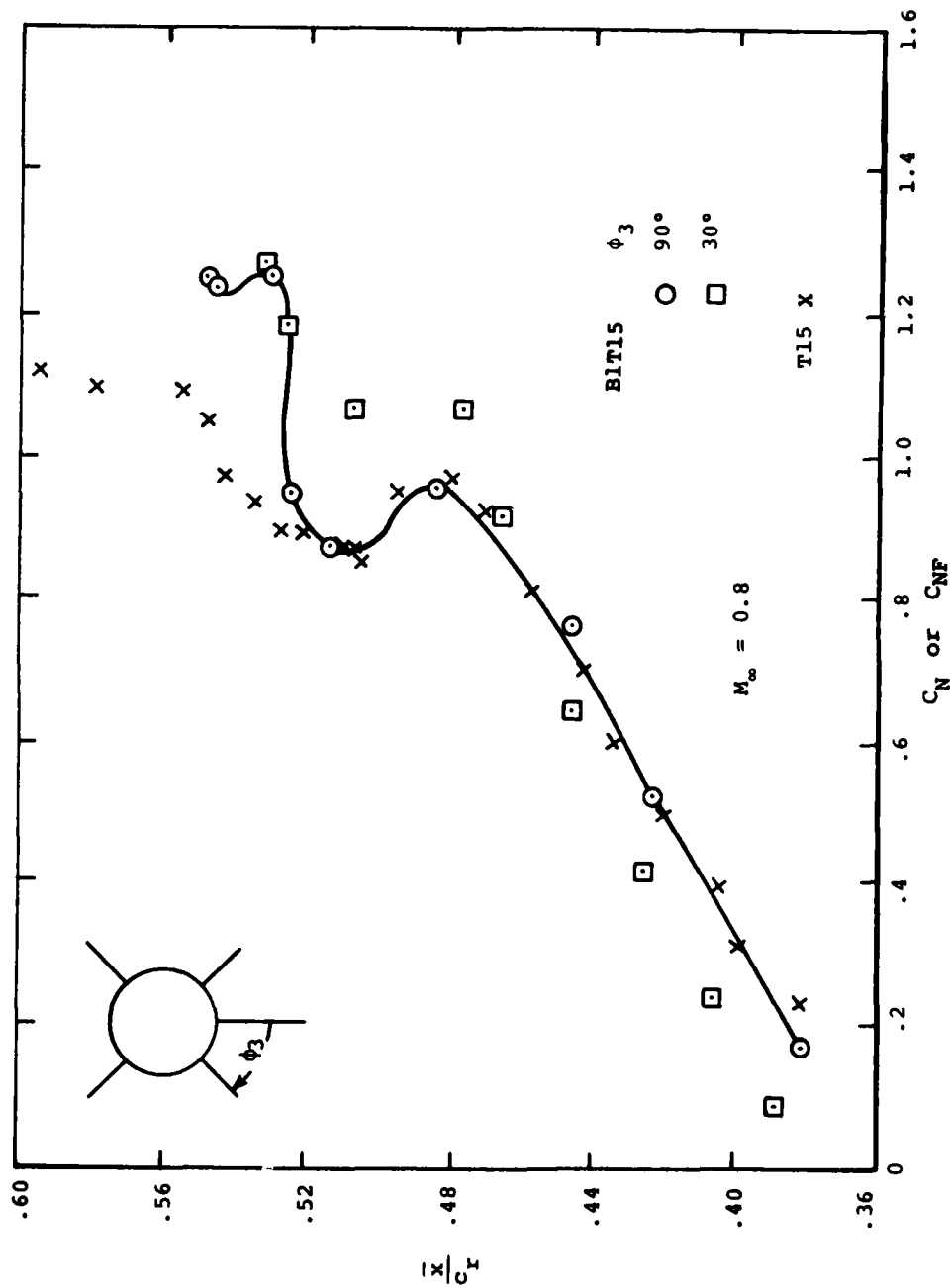


Figure 19.- Comparison of wing-alone nonlinear center-of-pressure travel with that for fin in presence of body; $R = 1$, $\lambda = 0.5$.

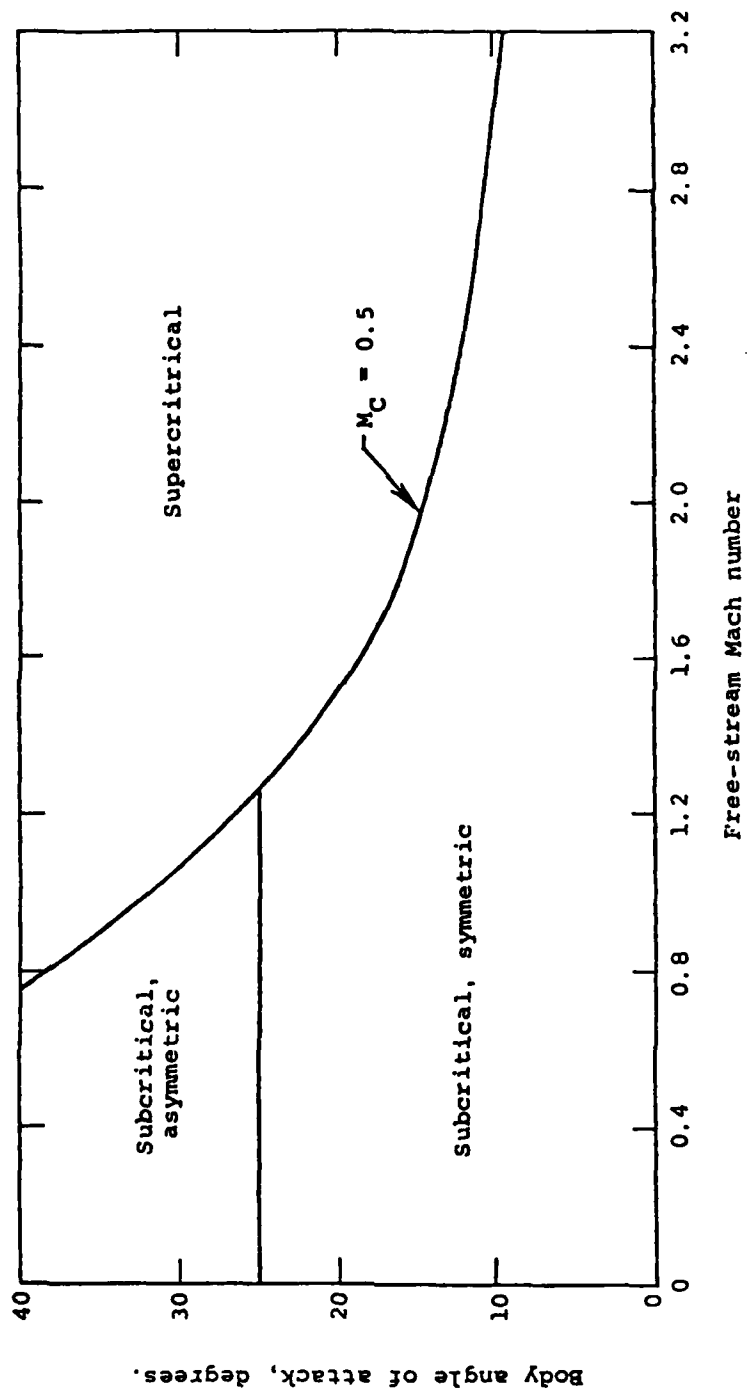


Figure 20.- Approximate regions for various types of body vortices.

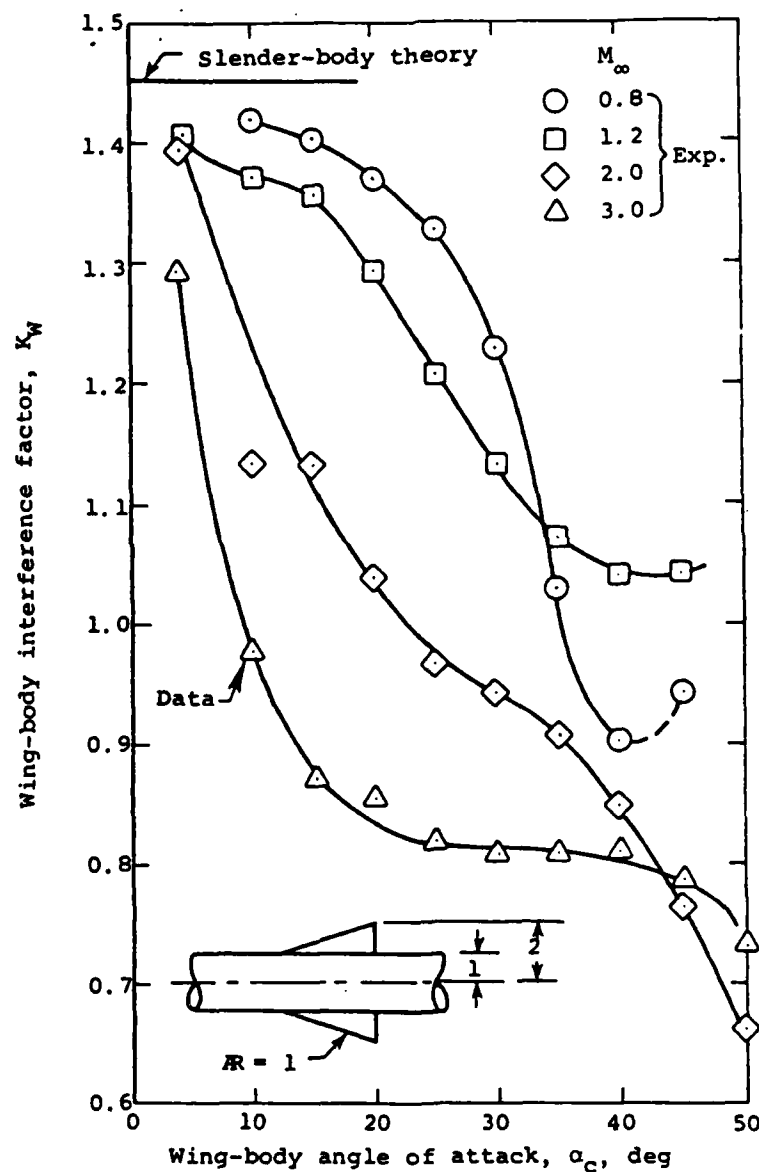


Figure 21.- Effect of angle of attack and free-stream Mach number on interference of body on wing.

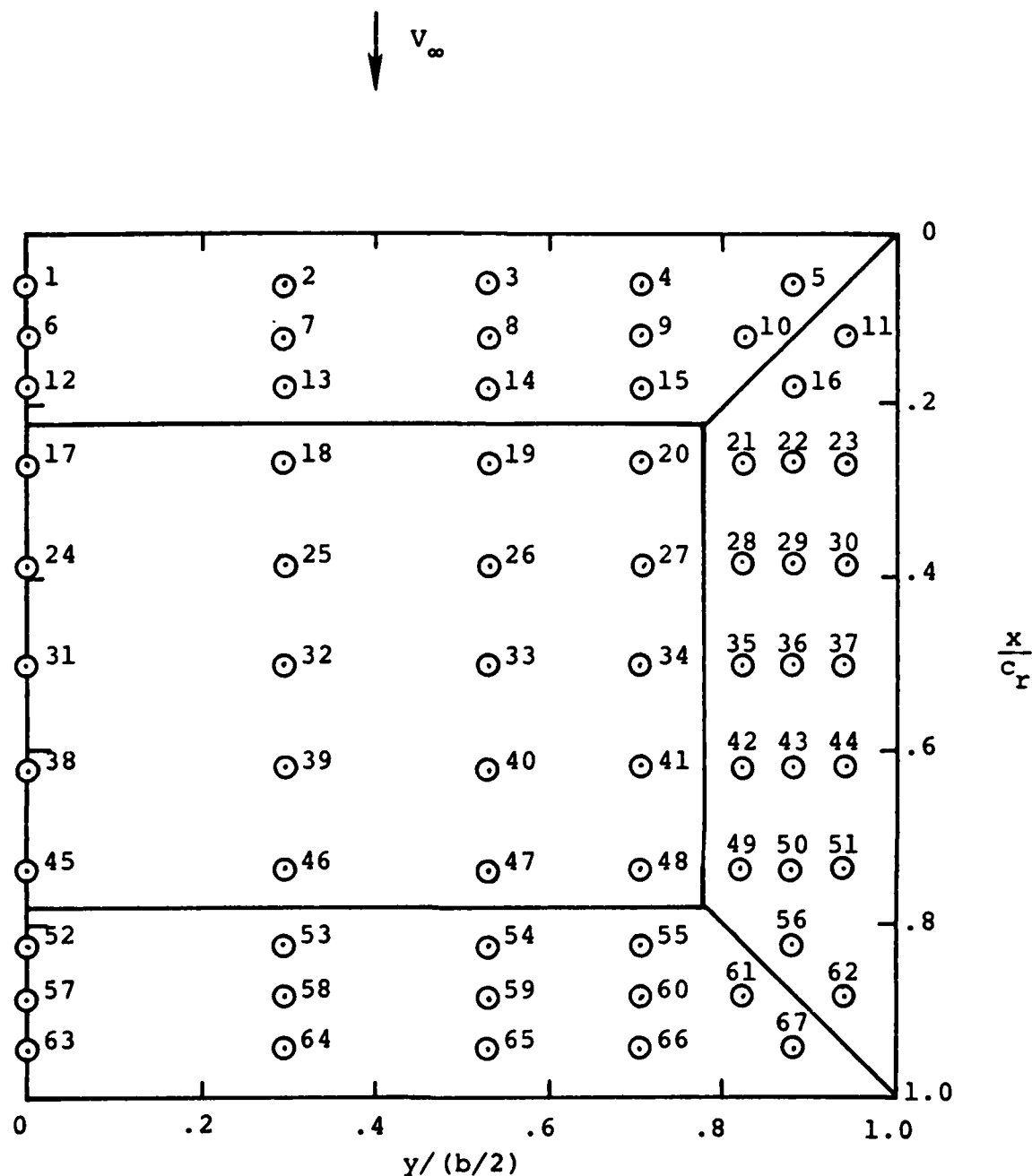
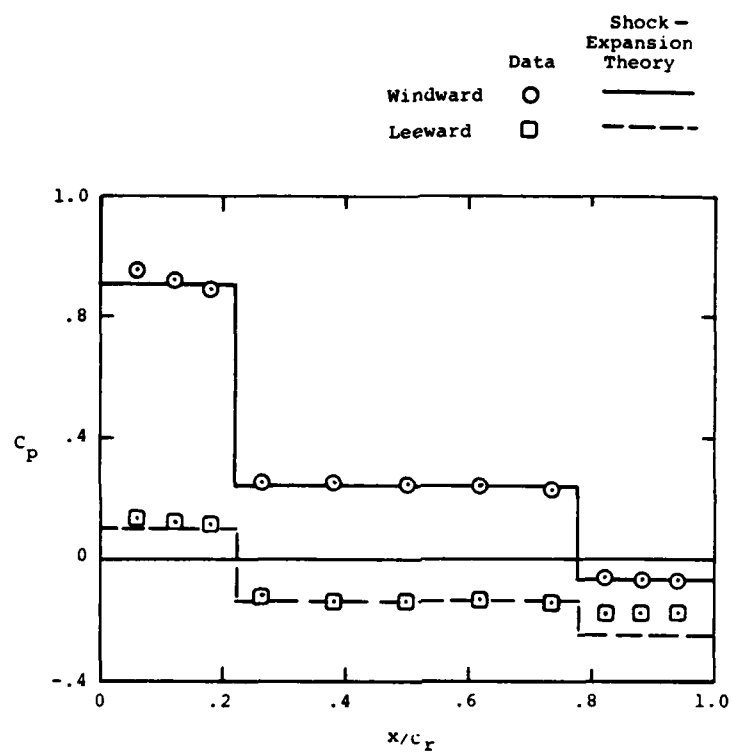
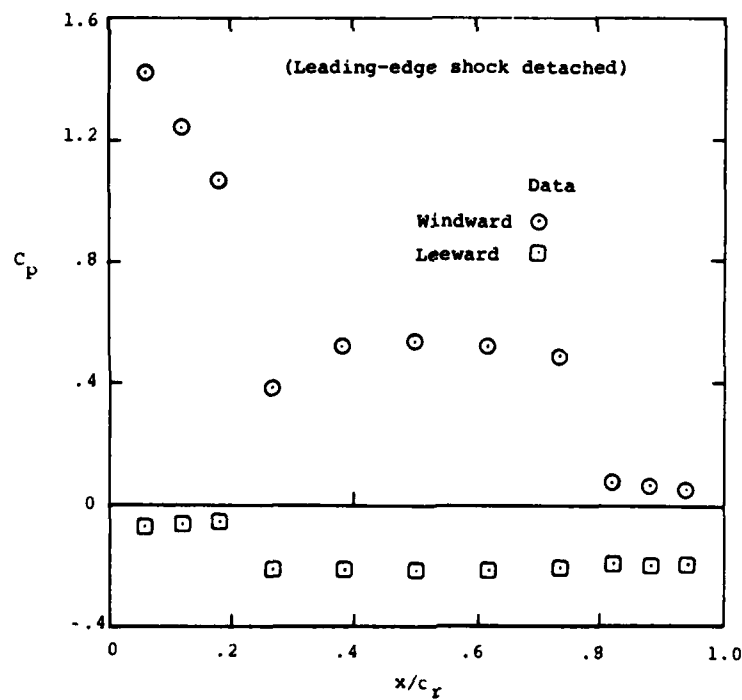


Figure 22.- Pressure orifice locations on an aspect ratio 2.0 rectangular wing

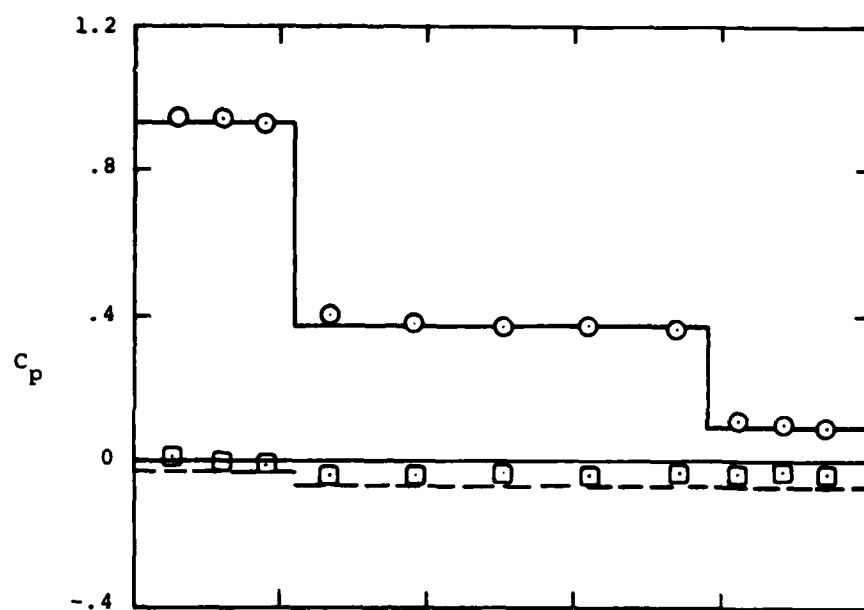


(a) $\alpha = 10^\circ$, $M_\infty = 2.16$, $y/(b/2) = 0$

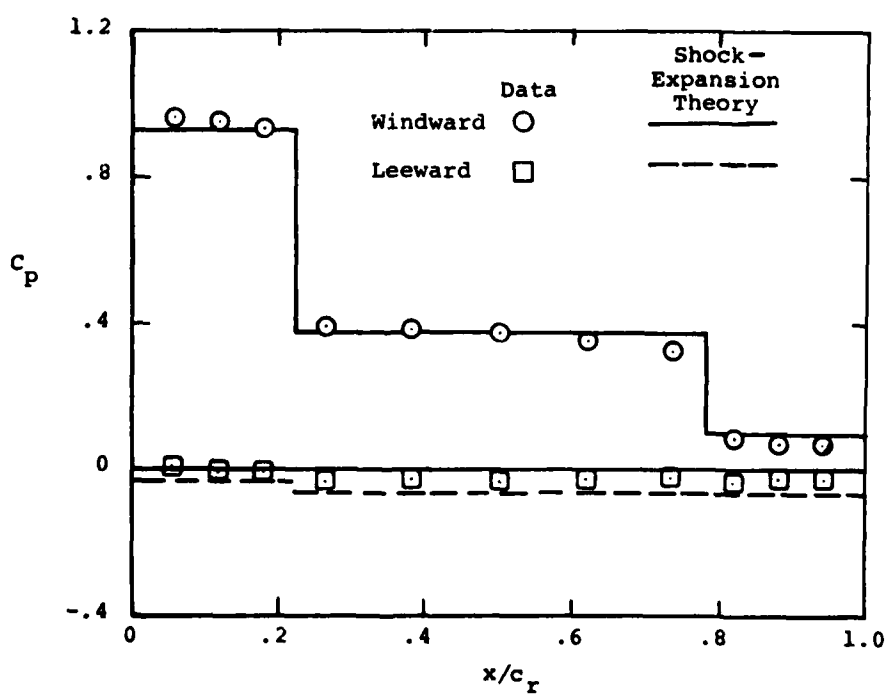


(b) $\alpha = 20^\circ$, $M_\infty = 2.16$, $y/(b/2) = 0$

Figure 23.- Longitudinal pressure distributions on an aspect ratio 2.0 rectangular wing.

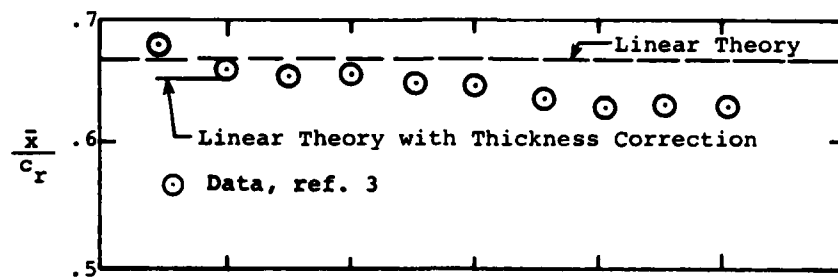


(c) $y/(b/2) = 0.0$, $M_\infty = 4.6$, $\alpha = 20^\circ$

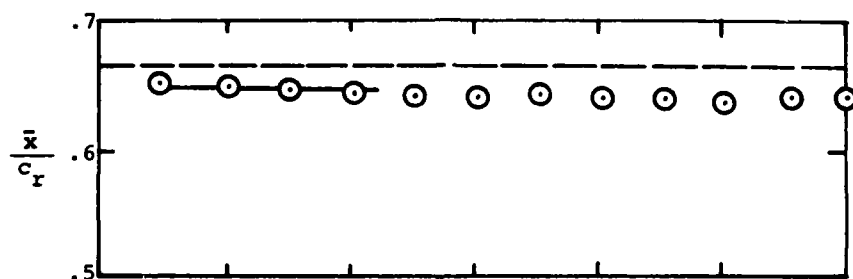


(d) $y/(b/2) = 0.530$, $M_\infty = 4.6$, $\alpha = 20^\circ$

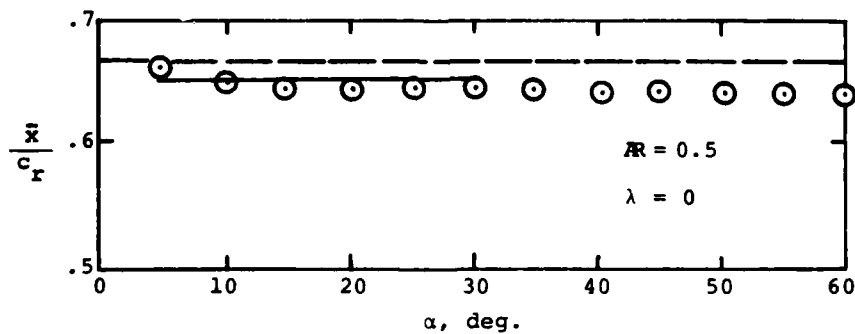
Figure 23.- Concluded



(a) $M_\infty = 1.60$

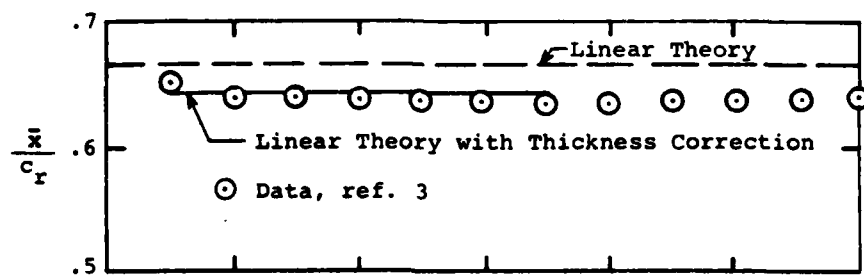


(b) $M_\infty = 2.16$

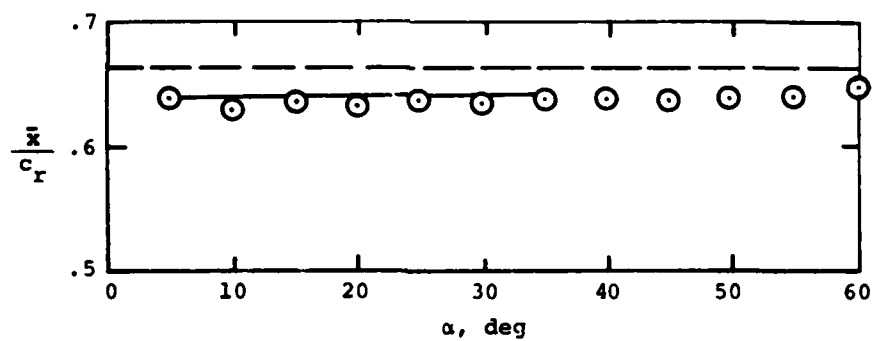


(c) $M_\infty = 2.86$

Figure 24.- Longitudinal center-of-pressure locations of aspect ratio 0.5 delta wing.



(d) $M_\infty = 3.50$



(e) $M_\infty = 4.60$

Figure 24.- Concluded

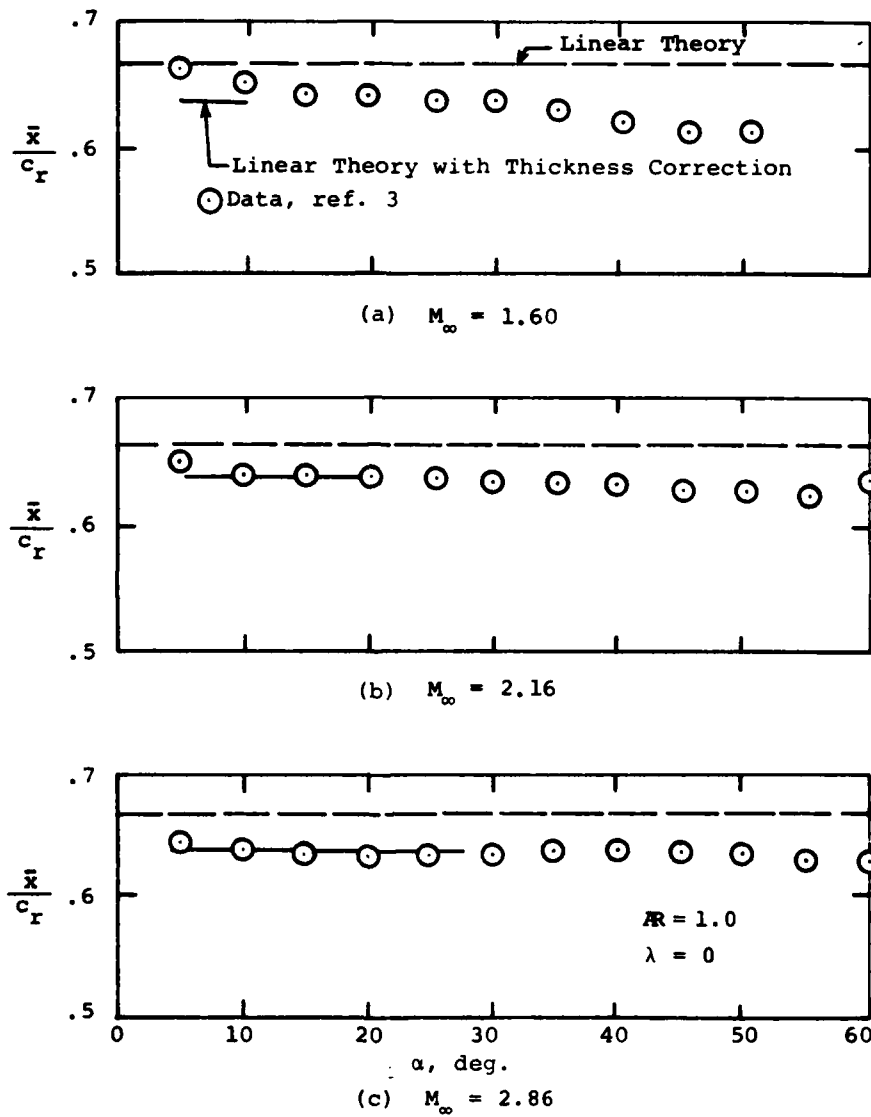
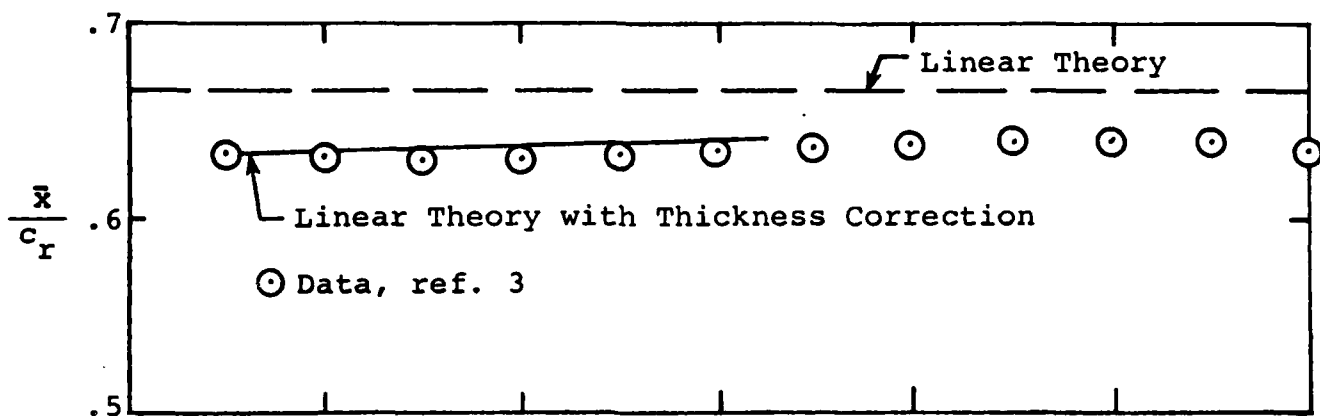
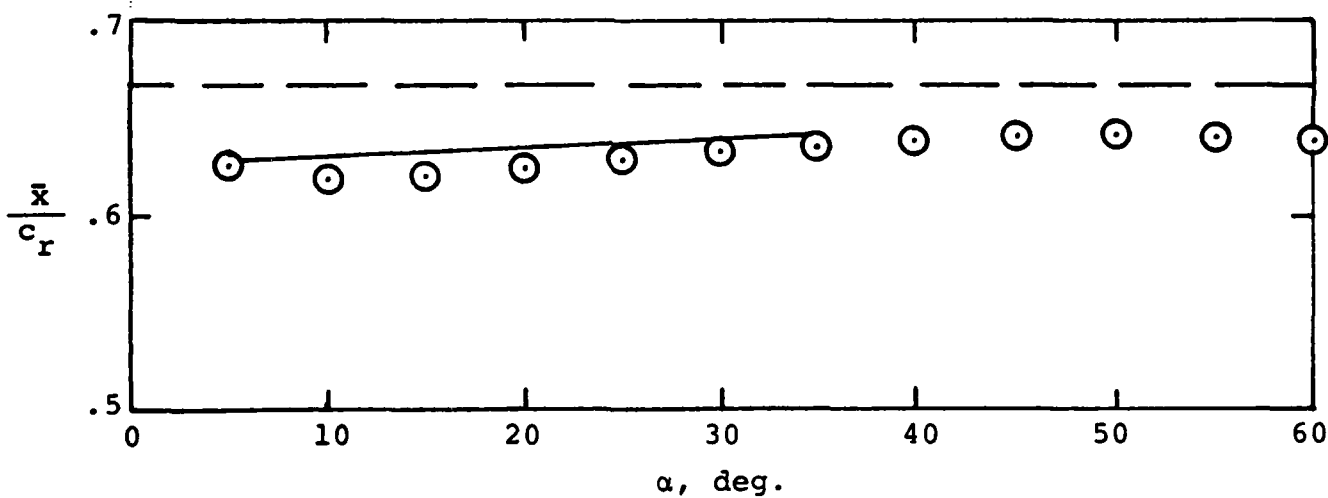


Figure 25.- Longitudinal center-of-pressure locations of aspect ratio 1.0 delta wing.

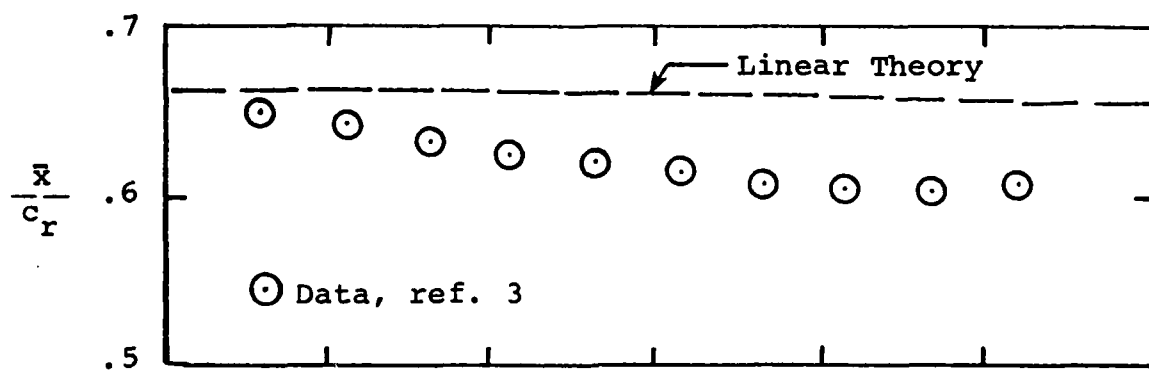


(d) $M_\infty = 3.50$

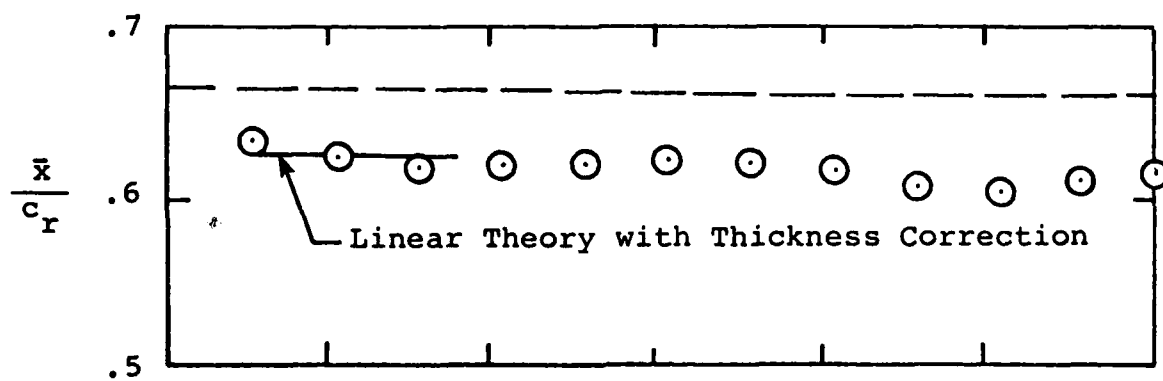


(e) $M_\infty = 4.60$

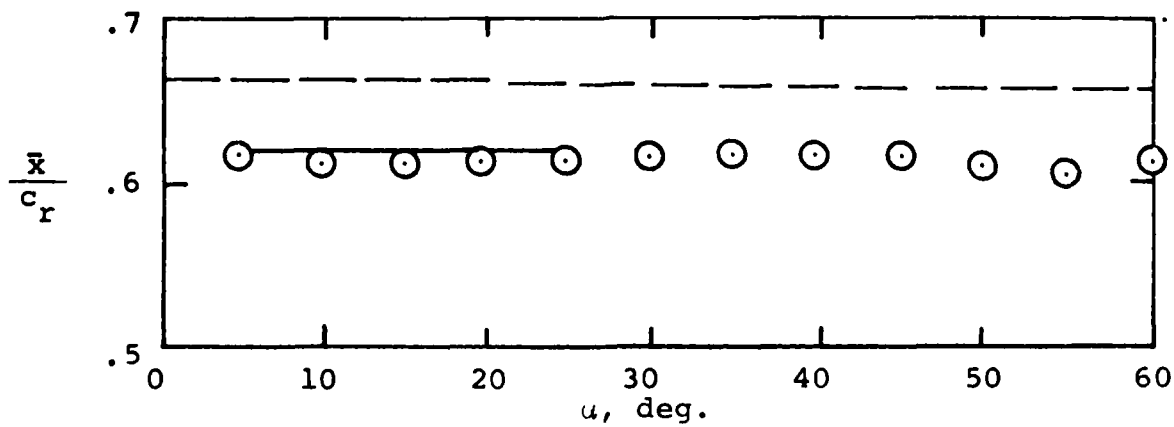
Figure 25.- Concluded.



(a) $M_\infty = 1.60$

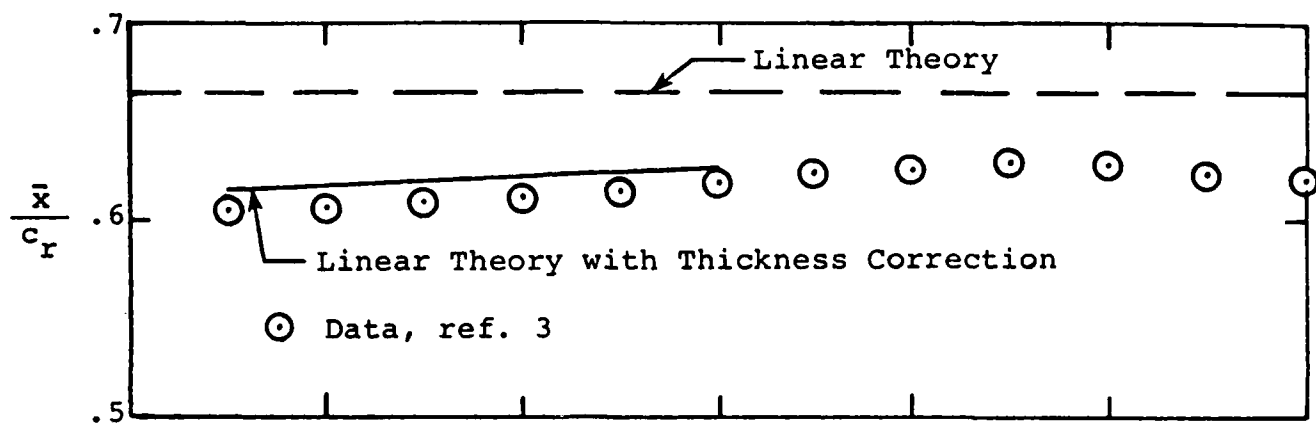


(b) $M_\infty = 2.16$

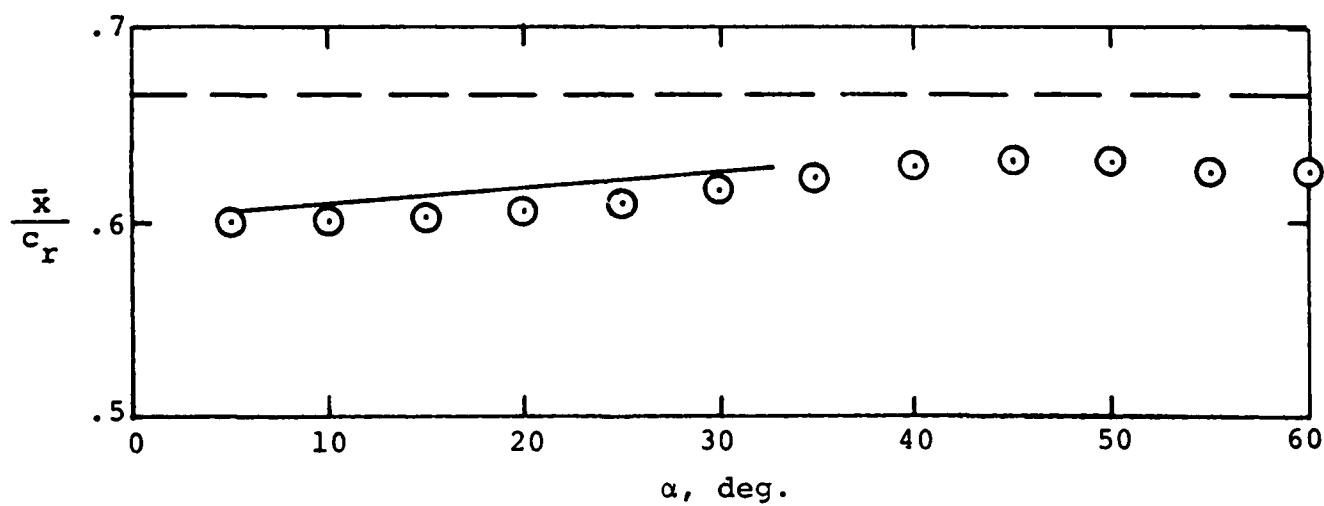


(c) $M_\infty = 2.86$

Figure 26.- Longitudinal center-of-pressure location of aspect ratio 2.0 delta wing.



(d) $M_\infty = 3.50$



(e) $M_\infty = 4.60$

Figure 26.- Concluded.

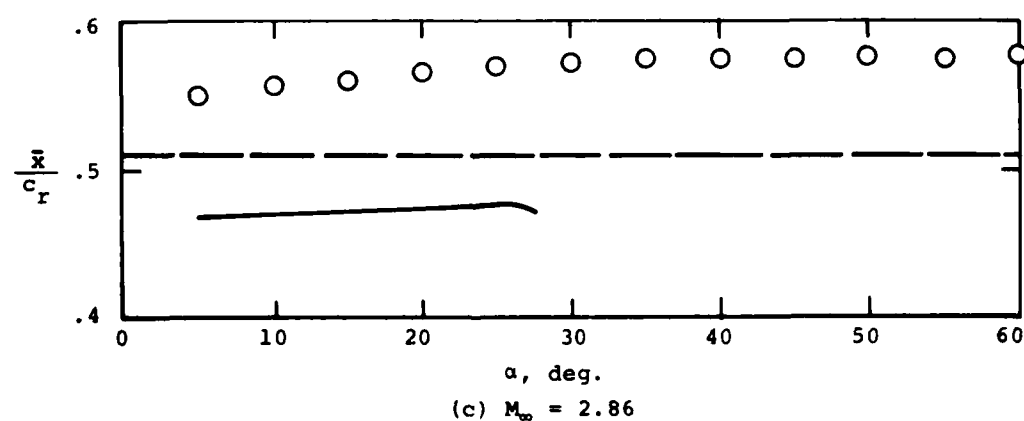
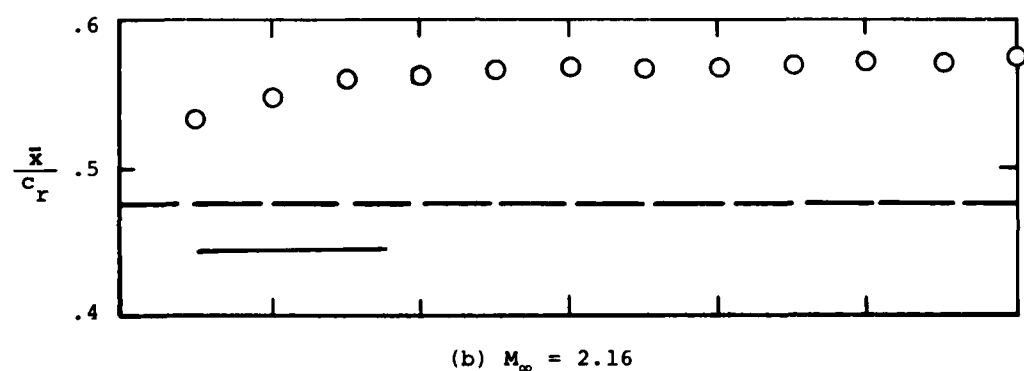
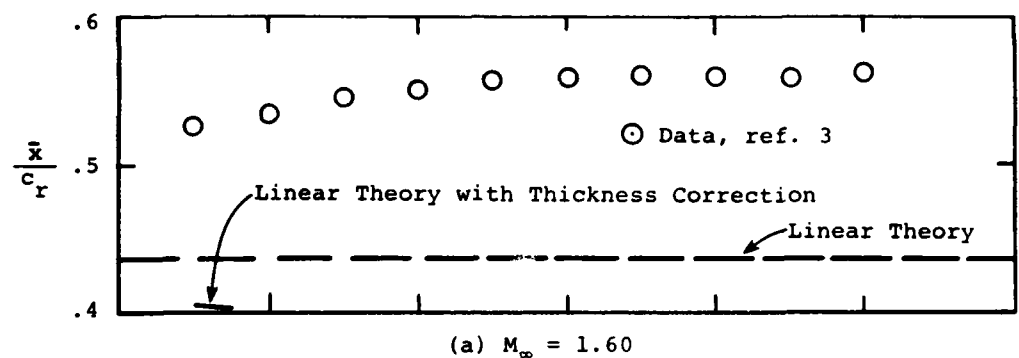
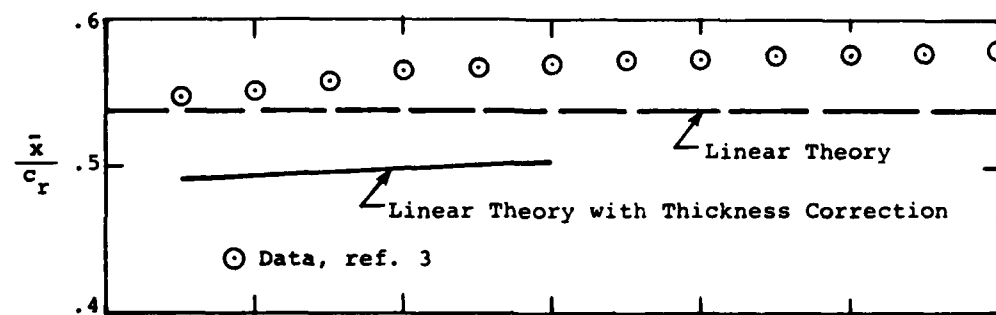
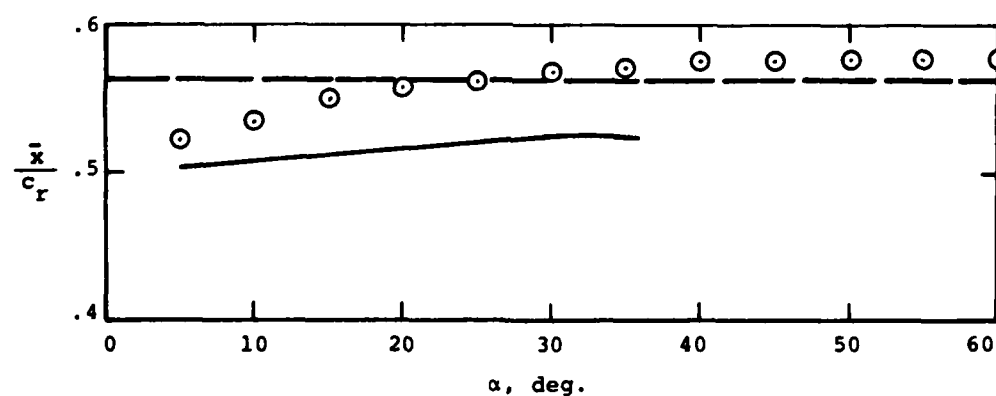


Figure 27.- Longitudinal center-of-pressure locations of an aspect ratio 0.5, taper ratio 0.5 cropped delta wing.



(d) $M_\infty = 3.50$



(e) $M_\infty = 4.60$

Figure 27.- Concluded.

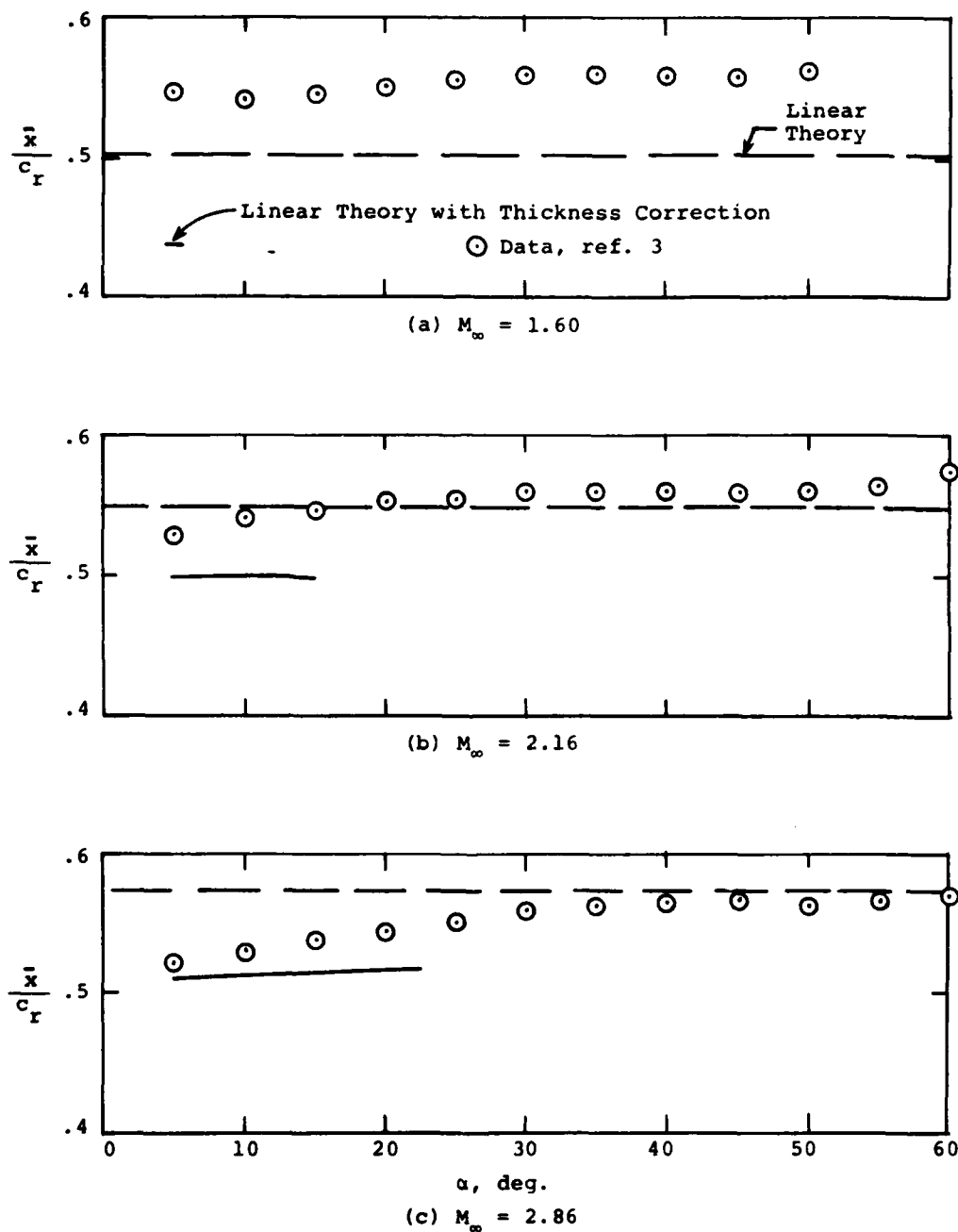
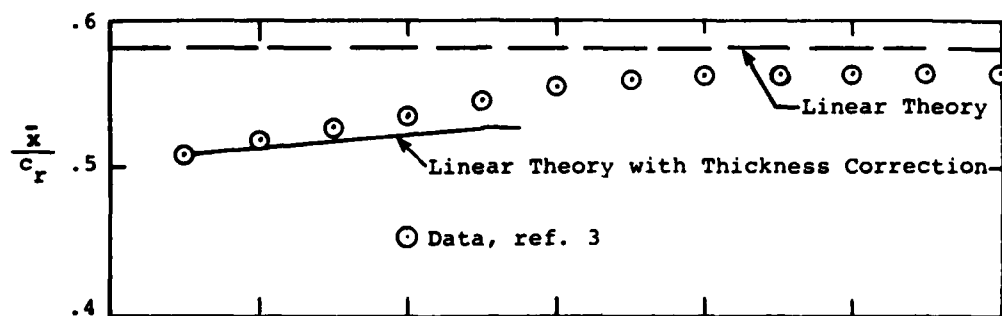
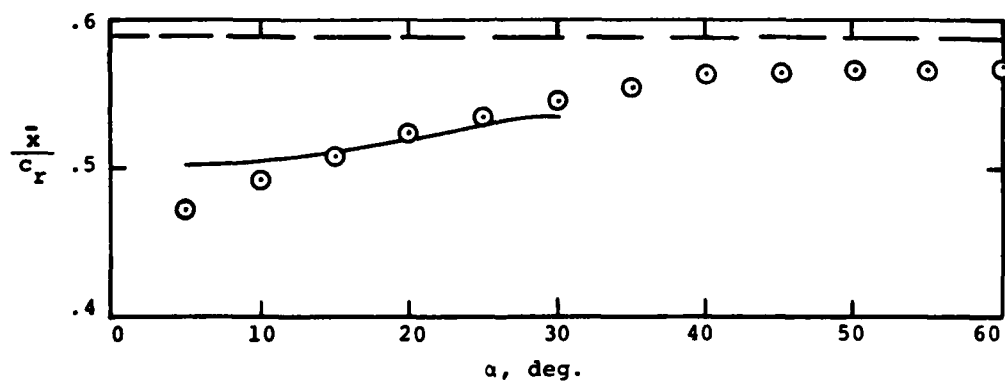


Figure 28.- Longitudinal center-of-pressure locations of an aspect ratio 1.0, taper ratio 0.5 cropped delta wing.



(d) $M_\infty = 3.50$



(e) $M_\infty = 4.60$

Figure 28.- Concluded.

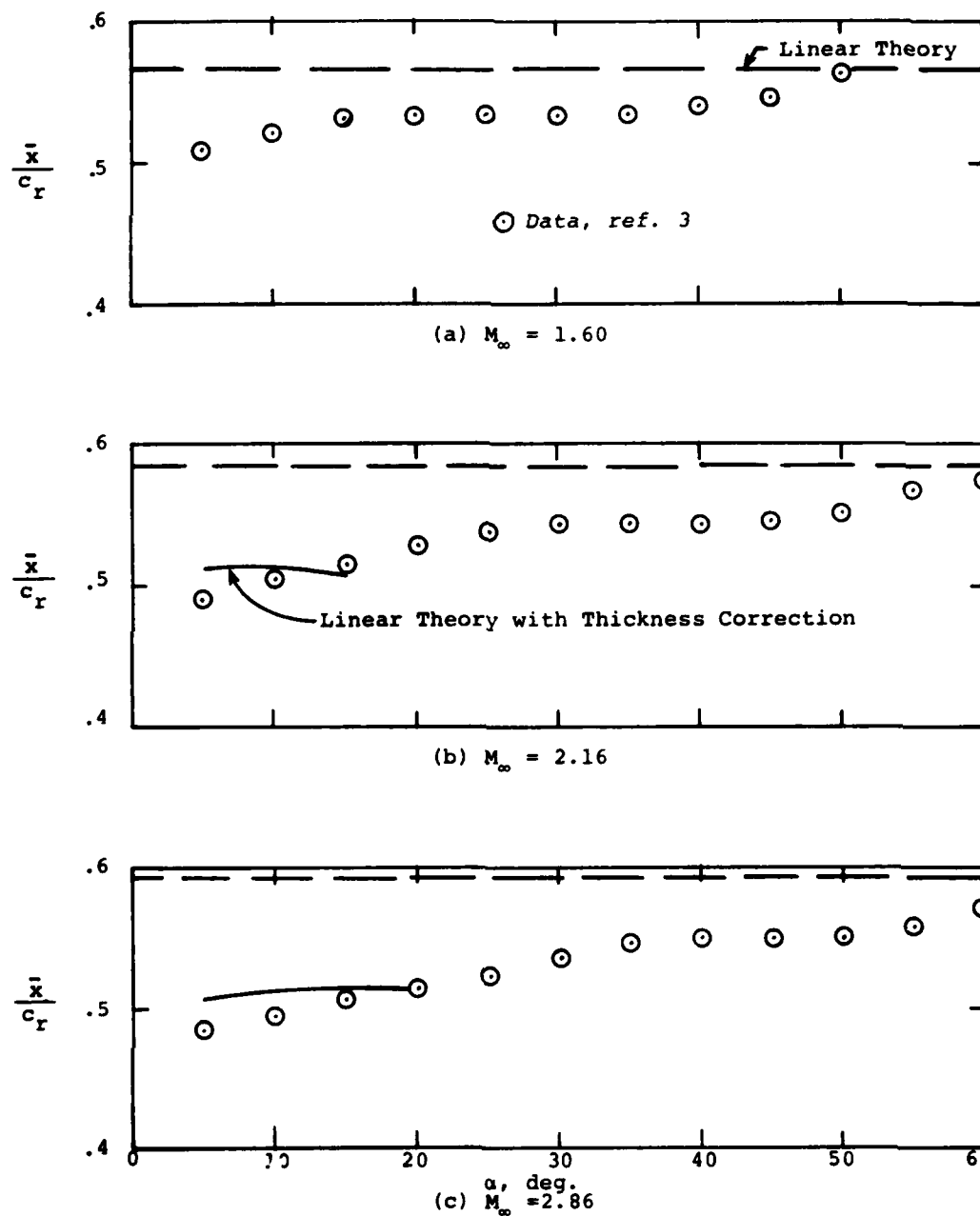


Figure 29.- Longitudinal center-of-pressure locations of an aspect ratio 2, taper ratio 0.5 cropped delta wing.

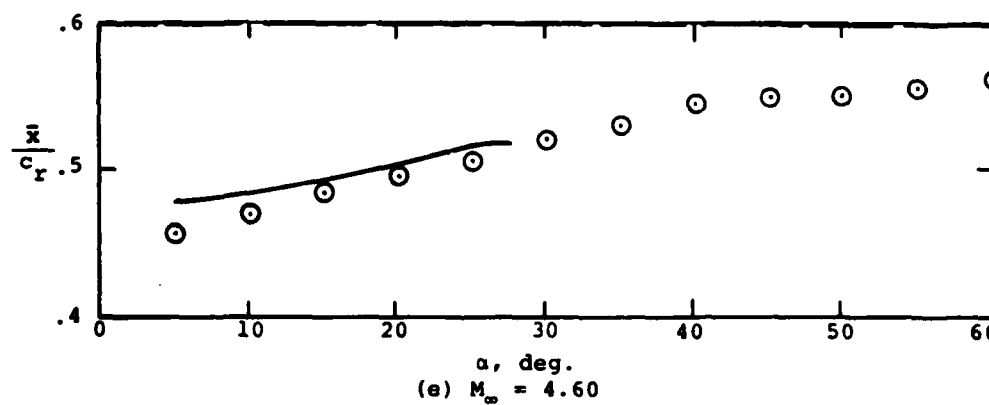
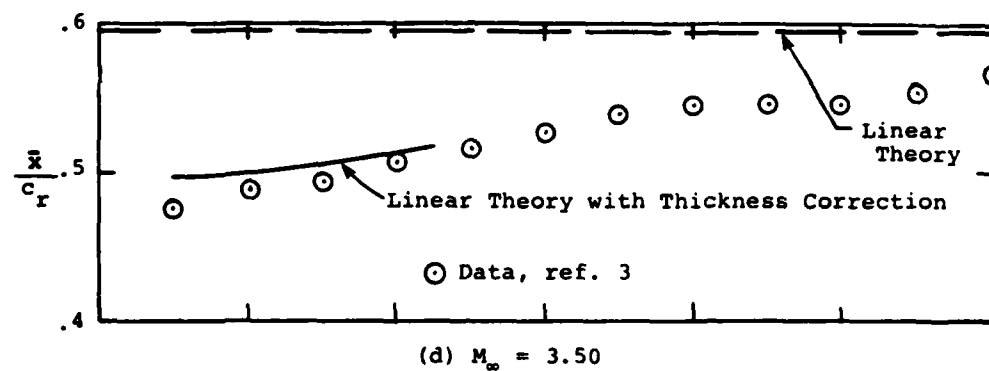
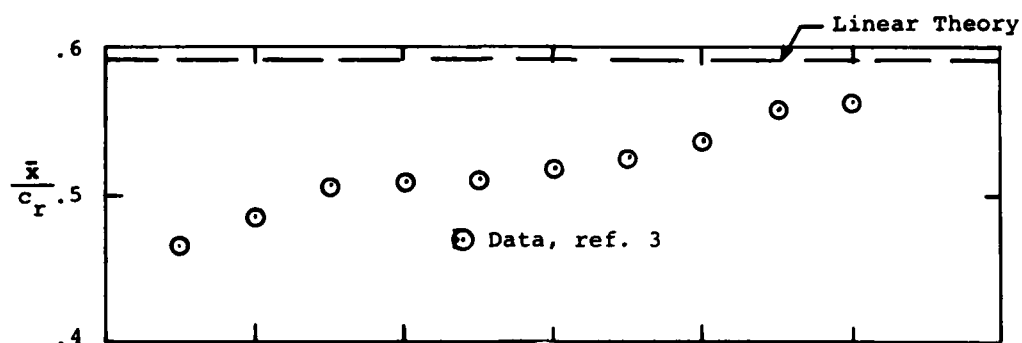
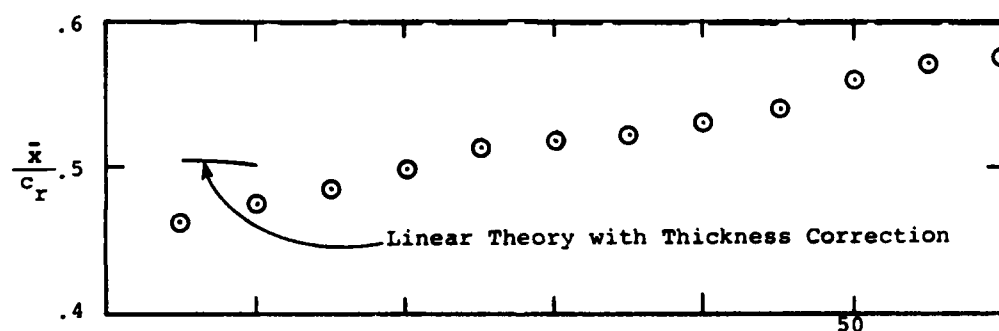


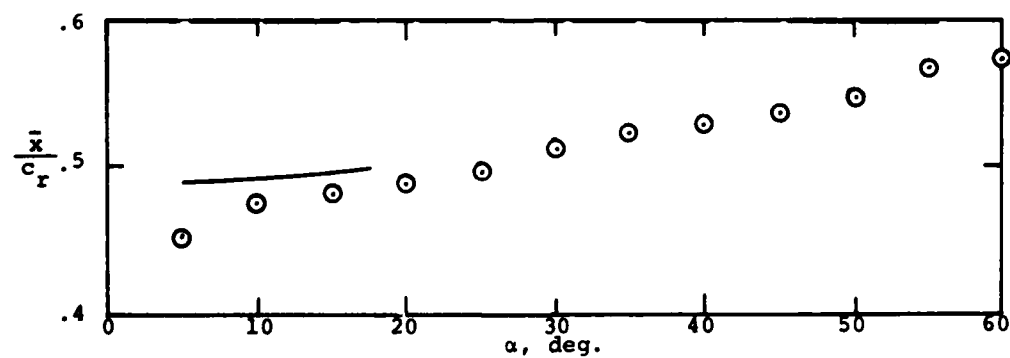
Figure 29.- Concluded



(a) $M_\infty = 1.60$



(b) $M_\infty = 2.16$



(c) $M_\infty = 2.86$

Figure 30.- Longitudinal center-of-pressure locations of an aspect ratio 4.0, taper ratio 0.5 cropped delta wing.

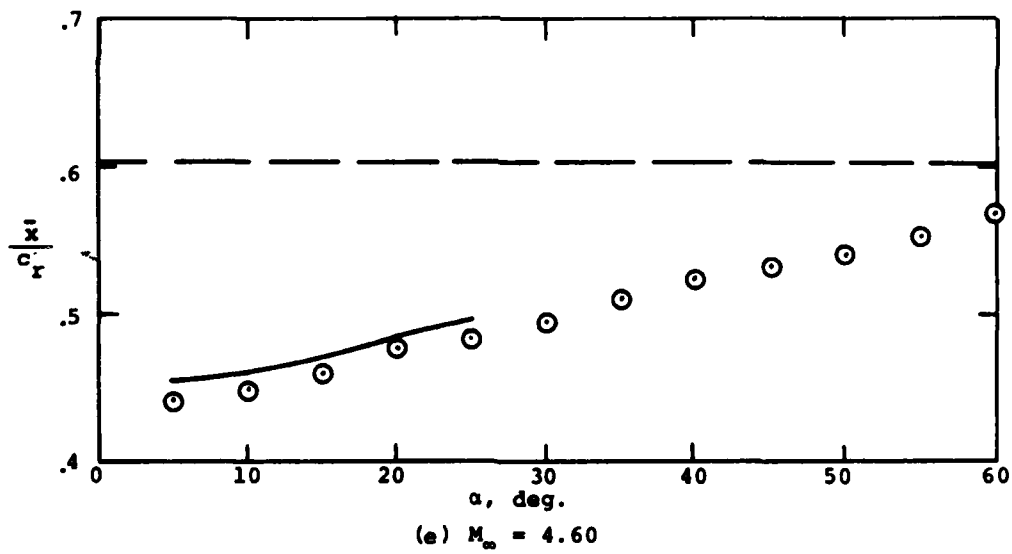
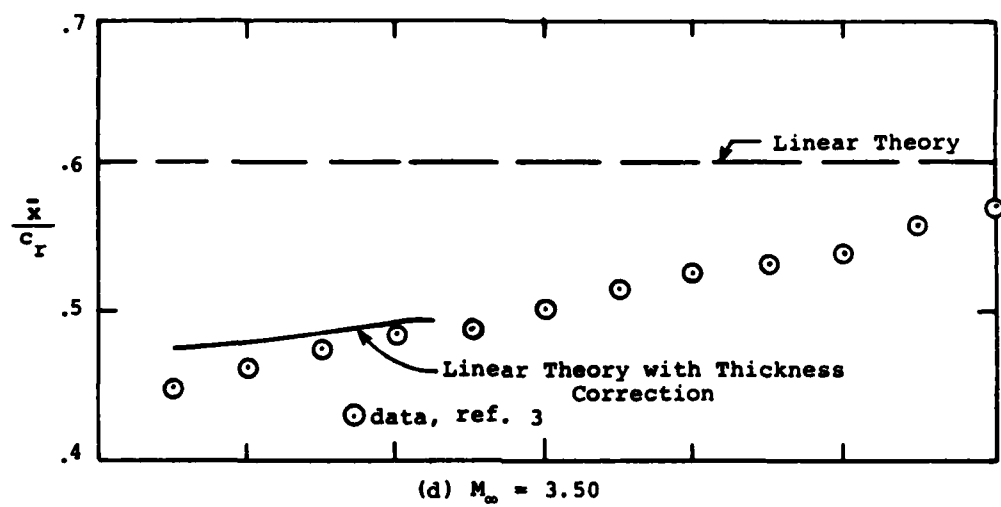


Figure 30.- Concluded

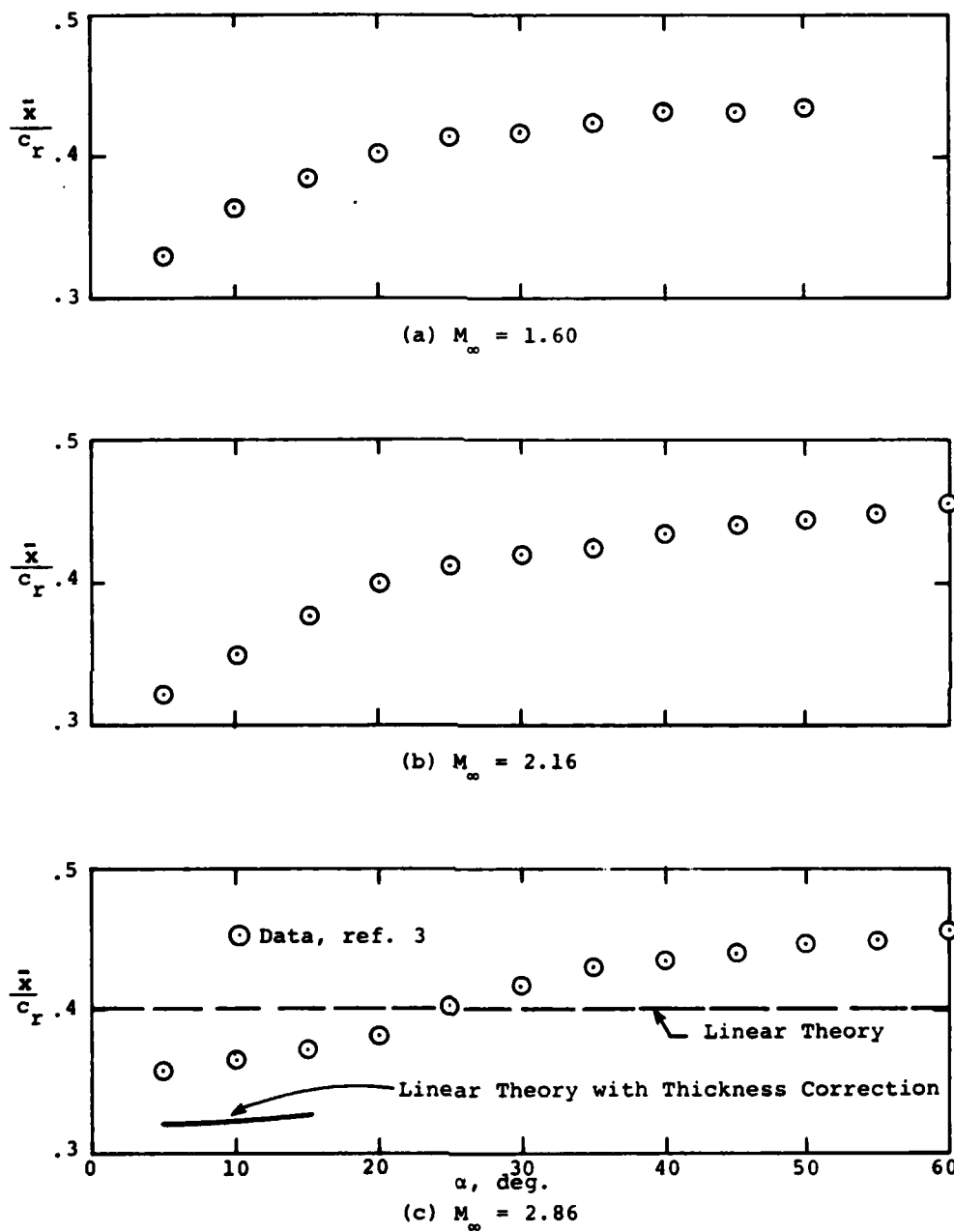
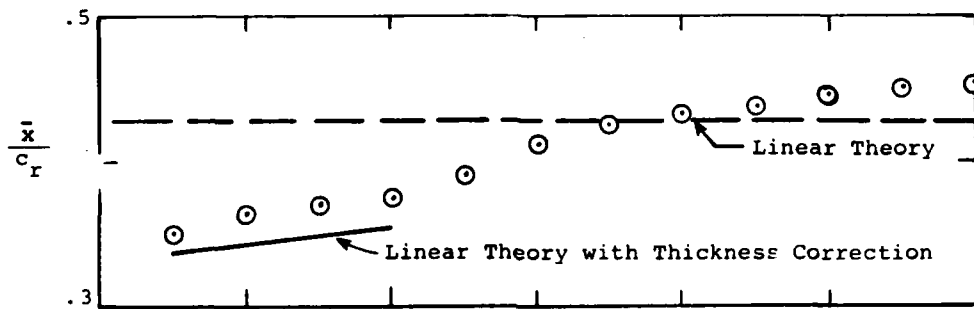
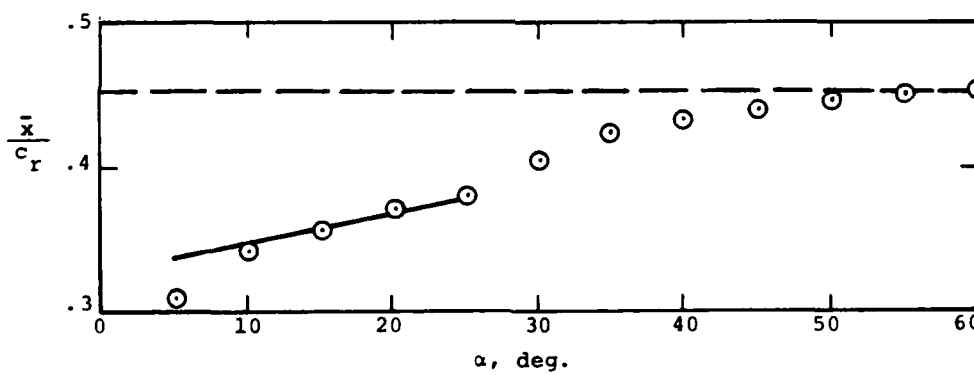


Figure 31.- Longitudinal center-of-pressure locations of an aspect ratio 0.5 rectangular wing.

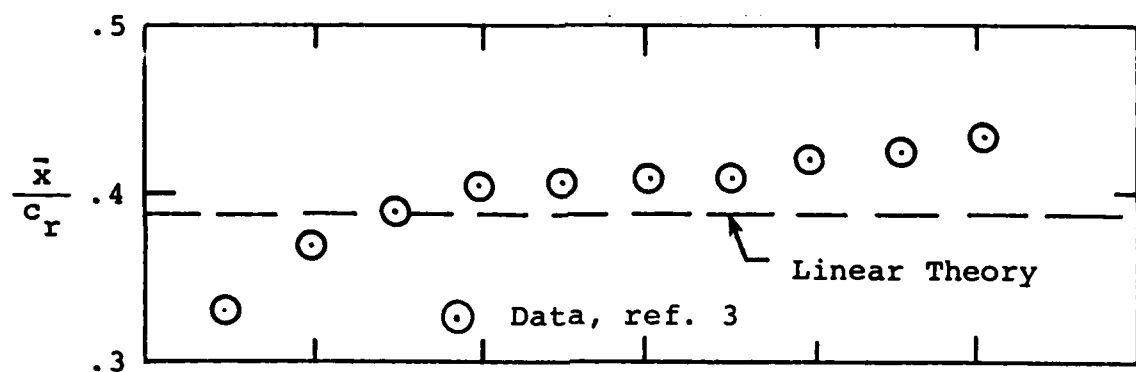


(d) $M_\infty = 3.50$

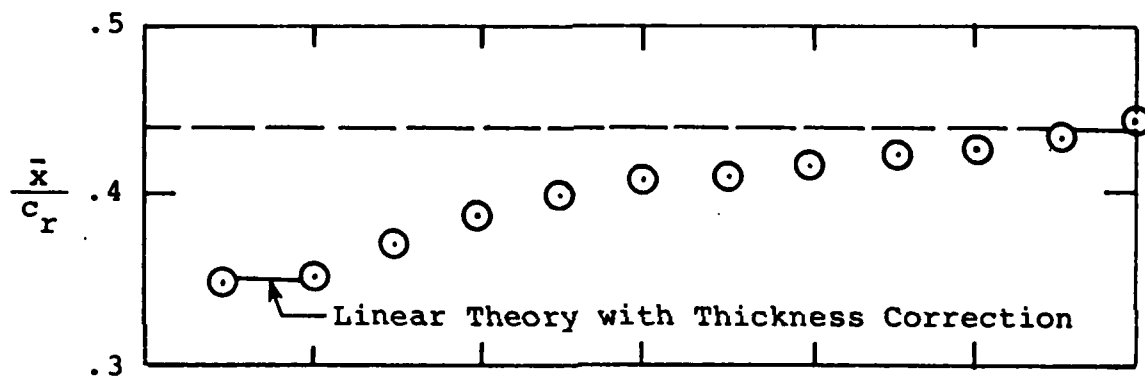


(e) $M_\infty = 4.60$

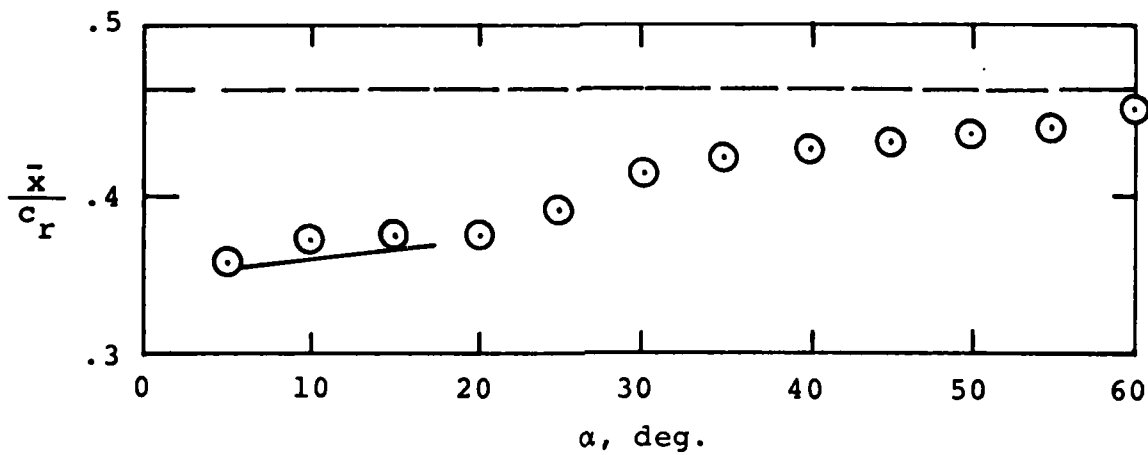
Figure 31.- Concluded.



(a) $M_\infty = 1.60$

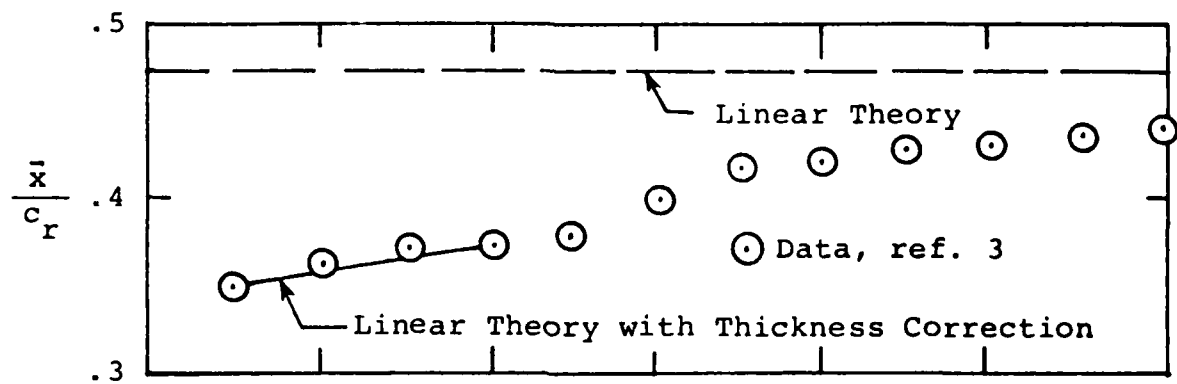


(b) $M_\infty = 2.16$

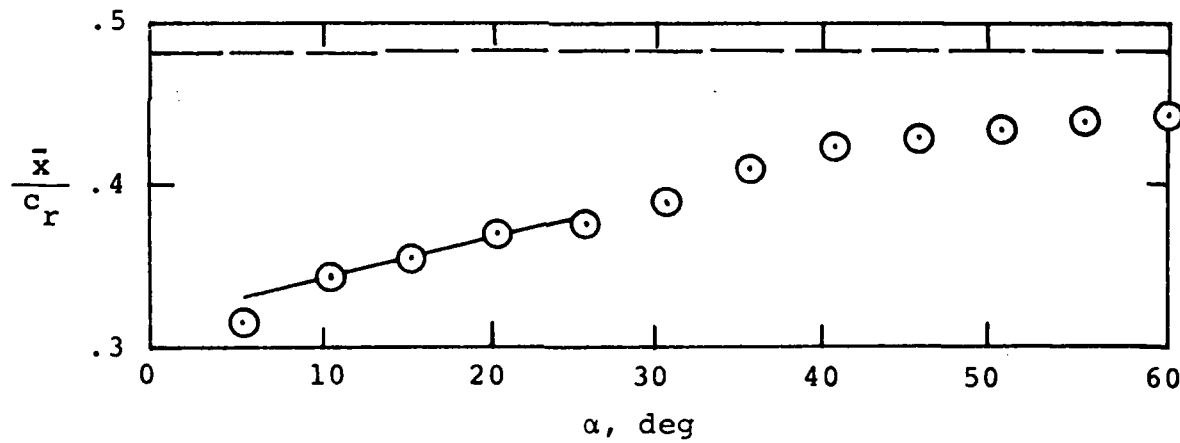


(c) $M_\infty = 2.86$

Figure 32.- Longitudinal center-of-pressure locations of an aspect ratio 1.0 rectangular wing.

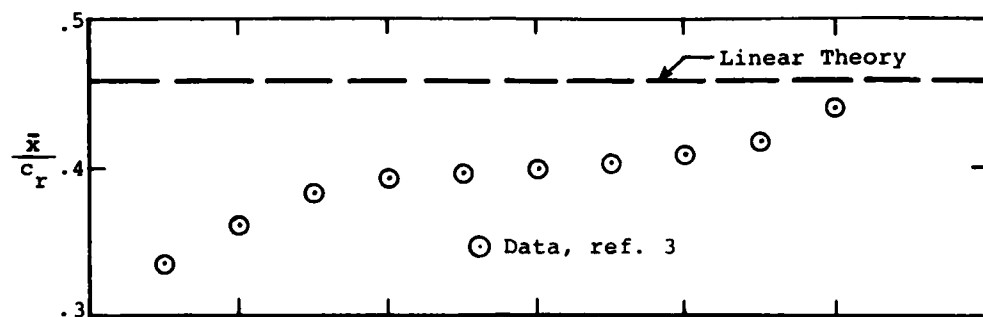


(d) $M_\infty = 3.50$

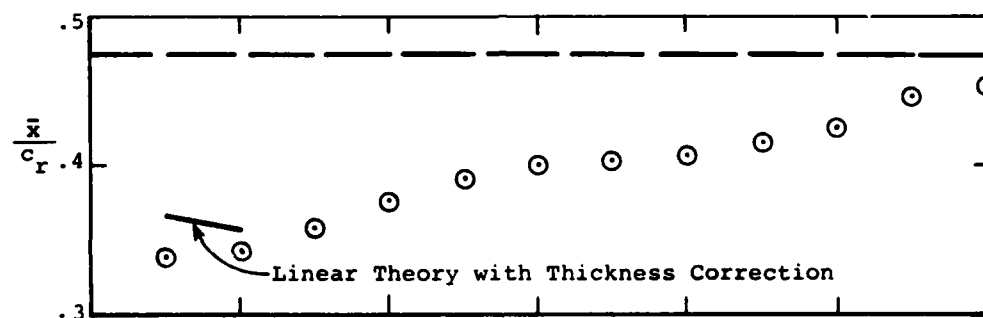


(e) $M_\infty = 4.60$

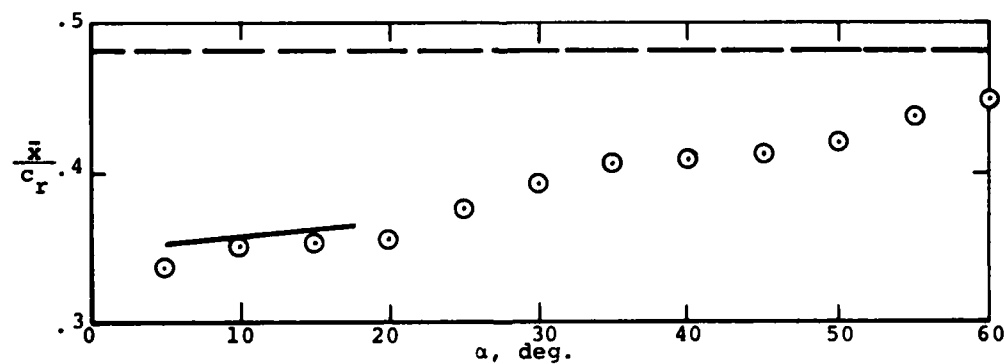
Figure 32.- Concluded



(a) $M_\infty = 1.60$



(b) $M_\infty = 2.16$



(c) $M_\infty = 2.86$

Figure 33.- Longitudinal center-of-pressure locations of an aspect ratio 2.0 rectangular wing.

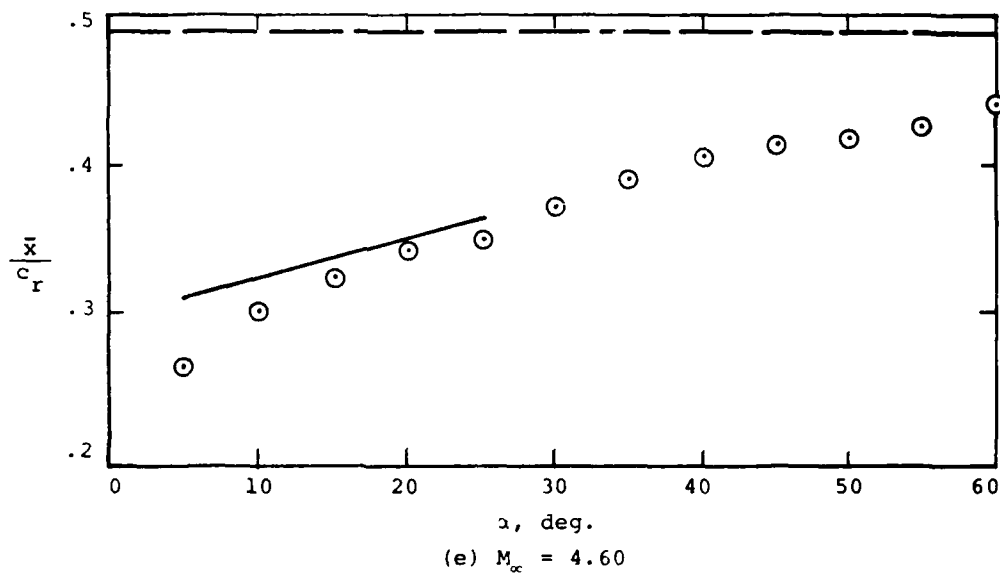
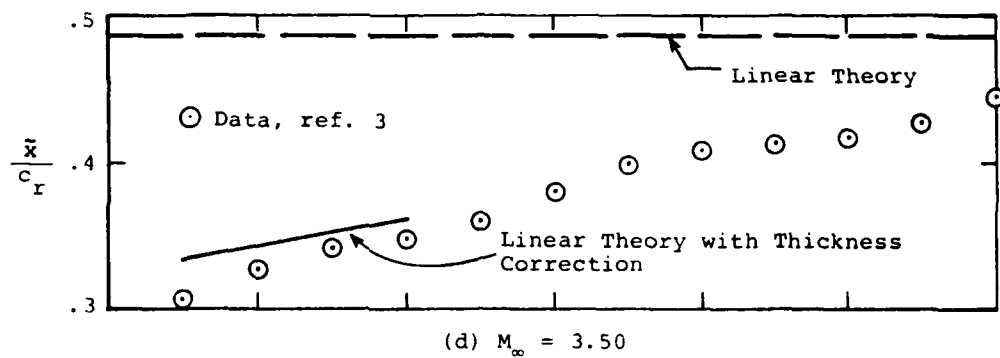


Figure 33.- Concluded.

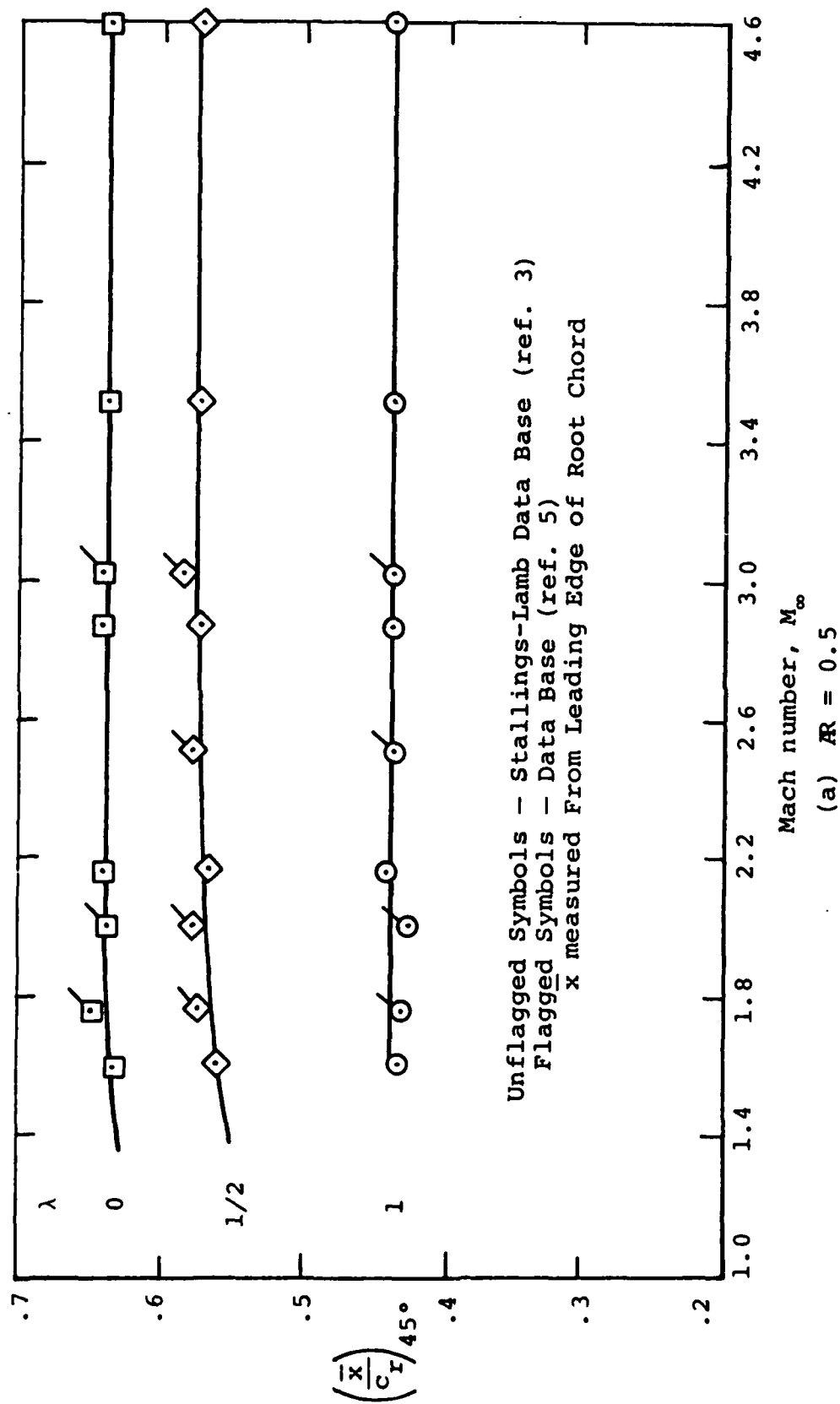
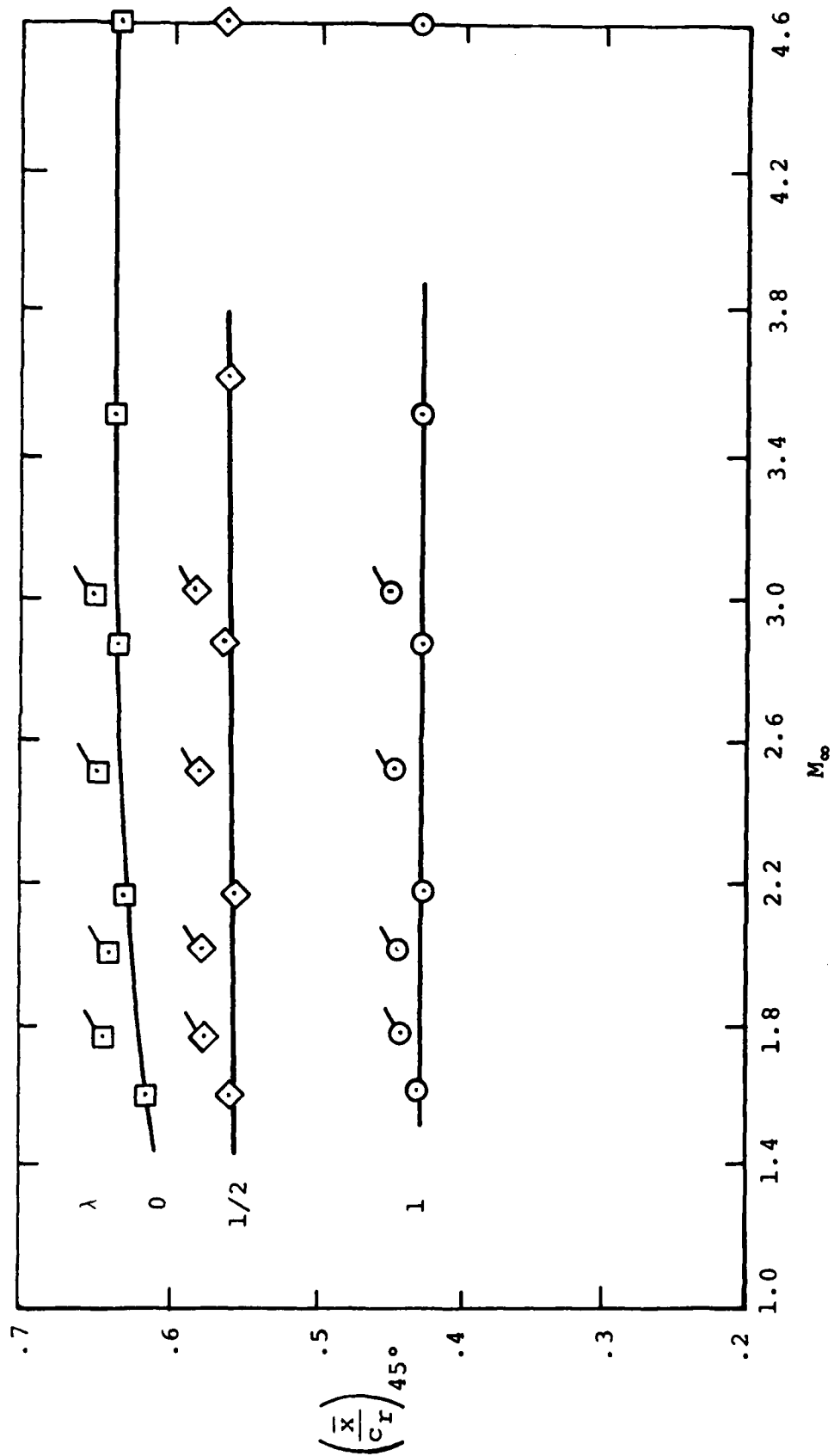
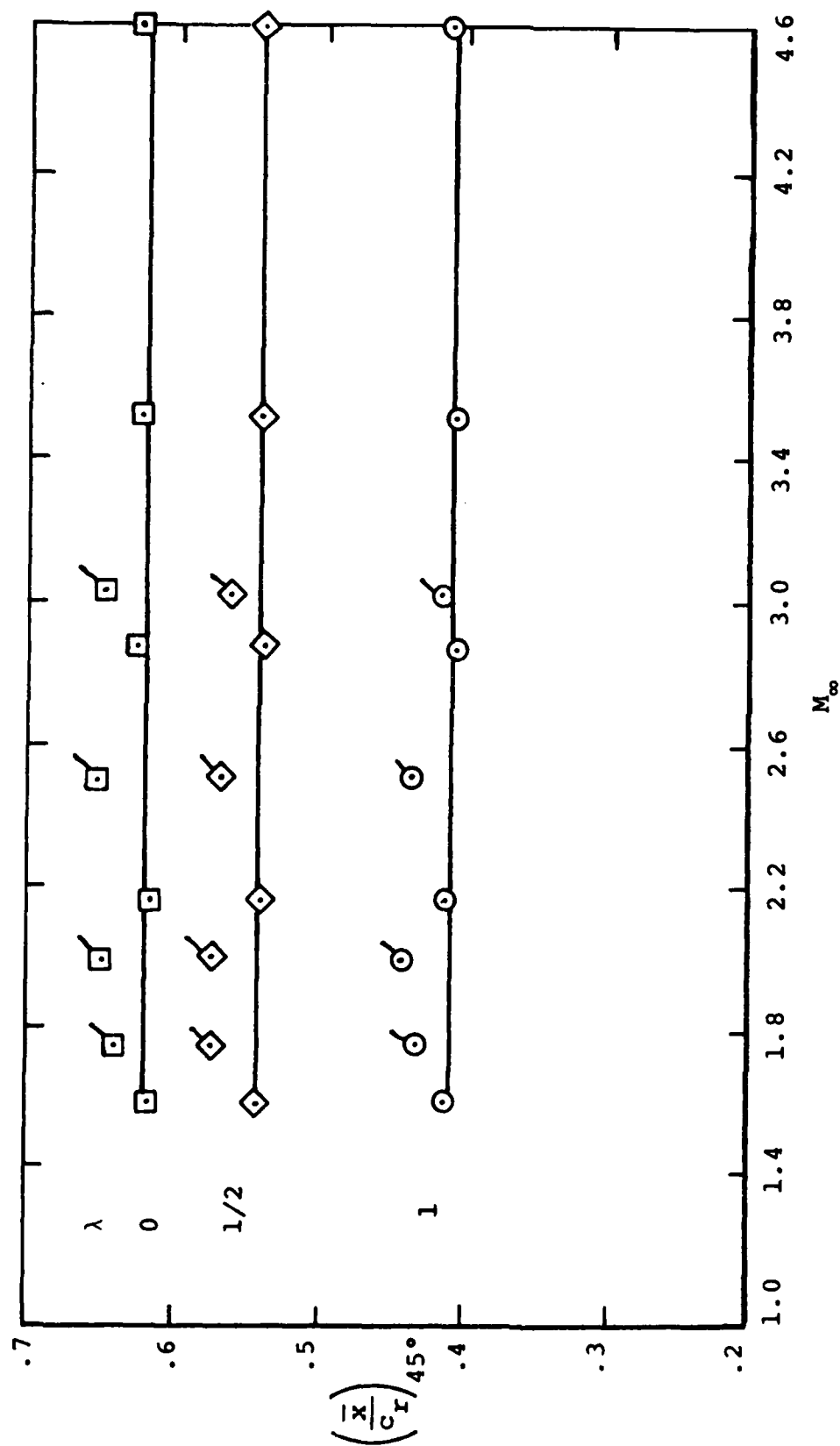


Figure 34.- Comparison of longitudinal center-of-pressure position at
 $\alpha = 45^\circ$ of wings of Stallings-Lamb and Fidler-Baker data bases;
 high Mach number range.



(b) $AR = 1.0$

Figure 34.- Continued.



(c) $AR = 2.0$
Figure 34.- Concluded.

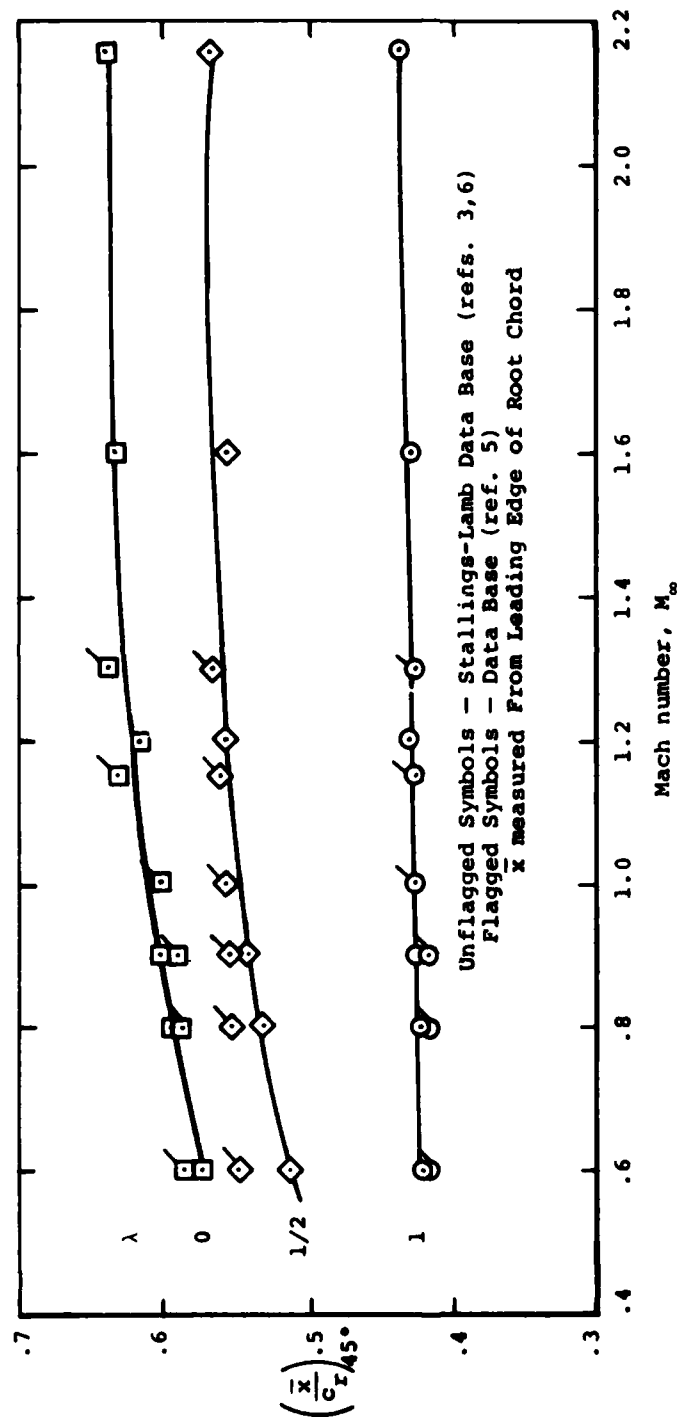


Figure 35.- Comparison of longitudinal center-of-pressure position at
 $\alpha = 45^\circ$ of wings of Stallings-Lamb and Fidler-Baker data bases;
 low Mach number range.

(a) $R = 0.5$

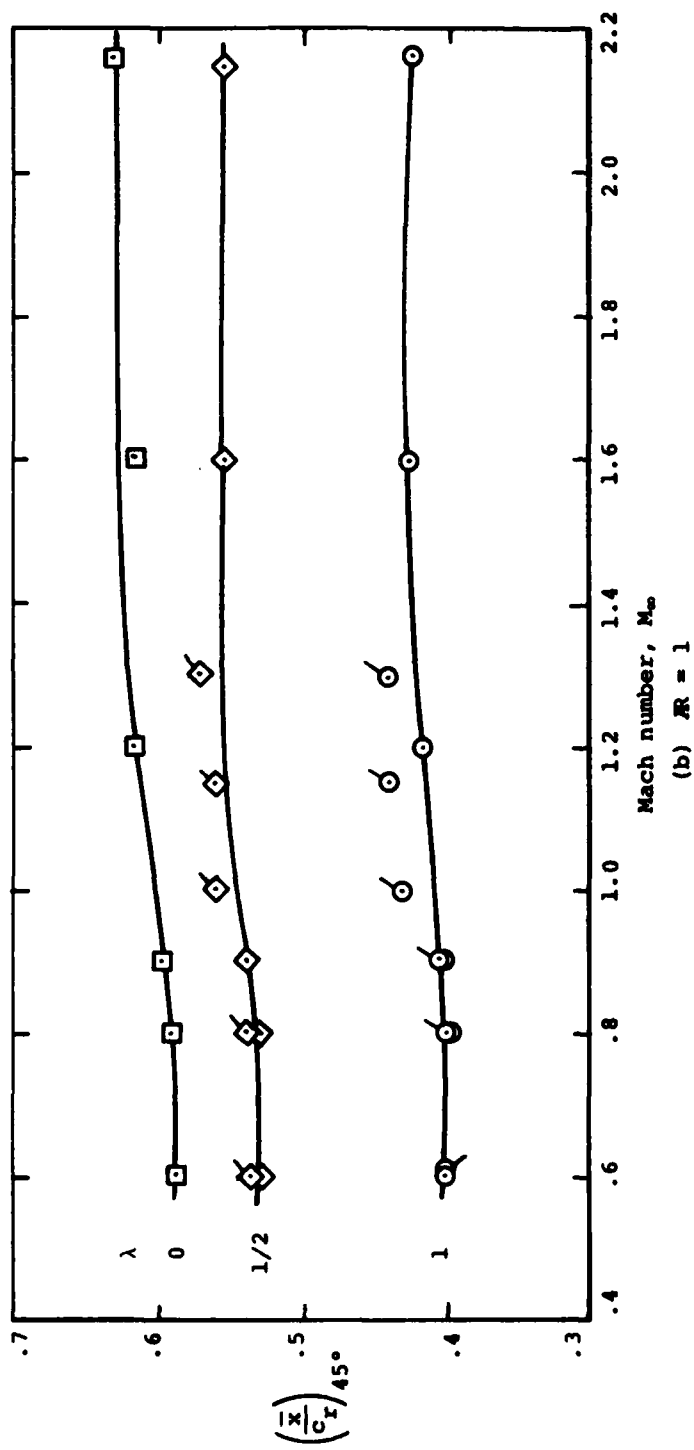
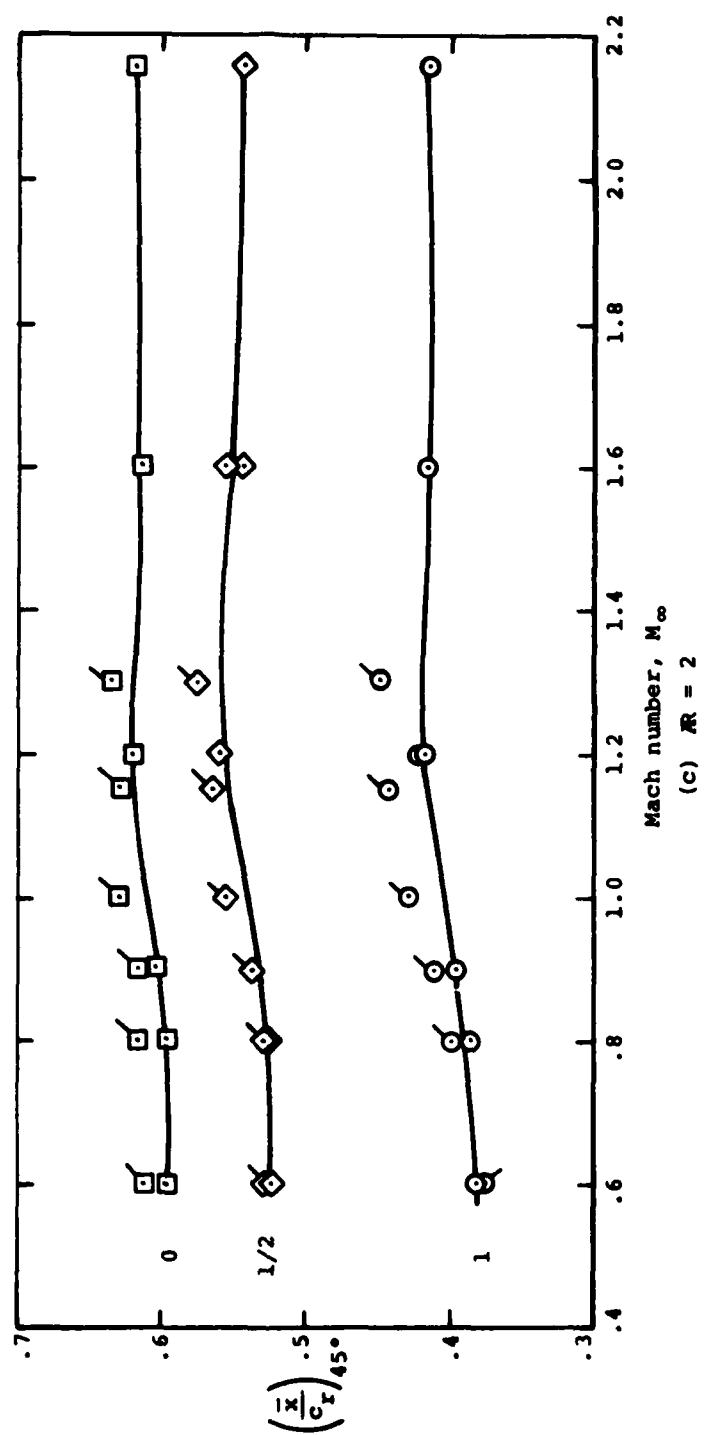


Figure 35.- Continued.



Mach number, M_∞

(c) $R = 2$

Figure 35.- Concluded.

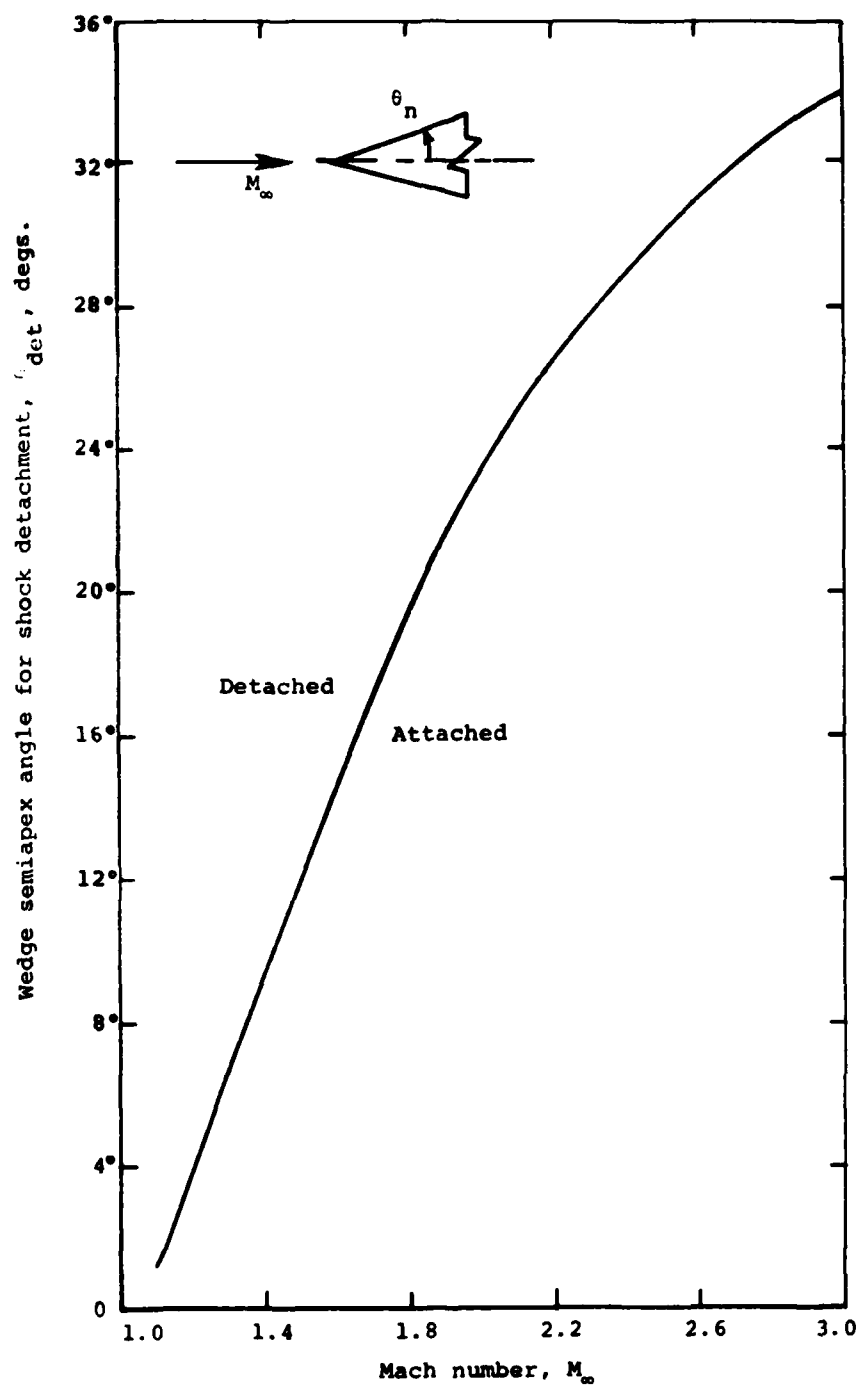


Figure 36.- Wedge semiapex angle for shock detachment in two-dimensional flow.

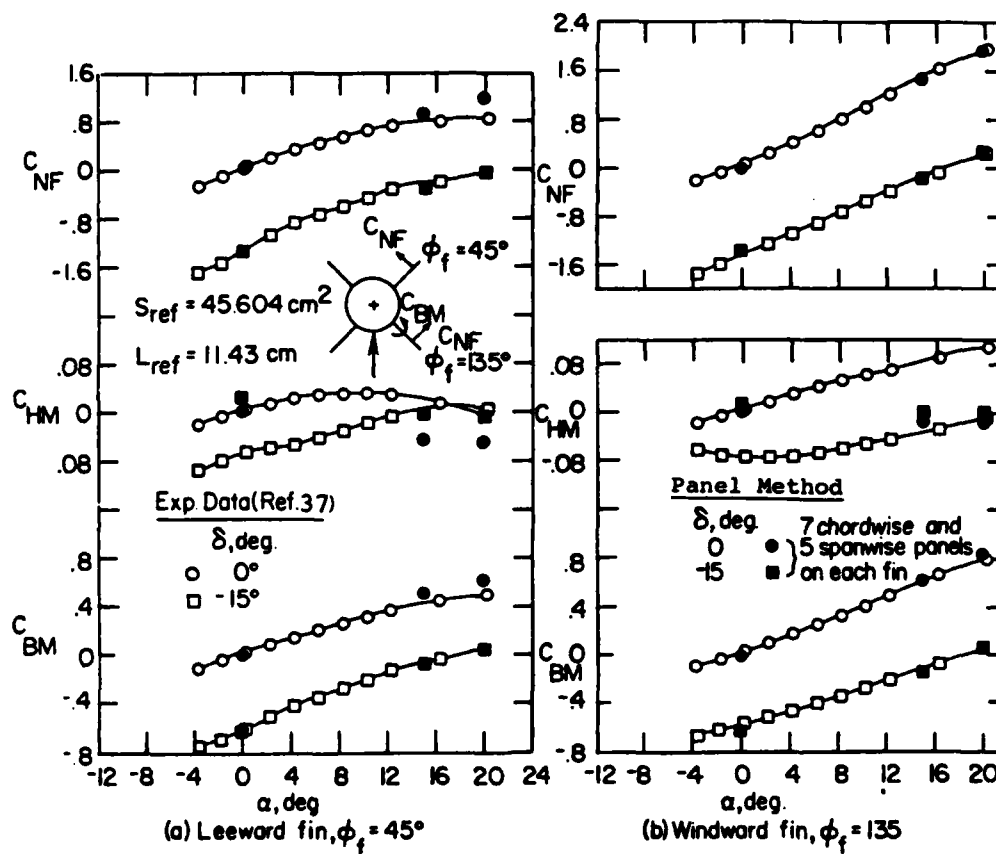
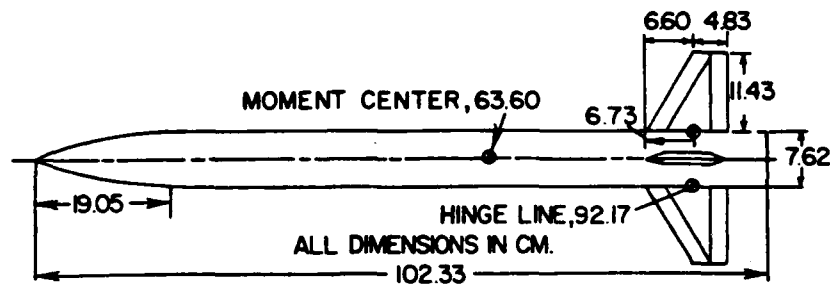


Figure 37.- Normal force, hinge moment and root bending moment acting on fins of a rolled fin-body combination, $M_\infty = 1.6$.

5 Spanwise Panels

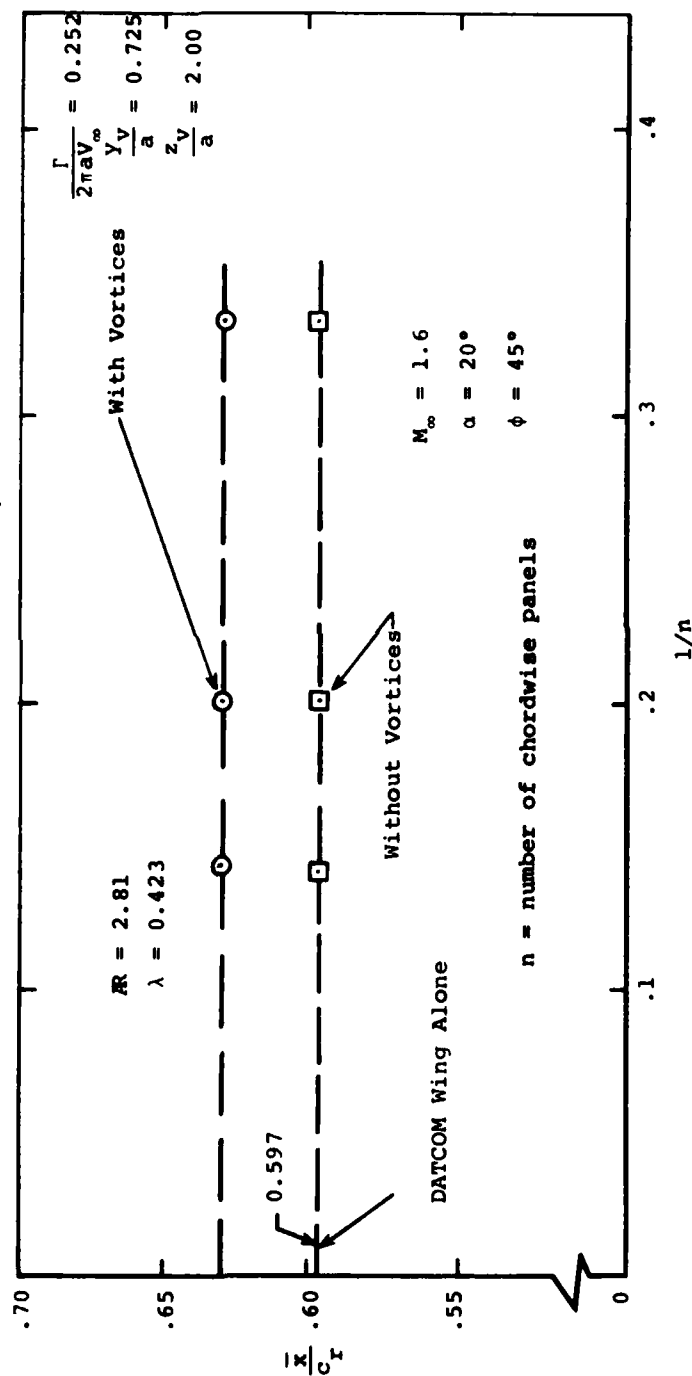
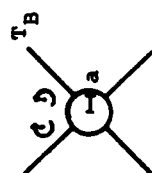
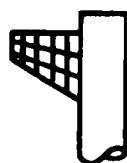


Figure 38.- Application of panel method to determine axial center-of-pressure position of fin T_B in presence of the body.

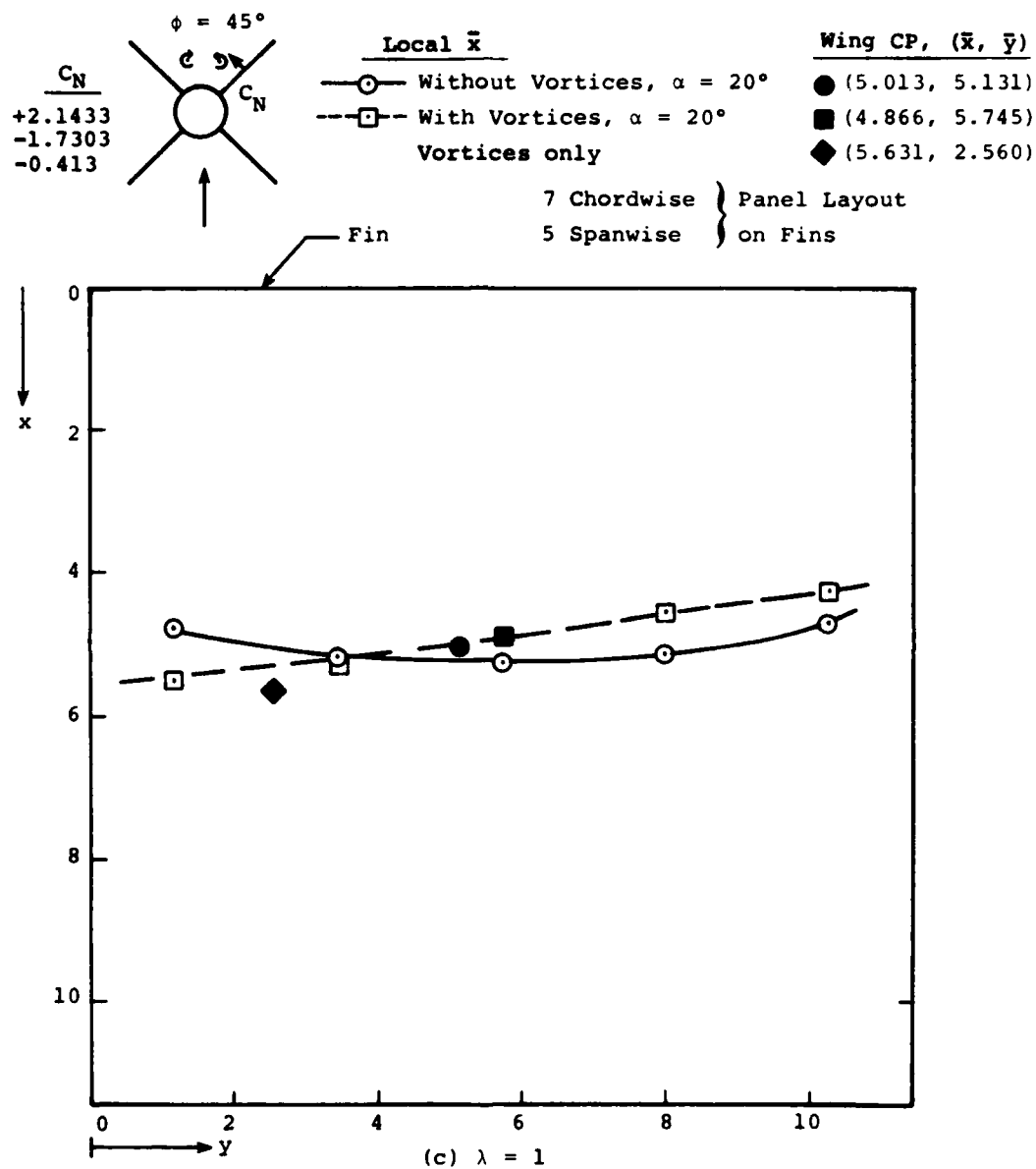
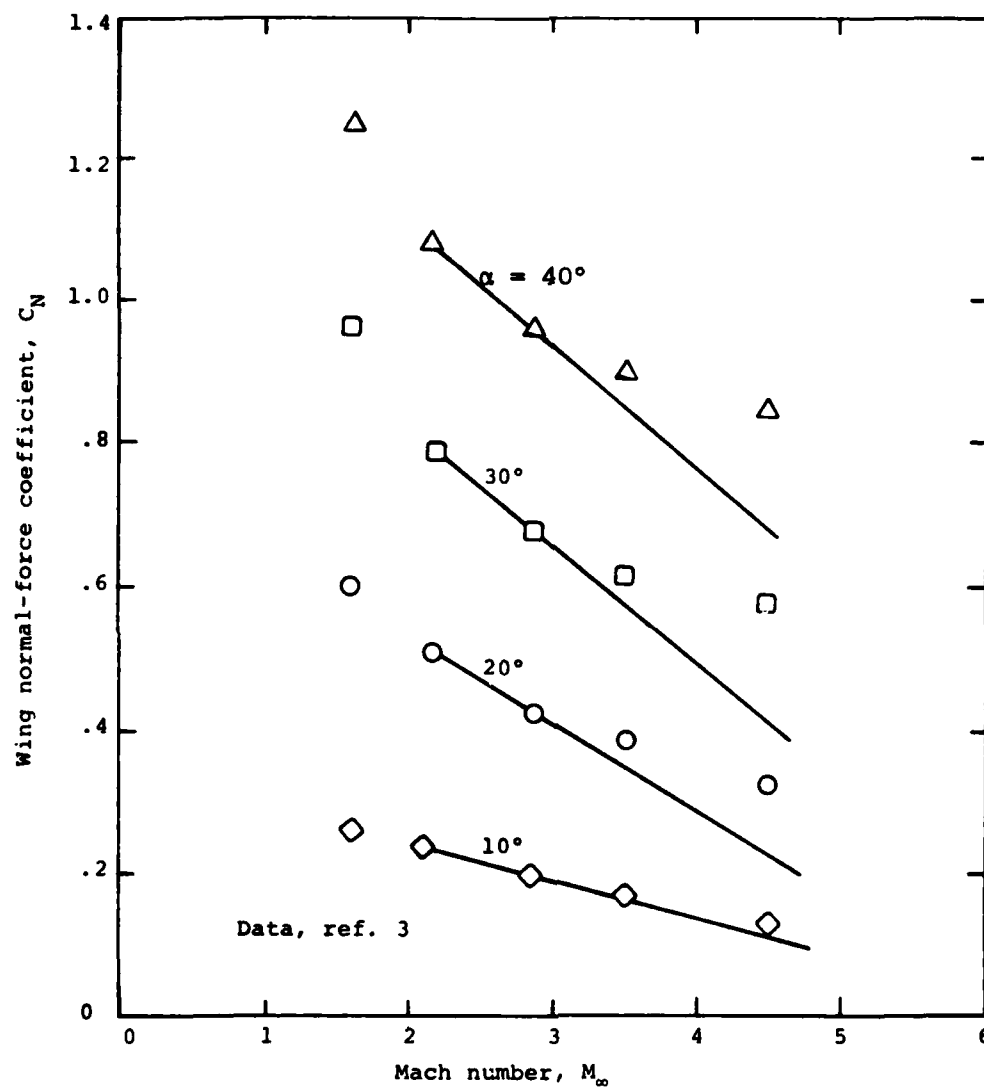
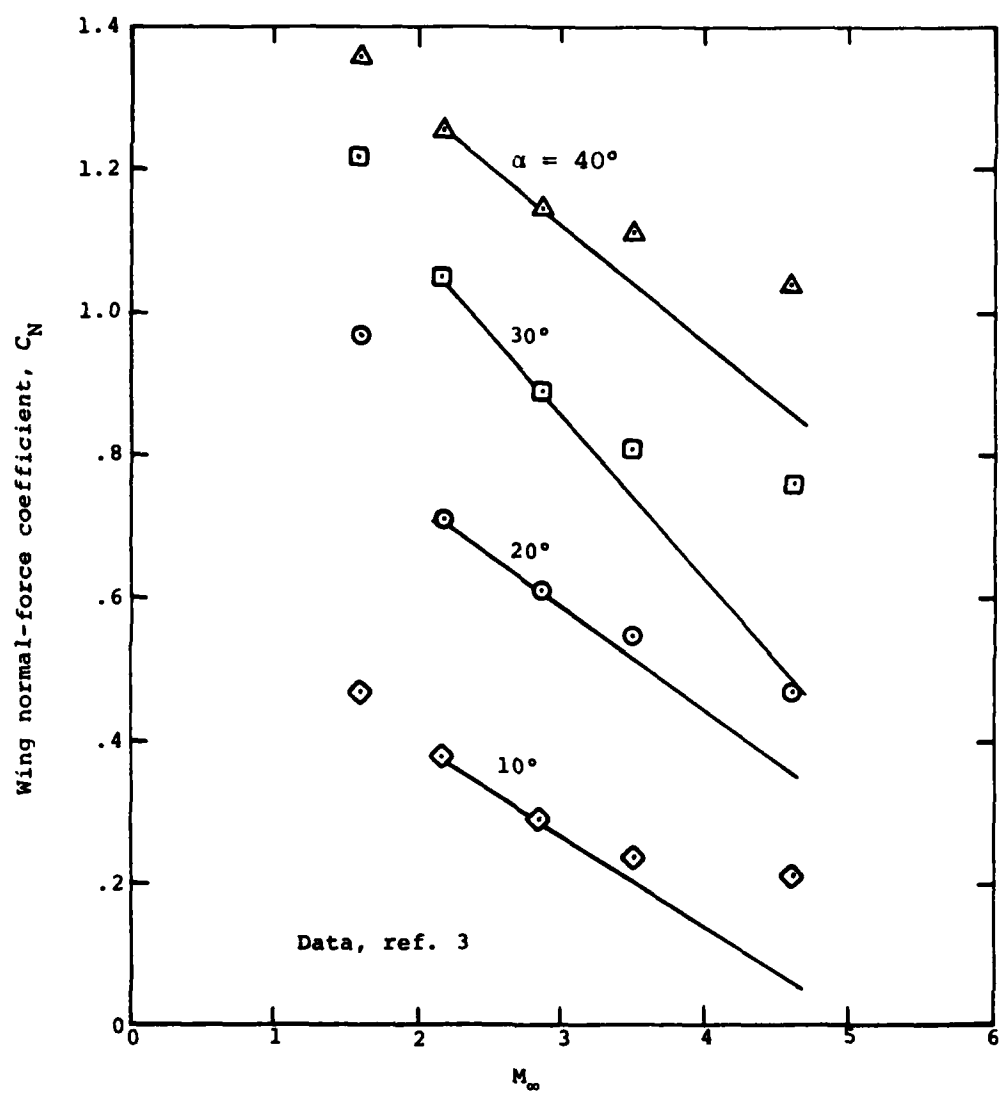


Figure 39.- Concluded.



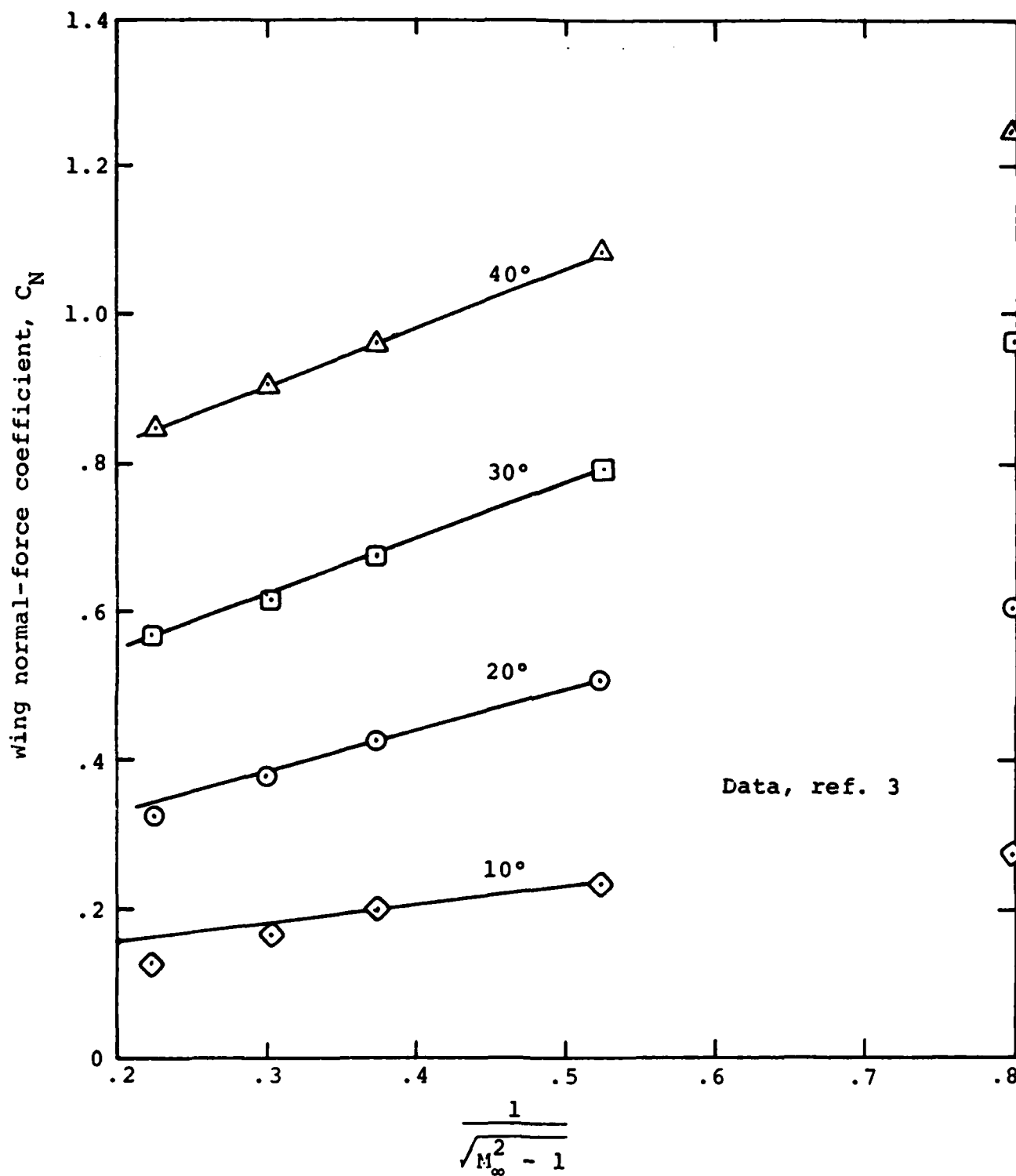
(a) $R = 0.5$, $\lambda = 1.0$

Figure 40.- Accuracy of linear extrapolation of wing-alone normal-force coefficient to Mach numbers greater than three.



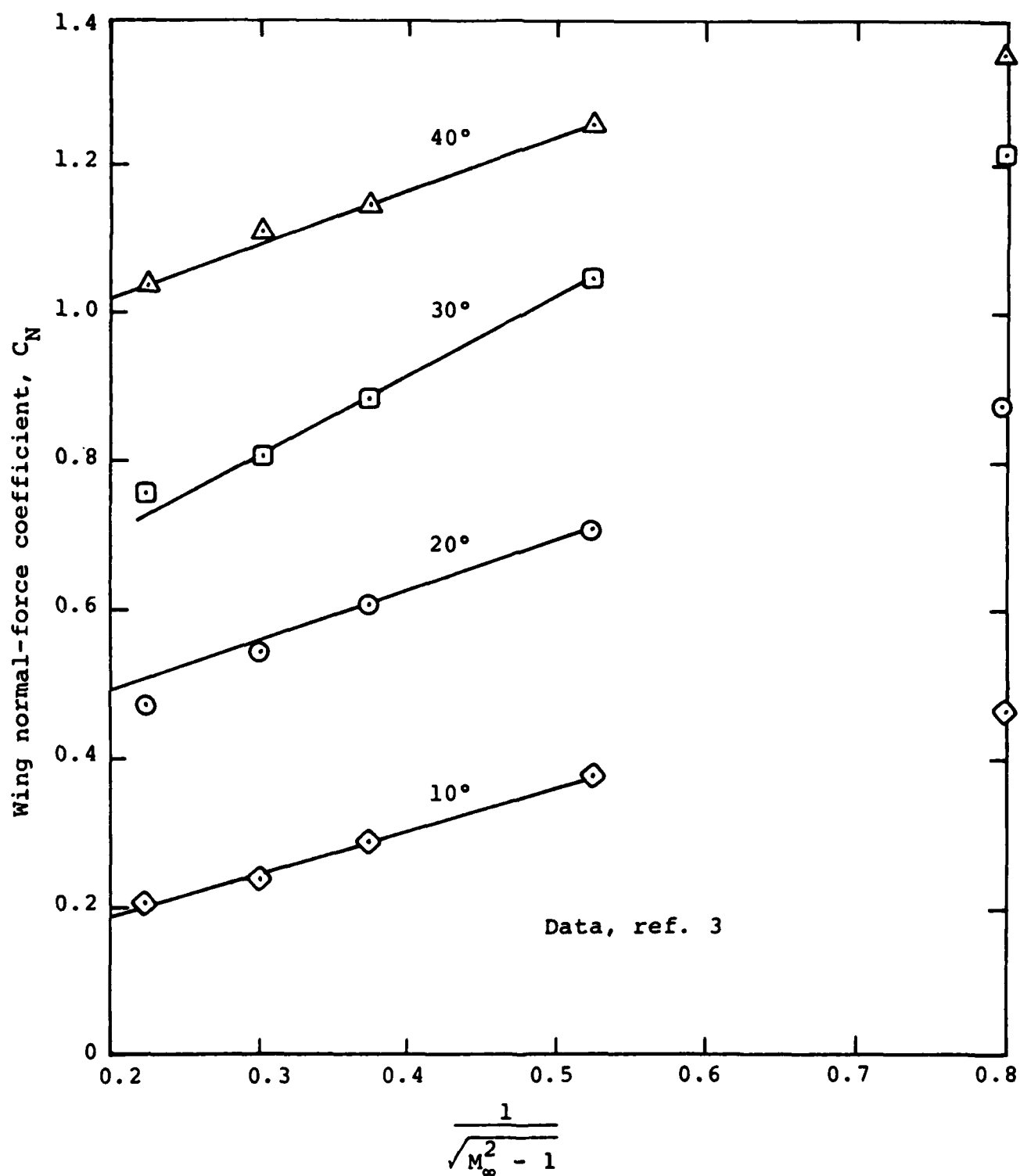
(b) $R = 4.0$, $\lambda = 0.5$

Figure 40.- Concluded.



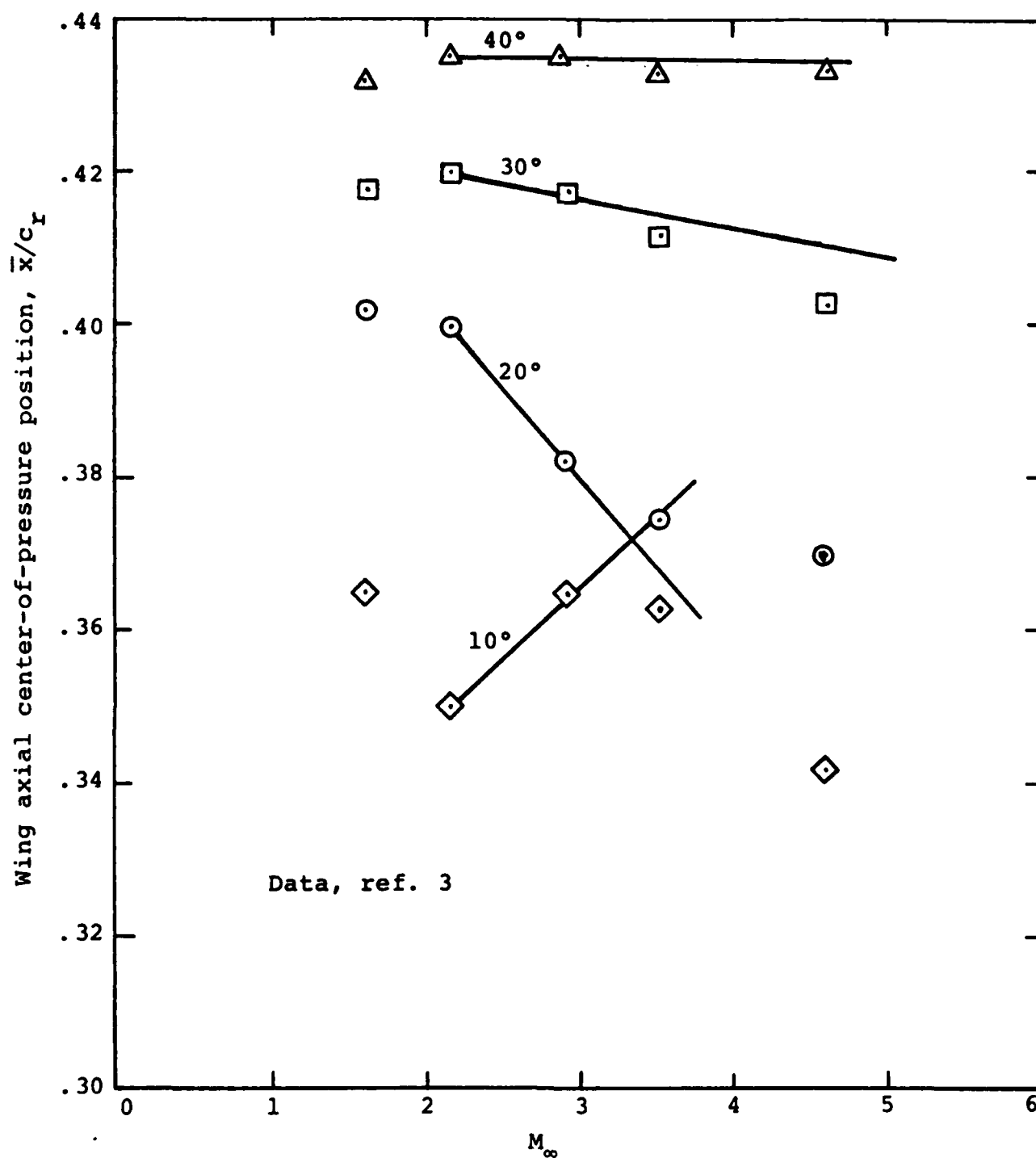
(a) $R = 0.5$, $\lambda = 1.0$

Figure 41.- Variation of wing normal-force coefficient with $(M_\infty^2 - 1)^{-1/2}$.



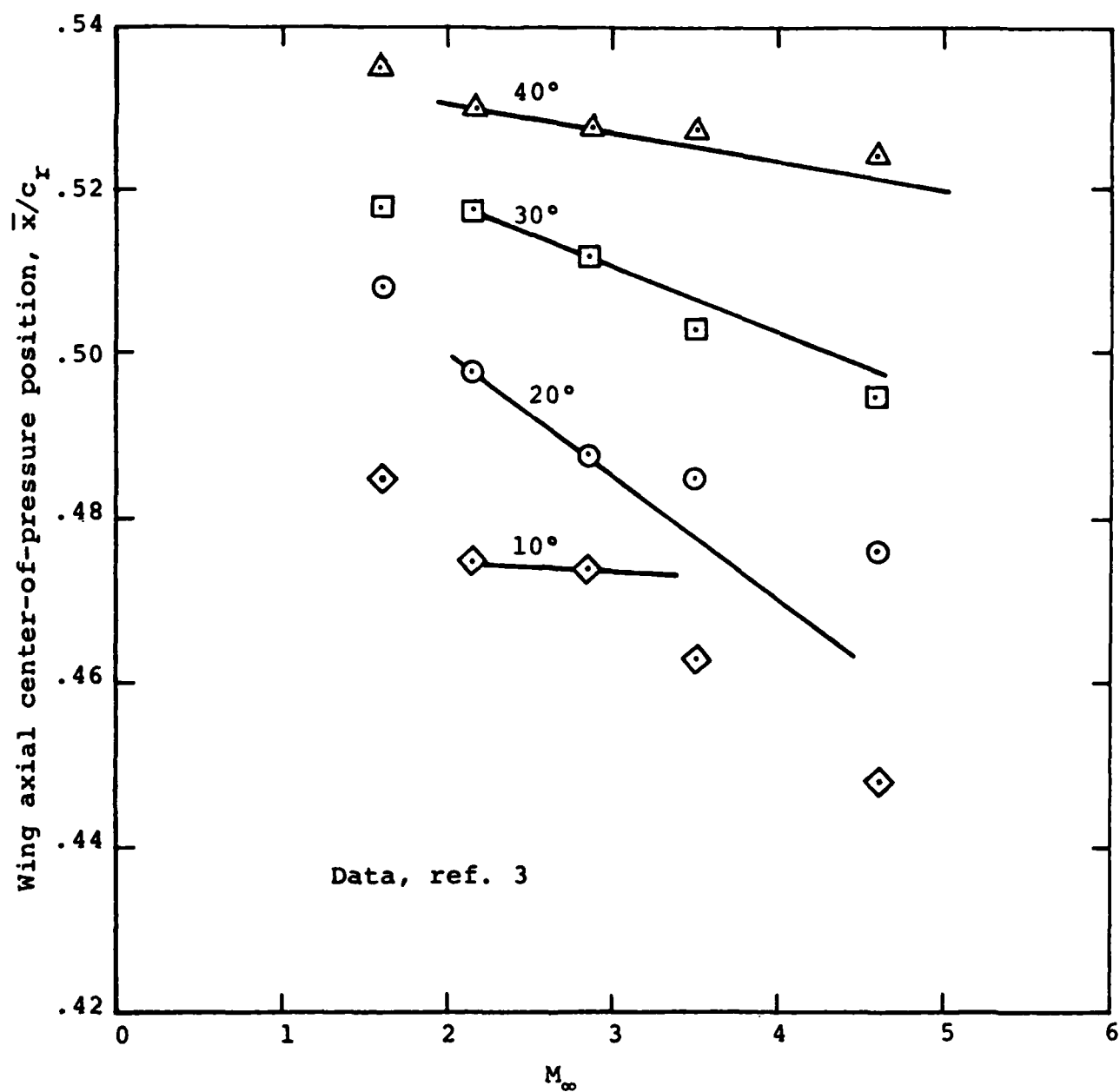
(b) $AR = 4.0$, $\lambda = 0.5$

Figure 41.- Concluded.

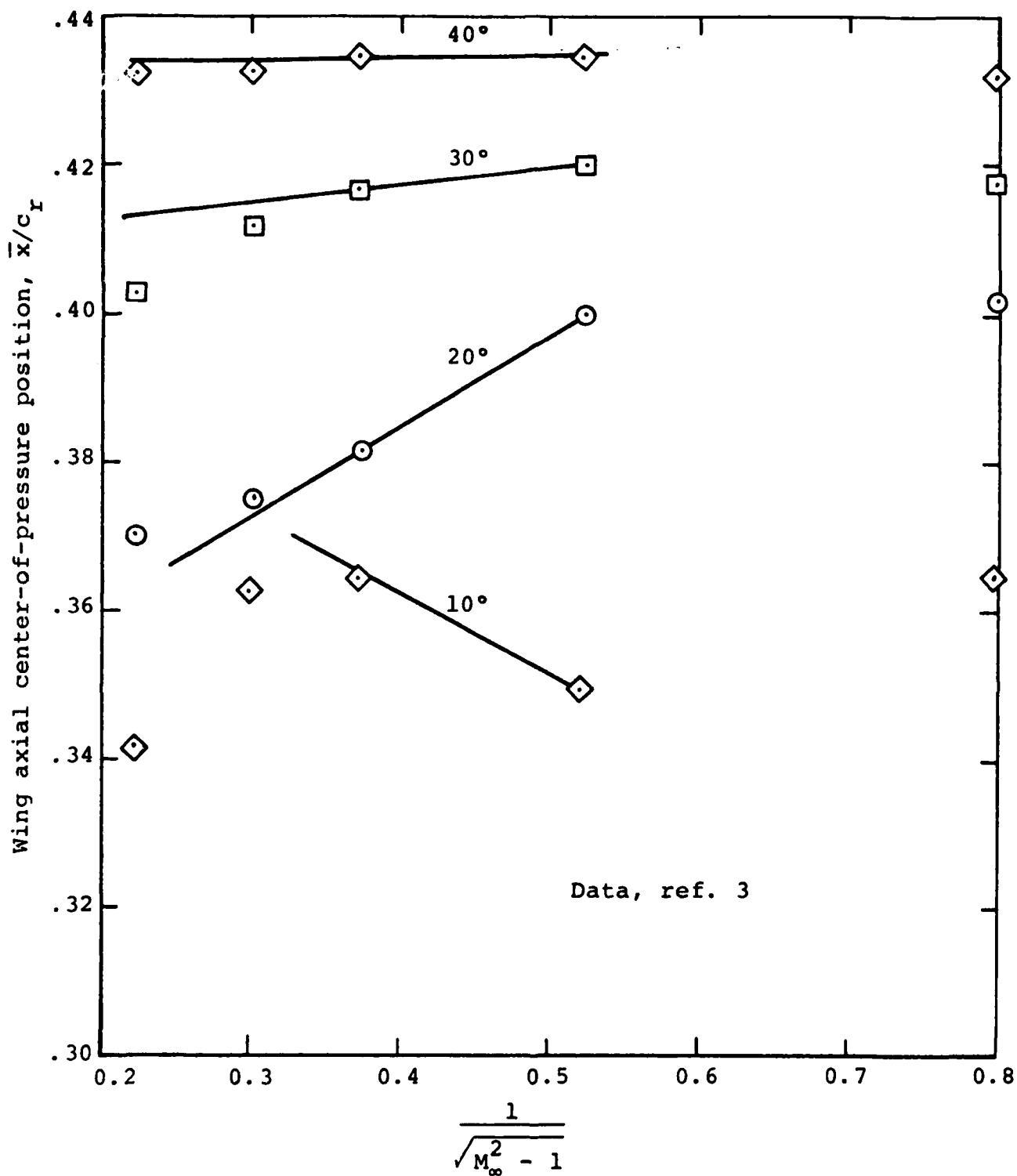


(a) $R = 0.5$, $\lambda = 1.0$

Figure 42.- Accuracy of linear extrapolation of wing-alone axial center-of-pressure position to Mach number greater than three.

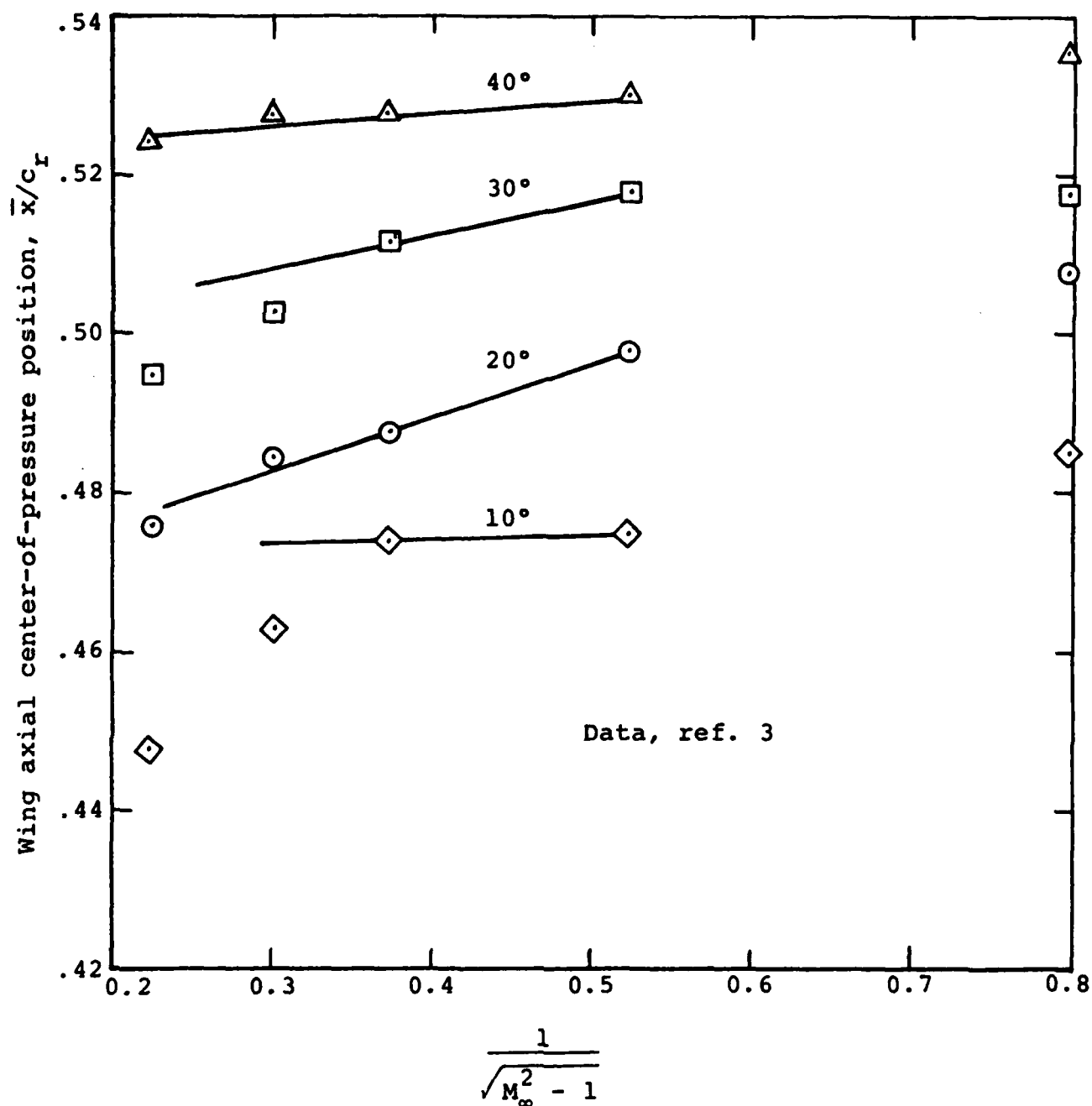


(b) $AR = 4, \lambda = 0.5$
Figure 42.- Concluded.



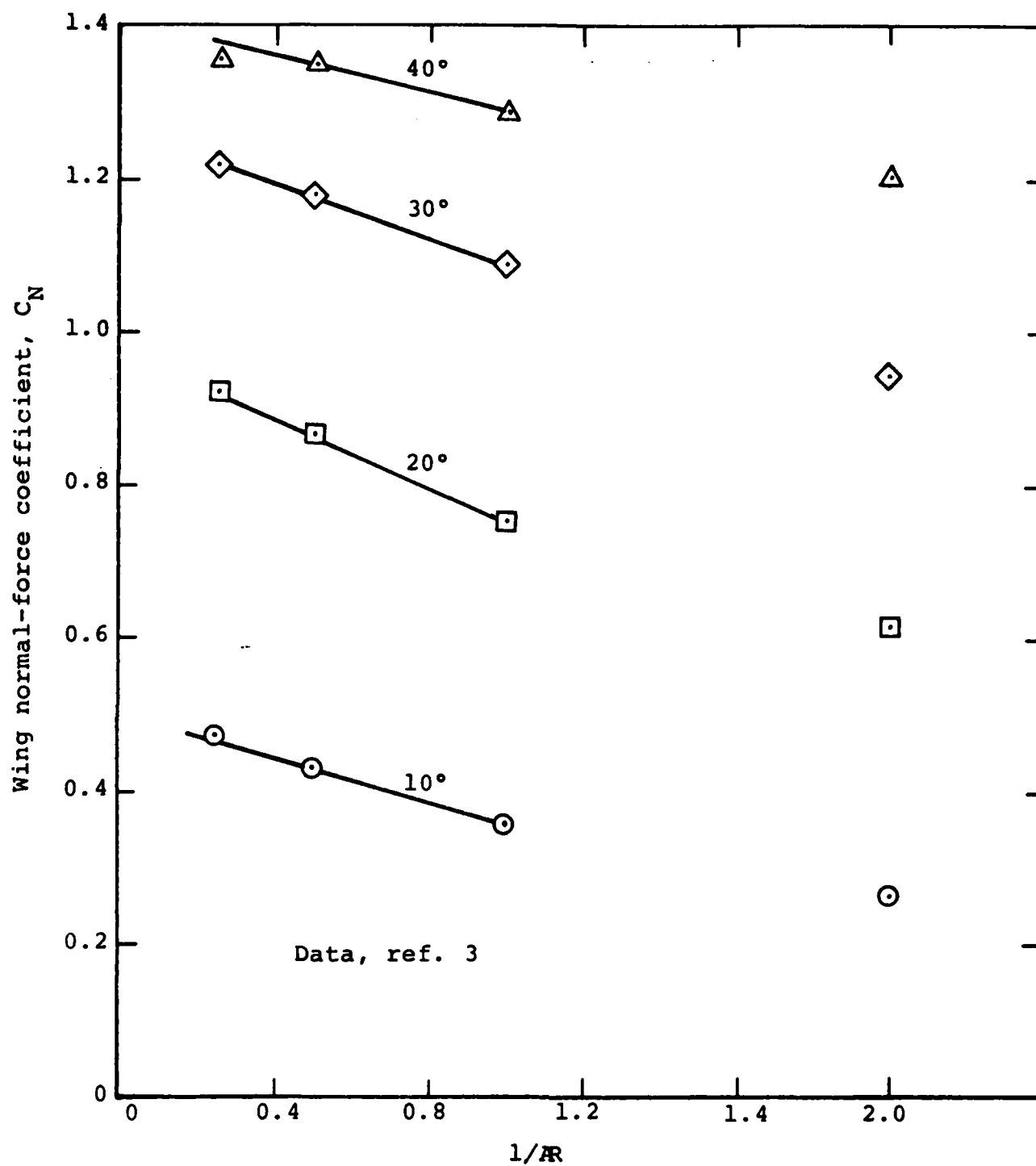
(a) $AR = 0.5$, $\lambda = 1.0$

Figure 43.- Variation of wing-alone axial center-of-pressure position with $1/\sqrt{M_\infty^2 - 1}$.



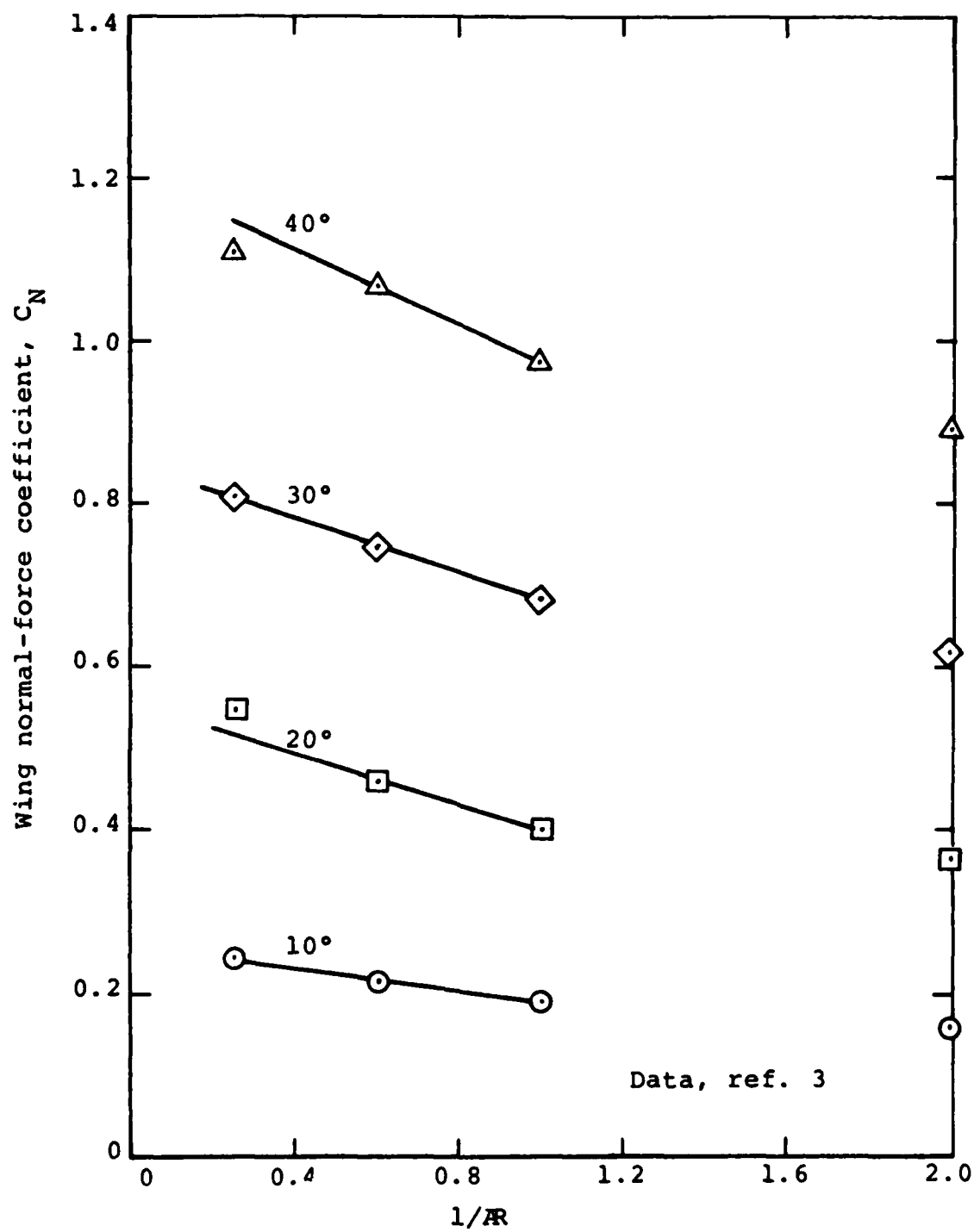
(b) $AR = 4, \lambda = 0.5$

Figure 43.- Concluded.



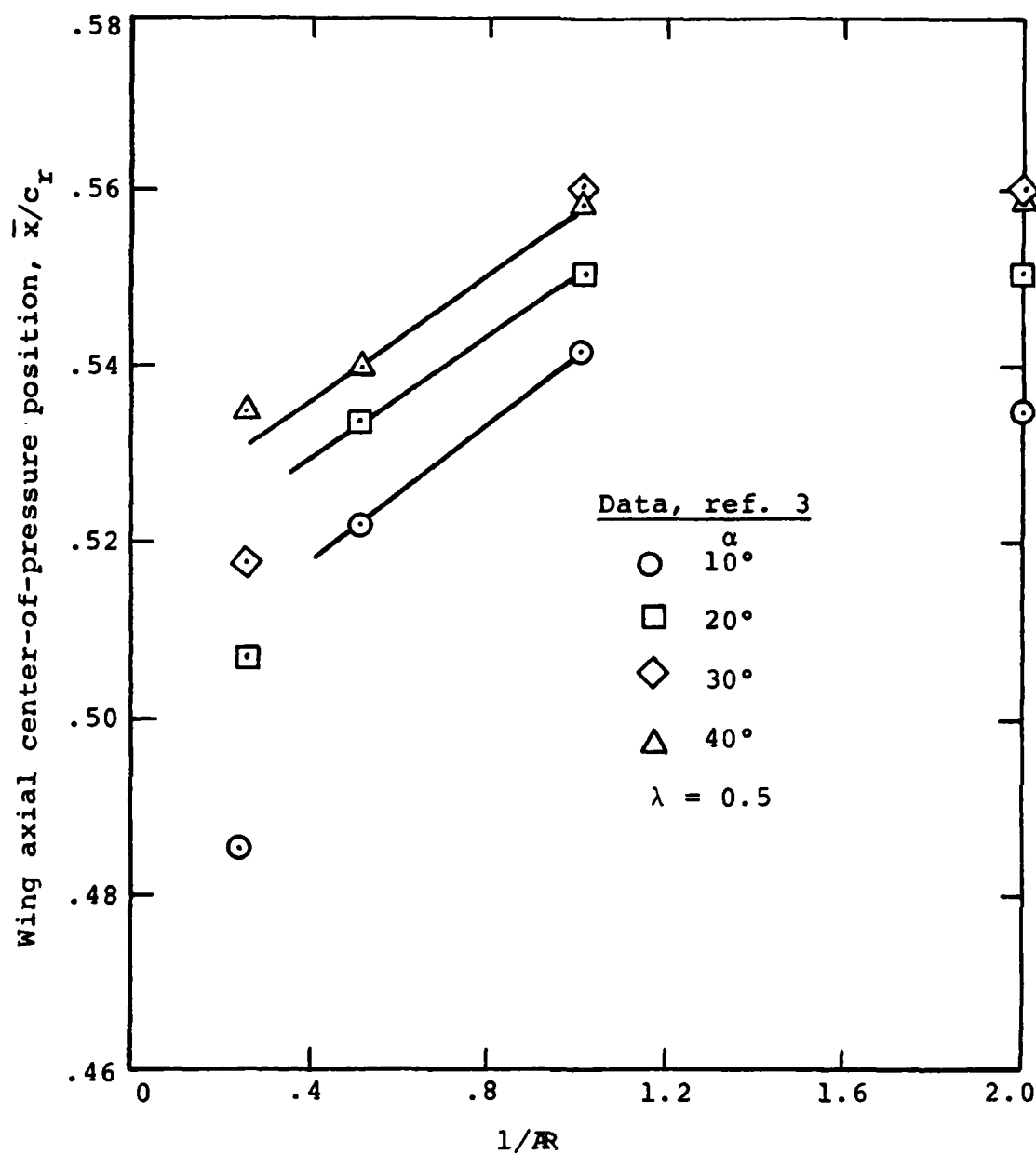
(a) $M_\infty = 1.6$

Figure 44.- Method of extrapolating wing-alone normal-force coefficient to aspect ratios greater than 2.0.



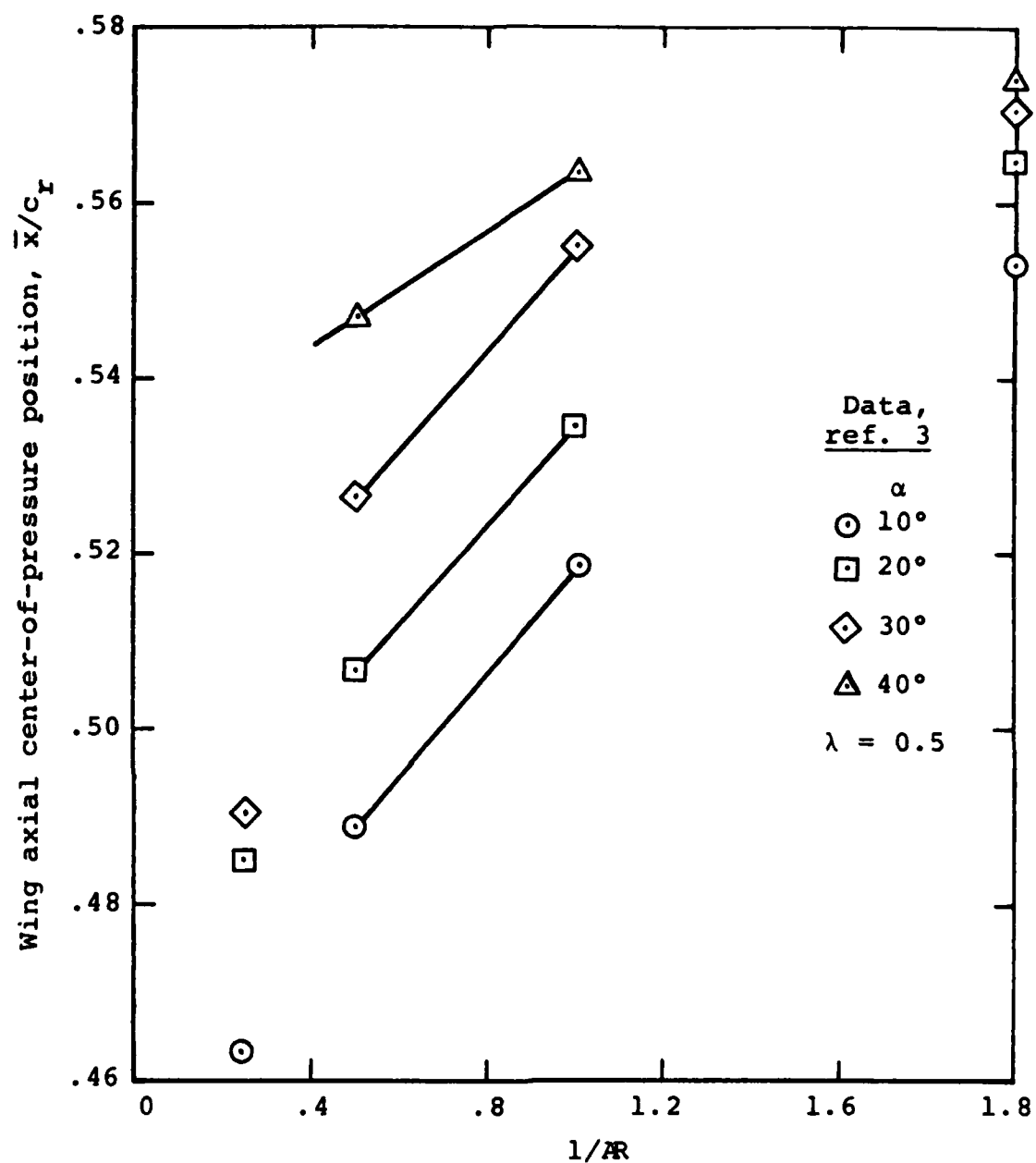
(b) $M_\infty = 3.5$

Figure 44.- Concluded.



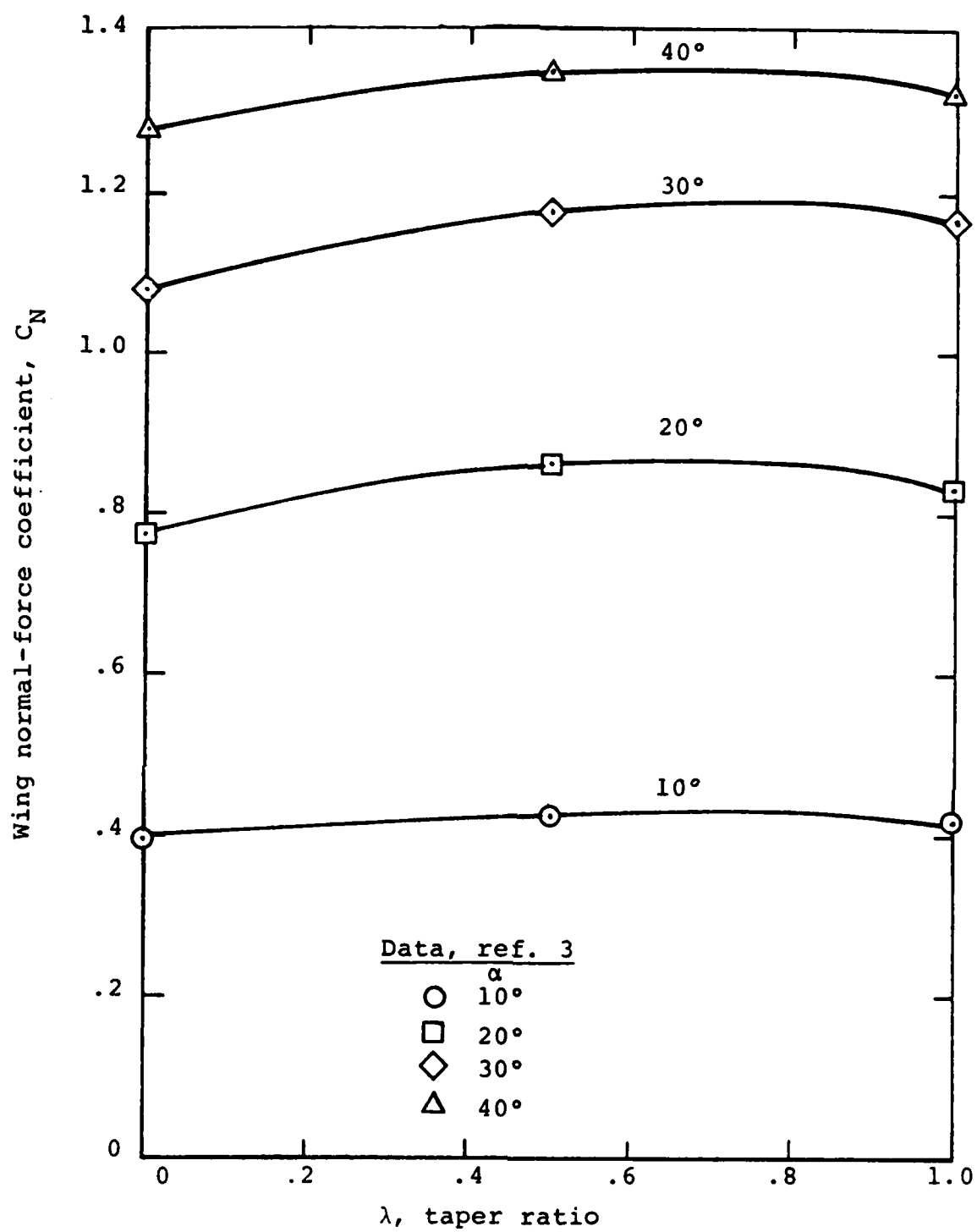
(a) $M_\infty = 1.6$

Figure 45.- Data illustrating accuracy of predicting wing axial center-of-pressure position for $R > 2$ from data for $R = 1$ and $R = 2$.



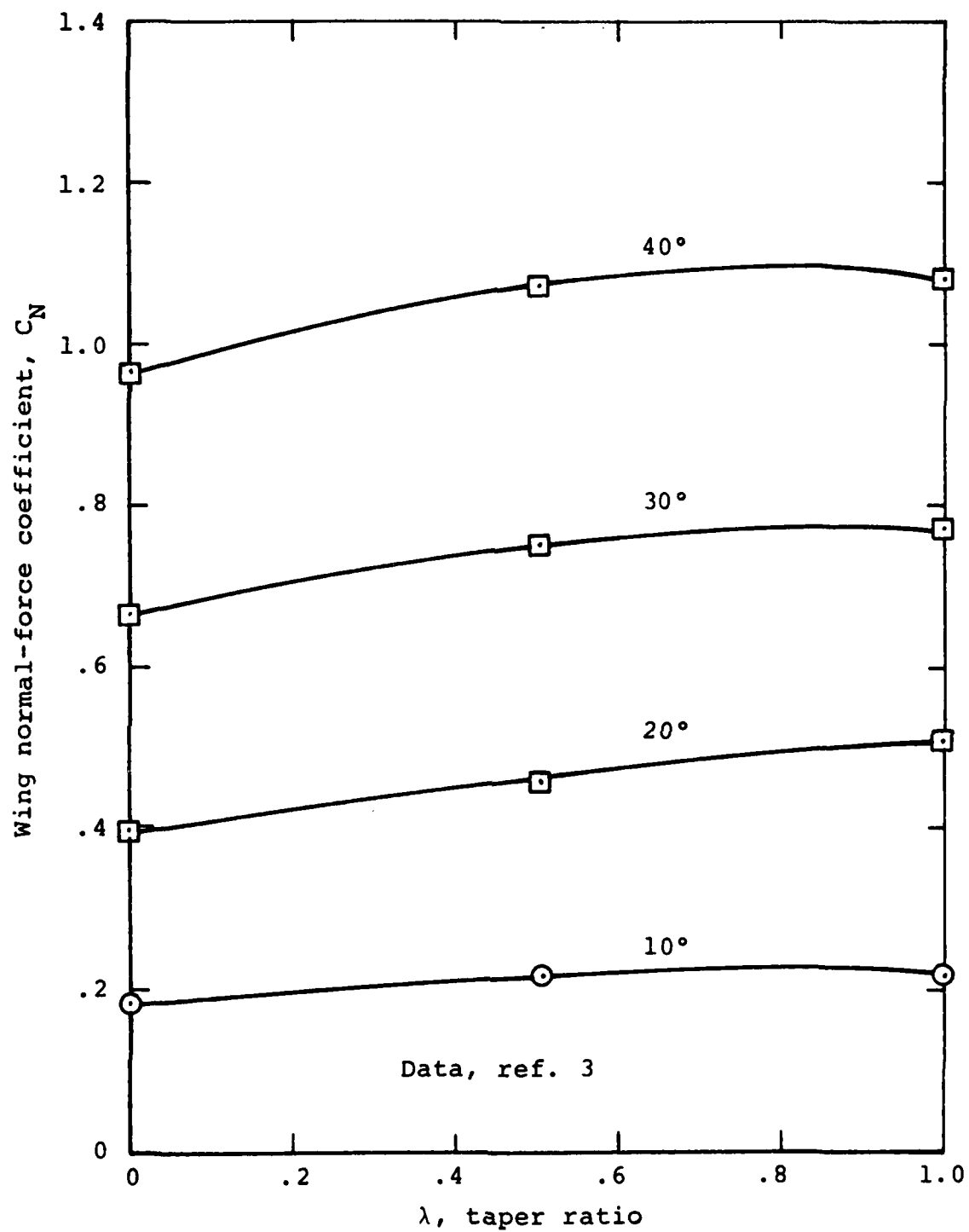
(b) $M_\infty = 3.5$

Figure 45.- Concluded.



(a) $M_\infty = 1.6$; $AR = 2$

Figure 46.- Variation of wing normal-force coefficient with taper ratio for $AR = 2$ wings of Stalling-Lamb data base.



(b) $M_\infty \approx 3.5$, $AR = 2.0$

Figure 46.- Concluded.

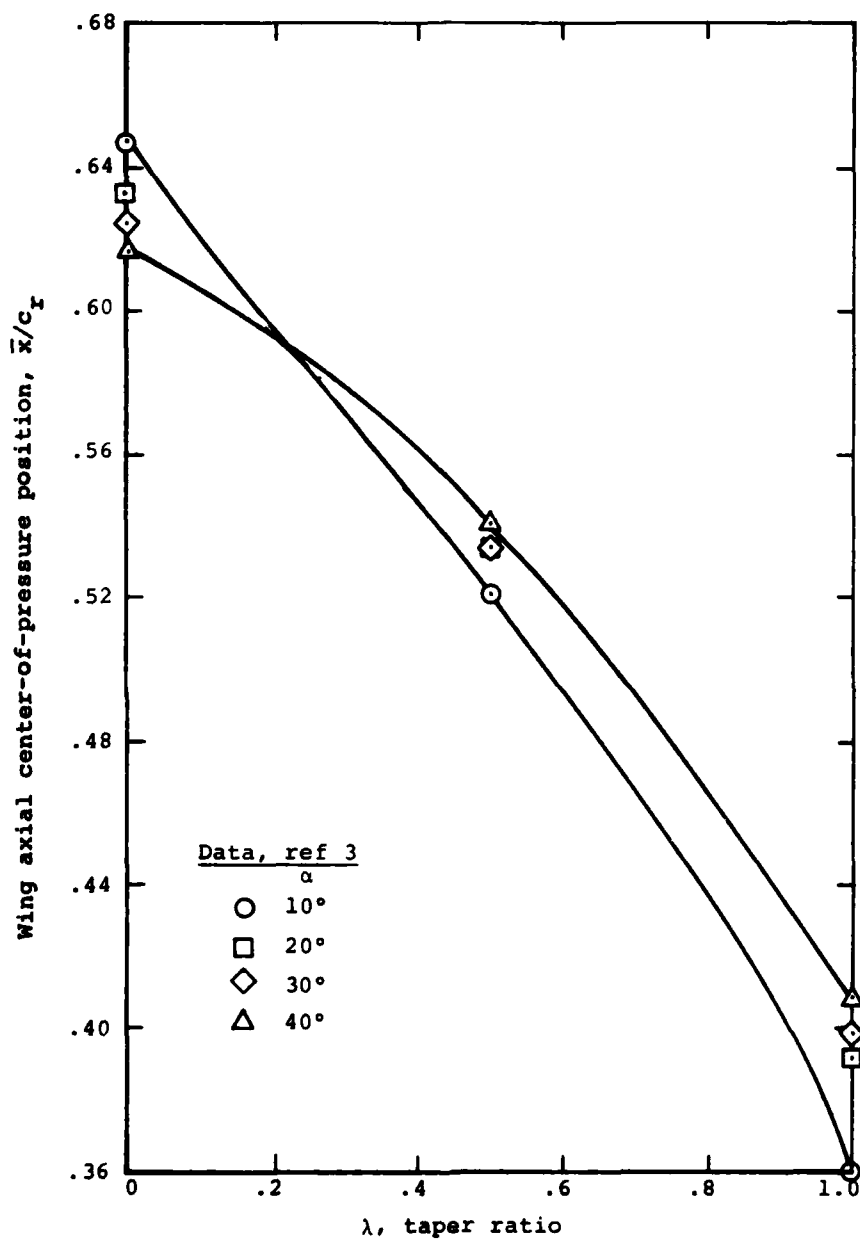
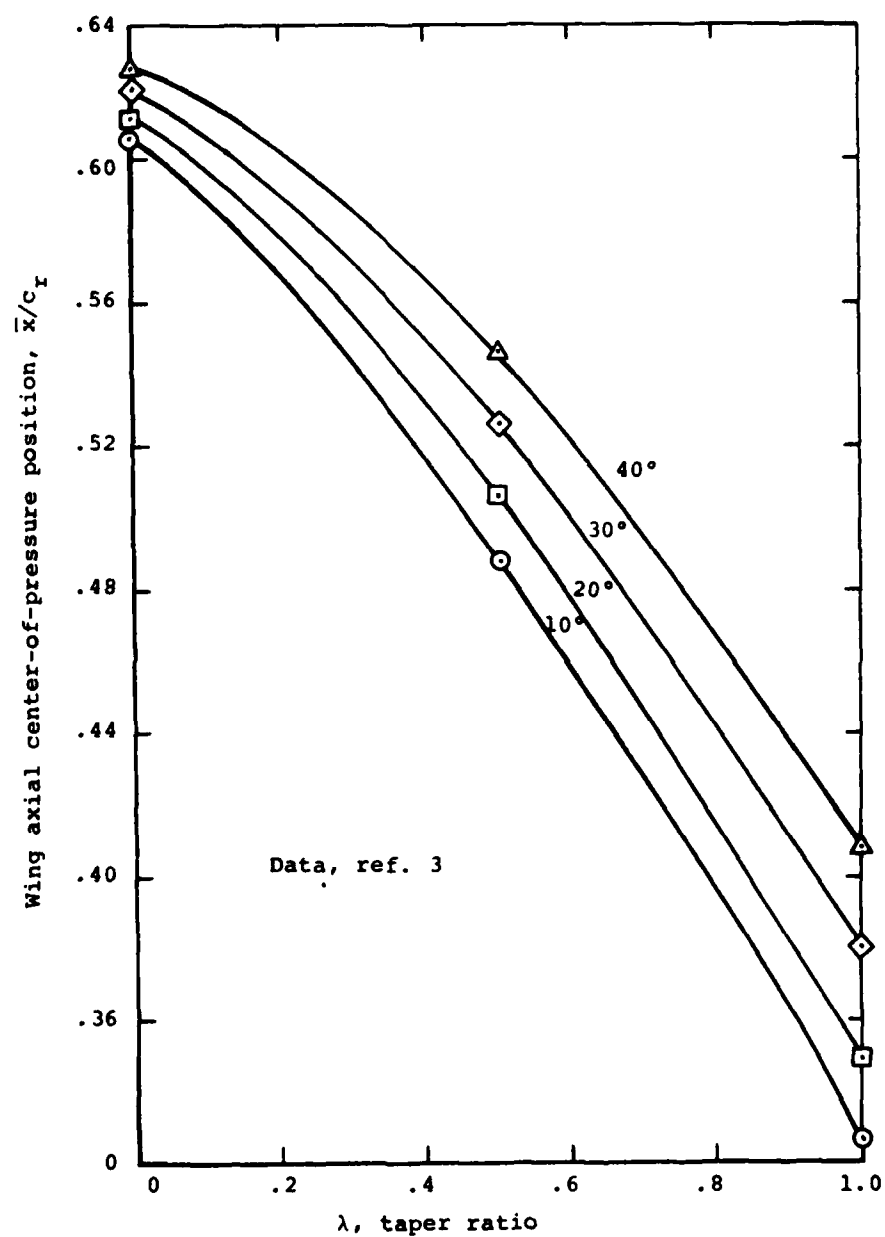


Figure 47.- Variation of wing axial center-of-pressure position with taper ratio for $R = 2$ wings of Stallings-Lamb data base.



(b) $M_\infty = 3.5$, $R = 2$

Figure 47.- Concluded.

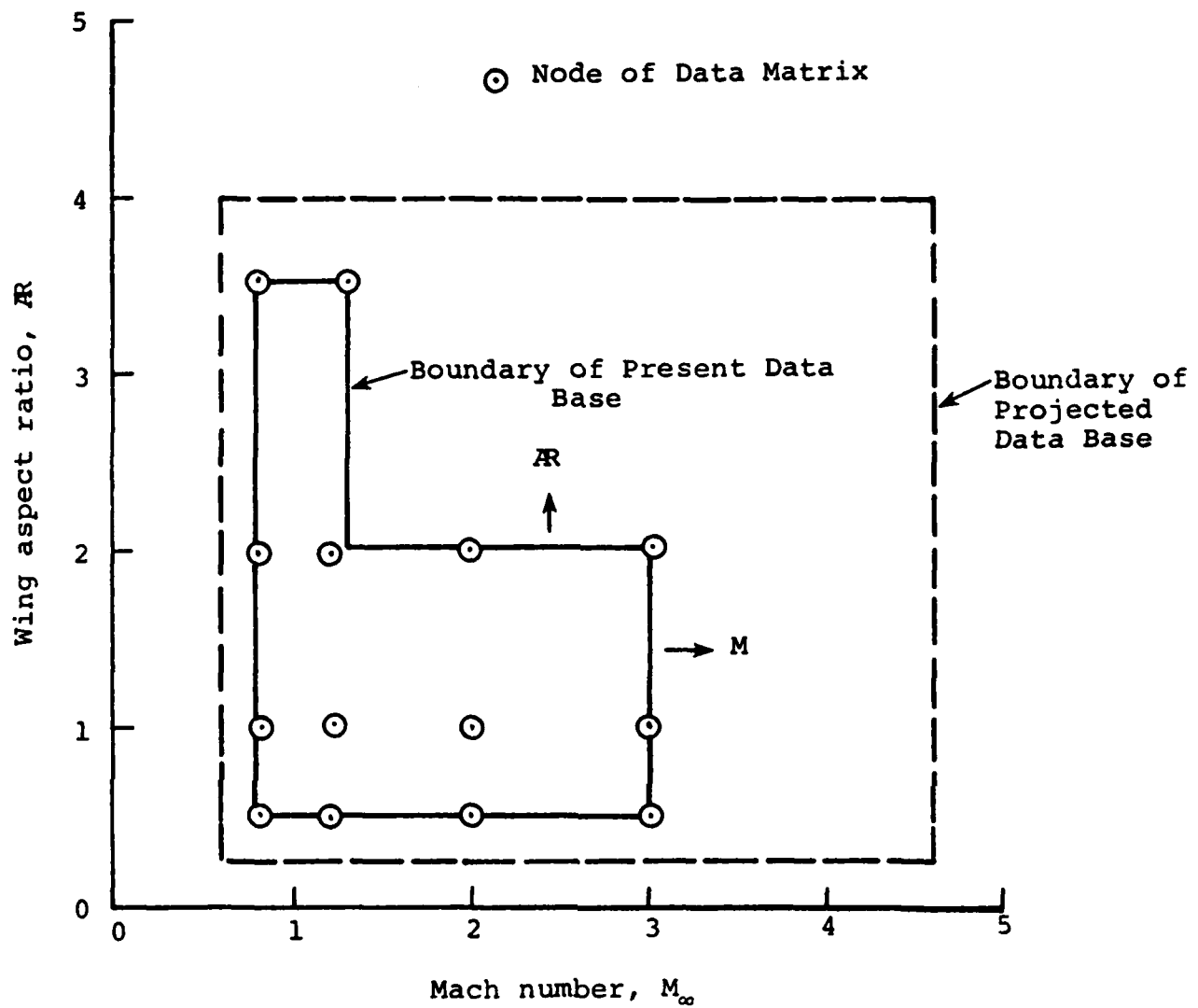


Figure 48.- Limits of present and future data bases.

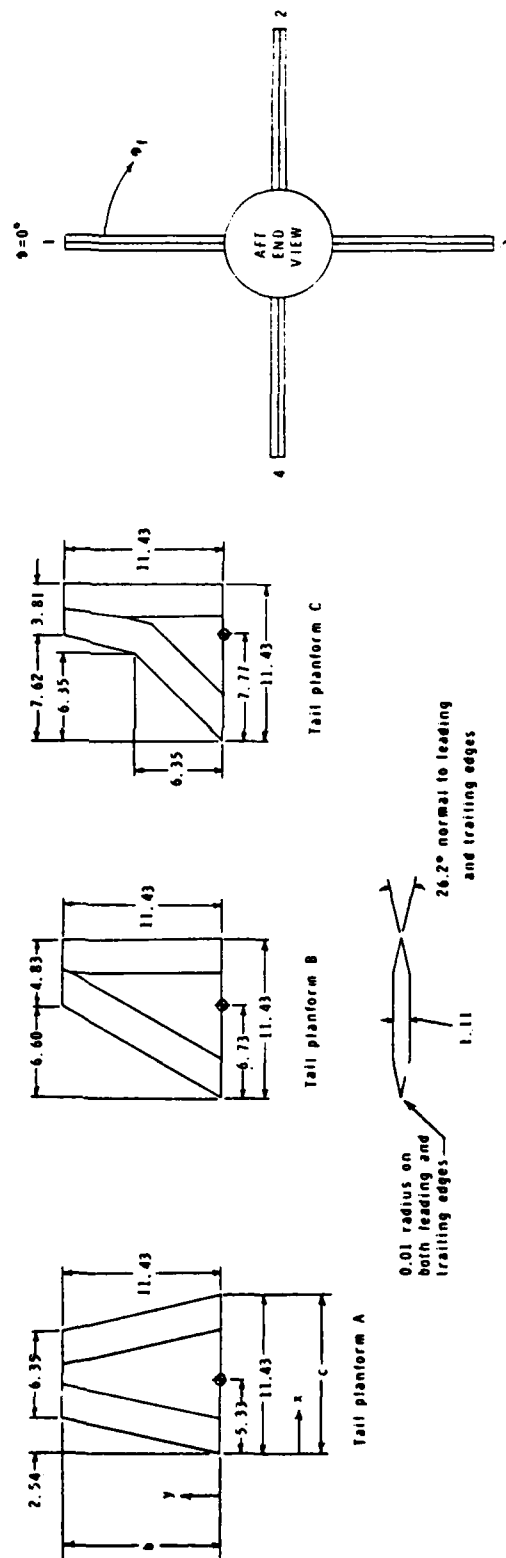
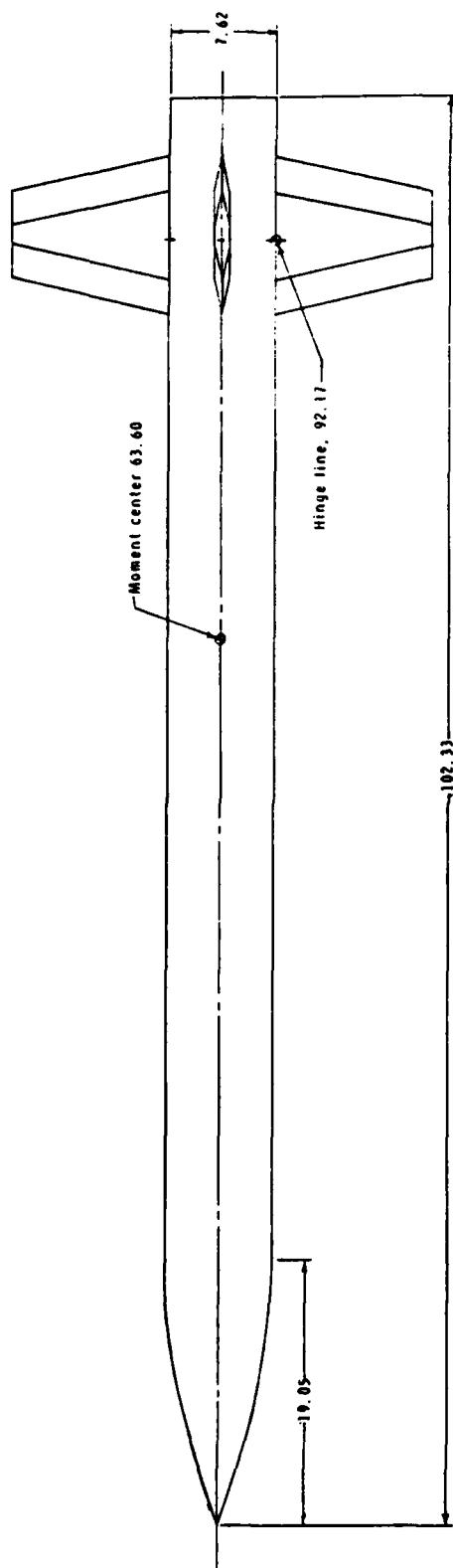


Figure 49.- Details of model. All linear dimensions are in centimeters.

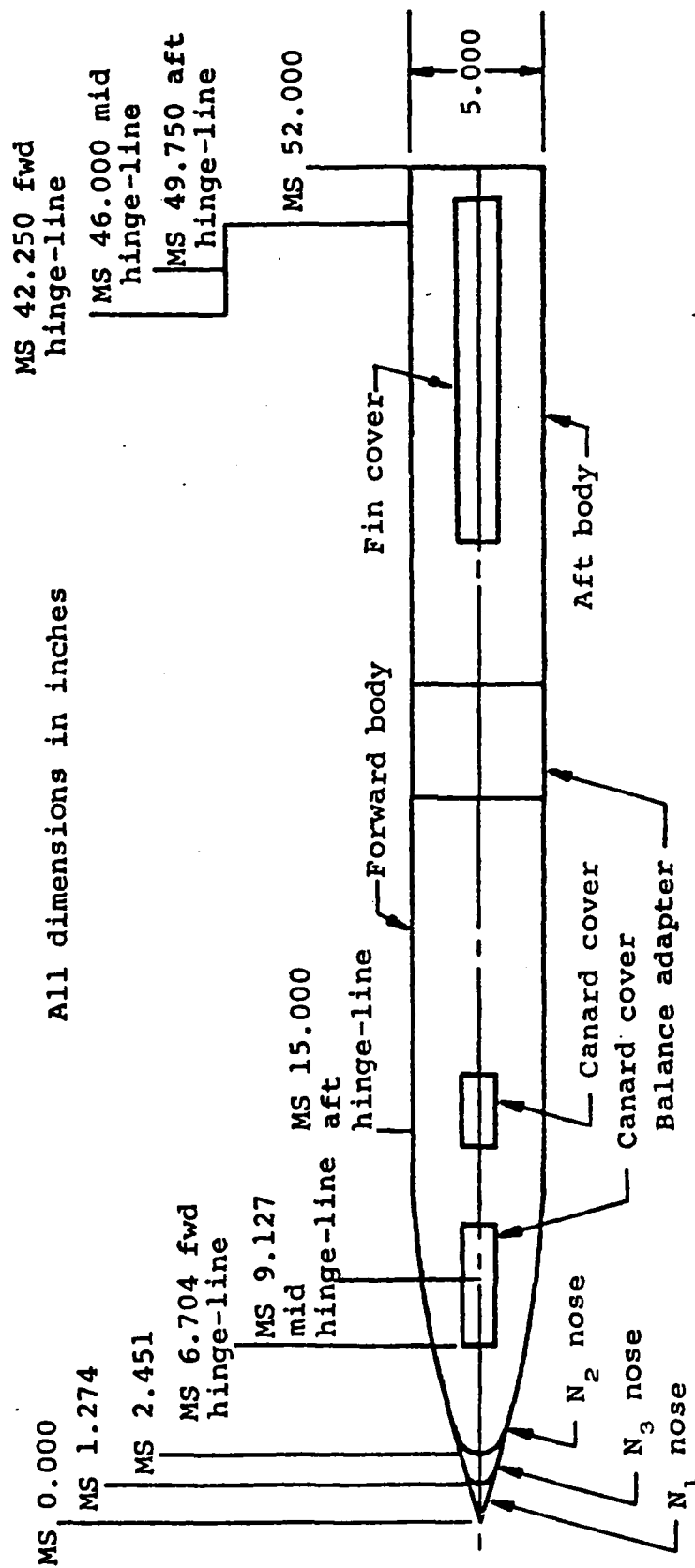
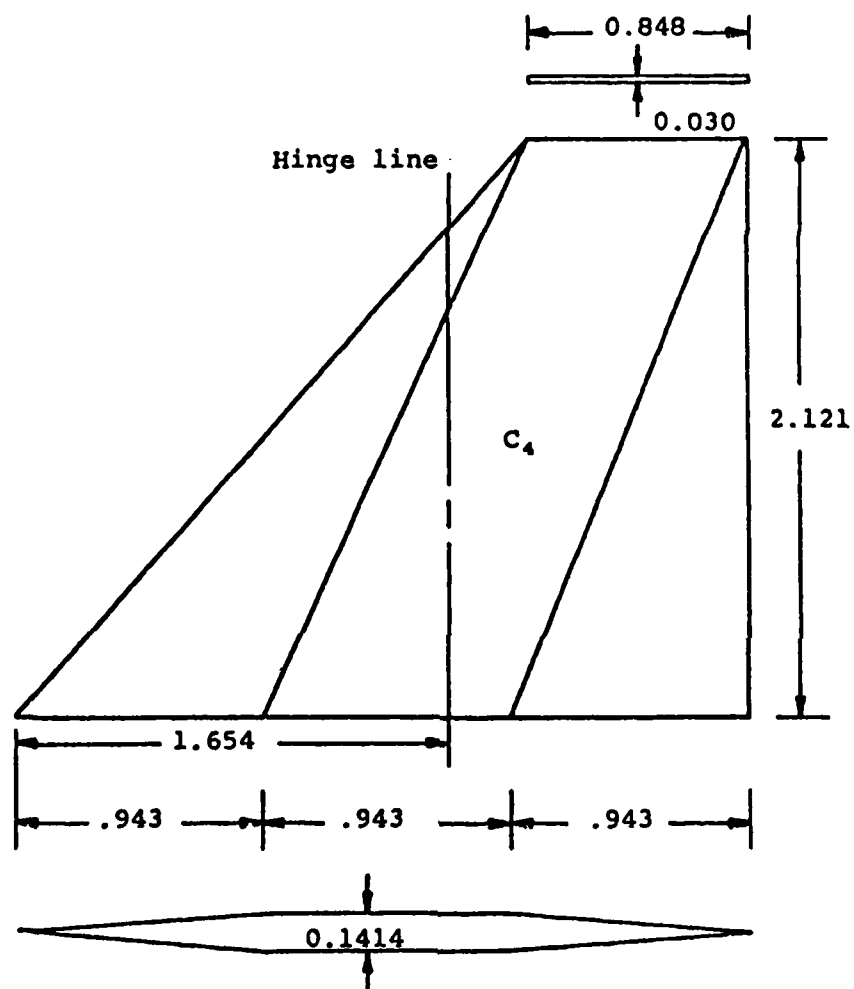


Figure 50.- Sketch of model body showing hinge-line positions for canard and tail panels.

Note 1: All dimensions are in inches.

Note 2: Leading and trailing-edge radii are 0.015.

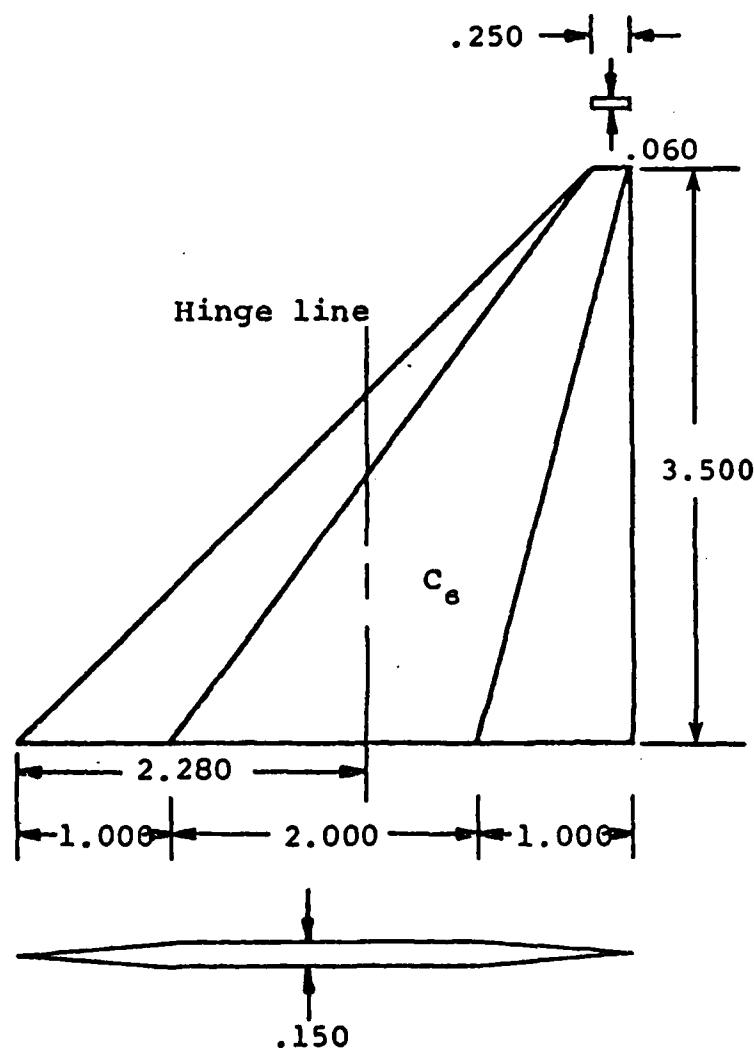


(a) Canard fin C_4

Figure 51.- Fins tested with Army Generalized Missile.

Note 1: All dimensions are in inches.

Note 2: Leading- and trailing-edge radii are 0.020.

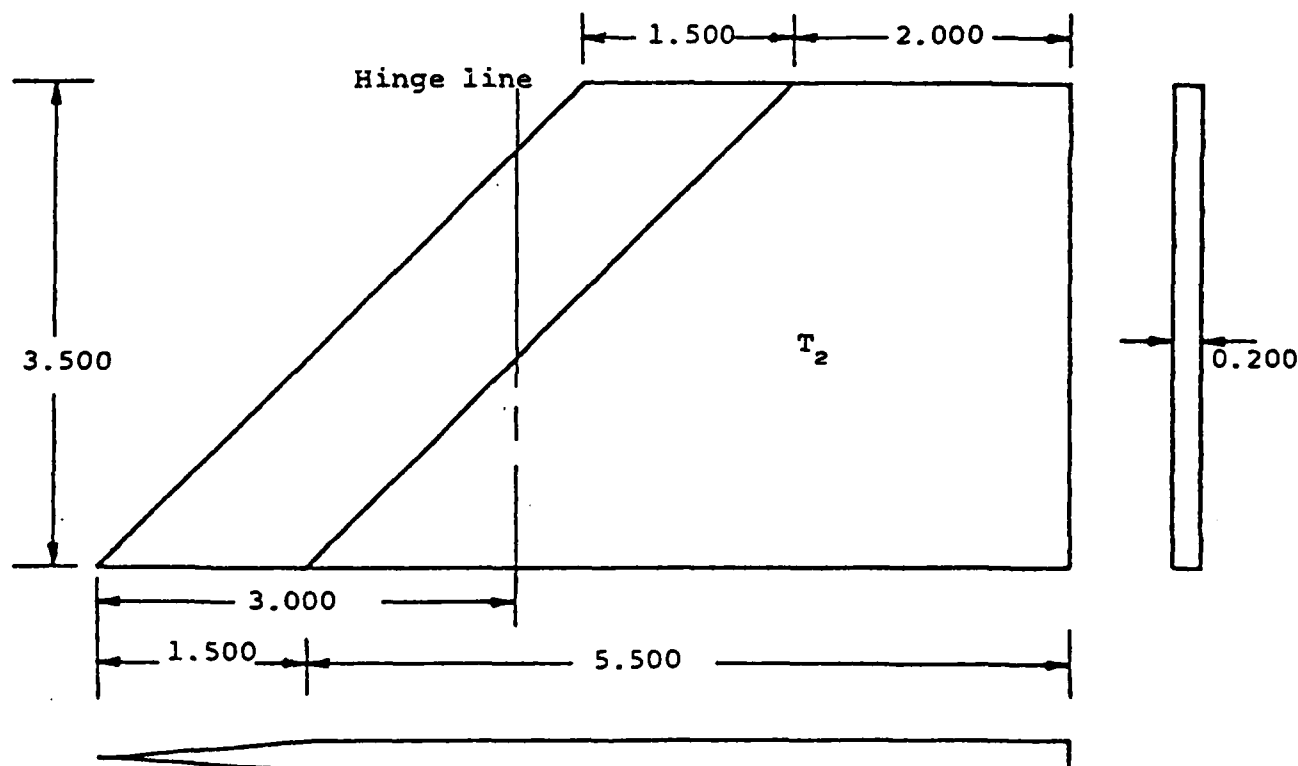


(b) Canard fin C_6 .

Figure 51.- Continued

Note 1: All dimensions are in inches.

Note 2: Leading- and trailing-edge radii are 0.020.



(c) Tail fin T_2

Figure 51.- Concluded.

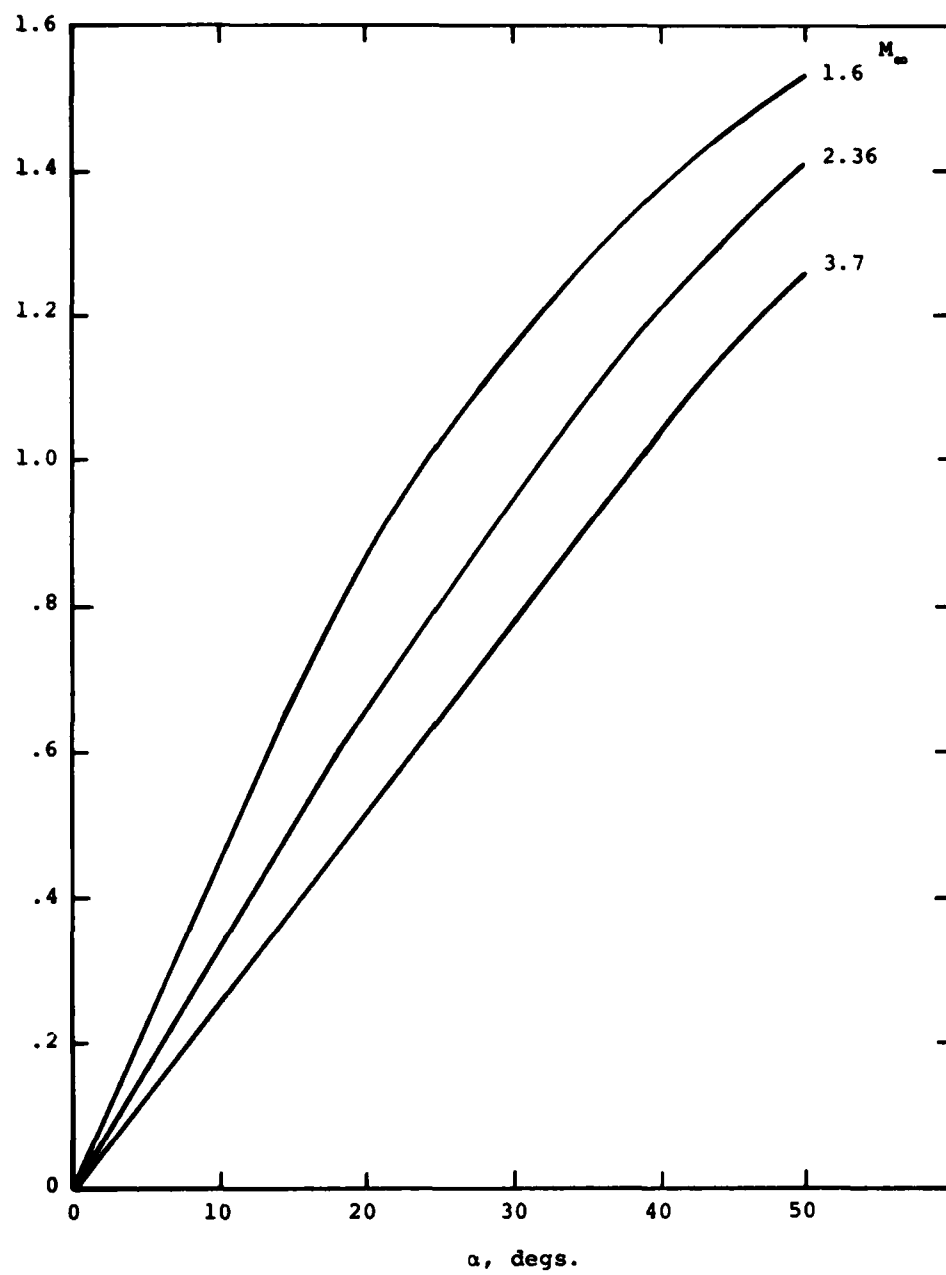


Figure 52.- Interpolated Normal-force curves for wing alone T_B .

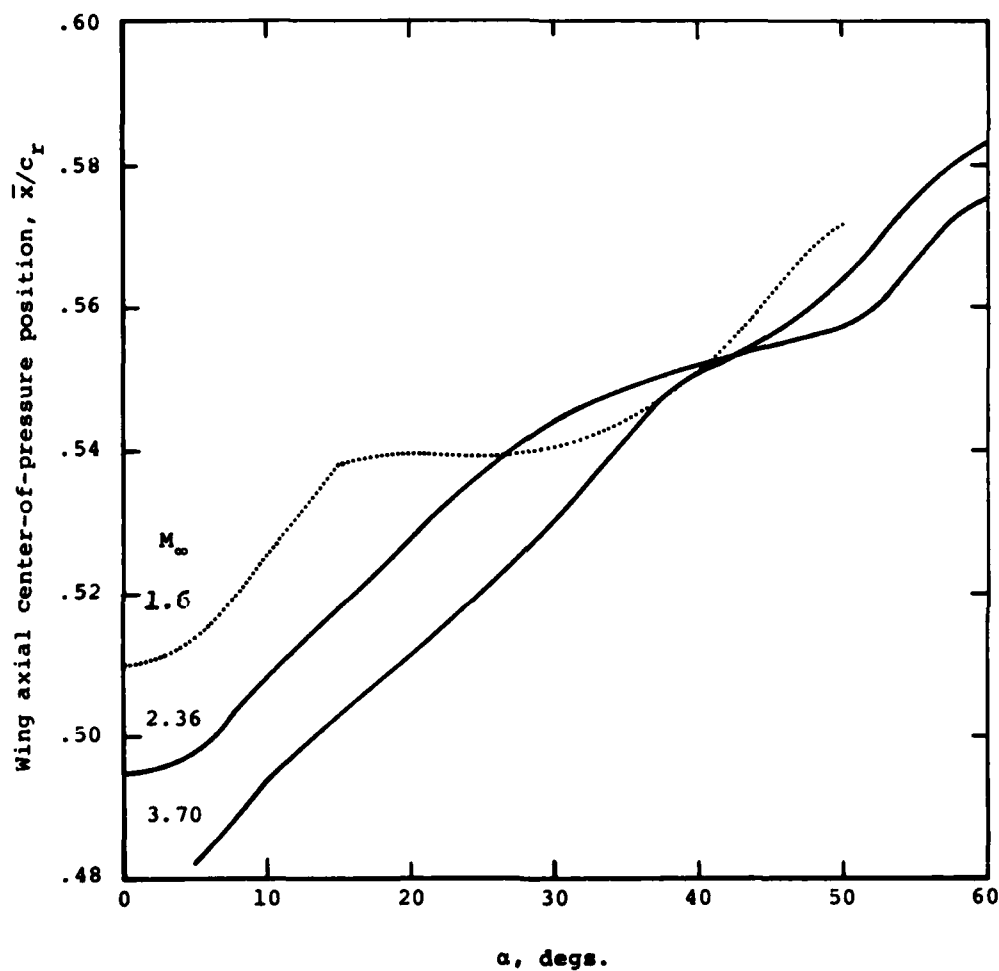
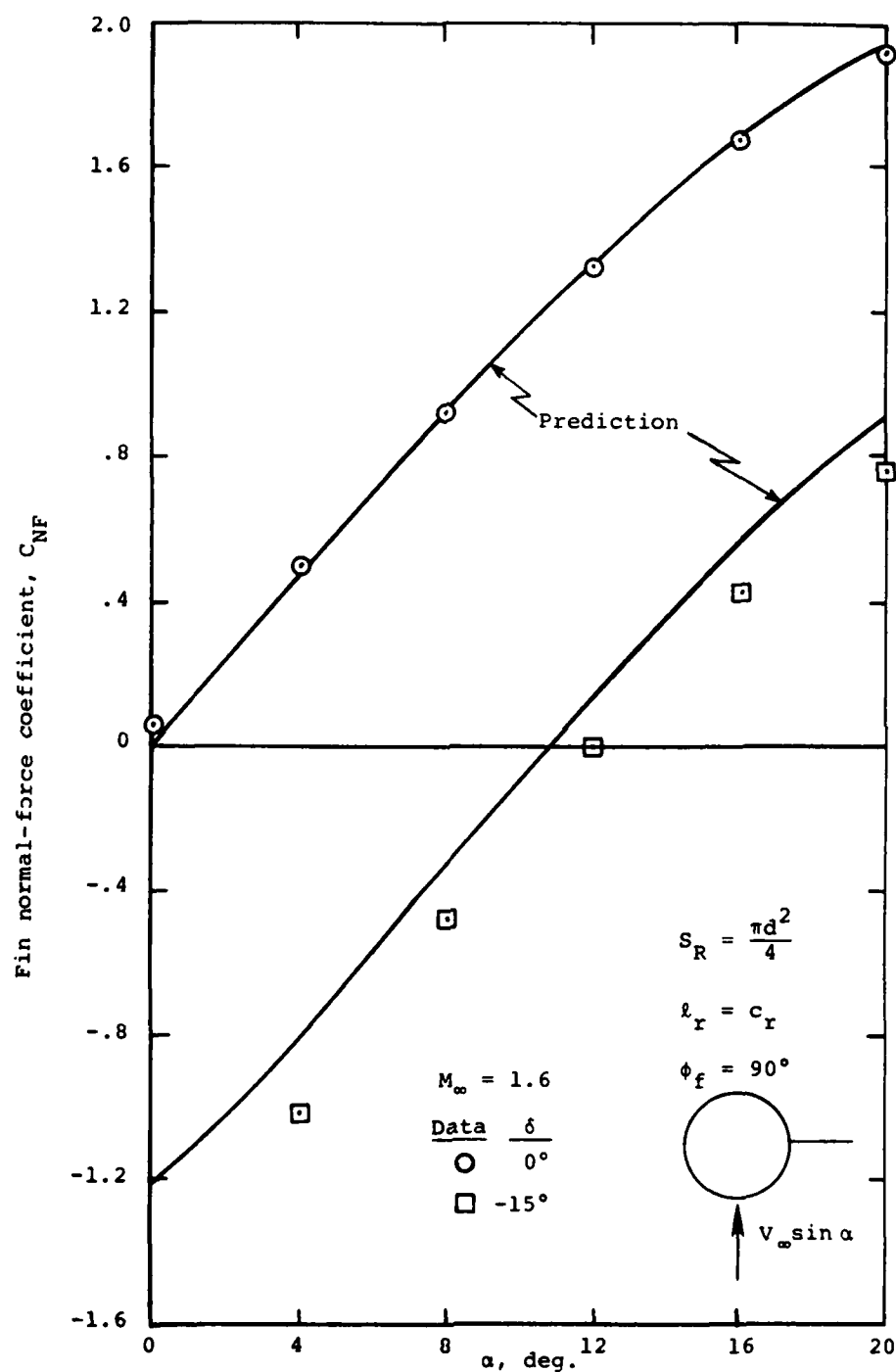
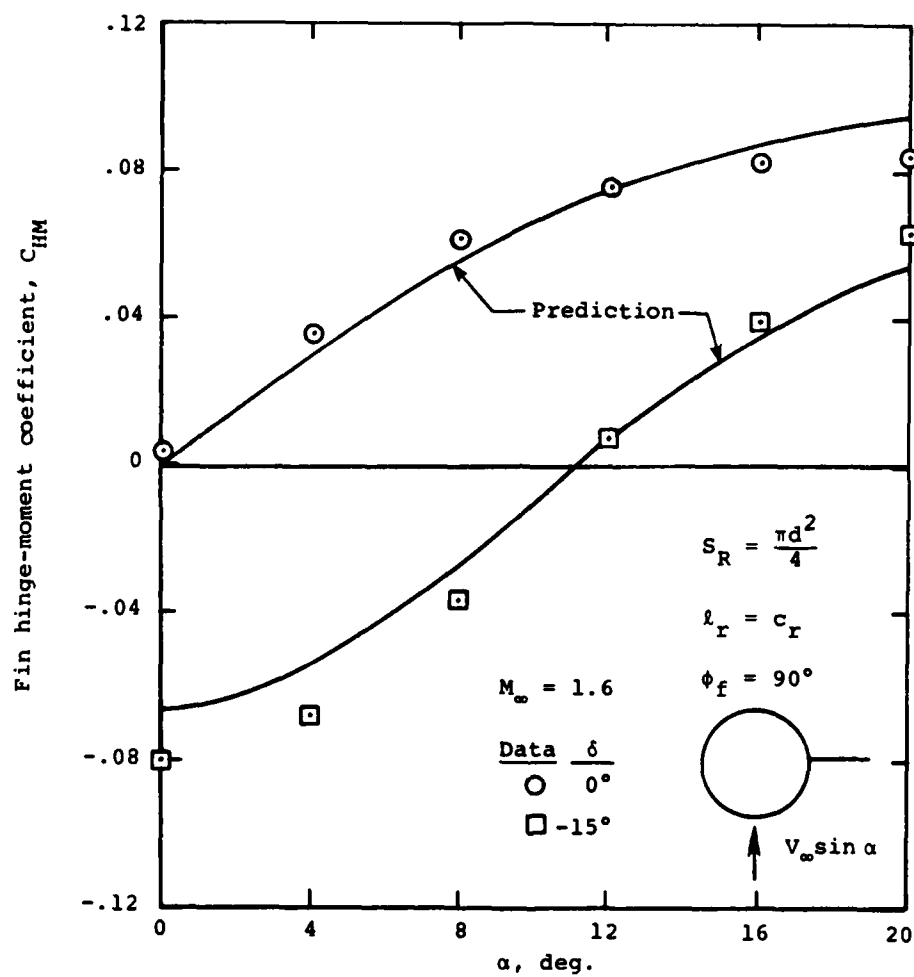


Figure 53.- Axial center-of-pressure position for wing alone T_B at several Mach numbers by interpolating in Stallings-Lamb data base.



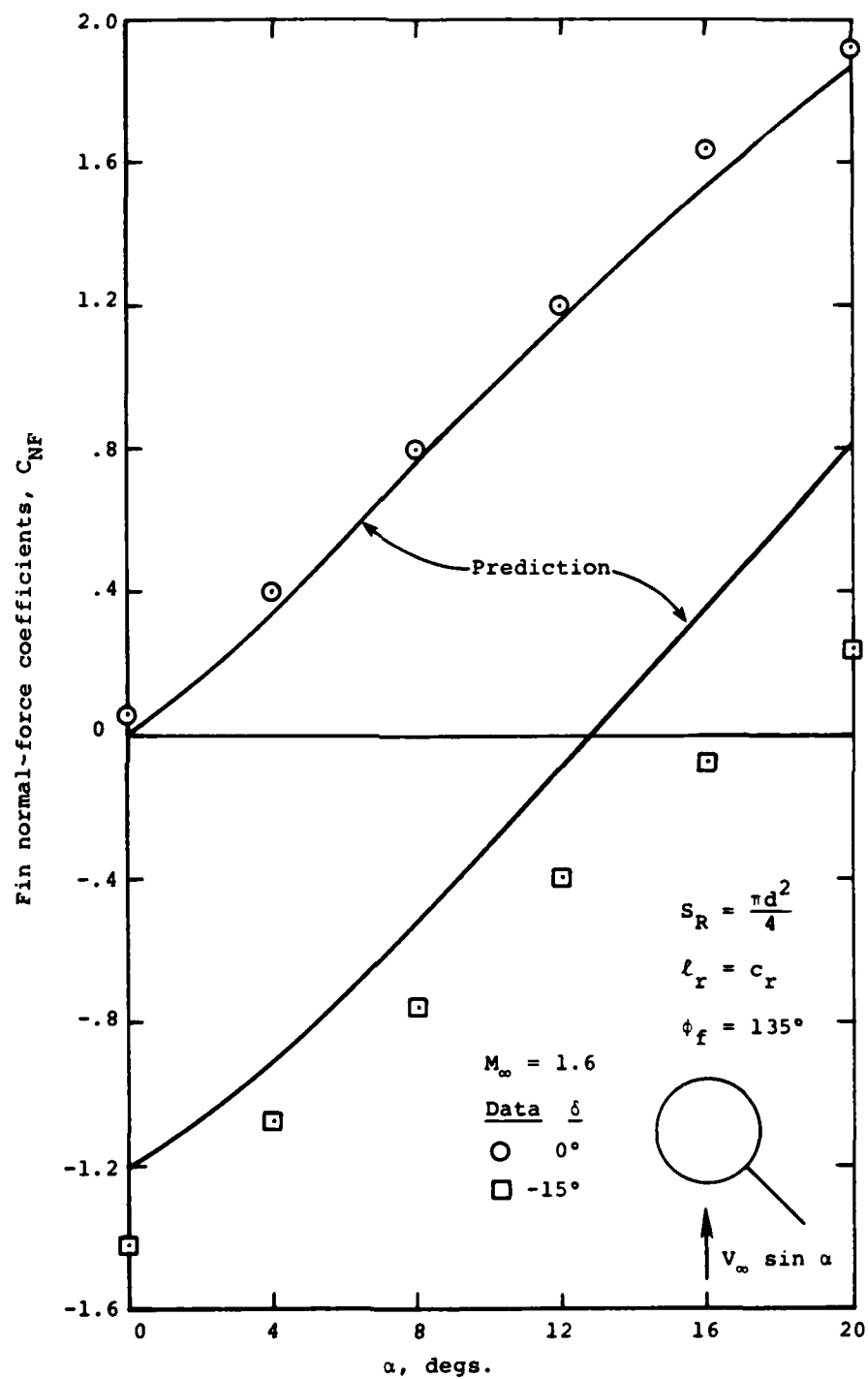
(a) Normal-force coefficient; $\phi_f = 90^\circ$; $\delta = 0^\circ, -15^\circ$

Figure 54.- Comparison of prediction and measurement for fin T_B characteristics at $M_\infty = 1.6$; Lamb-Trescott data.

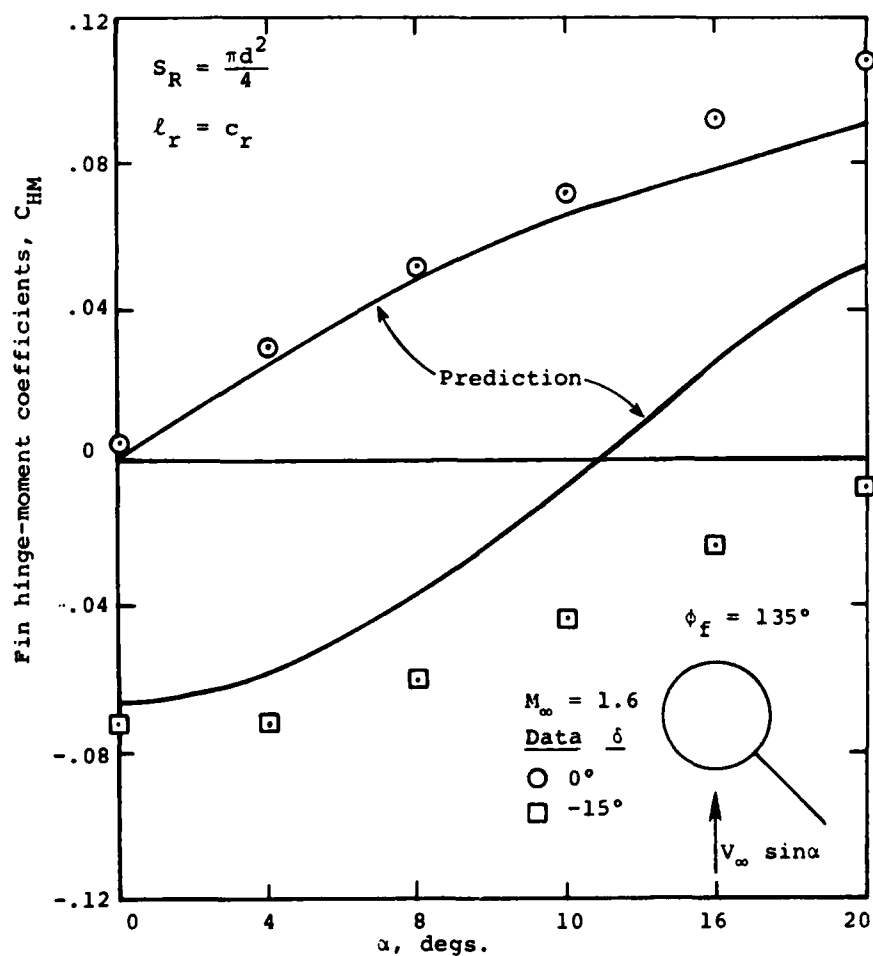


(b) Hinge-moment coefficient; $\phi_f = 90^\circ$; $\delta = 0^\circ, -15^\circ$

Figure 54.- Continued.

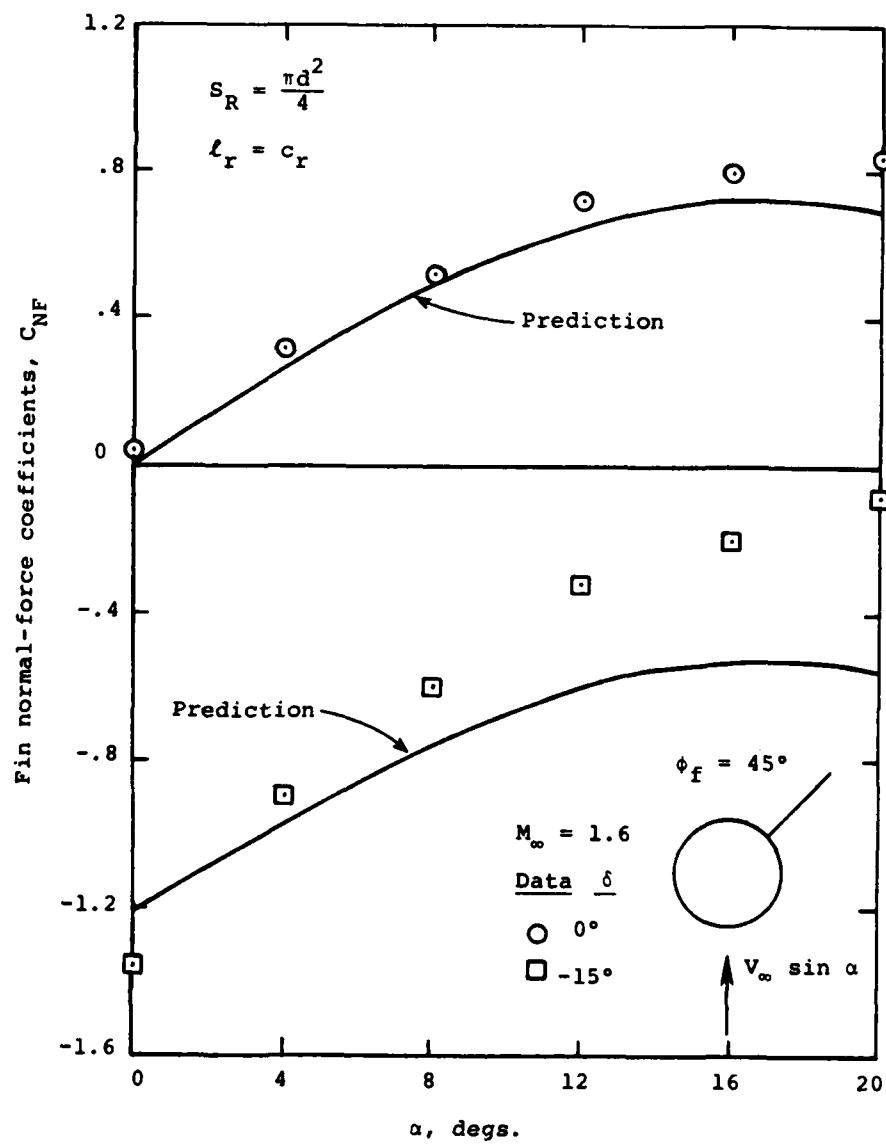


(c) Normal-force coefficient; $\phi_f = 135^\circ$, $\delta = 0^\circ, -15^\circ$
Figure 54.- Continued.



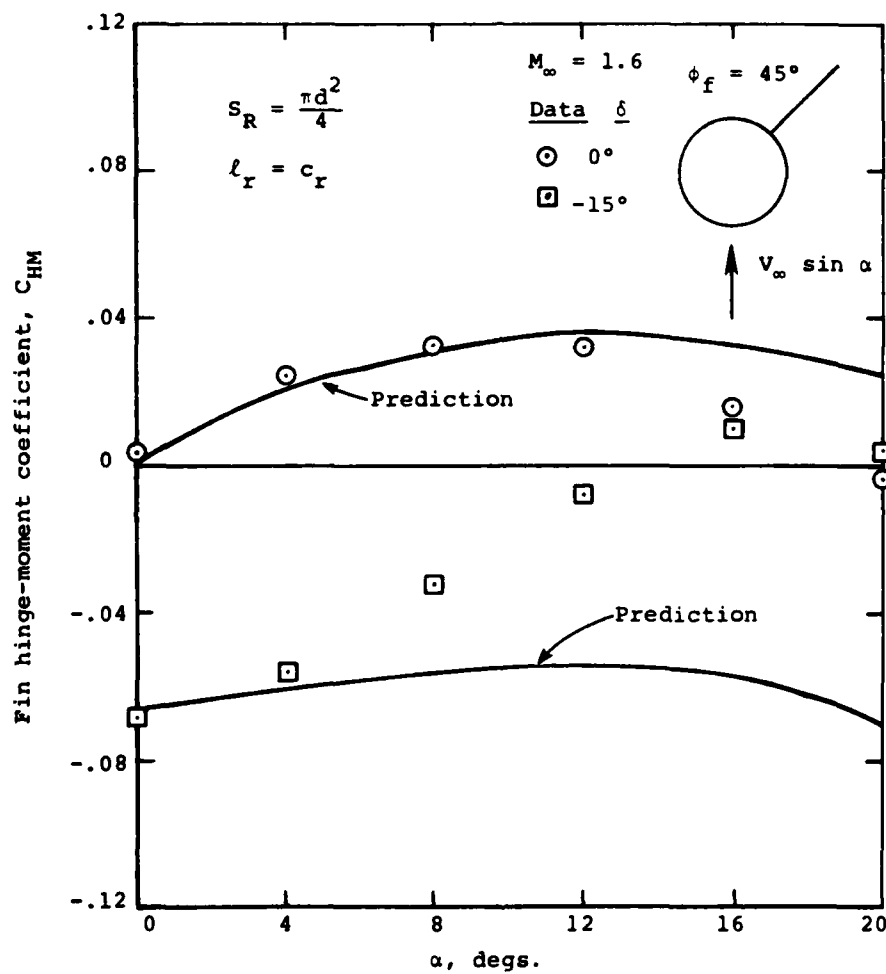
(d) Hinge-moment coefficients; $\phi_f = 135^\circ$, $\delta = 0^\circ, -15^\circ$

Figure 54.- Continued.



(e) Normal-force coefficients, $\phi_f = 45^\circ$, $\delta = 0^\circ, -15^\circ$

Figure 54.- Continued.



(f) Hinge-moment coefficients; $\phi_f = 45^\circ$, $\delta = 0^\circ, -15^\circ$

Figure 54.- Concluded.

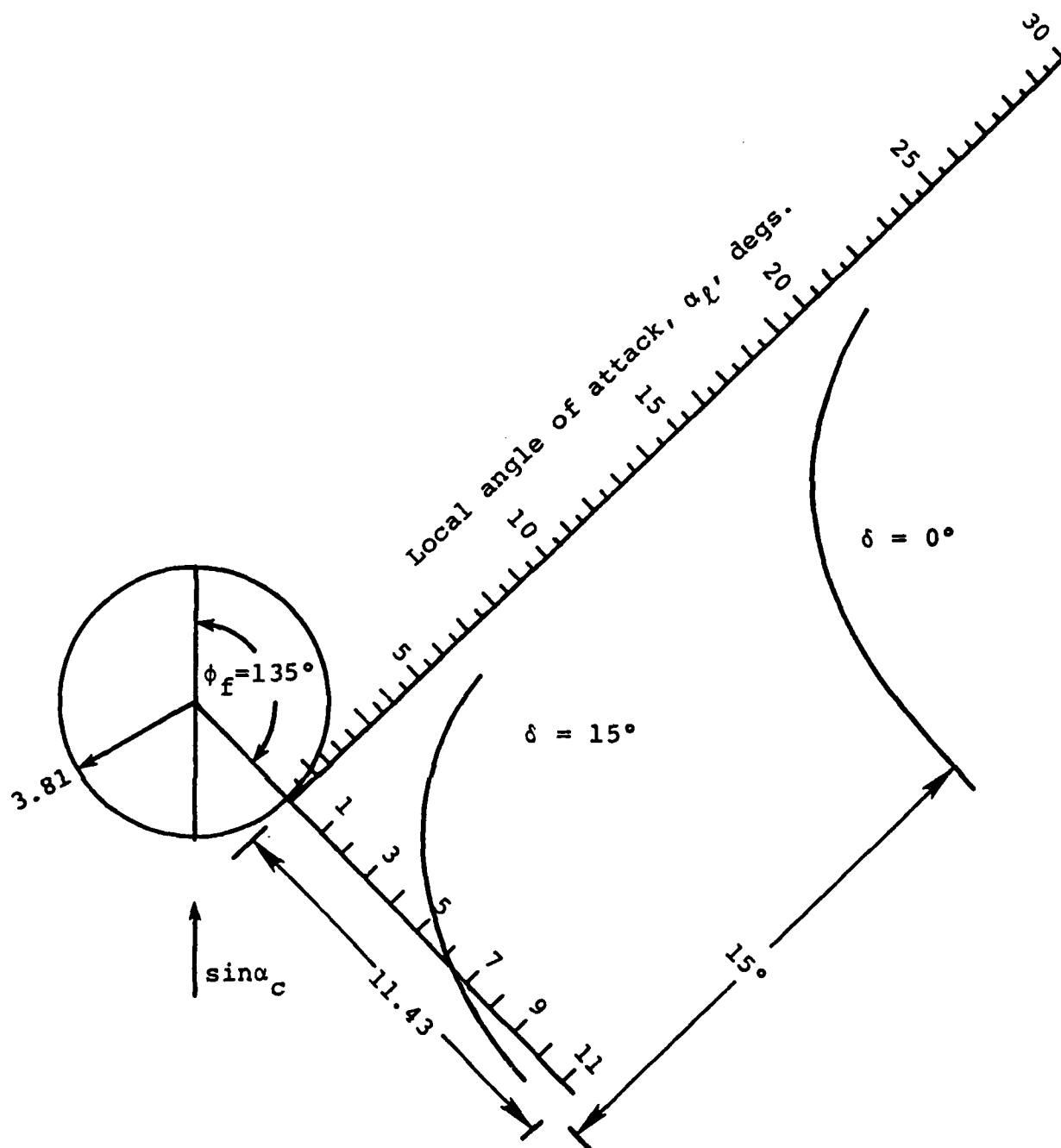


Figure 55.- Local angle-of-attack across span of fin T_B in planes normal to fin as calculated using supersonic line sources and doublets; $M_\infty = 1.6$, $\phi_f = 135^\circ$, $\delta = 0^\circ$, -15° , $\alpha_c = 18.76^\circ$.

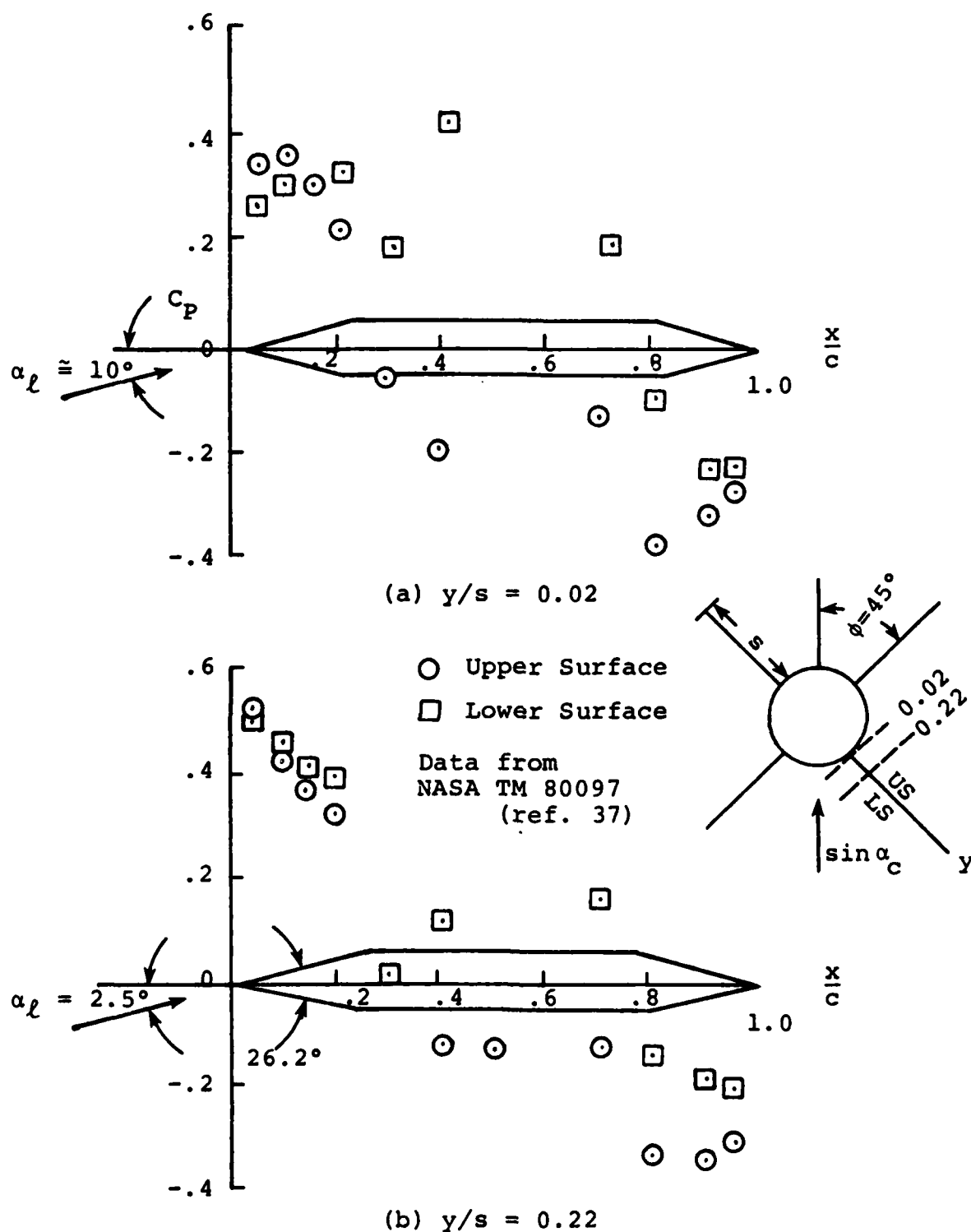
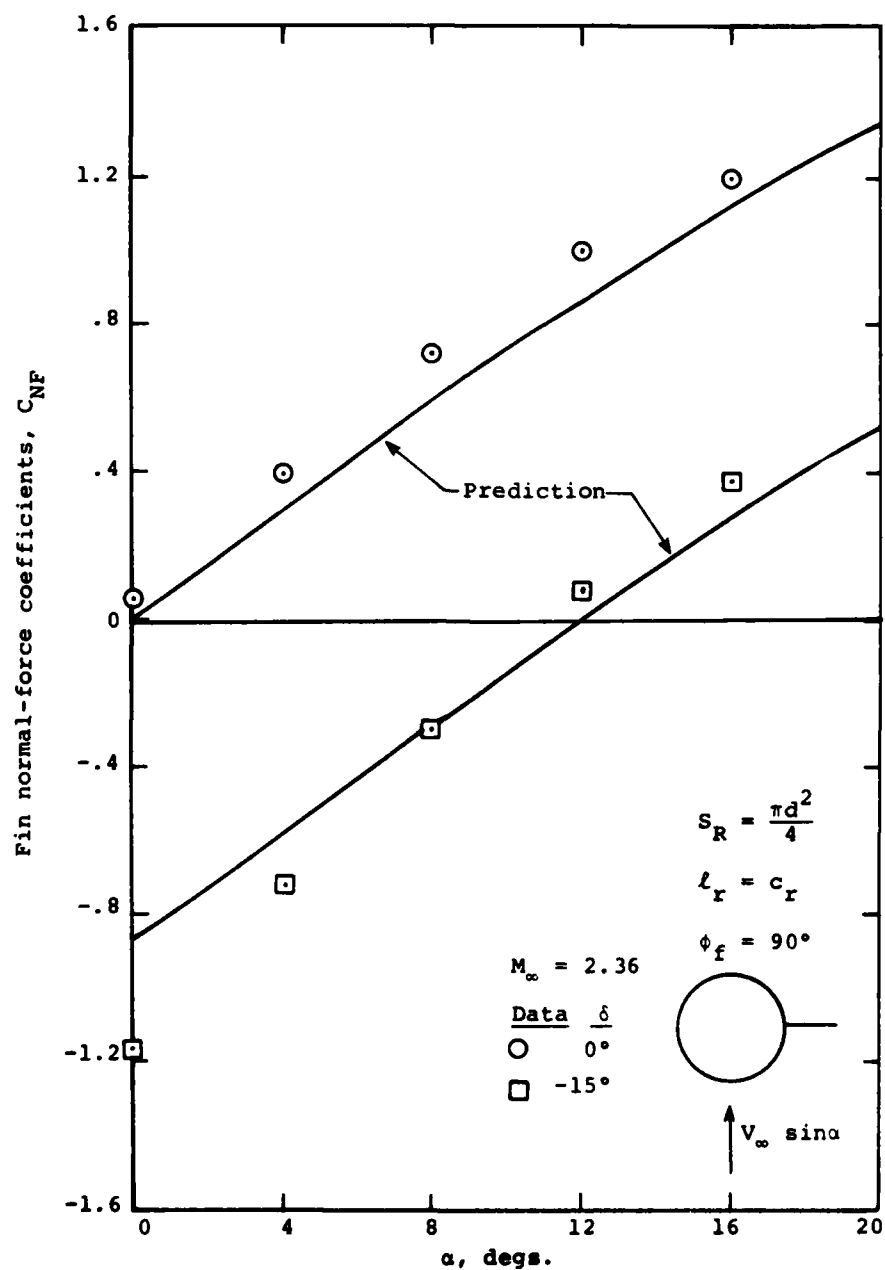
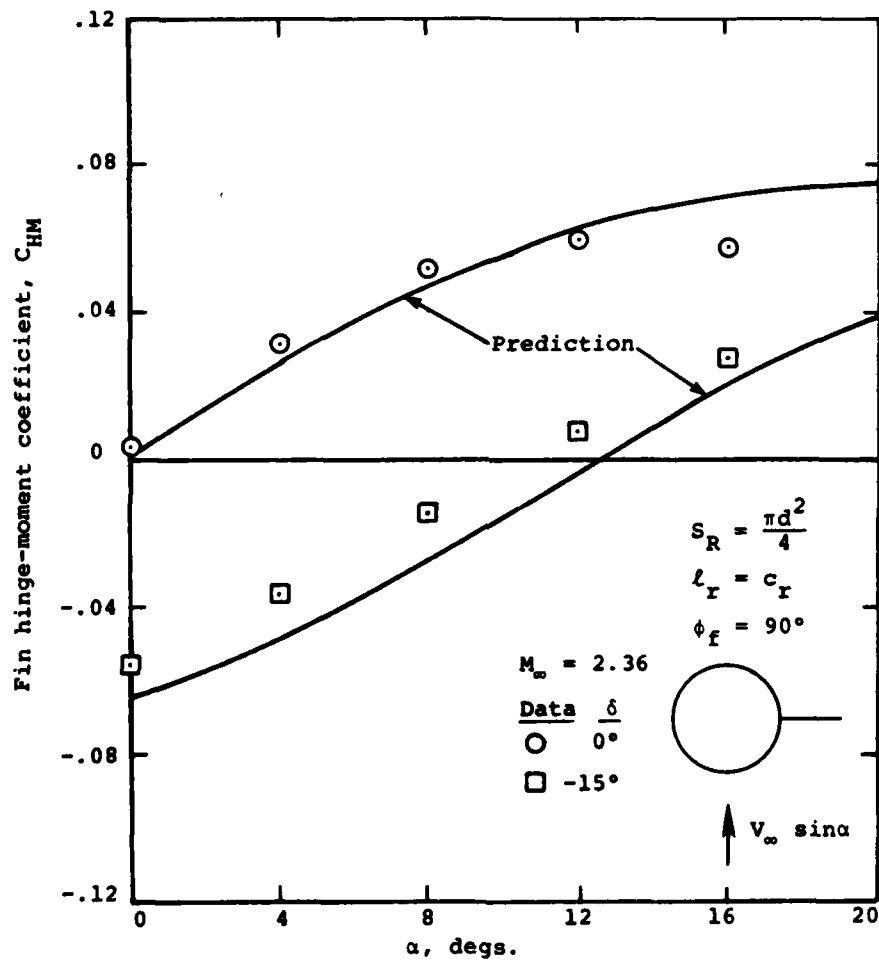


Figure 56.- Pressure distributions on windward fin near the root;
 $\alpha_c = 18.76^\circ$, $\phi_f = 135^\circ$, $\delta = -15^\circ$, $M_\infty = 1.6$.



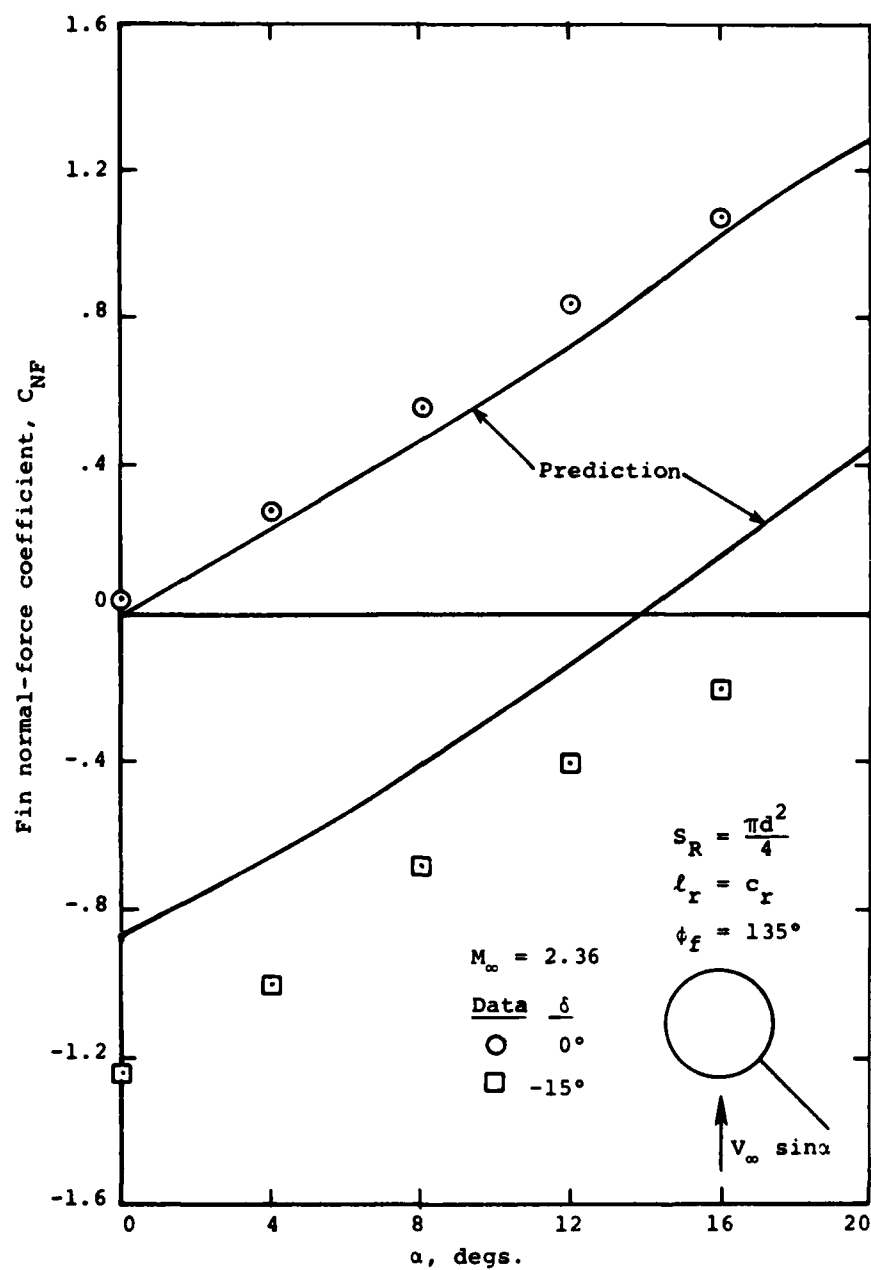
(a) Normal-force coefficient; $\phi_f = 90^\circ$, $\delta = 0^\circ, -15^\circ$

Figure 57.- Comparison of prediction and measurement for fin T_B characteristics at $M_\infty = 2.36$; Lamb-Trescott data.



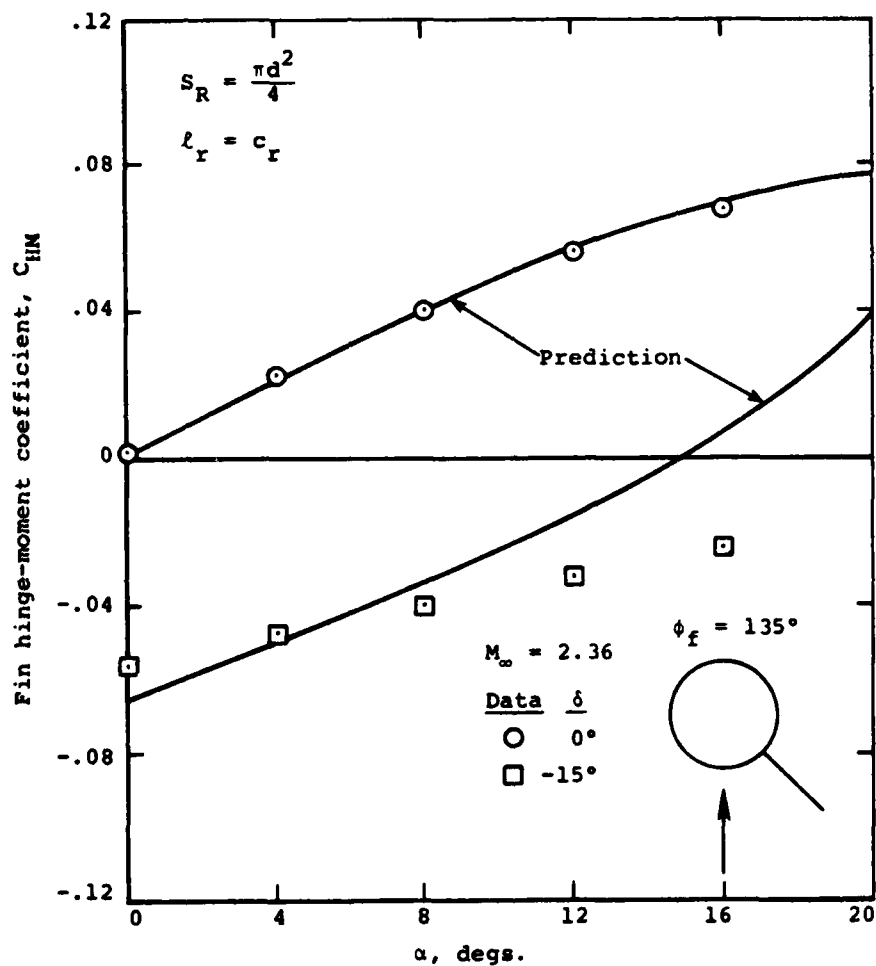
(b) Hinge-moment coefficient; $\phi_f = 90^\circ$; $\delta = 0^\circ, -15^\circ$

Figure 57.- Continued.



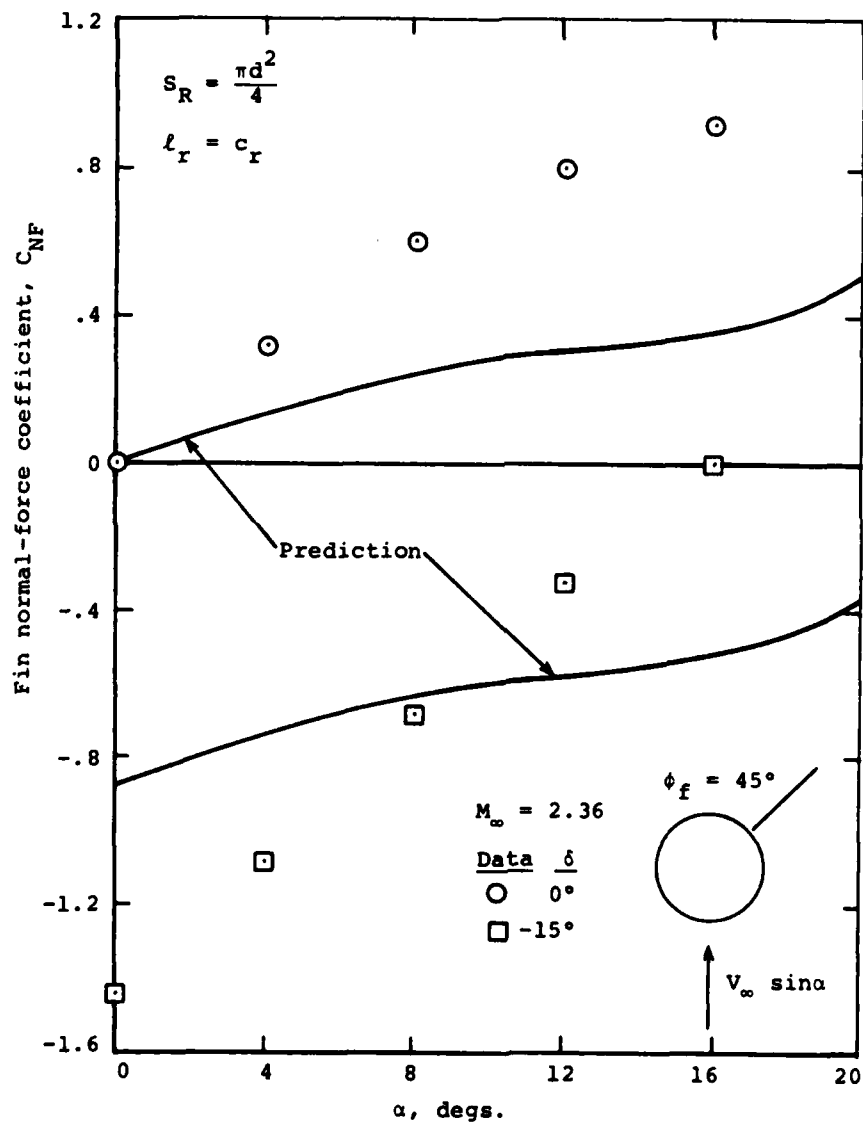
(c) Normal-force coefficient; $\phi_f = 135^\circ$; $\delta = 0^\circ, -15^\circ$

Figure 57.- Continued.



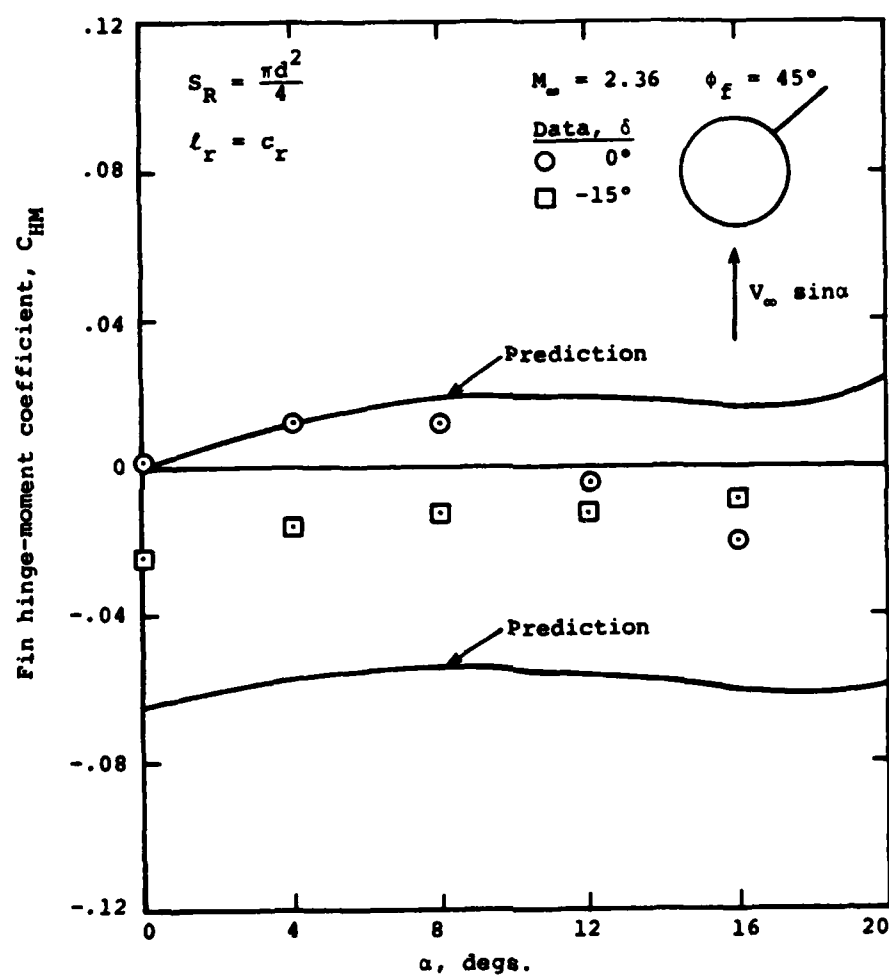
(d) Hinge-moment coefficient; $\phi_f = 135^\circ$; $\delta = 0^\circ, -15^\circ$

Figure 57.- Continued.



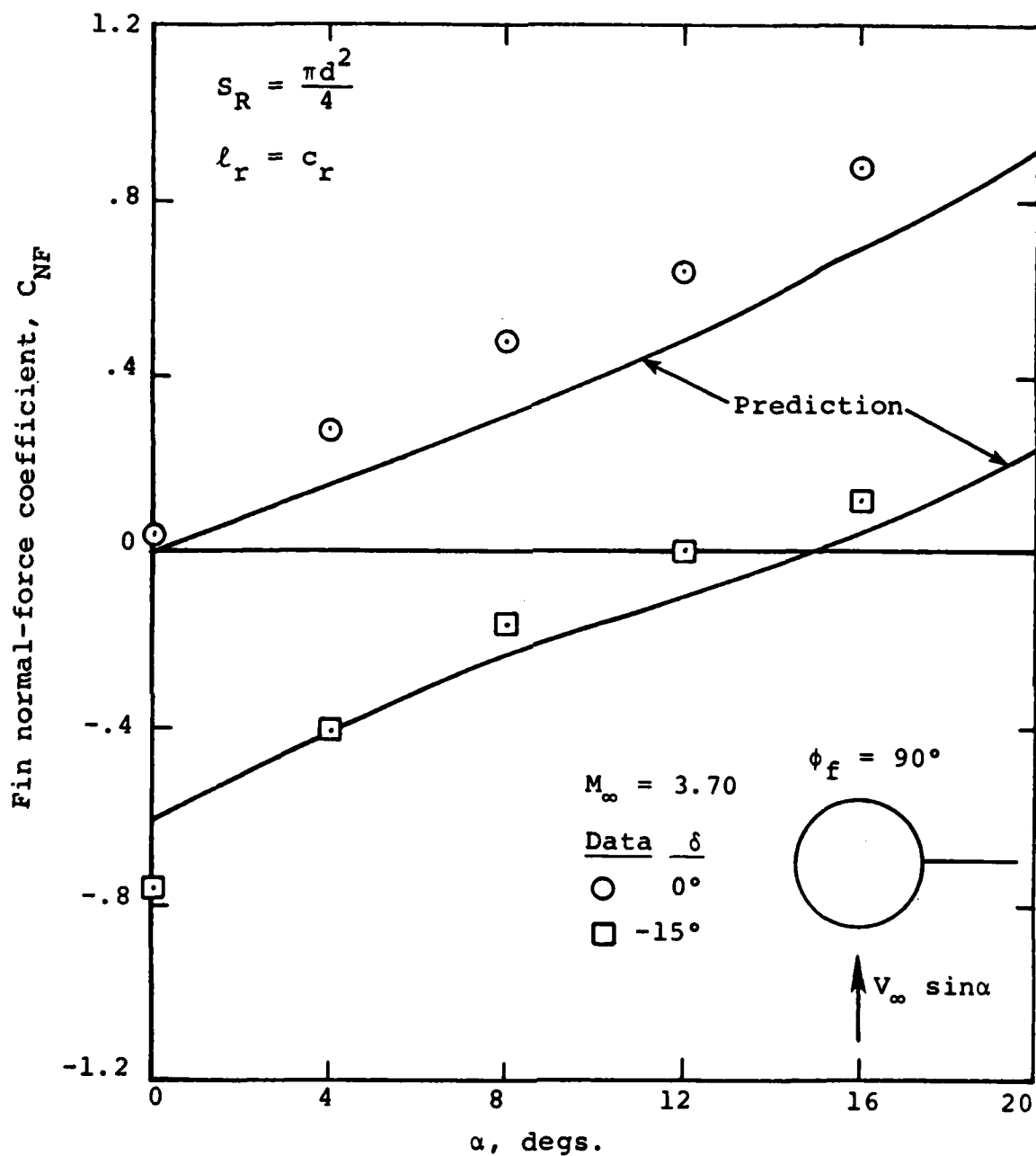
(e) Normal-force coefficient; $\phi_f = 45^\circ$; $\delta = 0^\circ, -15^\circ$

Figure 57.- Continued.



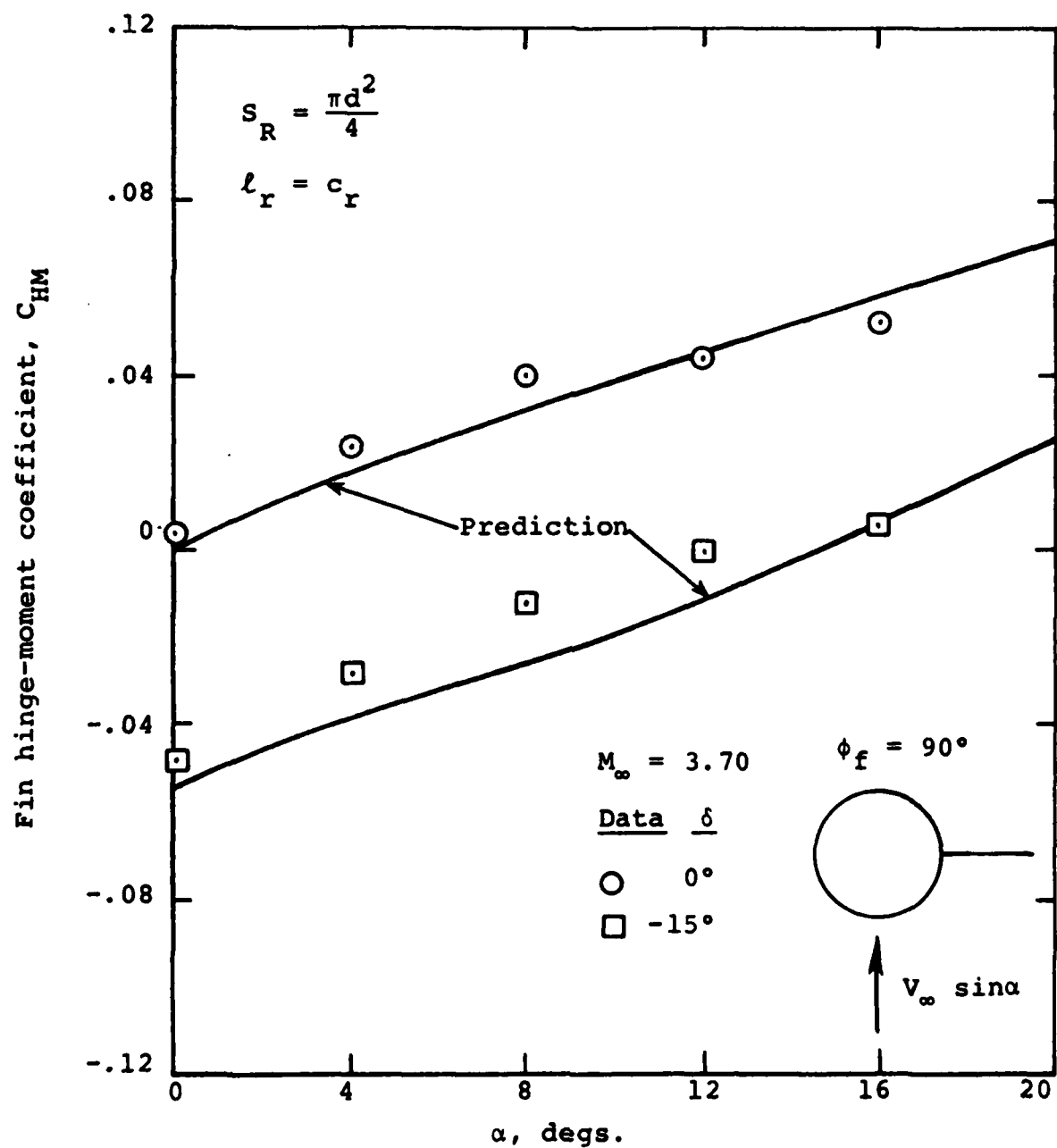
(f) Hinge-moment coefficient; $\phi_f = 45^\circ$; $\delta = 0^\circ, -15^\circ$

Figure 57.- Concluded.



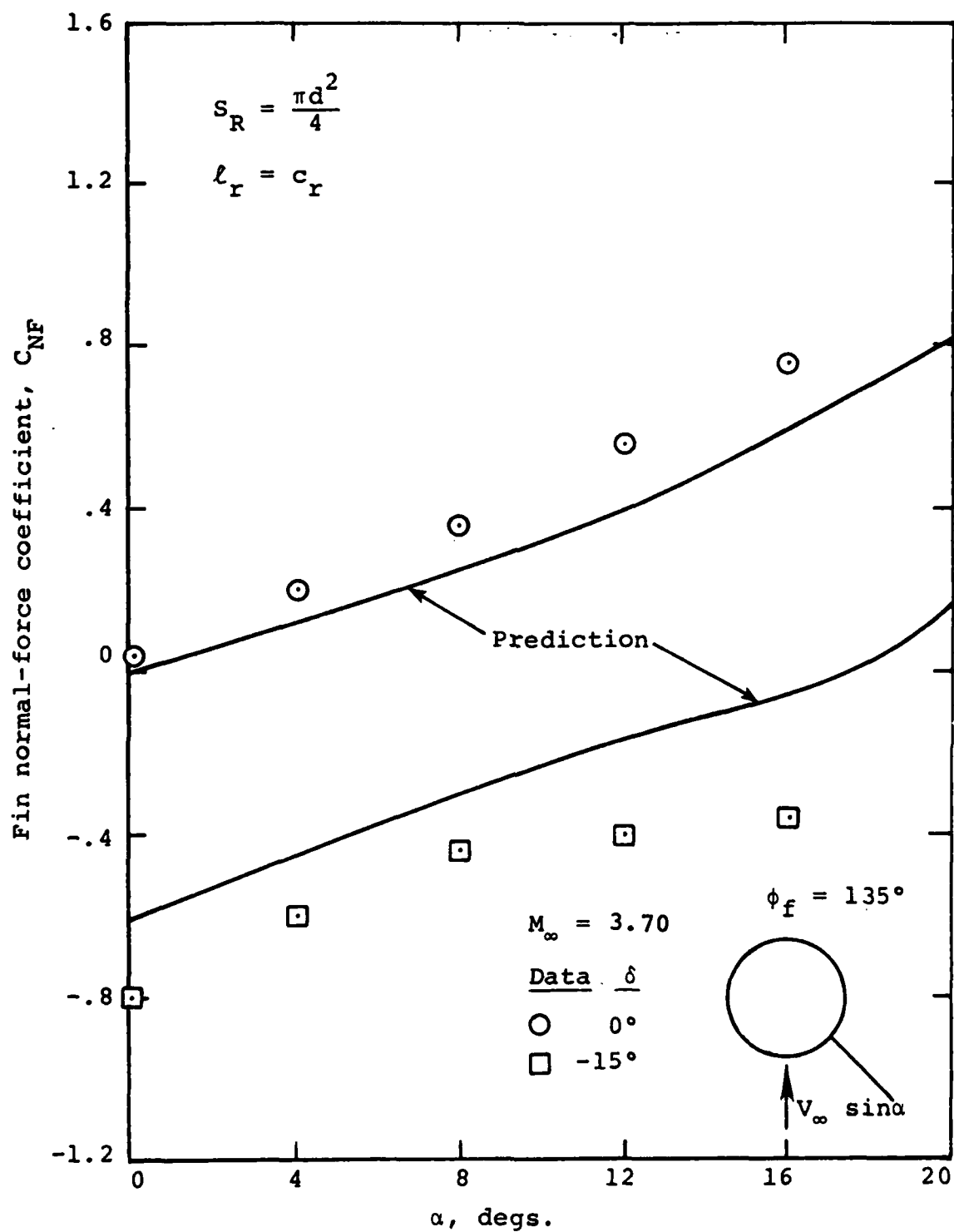
(a) Normal-force coefficient; $\phi_f = 90^\circ$; $\delta = 0^\circ, -15^\circ$

Figure 58.- Comparison of prediction and measurement for fin T_B characteristics at $M_\infty = 3.70$; Lamb-Trescott data.



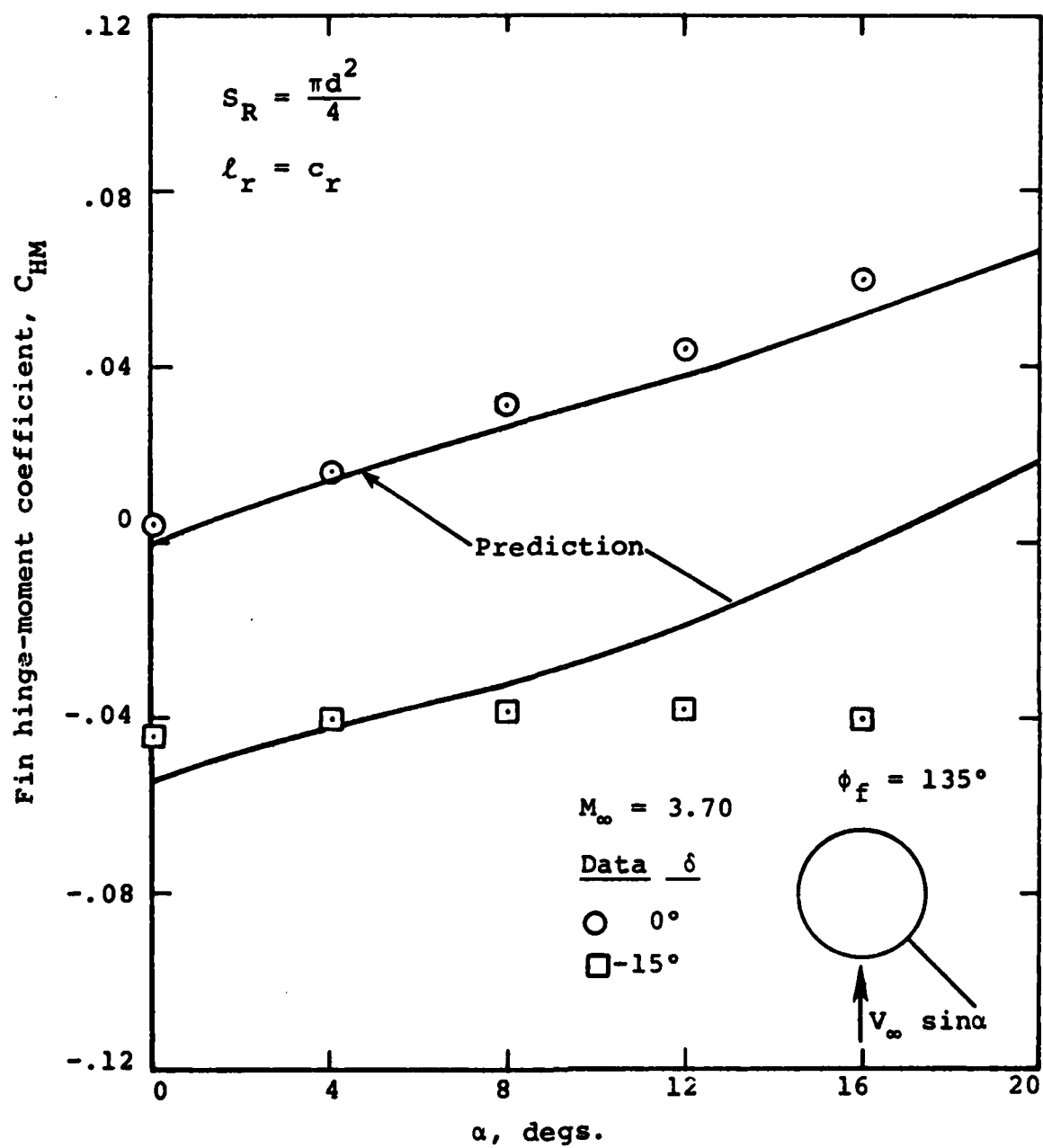
(b) Hinge-moment coefficient; $\phi_f = 90^\circ$; $\delta = 0^\circ, -15^\circ$

Figure 58.- Continued.



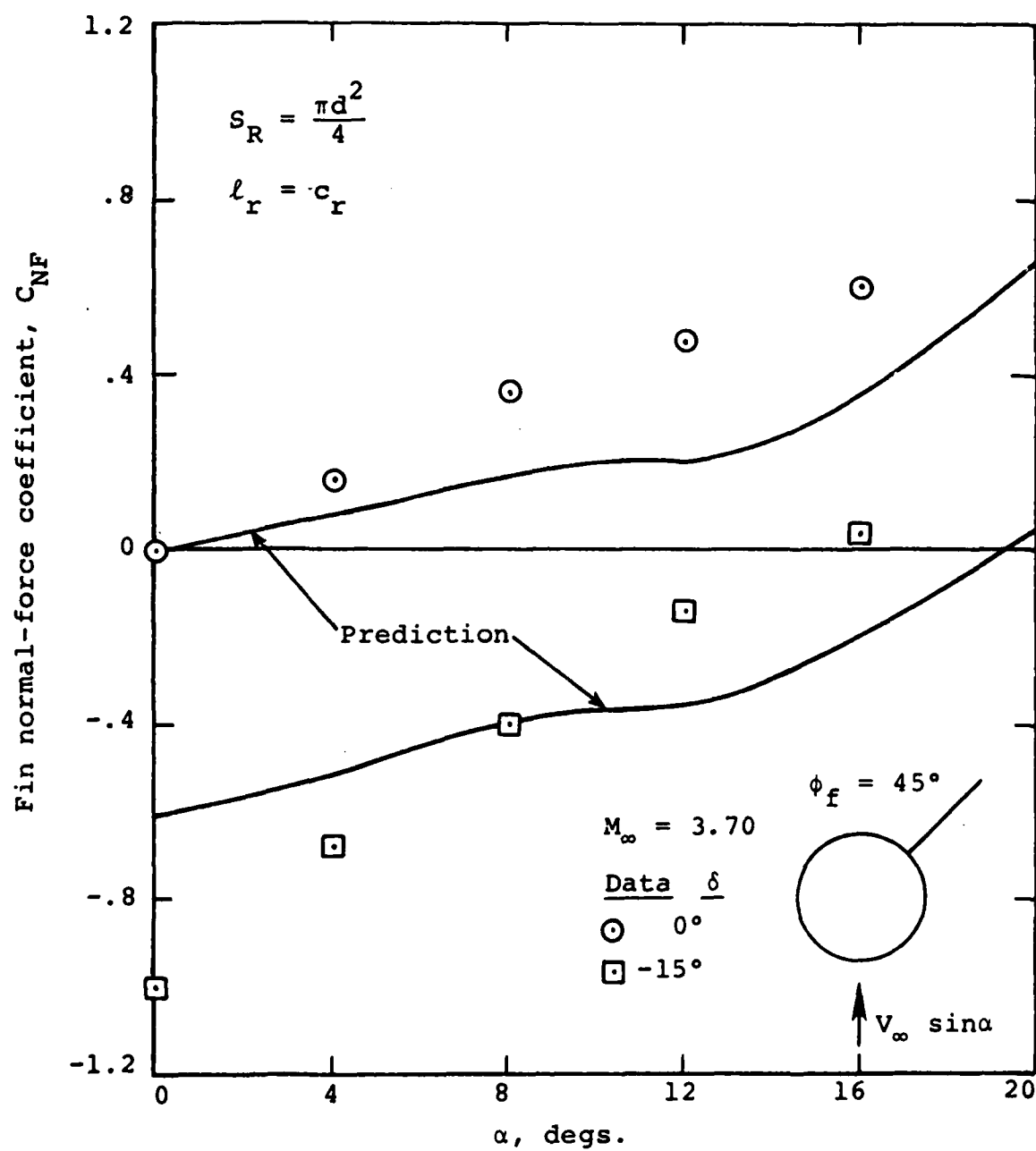
(c) Normal-force coefficient; $\phi_f = 135^\circ$; $\delta = 0^\circ, -15^\circ$

Figure 58.- Continued.



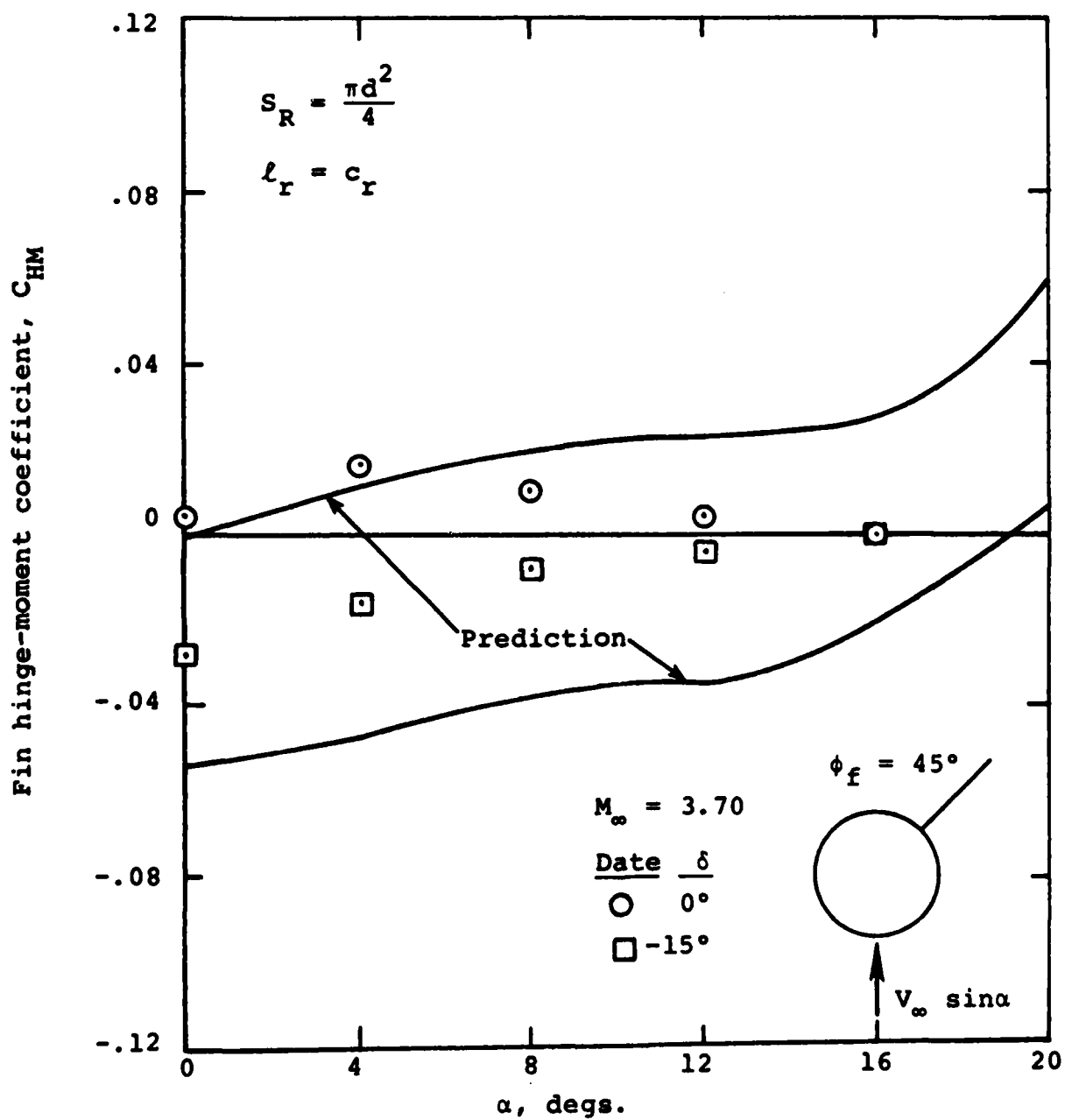
(d) Hinge-moment coefficient; $\phi_f = 135^\circ$; $\delta = 0^\circ$; -15°

Figure 58.- Continued.



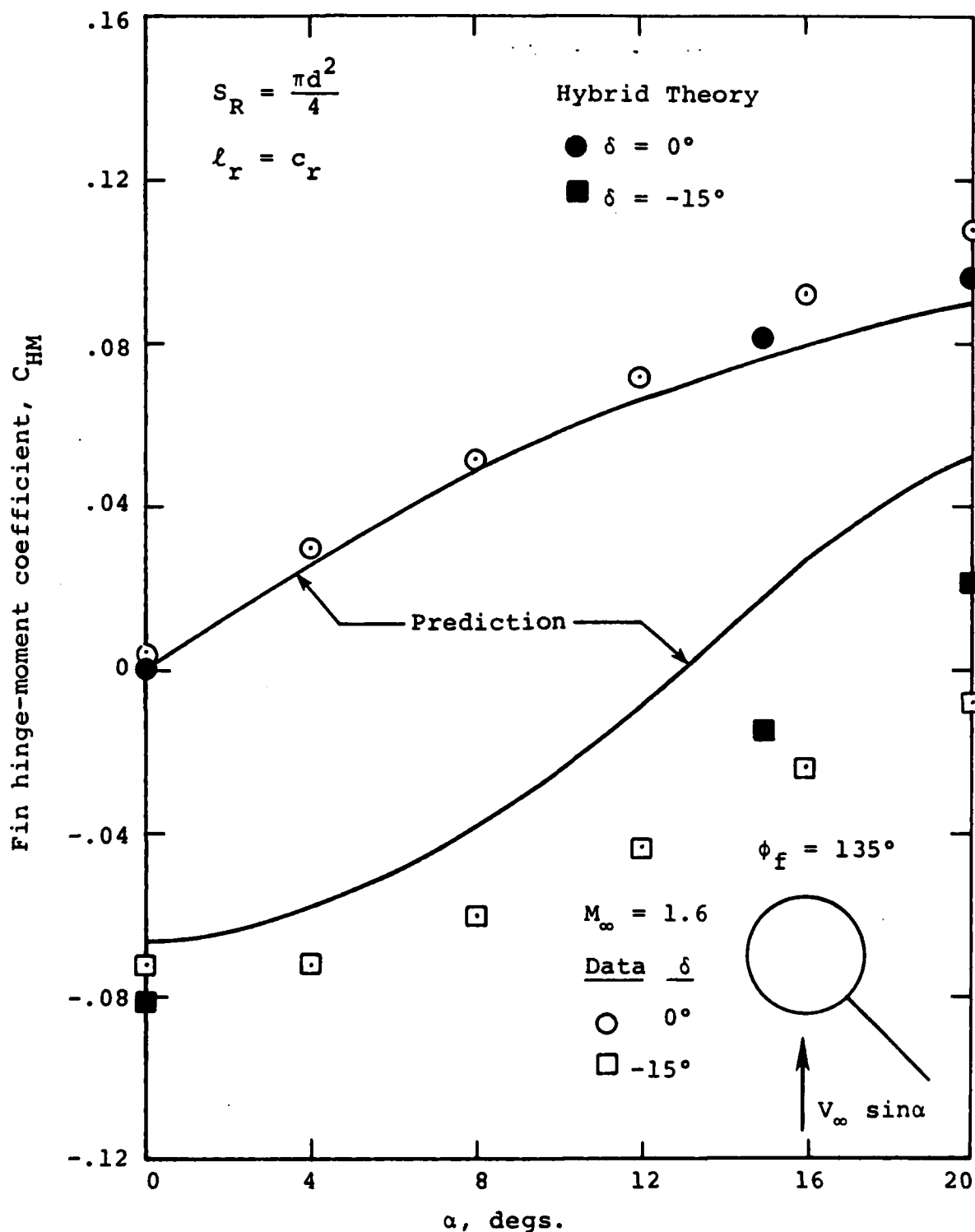
(e) Normal-force coefficient; $\phi_f = 45^\circ$; $\delta = 0^\circ, -15^\circ$

Figure 58.- Continued.



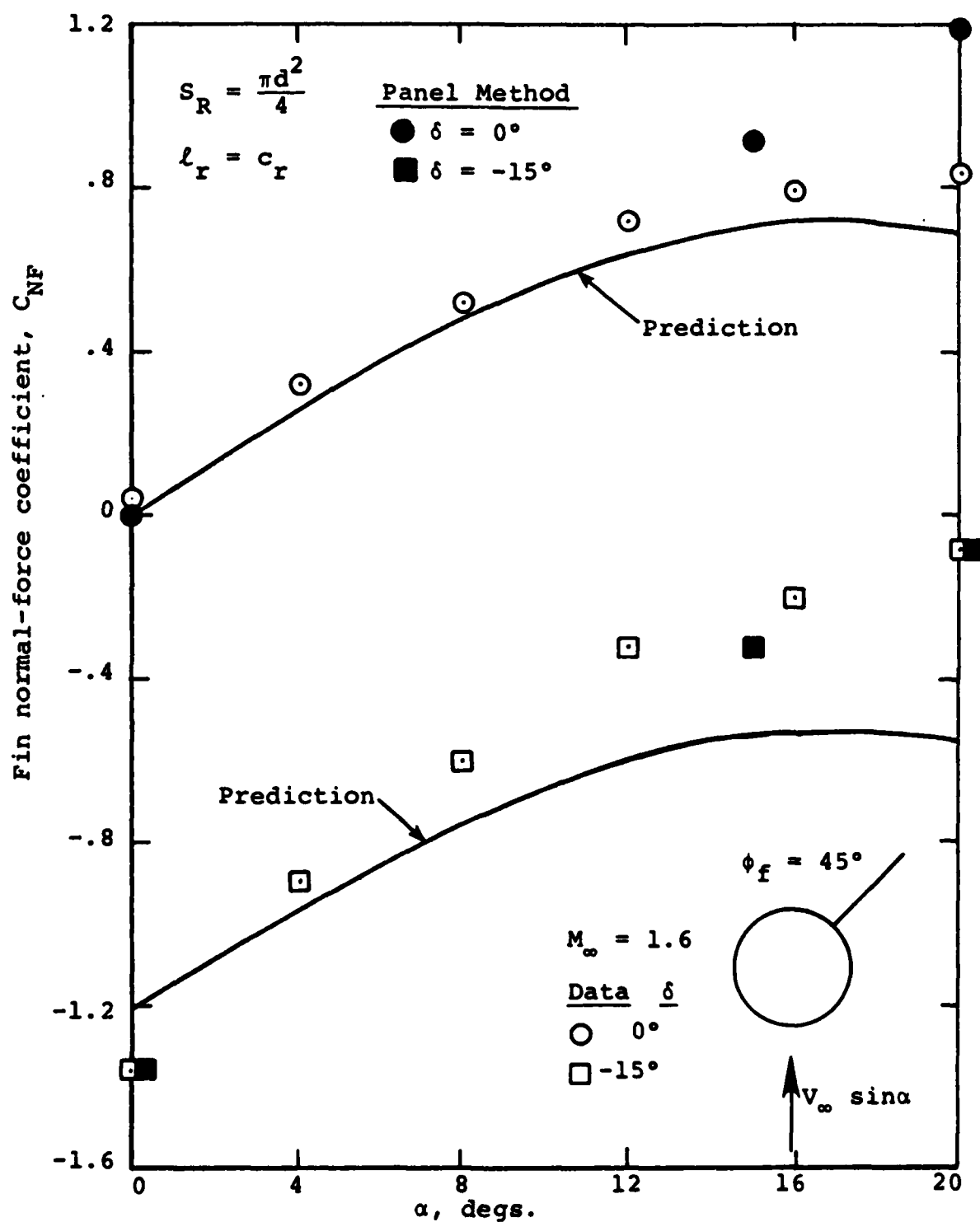
(f) Hinge-moment coefficient; $\phi_f = 45^\circ$; $\delta = 0^\circ, -15^\circ$

Figure 58.- Concluded.



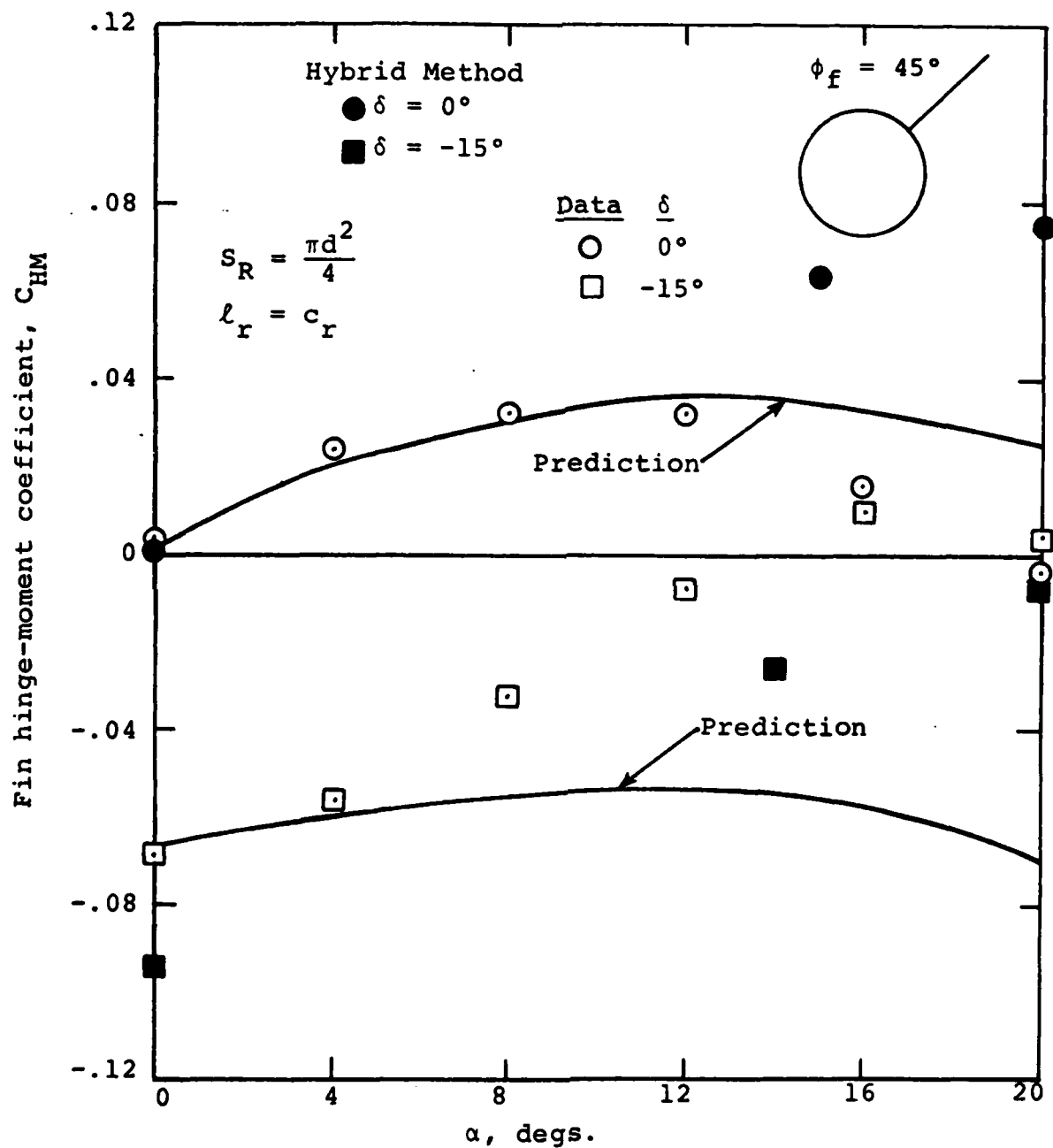
(a) Hinge-moment coefficients; $\phi_f = 135^\circ$; $\delta = 0^\circ, -15^\circ$

Figure 59.- Comparison of engineering prediction method and hybrid method with measurements for fin T_B characteristics at $M_\infty = 1.6$; Lamb-Trescott data.



(b) Normal-force coefficients; $\phi_f = 45^\circ$; $\delta = 0^\circ, -15^\circ$

Figure 59.- Continued.



(c) Hinge-moment coefficient; $\phi_f = 45^\circ$; $\delta = 0^\circ, -15^\circ$

Figure 59.- Concluded,

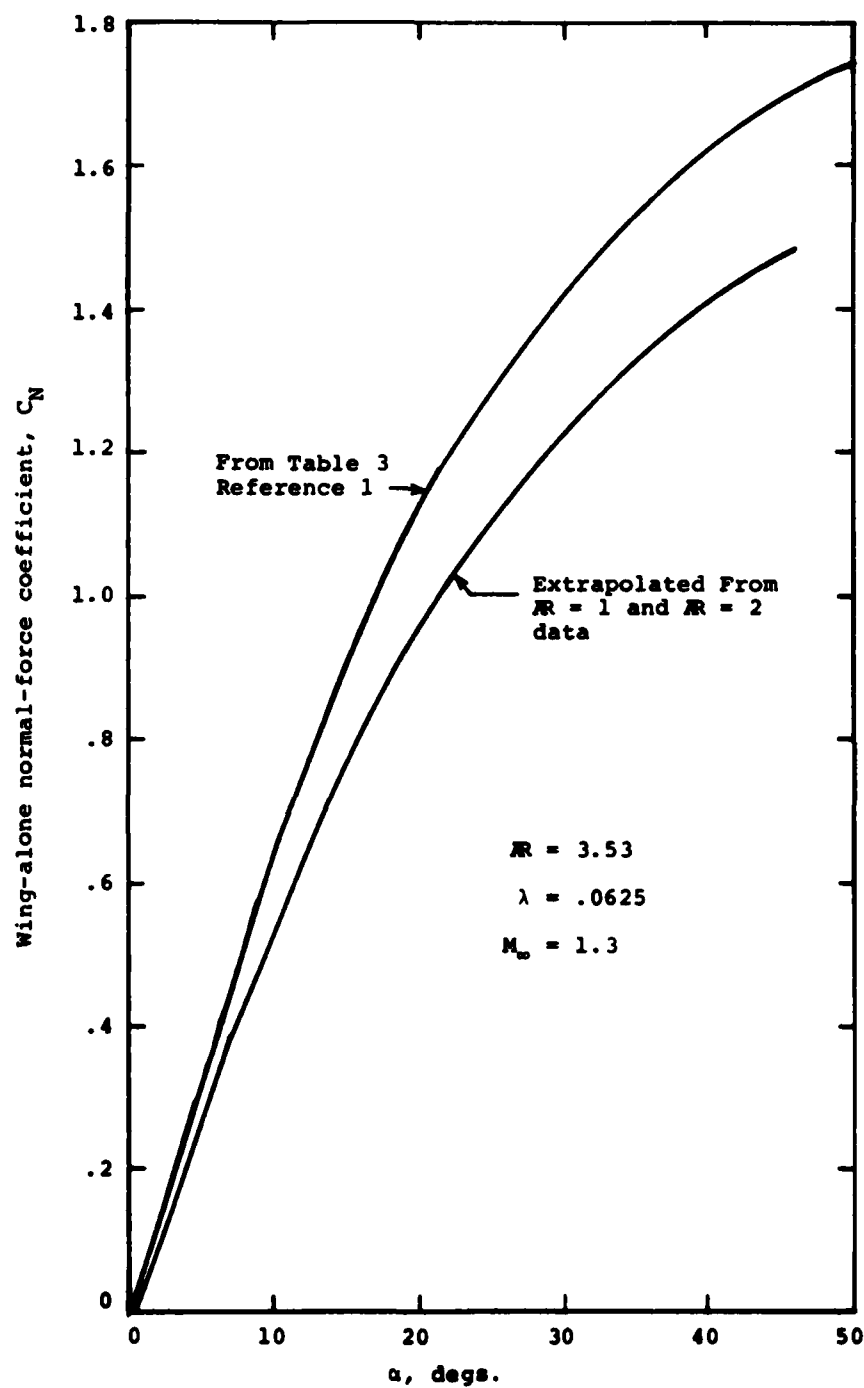


Figure 60.- Comparison of extrapolated normal-force curve for canard fin C_6 with one derived from experiment.

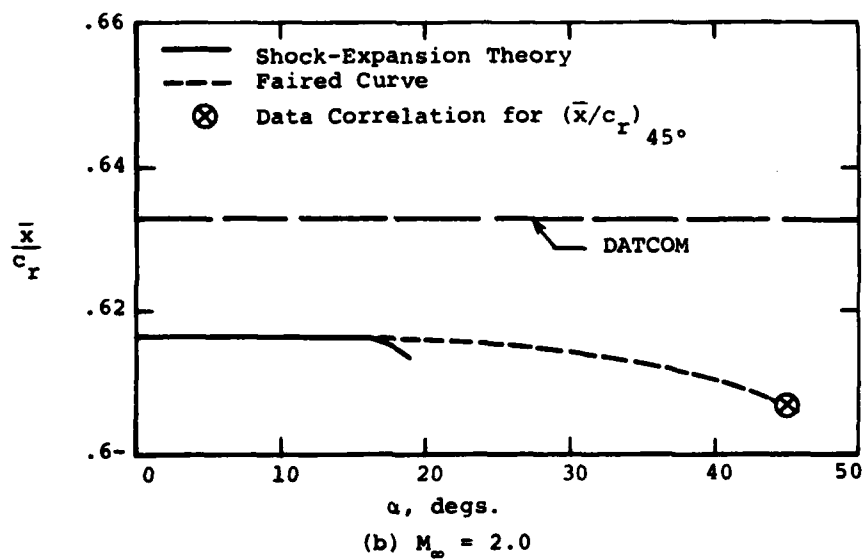
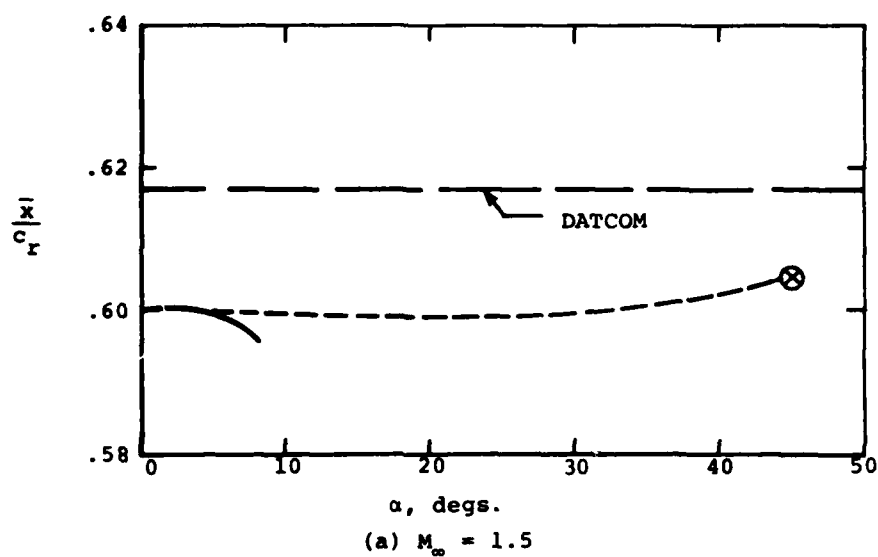
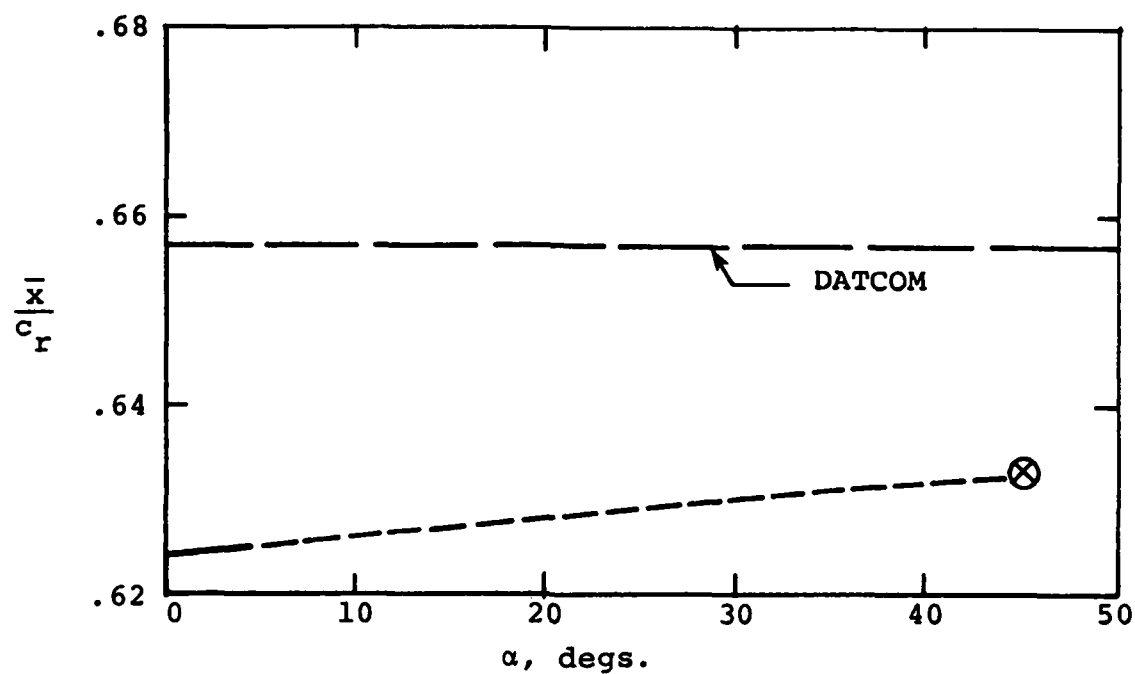
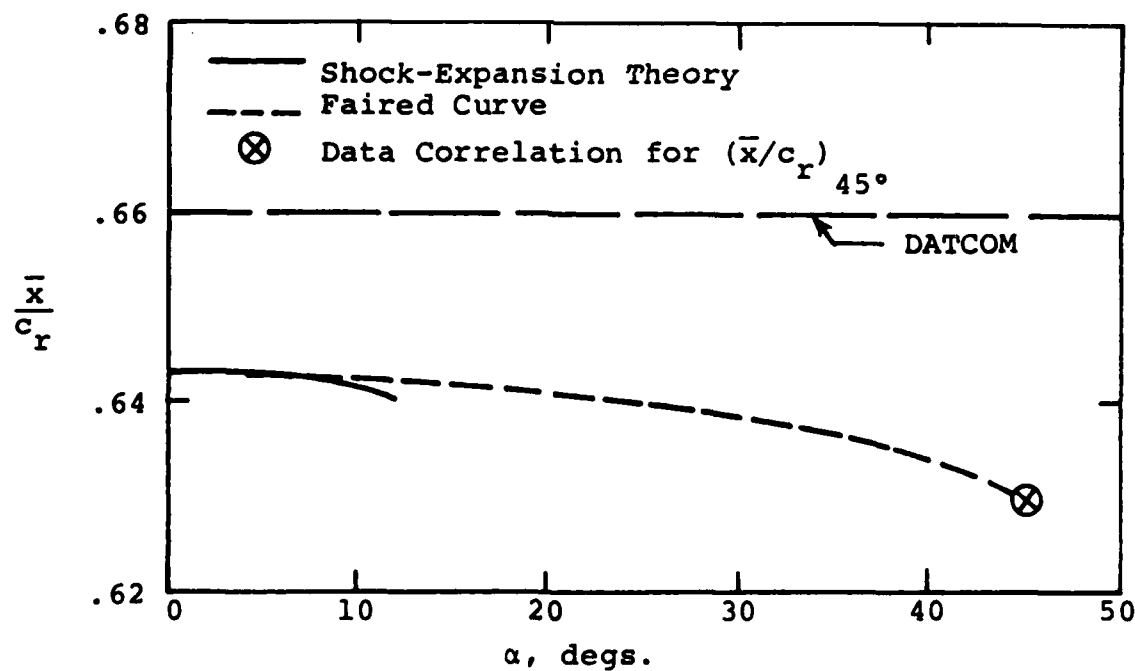


Figure 61.- Predicted center-of-pressure location for canard C_4 alone; $R = 2.31$, $\lambda = 0.3$.



(a) $M_\infty = 1.30$



(b) $M_\infty = 1.75$

Figure 62.- Predicted center-of-pressure location for canard C_6 alone: $AR = 3.529$, $\lambda = 0.0625$.

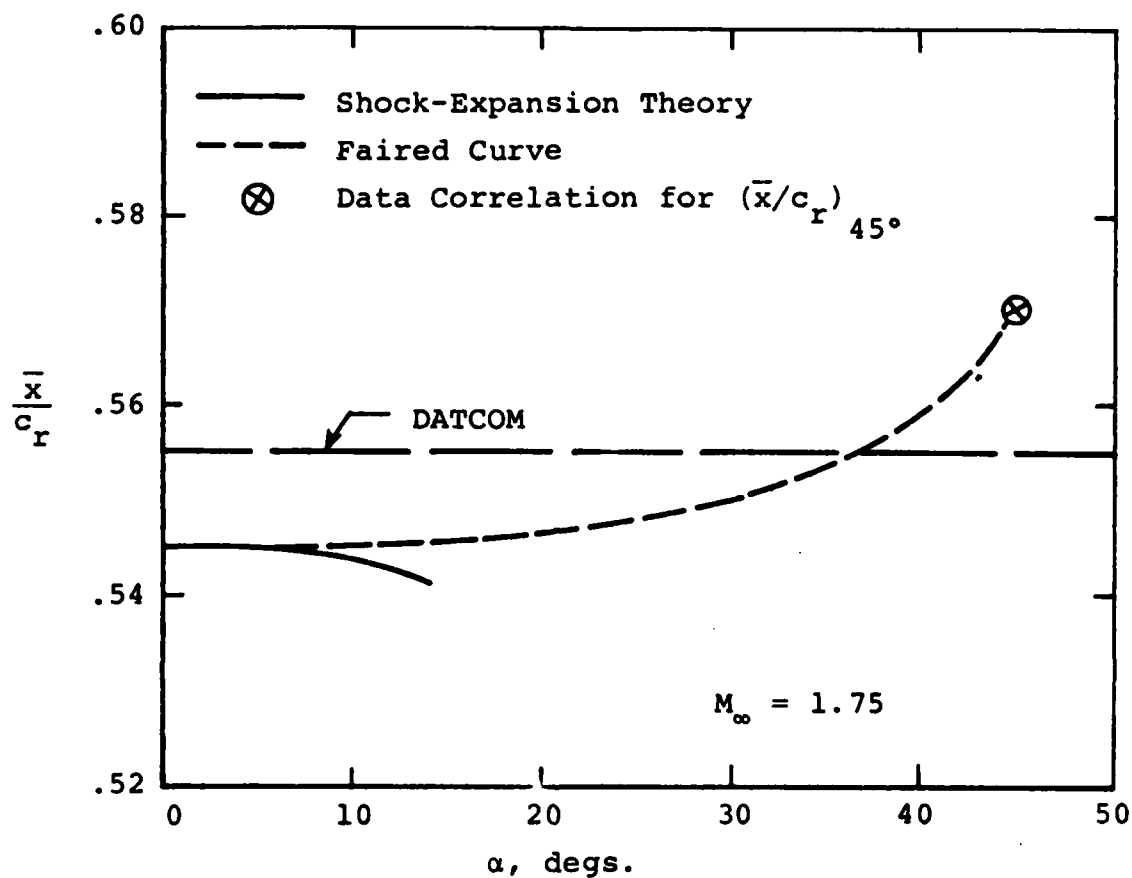
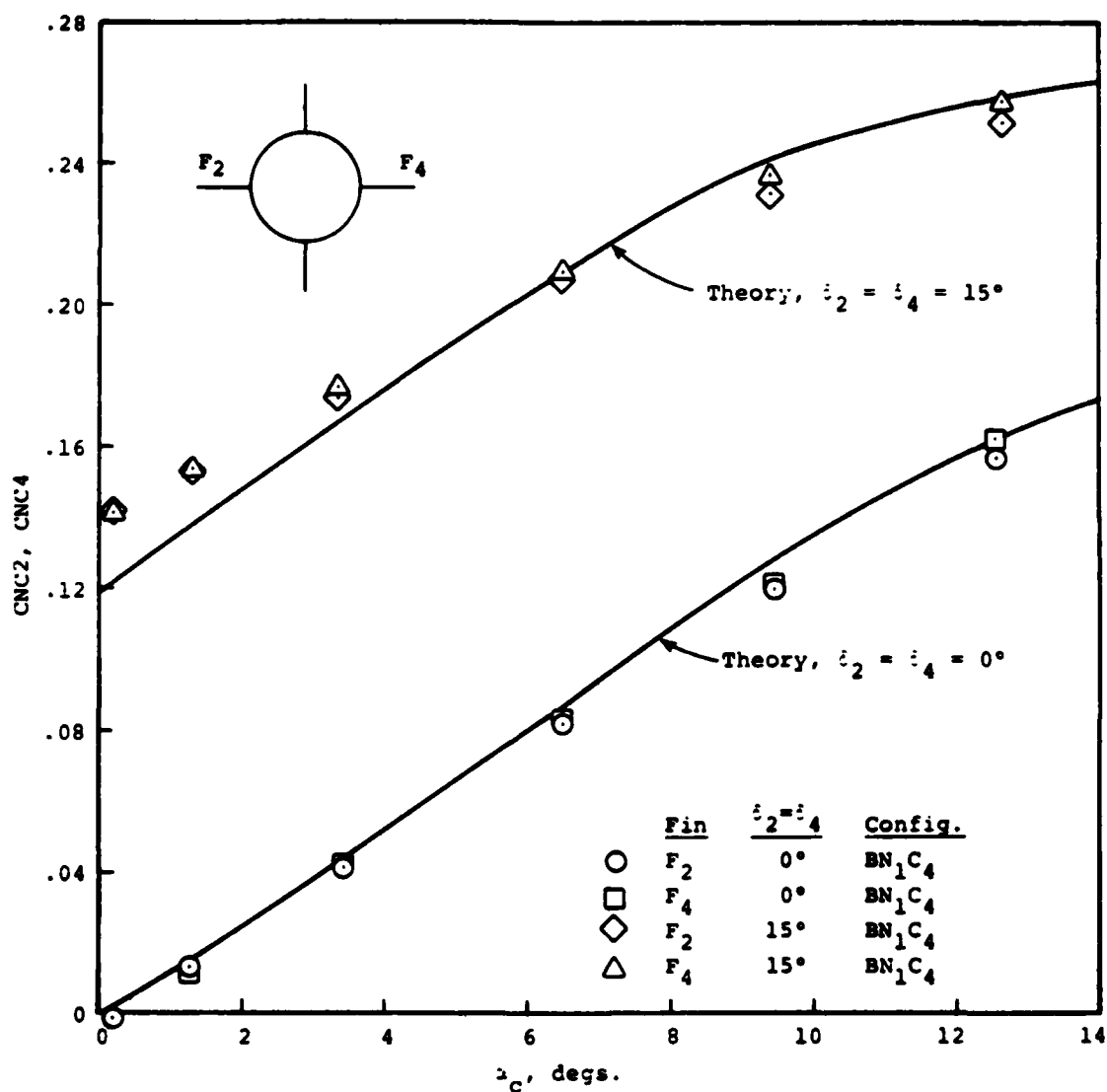
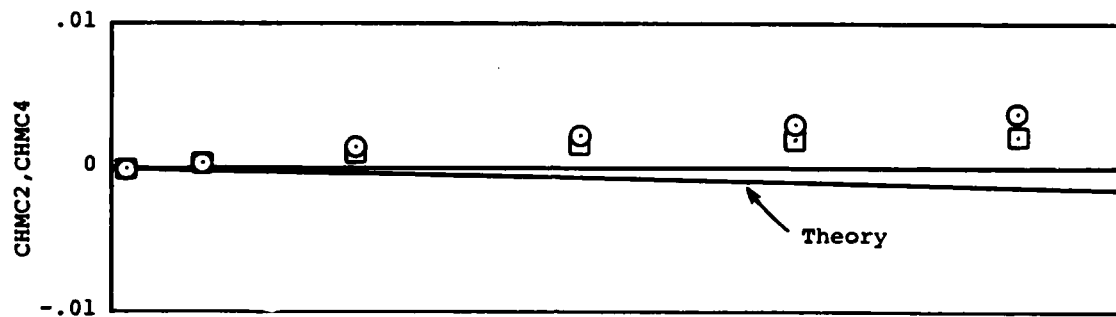
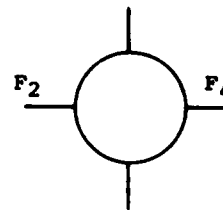


Figure 63.- Predicted center-of-pressure location for tail T_2 alone; $R = 1.33$, $\lambda = 0.5$.

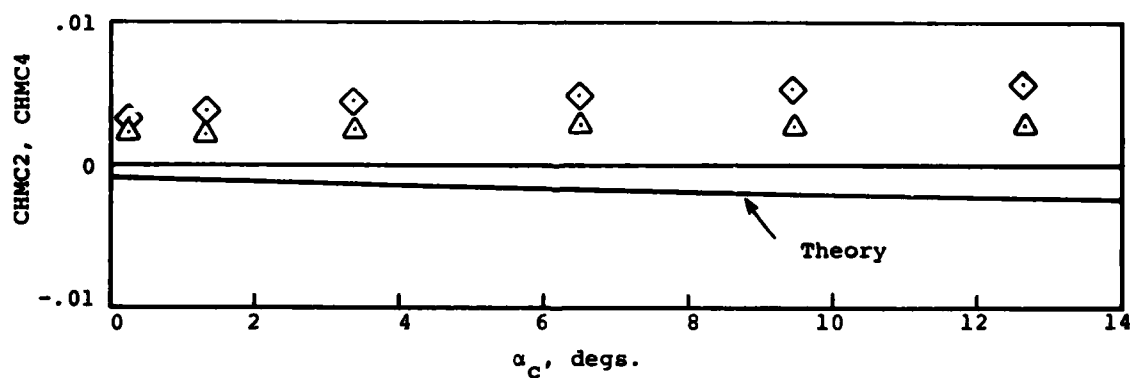


(a) Normal-force coefficient, $\alpha_2 = \alpha_4 = 0^\circ$ and 15°
 Figure 64.- Characteristics of canard C₄; $M_\infty = 1.5$, $\alpha_c = 0^\circ$,
 $\alpha_1 = \alpha_3 = 0^\circ$.

	<u>Fin</u>	<u>$\delta_2 = \delta_4$</u>	<u>Config.</u>
○	F_2	0°	BN_1C_4
□	F_4	0°	BN_1C_4
◇	F_2	15°	BN_1C_4
△	F_4	15°	BN_1C_4

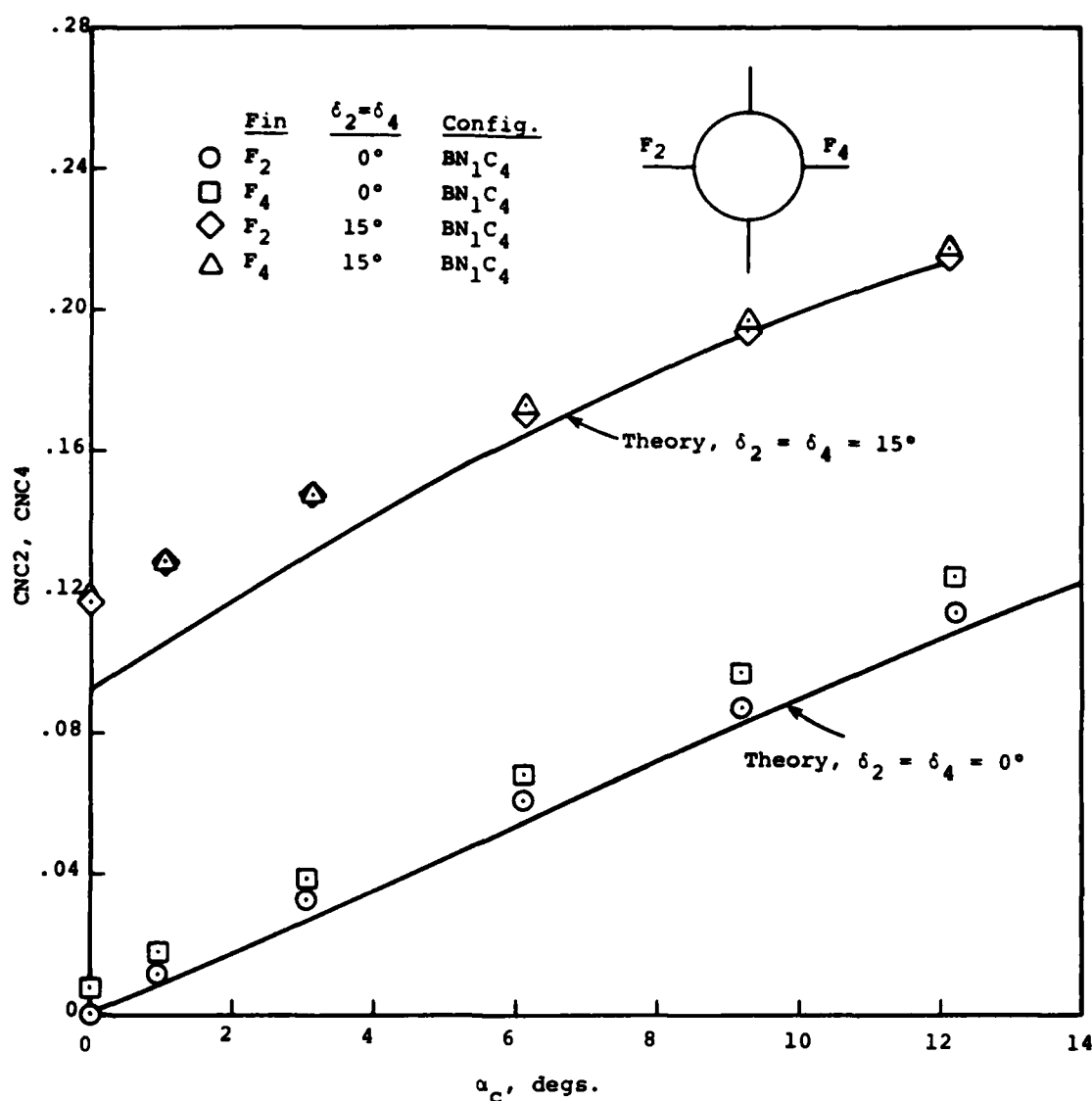


(b) Hinge-moment coefficient, $\delta_2 = \delta_4 = 0^\circ$



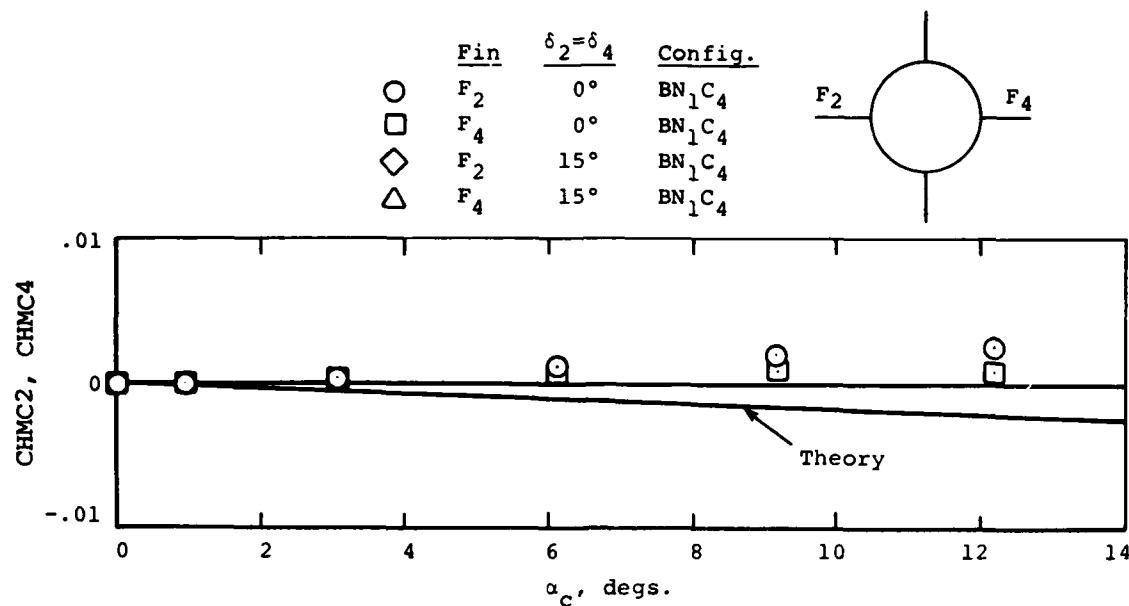
(c) Hinge-moment coefficient, $\delta_2 = \delta_4 = 15^\circ$

Figure 64.- Concluded.

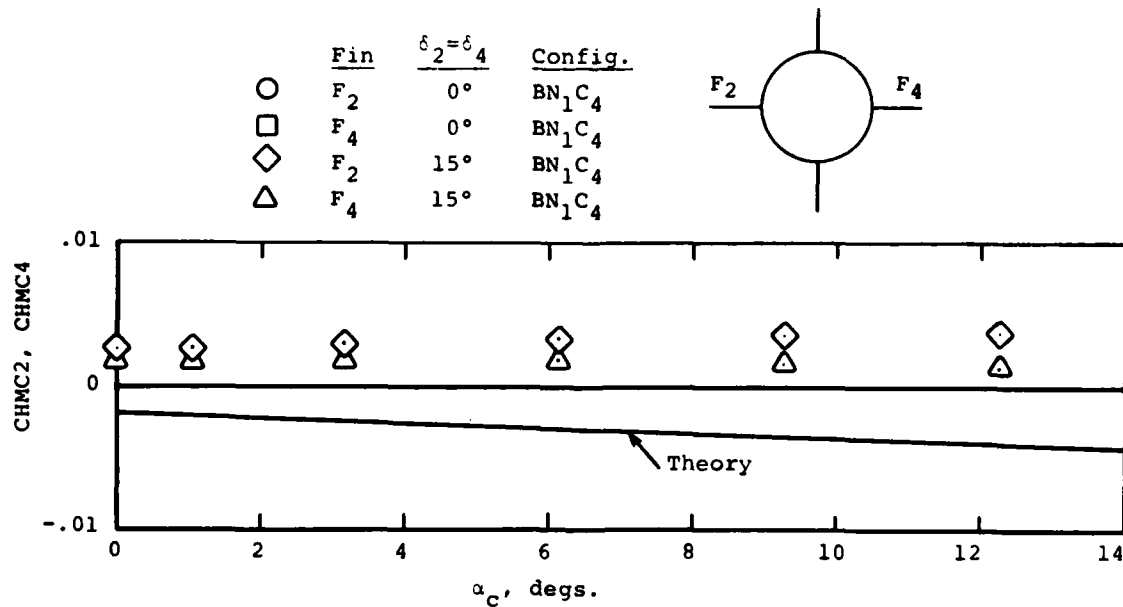


(a) Normal-force coefficient, $\delta_2 = \delta_4 = 0^\circ$ and 15°

Figure 65.- Characteristics of canard C_4 ; $M_\infty = 2.0$, $\phi_c = 0^\circ$, $\delta_1 = \delta_3 = 0^\circ$.



(b) Hinge-moment coefficient, $\delta_2 = \delta_4 = 0^\circ$.



(c) Hinge-moment coefficient, $\delta_2 = \delta_4 = 15^\circ$

Figure 65.- Concluded.

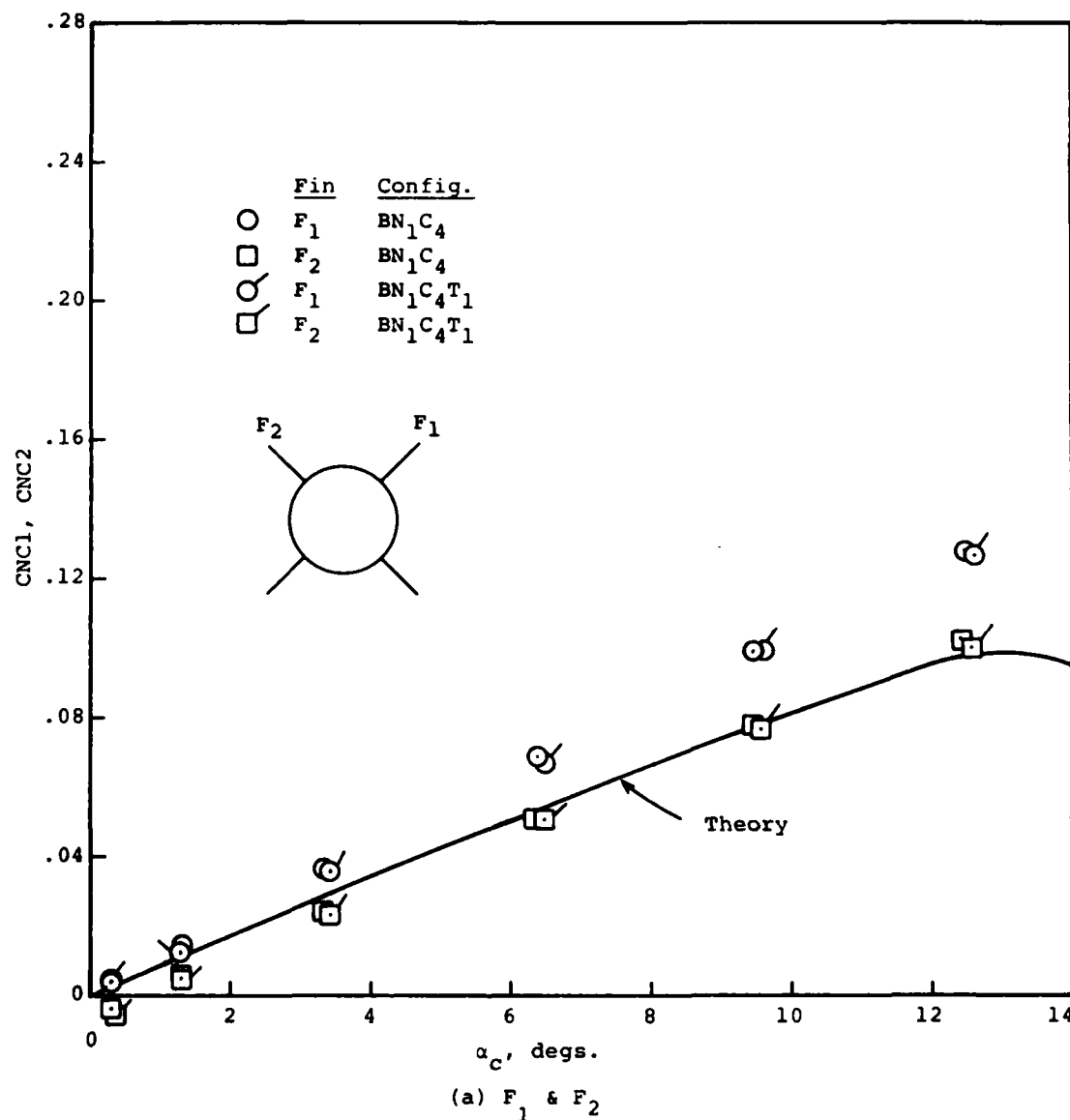
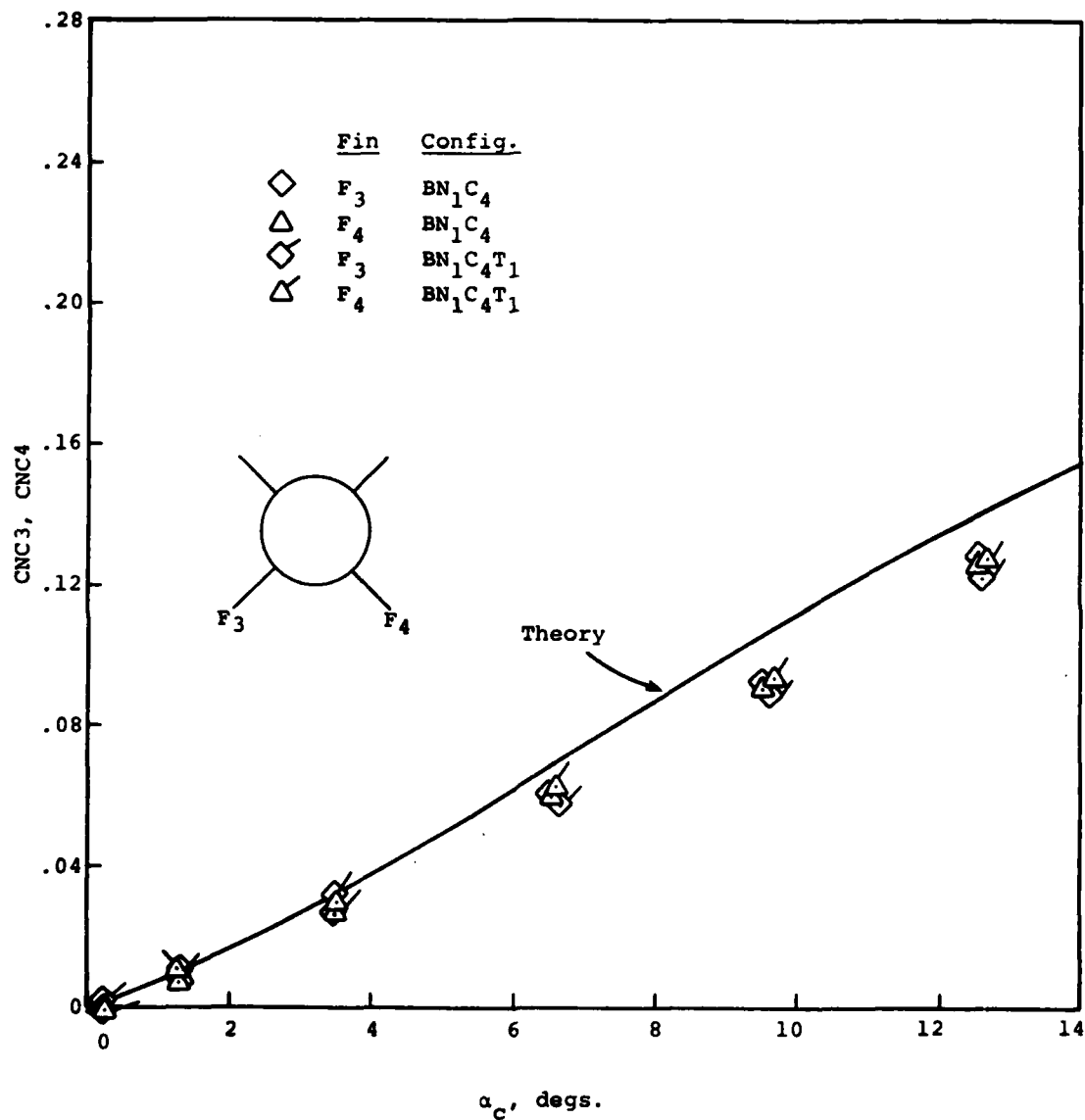
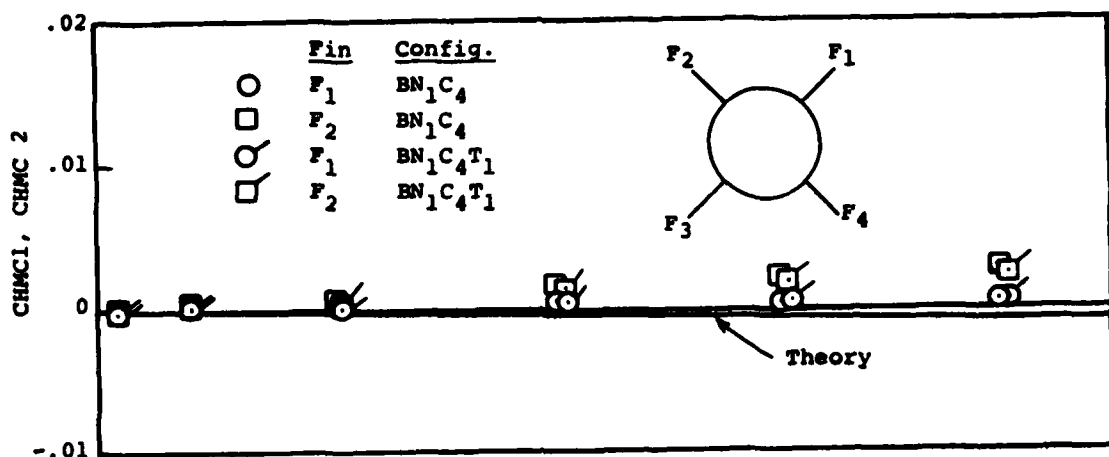


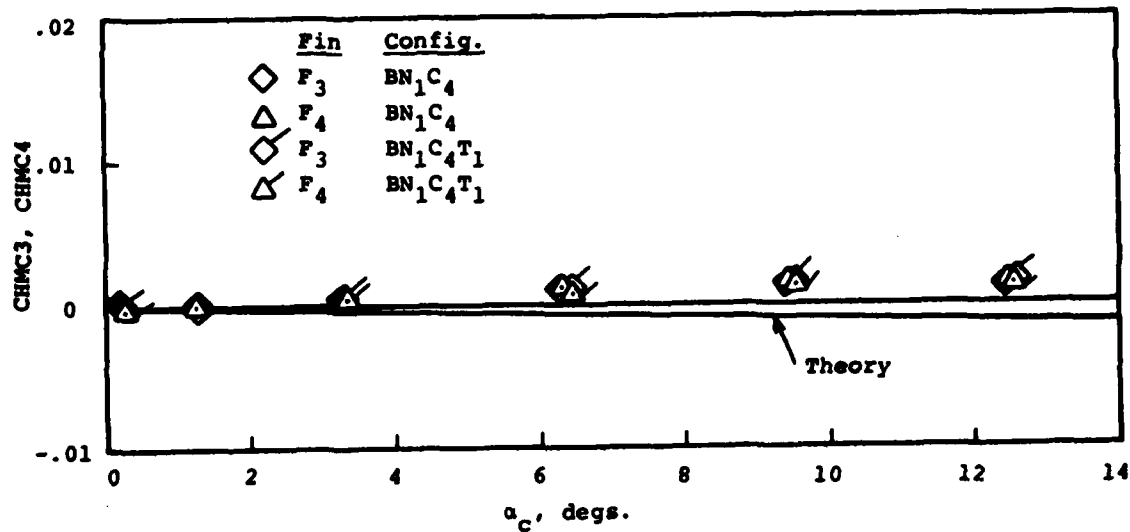
Figure 66.- Canard C₄ fins normal-force coefficients;
 $M_\infty = 1.5$, $\phi_c = 45^\circ$, $\delta_1 = \delta_2 = \delta_3 = \delta_4 = 0^\circ$.



(b) F_3 & F_4
Figure 66.- Concluded.



(a) F₁ and F₂



(b) F₃ & F₄

Figure 67.- Canard C, fins hinge-moment coefficients;
 $M_\infty = 1.5$, $\phi_c = 45^\circ$, $\delta_1 = \delta_2 = \delta_3 = \delta_4 = 0^\circ$.

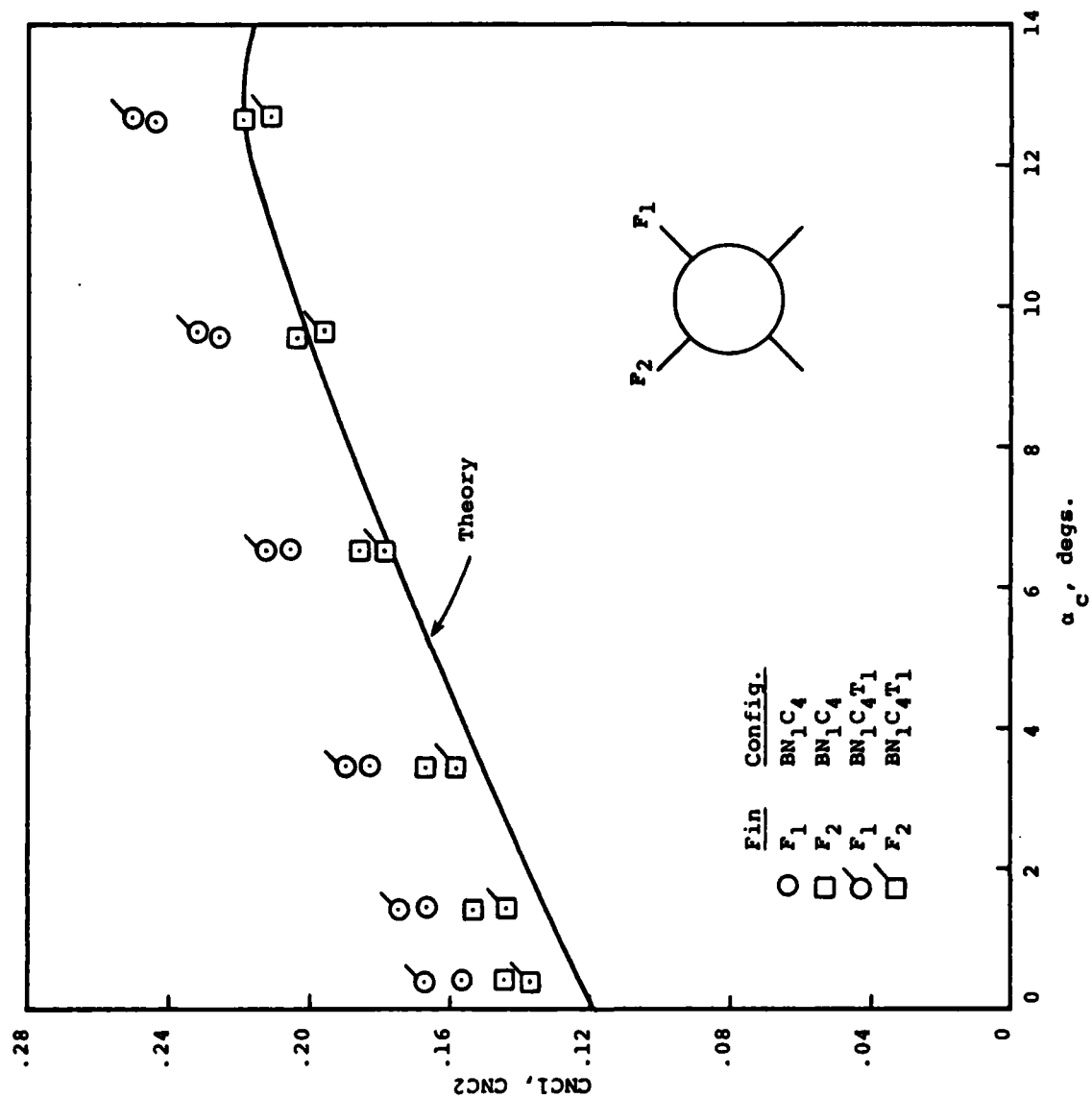
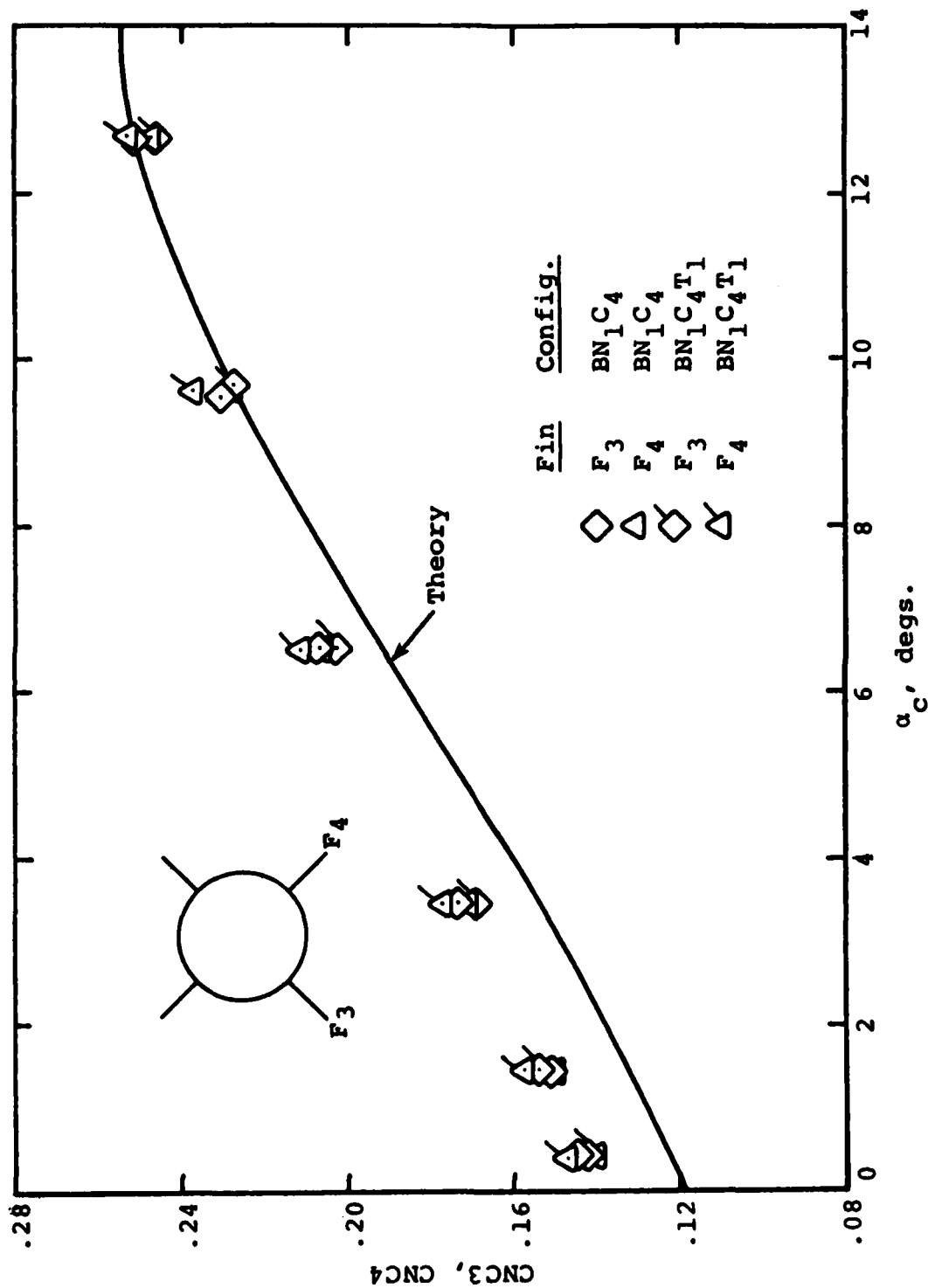


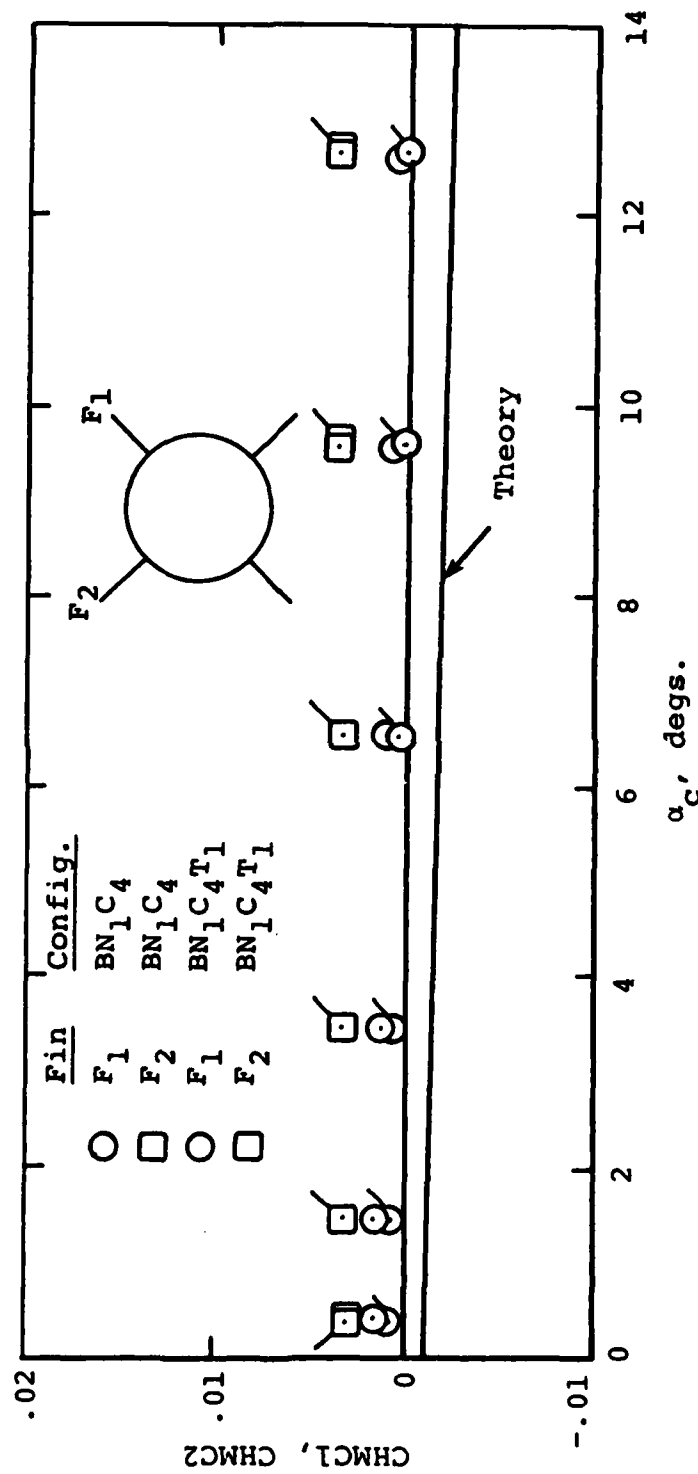
Figure 68.- Canard C fins normal-force coefficients;
 $M_\infty = 1.5$, $\phi_c = 45^\circ$, $\delta_1 = \delta_2 = \delta_3 = \delta_4 = 15^\circ$.



α_c , degs.

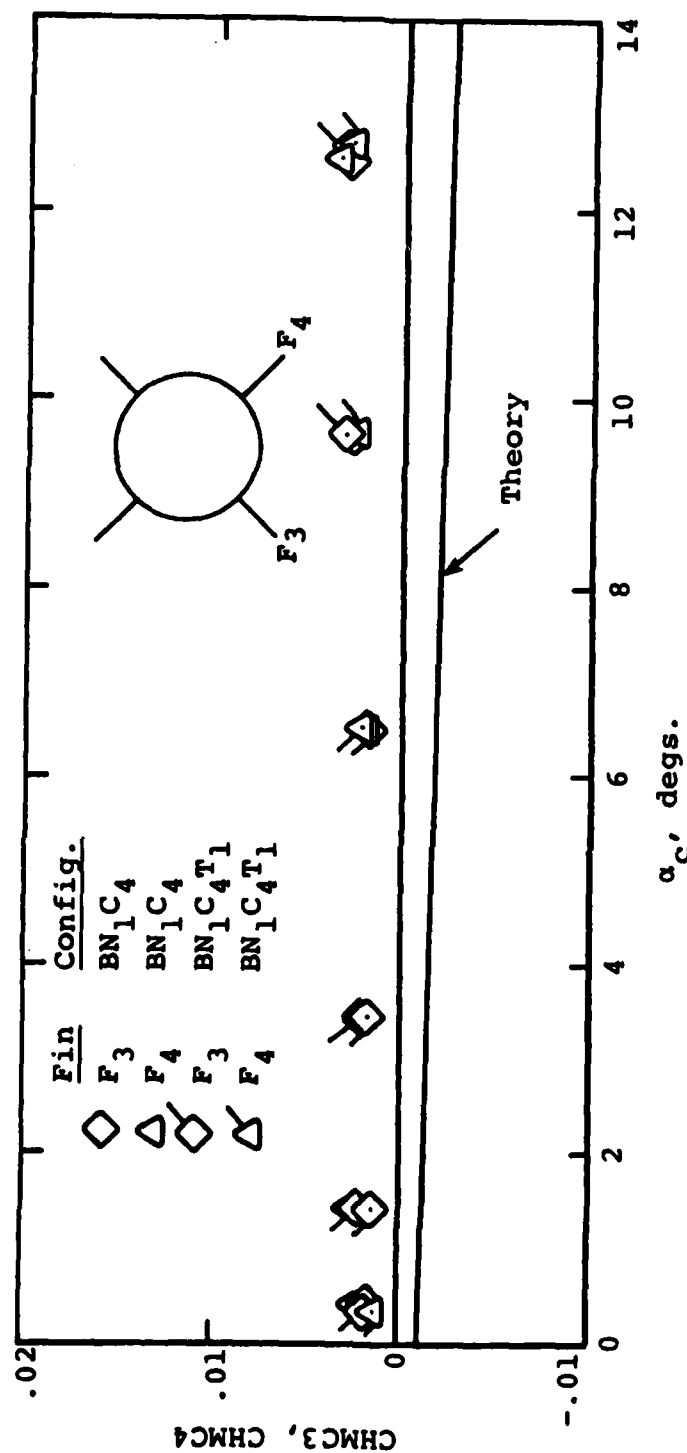
(b) F_3 & F_4

Figure 68.- Concluded.



(a) F_1 & F_2

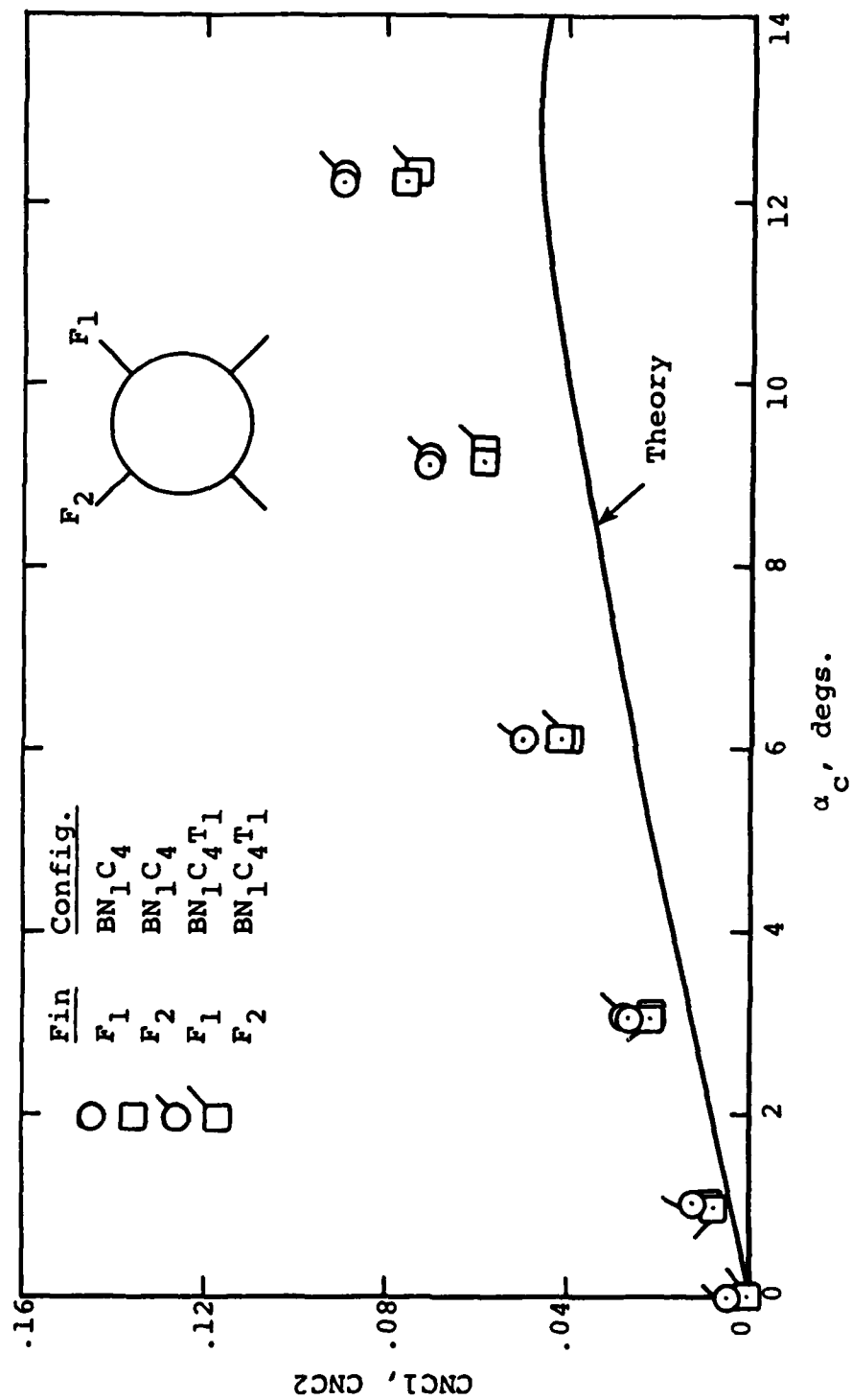
Figure 69.- Canard C_4 fins hinge-moment coefficient;
 $M_\infty = 1.5$, $\phi_c = 45^\circ$, $\delta_1 = \delta_2 = \delta_3 = \delta_4 = 15^\circ$.



$\alpha_{c'}$ degs.

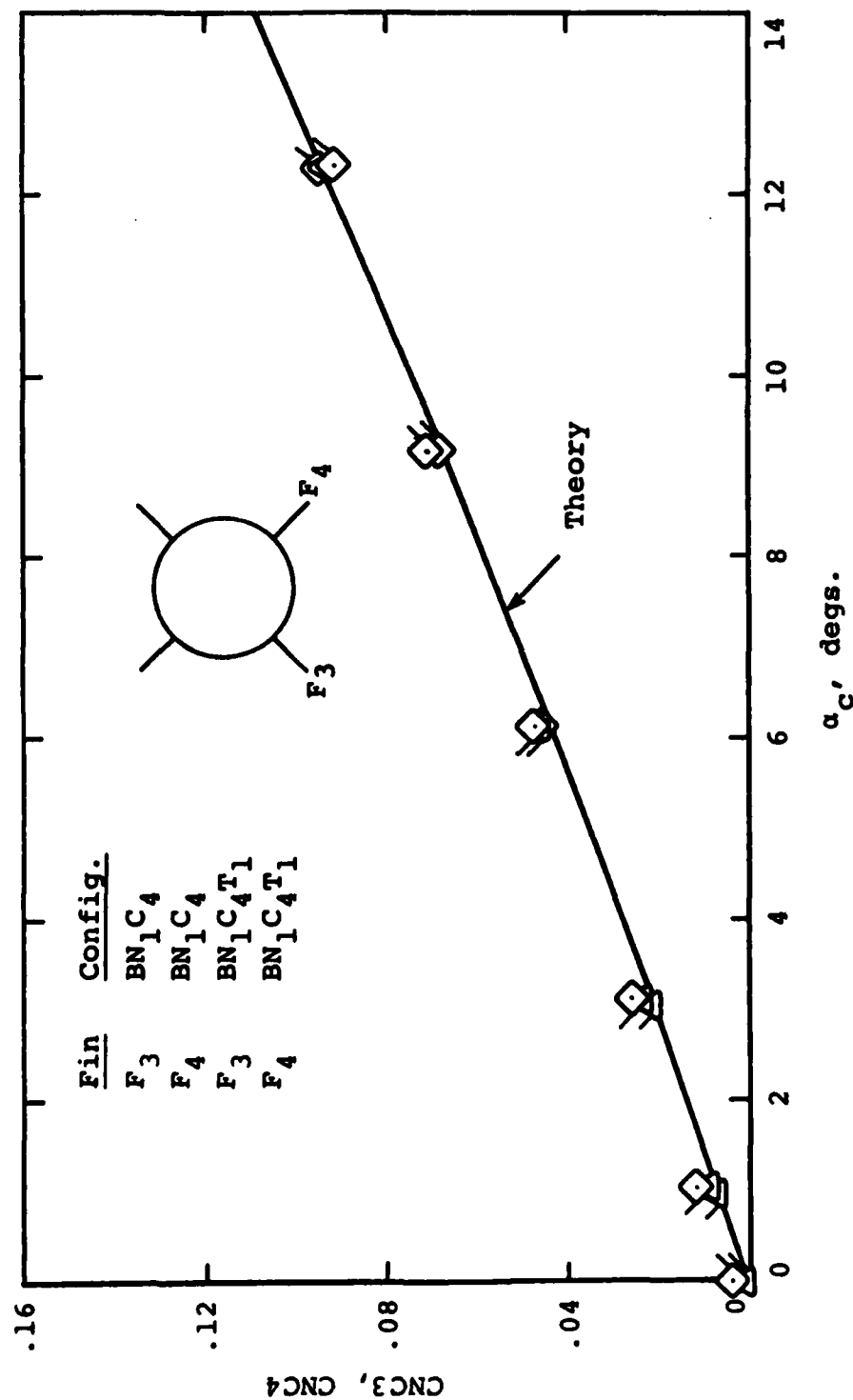
(b) F_3 & F_4

Figure 69.- Concluded.



(a) F_1 & F_2

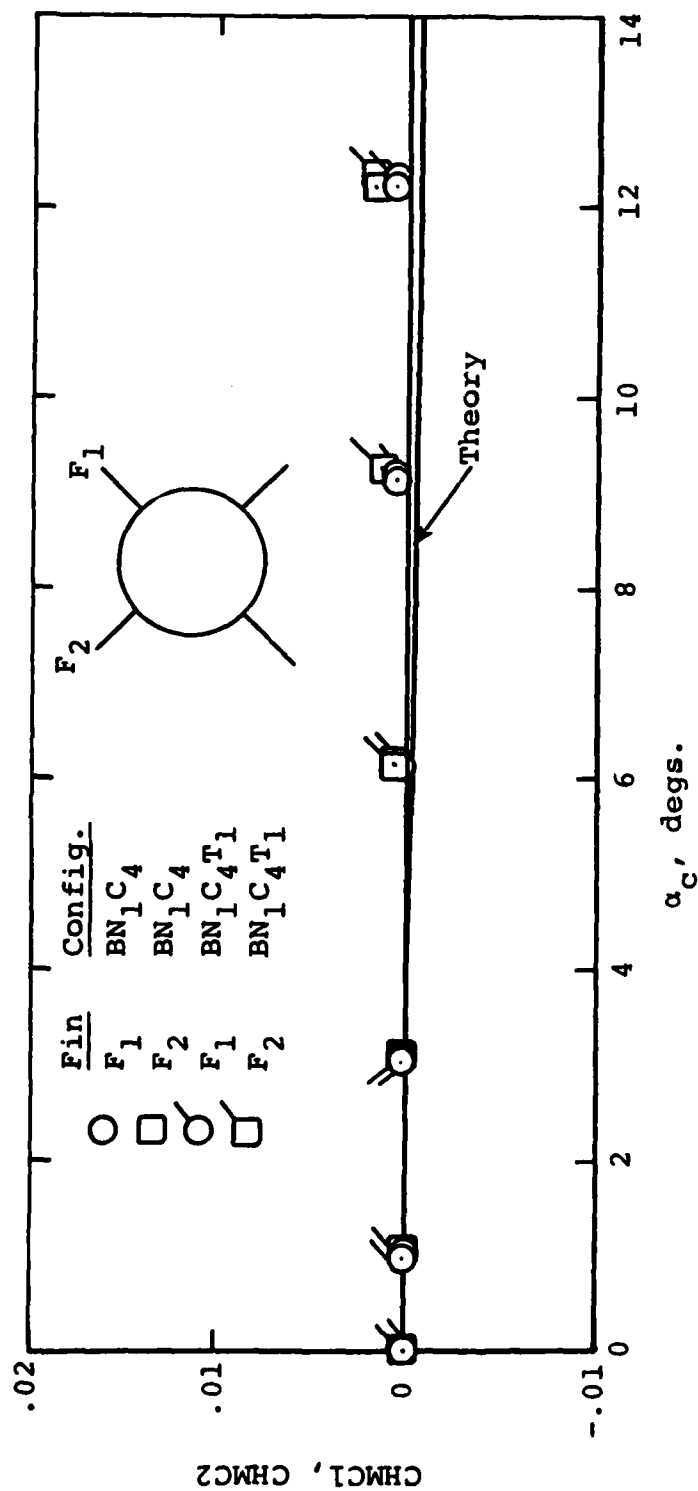
Figure 70.- Canard C_4 fins normal-force coefficients;
 $M_\infty = 2.0$, $\phi_c = 45^\circ$, $\delta_1 = \delta_2 = \delta_3 = \delta_4 = 0^\circ$.



$a_{C'}$, degs.

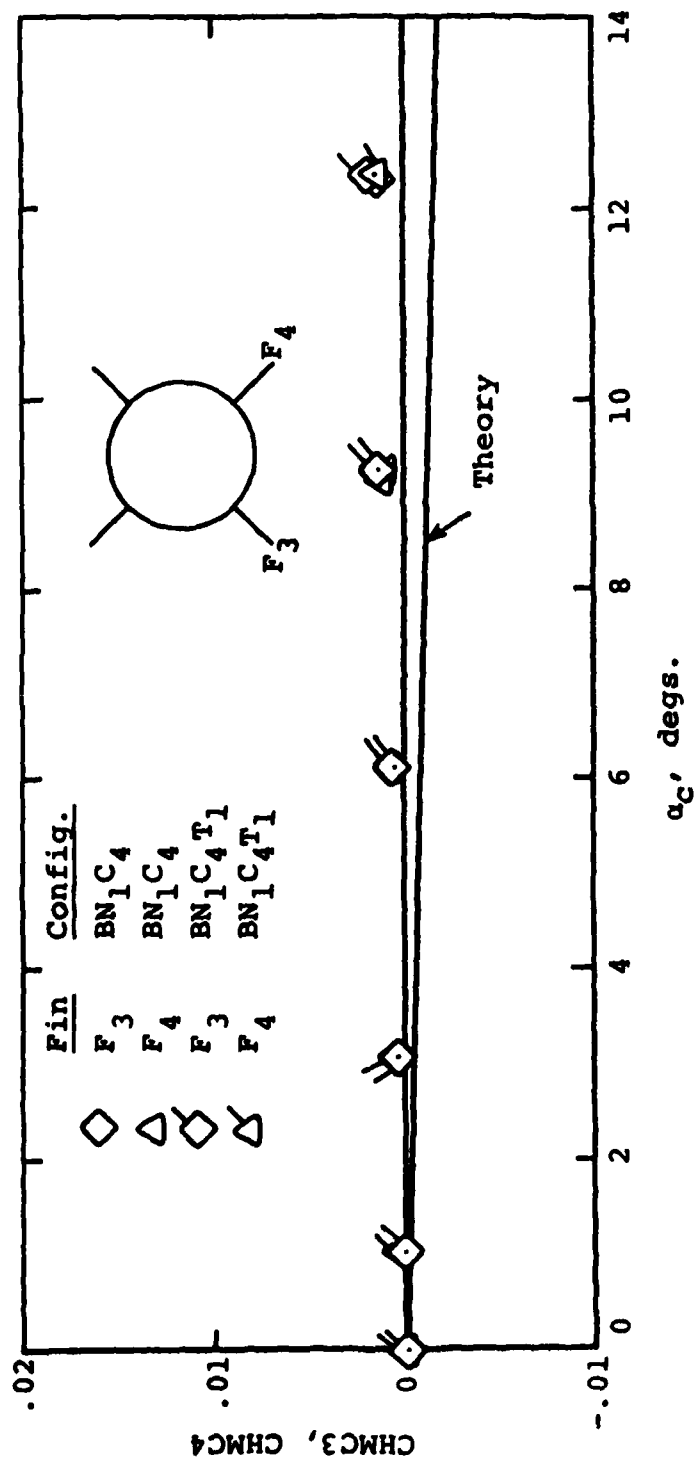
(b) F₃ & F₄

Figure 70.- Concluded.



(a) F₁ & F₂

Figure 71.- Canard C₄ fins hinge-moment coefficient;
 $M_{\infty} = 2.0$, $\phi_c = 45^\circ$, $\delta_1 = \delta_2 = \delta_3 = \delta_4 = 0^\circ$.



α_c' degs.

(b) F₃ & F₄

Figure 71.- Concluded.

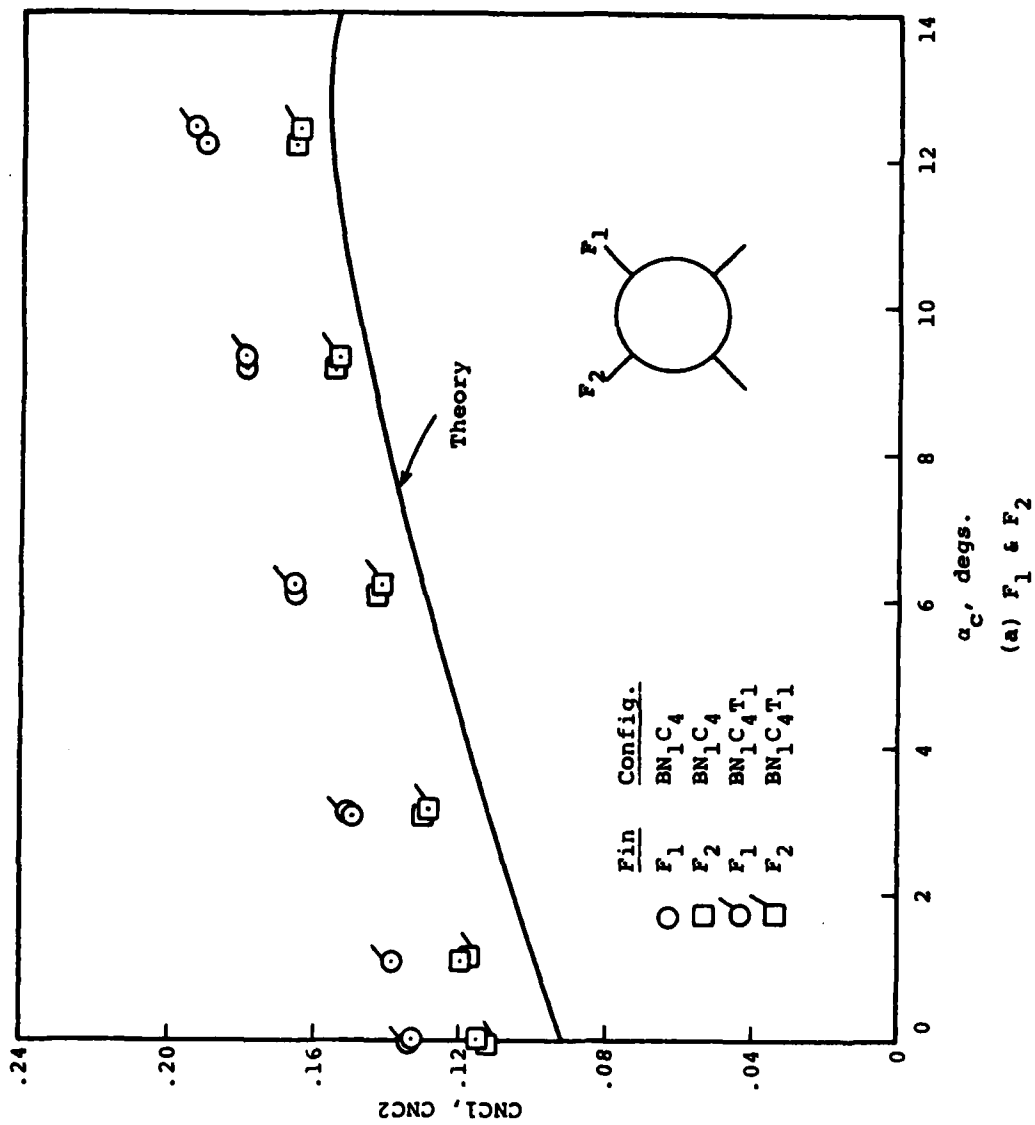
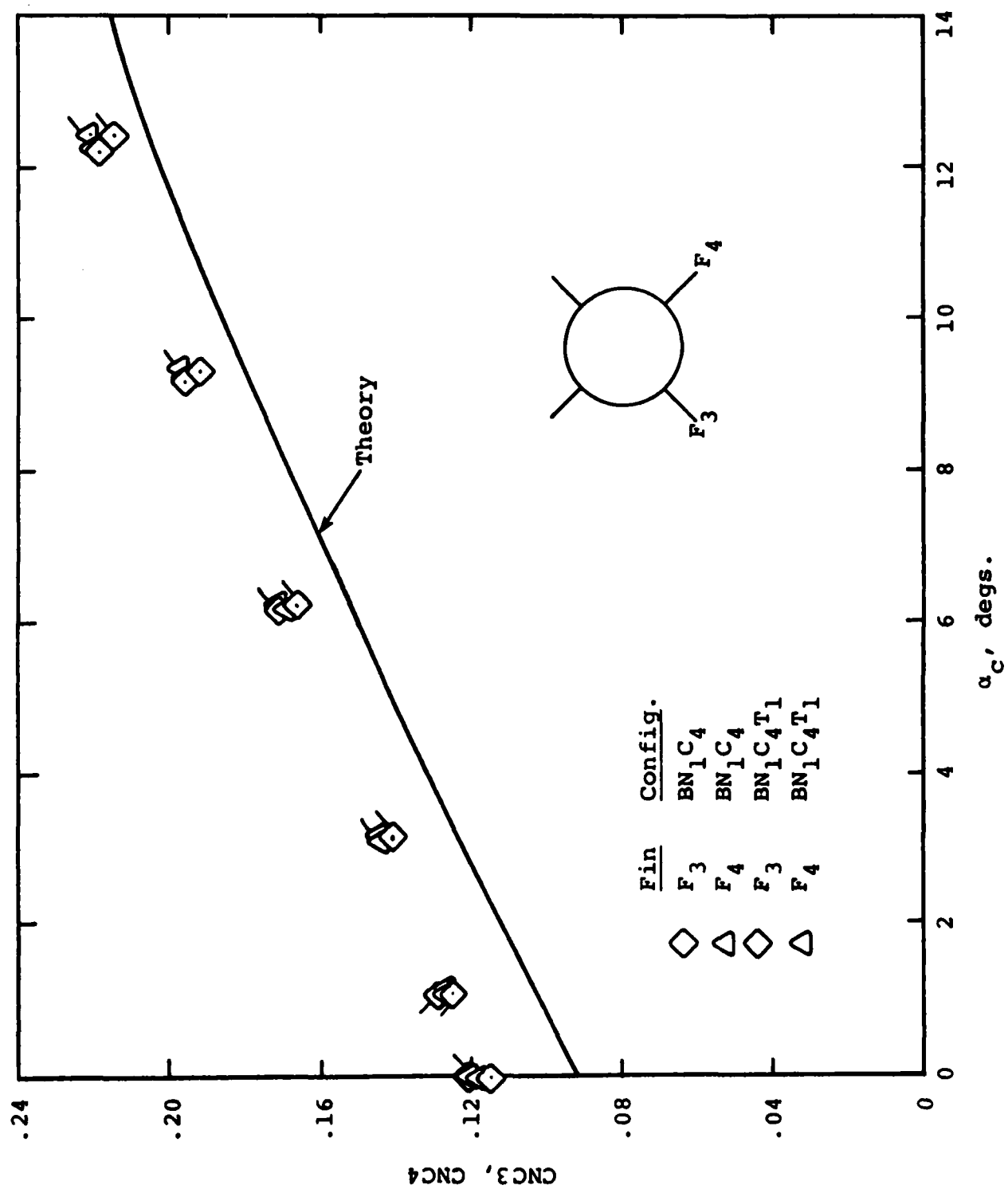


Figure 72.- Canard C4 fins normal-force coefficients;
 $M_\infty = 2.0$, $\phi_c = 45^\circ$, $\delta_1 = \delta_2 = \delta_3 = \delta_4 = 15^\circ$.



α_c' , degs.

(b) F_3 & F_4

Figure 72.- Concluded.

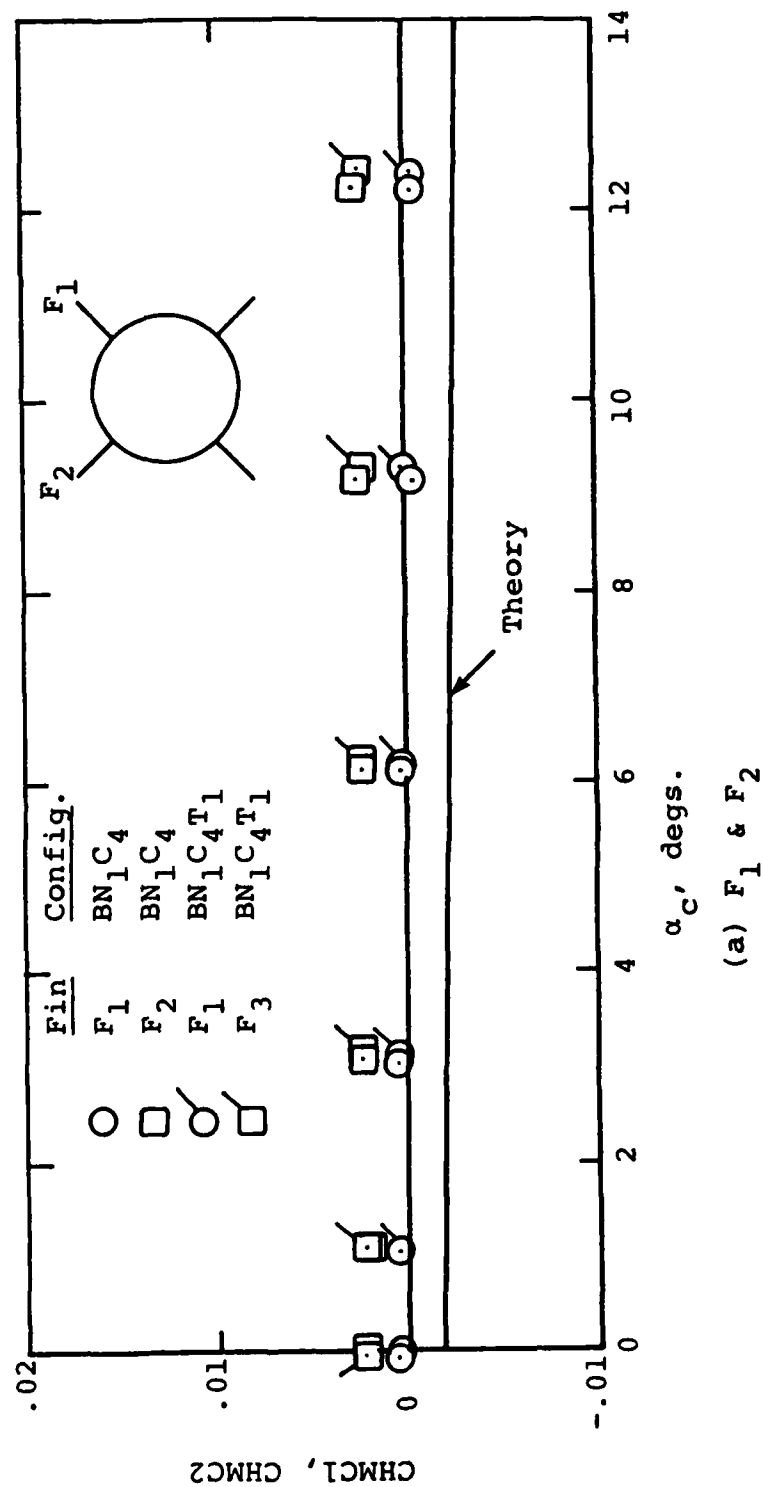
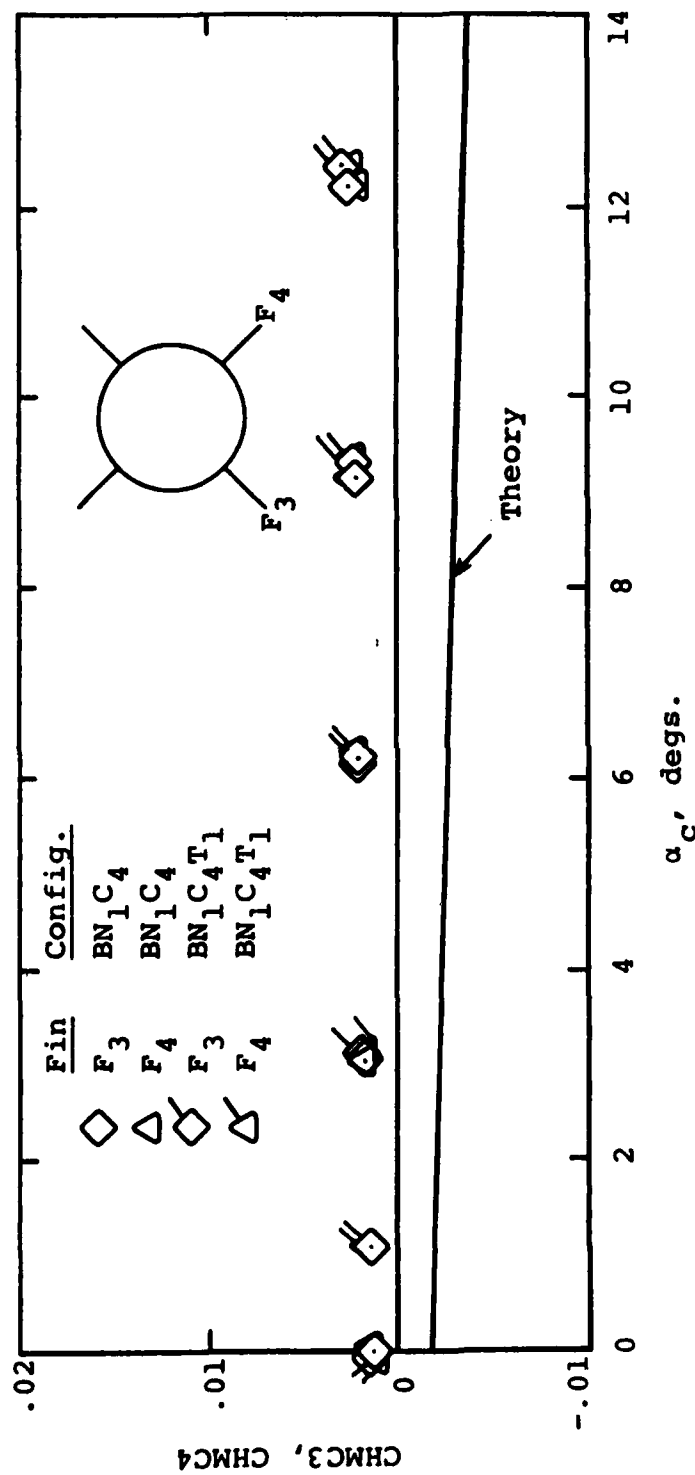


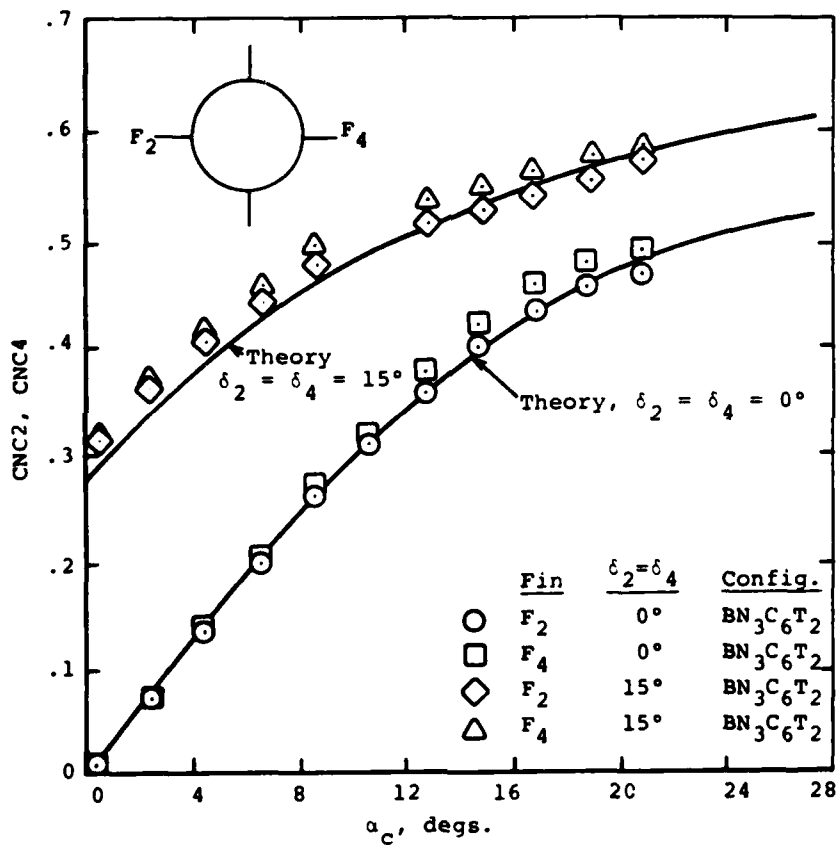
Figure 73.- Canard C4 fins hinge-moment coefficients;
 $M_\infty = 2.0$, $\phi_c = 45^\circ$, $\delta_1 = \delta_2 = \delta_3 = \delta_4 = 15^\circ$.



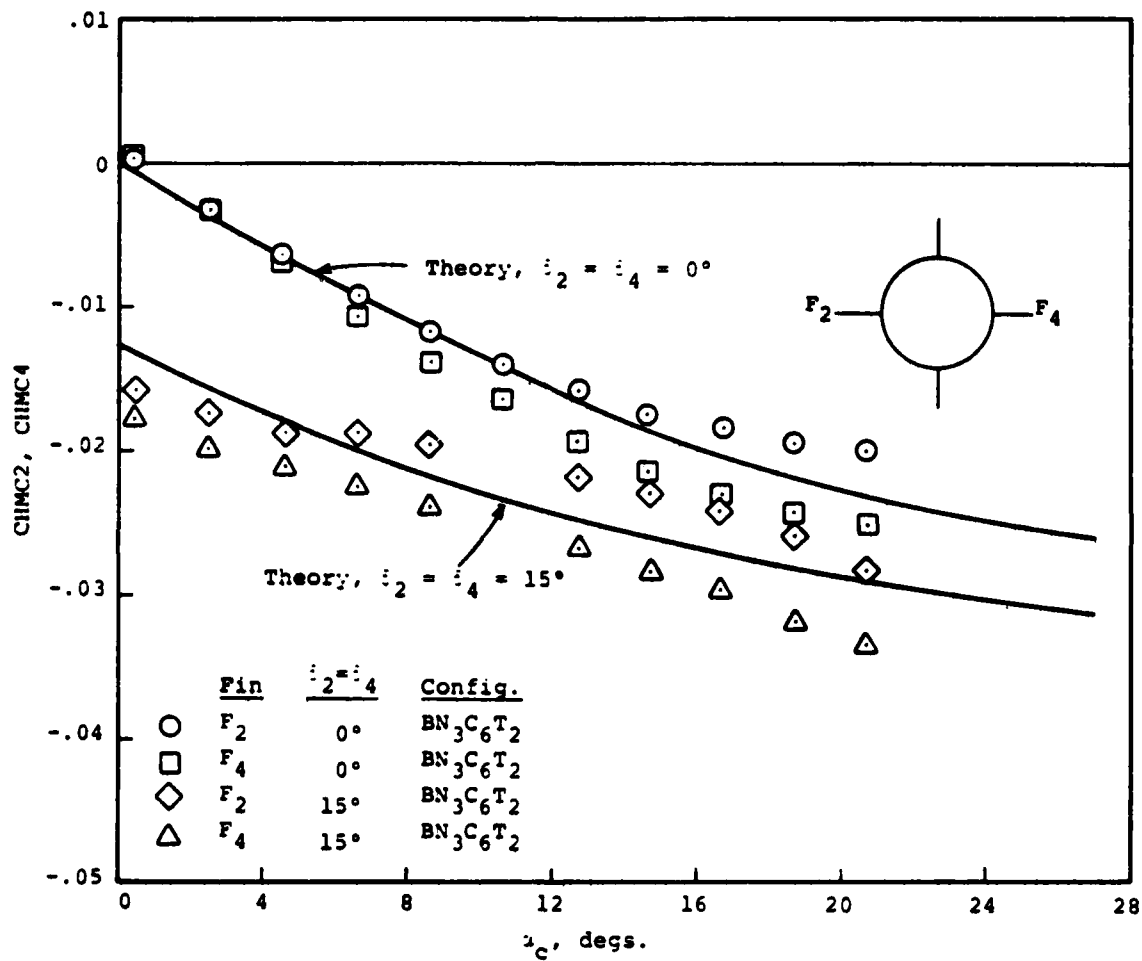
$\alpha_c', \text{ degs.}$

(b) F_3 & F_4

Figure 73.- Concluded.

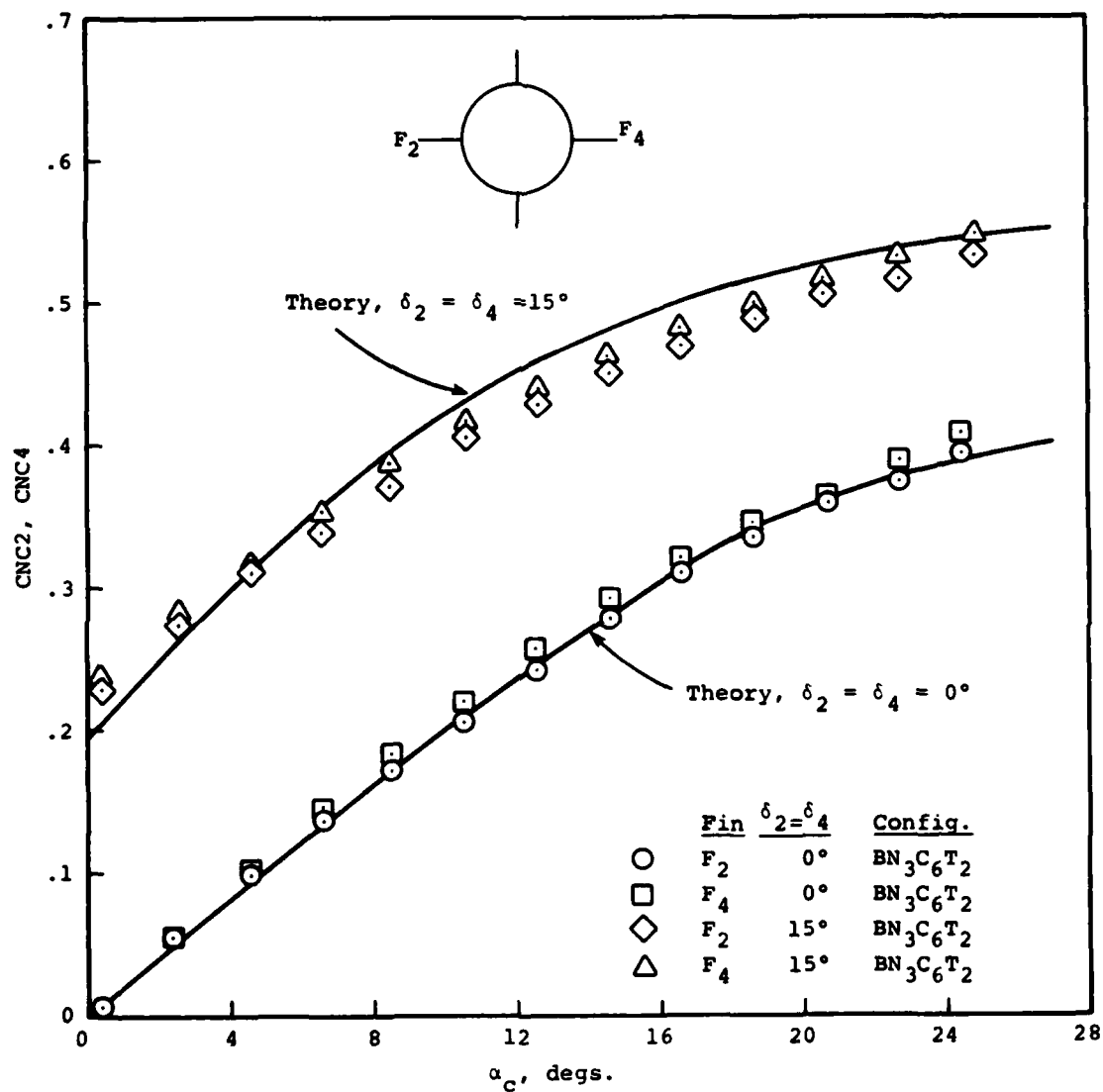


(a) Normal-force coefficient, $\delta_2 = \delta_4 = 0^\circ$ and 15°
 Figure 74.- Characteristics of canard C₆; $M_\infty = 1.3$, $\phi_c = 0^\circ$,
 $\delta_1 = \delta_3 = 0^\circ$.



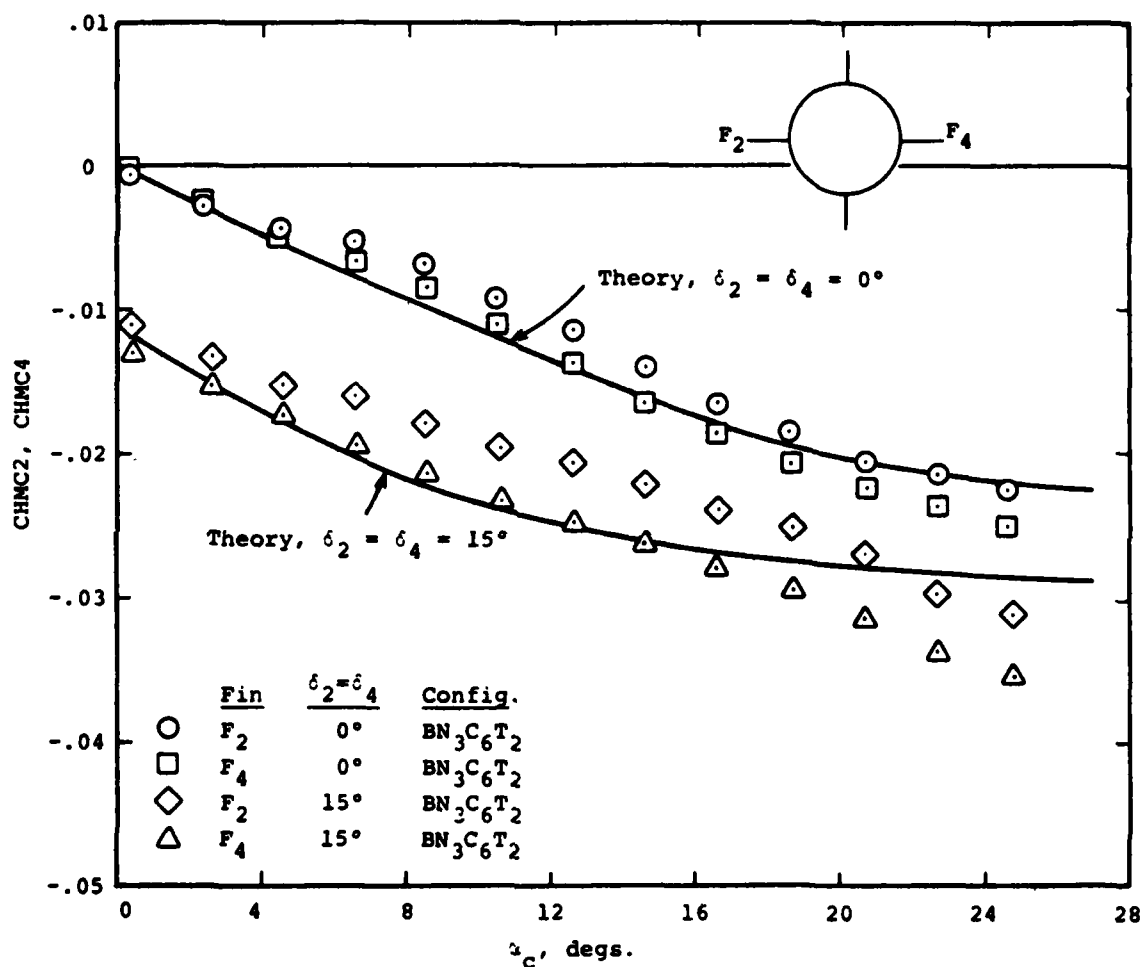
(b) Hinge-moment coefficient, $i_2 = i_4 = 0^\circ$ and 15°

Figure 74.- Concluded.



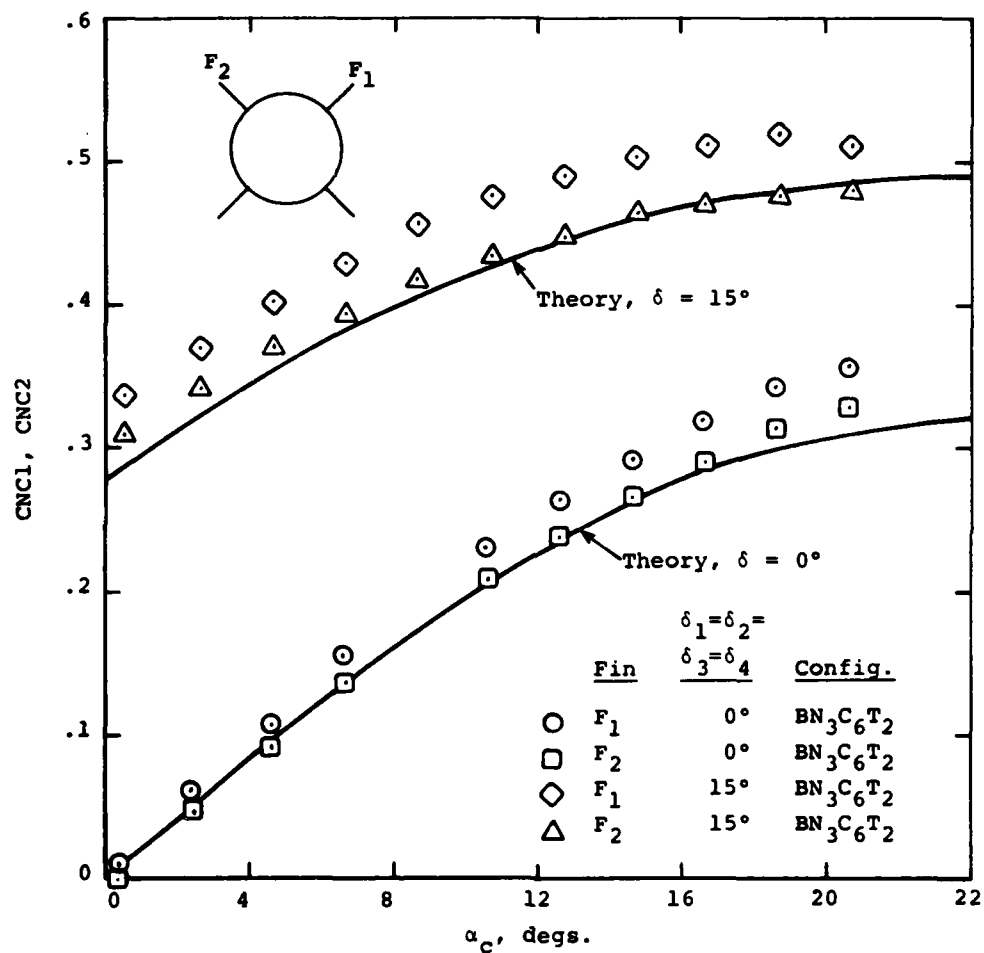
(a) Normal-force coefficient, $\delta_2 = \delta_4 = 0^\circ$ and 15°

Figure 75.- Characteristics of canard C₆; $M_\infty = 1.75$, $\phi_c = 0^\circ$,
 $\delta_1 = \delta_3 = 0^\circ$.



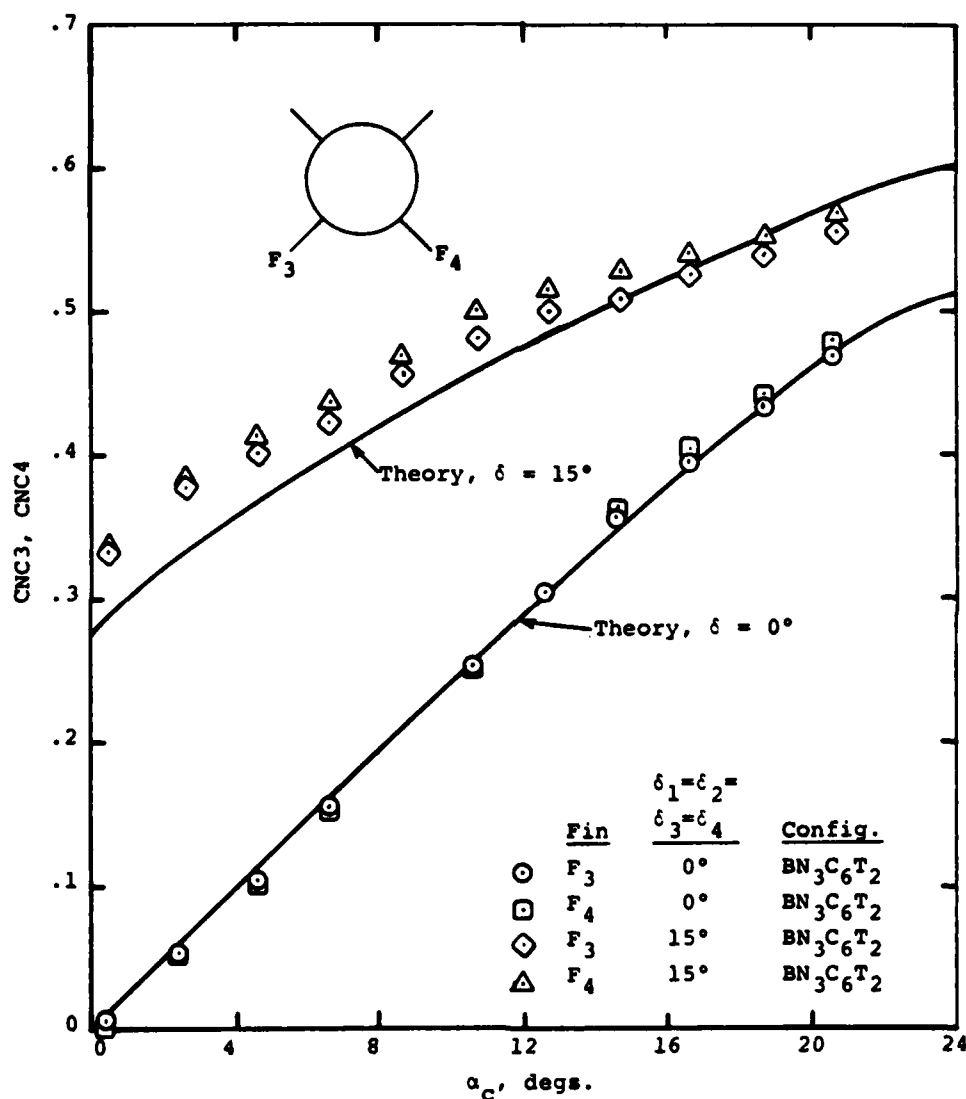
(b) Hinge-moment coefficient, $\delta_2 = \delta_4 = 0^\circ$ and 15°

Figure 75.- Concluded.



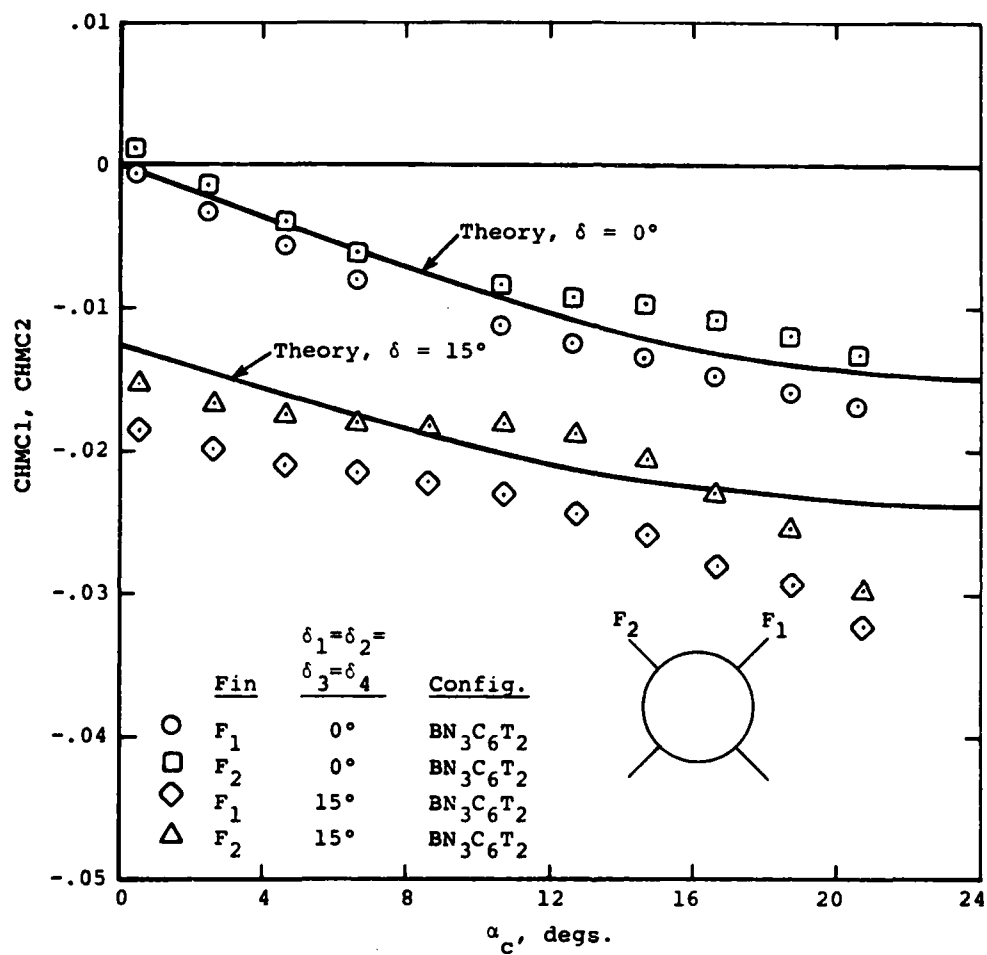
(a) Normal-force coefficient, fin 1 and fin 2

Figure 76.- Characteristics of canard C_6 ; $M_\infty = 1.3$, $\phi_c = 45^\circ$.



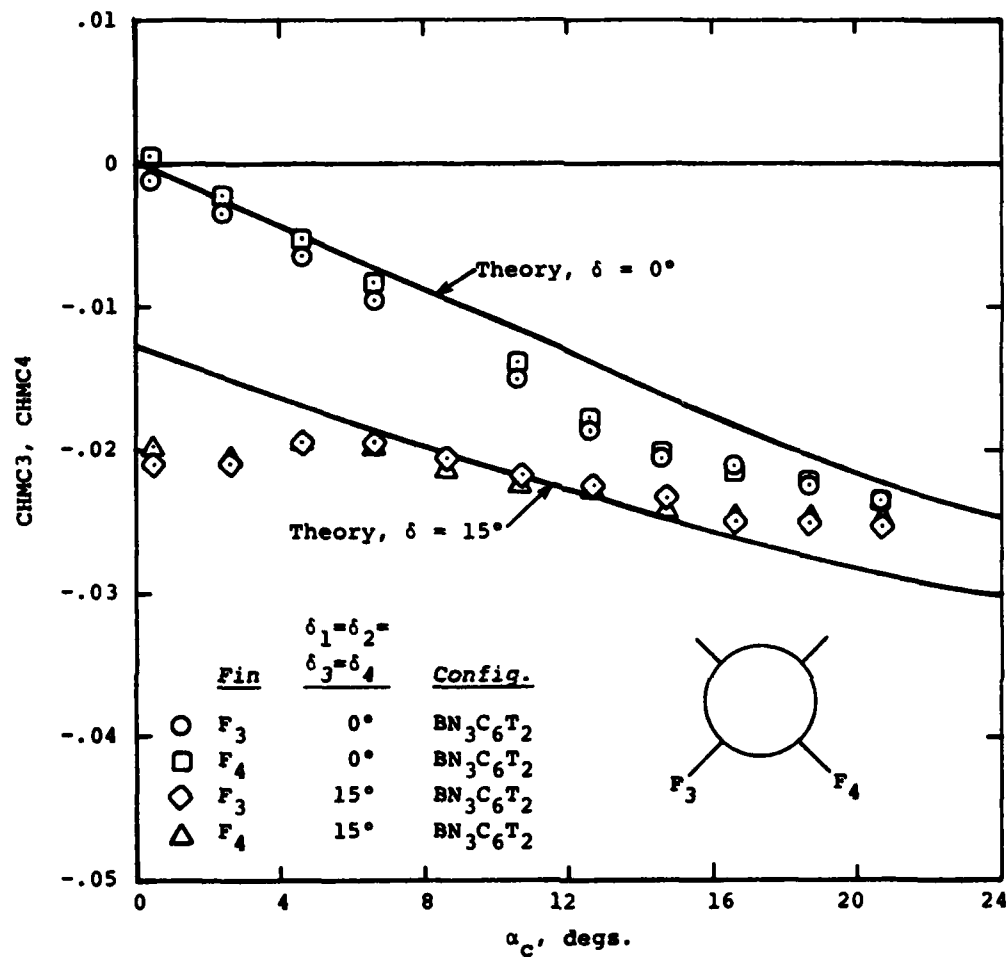
(b) Normal-force coefficient, fin 3 and fin 4

Figure 76.- Continued.



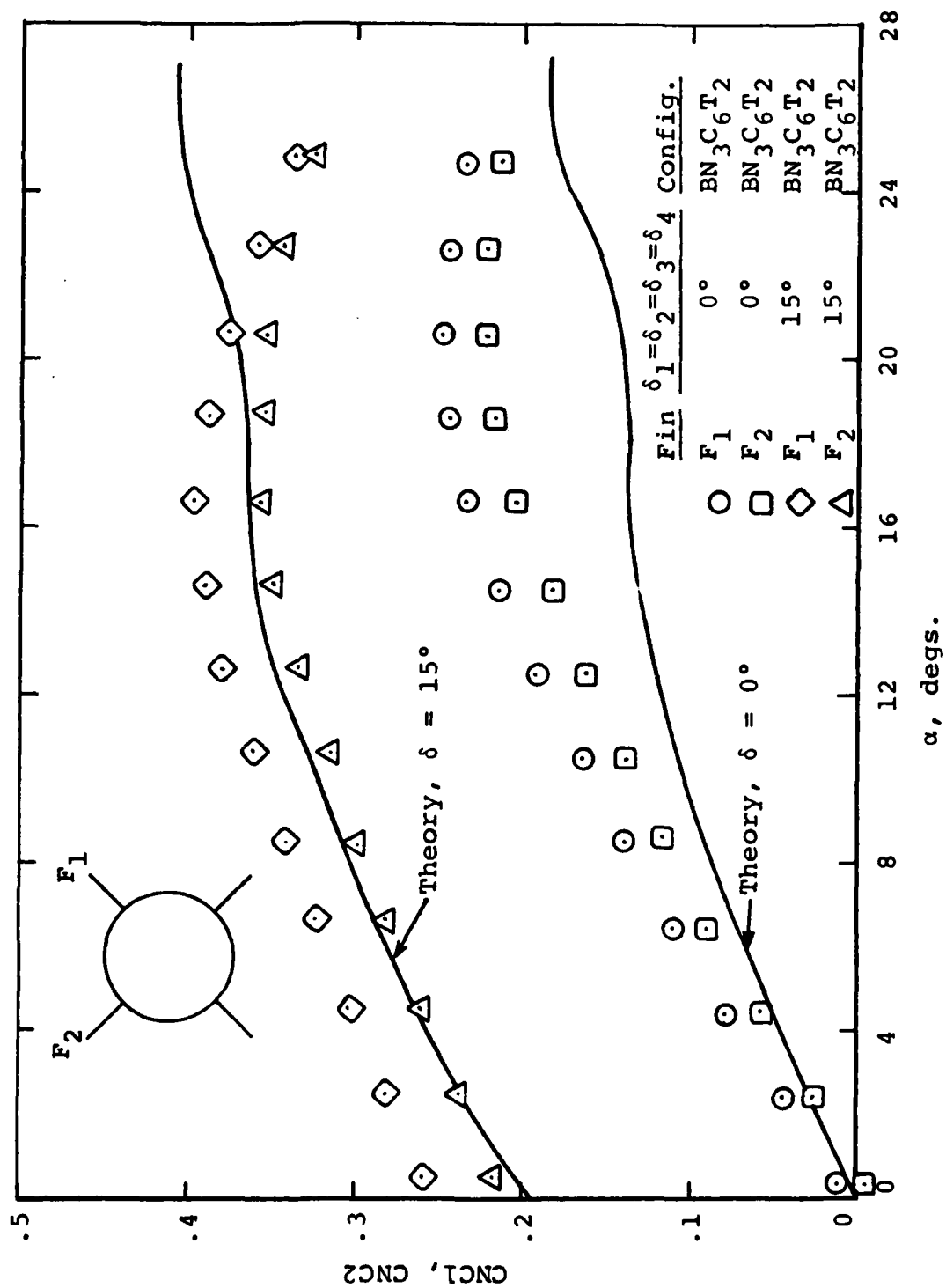
(c) Hinge-moment coefficient, fin 1 and fin 2

Figure 76.- Continued.



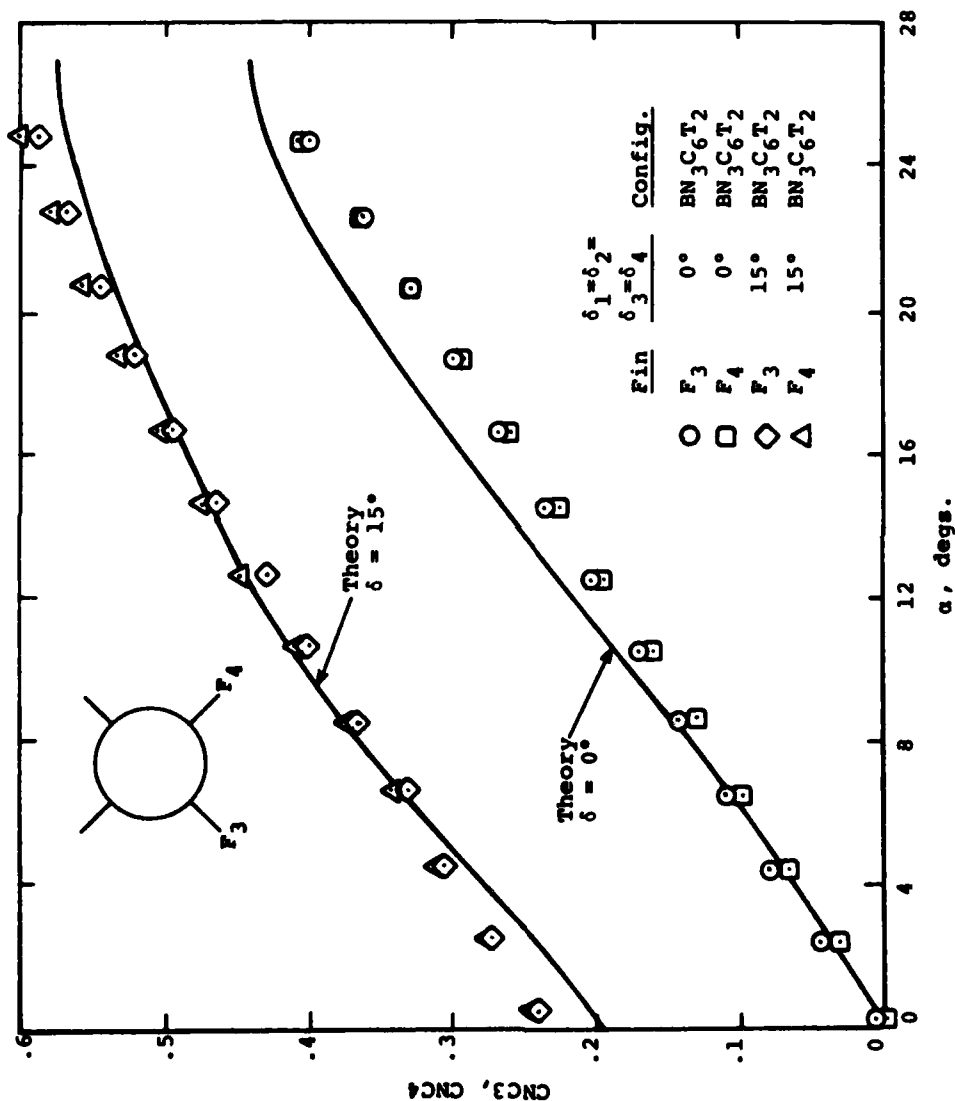
(d) Hinge-moment coefficient, fin 3 and fin 4

Figure 76.- Concluded.



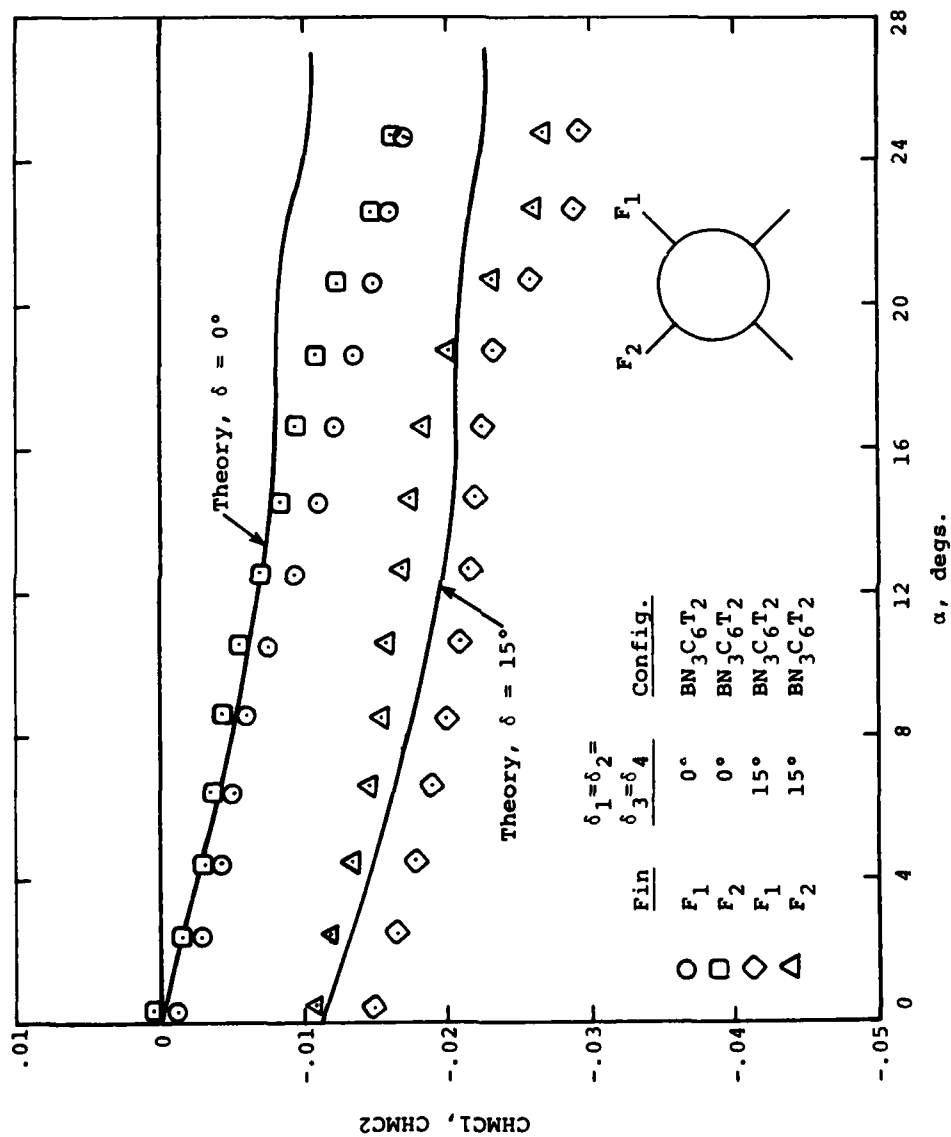
(a) Normal-force coefficient, fin 1 and fin 2

Figure 77.- Characteristics of canard C_6 ; $M_\infty = 1.75$, $\phi_c = 45^\circ$.



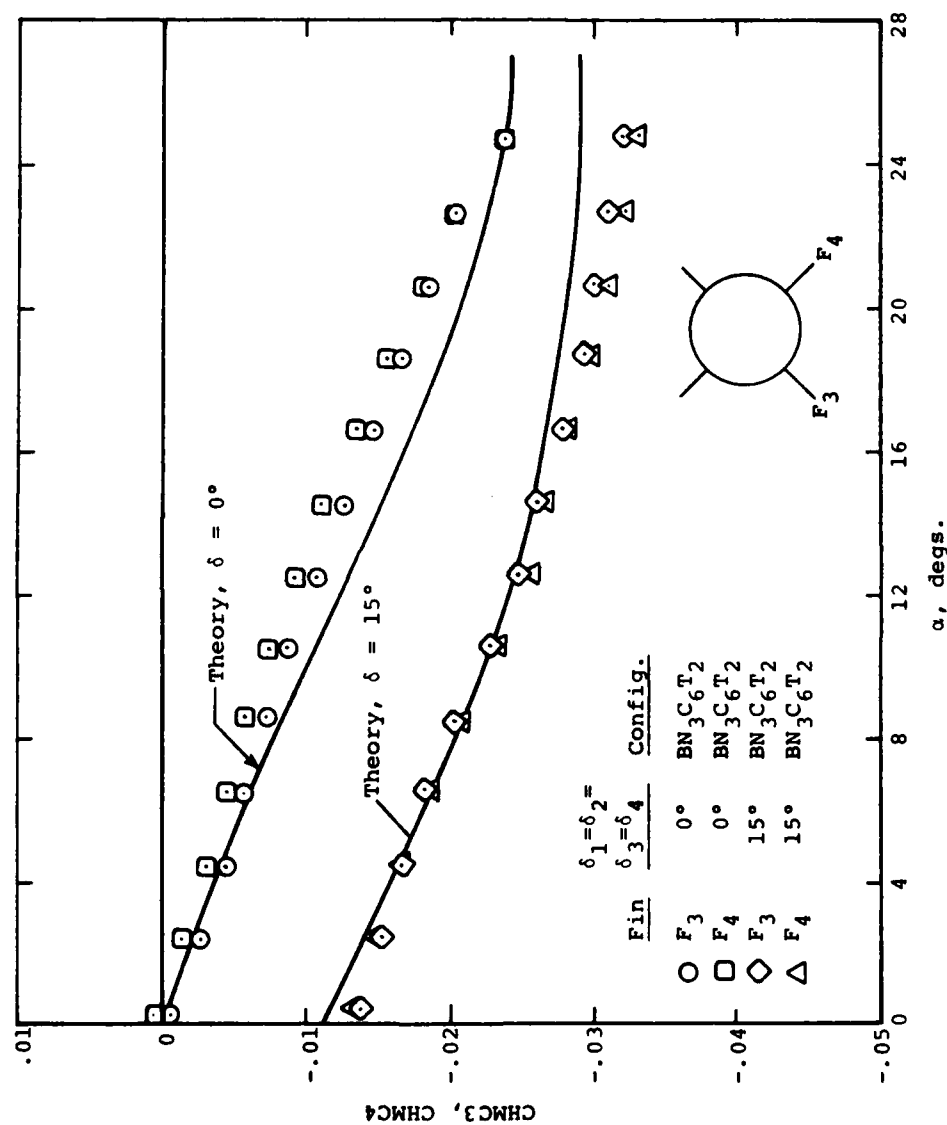
(b) Normal-force coefficient, fin 3 and fin 4

Figure 77.- Continued



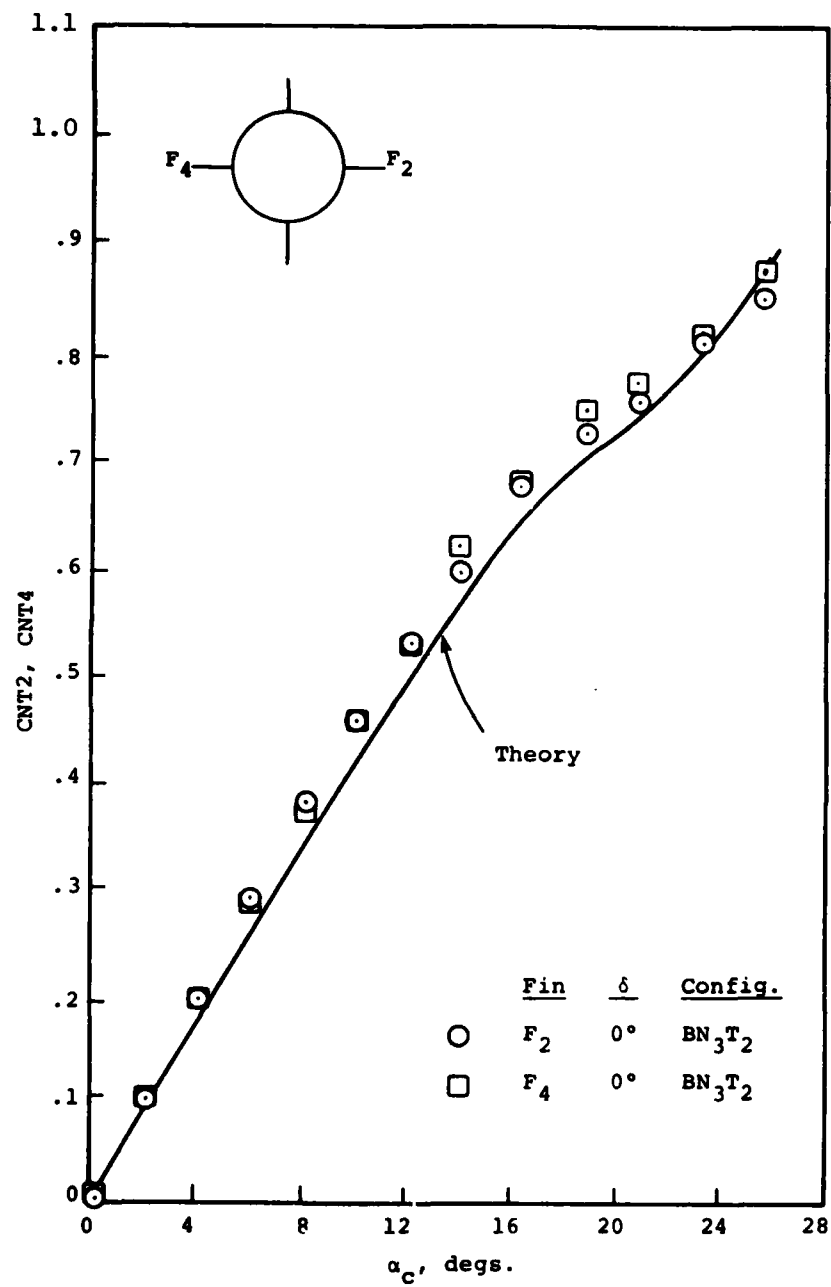
(c) Hinge-moment coefficient, fin 1 and fin 2

Figure 77.- Continued.



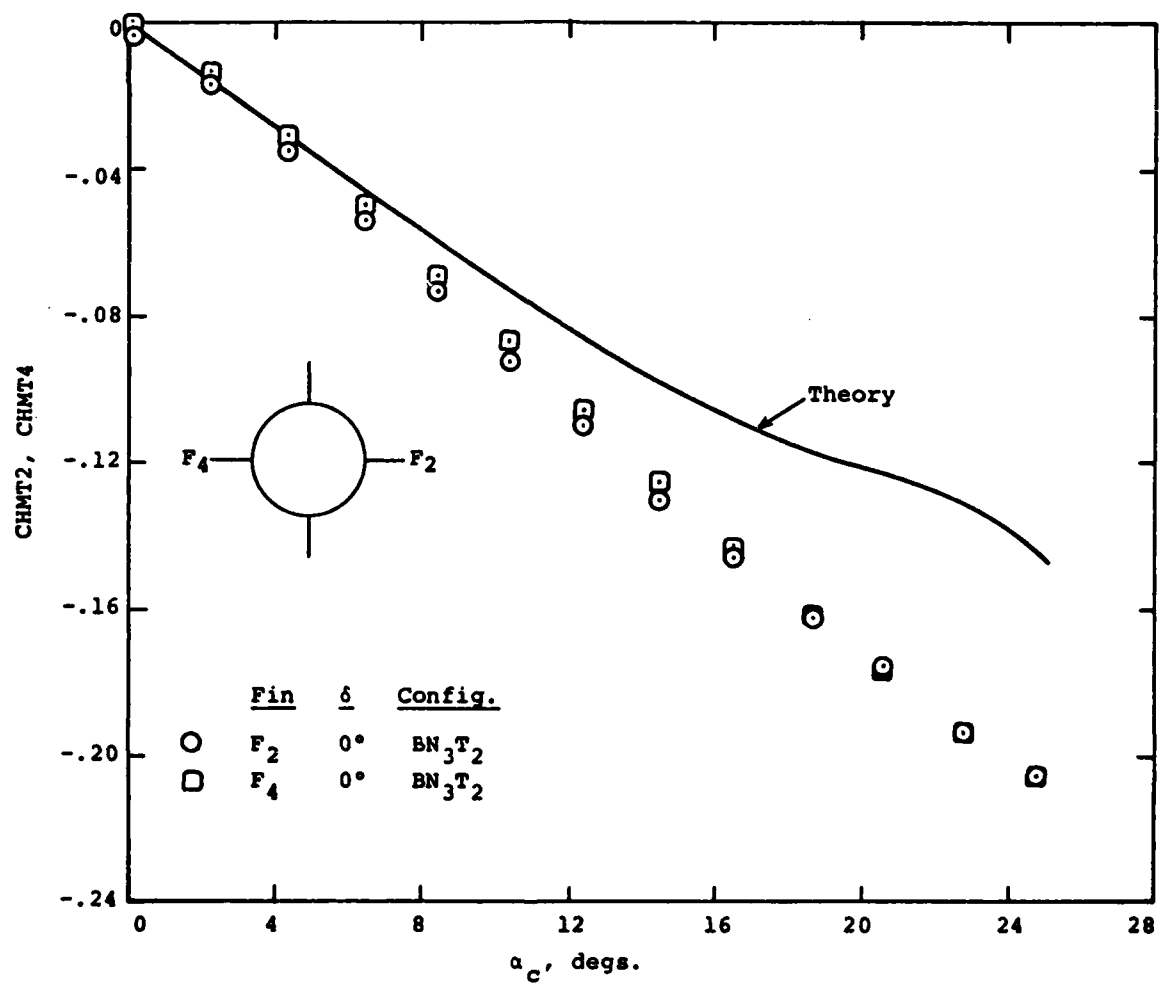
(d) Hinge-moment coefficient, fin 3 and fin 4

Figure 77.- Concluded.



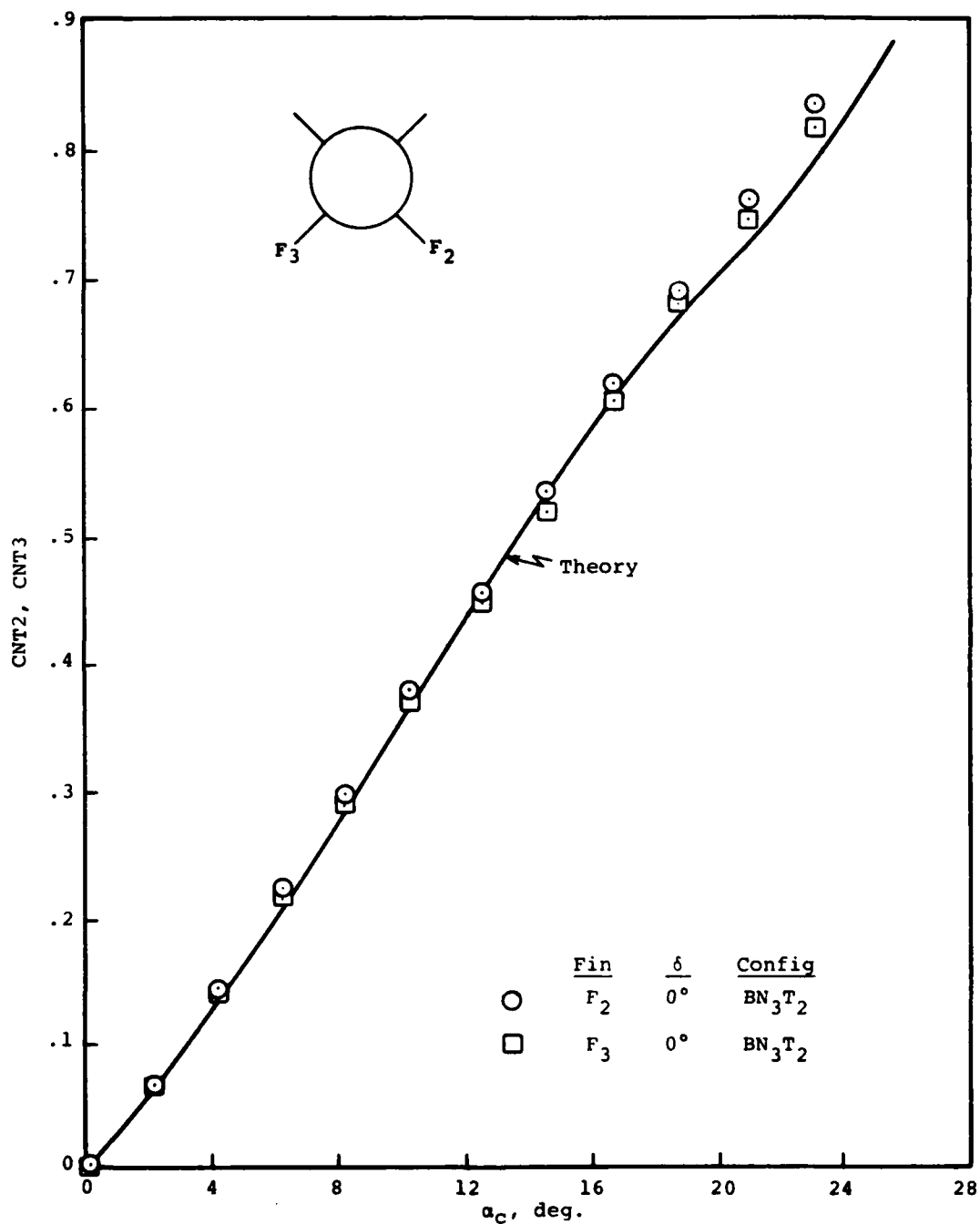
(a) Normal-force coefficient

Figure 78.- Characteristics of tail T_2 in the presence of the body; $M_\infty = 1.75$, $\phi_c = 0^\circ$.

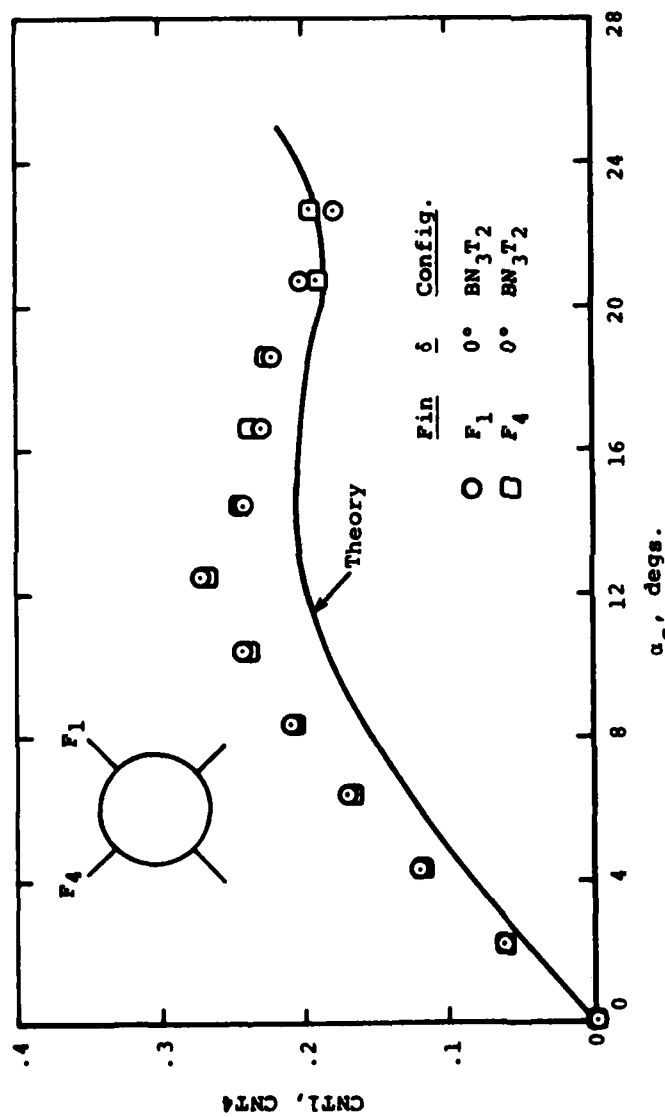


(b) Hinge-moment coefficient

Figure 78.- Concluded.

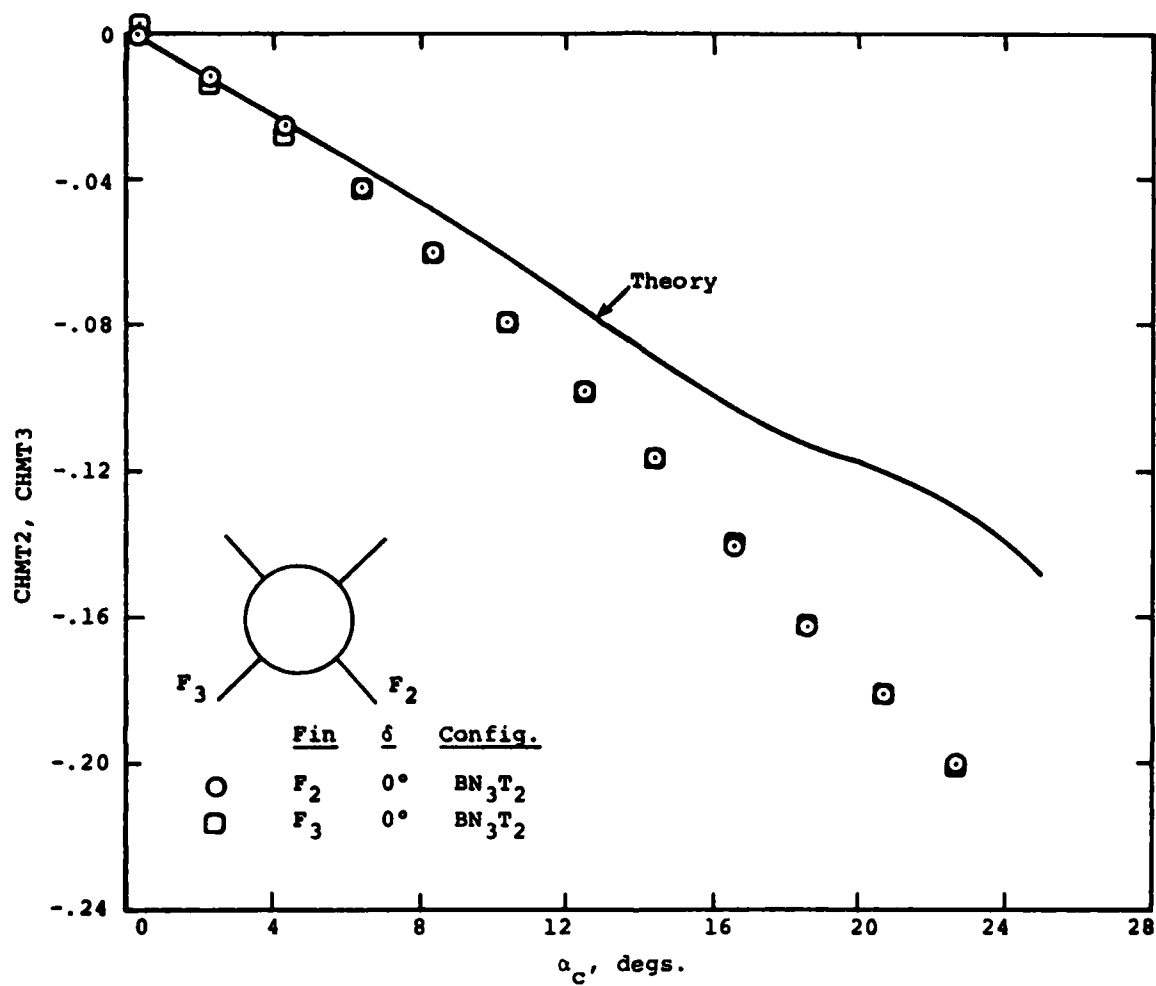


(a) Normal-force coefficient, fins 2 and 3
 Figure 79.- Characteristics of tail T_2 in the presence
 of the body; $M_\infty = 1.75$, $\phi_c = 45^\circ$



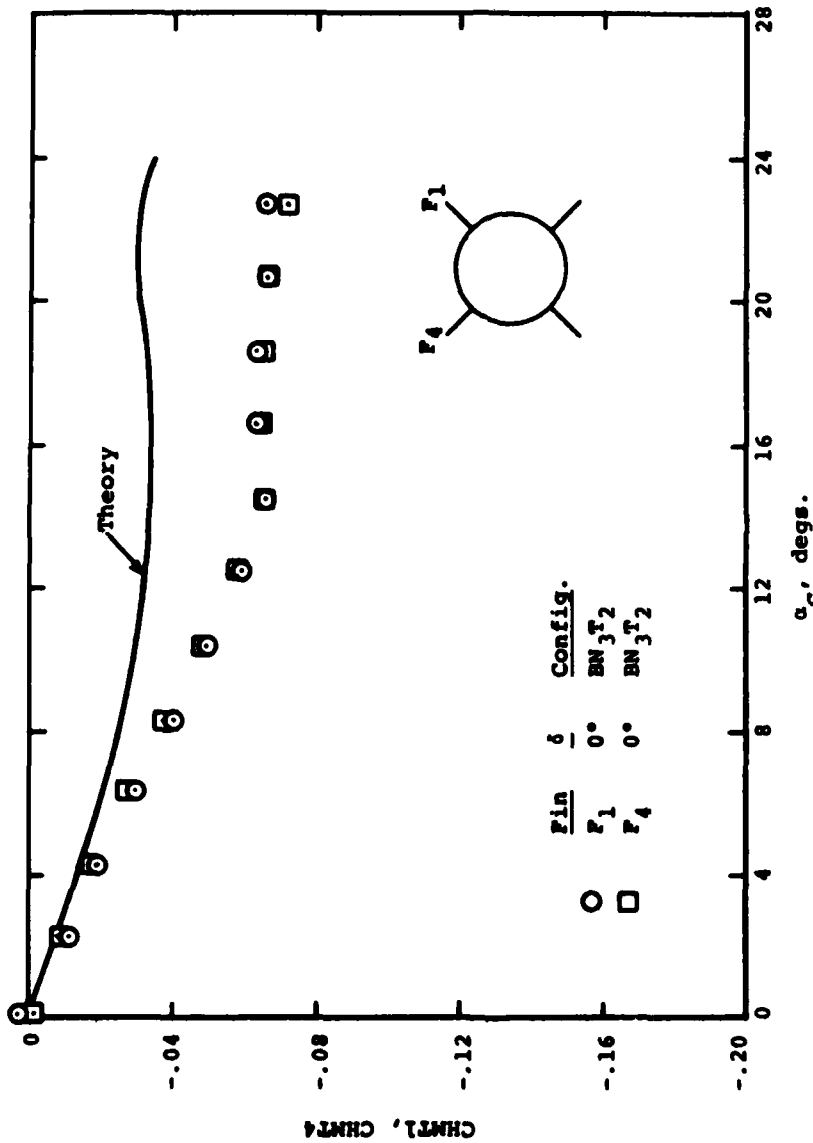
(b) Normal-force coefficient, fins 1 and 4

Figure 79.- Continued.



(c) Hinge-moment coefficients, fins 2 and 3

Figure 79.- Continued.



(d) Hinge-moment coefficient, fins 1 and 4

Figure 79.- Concluded.

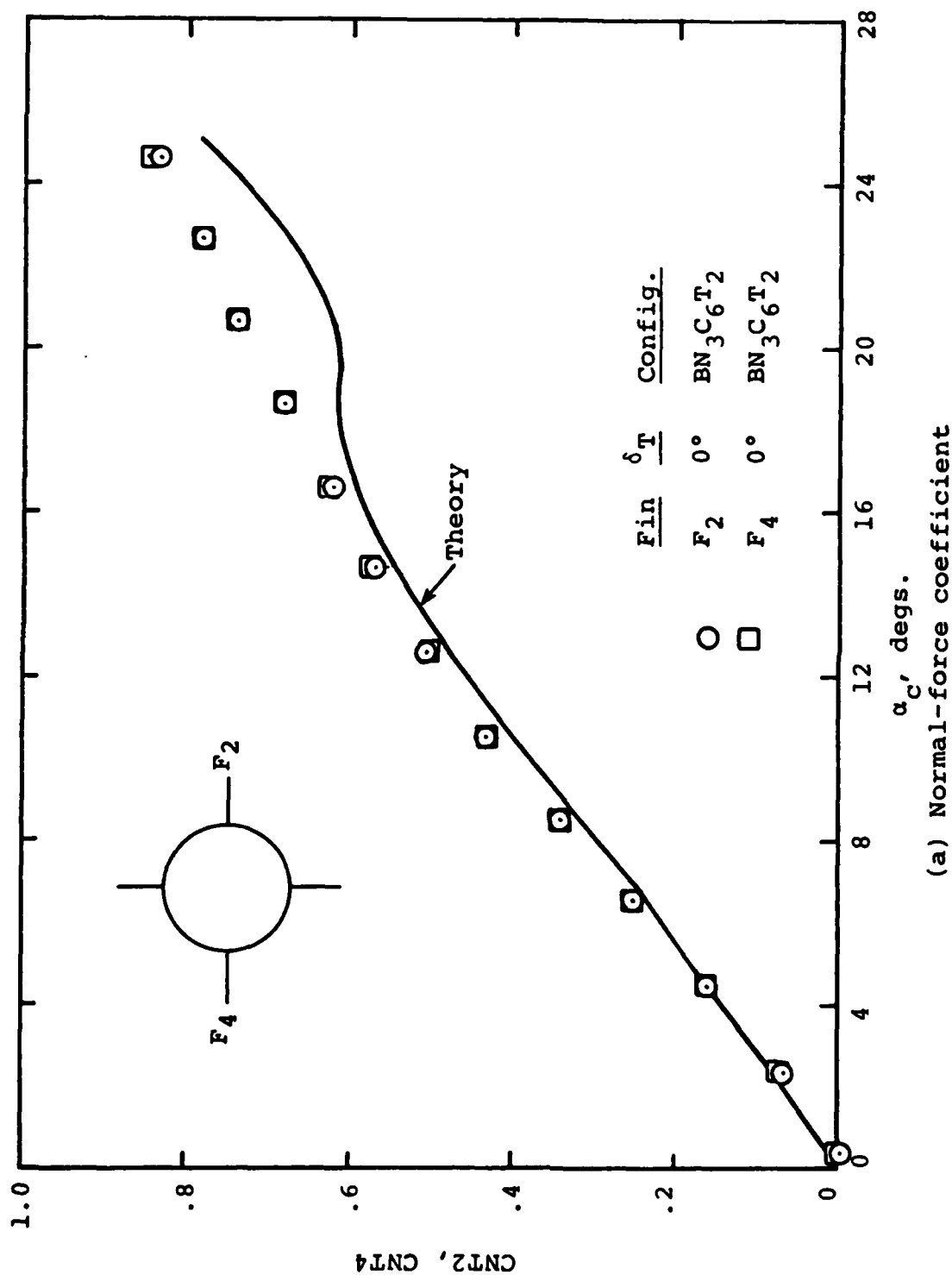
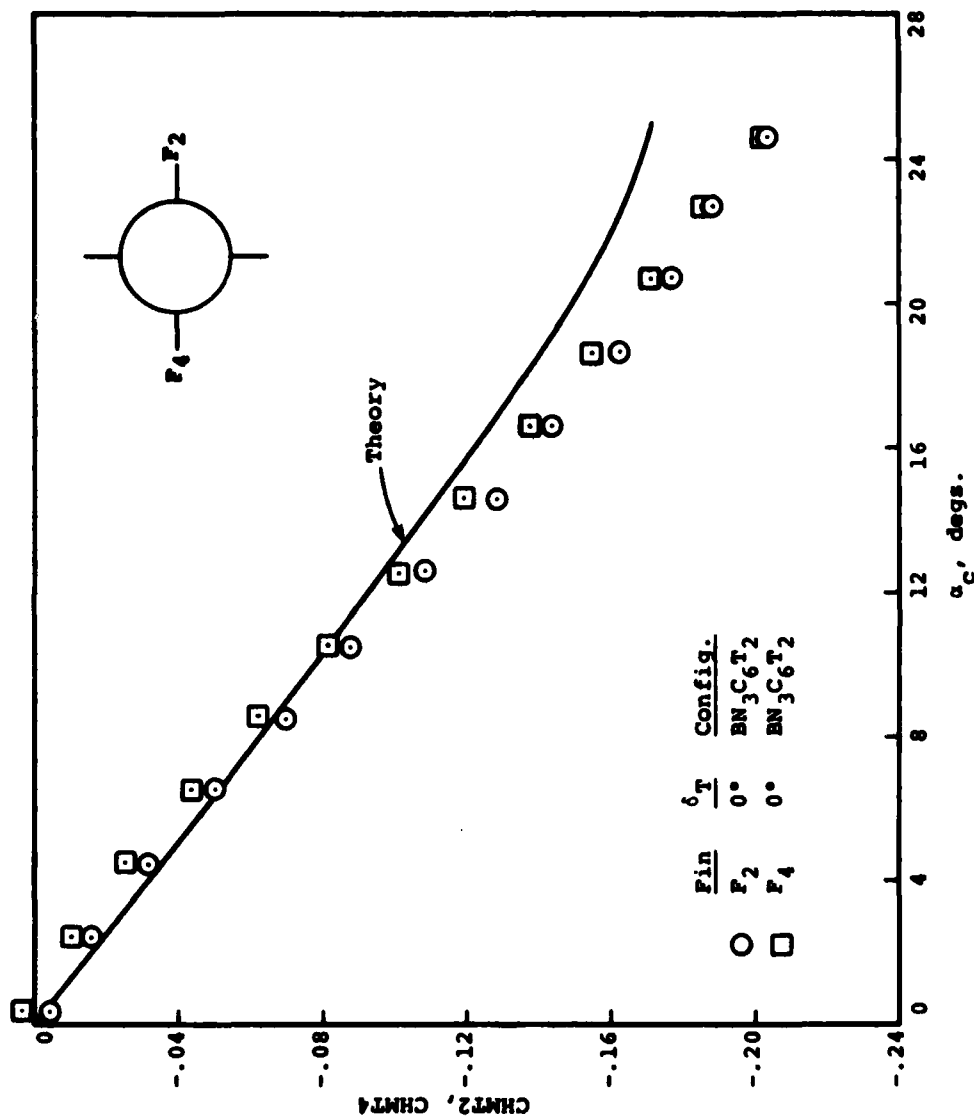


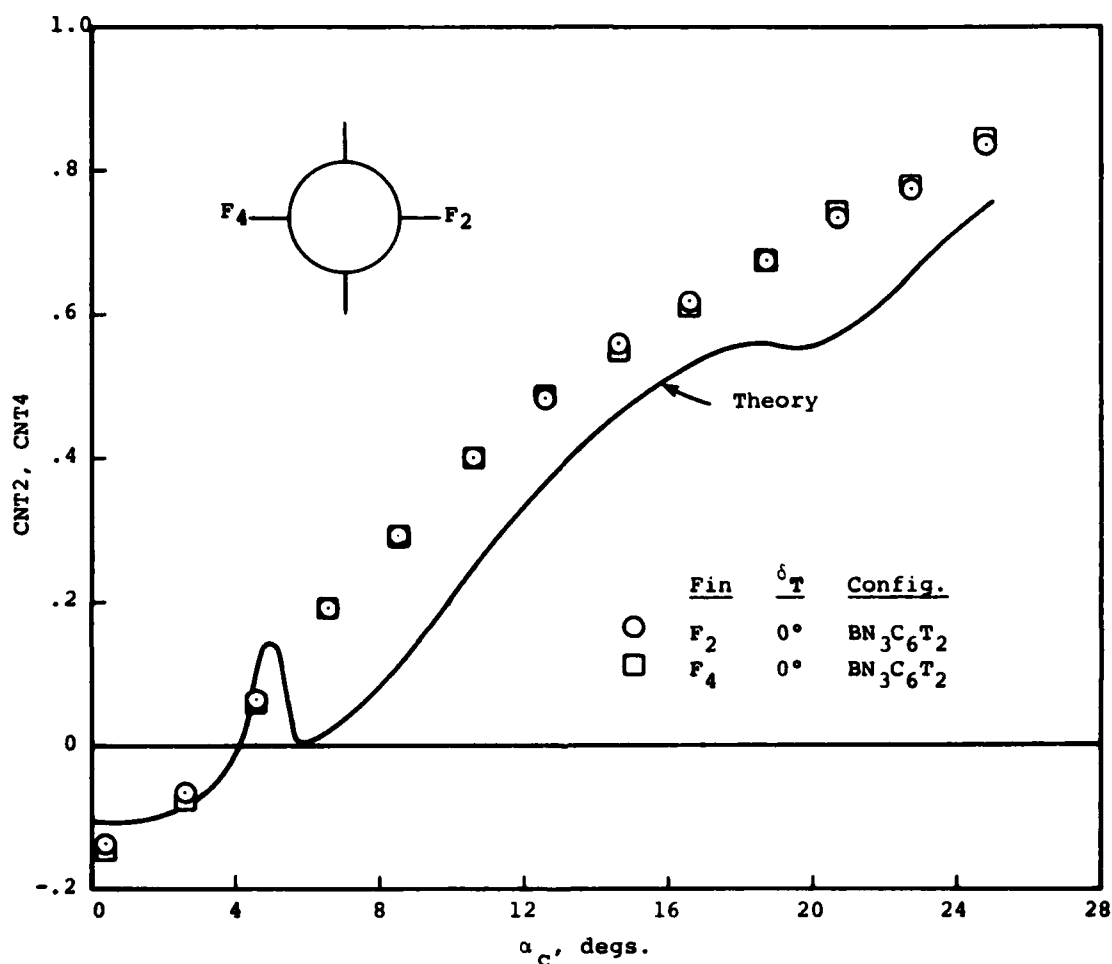
Figure 80.- Characteristics of tail T_2 in presence of canard
 C_6 ; $M_\infty = 1.75$, $\phi_c = 0^\circ$, $\delta_{1c} = \delta_2 = \delta_{3c} = \delta_{4c} = 0^\circ$.

(a) Normal-force coefficient



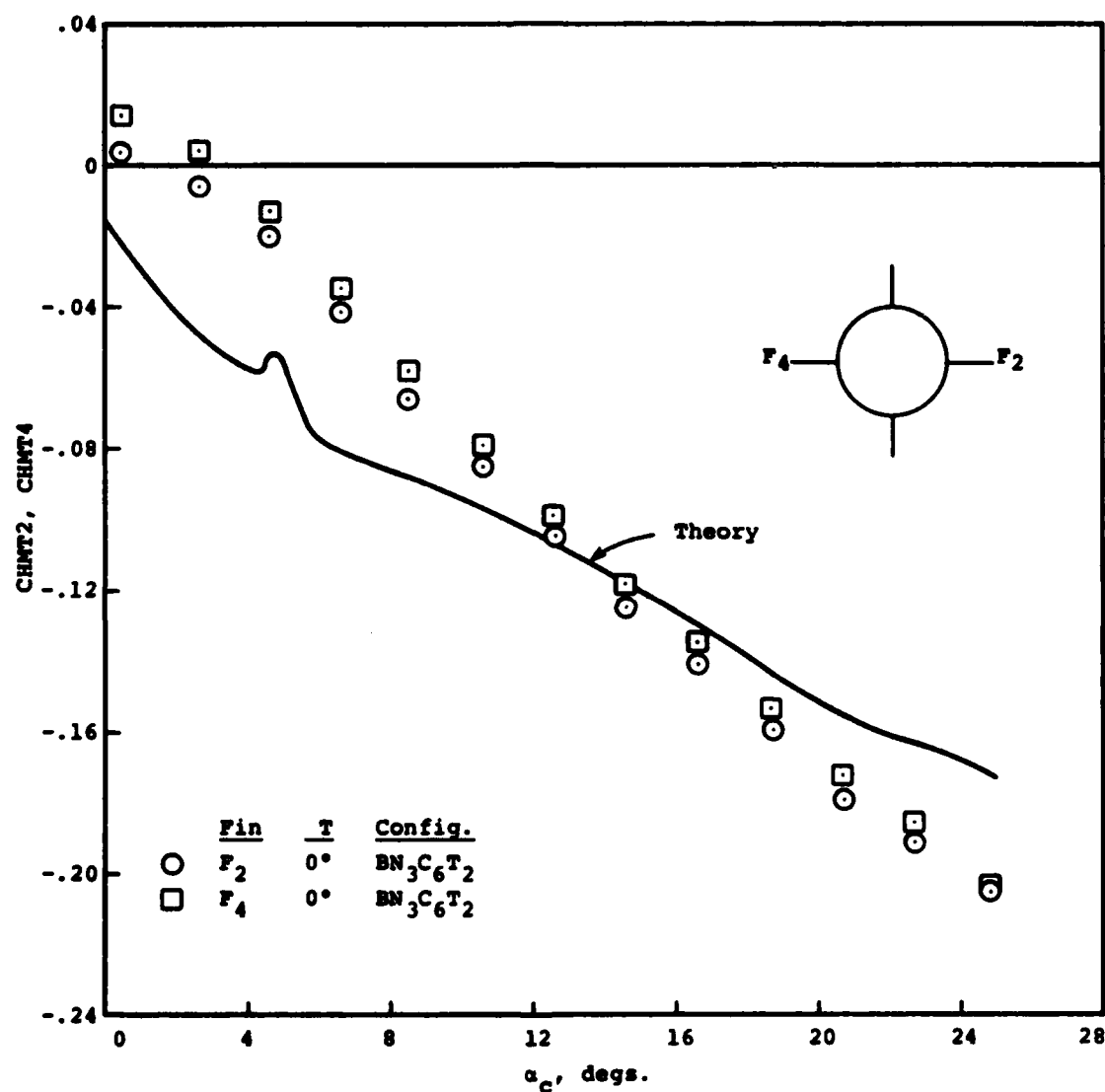
(b) Hinge-moment coefficient

Figure 80.- Concluded.



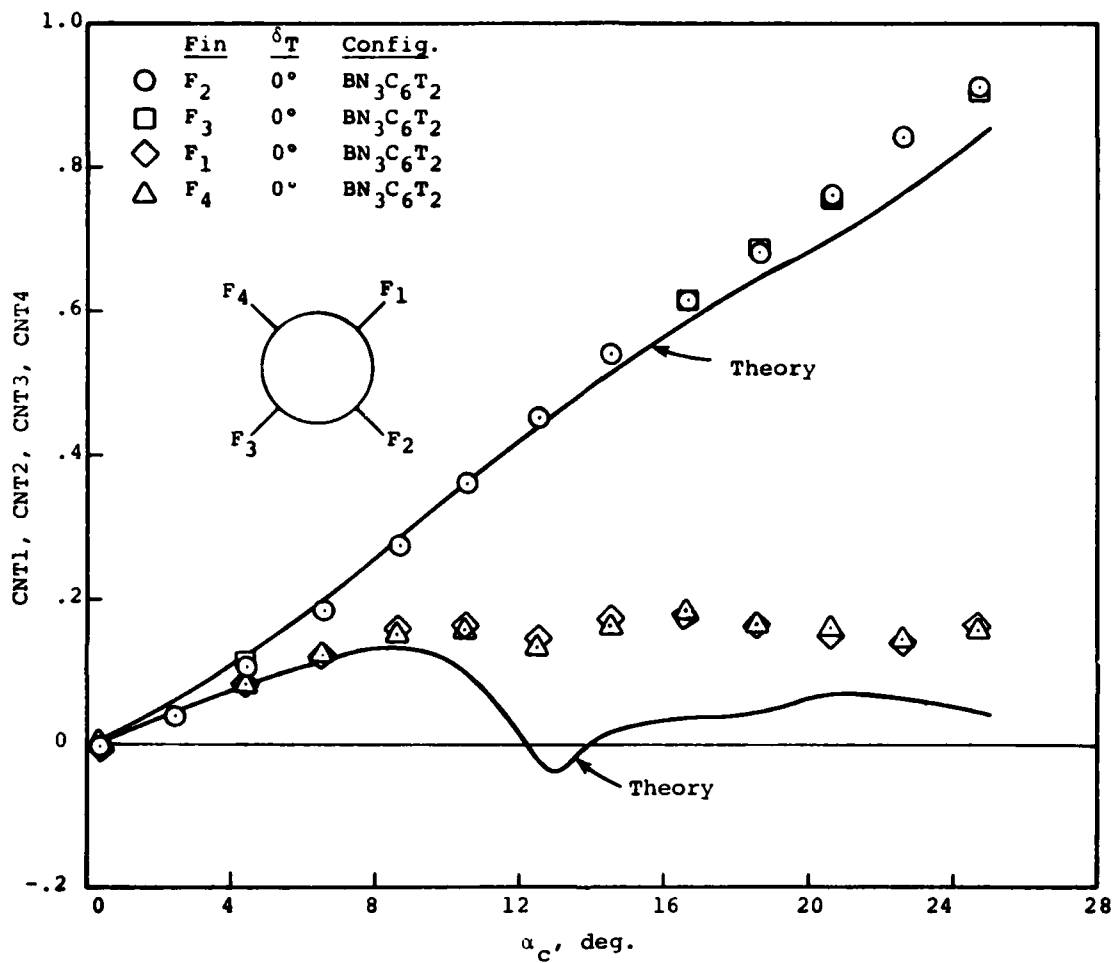
(a) Normal-force coefficient

Figure 81- Characteristics of tail T_2 in presence of canard C_6 ; $M_\infty = 1.75$, $\phi_c = 0^\circ$, $\delta_{1c} = \delta_{3c} = \delta_{2c} = \delta_{4c} = 15^\circ$.



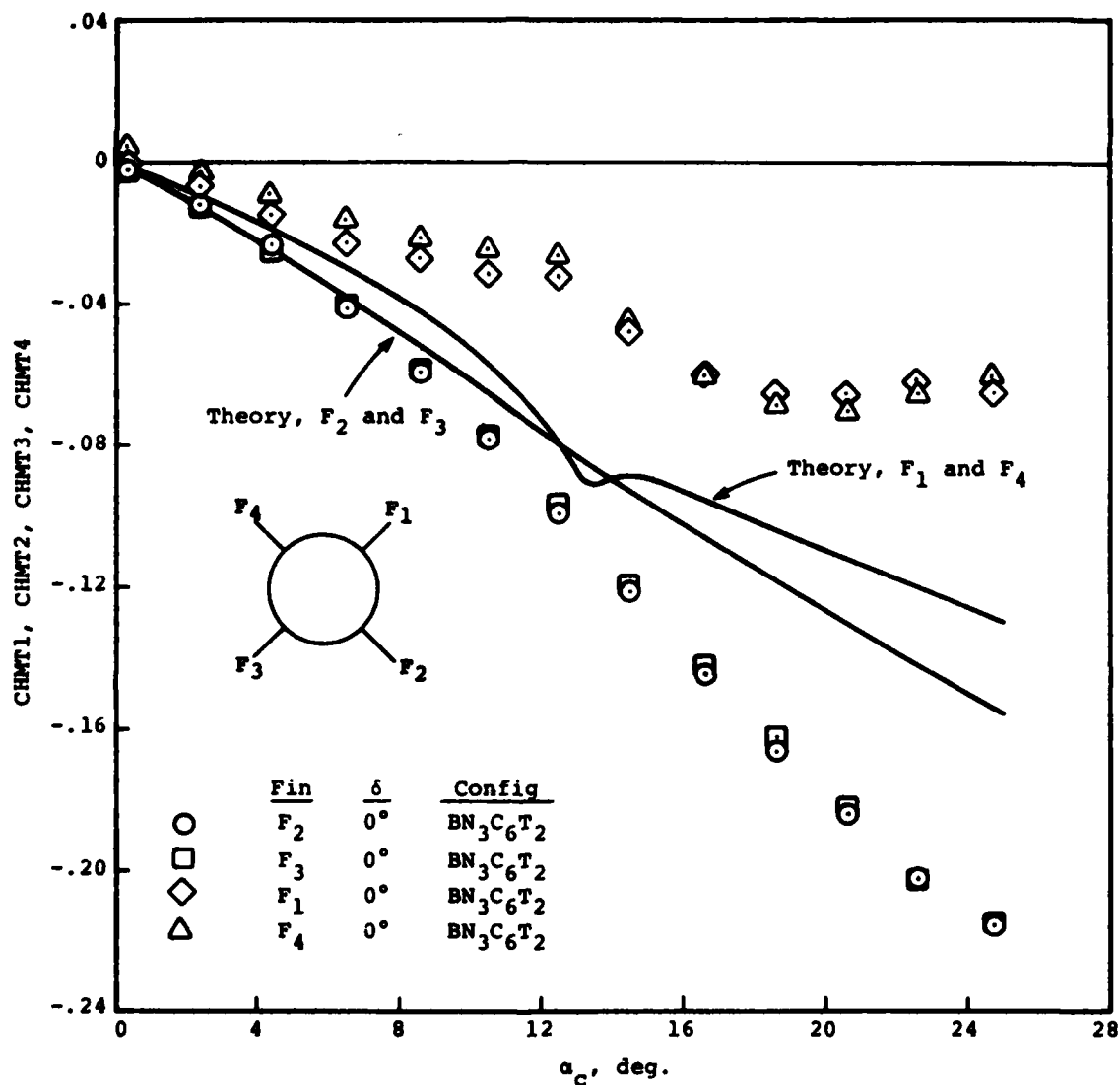
(b) Hinge-moment coefficient

Figure 81.- Concluded.



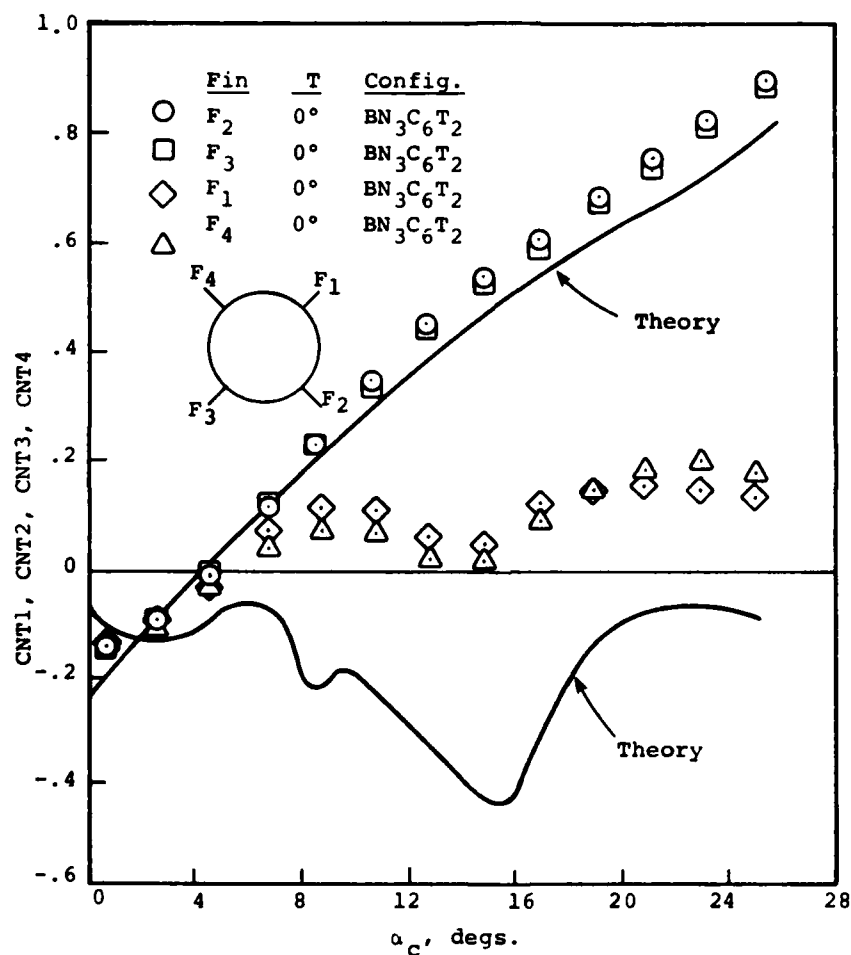
(a) Normal-force coefficient

Figure 82.- Characteristics of tail T₂ in presence of canard C₆; $M_\infty = 1.75$, $\phi_c = 45^\circ$, $\delta_{1c} = \delta_{2c} = \delta_{3c} = \delta_{4c} = 0^\circ$.



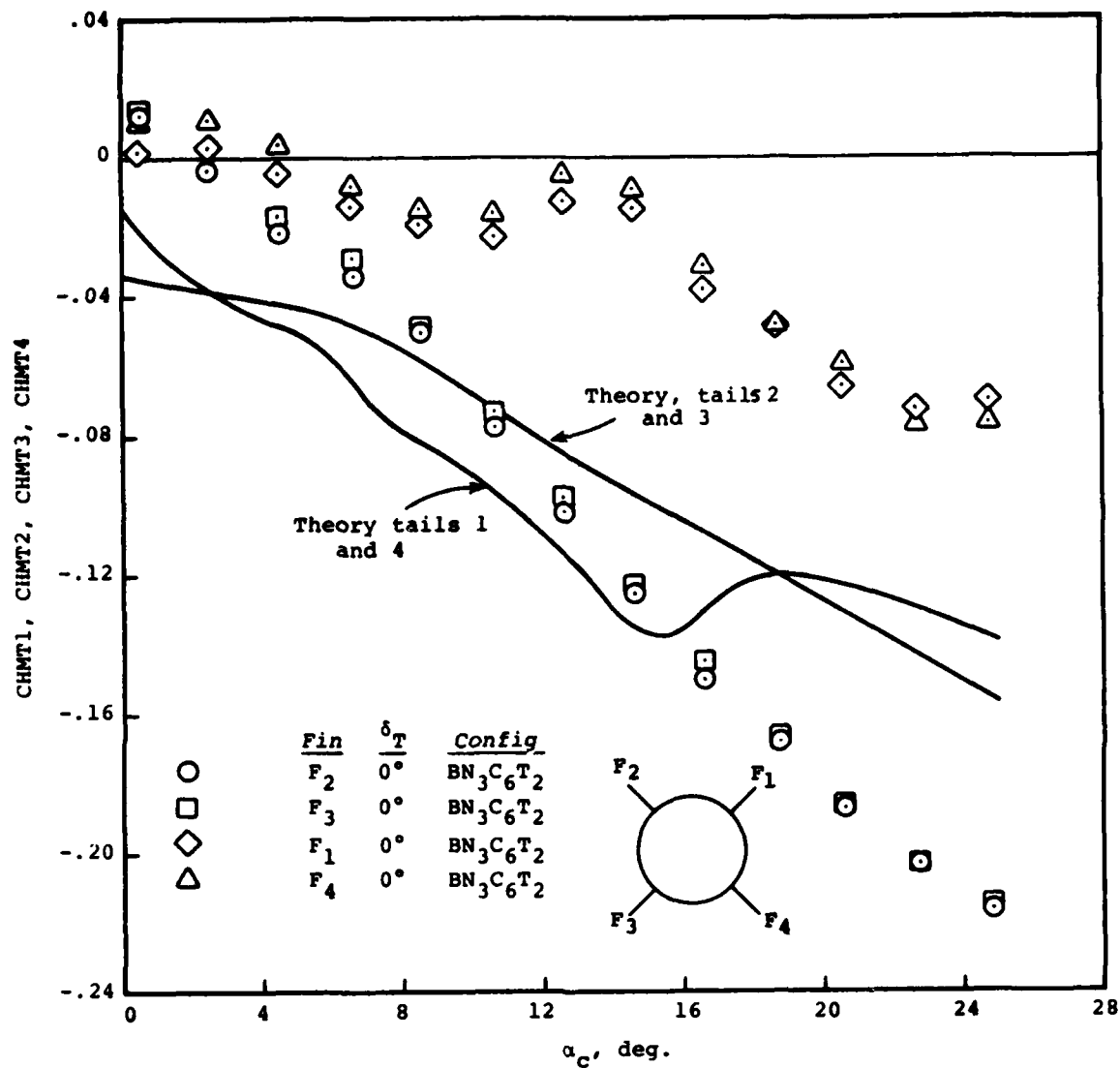
(b) Hinge-moment coefficient

Figure 82.- Concluded



(a) Normal-force coefficient

Figure 83.- Characteristics of tail T₂ in presence of canard C₆; M_∞ = 1.75, $\phi_c = 45^\circ$, $\delta_{1c} = \delta_{2c} = \delta_{3c} = \delta_{4c} = 15^\circ$.



(b) Hinge-moment coefficient

Figure 83.- Concluded

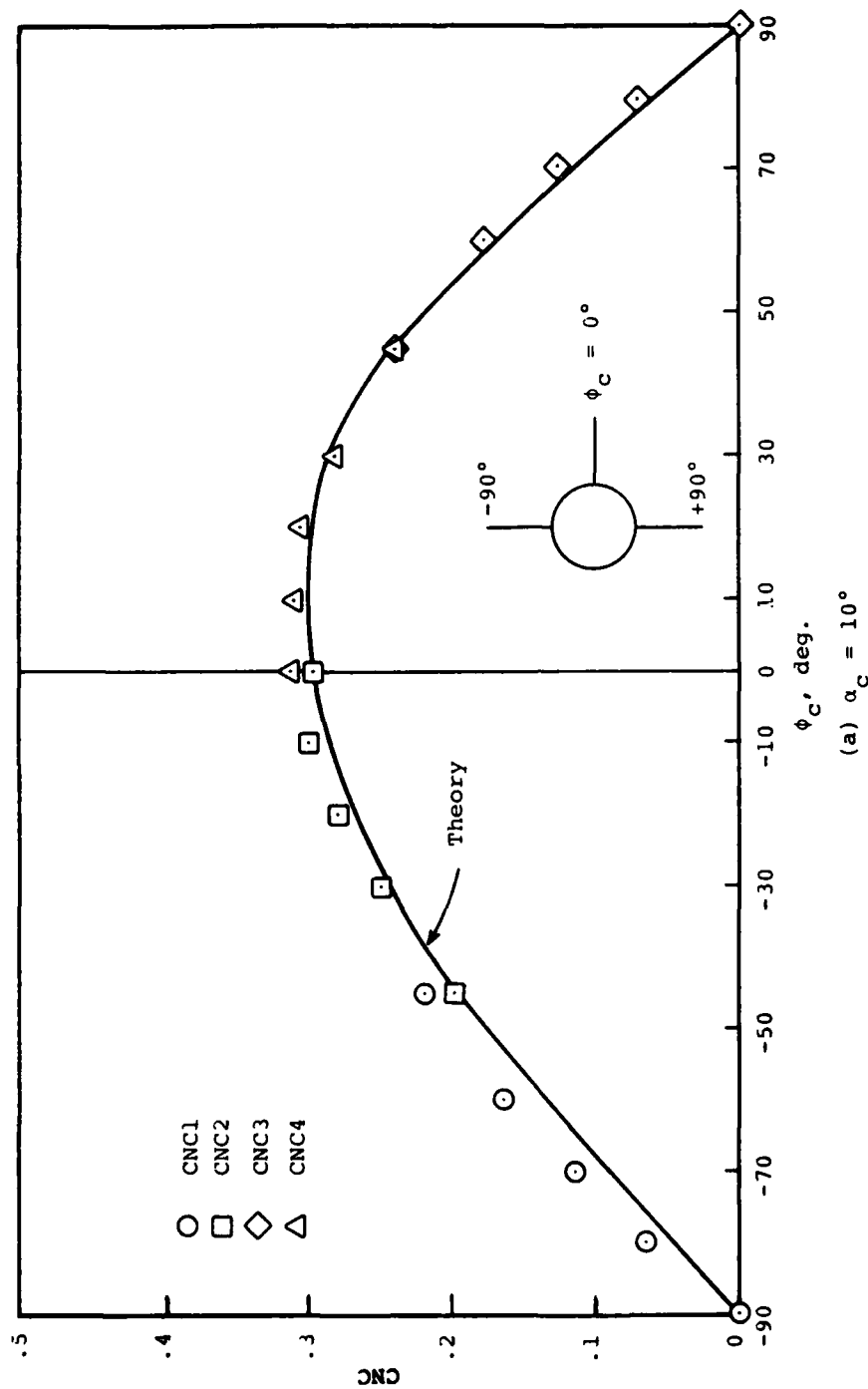
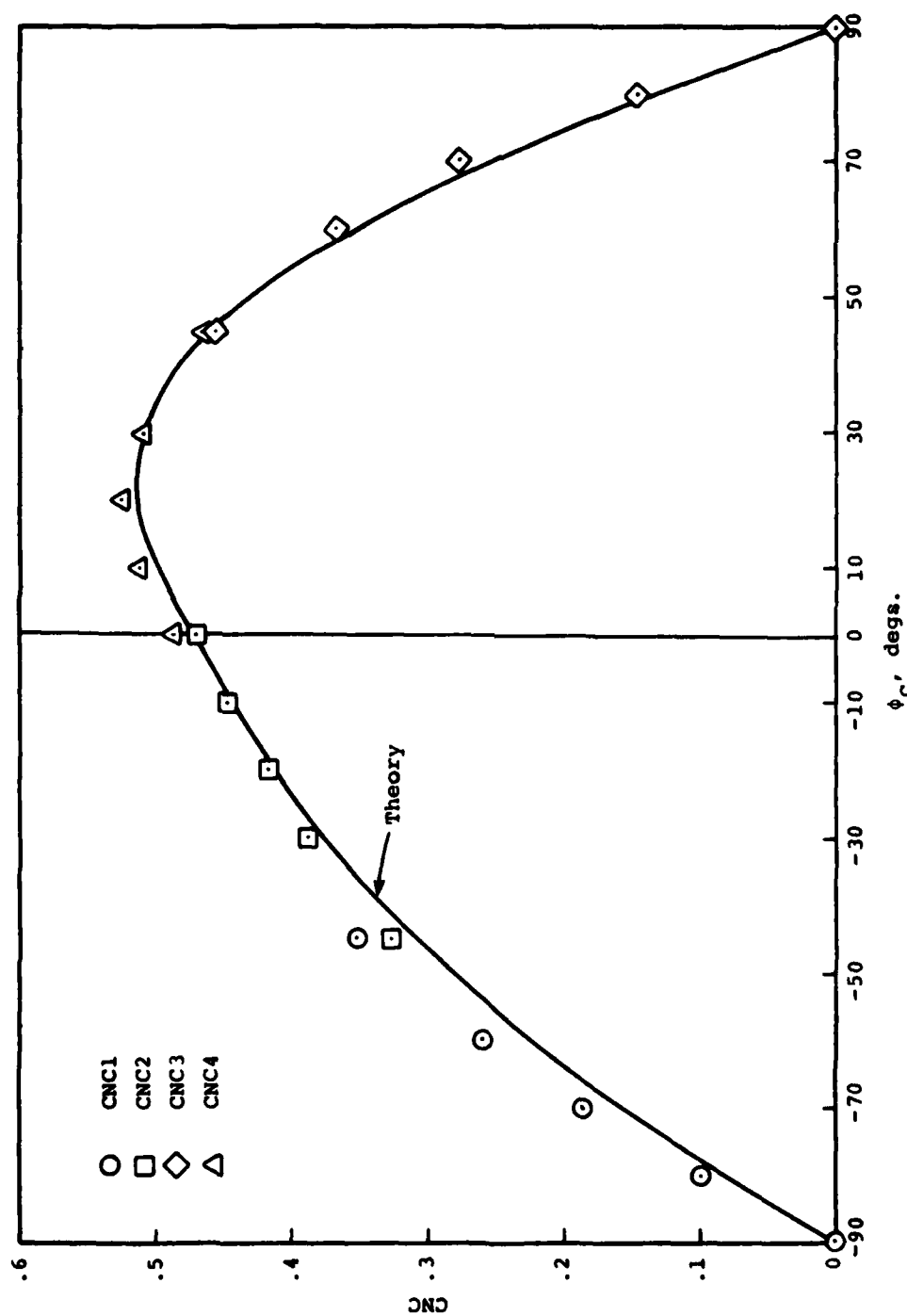


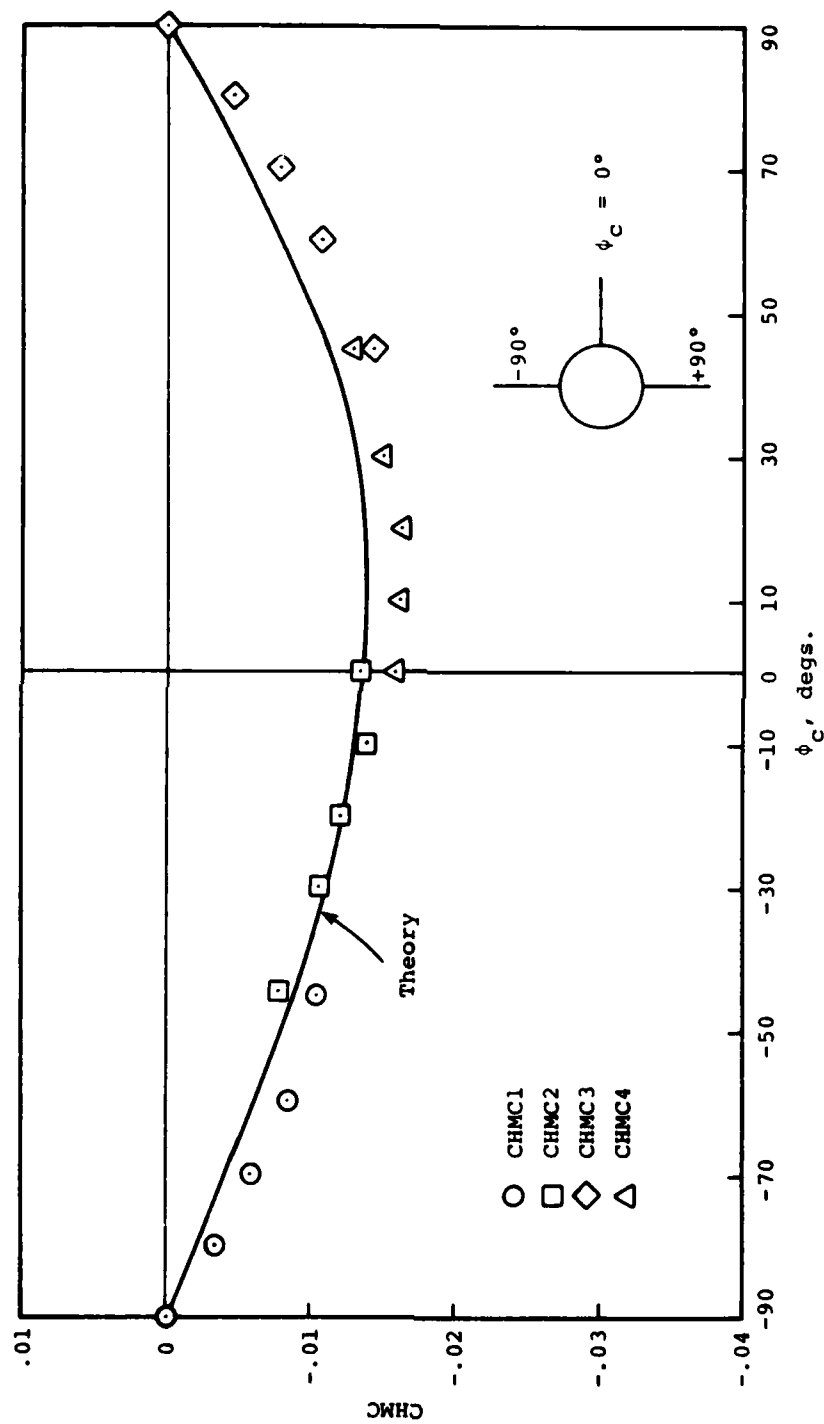
Figure 84.- Effect of roll angle on normal-force coefficient for canard C_6 mounted on body BN_3 ; $M_\infty = 1.3$, $\delta_1 = \delta_2 = \delta_3 = \delta_4 = 0^\circ$

(a) $\alpha_C = 10^\circ$

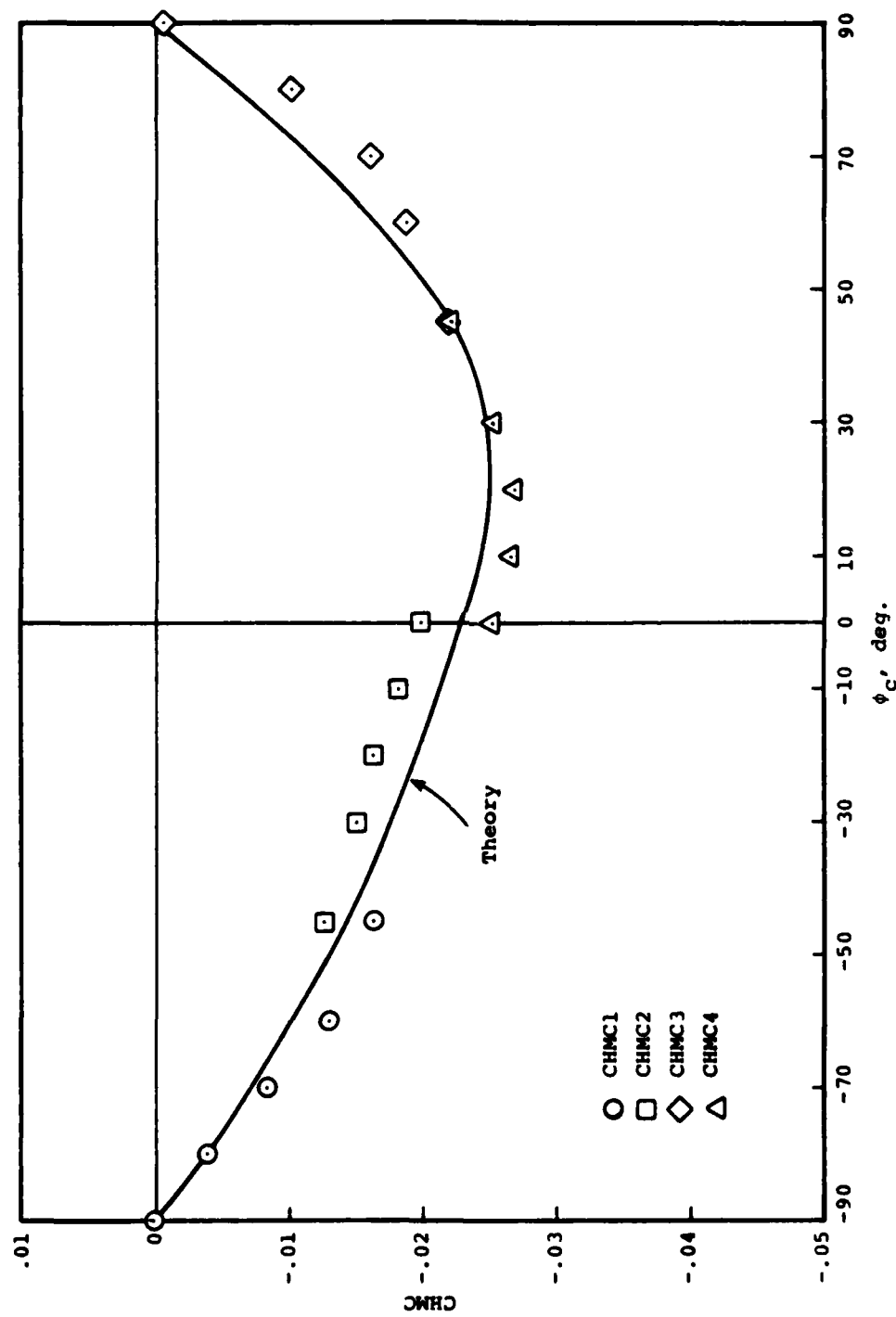


(b) $\alpha_C = 20^\circ$

Figure 84.- Concluded.



(a) $\alpha_C = 10^\circ$
 Figure 85.- Effect of roll angle on hinge-moment coefficient for canard C_6 mounted on body BN_3 ; $M_\infty = 1.3$, $\delta_1 = \delta_2 = \delta_3 = \delta_4 = 0^\circ$.



(b) $\alpha_C = 20^\circ$
Figure 85.- Concluded.

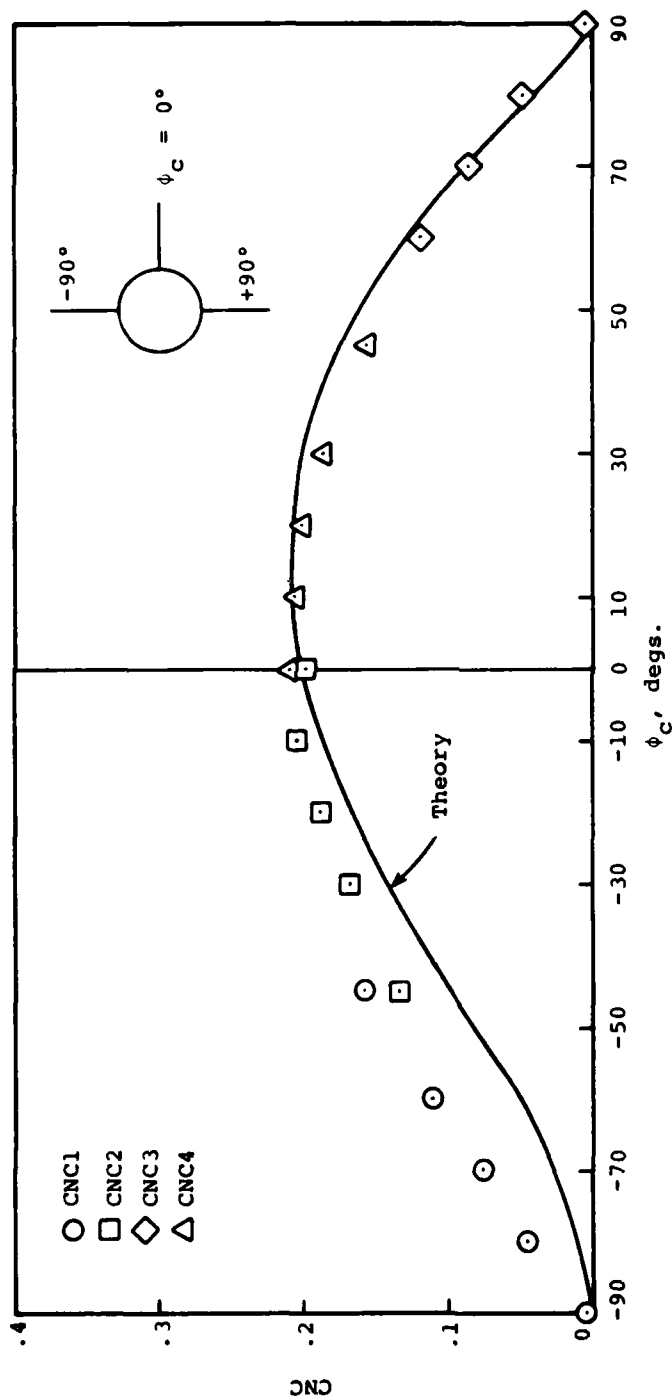
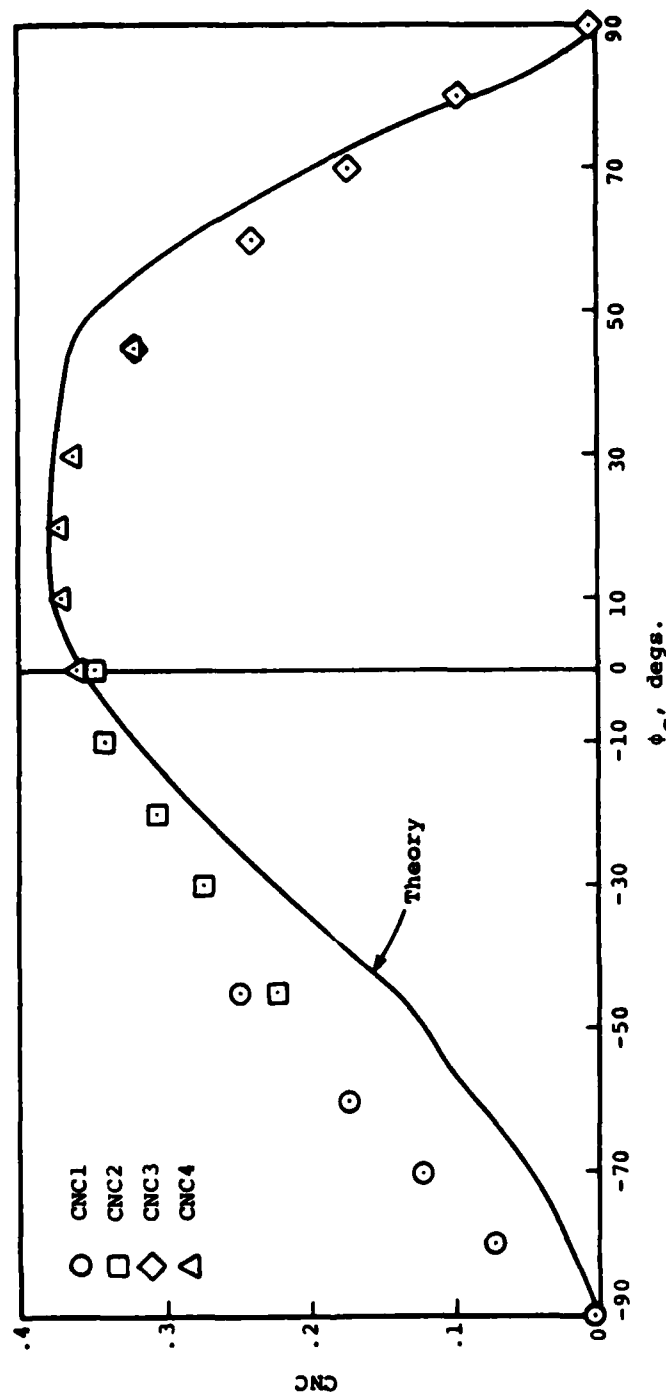


Figure 86.- Effect of roll angle on normal-force coefficient for canard C_6 mounted on body BN_3 ; $M_\infty = 1.75$, $\delta_1 = \delta_2 = \delta_3 = \delta_4 = 0^\circ$.

(a) $\alpha_C = 10^\circ$



(b) $\alpha_C = 20^\circ$
Figure 86.- Concluded.

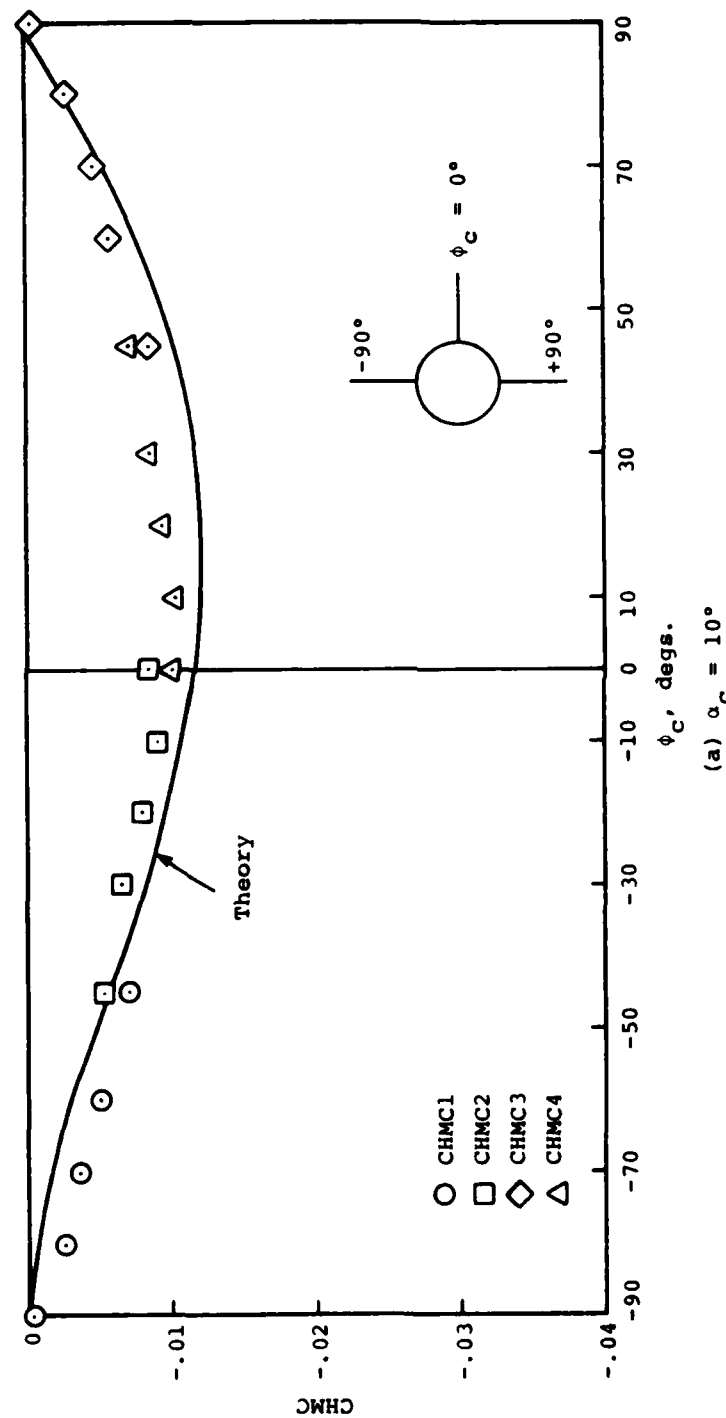
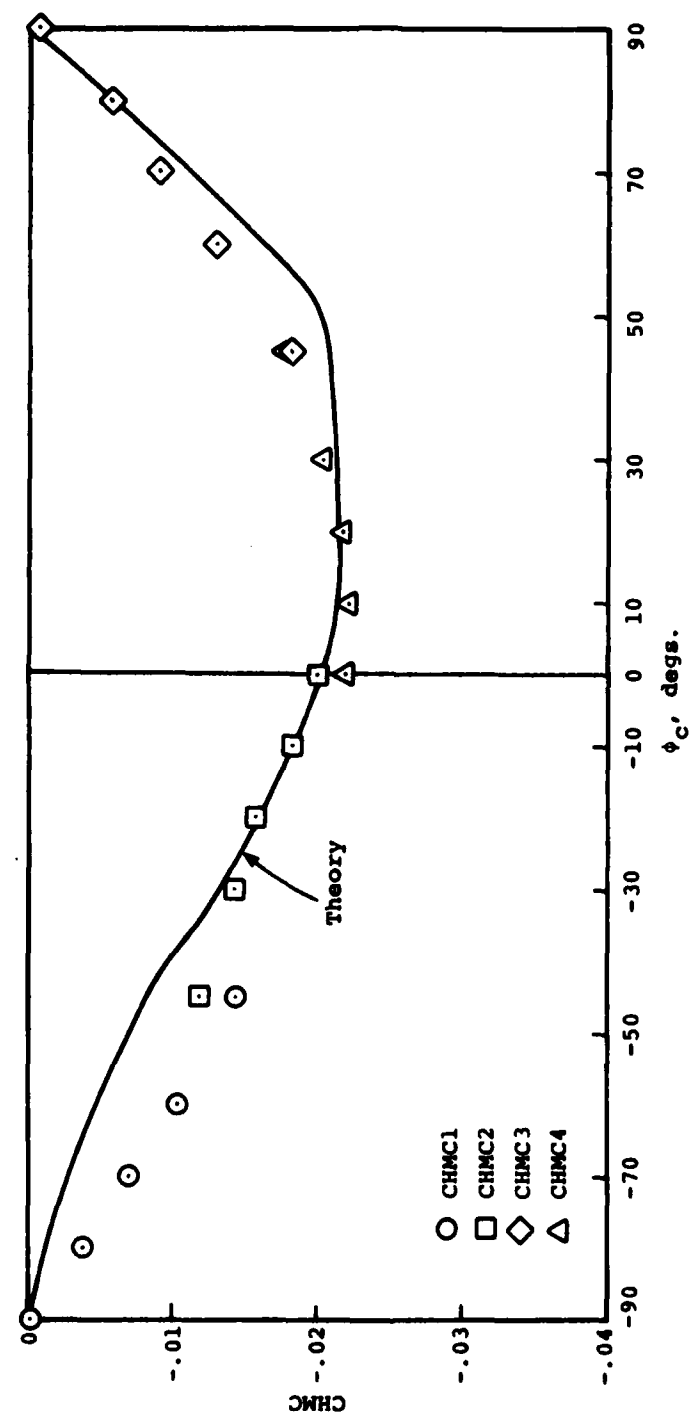
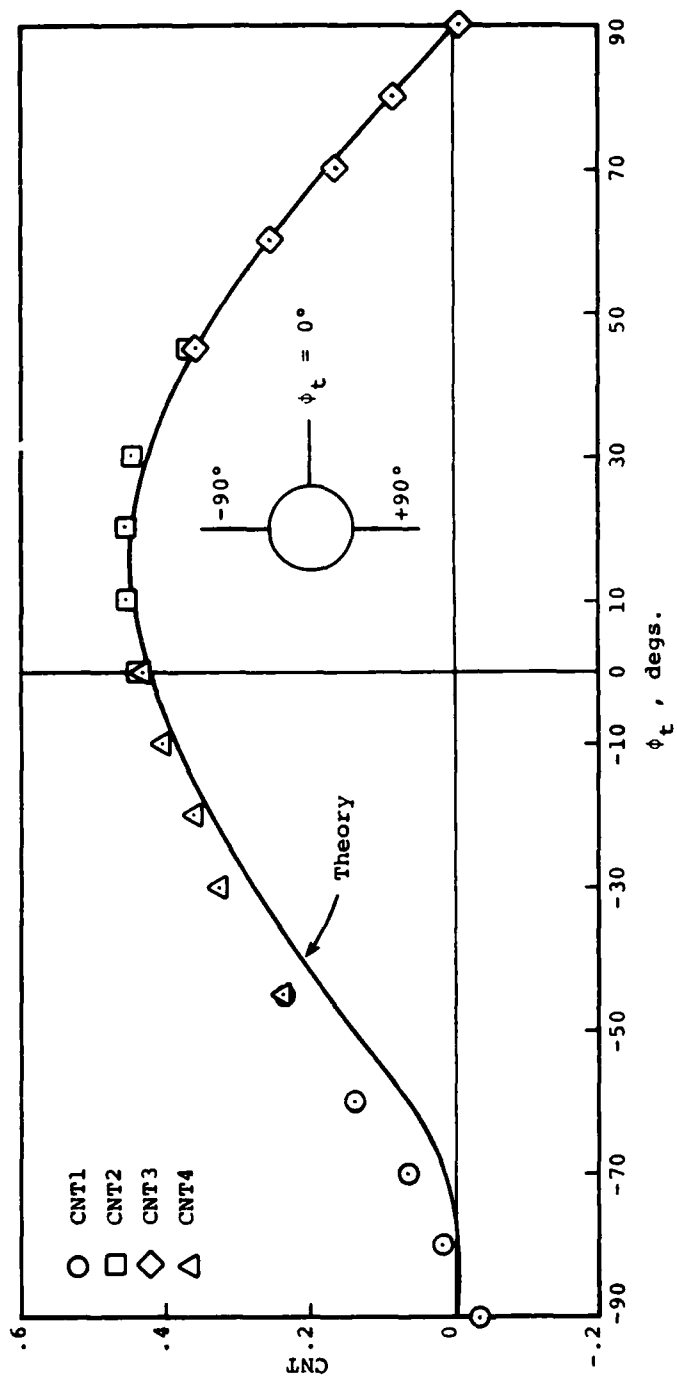


Figure 87.- Effect of roll angle on hinge-moment coefficient for canard C_6 mounted on body BN_3 ; $M_\infty = 1.75$, $\delta_1 = \delta_2 = \delta_3 = \delta_4 = 0^\circ$.

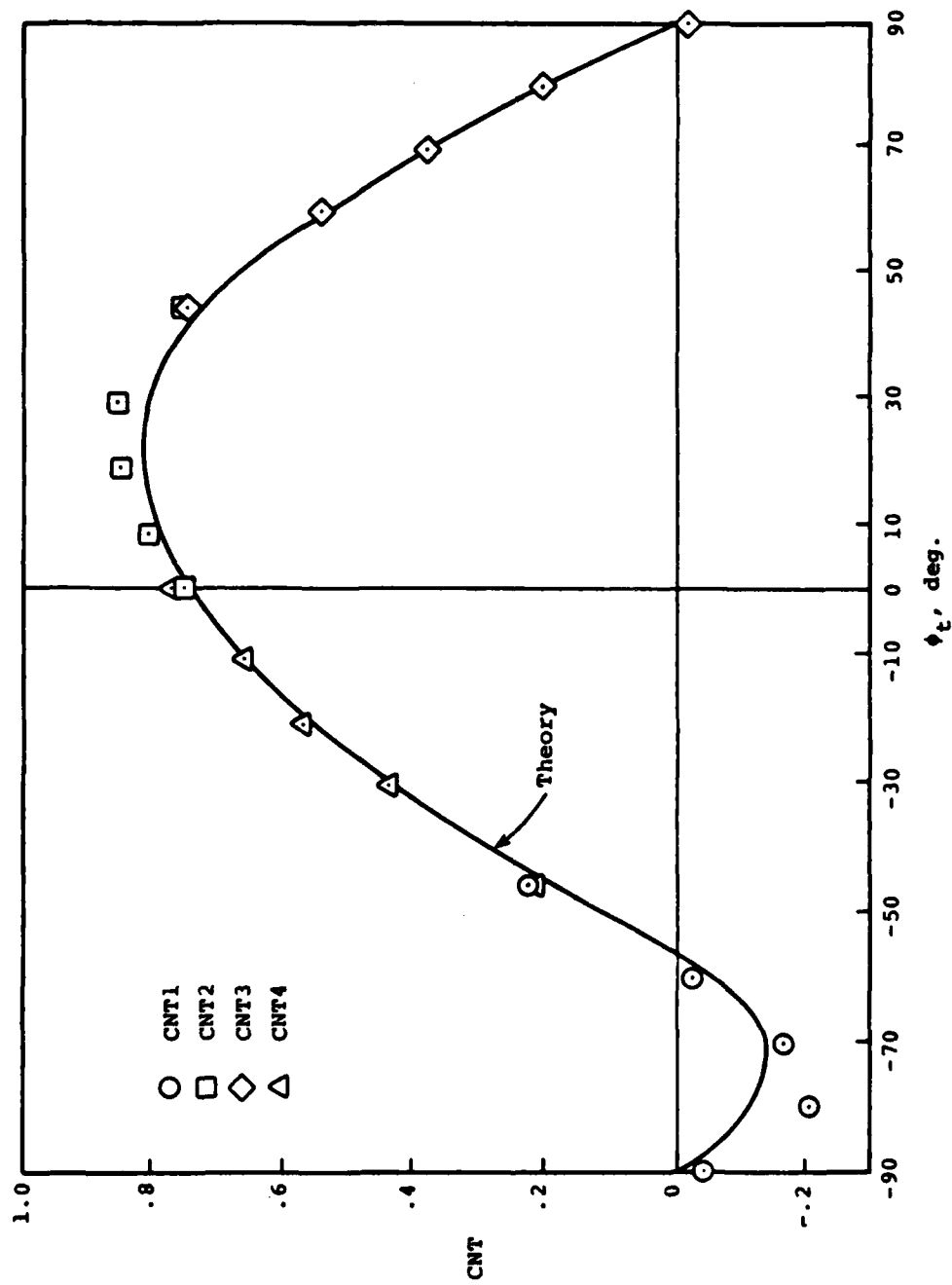


(b) $a_c = 20^\circ$
 Figure 87.- Concluded.

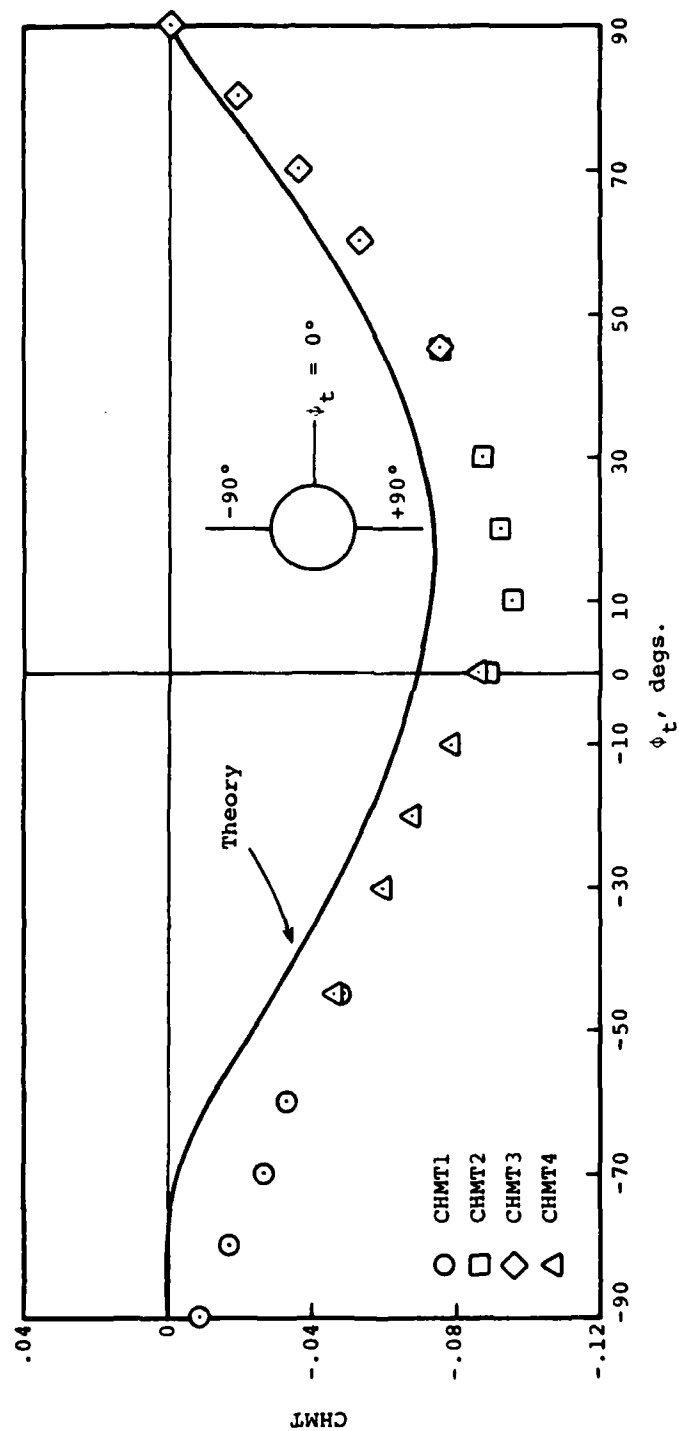


(a) $\alpha_C = 10^\circ$

Figure 88.- Effect of roll angle on normal-force coefficient for tail T_2 mounted on body BN_3 ; $M_\infty = 1.75$, $\delta_T = 0^\circ$.

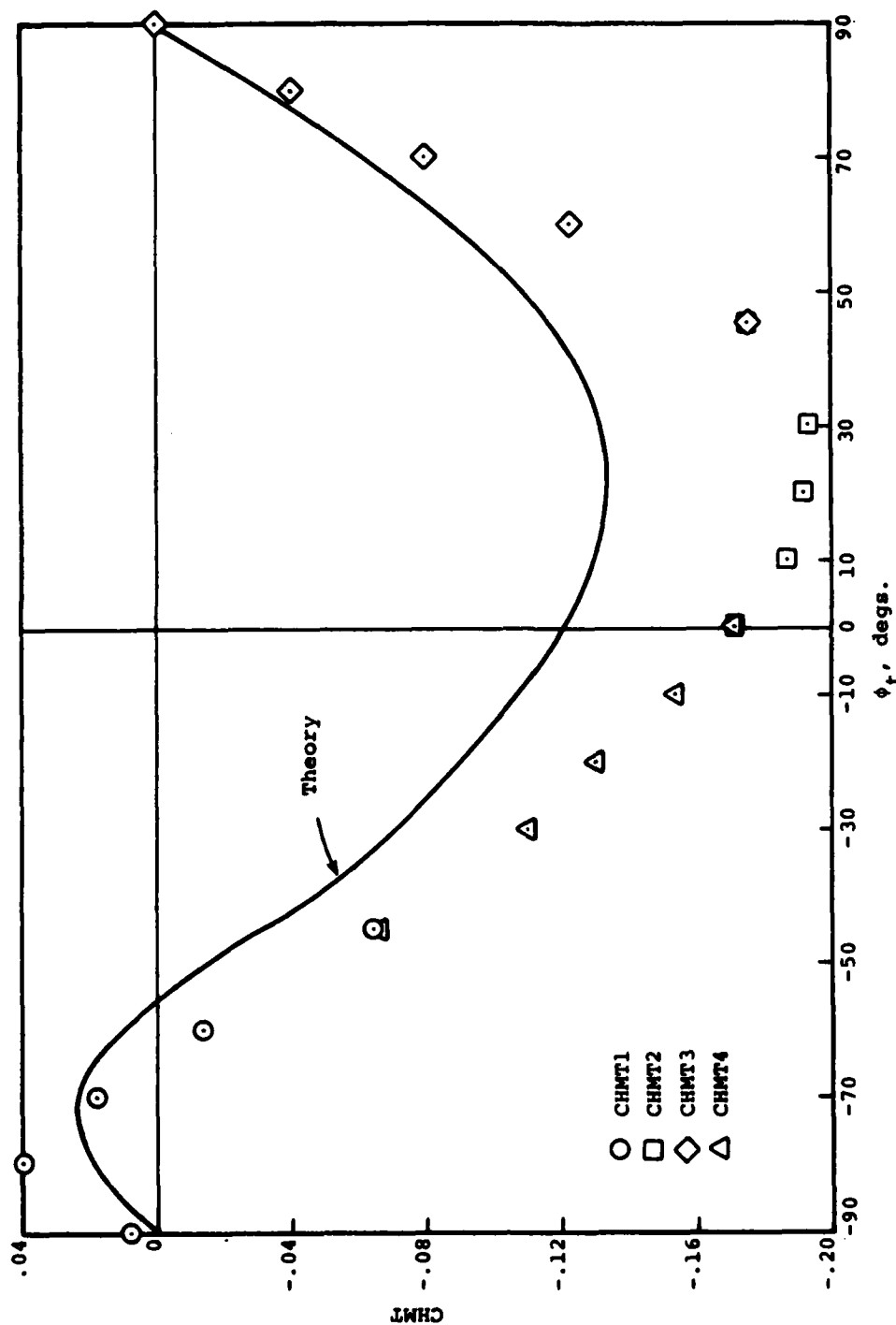


(b) $\alpha_c = 20^\circ$
Figure 88.- Concluded



(a) $\alpha_c = 10^\circ$

Figure 89.- Effect of roll angle on hinge-moment coefficient for tail T_2 mounted on body BN_3 ; $M_\infty = 1.75$, $\delta_T = 0^\circ$.



(b) $\alpha_c = 20^\circ$
Figure 89.- Concluded.

APPENDIX A

CONTROL HINGE-MOMENT BIBLIOGRAPHY

A. Gap Effects

1. Bleviss, Z. O. and Struble, R. A.: Some Aerodynamic Effects of Streamwise Gaps in Low-Aspect-Ratio Lifting Surfaces at Supersonic Speeds. Preprint No. 396, Jan. 1953. Presented at the 21st Annual Meeting, Jan. 26-20, 1953, Institute of the Aeronautical Sciences.
2. Bleviss, Z. O. and Struble, R. A.: Some Effects of Streamwise Gaps on the Aerodynamic Characteristics of Low-Aspect-Ratio Lifting Surfaces at Supersonic Speeds. Douglas Rept. SM-14627, Apr. 1953.
3. Drake, W. C.: Lift, Drag, and Hinge Moments at Supersonic Speeds of an All-Movable Triangular Wing and Body Combination. NACA RM A53F22, Sept. 1953.
4. Dugan, D. W. and Hikido, K.: Theoretical Investigation of the Effects Upon Lift of a Gap Between Wing and Body of a Slender Wing-Body Combination. NACA TN 3224, Aug. 1954.
5. Dugan, D. W.: Experimental Investigation of Some Aerodynamic Effects of a Gap Between Wing and Body of a Moderately Slender Wing-Body Combination at a Mach Number of 1.4. NACA RM A55D08, May 1955.
6. Michael, C. and Hancock, G. J.: On the Effects of Gaps on Control Surface Characteristics. AGARD-CP-262, Paper No. 28, May 1979.
7. Zarin, N. A.: Wind Tunnel Tests of Rectangular Finned Variable Gap Tangent Ogive-Cylinder Model at Mach Numbers 1.75 to 4.50. BRL Memorandum Rept. No. 1583, Aug. 1964.

B. Work at Ames Research Center

1. Drake, W. C.: Lift, Drag, and Hinge Moments at Supersonic Speeds of an All-Movable Triangular Wing and Body Combination. NACA RM A53F22, Sept. 1953.
2. Hill, W. A., Jr. and Kaattari, G. E.: Force and Pressure Distribution Investigation to High Angles of Attack on All-Movable Triangular and Rectangular Wings in Combination with a Body at Supersonic Speeds. NACA RM A56C12, 1956.

3. Kaattari, G. E., Hill, W. A., Jr., and Nielsen, J. N.: Controls for Supersonic Missiles. NACA RM A55D12, May 1955.
4. Katzen, E. D. and Pitts, W. C.: Load Distributions on Wings and Wing-Body Combinations at High Angles of Attack and Supersonic Speeds. NACA RM A55E17, July 1955.
5. Nielsen, J. N., Kaattari, G. E., and Drake, W. C.: Comparison Between Prediction and Experiment for All-Movable Wing and Body Combinations at Supersonic Speeds - Lift, Pitching Moment, and Hinge Moment. NACA RM A52D29, Aug. 1952.

C. Work at Langley Research Center

Forward Surfaces

1. Graves, E. B. and Fournier, R. H.: Stability and Control Characteristics at Mach Numbers from 0.20 to 4.63 of a Cruciform Air-to-Air Missile with Triangular Canard Controls and a Trapezoidal Wing. NASA TM X-3070, July 1974.
2. Spearman, L. M.: Component Tests to Determine the Aerodynamic Characteristics of an All-Movable 70° Delta Canard-Type Control in the Presence of a Body at a Mach number of 1.61. NACA RM L53I03, Oct. 1953.
3. Trescot, C. D., Jr., Foster, G. V., and Babb, C. D.: Effect of Fin Planform on the Aerodynamic Characteristics of a Wingless Missile with Aft Cruciform Controls at Mach 1.60, 2.36, and 2.86. NASA TM X-2774, July 1973.
4. Lamb, M., Sawyer, W. C., Wassum, D. L., and Babb, C. D.: Pressure Distributions on Three Different Cruciform Aft-Tail Control Surfaces of a Wingless Missile at Mach 1.60, 2.36, and 3.70. Vol. I - Trapezoidal Tail. NASA TM 80097, Vol. I, Aug. 1979.
5. Lamb, M., Sawyer, W. C., Wassum, D. L., and Babb, C. D.: Pressure Distributions on Three Different Cruciform Aft-Tail Control Surfaces of a Wingless Missile at Mach 1.60, 2.36, and 3.70. Vol. II - Clipped Delta Tail. NASA TM 80097, Vol. 2, Aug. 1979.
6. Lamb, M., Sawyer, W. C., Wassum, D. L., and Babb, C. D.: Pressure Distributions on Three Different Cruciform Aft-Tail Control Surfaces of a Wingless Missile at Mach 1.60, 2.36, and 3.70. Vol. III - Cranked Tail. NASA TM 80097, Vol. 3, Aug. 1979.

7. Lamb, M. and Trescot, C. D., Jr.: A study of Panel Loads and Centers of Pressure of Three Different Cruciform Aft-Tail Control Surfaces of a Wingless Missile from Mach 1.60 to 3.70. NASA TM 81787, May 1980.

Rearward Surfaces

1. Corlett, W. A. and Fuller, D. E.: Aerodynamic Characteristics at Mach 1.60, 2.00, and 2.50 of a Cruciform Missile Configuration with In-Line Tail Controls. NASA TM X-1112, July 1965.
2. Corlett, W. A.: Aerodynamic Characteristics of a Modified Missile Model with Cruciform Wings and In-Line Tail Controls at Mach 1.60 to 4.63. NASA TM X-1805, July 1969.
3. Corlett, W. A.: Aerodynamic Characteristics at Mach Numbers from 0.40 to 2.86 of a Maneuverable Missile with Cruciform Trapezoidal Wings and Aft Tail Controls. NASA TM X02681, Dec. 1972.
4. Corlett, W. A. and Howell, D. T.: Aerodynamic Characteristics at Mach 0.60 to 4.63 of Two Cruciform Missile Models, One Having Trapezoidal Wings with Canard Controls and the Other Having Delta Wings with Tail Controls. NASA TM X-2780, July 1973.

D. General

1. Hensch, M. J. and Nielsen, J. N.: Test Report for Canard Missile Test in Ames 6- by 6-Foot Supersonic Wind Tunnel. Nielsen Engineering & Research, Inc. TR 72, Aug. 1974.
2. Kirkpatrick, D. L. I. and Hepworth, A. G.: Experimental Investigation of the Effect of Trailing-Edge Sweepback on the Subsonic Longitudinal Characteristics of Slender Wings. ARC-CP-1130, Mar. 1970.
3. Lin, W. and Clarke, M. D.: Factors Influencing the Accuracy of Aerodynamic Hinge-Moment Prediction. AFFDL-TR-78-72, Aug. 1978.
4. Reichentahl, J. and Rom, J.: Lift and Hinge Moments of a Delta Control Surface in a Blunt-Nosed Canard Configuration. Israel Journal of Technology, Vol. 9, Nos. 1-2, Mar. 1971, pp. 165-175.
5. Schwind, R. G.: High Angle Canard Missile Test in the Ames 11-Foot Transonic Wind Tunnel. Nielsen Engineering & Research, Inc. TR 134, Aug. 1977.

6. Smith, C. A. and Nielsen, J. N.: Nonlinear Aerodynamics of All-Movable Controls. AGARD-CP-262, Paper No. 25, May 1979.
7. Whoric, J. M.: Aerodynamic Characteristics of Several Low-Aspect-Ratio Stabilizer Fins at Mach Numbers from 0.8 to 1.3. AEDC-TR-72-143, Sept. 1972 (AFATL-TR-72-189).

APPENDIX B

EFFECT OF THICKNESS ON AIRFOIL CENTER-OF-PRESSURE POSITION IN ATTACHED SHOCK REGION

B.1 CALCULATION OF PRESSURE DISTRIBUTION ON AN AIRFOIL USING SHOCK-EXPANSION THEORY

The method of calculating the pressure distribution on a symmetric airfoil using shock-expansion theory will be described. This method is valid up to the angle of attack at which the leading-edge shock wave becomes detached.

Figure B1 shows a symmetric airfoil section whose surface is made up of a series of straight line segments. The value of x , x_n , at which the segment ends is specified as is the surface angle θ_n . On the front of the airfoil θ_n is positive. Downstream of the point of maximum thickness θ_n is negative. On the lower surface, the flow in each region is characterized by

$C_{p_{\ell n}}$ = pressure coefficient, $(p_{\ell n} - p_{\infty})/q_{\infty}$

$M_{\ell n}$ = Mach number

$\nu_{\ell n}$ = local Prandtl-Meyer angle

Similarly, the flow in each region on the upper surface is characterized by

$C_{p_{u n}}$ = pressure coefficient, $(p_{u n} - p_{\infty})/q_{\infty}$

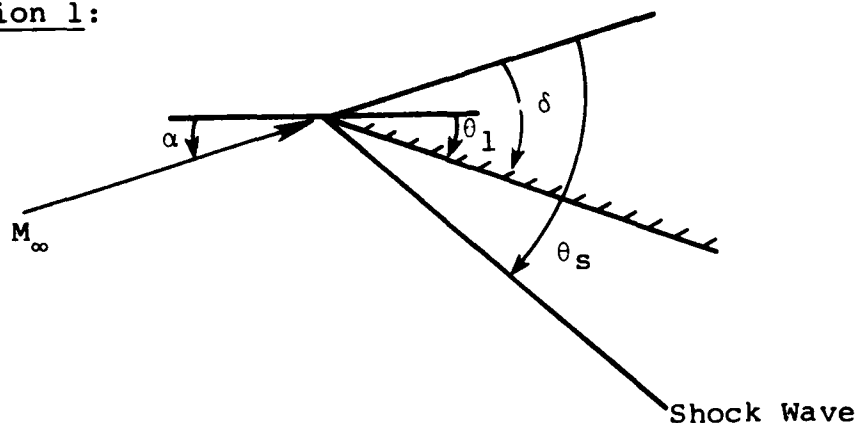
$M_{u n}$ = Mach number

$\nu_{u n}$ = local Prandtl-Meyer angle

The calculation of the N values of $C_{p_{\ell}}$ and the N values of C_{p_u} will now be described. Most of the equations used are taken from reference B1.

B.1.1 Lower Surface of Airfoil

Region 1:



On the lower surface in region 1 the free-stream flow is deflected through an angle δ where

$$\delta = \alpha + \theta_1 \quad (B-1)$$

To calculate the flow quantities in region 1, the shock wave angle, θ_s , which is a function of M_∞ and δ must be determined. This angle can be determined by an iterative solution of the following equation ($\gamma = 1.4$ for air)

$$\text{ctn}\delta = \tan\theta_s \left[\frac{(\gamma + 1)M_\infty^2}{2(M_\infty^2 \sin^2\theta_s - 1)} - 1 \right] \quad (B-2)$$

This equation is double valued in θ_s . Also, for a given value of M_∞ , there is a value of δ above which no solution can be found, the case of a detached shock wave. The maximum value of the wedge angle, δ , which will allow an attached shock occurs when, from Equation (B-2),

$$\frac{d\delta}{d\theta_s} = 0 \quad (B-3)$$

Therefore, the maximum value of θ_s for an attached shock wave for a given M_∞ can be found by differentiating Equation (B-2) and setting the derivative, $d\delta/d\theta_s$, to zero. If this is done

$$\sin \theta_{s_{\max}} = \left[\frac{-[4 - (\gamma + 1)M_{\infty}^2] + \sqrt{(\gamma + 1)^2 M_{\infty}^4 + 8(\gamma + 1)(\gamma - 1)M_{\infty}^2 + 16(\gamma + 1)}}{4\gamma M_{\infty}^2} \right]^{1/2} \quad (\text{B-4})$$

Using $\theta_{s_{\max}}$ and M_{∞} , Equation (B-2) can be used to find the maximum value of δ for an attached shock wave.

The procedure to be used in solving Equation (B-2) for θ_s for given values of M_{∞} and δ is:

1. Determine $\theta_{s_{\max}}$ using Equation (B-4)
2. Using $\theta_{s_{\max}}$ in Equation (B-2) compute δ_{\max}
3. If $\delta < \delta_{\max}$ solve Equation (B-2) for the value of θ_s which is less than $\theta_{s_{\max}}$

Pressure coefficient:

$$C_{p_{\ell_1}} = \frac{p_{\ell_1} - p_{\infty}}{q_{\infty}} = \frac{4(M_{\infty}^2 \sin^2 \theta_s - 1)}{(\gamma + 1)M_{\infty}^2} \quad (\text{B-5})$$

Mach number:

$$M_{\ell_1} = \left\{ \frac{(\gamma + 1)^2 M_{\infty}^4 \sin^2 \theta_s - 4(M_{\infty}^2 \sin^2 \theta_s - 1)(\gamma M_{\infty}^2 \sin^2 \theta_s + 1)}{[2\gamma M_{\infty}^2 \sin^2 \theta_s - (\gamma - 1)][(\gamma - 1)M_{\infty}^2 \sin^2 \theta_s + 2]} \right\}^{1/2} \quad (\text{B-6})$$

Prandtl-Meyer angle for M_{ℓ_1} :

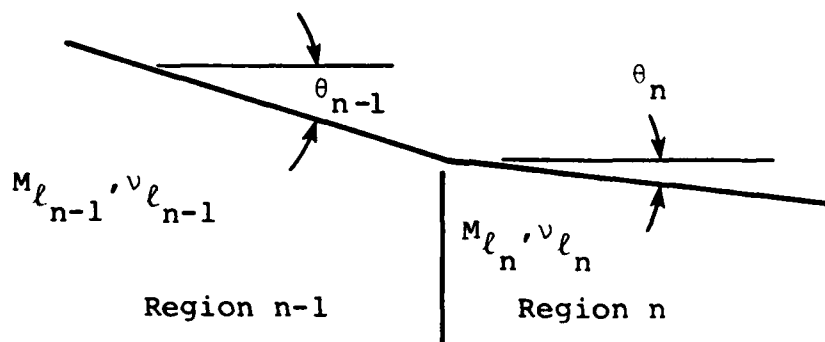
$$v_{\ell_1} = \sqrt{\frac{\gamma + 1}{\gamma - 1}} \tan^{-1} \sqrt{\frac{\gamma - 1}{\gamma + 1} (M_{\ell_1}^2 - 1)} - \tan^{-1} \sqrt{M_{\ell_1}^2 - 1} \quad (\text{B-7})$$

Ratio of total pressure to free-stream total pressure:

$$\frac{p_{t_{\ell_1}}}{p_{t_{\infty}}} = \left[\frac{(\gamma + 1)M_{\infty}^2 \sin^2 \theta_s}{(\gamma - 1)M_{\infty}^2 \sin^2 \theta_s + 2} \right]^{\frac{\gamma}{\gamma - 1}} \left[\frac{\gamma + 1}{2\gamma M_{\infty}^2 \sin^2 \theta_s - (\gamma - 1)} \right]^{\frac{1}{\gamma - 1}} \quad (\text{B-8})$$

Region n:

The procedure used to calculate the pressure coefficients in regions 2, 3,N on the lower surface is identical so that the following equations are written for region n where $n = 2, 3, \dots, N$.



The calculation is repeated sequentially for all these regions.

The flow, in going from region n-1 to region n, expands through angle $(\theta_{n-1} - \theta_n)$. Therefore, the Prandtl-Meyer angle in region n is

$$v_{\ell_n} = v_{\ell_{n-1}} + (\theta_{n-1} - \theta_n) \quad (B-9)$$

With this angle known, the Mach number in region n can be calculated using equations given in reference B2.

$$M_{\ell_n} = \frac{1 + 1.3604 \bar{v} + 0.0962 \bar{v}^2 - 0.5127 \bar{v}^3}{1 - 0.6722 \bar{v} - 0.3278 \bar{v}^2} \quad (B-10)$$

where

$$\bar{v} = \left(\frac{v_{\ell_n}}{v_{\max}} \right)^{2/3} ; \quad v_{\max} = \frac{\pi}{2} \left[\sqrt{\frac{\gamma+1}{\gamma-1}} - 1 \right] \quad (B-11)$$

The ratio of static pressure to total pressure in region n is then

$$\frac{p_{\ell_n}}{p_{t_{\ell_n}}} = \left(1 + \frac{\gamma-1}{2} M_{\ell_n}^2 \right)^{-\frac{\gamma}{\gamma-1}} \quad (\text{B-12})$$

and the pressure coefficient is

$$C_{p_{\ell_n}} = \frac{\left(\frac{p_{\ell_n}}{p_{t_{\ell_n}}} \right) \left(\frac{p_{t_{\ell_1}}}{p_{t_{\infty}}} \right) - \frac{p_{\infty}}{p_{t_{\infty}}}}{\frac{q_{\infty}}{p_{t_{\infty}}}} \quad (\text{B-13})$$

since $p_{t_{\ell_n}} = p_{t_{\ell_1}}$. Equation (B-8) gives $(p_{t_{\ell_1}}/p_{t_{\infty}})$ and

$$\frac{p_{\infty}}{p_{t_{\infty}}} = \left(1 + \frac{\gamma-1}{2} M_{\infty}^2 \right)^{-\frac{\gamma}{\gamma-1}} \quad (\text{B-14})$$

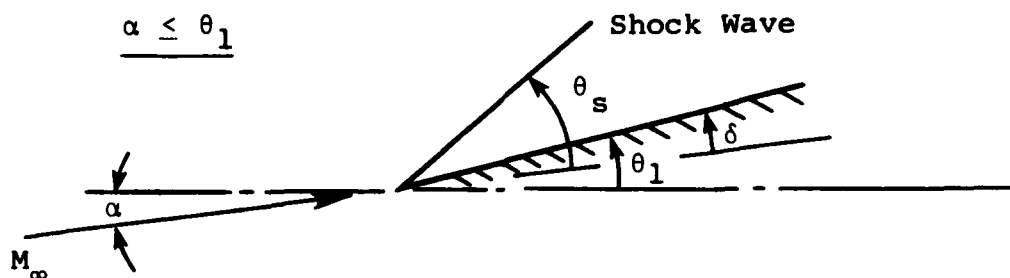
$$\frac{q_{\infty}}{p_{t_{\infty}}} = \frac{\gamma}{2} M_{\infty}^2 \left(\frac{p_{\infty}}{p_{t_{\infty}}} \right) \quad (\text{B-15})$$

After the calculations given by Equations (B-9) through (B-15) have been done sequentially for $n = 2, 3, \dots, N$, the complete pressure distribution on the lower surface has been determined.

B.1.2 Upper Surface of Airfoil

Region 1:

Two separate methods are used in calculating the pressure coefficient, $C_{p_{u_1}}$, in region 1 on the upper surface depending on whether the angle of attack, α , is less than or greater than the surface angle, θ_1 , shown in Figure B1. The two methods will now be described.



If $\alpha < \theta_1$ the free-stream flow is deflected through an angle where

$$\delta = -(\alpha - \theta_1) \quad (B-16)$$

and a shock wave exists on the upper surface. For this case the procedure described for region 1 on the lower surface is followed. The value of δ given by Equation (B-16) is used along with the free-stream Mach number, M_∞ , in Equation (B-2) to find the shock-wave angle, θ_s . Then

Pressure coefficient:

$$C_{p_{u_1}} = \frac{p_{u_1} - p_\infty}{q_\infty} = \frac{4(M_\infty^2 \sin^2 \theta_s - 1)}{(\gamma + 1)M_\infty^2} \quad (B-17)$$

Mach number:

$$M_{u_1} = \left\{ \frac{(\gamma + 1)^2 M_\infty^4 \sin^2 \theta_s - 4(M_\infty^2 \sin^2 \theta_s - 1)(\gamma M_\infty^2 \sin^2 \theta_s + 1)}{[2\gamma M_\infty^2 \sin^2 \theta_s - (\gamma - 1)][(\gamma - 1)M_\infty^2 \sin^2 \theta_s + 2]} \right\}^{1/2} \quad (B-18)$$

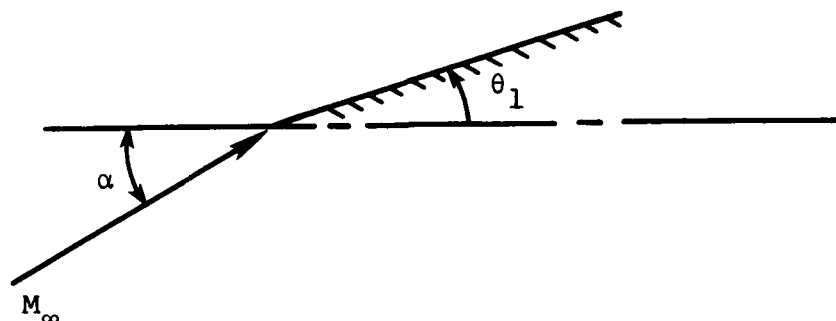
Prandtl-Meyer angle for M_{u_1} :

$$\nu_{u_1} = \sqrt{\frac{\gamma + 1}{\gamma - 1}} \tan^{-1} \sqrt{\frac{\gamma - 1}{\gamma + 1}} (M_{u_1}^2 - 1) - \tan^{-1} \sqrt{M_{u_1}^2 - 1} \quad (B-19)$$

Ratio of total pressure to free-stream total pressure:

$$\frac{p_{t_{u_1}}}{p_{t_\infty}} = \left[\frac{(\gamma+1)M_\infty^2 \sin^2 \theta_s}{(\gamma-1)M_\infty^2 \sin^2 \theta_s + 2} \right]^{\frac{\gamma}{\gamma-1}} \left[\frac{\gamma+1}{2\gamma M_\infty^2 \sin^2 \theta_s - (\gamma-1)} \right]^{\frac{1}{\gamma-1}} \quad (B-20)$$

$$\underline{\alpha > \theta_1}$$



If $\alpha > \theta_1$ the flow expands through angle $(\alpha - \theta_1)$ in going from the free stream to region 1 on the upper surface. Therefore, the Prandtl-Meyer angle in region 1 is

$$v_{u_1} = v_\infty + (\alpha - \theta_1) \quad (B-21)$$

where

$$v_\infty = \sqrt{\frac{\gamma+1}{\gamma-1}} \tan^{-1} \sqrt{\frac{\gamma-1}{\gamma+1} (M_\infty^2 - 1)} - \tan^{-1} \sqrt{M_\infty^2 - 1} \quad (B-22)$$

and the Mach number is

$$M_{u_1} = \frac{1 + 1.3604 \bar{v} + 0.0962 \bar{v}^2 - 0.5127 \bar{v}^3}{1 - 0.6722 \bar{v} - 0.3278 \bar{v}^2} \quad (B-23)$$

where

$$\bar{v} = \left(\frac{v_{u1}}{v_{\max}} \right)^{2/3} ; v_{\max} = \frac{\pi}{2} \left(\sqrt{\frac{\gamma+1}{\gamma-1}} - 1 \right) \quad (\text{B-24})$$

The ratio of static pressure to total pressure in region 1 is

$$\frac{p_{u1}}{p_{t_{u1}}} = \left(1 + \frac{\gamma-1}{2} M_{u1}^2 \right)^{-\frac{\gamma}{\gamma-1}} \quad (\text{B-25})$$

and the ratio of total pressure in region 1 to free-stream total pressure is, since there is no shock wave,

$$\frac{p_{t_{u1}}}{p_{t_{\infty}}} = 1.0 \quad (\text{B-26})$$

The pressure coefficient in region 1 on the upper surface is given by

$$C_{p_{u1}} = \frac{\left(\frac{p_{u1}}{p_{t_{u1}}} \right) \left(\frac{p_{t_{u1}}}{p_{t_{\infty}}} \right) - \frac{p_{\infty}}{p_{t_{\infty}}}}{\frac{q_{\infty}}{p_{t_{\infty}}}} \quad (\text{B-27})$$

The quantities $p_{\infty}/p_{t_{\infty}}$ and $q_{\infty}/p_{t_{\infty}}$ are obtained from Equations (B-14) and (B-15).

Region n:

The procedure for calculating the pressure coefficients in regions 2, 3, ..., N on the upper surface is the same as that described previously for the same regions on the lower surface. The following equations are written for region n where $n = 2, 3, \dots, N$.

The flow in going from region $n-1$ to region n expands through the angle $(\theta_{n-1} - \theta_n)$. The Prandtl-Meyer angle in region n is

$$v_{u_n} = v_{u_{n-1}} + (\theta_{n-1} - \theta_n) \quad (B-28)$$

If $n=2$, either Equation (B-19) or (B-21) is used to determine $v_{u_{n-1}}$ depending on whether α is less than or greater than θ_1 .

With v_{u_n} known, the Mach number in region n is:

$$M_{u_n} = \frac{1 + 1.3604 \bar{v} + 0.0962 \bar{v}^2 - 0.5127 \bar{v}^3}{1 - 0.6722 \bar{v} - 0.3278 \bar{v}^2} \quad (B-29)$$

where

$$\bar{v} = \left(\frac{v_{u_n}}{v_{\max}} \right)^{2/3} ; \quad v_{\max} = \frac{\pi}{2} \left(\sqrt{\frac{\gamma+1}{\gamma-1}} - 1 \right) \quad (B-30)$$

The ratio of static pressure to total pressure in region n is:

$$\frac{p_{u_n}}{p_{t_{u_n}}} = \left(1 + \frac{\gamma-1}{2} M_{u_n}^2 \right)^{-\frac{\gamma}{\gamma-1}} \quad (B-31)$$

and the pressure coefficient is

$$C_{p_{u_n}} = \frac{\left(\frac{p_{u_n}}{p_{t_{u_n}}} \right) \left(\frac{p_{t_{u_1}}}{p_{t_\infty}} \right) - \frac{p_\infty}{p_{t_\infty}}}{\frac{q_\infty}{p_{t_\infty}}} \quad (B-32)$$

The quantity $p_{t_{u_n}} = p_{t_{u_1}}$ with $p_{t_{u_1}}$ given by Equation (B-20) or (B-26) depending on whether α is less than or greater than θ_1 . The quantities p_∞/p_t and q_∞/p_{t_∞} are given by Equations (B-14) and (B-15).

After the calculations given by Equations (B-28) through (B-32) have been repeated sequentially for $n = 2, 3, \dots, N$, the complete pressure distribution on the upper surface of the airfoil has been determined.

B.2 CALCULATION OF CENTER-OF-PRESSURE SHIFT ON AN AIRFOIL DUE TO THICKNESS

With the pressure distribution calculated by the method described in the preceding section, the center-of-pressure location on the airfoil due to its thickness can be determined. For an airfoil with zero thickness, the center-of-pressure location is at the 50-percent chord. Thus, a shift due to thickness relative to this point will be calculated. The center-of-pressure is:

$$\left(\frac{\Delta \bar{x}}{c}\right)_t = \frac{C_m}{C_N} \quad (B-33)$$

where C_m is the sum of the pitching moments produced by the various regions describing the airfoil, taken about the 50-percent chord, and C_N is the sum of the normal forces.

Referring to Figure B1 the increment in normal-force coefficient produced by the n^{th} region is:

$$(C_N)_n = \frac{(C_{p_{\ell_n}} - C_{p_{u_n}})(x_n - x_{n-1})}{\ell} = \Delta C_{p_n} \frac{(x_n - x_{n-1})}{\ell} \quad (B-34)$$

where ℓ is some nondimensionalizing length. Similarly, the pitching moment produced by the n^{th} region, taken about the 50-percent chord, $c/2$, is

$$(C_m)_n = \Delta C_{P_n} \frac{(x_n - x_{n-1})}{\ell} \left[\frac{1}{2} - \frac{(x_n + x_{n-1})}{2c} \right] \quad (\text{B-35})$$

The total center-of-pressure shift due to the thickness distribution of the complete airfoil section is obtained by summing over the N regions

$$\left(\frac{\Delta \bar{x}}{c} \right)_t = \frac{\sum_{n=1}^N (C_m)_n}{\sum_{n=1}^N (C_N)_n} \quad (\text{B-36})$$

or

$$\left(\frac{\Delta \bar{x}}{c} \right)_t = \frac{\sum_{n=1}^N \Delta C_{P_n} (x_n - x_{n-1}) \left[\frac{1}{2} - \frac{(x_n + x_{n-1})}{2c} \right]}{\sum_{n=1}^N \Delta C_{P_n} (x_n - x_{n-1})} \quad (\text{B-37})$$

REFERENCES

- B1. NACA Ames Research Staff: Equations, Tables, and Charts for Compressible Flow. NACA Report 1135, 1953.
- B2. Hall, I. M.: Inversions of the Prandtl-Meyer Relation. Aero. Jour., Roy. Aero. Soc., UK, Sept. 1975, pp. 416-418.

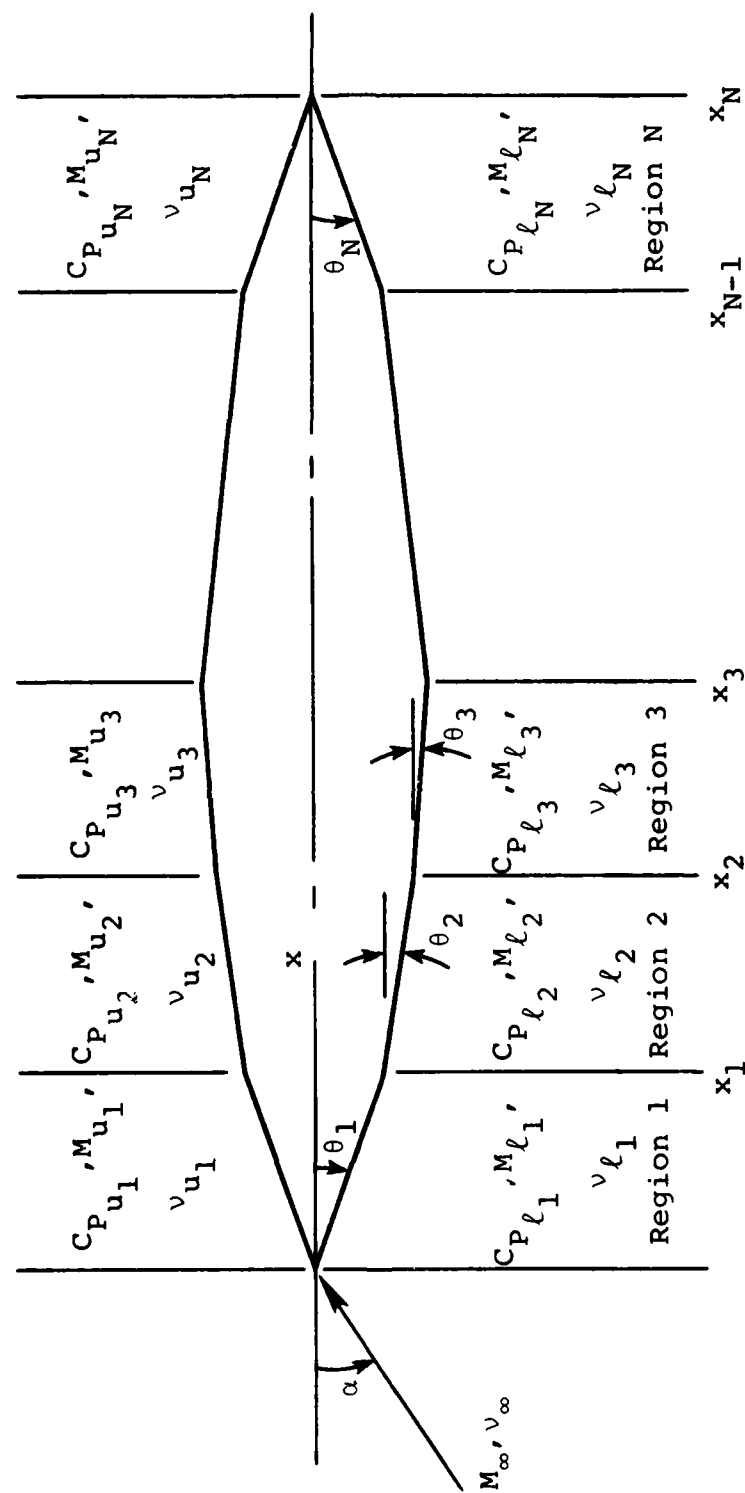


Figure B1.- Symmetric airfoil section made up of straight line segments.

APPENDIX C

EQUIVALENT ANGLE OF ATTACK FORMULATION FOR LARGE ANGLES OF ATTACK

C.1 INTRODUCTION

This appendix is a revised and expanded version of Appendix C of reference 1. The purpose of this appendix is to derive the equivalent angle-of-attack formulas and to show how they are used (1) to develop the tables to be incorporated in the present version of PROGRAM MISSILE and (2) to account for extrapolation from the measured data base. In particular, it is useful to rederive the formulas in order to handle the new control data base to be obtained in the future which was not available at the time reference 1 was written.

The equivalent angle-of-attack concept is based on the notion that the aerodynamic characteristics of an all-movable fin on a body should parallel those of a wing alone* with the same planform and the same Mach number, provided that the effective incidence of the flow seen by the fin is the same as that of the wing alone. We will want the derivation to include body angle, deflection and span effects as well as the effects of vortices; i.e., we want to find an α_{eq_i} for fin i such that

$$C_{N_W}(\alpha_{eq_i}) = C_{N_{F_i}}(B) [\alpha_c, \phi_i, \delta_1, \delta_2, \delta_3, \delta_4, a/s_m, (\Delta\alpha_{eq}) v_i]$$

The idea for α_{eq} was suggested by the earlier slender-body work of Pitts, Nielsen, and Kaattari (ref. 43) which found just such behavior for the linear range. However, for large angles of attack a nonlinear definition of α_{eq} is required. Since there is no unique way to derive a nonlinear formula from the linear

*The wing alone consists of two opposing fins joined at their root chords.

result, we are free to choose our approach provided that it gives the linear result in the limit of small angles. Our method is based on the use of average velocity components seen by the fin of interest. Those velocity components are put together to give α_{eq} . Extrapolation from the measured data base is accomplished as follows. First, the equivalent angle of attack, α_{eq_p} , corresponding to the vortex-free value of fin normal-force coefficient, $\hat{C}_{NF(B)}$, for no fin deflection is obtained from the wing-alone normal-force curve. Then, the value of $\Delta\alpha_{eq}$ corresponding to changes from that condition is determined and added to α_{eq_p} . The new value of α_{eq} is used together with the wing-alone curve to obtain the corresponding fin normal-force coefficient, $C_{NF(B)}$. The procedure is illustrated in the sketch below. The details are given in the following section.

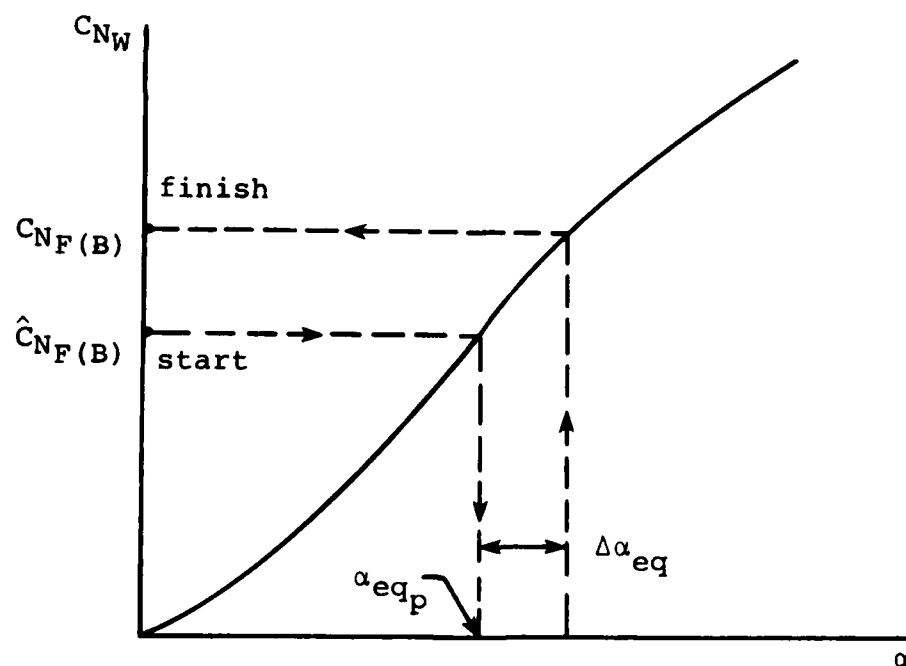
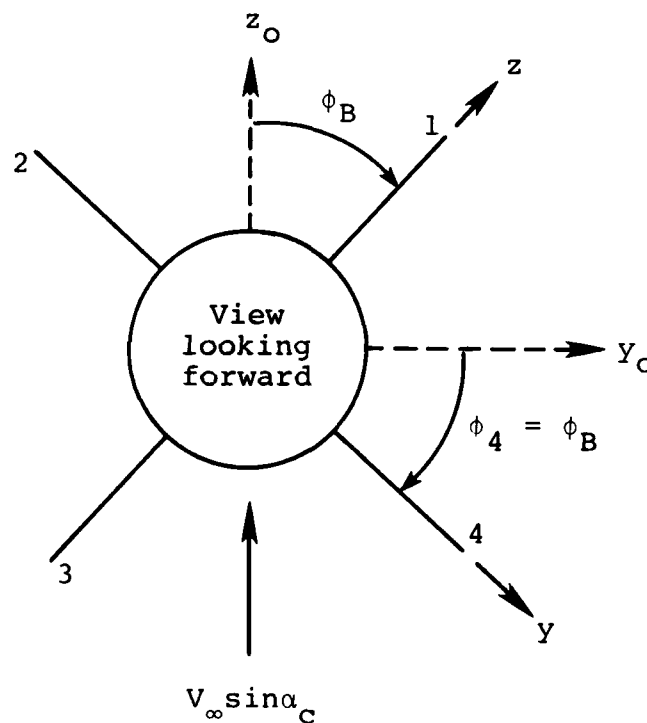


Illustration of equivalent angle of attack concept

C.2 DERIVATION

Consider a cruciform wing-body combination with the x-axis rearward along the body axis, the y-axis lateral along the right horizontal fin (fin 4) and the z-axis vertical along the upper fin (fin 1). Let the combination first be pitched in a plane containing the free-stream velocity and the x-axis by an angle α_c . Let it then be rolled right wing down by angle ϕ_B . In a plane normal to the body axis we now have the following picture:



We determine first the flow field seen by the fins with no fin deflection and then consider the effects of rotating (deflecting) the fins in that flow field. Referring to the sketch above, we see that the components of the free-stream velocity along x, y,

and z are $V_\infty \cos \alpha_c$, $-V_\infty \sin \alpha_c \sin \phi_4$ and $V_\infty \sin \alpha_c \cos \phi_4$, respectively.* Hence, the component of free-stream velocity normal to the plane of fin 4, V_{n4} , is $V_\infty \sin \alpha_c \cos \phi_4$. Thus, the angle of attack induced on fin 4 if it sees the free-stream only is

$$\begin{aligned} \tan \alpha_{eq4} &= \frac{V_{n4}}{V_{p4}} \\ &= \tan \alpha_c \cos \phi_4 \end{aligned} \quad (C-1)$$

Equation (C-1) does not yet represent the actual angle of attack induced on fin 4 with no fins deflected because effects of the body, sideslip and vortices have not been incorporated. We now consider these one at a time.

The presence of the body affects the flow in the crossflow plane (wing-body interference). We account for this effect by multiplying V_{n4} by the factor K_W , i.e.

$$V_{n4} \Big|_{\text{free-stream+body}} = K_W V_\infty \sin \alpha_c \cos \phi_4 \quad (C-2)$$

For favorable interference, $K_W > 1$. With increasing α_c and M_∞ , K_W tends to decrease (ref. 1). We will assume that K_W is independent of ϕ .

Any fin for which ϕ is not zero is sideslipping. Spreiter and Sacks (ref. 45) investigated this effect and found that the increment in the fin normal force was proportional to the product of α and β for the fin, i.e. $\alpha_c^2 \sin \phi_4 \cos \phi_4$. We use the same idea here to account for changes in V_{n4} due to sideslip, i.e.

$$V_{n4} \Big|_{\text{sideslip}} = \frac{4}{AR} K_\phi V_\infty \sin^2 \alpha_c \sin \phi_4 \cos \phi_4 \quad (C-3)$$

* Note that we are using the sine definition of the angle of attack (see pg. 5 of reference 44).

The introduction of the $4/AR$ coefficient makes the slender body value of K_ϕ independent of AR for delta fins.

To account for the effects of body vortices and vortices generated by upstream fins, we need a method for determining the equivalent angle of attack, $(\Delta\alpha_{eq})_{v_i}$, induced on fin i by the vortical flow field. The method used in PROGRAM MISSILE is described in reference 1 and is given next. By definition, we have

$$\left(\frac{V_{n_4}}{V_{p_4}} \right)_{\text{vortices}} = \tan(\Delta\alpha_{eq})_{v_4} \quad (C-4)$$

The method assumes that the vortices are rectilinear and parallel to the body axis. Hence, $(V_{p_4})_{\text{vortices}}$ is equal to the component of the free-stream velocity which is parallel to the fin chord and we can write

$$V_{n_4} \Big|_{\text{vortices}} = V_\infty \cos\alpha_c \tan(\Delta\alpha_{eq})_{v_4} \quad (C-5)$$

Using relations (C-2,3,5) we can define an equivalent angle of attack, $\hat{\alpha}_{eq_4}$, for body, sideslip, and vortex effects but without fin deflection, i.e.

$$\begin{aligned} \tan\hat{\alpha}_{eq_4} &= \frac{V_{n_4} \Big|_{\text{free-stream+body}} + V_{n_4} \Big|_{\text{sideslip}} + V_{n_4} \Big|_{\text{vortices}}}{V_{p_4}} \\ &= K_W \tan\alpha_c \cos\phi_4 + \frac{4}{AR} K_\phi \tan\alpha_c \sin\alpha_c \sin\phi_4 \cos\phi_4 + \tan(\Delta\alpha_{eq})_{v_4} \end{aligned} \quad (C-6)$$

Note that the sideslip and vortex terms in equation (C-6) cannot increase $\hat{\alpha}_{eq_4}$ beyond ninety degrees.

To account for the change in equivalent angle of attack due to fin deflection, we define a new quantity, Λ_{ji} , such that the

effect on fin i of the deflection of fin j is given by

$$(\Delta\alpha_{eq})_{ji} = \Lambda_{ji}\delta_j \quad (C-7)$$

where Λ_{ji} is to be obtained experimentally and will be a function of δ_j . Then the final expression for the equivalent angle of attack of fin 4 which includes fin deflection is

$$\alpha_{eq_4} = \hat{\alpha}_{eq_4} + \sum_{j=1}^4 \Lambda_{j4}\delta_j \quad (C-8)$$

By using an angle addition theorem rather than a tangent addition theorem we allow for the possibility of α_{eq_4} exceeding ninety degrees due to large fin deflection. In the definition of Λ_{ji} as incorporated in equations (C-7) and (C-8), we have assumed implicitly that any vortex effects on fin i are not changed by deflecting the fins.

We can generalize equations (C-6) and (C-8) by defining ϕ_i to be the bank angle of fin i measured positive to windward from the horizontal plane. The horizontal plane is defined as that plane which is perpendicular to the wind plane and contains the body axis. The generalized equations are

$$\begin{aligned} \tan\hat{\alpha}_{eq_i} = & K_W \tan\alpha_c \cos\phi_i + \frac{4}{AR} K_\phi \tan\alpha_c \sin\alpha_c \sin\phi_i \cos\phi_i \\ & + \tan(\Delta\alpha_{eq}) v_i \end{aligned} \quad (C-9)$$

and

$$\alpha_{eq_i} = \hat{\alpha}_{eq_i} + \sum_{j=1}^4 \Lambda_{ji}\delta_j \quad (C-10)$$

Equations (C-9) and (C-10) represent the mathematical formulation of the equivalent angle of attack.

LIST OF SYMBOLS

a	body radius at cylindrical section
A_1, A_2, A_3	empirical coefficients in curve fit to normal-force curve; see Table 3
R	aspect ratio
b	total wing span
BM	bending moment of fin about root chord, positive tip upward
c	local wing chord
c_ℓ	local wing section lift coefficient
c_r	wing or fin root chord
c_t	wing or fin tip chord
C_N	normal-force coefficient, $N/q_\infty S_R$
C_P	pressure coefficient, $(p - p_\infty)/q_\infty$
C_{BM}	root bending-moment coefficient, $BM/q_\infty S_R \ell_r$
C_{HM}	hinge-moment coefficient, $HM/q_\infty S_R \ell_r$
C_{NF}	fin normal-force coefficient, $N/q_\infty S_R$
$C_{NW(B)}$	fin normal-force coefficient, $N/q_\infty S_R$
$CNC1, CNC2$	values of C_{NF} for canard fins F_1, F_2, \dots
$CHMC1, CHMC2, \dots$	values of C_{HM} for canard fins F_1, F_2, \dots
$CNT1, CNT2, \dots$	values of C_{NF} for tail fins F_1, F_2, \dots
$CHMT1, CHMT2, \dots$	values of C_{HM} for tail fins F_1, F_2, \dots
d	diameter of missile body on cylindrical section; $2a$
F_1, F_2, F_3, F_4	fins in a cruciform arrangement with F_1 at top; numbering is clockwise for tail fins and counterclockwise for canard fins

HM	hinge moment
K_W	ratio of twice fin-on-body normal force at $\delta = 0$ to that for wing alone for same angle of attack
l_r	reference length
M_c	crossflow Mach number, $M_\infty \sin \alpha$
M_∞	free-stream Mach number
n	number of equally spaced fins in an empennage; also number of panels on chordwise row on wing or fin
N	normal force
p	local static pressure
p_∞	free-stream static pressure
q_∞	free-stream dynamic pressure
s	semispan of wing; exposed semispan of fin on body
s_m	semispan from body axis to fin tip of wing-body combination
S_R	reference area
S_W	wing-alone planform area
t_{\max}	maximum thickness of a wing
$(t/c)_{\max}$	thickness ratio of airfoil section
x, y	coordinate system with origin at leading edge of fin root chord with x positive rearward and y positive laterally towards tip looking forward (see Fig. 5)
\bar{x}, \bar{y}	x, y coordinates of fin or wing center of pressure
\bar{x}_v, \bar{y}_v	x, y coordinates of fin or wing center of pressure
x_{le}	x coordinate of wing or fin leading edge

x_{HL}	x coordinate of fin hinge line
x'	axial distance of orifice in front of fin trailing edge
\bar{x}/c_r	axial position of center of pressure as a fraction of fin or wing root chord
$\bar{x}_{W(B)}$	value of \bar{x} for fin mounted on body with $\delta = 0$
$(\bar{x}/c_r)_{W(B) \delta}$	value of \bar{x}/c_r for loading on fin in presence of body due to fin deflection δ
$(\Delta \bar{x})_t$	change in value of \bar{x} due to adding thickness to an airfoil or wing
$(\bar{x}/c_r)_{LT}$	value of \bar{x}/c_r from linear theory for wing with no thickness
$(\bar{x}/c_r)_{45^\circ}$	value of \bar{x}/c_r for wing at $\alpha = 45^\circ$ determined experimentally
y_v	lateral distance of body vortex from body longitudinal axis
z_v	vertical distance of body vortex above x-y plane
α	angle of attack
α_c	angle of attack of missile between body longitudinal axis and free-stream velocity; different from α if $\phi \neq 0$
α_{eq_i}	equivalent angle of attack of fin F_i with no fin deflections
$\hat{\alpha}_{eq_i}$	equivalent angle of attack of fin F_i with any or all fins deflected
α_{det}	angle for shock detachment
α_ℓ	local angle of attack of flow approaching fin leading edge in plane parallel to body axis and normal to fin planform

β	$\sqrt{M_\infty^2 - 1}$
βAR	effective aspect ratio
Γ	strength of body vortex
δ	fin deflection; positive trailing edge down for horizontal fins and trailing edge to the right for vertical fins
$\delta_1, \delta_2, \delta_3, \delta_4$	fin deflections for F_1, F_2, F_3 , and F_4 , respectively
δ_c	fin deflection for canard fin
δ_j	fin deflection of j^{th} fin
δ_t	fin deflection for tail fin
θ_n	nose semiapex angle of wing section in plane normal to wing or fin planform and parallel to root chord
θ_{det}	value of θ_n for shock detachment in two-dimensional wedge flow at $\alpha = 0^\circ$
λ	wing or fin taper ratio, c_t/c_r
Λ_{ij}	average angle of attack induced on fin F_i due to unit deflection of fin F_j
τ	fraction of the local chord of the fin center-of-pressure position with no vortex effects
ϕ	roll angle of missile, positive clockwise viewed from rear
ϕ_f	roll angle of fin, measured positive clockwise from positive z axis
ϕ_c	roll angle of canard fin measured positive clockwise from positive y axis
ϕ_t	roll angle of tail fin measured positive clockwise from positive y axis

DISTRIBUTION LIST

All addresses receive one copy unless otherwise specified.

Building 313
Ballistic Research Laboratories
Aberdeen Proving Ground, MD 21005

Mr. Aviars Celmins
Ballistic Research Laboratory
Ballistic Modelling Division
Aberdeen Proving Ground, MD 21005

Dr. P. J. Roache
Ecodynamics Research Associates, Inc.
P. O. Box 8172
Albuquerque, NM 87108

Defense Technical Information Center
Cameron Station, Building 5
Alexandria, VA 22314

12 copies

Library
Naval Academy
Annapolis, MD 21402

Director, Tactical Technology Office
Defense Advanced Research Projects
Agency
1400 Wilson Boulevard
Arlington, VA 22209

Code 200B
Office of Naval Research
800 N. Quincy Street
Arlington, VA 22217

Code 438
Office of Naval Research
800 N. Quincy Street
Arlington, VA 22217

2 copies

Dr. J. L. Potter
Deputy Director, Technology
von Karman Gas Dynamics Facility
Arnold Air Force Station, TN 37389

Professor J. C. Wu
School of Aerospace Engineering
Georgia Institute of Technology
Atlanta, GA 30332

Aerojet-General Corporation
6352 North Irwindale Avenue
Azusa, CA 91702

NASA Scientific and Technical
Information Facility
P. O. Box 8757
Baltimore/Washington International
Airport, MD 21240

Dr. K. C. Wang
College of Engineering
San Diego State University
San Diego, CA 92182

Professor A. J. Chorin
Department Mathematics
University of California
Berkeley, CA 94720

Professor M. Holt
Department of Mechanical Engineering
University of California
Berkeley, CA 94720

Dr. H. R. Chaplin
Code 1600
David W. Taylor Naval Ship Research
and Development Center
Bethesda, MD 20084

Dr. Hans Lugt
Code 1802
David W. Taylor Naval Ship Research
and Development Center
Bethesda, MD 20084

Dr. Francois Frenkiel
Code 1802
David W. Taylor Naval Ship Research
and Development Center
Bethesda, MD 20084

Dr. T. C. Tai
Code 1606
David W. Taylor Naval Ship
Research and Development Center
Bethesda, MD 20084

Page 2

Dr. G. R. Inger
Department of Aerospace Engineering
Virginia Polytechnic Institute and
State University
Blacksburg, VA 24061

Professor C. H. Lewis
Department of Aerospace and Ocean
Engineering
Virginia Polytechnic Institute and
State University
Blacksburg, VA 24061

Professor A. H. Mayfeh
Department of Engineering Science
Virginia Polytechnic Institute and
State University
Blacksburg, VA 24061

Dr. A. Rubel
Research Department
Grumman Aerospace Corporation
Bethpage, NY 11714

Commanding Officer
Office of Naval Research Eastern/Central
Regional Office
666 Summer Street, Bldg. 114, Section D
Boston, MA 02210

Dr. J. C. Erickson, Jr.
CALSPAN Corporation
Advanced Technology Center
P. O. Box 400
Buffalo, NY 14225

Dr. T. J. Falk
CALSPAN Corporation
Advanced Technology Center
P. O. Box 400
Buffalo, NY 14225

Dr. C. Witliff
CALSPAN Corporation
Advanced Technology Center
P. O. Box 400
Buffalo, NY 14225

Professor R. F. Probst
Department of Mechanical Engineering
Massachusetts Institute of Technology
Cambridge, MA 02139

Commanding Officer
Office of Naval Research Branch Office
536 South Clark Street
Chicago, IL 60605

Code 753
Naval Weapons Center
China Lake, CA 93555

Mr. J. Marshall
Code 4063
Naval Weapons Center
China Lake, CA 93555

Professor R. T. Davis
Department of Aerospace Engineering
University of Cincinnati
Cincinnati, OH 45221

Professor S. G. Rubin
Department of Aerospace Engineering
and Applied Mechanics
University of Cincinnati
Cincinnati, OH 45221

Library MS 60-3
NASA Lewis Research Center
21000 Brookpark Road
Cleveland, OH 44135

Dr. J. D. Anderson, Jr.
Chairman, Department of Aerospace
Engineering
College of Engineering
University of Maryland
College Park MD 20742

Professor O. Burggraf
Department of Aeronautical and
Astronautical Engineering
Ohio State University
1314 Kinnear Road
Columbus, OH 43212

Technical Library
Naval Surface Weapons Center
Dahlgren Laboratory
Dahlgren, VA 22448

Dr. F. Moore
Naval Surface Weapons Center
Dahlgren Laboratory
Dahlgren, VA 22448

Technical Library 2-51131
LTV Aerospace Corporation
P. O. Box 5907
Dallas, TX 75222

Library, United Aircraft Corporation
Research Laboratories
Silver Lane
East Hartford, CT 06108

Professor G. Moretti
Polytechnic Institute of New York Long
Island Center
Department of Aerospace Engineering and
Applied Mechanics
Route 110
Framingdale, NY 11735

Dr. W. R. Briley
Scientific Research Associates, Inc.
P. O. Box 498
Glastonbury, CT 06033

Professor P. Gordon
Calumet Campus
Department of Mathematics
Purdue University
Hammond, IN 46323

Library (MS 185)
NASA Langley Research Center
Langley Station
Hampton, VA 23665

Professor A. Chapmann
Chairman, Mechanical Engineering
Department
William M. Rice Institute
Box 1892
Houston, TX 77001

Technical Library
Naval Ordnance Station
Indian Head, MD 20640

Professor D. A. Caughey
Sibley School of Mechanical and
Aerospace Engineering
Cornell University
Ithaca, NY 14850

Professor E. L. Resler
Sibley School of Mechanical and
Aerospace Engineering
Cornell University
Ithaca, NY 14850

Professor S. F. Shen
Sibley School of Mechanical and
Aerospace Engineering
Cornell University
Ithaca, NY 14850

Library
Midwest Research Institute
425 Volker Boulevard
Kansas City, MO 64110

Dr. M. M. Hafez
Flow Research, Inc.
P. O. Box 5040
Kent, WA 98031

Dr. E. M. Murman
Flow Research, Inc.
P. O. Box 5040
Kent, WA 98031

Dr. J. J. Riley
Flow Research, Inc.
P. O. Box 5040
Kent, WA 98031

Dr. S. A. Orszag
Cambridge Hydrodynamics, Inc.
54 Baskin Road
Lexington, MA 02173

Dr. P. Bradshaw
Imperial College of Science and
Technology
Department of Aeronautics
Prince Consort Road
London SW7 2BY, England

Professor T. Cebeci
Mechanical Engineering Department
California State University, Long
Beach
Long Beach, CA 90840

Dr. H. K. Cheng
University of Southern California,
Department of Aerospace Engineering
University Park
Los Angeles, CA 90007

Professor J. D. Cole
Mechanics and Structures Department
School of Engineering and Applied
Science

University of California
Los Angeles, CA 90024

Engineering Library
University of Southern California
Box 77929
Los Angeles, CA 90007

Dr. C. -M. Ho
Department of Aerospace Engineering
University of Southern California
University Park
Los Angeles, CA 90007

Dr. T. D. Taylor
The Aerospace Corporation
P. O. Box 92957
Los Angeles, CA 90009

Commanding Officer
Naval Ordnance Station
Louisville, KY 40214

Mr. B. H. Little, Jr.
Lockheed-Georgia Company
Department 72-74, Zone 369
Marietta, GA 30061

Professor E. R. G. Eckert
University of Minnesota
241 Mechanical Engineering Building
Minneapolis, MN 55455

Dr. Gary Chapman
Mail Stop 227-4
Ames Research Center
Moffett Field, CA 94035

Library
Naval Postgraduate School
Monterey, CA 93940

Dr. J. L. Steger
Flow Simulations, Inc.
735 Alice Avenue
Mountain View, CA 94041

Dr. S. S. Stahara
Nielsen Engineering and Research
Inc.
510 Clyde Avenue
Mountain View, CA 94043

Engineering Societies Library
345 East 47th Street
New York, NY 10017

Professor A. Jameson
Courant Institute of Mathematical
Sciences
New York University
251 Mercer Street
New York, NY 10012

Professor G. Miller
Department of Applied Science
New York University
26-36 Stuyvesant Street
New York, NY 10003

Office of Naval Research
New York Area Office
715 Broadway - 5th Floor
New York, NY 10003

Dr. A. Vaglio-Laurin
Department of Applied Science
New York University
26-36 Stuyvesant Street
New York, NY 10003

Mr. D. Farmer
Naval Ocean Research and Development
Activity
Code 332
NSTL Station, MS 39522

Librarian, Aeronautical Library
National Research Council
Montreal Road
Ottawa 7, Canada

Lockheed Missiles and Space Company
Technical Information Center
3251 Hanover Street
Palo Alto, CA 94304

Commanding Officer
Office of Naval Research Western Regional
1030 East Green Street Office
Pasadena, CA 91106

Engineering Division
California Institute of Technology
Pasadena, CA 91109

Library

Jet Propulsion Laboratory
4800 Oak Grove Drive
Pasadena, CA 91103

Professor H. Liepmann
Department of Aeronautics
California Institute of Technology
Pasadena, CA 91109

Mr. L. I. Chasen, MGR-MSD Lib.
General Electric Company
Missile and Space Division
P. O. Box 8555
Philadelphia, PA 19101

Technical Library
Naval Missile Center
Point Mugu, CA 93042

Professor S. Bogdonoff
Gas Dynamics Laboratory
Department of Aerospace and
Mechanical Sciences
Princeton University
Princeton, NJ 08540

Professor S. I. Cheng
Department of Aerospace and
Mechanical Sciences
Princeton University
Princeton, NJ 08540

Dr. J. E. Yates
Aeronautical Research Associates
of Princeton, Inc.
50 Washington Road
Princeton, NJ 08540

Professor L. Sirovich
Division of Applied Mathematics
Brown University
Providence, RI 02912

Redstone Scientific Information Center
Chief, Document Section
Army Missile Command
Redstone Arsenal, AL 35809

U.S. Army Research Office
P. O. Box 12211
Research Triangle, NC 27709

Editor, Applied Mechanics Review
Southwest Research Institute
8500 Culebra Road
San Antonio, TX 78228

Library and Information Services
General Dynamics-CONVAIR
P. O. Box 1128
San Diego, CA 92112

Dr. R. Magnus
General Dynamics-CONVAIR
Kearny Mesa Plant
P. O. Box 80847
San Diego, CA 92138

Office of Naval Research
San Francisco Area Office
One Hallidie Plaza, Suite 601
San Francisco, CA 94102

Library
The RAND Corporation
1700 Main Street
Santa Monica, CA 90401

Dr. P. E. Rubbert
Boeing Aerospace Company
Boeing Military Airplane Development
Organization
P. O. Box 3707
Seattle, WA 98124

Dr. H. Yoshihara
Boeing Aerospace Company
P. O. Box 3999
Mail Stop 41-18
Seattle, WA 98124

Librarian
Naval Surface Weapons Center
White Oak Laboratory
Silver Spring, MD 20910

Dr. J. M. Solomon
Naval Surface Weapons Center
White Oak Laboratory
Silver Spring, MD 20910

Professor J. H. Ferziger
Department of Mechanical Engineering
Stanford University
Stanford, CA 94305

Page 6

Professor K. Karamcheti
Department of Aeronautics and
Astronautics
Stanford University
Stanford, CA 94305

Professor O. Bunemann
Institute for Plasma Research
Stanford University
Stanford, CA 94305

Engineering Library
McDonnell Douglas Corporation
Department 218, Building 101
P. O. Box 516
St. Louis, MO 63166

Dr. R. J. Hakkinen
McDonnell Douglas Corporation
Department 222
P. O. Box 516
St. Louis, MO 63166

Dr. N. Malmuth
Rockwell International Science Center
1049 Camino Dos Rios
P. O. Box 1085
Thousand Oaks, CA 91360

Library
Institute of Aerospace Studies
University of Toronto
Toronto 5, Canada

Professor W. R. Sears
Aerospace and Mechanical Engineering
University of Arizona
Tucson, AZ 85721

Professor A. R. Seebass
Department of Aerospace and
Mechanical Engineering
University of Arizona
Tucson, AZ 85721

Dr. K. T. Yen
Code 3015
Naval Air Development Center
Warminster, PA 18974

Air Force Office of Scientific
Research (SPRM)
Building 1410, Bolling AFB
Washington, DC 20332

Chief of Research and Development
Office of Chief of Staff
Department of the Army
Washington, DC 20310

Library of Congress
Science and Technology Division
Washington, DC 20540

Director of Research (Code RR)
National Aeronautics and Space
Administration
600 Independence Avenue, SW
Washington, DC 20546

Library
National Bureau of Standards
Washington, DC 20234

National Science Foundation
Engineering Division
1800 G Street, NW
Washington, DC 20550

AIR 320D
Naval Air Systems Command
Washington, DC 20361

AIR 950D
Naval Air Systems Command
Washington, DC 20375

Code 2627
Naval Research Laboratory
Washington, DC 20375

SEA 03512
Naval Sea Systems Command
Washington, DC 20362

SEA 09G3
Naval Sea Systems Command
Washington, DC 20362

Dr. Charles Watkins
Head, Mechanical Engineering Dept.
Howard University
Washington, DC 20059

Page 7

Dr. A. L. Slafkosky
Scientific Advisor
Commandant of the Marine Corps
(Code AX)
Washington, DC 20380

Director
Weapons Systems Evaluation Group
Washington, DC 20350

Research Library
AVCO Corporation
Missile Systems Division
201 Lowell Street
Wilmington, MA 01887

AFAPL (APRC)
AB
Wright Patterson, AFB, OH 45433

Dr. Donald J. Harney
AFFDL/FX
Wright Patterson AFB, OH 45433

Flow Research
1320 Fenwick Lane
Suite 401
Silver Spring, MD 20910